CORA Cork Open Research Archive
Cartlann Taighde Oscailte Chorcaí

Title	Metallogenesis of Cu deposits in Upper Palaeozoic sedimentary rocks, southern Ireland
Authors	Lang, Jürgen
Publication date	2022-01-26
Original Citation	Lang, J. 2022. Metallogenesis of Cu deposits in Upper Palaeozoic sedimentary rocks, southern Ireland. PhD Thesis, University College Cork.
Type of publication	Doctoral thesis
Rights	© 2022, Jürgen Lang. - https://creativecommons.org/licenses/by-nc-nd/4.0/
Download date	2026-11-02 09:02:46
Item downloaded from	https://hdl.handle.net/10468/13191

UCC
University College Cork, Ireland
Coláiste na hOllscoile Corcaigh

Ollscoil na hÉireann, Corcaigh
National University of Ireland, Cork
And Irish Centre for Research in Applied Geosciences





Metallogenesis of Cu deposits in Upper Palaeozoic sedimentary rocks, Southern Ireland

Thesis presented by

Jürgen Lang, M.Sc. Geologist

ORCHID iD: https://orcid.org/0000-0003-0086-0193

for the degree of

Doctor of Philosophy

University College Cork

School of Biological, Earth and Environmental Sciences
Geology Department

Head of School: Prof. Andrew J. Wheeler

Supervisors: Dr. Patrick A. Meere, Dr. Richard P. Unitt, Dr. Giulio Solferino

Advisor: Dr. David E. Jarvis

January 2022

[This page intentionally left blank]

Table of Contents

	Page
Table of Contents	**III**
List of Figures	**IX**
List of Tables	**XVIII**
List of Abbreviations	**XIX**
Declaration	**XXI**
Acknowledgement of Funding	**XXII**
Acknowledgements	**XXII**
Abstract	**XXVI**
Chapter 1: Introduction	**1**
1.1 Historical Background	**1**
1.2 Scope of Study	**7**
1.3 Chapter References	**9**
Chapter 2: Geological Setting	**11**
2.1 Sediment-Hosted Stratiform Copper Deposits	**11**
2.2 Upper Palaeozoic Basin Development in Southern Ireland	**13**
2.3 Variscan Orogeny	**17**
2.4 Magmatism in Southern Ireland	**18**
2.5 Copper Mineralization in Southern Ireland	**18**
2.5.1 Sediment hosted deposits	**18**
2.5.2 Vein hosted deposits	**19**
2.5.3 Mineralization and Microthermometry	**21**
2.5.4 Geochemistry	**22**

2.6 Fluid mobility and structural models **23**
2.7 Chapter References **24**

Chapter 3: The Vein Hosted Copper Deposits of the Allihies Mining Area, Southwest Ireland – A New Structural and Chronological Evaluation **31**

3.1 Abstract **32**
3.2 Introduction **32**
3.3 Geological Setting **35**
3.4 Methodology **39**
3.5 Results **42**
3.5.1 Field Observations **42**
3.5.2 Vein petrography and microstructures **52**
3.5.3 Fluid inclusion microthermometry **56**
3.5.4 Re-Os molybdenite geochronology **66**
3.6 Discussion **68**
3.6.1 Timing of the copper mineralization **76**
3.7 Conclusions **77**
3.8 Acknowledgements **78**
3.9 Chapter References **80**

Chapter 4: The Copper Mineralization of West Cork **89**

4.1 Abstract **90**
4.2 Introduction **90**
4.3 Geological Setting **91**
4.3.1 Sediment hosted mineralization **96**
4.3.2 Vein hosted mineralization **96**
4.4 Methodology **98**
4.5 Results **101**
4.5.1 Baurearagh **104**
4.5.2 Caha Pass **108**
4.5.3 Gortavallig **111**

4.5.4 Dhurode **117**
4.5.5 Crookhaven **122**
4.5.6 Ballycummisk **128**
4.5.7 Fluid inclusion microthermometry **135**
4.6 Discussion **145**
4.6.1 Basinal kinematics and fluid flow – A basinal crustal N-S extension provides E-W to ENE-WSW fluid pathways **145**
4.6.2 Regional and microscopic evidence for a pre- and syn-Variscan mineralization **150**
4.6.3 Fluid inclusions microthermometry of the pre-Variscan and syn-Variscan quartz veins **152**
4.6.4 Magmatism and mineralization **154**
4.6.5 Timing of the copper emplacement and previous mineralization models **155**
4.6.6 Sediment-hosted stratiform copper (SSC) deposits and exploration potential **158**
4.6.7 Comparison with Zn-Pb Deposits of the Irish Midlands **159**
4.7 Conclusions **160**
4.8 Acknowledgements **161**
4.9 Chapter References **163**

Chapter 5: Synthesis **176**

5.1 Geomorphology, Supergene Leaching and Historical Exploration – An important key for the new model **179**
5.2 Structural Evolution and Re-Os Geochronology **181**
5.3 Intrusion related Mineralization? **182**
5.4 The Copper Mineralization in SW Ireland – A Sediment-Hosted Stratiform Copper Ore System? **183**
5.4.1 Metal Sources and Fluid Flow **187**
5.4.2 Exploration Guidelines **189**

5.5 Copper Mineralization in SW Ireland and their Relation to the Irish Orefield (Irish Midlands Zn-Pb Deposits) **190**
5.6 Possibly linked Fluid Systems **196**
5.7 Chapter References **198**

Chapter 6: Summary of Conclusions **210**

Appendix **213**

Appendix A: Field Data (Chapter 1) **213**
Excel Spreadsheet:
Appendix_A_Field_Data_Thesis_JLang.xlsx:
A.1 Allihies (Chapter 3)
A.2 Caherdaniel
A.3 Pass of Keimaneigh
A.4 Caha Pass (Chapter 4)
A.5 Baurearagh (Chapter 4)
A.6 Healy Pass
A.7 Gortavallig (Chapter 4)
A.8 Durrus
A.9 Mt. Corin
A.10 Dunmanus
A.11 Ballycummisk (Chapter 4)
A.12 Dhurode (Chapter 4)
A.13 Goleen
A.14 Crookhaven (Chapter 4)
A.15 Mizen Peninsula
A.16 Seven Heads

Appendix B: Fluid Inclusions Allihies (Chapter 3) **215**
B.1 Fluid inclusions measurements of the Allihies Copper Mining District **216**
B.2 Fluid inclusions assemblages of the Allihies Copper Mining District

238

B.3 Fluid inclusions measurement plots salinity vs. homogenisation temperatures of the Allihies Copper Mining District **266**

Appendix C: Sample locations of the Allihies Copper Mining District (Chapter 3) **280**

Appendix D: Supporting petrography of the Allihies Copper Mining District (Chapter 3) **282**

Appendix E: Fluid Inclusions West Cork (Chapter 4) **288**

E.1 Fluid inclusions measurements of West Cork samples **288**

E.2 Fluid inclusions assemblages of West Cork samples **308**

E.3 Fluid inclusions measurement plots salinity vs. homogenisation temperatures of West Cork samples **328**

Appendix F: Locations of selected samples from West Cork, SW Ireland **341**

Appendix G: Additional Field Locations **343**

G.1 Research Locations **345**

G.1.1 Caherdaniel (Behaghane) **345**

G.1.2 Healy Pass **348**

G.1.3 Pass of Keimaneigh **350**

G.1.4 Goleen **352**

G.1.5 Dunmanus **354**

G.1.6 Mount Corin (Dereennalomane) **356**

G.1.7 Durrus **358**

G.1.8 Seven Heads **360**

G.2 Chapter References **363**

Appendix H: Stable Isotopes Geochemistry **365**

H.1 Methodology **365**

H.2 Sample List and Calibration Settings **367**
H.3 Results **370**
H.4 References **370**

Appendix I: Trace Element Analysis (LA-ICP-MS) **371**
I.1 Methodology **371**
I.2 Sample list + Slides images **378**
I.3 (Laser Ablation ICP-MS) Additional Quality Control:
Micro Inclusions – Element plots **398**
I.4 Results: Excel Spreadsheet: **428**
Appendix_I_4_LA-ICP-MS_West_Cork_Thesis_JLang
I.5 Chapter References **429**

Appendix J: Figures as High-Resolution PDF Files **430**
Supplementary folder:
Appendix_J_Thesis_JLang

List of Figures

*Note: Due to the format requirements some of the figures (especially Maps) appear too small on a standard A4 page. These selected figures are attached to this thesis as high-resolution PDF files in a separate folder **Appendix J**. The figures are marked with (*) in the list below.*

		Page
Figure 1.1a+b	Overview of the research areas and the examined copper mines in SW Ireland	**1-2**
Figure 1.2a	Drone image of the Dooneen cliff face at Allihies	**3**
Figure 1.2b	The historical Mountain Mine Engine House at Allihies (Beara Peninsula)	**3**
Figure 1.2c	Underground workings of Mountain Mine (Gunpowder Mine Adit)	**4**
Figure 1.2d	Historic mining kibble from the Coom Mine tailings (Allihies)	**4**
Figure 1.3a	Adit entrance at the Gortavallig cliff face (Sheep's Head Peninsula)	**6**
Figure 1.3b	Original mining share of the West Cork Mining Company (1835)	**6**
Figure 2.1	World map showing the most prominent sediment-hosted stratiform copper deposits (SSC)	**12**

Figure 2.2*	Simplified geological map of the Munster Basin and the South Munster Basin in SW Ireland	**13**
Figure 2.3a*	Geological map with research localities and major lithologies of the South Munster Basin	**15**
Figure 2.3b*	Simplified profile of the Munster Basin sedimentary formations	**15**
Figure 2.3c*	Simplified geological map with the historically mined sediment hosted copper deposits in SW Ireland	**16**
Figure 2.4*	Overview of the historical copper mines at Allihies (Beara Peninsula)	**20**
Figure 3.1*	Simplified map of the Munster Basin and the South Munster Basin in Southwest Ireland	**34**
Figure 3.2*	Overview of the historical copper mines at Allihies (Beara Peninsula, see Fig. 2.4*)	**37**
Figure 3.3a*	The major lodes and mineralized veins of the Mountain Mine Area with pre-deformation structures	**43**
Figure 3.3b	Outcrop of pre-Variscan, extensional faults (graben structure, Allihies)	**43**
Figure 3.4a-f	Equal angle stereoplots of structural features of the Allihies Mining District	**45**
Figure 3.5*	3D model of the major lodes and the underground workings at Mountain Mine	**46**
Figure 3.6	Outcrop at Marion Lode (Allihies) with 3 different vein generations	**47**

Figure 3.7a-c*	Map with syn-Variscan structures affecting the pre-Variscan faults and veins at Allihies	**49**
Figure 3.8a	Cleavage within the Northern Lode of Great Mountain Mine (Allihies)	**51**
Figure 3.8b	Smaller E-W vein (cleaved) north of Mountain Mine, Allihies	**51**
Figure 3.8c	Cataclastic deformation at the eastern end of Coom Lode, Allihies	**51**
Figure 3.8d	Syn-compressional saddle reef quartz veins, Great Mountain Mine, Allihies	**51**
Figure 3.9a	Microphotograph of mineralized quartz veins from Allihies Mining District	**53**
Figure 3.9b	Historic quartz vein with molybdenite from National History Museum of London (BM.1964,R231)	**53**
Figure 3.9c	Paragenetic sequence of the pre-Variscan mineralization, Allihies Mining District	**53**
Figure 3.10*	False colour microphotographs of mineralized E-W veins (north of Mountain Mine)	**55**
Figure 3.11a-l	Fluid inclusions assemblages from pre-Variscan samples of the Allihies District: salinity versus homogenisation temperatures	**59-63**
Figure 3.11m-o	Fluid inclusions assemblages from syn-Variscan samples of the Allihies District: salinity versus homogenisation temperatures	**64-65**

Figure 3.12a* Schematic model of the vein development, mineralization and structural evolution of the Munster Basin and South Munster Basin (pre-Variscan) **74**

Figure 3.12b* Schematic model of the vein development, mineralization and structural evolution of the Munster Basin and South Munster Basin (Syn-Variscan) **74**

Figure 4.1* Simplified map of the Munster Basin and the South Munster Basin in Southwest Ireland (see Fig. 3.1) **92**

Figure 4.2a* Geological map with research localities and major lithologies of the South Munster Basin (see Fig. 2.3a) **94**

Figure 4.2b* Simplified profile of the Munster Basin sedimentary formations (see Fig. 2.3b) **94**

Figure 4.3* Geological map of West Cork with E-W faults and their relation to historic copper lodes and mineralized sediments **103**

Figure 4.4a* Structural drone map of Bauregragh **106**

Figure 4.4b* 3D photogrammetry model of Bauregragh **106**

Figure 4.4c Stockwork quartz veining and hydraulic vein breccia (Bauregragh) **107**

Figure 4.4d Syn-compressional en echelon quartz veins (Bauregragh) **107**

Figure 4.4e* E-W striking quartz veins with reverse syn-compressional movement (Bauregragh) **107**

Figure 4.4f	Microphotograph of deformed specular hematite within quartz vein (Baurearagh)	**108**
Figure 4.4g	Quartz vein with stylolites (Baurearagh)	**108**
Figure 4.5a*	Structural drone map of Caha Pass	**110**
Figure 4.5b*	E-W striking quartz veins with syn-compressional stylolites (Caha Pass)	**110**
Figure 4.5c	Polished slide of quartz veins with two generations (Caha Pass)	**111**
Figure 4.6a*	Structural drone map of Gortavallig	**114**
Figure 4.6b	Syncline with reverse fault and en echelon veins (Gortavallig)	**114**
Figure 4.6c	Iron-stained quartz vein cut off by bedding parallel thrust (Gortavallig)	**115**
Figure 4.6d-g	Microphotographs of mineralized quartz veins and mineralized slate (Gortavallig)	**115**
Figure 4.6h-k*	Microphotographs of conglomerate clasts with elongated fossilised (chalcopyrite) plant cells (Killeen North)	**116-117**
Figure 4.7a*	Structural drone map of Dhurode	**120**
Figure 4.7b*	Aerial drone image with structures of Dhurode	**120**
Figure 4.7c*	Microstructures within mineralized quartz vein from Dhurode	**121**
Figure 4.7d	Microphotograph of mineralized quartz vein (Dhurode tailings)	**121**

Figure 4.8a*	Structural drone map of Crookhaven	**124**
Figure 4.8b	Splaying horsetail quartz veinlets with vein cleavage (Crookhaven)	**124**
Figure 4.8c	Folded, mineralized quartz veins with chalcopyrite (Crookhaven)	**125**
Figure 4.8d	Mineralized quartz vein within malachite-stained siltstone: vein hosted + sediment hosted mineralization (Crookhaven)	**125**
Figure 4.8e*	Microphotograph of a quartz vein with bornite showing a microfracture (Crookhaven)	**126**
Figure 4.8f	Quartz vein with chalcopyrite, chlorite, goethite and stylolites (Crookhaven)	**126**
Figure 4.8g	Fibrous quartz vein with parallel siderite and minor chalcopyrite (Crookhaven)	**127**
Figure 4.9a*	Structural map of Ballycummisk	**129**
Figure 4.9b+c	Microphotographs of mineralized quartz veins from Ballycummisk with chalcopyrite, hematite, barite, molybdenite and goethite (Ballycummisk)	**130**
Figure 4.9d*+e*	Mineralized quartz vein with molybdenite and stylolites (Ballycummisk)	**131**
Figure 4.9f*	Folded quartz vein within slate with cleavage-parallel quartz-barite-hematite-chalcopyrite mineralization (Ballycummisk)	**132**
Figure 4.10a-d	Microphotographs of fluid inclusions within quartz veins from West Cork	**137**

Figure 4.11a-h Fluid inclusions assemblages measurements from selected research areas in West Cork – Pre-Variscan: Salinity versus homogenisation temperatures **138-141**

Figure 4.11i-n Fluid inclusions assemblages measurements from selected research areas in West Cork – Syn-Variscan: Salinity versus homogenisation temperatures **142-144**

Figure 4.12a* Block model of the South Munster Basin in West Cork: Pre-Variscan **148**

Figure 4.12b* Block model of the South Munster Basin in West Cork: Syn-Variscan **149**

Figure 4.13 Solubility of metals in hydrothermal fluids – Temperature versus metal in fluid **157**

Figure 5.1* Map of West Cork with the major research areas with the E-W extensional faults and the historically documented Cu occurrences **180**

Figure 5.2 Modification of Fig. 2.3b showing a simplified model of the Munster Basin as an SSC deposit **184**

Figure 5.3* Geological map of Ireland with a selection of the geochronological dated Zn-Pb deposits and the Re-Os dating results of this study for the Cu mineralization in SW Ireland **192**

Appendix:

Figure D.1 Sample JL_AH_60 Mountain Mine Underground **283**

Figure D.2 Sample JL_AH_220 Mountain Mine Spoil **284**

Figure D.3	Sample JL_AH_220 Mountain Mine Spoil	**285**
Figure D.4	Sample JL_AH_367 Mountain Mine - Gunpowder Mine	**286**
Figure D.5	Sample BM.1964,R231 Mountain Mine	**287**
Figure G.1*	Simplified geological map of the Munster Basin and the South Munster Basin in SW Ireland showing additional field locations	**344**
Figure G.2a*	Structural map of Behaghane (Caherdaniel, Kerry)	**346**
Figure G.2b	Hydrobreccia of veining quartz with host rock clasts and green malachite staining (Behaghane)	**346**
Figure G.2c	Folded and cleaved quartz veins with specular hematite (Behaghane)	**347**
Figure G.2d	Hand specimen of mineralized quartz vein from Behaghane	**347**
Figure G.3a*	Structural map of the location Healy Pass (Beara Peninsula)	**349**
Figure G.3b	Pre-Variscan quartz veins with cataclastic deformation, folding and cleavage (Healy Pass)	**349**
Figure G.4a*	Structural drone map of extensional fault with related quartz veining near Pass of Keimaneigh	**351**
Figure G.4b	Syn-Variscan quartz veins (near Pass of Keimaneigh)	**351**

Figure G.4c Microphotograph of folded specular hematite within Pre-Variscan quartz vein (near Pass of Keimaneigh) **352**

Figure G.5a* Structural drone map from area located west of Goleen (Mizen Peninsula) **353**

Figure G.5b Hydrobrecciated quartz vein with small amounts of specular hematite (Goleen) **353**

Figure G.5c Folded and cleaved quartz vein (Goleen) **354**

Figure G.6a* Structural map of Dunmanus (Mizen Peninsula) **355**

Figure G.6b Outcrop of large E-W striking quartz veins (Dunmanus) **355**

Figure G.7a* Structural (drone) map of Mount Corin (Dereennalomane, Mizen Peninsula) **357**

Figure G.7b Euhedral quartz twins from historically mined trenches (Mount Corin) **358**

Figure G.8a Fibrous quartz crystals with kinks growing along mudstone (Durrus, Mizen Peninsula) **359**

Figure G.8b Euhedral quartz crystals with minor chalcopyrite and radial crystallized yellow muscovite (Durrus) **359**

Figure G.9a* Structural drone map of the Seven Heads coastal outcrop (South Cork) **361**

Figure G.9b Outcrop showing coastal erosion of extensional fault with larger quartz veins (Seven Heads) **362**

Figure H.1 Map of Allihies Mining Area showing the stable isotopes sample locations **366**

Figure I.1 Sample localities for chalcopyrite LA-ICP-MS trace element measurements **374**

Figure I.2 Accuracy of the UQAC-FeS-1 quality control standard, calibrated with the MASS1 calibration standard **377**

List of Tables

Page

Table 3.1 Re-Os isotope data and model ages for the molybdenite samples from Allihies Mountain Mine (BM.1964,R231) and Caminches Mine **67**

Table 4.1 Re-Os isotope data for the molybdenite samples BM.1964,R230 and JL_BC_525 from Ballycummisk Mine **134**

Table G.1 Additional Field Locations in County Cork and County Kerry; Munster Basin, SW Ireland **343**

Table I.1 QAQC using MASS1 as calibration standard and UQAC-FeS-1 as quality control standard **375**

Additional tables with measured and standardised data can be found in the **Appendices A-I**.

List of Abbreviations

Apy	-	arsenopyrite
Bn	-	bornite
Brt	-	barite
Ccp	-	chalcopyrite
Cct	-	chalcocite
Chl	-	chlorite
CKFZ	-	Cork-Kenmare Fault Zone
CKMFZ	-	Coomnacronia-Killarney-Mallow Fault Zone
DB-GFZ	-	Dingle Bay-Galtee Fault Zone
Fm.	-	formation
Gn	-	galena
Gth	-	goethite
Hem	-	hematite (mostly specular hematite)
iCRAG	-	Irish Centre for Research in Applied Geosciences
Mlc	-	malachite
Mol	-	molybdenite
NHM	-	National History Museum London
Py	-	pyrite

Qz/Qtz	-	quartz
S_0 =	-	bedding orientation
S_1 =	-	cleavage orientation
Sd	-	siderite
Sl.	-	slate
Sltst	-	siltstone
SSC	-	sediment-hosted stratiform copper
Sst	-	sandstone
Ttr	-	tetrahedrite/tennantite
UCC	-	University College Cork
V =	-	vein orientation
V_1 =	-	veining cleavage orientation

Declaration

This is to certify that the work I am submitting is my own and has not been submitted for another degree, either at University College Cork or elsewhere. All external references and sources are clearly acknowledged and identified within the contents. I have read and understood the regulations of University College Cork concerning plagiarism.

This thesis is submitted in fulfilment of the requirement of the degree of Doctor of Philosophy at the National University of Ireland, Cork in the School of Biological, Earth and Environmental Sciences (Geology Department), College of Science, Engineering and Food Science.



Signed: ……..... Date: 26/01/2022

Jürgen Lang

Acknowledgement of Funding

This PhD Thesis has emanated from research supported in part by a research grant from Science Foundation Ireland (SFI) under Grant Number 13/RC/2092 and is co-funded under the European Regional Development Fund and by iCRAG industry partners.

Acknowledgements

Doing a Ph.D. is not only writing a thesis, crunching numbers and developing new theories – a Ph.D. is about making new friendships with people from all over the world. There is no border in science! A Ph.D. is diving into a new culture, enjoying its lifestyle and experiencing unforgettable adventures. This is the story of an amazing country called Ireland where I have spent four and a half years of my life. Hopefully there will be more!

First of all, I would like to thank my supervisors Dr. Pat Meere and Dr. Richard Unitt. From the very first warm welcome in Cork after my arrival, over inspiring enthusiastic discussions about the correct timing of copper mineralization, to the final submission of this thesis; you guided me all the way to the final goal. Thank you very much for the multiple amazing trips to Allihies, the Mountain Mine Underground visits, the great fun with the RTE “10 Things you need to know about” filming, the mineral hunting at Ardmore Mine and exploring the Copper Coast. Pat, I hereby can officially confirm that we had many sunny days in the field, so the curse must be over now (😉). Thank you also for providing me the opportunity to go to many national and international conferences, short courses and field trips. Richard, thanks for the many minerals collectors chats and the recommendations for the best mineral hunting sites. There are so many exciting stories with both of you Pat and

Richard. So, I am very grateful for not only having you as perfect supervisors, but also as very good friends! Thanks a million for that!

Thanks to Dr. Giulio Solferino for being my internal and later external supervisor. Thank you very much for your support, the interesting discussions, organizing the short course trip to Naples (Fluids in the Earth) and guiding me through the geochemical laboratories in Dublin at the very beginning. Thank you as well for the valuable input for my first publication and the excellent career tips you gave me after a great evening in the pub.

A special thanks goes to my advisor Dr. David (Ed) Jarvis. Ed, you always have (literally) an open door for everybody. You always take the time for some friendly words, a pleasant chat and caring about each individual person you know. Thanks a million for having me as demonstrator on several Antrim field trips. I really enjoyed every single trip, and I am hoping for an Antrim reunion event in near future. Thank you very much for the hilarious Wassail and BBQ parties at your house in Bandon!

Many thanks to the postdocs Dr. Pedro Cordeiro and Dr. Sean Johnson for accompanying me on my journey through the Ph.D. research. Thank you very much for your expertise, the great copper meetings and for building up new connections with other international researchers.

I greatly appreciated the public presentations, Science Weeks (Cork Science Festival) and outreach courses with Dr. Fergus McAuliffe. These events raised my interest in public engagement which was always great fun!

During the last couple of years, I got the privilege to visit several national and international laboratories and received excellent training in various geochemical techniques. Many thanks to Prof. Clemente Recio, his team and Prof. Antonio M. Álvarez-Valero for the warm welcome at the University of Salamanca in Spain and your detailed introduction into the stable isotope geochemistry. Many thanks to Prof. David Selby from Durham University for the great experience in geochronology and mineral preparation. I am very grateful to Prof. Seán McClenaghan from Trinity College Dublin for his

expertise and support in LA-ICP-MS trace elements geochemistry. Thank you very much to Maurice Brodbeck from Trinity College Dublin for the LA-ICP-MS data reduction and to Dr. Lingli Zhou (Trinity College Dublin) for the precise SEM-EDS classification of the tennantite/tetrahedrite mineralization.

I would like to acknowledge the great support from Tadhg O'Sullivan, Tara O'Sullivan and the entire team from the Allihies Copper Mine Museum. Thank you very much for the many exciting stories about the Puxley Family, the mining history at Allihies and for granting us the privileged access to the beautiful Mountain Mine underground workings.

A special thanks goes to Dr. Simon Kocher from National History Museum in London (NHM) and Dr. David van Acken from University College Dublin. They both initiated the idea and the processes for the successful Re-Os geochronology. Thanks to Simon for hosting me in London and guiding me through the sample probing applications at the NHM. Thanks as well to Ms Robin Hansen from NHM for granting me access to the famous historical Sir Arthur Russell collection. Many thanks to Dr. Kate Kiseeva for donating her recent finding of a molybdenite sample from Allihies for my research purposes.

I would like to thank our industrial partners from Adventus Mining Mr Wilson Robb and Mr Vaughan Williams, as well as Mr Tom Wesby from First Quantum for the fieldtrips to West Cork and the open-minded brainstorming about the formation of the copper deposits.

Research life is so much easier and more pleasant if you have amazing colleagues and friends. Therefore, a big thank you goes to: Josh, Austin, Zaheeda, Dan, Nidia, Luke, Ninon, Aaron, Odhrán, Siobhán, Frank, Gerard, Daniel, John, Greg, Darren, Ruaihri, Evan, Eileen, Aude, Larissa, Tiffany, Brenton, Ben and many, many more. Thanks a million for the craic!

Dr. Mohit Tunwal, thank you for being a great colleague and guiding me through various UCC administration challenges (Agresso System); thank you as well for being the housemate No. 1 for over 4.5 years, the tasty Indian food

and the relaxing BBQ's together with Kim, Jenni and Bhuvan. We made it together through the first COVID-19 lockdown!

There is a special group in the School of BEES administrative staff, keeping the engine running, even in difficult times. I am very grateful for your endless friendly support: Ms Elaine Kelly, Ms Christine Dennehy, Ms Mary McSweeney, Ms Maggie O'Sullivan and Ms Philomena Fogarty.

Many thanks to the Head of School Prof. Andy Wheeler for your friendly, uncomplicated, and quick support in administrative tasks. Thank you very much as well for your keen interest in each student's research topic and the great discussions on several fieldtrips!

The technical staff from School of BEES made impossible things possible and always maintained a keen sense of humour: Mr Don Kelleher, Mr Luke Harman, Ms Mary Lehane and Mr Allen Whitaker. A special thanks goes to Dr. Ronan Hennessy. Thank you for your expertise in mineral preparation, your incredible knowledge in GIS, and for the help with abseiling on Sheep's Head!

I want to express my gratitude to my brother Dr. Manuel Lang and his wife Carolin for supporting my crazy ideas and field experiments (underwater mine filming and photography), as well as for solving problems back home in Germany when I was abroad.

Last, but certainly not least, the biggest thank you goes to my parents Ingrid Lang and Herbert Lang. Without your help this thesis would not exist. You guided me all the long way up to this stage. You always believed in me and supported me with my dreams and goals. I know there is always a place which I can call home!

Thanks a million!

Abstract

Copper has been exploited in SW Ireland for thousands of years. The increased demand for copper world-wide has led to renewed interest in these occurrences and their overall implication for copper metallogenesis in Ireland.

This PhD research study focuses on historically mined, mainly vein-hosted copper deposits of SW Ireland. Central to this is the identification of the dominant structural control on mineralization, which is found to be associated with the development of the Upper Palaeozoic Munster and South Munster Basins.

Detailed geological mapping, including drone mapping and 3D modelling of selected mine sites in SW Ireland have led to a new interpretation of the chronological development of quartz veins hosting copper mineralization. Macro- and microstructural investigations of the West Cork peninsulas and the mining areas reveal the development of two distinct ore forming episodes.

The first of these is related to metre- to kilometre-scale early extensional, basinal normal faults that pre-date the late Carboniferous Variscan Orogeny. The copper sulphide bearing, mainly E-W to ENE-WSW striking, quartz veins are directly associated with these extensional faults. This early vein system experienced subsequent late Carboniferous deformation during the Variscan Orogeny, including folding, cleavage development, stylolitisation, sinistral SW-NE strike-slip faulting, cataclastic fracturing and recrystallization. Smaller sediment hosted copper sulphide occurrences are also related to the early extensional fault systems.

The second mineralization phase occurred during the early stages of late Carboniferous Variscan compression during reactivation of the early extensional, basinal fault systems. This localised reactivation precipitates quartz hosted copper lodes (e.g. Ballycummisk on Mizen Peninsula). Metre-

scale syn-Variscan quartz veins in SW Ireland are predominantly formed as tension gashes (saddle reefs, en echelon veins) in semi-brittle shear zones.

The copper sulphides within the quartz veins from both episodes are mainly syn-genetic chalcopyrite, tetrahedrite/tennantite, minor bornite and chalcocite.

Re-Os geochronology measurements on molybdenite samples, associated with the vein hosted copper sulphides, reveal ages of 367.3 ± 5.5 to 366.4 ± 1.9 Ma (Upper Devonian, syn-basinal) for the Allihies deposit on Beara Peninsula, and from 315.5 ± 1.6 Ma to 311.8 ± 1.6 Ma (Pennsylvanian, late Carboniferous, syn-Variscan) for the Ballycummisk copper mines on the southern coast of Mizen Peninsula.

Fluid inclusion studies on mineralized, pre-Variscan quartz veins reveal multiple fluid pulses with homogenisation temperatures (T_h LV-L) ranging from 74 to 335 °C. Salinities vary between 3.2 and 28.5 wt% $NaCl_{equiv}$. Syn-Variscan quartz veins have a T_h range from 101 to 270 °C with salinities between 4.8 and 19.1 wt% $NaCl_{equiv}$.

The petro-stratigraphic architecture of the Munster and South Munster Basins suggests similarities to a Redbed-Type copper deposit, a sub-type of sediment-hosted stratiform copper ore systems (SSC). Predominantly vein-hosted copper emplacement is caused by an advanced diagenetic stage of the host rock sediments.

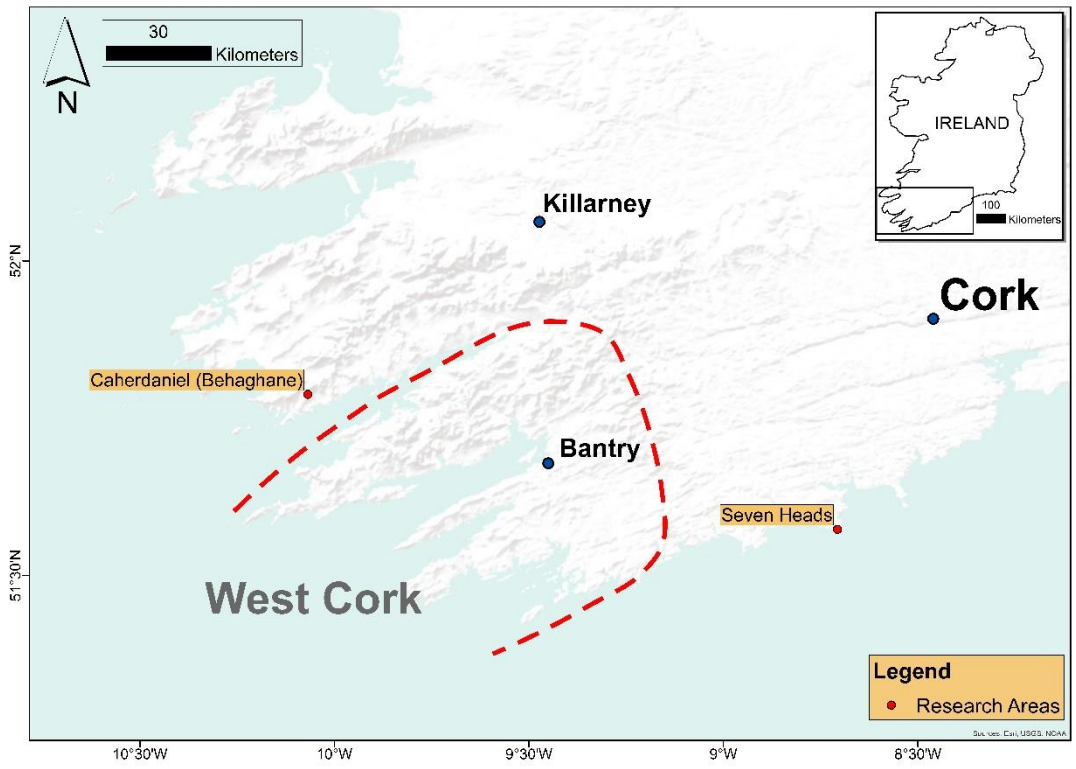
The new structural, chronological and geochemical model of copper mineralization in SW Ireland has major implications for its genetic relationship to the base metal deposits of the Irish Midlands.

Chapter 1: Introduction

1.1 Historical Background

Mineral deposits within the European Variscan fold/thrust belt have been utilised for over 3500 years (Williams 1991). Metals, especially copper, in southwest Ireland have been mined as far back as the Bronze Age (O'Brien 1987). Historic sites on the Mizen Peninsula (Fig. 1.1a+b) show that the original extraction of Cu ore targeted surficial malachite mineralization (O'Brien 1987). In 1812, malachite-stained cliff faces at Dooneen (Allihies) on the Beara Peninsula (Fig. 1.1a+b and 1.2a) led to the discovery of copper lodes (Blenkinsop 1902; Reilly 1986). These were exploited by extensive networks of numerous adits and shafts (Fig. 1.2a). As miners progressed further inland, they uncovered metal-rich, steeply dipping, E-W striking quartz veins in the vicinity of Allihies.

Fig. 1.1a)



1.1b)

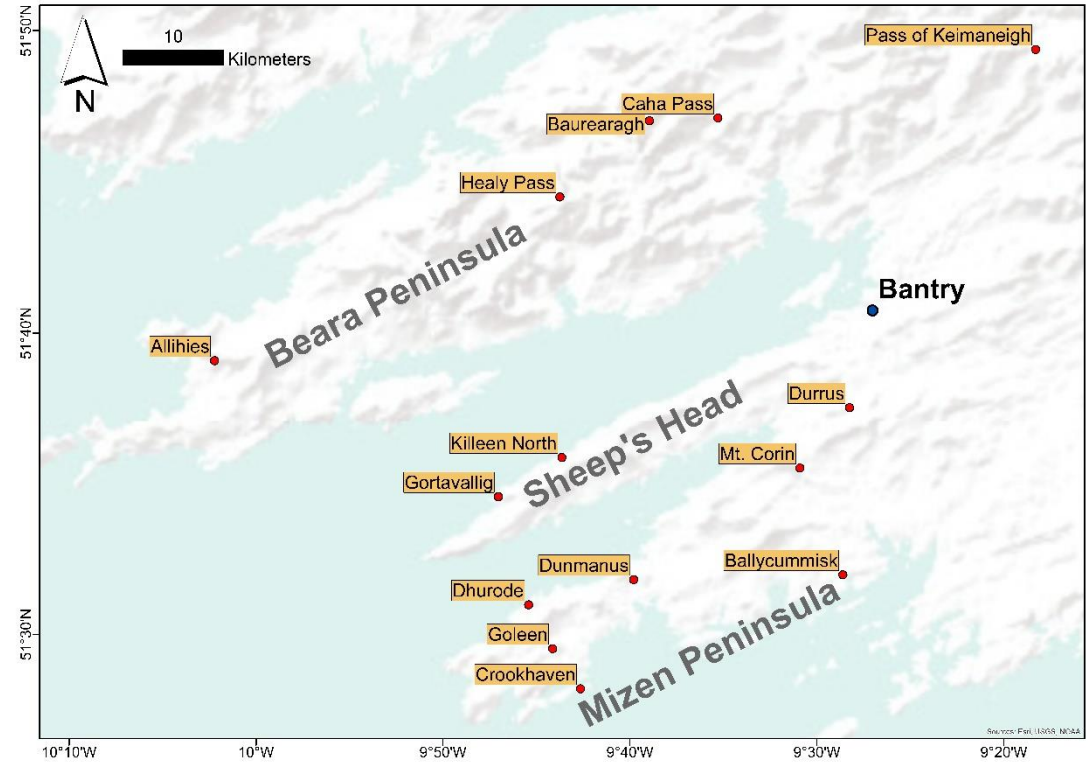
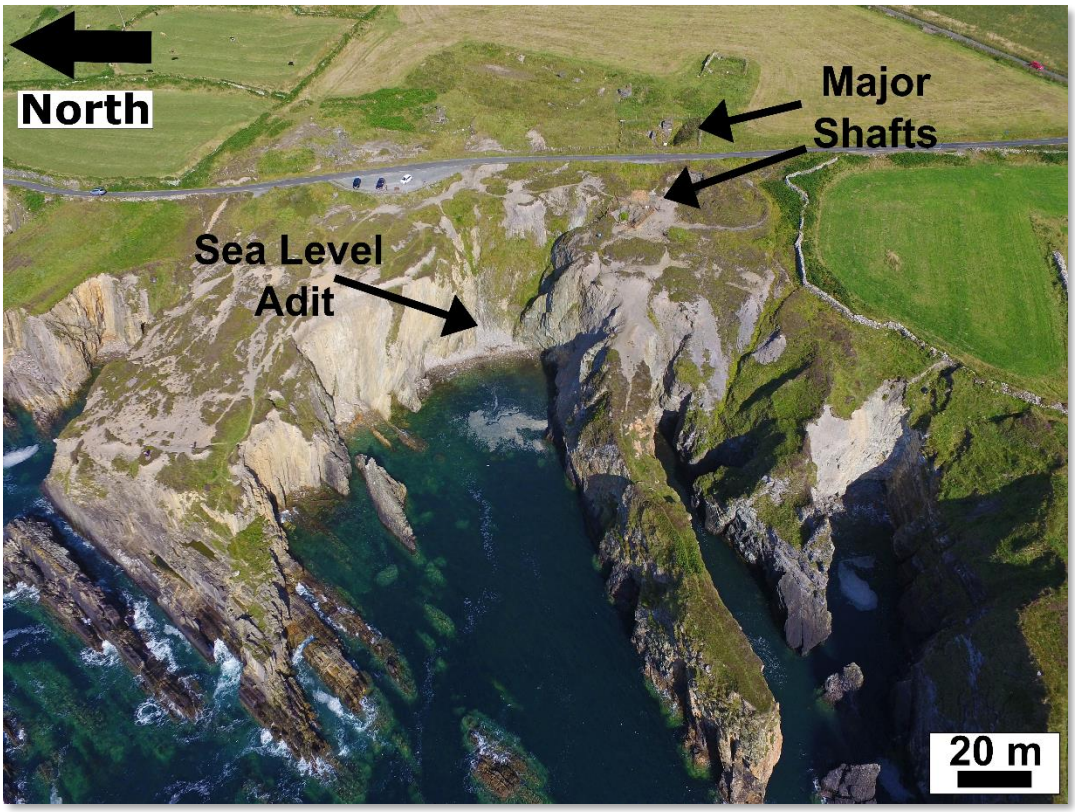


Fig. 1.1a+b) Overview of the research areas and the examined copper mines in SW Ireland.

The largest vein was worked at Mountain Mine (Fig. 1.2b) which at the time became the largest copper mine in the region with over 284,500 tonnes of ore extracted (O'Brien 1959). The main lode was mined in shafts of over 450 m depth, going well below the sea level (Reilly 1986, Fig. 1.2c). Cornish mining technology is still visible at the well-preserved Man Engine House of Mountain Mine (Fig. 1.2b), which was built in about 1862 (Williams 1991), and the recently re-discovered Cornish kibble from Coom Mine (Fig. 1.2d). Many smaller mines were also active throughout West Cork during the 19th century (Reilly 1986). The Gortavallig Mine on Sheep's Head (Fig. 1.1b), for example, only produced 88 tons of copper ore in 1848 before it was abandoned again due to economic inefficiency (Hodnett 2012). Narrow adits and small shafts can be found along the steep cliffs of Gortavallig (Fig. 1.3a).

Fig. 1.2a)



1.2b)



1.2c)



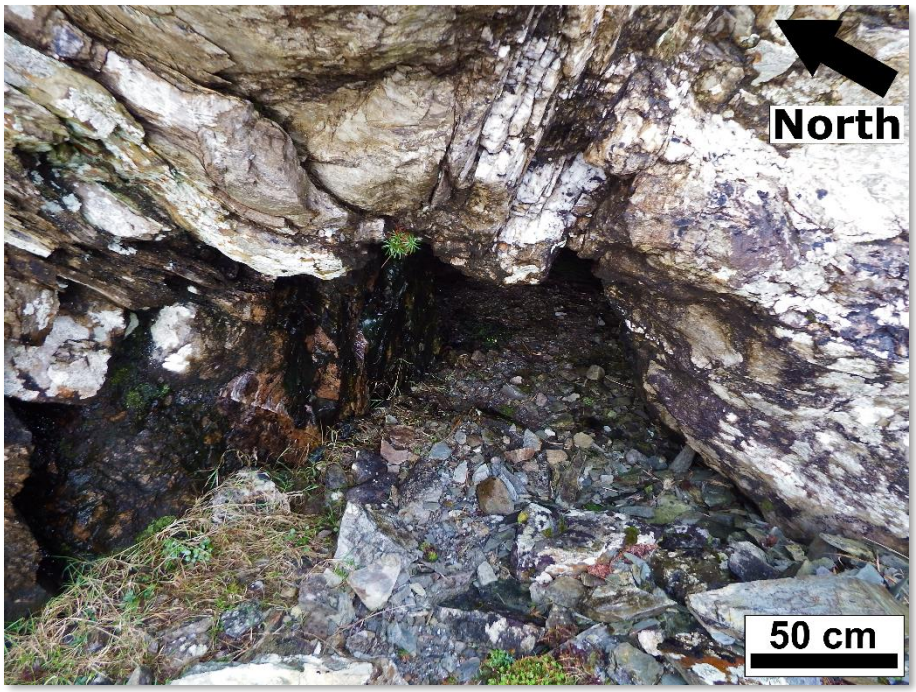
1.2d)



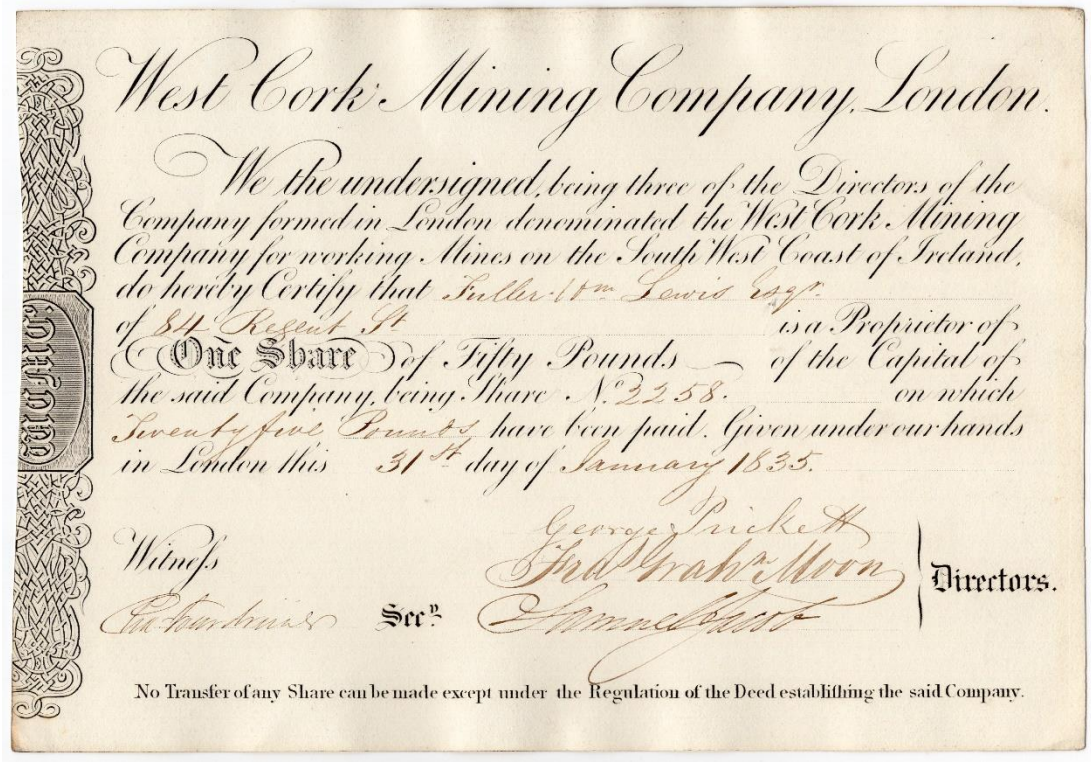
Fig. 1.2a) Aerial drone image of the Dooneen cliff face at Allihies showing the sea level adit and historical mine shafts. b) The historical Mountain Mine Engine House between the major shafts and Allihies Village in the background. c) Underground workings of Mountain Mine (Gunpowder Mine Adit) showing the extracted quartz lode and walls with secondary copper mineralization (e.g. blue langite and green malachite). d) Recent finding of a historic mining kibble from the Coom Mine tailings (Allihies).

During the zenith of mining industry in SW Ireland a number of public companies were formed (Hodnett 2012). Ballycummisk on Mizen Peninsula (Fig. 1.1b), for example, became part of the West Cork Mining Company (former Audley Mines) in 1834 (Hodnett 2012, Fig. 1.3b). Despite dubious legal activities with the share trading, Ballycummisk was one of the most productive mines on the Mizen Peninsula which sold up to 648 tons of copper ore in one year at its peak between 1872 and 1873 (Hodnett 2012). In the more recent past between 1956 and 1962 the Allihies Mines were explored by the Emerald Isle Mining Company, a subsidiary of the Canadian Can Erin company (Williams 1991). The shafts of Mountain Mine (Fig. 1.2c) were dewatered, and the copper lode was probed by diamond drilling up to 3000 feet (914 m) below the surface. Nevertheless, only 1.5 million tons of 1.9 % copper ore was proven (Williams 1991). In the late 1970's the neighbourhood of Allihies moved into focus for uranium exploration (GSI Goldmine 2020: Sullivan 1979, Williams 1991). A weak anomaly was found about 1 mile (1.6 km) north of Allihies village (Williams 1991). At the same time (late 1970's to early 1980's) Dresser Minerals focussed on exploration drillings at the historic copper mines of Mizen Peninsula (e.g. Ballycummisk, Fig. 1.1b; GSI Goldmine 2020: Dresser 1979-81, Rothery and Coates 1988). The exploration targets included not only copper, but also the baryte occurrences. Dana Exploration PLC was one of the most recent companies (1987-1988) that looked for the copper deposits of Mizen Peninsula (Rothery and Coates 1988). The exploration work included soil geochemistry and diamond drilling (including works at Dhurode Mine, Fig. 1.1b).

Fig. 1.3a)



1.3b)


West Cork Mining Company, London.

We the undersigned, being three of the Directors of the Company formed in London denominated the West Cork Mining Company for working Mines on the South West Coast of Ireland, do hereby Certify that Fuller Wm Lewis Esqr. of 84 Regent St is a Proprietor of One Share of Fifty Pounds — of the Capital of the said Company, being Share N.2258. on which Twenty five Pounds have been paid. Given under our hands in London this 31st day of January 1835.

Witness — George Pricket, Fred Grabe Moon, James Scott — Directors.

No Transfer of any Share can be made except under the Regulation of the Deed establishing the said Company.

Fig. 1.3a) Shallow adit entrance at the Gortavallig cliff face following a lode of mineralized quartz veins. b) Original mining share of the West Cork Mining Company, London over fifty pounds from 1835 (author's private collection).

1.2 Scope of Study

New technologies for environmentally friendly energy sources, e-mobility and smart communication require an enormous and increasing number of base metals, especially copper. This PhD research thesis targets the historically mined, copper deposits of SW Ireland (Fig. 1.1a+b). The aim is to understand the structural and geochemical processes which lead to the metal precipitation. The outcomes of this thesis should help to find similarities with other sediment-hosted stratiform copper (SSC) deposits, as well as detecting a possible link to the Irish Midlands Pb-Zn Deposits. This will add an important piece of puzzle to the complex Irish geological history. The new developed genetic model can be utilized for further mineral exploration in this region. To this end, a variety of methods, ranging from structural field mapping, petrography, microtextural analysis and microthermometry, to modern drone mapping techniques, 3D modelling, as well as stable isotopes and trace elements geochemistry were employed.

Structural field mapping, including sampling and drone mapping are the key procedures to provide a base construct for this thesis. Altogether 68 days were spent at various selected locations in SW Ireland (Figs. 1.1a and 1.1b) to gather a sum of 584 structural measurements (Appendix A). The workflow incorporates initial structural data acquisition and field mapping, followed by drone imaging (see Chapter 3 and 4 for further details). Structural maps (Appendix J) were created by implementing the field data into the high-resolution drone maps. Following the map drafting, a renewed field assessment including further field measurements and sampling reassured the completeness of the structural field models. As a result, 17 individual maps were created (Chapter 3, Chapter 4 and Appendix G). The maps are attached to this thesis as high-resolution PDF (Appendix J).

This thesis is based on the following major research sections:

- The vein-hosted copper deposits of the Allihies mining area in SW Ireland (Fig. 1.1b): Excellent outcrop, intensive historical mining and a

long research history (e.g. Sheridan 1964, Fletcher 1969, Reilly 1986, Meere and Banks 1997) provided an outstanding field area to develop a new genetic mineralization model. New structural and geochronological discoveries provided the critical data that allowed a significant re-interpretation of this deposit.

- The new mineralization model from Allihies was then tested by looking at additional historical Cu mines and localities in West Cork, South Kerry and South Cork (Fig. 1.1a+b).
- A comparison of the structures and geochronology from the Allihies Mines and other West Cork deposits combined with sediment-hosted stratiform copper (SSC) deposits, as well as the Irish Midlands Pb-Zn Deposits allows the development of a regional Cu mineralization model. A comprehensive interpretation of the Cu mineralization in SW Ireland is the outcome of this thesis.
- Supporting geochemical data (stable isotopes and trace elements) from selected locations in SW Ireland is provided in Appendix H and Appendix I.

1.3 Chapter References

Blenkinsop, H.G. 1902. Notes on the Berehaven copper mines. Transactions of the Institution of Mining and Metallurgy, 12, 1–7.

Fletcher, C.I. 1969. The sulphide mineralization in the Allihies region, County Cork, Eire. Ph.D. Dissertation, University of Leicester, 128–129.

GSI Goldmine (Geological Survey of Ireland) 2020. Last accessed 08/12/2020. https://secure.dccae.gov.ie/goldmine/index.html:

- Rothery, E. and Coates, D. 1988. Dana Exploration PLC. South West Cork Area Interim Report to the Geological Survey. October 1988.
- Sullivan, J.L. 1979. Uranium Survey - Allihies Project. License Areas X5, X6, County Cork, Ireland. Progress Report 2 October 1978 - 31 March 1979.
- Unknown author, Dresser 1979 – 1981. Map description: Ballycummisk (Structure).

Hodnett, D., O'Sullivan, P. 2012. The Metal Mines of West Cork. The Trevithick Society. UK.

Meere, P.A. and Banks, D.A. 1997. Upper crustal fluid migration: an example from the Variscides ofSW Ireland. Journal of the Geological Society, London, 154, 975–985, https://doi.org/10.1144/gsjgs.154.6.0975

O'Brien, M.V. 1959. The future of non-ferrous mining in Ireland. In: The Future of Non-Ferrous Mining in Great Britain and Ireland. Institution of Mining and Metallurgy Symposium, 5–26.

O'Brien, W.F. 1987. The dating of the Mt Gabriel-type copper mines of West Cork. Journal of the Cork Historical and Archaeological Society, 92, 50–70.

Reilly, T.A. 1986. A review of vein mineralization in SW County Cork, Ireland. In: Andrew, C.J., Crowe, R.W.A., Finlay, S., Pennell, W.M. and Pyne, J.F. (eds) Geology and Genesis of Mineral Deposits in Ireland. Irish Association for Economic Geology, Dublin, 513–544.

Sheridan, D.J. 1964. The structure and mineralisation of the Mountain Mine area, Allihies, west Co. Cork, Ireland. Scientific Proceedings, Royal Dublin Society, Series A, 2, 21–27.

Williams, R.A. 1991. The Berehaven copper mines. British Mining, 42. Northern Mine Research Society, Sheffield.

Chapter 2: Geological Setting

2.1 Sediment-Hosted Stratiform Copper Deposits

Sediment-hosted stratiform copper deposits (SSC) are highly important for the global distribution of economically valuable copper resources (Hayes *et al.* 2015). The Paleozoic Polish-German Kupferschiefer within the Permian Basin is the most prominent example of European SSC deposits (Fig. 2.1, Vaughan *et al.* 1989, Kucha 2003, Hitzman *et al.* 2005). The Kupferschiefer deposit shows an estimated amount of 350 million metric tons (Mt) of copper metal in Poland (Cathles *et al.* 1993, Brown 2014). The Neoproterozoic basin mineralization of the Central African Copper Belt of Zambia and the Democratic Republic of Congo hosts several giant and supergiant deposits with over 24 million metric tons of copper metal (Fig. 2.1, Singer 1995, Selley *et al.* 2005, Hitzman *et al.* 2005, Brown 2014). The Paleoproterozoic Udokan District of Siberia also contains a supergiant, but poorly documented copper deposit (Fig. 2.1, Volodin *et al.* 1994, Hitzman *et al.* 2005, Brown 2014).

SSC deposits are generally formed within rift-related extensional basins (e.g. Hitzman *et al.* 2005). The basement is unconformably filled with oxidized hematitic, continental siliciclastic red bed sedimentary rocks (e.g. Kirkam 1989, Hitzman *et al.* 2005, Brown 2014 and references herein). Nonreddish transgressive marine sandstones, siltstones, carbonates and/or carbonaceous shales overlay and seal the red bed sediments (e.g. Hitzman *et al.* 2005, Brown 2014). These nonreddish sediments are generally *sulphide*-rich reduced beds which are called graybeds (e.g. Brown 2014). Typically, the major Cu mineralization is stratiform widespread along the basal portions of the graybeds (e.g. Brown 2014). Interbedded and/or the red bed sequence overlying lacustrine to marine evaporites are seen as a major source of salinity and sulfur for the SSC mineralization (Hitzman *et al.* 2005).

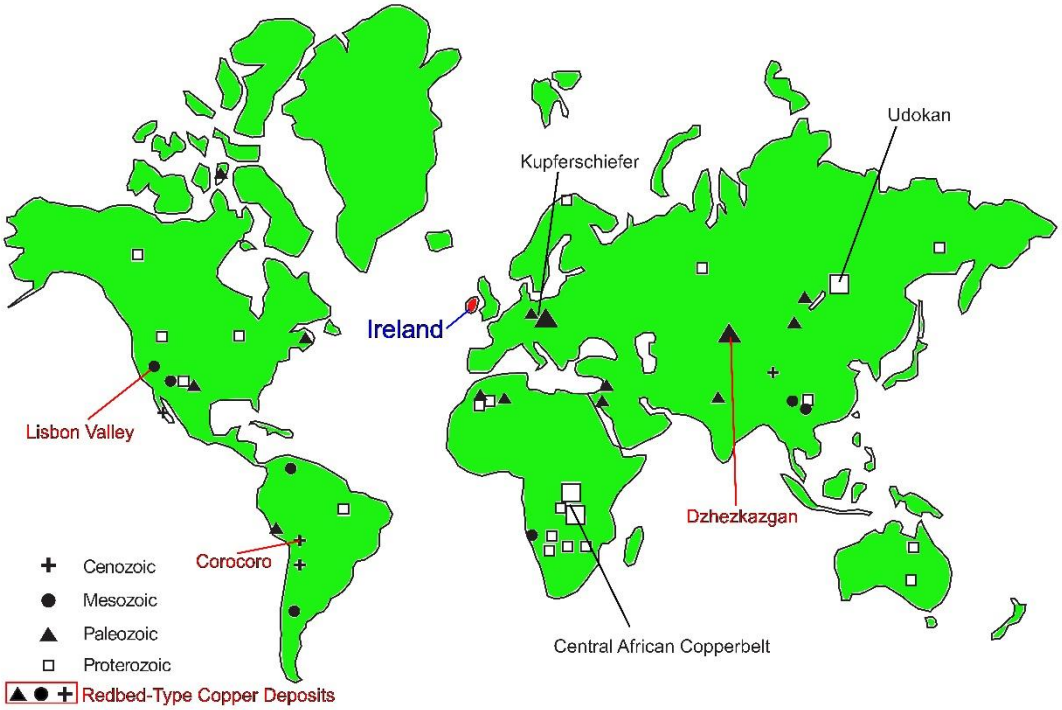


Fig. 2.1) World map showing the most prominent sediment-hosted stratiform copper deposits (SSC), as well as Redbed-Type Copper deposits (modified from Hitzman et al. 2005 and Brown 2014).

Some minor to subeconomic SSC deposits are classified as Redbed-Type Copper Deposits (Brown 2014). The copper mineralization of these deposits is directly hosted within the red bed sequence of the basin filling. Economically important examples for this sub-type of SSC deposits are Dzhezkazgan in Kazakhstan with 22 Mt metal copper, Corocoro in Boliva with 0.5 Mt metal copper and Lisbon Valley in Utah 0.6 Mt metal copper (Fig. 2.1, Brown 2014, Hitzman *et al.* 2005).

The following paragraphs provide a detailed description about the formation and mineralization of the Munster and South Munster Basins in Southern Ireland. Potential similarities to the prominent SSC deposits (Fig. 2.1) are discussed in Chapter 5.

2.2 Upper Palaeozoic Basin Development in Southern Ireland

North-south crustal extension between the Middle and Upper Devonian, led to the development of a large half-graben basin in southern Ireland, the Munster Basin (Naylor & Jones 1967). The east-west trending listric Coomnacronia-Killarney-Mallow Fault Zone marks the northern bounding structure of this intracratonic basin (Fig. 2.2; Naylor & Jones 1967; Capewell 1975; Price & Todd 1988; Meere 1995c; Vermeulen *et al.* 2000; Landes *et al.* 2003; MacCarthy 2007; Ennis *et al.* 2015). Williams (2000) alternatively described the Dingle Bay-Galtee Fault Zone as major margin to the north (Fig. 2.2).

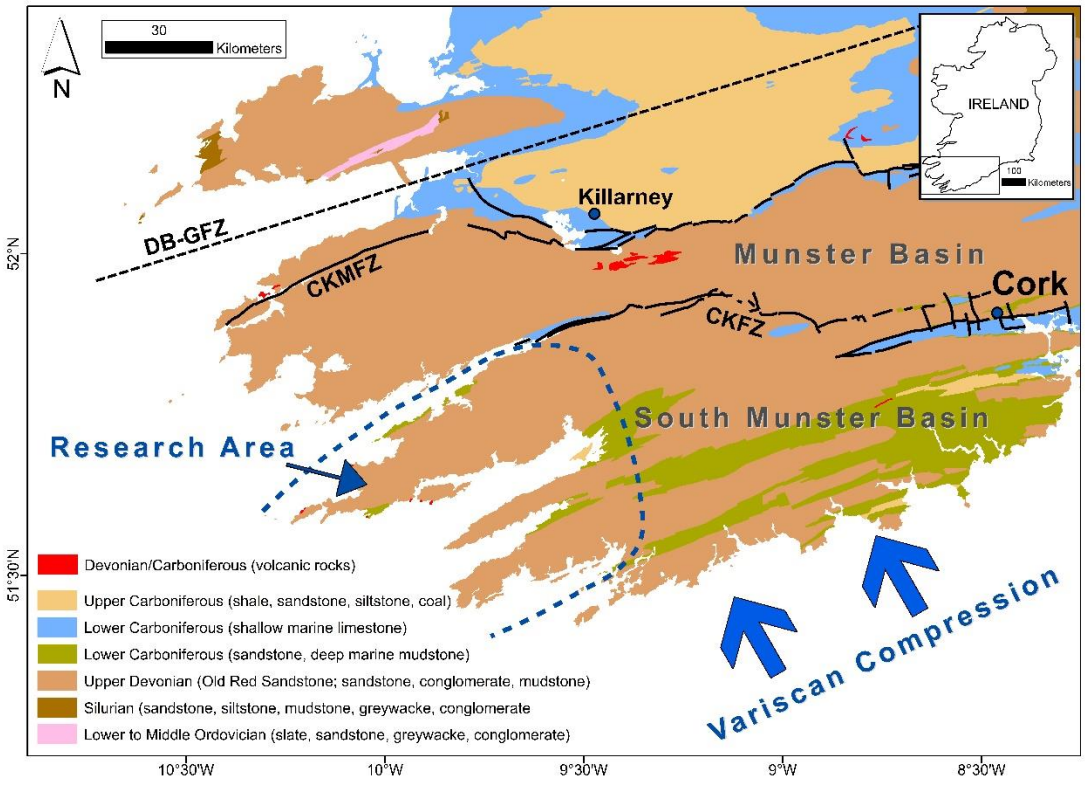


Fig. 2.2) Simplified geological map of the Munster Basin and the South Munster Basin in SW Ireland. The Munster Basin is defined by the Coomnacronia-Killarney-Mallow Fault Zone (CKMFZ) or alternatively by the Dingle Bay-Galtee Fault Zone (DB-GFZ) in the North. The Cork-Kenmare Fault Zone (CKFZ) indicates the rim to the South Munster Sub-Basin. An NNW directed compression indicates the Variscan Orogeny (modified from Sanderson 1984; Williams 2000; MacCarthy et al. 2002; Landes et al. 2003; MacCarthy 2007; Ennis et al. 2015).

The basin infill is dominated by late Middle to Upper Devonian alluvial and fluvial siliciclastic sediments (Fig. 2.3, MacCarthy 1990). These sediments were mainly transported from the north into the Munster Basin. Detailed stratigraphic nomenclature is described by Williams *et al.* (1989), MacCarthy (1990), Williams (2000), MacCarthy *et al.* (2002) and Pracht & Sleeman (2002, Fig. 2.3a and 2.3b): The siliciclastic Valentia Slate and Bird Hill Formation form the base of the north western basin infill (Pracht & Sleeman 2002). Both formations belong to the early facies association formed by basin margin alluvial fans to floodplain-sheetfloods and ephemeral lakes (MacCarthy 1990). A first fluvial influx from the northwest and west deposited sandstones and siltstones of the Slaheny Formation in the north and the sandstones with interbedded mudstones of the Sherkin Formation to the south of the Munster Basin (Pracht & Sleeman 2002, MacCarthy 1990). These formations are followed by an alluvial infill, which is formed by sandstones and siltstones of the fine-grained Caha Mountain, Castlehaven and Gun Point Formations (Pracht & Sleeman 2002). These formations are classified as “background” basin infill, which was deposited by unconfined sheetfloods across the floodplains of the rivers (Pracht & Sleeman 2002). The alluvial formations are assigned to the Upper Old Red Sandstone magnafacies, which formed a basinal infill of over 6 km (Williams *et al.* 1989, Meere & Banks 1997, Williams 2000). The cross-bedded sandstones of the Toe Head Formation mark a transition zone between the underlying non marine Old Red Sandstone Magna-Facies and the overlain marine Old Head Sandstone Formation (Pracht & Sleeman 2002). The Toe Head Formation belongs to the late fluvial influx from the west and mainly formed coastal plains within the newly developed South Munster Basin (MacCarthy 1990).

Fig. 2.3)

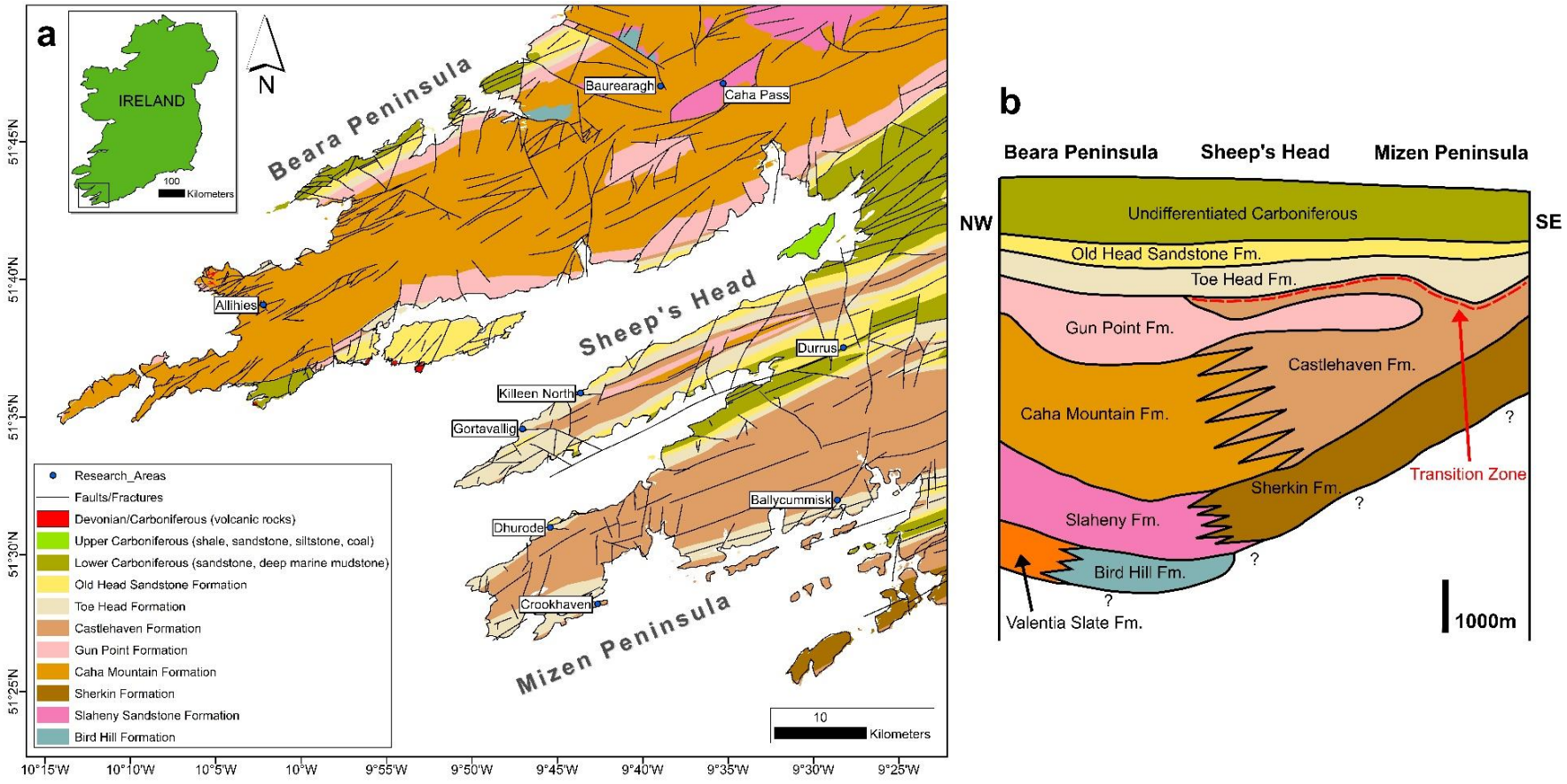

a
IRELAND
100
Kilometers
N
Beara Peninsula
Sheep's Head
Mizen Peninsula
Baurearagh
Caha Pass
Allihies
Durrus
Killeen North
Gortavallig
Ballycummisk
Dhurode
Crookhaven
Research_Areas
Faults/Fractures
Devonian/Carboniferous (volcanic rocks)
Upper Carboniferous (shale, sandstone, siltstone, coal)
Lower Carboniferous (sandstone, deep marine mudstone)
Old Head Sandstone Formation
Toe Head Formation
Castlehaven Formation
Gun Point Formation
Caha Mountain Formation
Sherkin Formation
Slaheny Sandstone Formation
Bird Hill Formation
10
Kilometers
51°45'N
51°40'N
51°35'N
51°30'N
51°25'N
10°15'W
10°10'W
10°5'W
10°W
9°55'W
9°50'W
9°45'W
9°40'W
9°35'W
9°30'W
9°25'W
b
Beara Peninsula
Sheep's Head
Mizen Peninsula
NW
SE
Undifferentiated Carboniferous
Old Head Sandstone Fm.
Toe Head Fm.
Gun Point Fm.
Castlehaven Fm.
Caha Mountain Fm.
Sherkin Fm.
Slaheny Fm.
Bird Hill Fm.
Valentia Slate Fm.
Transition Zone
?
1000m

Fig. 2.3c)

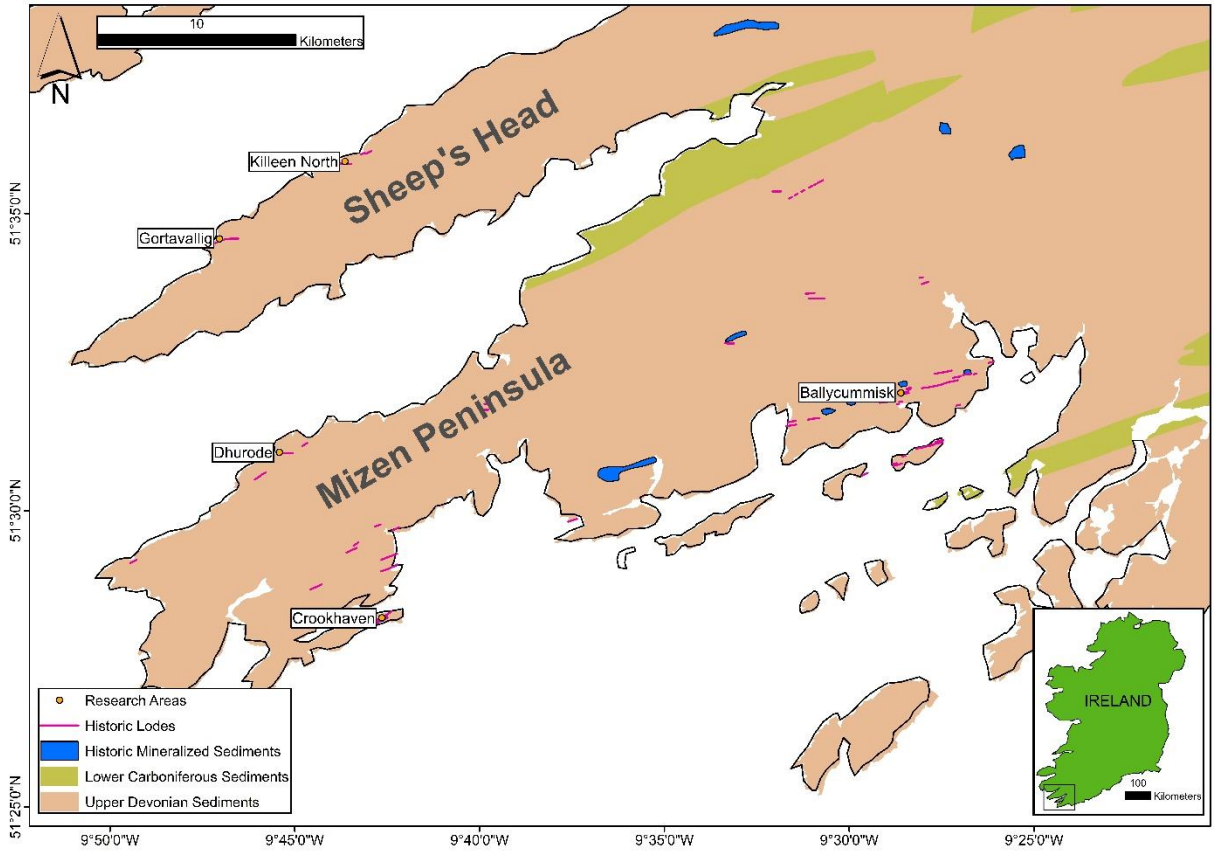


Fig. 2.3a) Geological map with research localities, major lithologies of the South Munster Basin and mainly Variscan NE-SW striking fractures (modified from GSI 2016). b) Simplified profile of the Munster Basin sedimentary formations including the copper hosting transition zone at the top of the Castlehaven Formation (modified from Snodin 1972; MacCarthy 1990; Wen et al. 1996; MacCarthy et al. 2002; Pracht & Sleeman 2002; GSI 2016 and Spinks et al. 2016). c) Simplified geological map (modified from GSI 2016 and GSI Jetstream 2019) showing the historically mined sediment hosted copper deposits in SW Ireland.

Continuous subsidence and formation of the South Munster Basin was initiated by the development of the east-west trending Cork-Kenmare Fault Zone (CKFZ) at the end of the Devonian (Fig. 2.2, MacCarthy 2007). Seismic interpretations from Landes *et al.* (2003) show a possible depth of 13–14 km for the basin-controlling Cork–Kenmare Fault Zone. The concomitant marine transgression from the south resulted in the accumulation of marine siliciclastics within the South Munster Basin south of the CKFZ and shelf limestones on a more stable platform to the north (Fig. 2.3; MacCarthy 2007).

2.3 Variscan Orogeny

An NNW-directed compression (Fig. 2.2) terminated sedimentation towards the end of the Carboniferous and marked the beginning of the Variscan Orogeny (Sanderson 1984; Ford 1987; Meere 1995b; Quinn *et al.* 2005). According to Ar-Ar dates of cleaved and deformed intrusive rocks on the Beara Peninsula (Fig. 2.3a, Quinn *et al.* 2005), the initial effect of the Variscan compression started before 314.4 Ma. The orogeny resulted in crustal shortening of over 52 % with the development of a pervasive cleavage, followed by kilometre scale buckling and faulting (Fig. 2.3a, Cooper & Trayner 1986; Ford 1987). The folding and faulting followed a general NE-SW strike (Fig. 2.3a, GSI 2016). High-angle basin-controlling faults were reactivated during compression (Price & Todd 1988). Reverse NE-SW-trending faults, as well as rarer NW-SE-trending strike slip faults are described by Meere (1995c) occurring in the west of the Munster Basin. The sediments underwent metamorphism to sub-greenschist facies (Meere 1995b).

E-W and ENE-WNW trending faults were interpreted by Wen *et al.* (1996) as late orogenic events. Daltry (1985) described a possible relationship of these fault systems with Post-Hercynian (Post-Variscan) wrench movements, associated with the North Atlantic opening in the Permian.

2.4 Magmatism in Southern Ireland

Minor intrusions ranging from dioritic to trachytic occur around Beara Peninsula and the northern Sheep's Head coastline (Boldy 1955, Viswanathiah 1959 and Reilly 1986, Figs. 2.1 and 2.2). These sheet-like intrusions were described by Pracht (2000) as mainly alkali basalts, trachytes and phonolites. Basalts formed high level shallow intrusions during the subsidence phase of the Munster Basin. Ductile deformed, pipe-like lamprophyric intrusions dated at 314.44 ± 1.00 Ma (Ar/Ar phlogopite, Quinn *et al.* 2005) have been found at Black Ball Head (5.6 km south of Allihies, Fig. 2.3) and were formed during the early Variscan compression (Pracht & Kinnaird 1995; Pracht 2000). Undeformed trachytic dykes from White Ball Head (400 m northwest of Black Ball Head) show ages of 296.88 ± 0.60 Ma (Ar/Ar phlogopite), which confine and therefore post-date the Variscan Orogeny (Quinn *et al.* 2005).

2.5 Copper Mineralization in Southern Ireland

The copper deposits and smaller copper occurrences in southern Ireland have been described by several authors (e.g. Sheridan 1964, Fletcher 1969, Snodin 1972, Sanderson 1984, Reilly 1986, Wen *et al.* 1996, Spinks *et al.* 2016). In general, the authors distinguished two major copper mineralization types: The sediment hosted, strata-bound copper deposits (e.g. Snodin 1972), and the quartz(-barite) vein hosted copper deposits (e.g. Reilly 1986). The major contentious points between the authors are the contradictory interpretations in timing and formation of both deposit types:

2.5.1 Sediment hosted deposits

Most of the sediment hosted, disseminated copper mineralization occurs on Sheep's Head and Mizen Peninsula (Fig. 2.3c, e.g. Wen *et al.* 1996 and GSI Jetstream 2019). A proximal distance of sediment hosted and vein hosted Cu mineralization is quite common (e.g. Crookhaven and Ballycummisk, Fig. 2.3c, Reilly 1986 and Wen *et al.* 1996).

According to Snodin (1972) interstitial brines from the marine basin migrated through the uppermost red-bed sediments and produced sulphite with anaerobic bacteria. The Cu deposits were assumed to be diagenetic in origin (Snodin 1972). Wen *et al.* (1996) and Snodin (1972) identified sediment hosted mineralization in stratigraphically bound, reduced green sandstone zones (green beds) within the upper Castlehaven Formation (Fig. 2.3b). The green to grey sandstone lithologies form beds with < 3 m thickness and have Cu grades of up to 6.4 wt% (Snodin 1972). Occasionally, e.g. at Killeen North on Sheep's head (Fig. 2.3c) copper can occur within carbonate rock (Wen *et al.* 1996). The sedimentary Cu occurrences are related to channel sandstones near the base of the Toe Head Formation and within the upper part of the Castlehaven Formation (Reilly 1986, Fig. 2.3a+b). According to Wen *et al.* (1996) these deposits were formed pre-metamorphic before the Variscan Orogeny. The disseminated mineralization is generally associated with minor quartz veins and veinlets (Wen *et al.* 1996). The sediments, veinlets and veins usually carry the same copper minerals (Snodin 1972). Spinks *et al.* (2016) measured negative $\delta^{34}S$ values at Allihies caused by biogenically-induced reduction within the Old Red Sandstone Facies resulting in syngenetic-diagenetic sulphide mineralization. Historically, the major sedimentary deposits were mined from green sandstones and slates (Fig. 2.3c, GSI 2016 & GSI Jetstream 2019).

2.5.2 Vein hosted deposits

The most prominent and largest known vein hosted copper mineralization in SW Ireland is Allihies on Beara Peninsula with over 284,500 tonnes of ore extracted (O'Brien 1959). Further historically mined quartz-copper veins are located on Sheep's Head and Mizen Head Peninsulas (e.g. Wen *et al.* 1996). The vein hosted deposits at Crookhaven (Mizen Peninsula, Fig. 2.3) have been described as saddle reef tension gashes exposed in an anticlinal (syn-Variscan) core (Duffy 1932 & Reilly 1986). Halliday and Mitchell (1983) dated clay minerals from Allihies (Fig. 2.3), which were sampled from the wall rock next to the quartz veins. The K-Ar dates showed post-Variscan results

between 290 and 261 Ma for the Mountain Mine Lode. An older, pre-Variscan age of 321 Ma was measured for an apparently unmineralized quartz vein (Halliday and Mitchell 1983). In contrary, Sanderson (1984) described N-S trending mineralized veins on Beara Peninsula with strong folding and cleavage, which led to a proposed pre/syn-Variscan age. Faulting and brecciation of mineralized veins occurring at deposits on Mizen Peninsula (Fig. 2.3) has been confirmed by Reilly (1986). For Crookhaven Reilly (1986) considered a late syntectonic mineralization. According to Wen *et al.* (1996) and Spinks *et al.* (2016) the sediment-hosted sulphides were remobilised into late- or post-Variscan quartz veins. Model age measurements (Pb/Pb) on vein-hosted copper occurrences from Ross Island (Northern Munster Basin at Killarney, Kerry, Fig. 2.2) yield to a syn-Variscan vein mineralization between 290 and 270 Ma (Kinnaird *et al.* 2002).

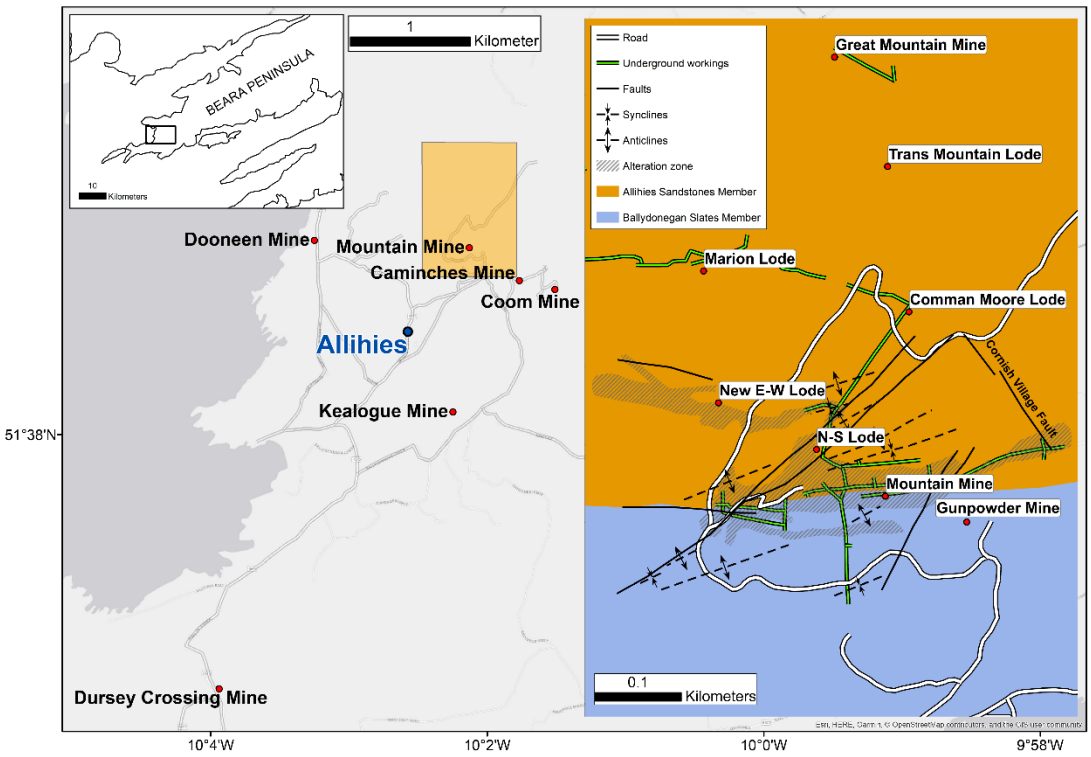


Fig. 2.4) Left: overview of the historical copper mines around Allihies Village on the western end of Beara Peninsula. Right: close-up view of the mining area at Mountain Mine, showing the bedrock geology, major structures, alteration zones and the traces of mapped underground workings (modified from Reilly 1986; historical mining map, Allihies Copper Mines, Unknown Author 1919).

2.5.3 Mineralization and Microthermometry

The mineral paragenesis of the major quartz vein hosted deposits in West Cork was well documented during active mining operations in the past (Sheridan 1964, Fletcher 1969, Snodin 1972), as well as more recent studies on tailings material and accessible historic mine sites (Reilly 1986, Spinks *et al.* 2016).

At Allihies Mountain Mine Reilly (1986; Fig. 2.4) describes the major copper lodes, the E-W Lode, N-S Lode and New E-W Lode together defining a Z-shaped surficial outcrop with bleached, altered, wall-rock zones up to 21 m in width. The mineralization has been described in detail by Sheridan (1964) as consisting of mainly chalcopyrite, tetrahedrite and bornite within “compact silica” gangue (quartz) material. Reilly (1986) described the distribution of “molybdenum mineralization” on the 1400 feet level of Mountain Mine, associated with high-grade copper mineralization. Zones with a “cherty” appearance of quartz were identified as “dust-like” grains of molybdenite and pyrite (Fletcher 1969). Selenium and tellurium minerals, as well as molybdenum and traces of gold, silver and mercury have been identified from the Allihies Mines (Reilly 1986; Spinks *et al.* 2016).

Chalcopyrite is described as the dominant Cu ore at the Sheep’s Head and Mizen Head locations (Fig. 2.3, Snodin 1972). Tennantite-tetrahedrite, as well as euhedral arsenopyrite has been found at Gortavallig and Dhurode Mine (Snodin 1972). The latter also has traces of galena. The mines at Crookhaven show mainly a chalcopyrite-bornite-quartz assemblage (Reilly 1986). Next to the primary Cu ore (chalcopyrite), Snodin (1972) described significant quantities of barite and specular hematite occurring at Ballycummisk Mine (Fig. 2.3). Fletcher (1969) recognized molybdenite in copper-bearing quartz veins at Ballycummisk, Dhurode and Crookhaven, similar to the Allihies veins.

Detailed fluid inclusion studies from Allihies (near Mountain Mine, Fig. 2.4) by Meere and Banks (1997) indicate medium to moderate salinities (4-16 wt% $NaCl_{equiv}$) for syn-Variscan quartz veins and high salinities (22-27 wt% $NaCl_{equiv}$) for post-orogenic extensional quartz veins. At Hungry Hill (about 19 km ENE of Allihies) Rogers (2002) compared early quartz veins (T_h = 230 °C)

with the syn-buckling veins (syn-Variscan, T_h = 190 °C) and late-stage quartz veins (T_h = 170 °C). All 3 vein types have a moderate salinity of about 10 wt% $NaCl_{equiv}$. Microthermometry measurements of quartz veins from Mizen Peninsula suggest peak-metamorphic conditions of between 300-400 °C (Wen *et al.* 1996). Homogenisation temperatures T_h can be as low as 100 °C (Crookhaven, Wen *et al.* 1996).

2.5.4 Geochemistry

Stable isotopes measurements on mineralized quartz veins from Allihies show consistent negative $\delta^{34}S_{CDT}$ values (−16.9 to −10.4 ‰) for chalcopyrite (Spinks *et al.* 2016). Wen *et al.* (1996) described wide-ranging and mostly negative $\delta^{34}S_{CDT}$ sulphide values (- 21.0 to + 5.1 ‰) for vein- and stratiform-disseminated deposits from West Cork (e.g. Crookhaven, Ballycummisk, Dhurode, Fig. 2.3). Both Wen *et al.* (1996) and Spinks *et al.* (2016) presumed a bacteriogenic sedimentary source causing the negative $\delta^{34}S$ values.

Wen *et al.* (1996) measured fluid inclusions within the mineralized veining quartz for δD_{SMOW} values ranging from -27.3 to -52.2 ‰. The veining quartz from mine localities on Mizen Head and Sheep's Head Peninsulas (Fig. 2.3) revealed $\delta^{18}O_{SMOW}$ values from +8.00 to +13.31 ‰ (calculated, Wen *et al.* 1996). Owing to these values Wen *et al.* (1996) assumed that the mineralized veins were deposited by metamorphic fluids.

Very little trace element geochemistry on Cu sulphides has been implemented on the historic copper mines of West Cork. Spinks *et al.* (2016) presented anomalously high selenium values within chalcopyrite with up to 291 ppm from Caminches Mine at Allihies (Fig. 2.4). These very high selenium concentrations around the area of Allihies were also mapped by Fay *et al.* (2007) occurring within regolith samples. Spinks *et al.* (2016) presumed oxidizing metamorphic conditions forming a selenium-rich roll-front-envelope within the Old Red Sandstones (Fig. 2.3b). Further measurements show up to 1399.9 ppm Zn and 21138.8 ppm Sb at Allihies Mountain Mine (chalcopyrite), and up to 67.667 ppm Cd and 1278.48 ppm Bi within a mineralized quartz vein from Ballycummisk (Spinks *et al.* 2016, Fig. 2.3).

2.6 Fluid mobility and structural models

Several authors developed fluid flow and structural models to explain the ore precipitating processes in southern Ireland.

A strong sea water Br/Cl signature from quartz vein fluid inclusions from Allihies (Fig. 2.3) indicates an early marine brine which perculated into the underlying sediments during the Munster Basin formation (Meere & Banks 1997). During the Variscan compression, these brines migrated by a gravity driven flow though the sediments (Meere & Banks 1997). Later, during the post orogenic extension, the fluids followed an upwards flow along normal extensional faults (Meere & Banks 1997).

A structural model from Hitzman (1999) describes the formation of syndiagentic Zn-Pb deposits of south-central Ireland. Hitzman (1999) postulated that the major Zn-Pb deposits are related to north-side-down (northwards dipping) east-west striking normal faults. The south-side-down normal faults, including the Munster Basin controlling listric Coomnacronia-Killarney-Mallow Fault Zone (CKMFZ, Fig. 2.2; Naylor & Jones 1967; Capewell 1975; Price & Todd 1988; Meere 1995c; Vermeulen *et al.* 2000; Landes *et al.* 2003; MacCarthy 2007; Ennis *et al.* 2015) was reactivated during the Variscan compression (Hitzman 1999). This reverse movement with the inherent uplift of the Munster Basin sediments caused the loss of any possible deposits related to the CKMFZ due to erosion (Hitzman 1999).

2.7 Chapter References

Boldy, G.D.J. 1955. The Petrology of the Igneous rocks near Castletownbere, West Co. Cork and their relationship with the Armorican Orogenesis in S.W. England. Unpublished M.Sc. Thesis. Trinity College, Dublin.

Brown, A.C. 2014. Low-Temperature Sediment-Hosted Copper Deposits. Editors: Heinrich, D., Holland, Karl, Turekian, K., Treatise on Geochemistry (Second Edition), Elsevier, 251-271. https://doi.org/10.1016/B978-0-08-095975-7.01110-4

Capewell, J. 1975. The Old Red Sandstone Group of Iveragh, Co. Kerry. Proceedings of the Royal Irish Academy, Section B, 75, 155–171. Cardozo, N. and Allmendinger, R.W. 2013. Spherical projections with OSXStereonet. Computers & Geosciences, 51, 193–205, https://doi.org/10.1016/j.cageo.2012.07.021

Cathles, L.M., III, Oszczepaliski, S., and Jowett, E.C. 1993. Mass balance evaluation of the late diagenetic hypothesis for Kupferschiefer Cu mineralization in the Lubin basin of southwestern Poland. Economic Geology, 88, 948–956.

Cooper, M.A. and Trayner, P.M. 1986. Thrust-surface geometry: implications for thrust-belt evolution and section-balancing techniques. Journal of Structural Geology, 8, 305–312, https://doi.org/10.1016/0191-8141(86)90051-9

Daltry, V.D.C. 1985. A structural, geochemical and mineralogical appraisal of the stratabound ore deposits in western County Cork, Ireland. Ph.D. Thesis, University College Cardiff.

Duffy, T.J. 1932. Copper Deposits in Southwest Ireland. Unpublished report and field sheets. Geol. Surv. Ireland.

Ennis, M., Meere, P.A., Timmerman, M.J. and Sudo, M. 2015. Post-Acadian sediment recycling in the Devonian Old Red Sandstone of Southern Ireland. Gondwana Research, 28, 1415–1433, https://doi.org/10.1016/j.gr.2014.10.007

Fay, D., Kramers, G., Zhang, C., McGrath, D., Grennan, E. 2007. Soil Geochemical Atlas of Ireland. Teagasc and Environmental Protection Agency, Dublin.

Fletcher, C.I. 1969. The sulphide mineralization in the Allihies region, County Cork, Eire. Ph.D. Dissertation, University of Leicester, 128–129.

Ford, M. 1987. Practical application of the sequential balancing technique: an example from the Irish Variscides. Journal of the Geological Society, London, 144, 885–891, https://doi.org/10.1144/gsjgs.144.6.0885

Geological Survey of Ireland, GSI 2016. Bedrock 100k (scale 1:100,000), Bedrock Geology, Coordinate System: Irish Transverse Mercator / ITM. https://www.gsi.ie/en-ie/data-and-maps/Pages/Bedrock.aspx# [last accessed 20/04/2020]

Geological Survey of Ireland, GSI Jetstream 2019. Historical Maps of Copper Deposits in SW Ireland. https://jetstream.gsi.ie [last accessed 08/03/2019]

Halliday, A.N. and Mitchell, J.G. 1983. K–Ar ages of clay concentrates from Irish orebodies and their bearing on the timing of mineralisation. Earth and Environmental Science Transactions of the Royal Society of Edinburgh, 74, 1–14, https://doi.org/10.1017/S0263593300009858

Hayes, T.S., Cox, D.P., Piatak, N.M., and Seal, R.R., II 2015. Sediment hosted stratabound copper deposit model: U.S. Geological Survey Scientific Investigations Report 2010–5070–M, 147 p.

Hitzman, M.W. 1999. Extensional faults that localize Irish syndiagenetic Zn-Pb deposits and their reactivation during Variscan compression. In: McCaffrey, K.J.W., Lonergan, L. and Wilkinson, J.J. (eds) Fractures, Fluid Flow and Mineralization. Geological Society, London, Special Publications, 155, 233-245.

Hitzman, M.W., Kirkham, R., Broughton, D., Thorson, J., and Selley, D. 2005. The sediment hosted stratiform copper ore system. In: Hedenquist, J.W., Thompson, J.F.H., Goldfarb, R.J., and Richards, J.P. (eds.). Economic Geology 100th Anniversary Volume 1905–2005, 609–642. Littleton, CO: Society of Economic Geologists, Inc.

Kinnaird, J.A., Ixer, R.A., Barreiro, B. and Nex, P.A. 2002. Contrasting sources for lead in Cu-polymetallic and Zn–Pb mineralisation in Ireland: constraints from lead isotopes. Mineralium Deposita, 37, 495–511, https://doi.org/10.1007/s00126-001-0252-5

Kirkham, R.V. 1989. Distribution, setting and genesis of sediment-hosted stratiform copper deposits. In: Boyle, R.W., Brown, A.C., Jefferson, C.W., Jowett, E.C., and Kirkham, R.V. (eds.), Sediment-Hosted Stratiform Copper Deposits, Geological Association of Canada Special Paper 36, 3–38. Ottawa: Geological Association of Canada.

Kucha, H. 2003. Geology, mineralogy and geochemistry of the Kupferschiefer, Poland. In: Kelly, J.G., Andrew, C.J., Ashton, J.H., Boland, M.B., Earls, G., Fusciardi, L., and Stanley, G., eds., Europe's major base metal deposits: Dublin, Irish Association for Economic Geology, 215–238.

Landes, M., O'Reilly, B.M., Readman, P.W., Shannon, P.M. and Prodehl, C. 2003. VARNET-96: three-dimensional upper crustal velocity structure of SW Ireland. Geophysical Journal International, 153, 424–442, https://doi.org/10.1046/j.1365-246X.2003.01911.x

MacCarthy, I.A.J. 1990. Alluvial sedimentation patterns in the Munster Basin, Ireland. Sedimentology, 37, 685–712, https://doi.org/10.1111/j.1365-3091.1990.tb00629.x

MacCarthy, I.A.J. 2007. The South Munster Basin of southwest Ireland. Journal of Maps, 3, 149–172, https://doi.org/10.1080/jom.2007.9710835

MacCarthy, I.A.J., Pracht, M. and Sleeman, A.G. 2002. Geology of West Cork, Scale 1:100000, Sheet 24. Geological Survey of Ireland, Dublin.

Meere, P.A. 1995a. High and low density fluids in a quartz vein from the Irish Variscides. Journal of Structural Geology, 17, 435–446, https://doi.org/10.1016/0191-8141(94)00066-9

Meere, P.A. 1995b. Sub-greenschist facies metamorphism from the Variscides of SW Ireland an early syn-extensional peak thermal event. Journal of the Geological Society, London, 152, 511–521, https://doi.org/10.1144/gsjgs.152.3.0511

Meere, P.A. 1995c. The structural evolution of the western Irish Variscides: an example of obstacle tectonics? Tectonophysics, 246, 97–112, https://doi.org/10.1016/0040-1951(94)00267-D

Meere, P.A. and Banks, D.A. 1997. Upper crustal fluid migration: an example from the Variscides ofSW Ireland. Journal of the Geological Society, London, 154, 975–985, https://doi.org/10.1144/gsjgs.154.6.0975

Naylor, D. and Jones, P.C. 1967. Sedimentation and tectonic setting of the Old Red Sandstone of southwest Ireland. In: Oswald, D. (ed.) International Symposium on the Devonian System (Calgary). Society of Petroleum Geology 2, Calgary, Alberta, 1089–1099.

O'Brien, M.V. 1959. The future of non-ferrous mining in Ireland. In: The Future of Non-Ferrous Mining in Great Britain and Ireland. Institution of Mining and Metallurgy Symposium, 5–26.

Pracht, M. 2000. Controls on magmatism in the Munster Basin, SW Ireland. Geological Society, London, Special Publications, 180, 303–317, https://doi.org/10.1144/GSL.SP.2000.180.01.14

Pracht, M. and Kinnaird, J.A. 1995. Mineral chemistry of megacrysts and ultramafic nodules from an undersaturated pipe at Black Ball Head, County Cork. Irish Journal of Earth Sciences, 14, 47–58.

Pracht, M. and Sleeman, A.G. 2002. A geological description of West Cork and adjacent parts of Kerry to accompany the Bedrock Geology, 1:100,000 Scale Map Series, Sheet 24, West Cork. With accompanying contributions by Wright G (Groundwater) and CoxW (Minerals). Geological Survey of Ireland, Dublin.

Price, C.A. and Todd, S.P. 1988. A model for the development of the Irish Variscides. Journal of the Geological Society, London, 145, 935–939, https://doi.org/10.1144/gsjgs.145.6.0935

Quinn, D., Meere, P.A. and Wartho, J.A. 2005. A chronology of foreland deformation: Ultra-violet laser 40Ar/39Ar dating of syn/late-orogenic intrusions from the Variscides of southwest Ireland. Journal of Structural Geology, 27, 1413–1425, https://doi.org/10.1016/j.jsg.2005.02.003

Reilly, T.A. 1986. A review of vein mineralization in SW County Cork, Ireland. In: Andrew, C.J., Crowe, R.W.A., Finlay, S., Pennell, W.M. and Pyne, J.F. (eds) Geology and Genesis of Mineral Deposits in Ireland. Irish Association for Economic Geology, Dublin, 513–544.

Rogers, J.G. 2002. Regional veining in the Upper Palaeozoic Munster and South Munster Basins, Ireland; the evolution of palaeofluids and palaeofluid flow during basin inversion. Ph.D. Dissertation, University College Cork.

Sanderson, D.J. 1984. Structural variation across the northern margin of the Variscides in NW Europe. Geological Society, London, Special Publications, 14, 149–165, https://doi.org/10.1144/GSL.SP.1984.014.01.15

Selley, D., Broughton, D., Scott, R., Hitzman, M., Bull, S., Large, R., McGoldrick, P., Croaker, M., Pollington, N., and Barra, F. 2005. A new look at the geology of the Zambian Copperbelt Economic Geology 100Th Anniversary Volume, 965–1000.

Sheridan, D.J. 1964. The structure and mineralisation of the Mountain Mine area, Allihies, west Co. Cork, Ireland. Scientific Proceedings, Royal Dublin Society, Series A, 2, 21–27.

Singer, D.A. 1995. World-class base and precious metal deposits: A quantitative analysis: Economic Geology, 90, 88–104.

Snodin, S.R. 1972. Copper and other mineralisation in the Upper Palaeozoic strata of south-west Cork, Ireland, and related areas. Unpublished Ph.D. Thesis. University of Leicester.

Spinks, S.C., Parnell, J., Bellis, D. and Still, J. 2016. Remobilization and mineralization of selenium–tellurium in metamorphosed red beds: Evidence from the Munster Basin, Ireland. Ore Geology Reviews, 72, 114–127, https://doi.org/10.1016/j.oregeorev.2015.07.007

Unknown Author 1919. Historic mining map, Allihies Copper Mines. Geological Survey of Ireland, GSI Goldmine, https://secure.dccae.gov.ie/goldmine/docpage.html?id1=8260590&id2=9553634&id3=9556911 [last accessed 16 July 2017].

Vaughan, D.J., Sweeney, M., Diedel, F.R., and Haranczyk, C. 1989. The Kupferschiefer: An overview with an appraisal of the different types of mineralization. Economic Geology 84, 1003–1027.

Vermeulen, N.J., Shannon, P.M., Masson, F. and Landes, M. 2000. Wide-angle seismic control on the development of the Munster Basin, SW Ireland. Geological Society, London, Special Publications, 180, 223–237, https://doi.org/10.1144/GSL.SP.2000.180.01.11

Viswanathiah, M.N. 1959. Geology and Mineralisation around Allihies – Castletownbere Area. Co. Cork, Ireland. Unpublished Ph.D. Thesis, London University.

Volodin, R.N., Chechetkin, V.S., Bogdanov, Y.V., Narkelyun, L.F., and Trubachev, A.I. 1994. The Udokan cupriferous sandstones deposit (eastern Siberia). Geology of Ore Deposits, 36, 1–25.

Wen, N., Boyce, A.J., Fallick, A.E., Ashworth, J.R. and Ixer, R.A. 1996. The genesis of Cu-bearing quartz veins by metamorphic remobilization from stratiform red bed deposits, SW County Cork, Ireland. Mineralogy and Petrology, 57, 73–89, https://doi.org/10.1007/BF01161622

Williams, E.A., Bamford, M.L.F., Cooper, M.A., Edwards, H.E., Ford, M., Grant, G.G., MacCarthy, I.A.J., McAfee, A.M., and O'Sullivan, M.J., 1989. Tectonic controls and sedimentary response in the Devonian-Carboniferous Munster and South Munster basins, south-west Ireland. In: R.S. Arthurson, P. Gutteridge and S.C. Nolan (Editors), Role of Tectonics in Devonian and Carboniferous Sedimentation in the British Isles. Spec. Publ. Yorkshire Geol. Soc., 6, 123-141.

Williams, E.A. 2000. Flexural cantilever models of extensional subsidence in the Munster Basin (SW Ireland) and Old Red Sandstone fluvial dispersal systems. Geological Society, London, Special Publications, 180, 239–268, https://doi.org/10.1144/GSL.SP.2000.180.01.12

Chapter 3: The Vein Hosted Copper Deposits of the Allihies Mining Area, Southwest Ireland – A New Structural and Chronological Evaluation

Status: Published in the *Journal of the Geological Society (2020),177(4):671*

DOI: https://doi.org/10.1144/jgs2019-154

Author list:

Jürgen Lang[1]*, Patrick A. Meere[1], Richard P. Unitt[1], Sean C. Johnson[2], Giulio Solferino[3], Koen Torremans[2], David Selby[4,5] & Roisin Kyne[6]

[1] *Irish Centre for Research in Applied Geosciences (iCRAG), School of Biological, Earth and Environmental Sciences, University College Cork, Distillery Fields, North Mall, Cork, Ireland*

[2] *Irish Centre for Research in Applied Geosciences (iCRAG), University College Dublin, Belfield, Dublin 4, Ireland*

[3] *Department of Earth Sciences, Royal Holloway University of London, Egham, Surrey, United Kingdom*

[4] *Department of Earth Sciences, University of Durham, Durham, United Kingdom*

[5] *State Key Laboratory of Geological Processes and Mineral Resources, School of Earth Resources, China University of Geoscience Wuhan, Hubei Province, 430074, China*

[6] *Teck Resources Limited, Suite 3300, Bentall 5. 550 Burrard Street, Vancouver, B.C., Canada, V6C 0B3*

**Corresponding author (e-mail: juergen.lang@icrag-centre.org)*

Appendix B1-3: Fluid inclusions measurements of the Allihies Copper Mining District. Locations are as shown in Fig. 3.2 and 3.7.

Appendix C: Sample locations of the Allihies Copper Mining District.

Appendix D: Supporting petrographical images from samples of the Allihies Copper Mining District.

3.1 Abstract

This paper presents new data for historic vein-hosted copper sulphide deposits in the Upper Palaeozoic Munster and South Munster Basins of southwest Ireland. Detailed mapping, 3D modelling, fluid inclusion microthermometry and geochronology from the Allihies area of the Beara Peninsula, have led to a new interpretation of the timing and development of ore mineralization. Macro- and microstructural studies reveal that the ore-bearing, mainly E-W striking quartz veins are directly related to early extensional, basinal normal faults. Molybdenite Re-Os dating of the main-stage Cu lode yield ages from 367.3 ± 5.5 to 366.4 ± 1.9 Ma. This early vein system experienced subsequent late Carboniferous Variscan deformation, including cleavage development, sinistral SW-NE strike slip faulting, cataclastic deformation and recrystallization. The new timing of Cu mineralization in SW Ireland has major implications for its relationship to the base metal deposits of the Irish Midlands.

3.2 Introduction

The mineral deposits of the Irish Variscan fold/thrust belt have been exploited for over 3500 years (Williams 1991). In southwest Ireland copper has been mined as far back as the Bronze Age (O'Brien 1987). In 1812, malachite stained cliff faces at Dooneen on the Beara Peninsula (Fig. 3.1 and 3.2) led to the discovery of significant copper lodes (Blenkinsop 1902; Reilly 1986). As

miners progressed further inland, they uncovered metal-rich, steeply dipping, E-W striking quartz veins in the vicinity of Allihies (Fig. 3.1 and 3.2). The biggest vein was worked at Mountain Mine which at the time became the largest copper mine in the region with a total estimated 284,500 tonnes ore extracted (O'Brien 1959).

This paper focusses on the copper deposits of the Allihies mining district in West Cork (Fig. 3.2) where previous authors studied the structure and chronology of the vein mineralization (Sheridan 1964; Sanderson 1984; Spinks *et al.* 2016).

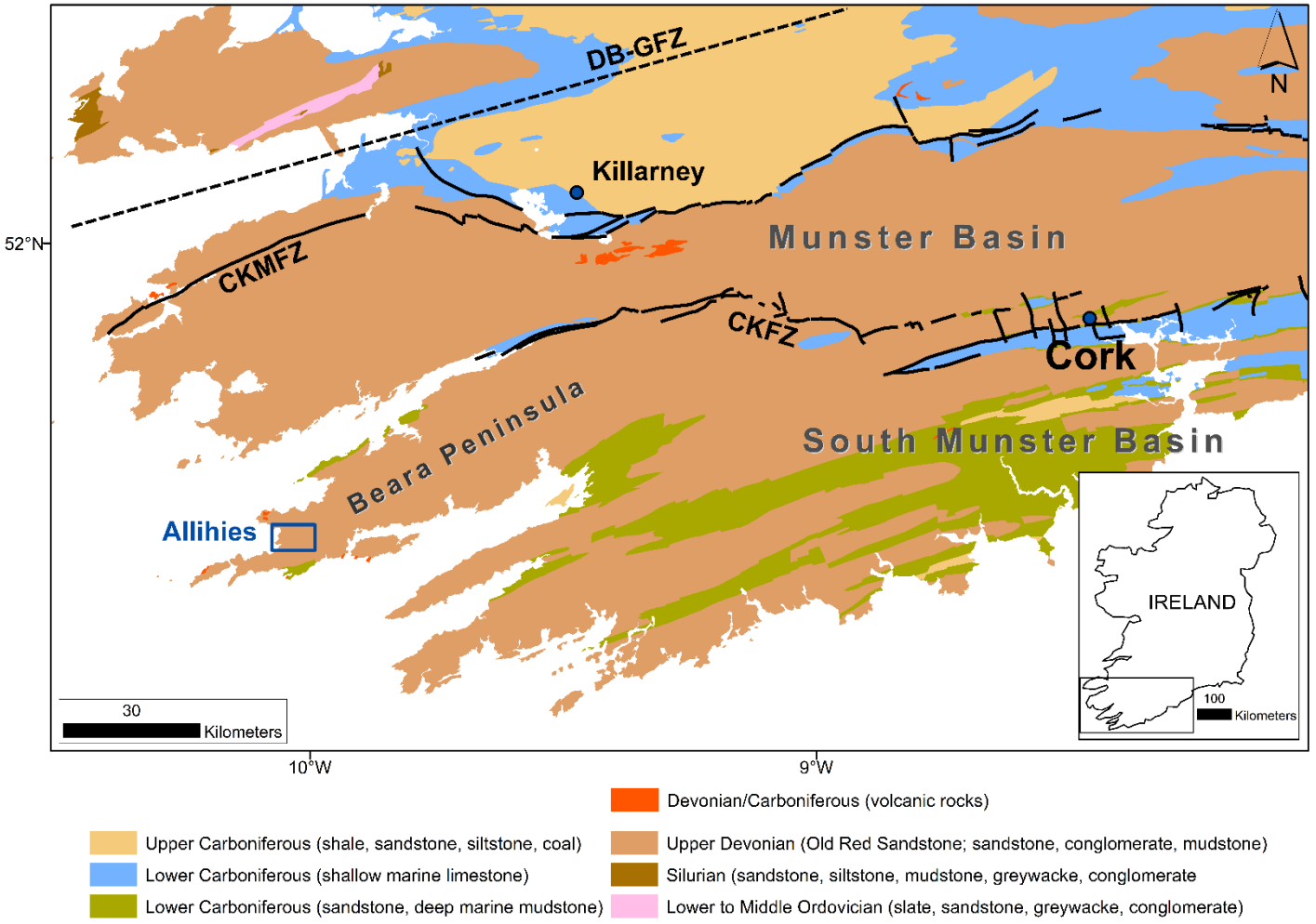


Fig. 3.1) Simplified map of the Munster Basin and the South Munster Basin in Southwest Ireland. The northern margin of the Munster Basin is defined by the Coomnacronia-Killarney-Mallow Fault Zone (CKMFZ) or alternatively by the Dingle Bay-Galtee Fault Zone (DB-GFZ). The Cork-Kenmare Fault Zone (CKFZ) indicates the rim to the South Munster Sub-Basin (modified from MacCarthy et al. (Geological Survey of Ireland) 2002; Williams 2000; Landes et al. 2003; MacCarthy 2007; Ennis et al. 2015).

3.3 Geological Setting

Between the Middle and early Upper Devonian, north-south crustal extension led to the development of a half-graben structure in southern Ireland that comprises the Munster Basin (Naylor & Jones 1967). The northern bounding structure of this intracratonic basin has been described as the east-west trending, listric Coomnacronia-Killarney-Mallow Fault Zone (Fig. 3.1; Naylor & Jones 1967; Capewell 1975; Price & Todd 1988; Meere 1995c; Vermeulen *et al.* 2000; Landes *et al.* 2003; MacCarthy 2007; Ennis *et al.* 2015) or the Dingle Bay-Galtee Fault Zone Williams (2000).

The lithostratigraphic nomenclature of the basin sediments is described in detail by MacCarthy 1990, MacCarthy *et al.* 2002 and Pracht & Sleeman 2002. Late Middle to Upper Devonian alluvial and fluvial siliciclastic sediments derived mainly from the north were transported into the Munster Basin (MacCarthy 1990). These 'Upper Old Red Sandstone' sediments formed a basinal infill of over 6 km (Meere & Banks 1997). MacCarthy (1990) divided these siliciclastic sediments into 5 facies associations which evolved from early basin margin alluvial fans to floodplain-sheetfloods and ephemeral lakes.

Towards the end of the Devonian the formation of another east-west trending fault system, the Cork-Kenmare Fault Zone (Fig. 3.1) resulted in continuous subsidence of the South Munster Basin (MacCarthy 2007). This was accompanied by a marine transgression from the south with resulting accumulation of marine siliciclastics within the South Munster Basin and limestones on a more stable platform to the north (Fig. 3.1; MacCarthy 2007).

At the end of the Carboniferous NNW-directed compression terminated sedimentation in the region and marked the beginning of the Variscan Orogeny (Sanderson 1984; Ford 1987; Meere 1995b; Quinn *et al.* 2005). Bulk shortening of over 52 % was achieved by pervasive cleavage development followed by kilometre scale buckling and faulting (Cooper & Trayner 1986; Ford 1987). This resulted in the reactivation of high-angle basin-controlling faults (Price & Todd 1988). In the west of the Munster Basin, Meere (1995c) identified NE-SW-trending reverse faults, as well as rarer NW-SE-trending

strike slip faults. The sediments underwent metamorphism to sub-greenschist facies (Meere 1995b).

E-W and ENE-WNW trending faults were interpreted by Wen *et al.* (1996) as late orogenic events. Daltry (1985) described a possible relationship of these fault systems with Post-Hercynian (Post-Variscan) wrench movements, associated with the North Atlantic opening in the Permian.

A series of minor sheet-like intrusions of mainly alkali basalts, trachytes and phonolites have been found along the northern coastline of Beara Peninsula (Pracht 2000; Fig. 3.1). These basalts are interpreted as surficial intrusions during the subsidence phase of the Munster Basin. Pipe-like lamprophyric intrusions dated at 314.44 ± 1.00 Ma (Ar/Ar phlogopite, Quinn *et al.* 2005) occur at Black Ball Head (5.6 km south of Allihies), which were formed during the early Variscan compression (Pracht & Kinnaird 1995; Pracht 2000).

The Allihies Mining District is located near the western end of the Beara Peninsula (Fig. 3.2). The predominant lithologies are purple and green siltstones and sandstones of the Caha Mountain Formation (MacCarthy *et al.* 2002). The Caha Mountain Formation can be subdivided into the Allihies Sandstone Member, which mainly outcrops north of Mountain Mine (Fig. 3.2) and has an approximate thickness of 1200 m, and the underlying Ballydonegan Slate Member (south of Mountain Mine) that has an approximate thickness of 1500 m (Reilly 1986).

The Allihies copper mines are positioned on the northern limb of the Beara Anticline (Sheridan 1964). Around the mines, third-order open symmetrical folds with wavelengths of 90 to 150 m, trending SW-NE can be found associated with fault zones following similar strike (Reilly 1986; Fig. 3.2). Penetrative cleavage is sub-vertical and strikes SW-NE (Reilly 1986). The Cornish Village Fault is one of the rare NW-trending faults and was previously interpreted as a pre-mineralization structure (Reilly 1986; Fig. 3.2).

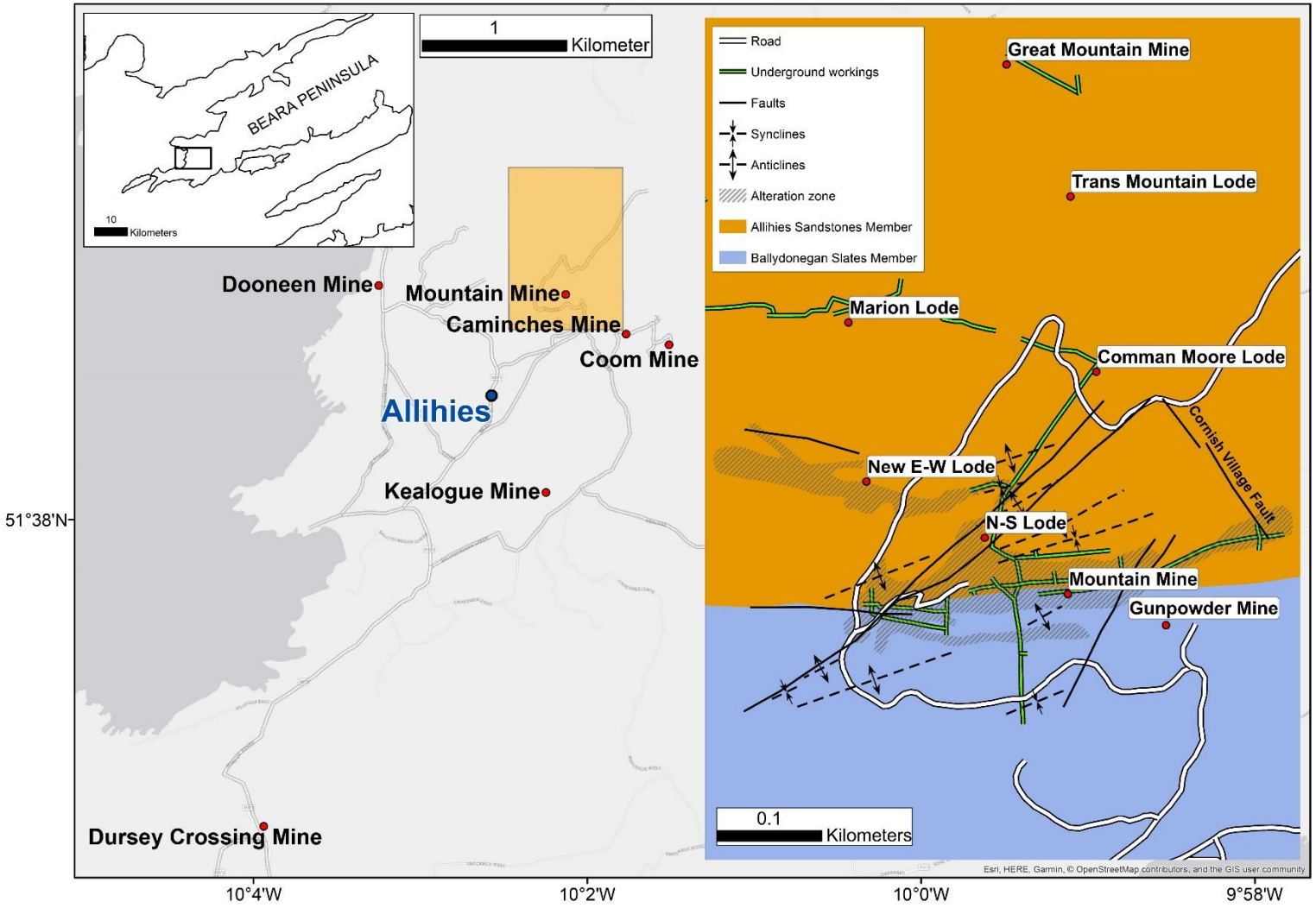


Fig. 3.2) Left: Overview of the historic copper mines around Allihies Village on the western end of Beara Peninsula. Right: Zoom into the mining area at Mountain Mine, showing the bedrock geology, major structures, alteration zones and the traces of mapped underground workings (modified from Reilly 1986; historic mining map, Allihies Copper Mines 1919).

There has been differing opinions about the timing of the vein structures and the copper mineralization of the Allihies region. For example, mineralized veins were considered to post-date the barren veins and Variscan compression tectonics (Sheridan 1964). In direct contrast is the observation by Sanderson (1984) that mineralized (chalcopyrite and siderite) N-S trending quartz veins are both strongly folded and cleaved, suggesting a pre/syn-Variscan age. Sanderson (1984) also proposed that the east-west veins, which include the main lodes of the mining area, were formed in association with the cleavage development and the folding. Rogers (2002) divided the quartz veins of the Beara Peninsula into 3 different genetic events; early buckled veins, syn-buckled (syn-Variscan) and late stage extension. Wen *et al.* (1996) and Spinks *et al.* (2016) suggested remobilisation of sediment-hosted sulphides into late- or post-Variscan quartz veins.

At Mountain Mine Reilly (1986; Fig. 3.2) describes the major copper lodes, the E-W Lode, N-S Lode and New E-W Lode together defining a Z-shaped surficial outcrop. On the surface, these lodes are up to 18 m wide and 240 m long with bleached, altered, wall-rock zones up to 21 m in width. The mineralization has been described in detail by Sheridan (1964) as consisting of mainly chalcopyrite, tetrahedrite and bornite within “compact silica” gangue (quartz) material. Reilly (1986) described the distribution of “molybdenum mineralization” on the 1400 feet level of Mountain Mine, associated with high-grade copper mineralization. Zones with a “cherty” appearance of quartz were identified as “dust-like” grains of molybdenite and pyrite (Fletcher 1969). Selenium and tellurium minerals, as well as molybdenum and traces of gold, silver and mercury have been identified from the Allihies Mines (Reilly 1986; Spinks *et al.* 2016).

Previous microthermometry measurements of syn-Variscan quartz veins from Mizen Peninsula suggest peak-metamorphic conditions of between 300-400 °C (Wen *et al.* 1996). Detailed fluid inclusion studies from Allihies (near Mountain Mine) by Meere and Banks (1997) indicate medium to moderate salinities (4-16 wt% $NaCl_{equiv}$) for syn-Variscan quartz veins and high salinities (22-27 wt% $NaCl_{equiv}$) for post-orogenic extensional veins. At Hungry Hill

(about 19 km ENE of Allihies) Rogers (2002) compared early veins (T_h = 230 °C) with the syn-buckling veins (syn-Variscan, T_h = 190 °C) and late stage veins (T_h = 170 °C). All 3 vein types have a moderate salinity of about 10 wt% $NaCl_{equiv}$.

3.4 Methodology

Field mapping focussed primarily on the classification, measuring and sampling of quartz veins to establish a paragenesis and a structural chronology. Aerial drone mapping was utilised to investigate the area around the Allihies copper mines and to contextualise features identified in the field. A DJI Phantom 3 Professional with a 4K, 12.4-megapixel camera was flown at a vertical height of between 20 to 50 m, depending on the surface topography, over a defined area of approximately 30,000 m^2 per flight. Several flights were necessary to cover the entire mining area (Fig. 3.3a). The high-resolution images were captured with two thirds overlap. The geotagged images were processed with the photogrammetry software 3Dsurvey by Modri planet to calculate a 3-dimensional (3-D) digital terrain model (DTM) and a 2-D high-resolution orthorectified photograph, subsequently georeferenced in ArcGIS (Fig. 3.3a). The high-resolution drone orthophotography and aerial photography aided the field mapping of the faults and veins. The low capturing elevation facilitated the identification of veins and structures as small as 6 cm wide.

The 3-D DTM point cloud and historical mining maps (Wilson & Powell 1956) were used to create a 3-D model of Mountain Mine and its mineralized veins (see digital appendix). Data entry and 3-D modelling was done using SKUA-GoCAD (Emerson Paradigm) and the Mining Suite plugins of Mira Geoscience, using the discrete smooth interpolator to model the veins (Caumon *et al.* 2009). Data entry and georeferencing was performed in ArcMap (ESRI). Data validation and visualization were carried out with Leapfrog3DGeo (ARANZ Geo Ltd., now Seequent).

Sampling of mineralized and unmineralized quartz veins was conducted in the entire area around Allihies. Whenever possible, in-situ vein samples were taken, but in some cases the historic mine shafts were not accessible, collapsed or filled with water. This necessitated the collection and analysis of some samples from spoil material.

The samples were petrographically analysed as polished blocks and polished thin sections via reflected and transmitted light microscopy. Images were captured using a Leica (DVM2500) digital microscope with an attached VZ700C lens in the Geomicroscopy Facility at University College Cork.

Four spatially oriented samples from East-West striking mineralized quartz veins were collected and cut perpendicularly to cleavage $S_{1,vein}$ (sample 418; Fig. 3.3a). Thin section images were captured and stitched for the entire width of the veins with the Leica DVM2500 digital microscope as false colour images to identify different generations and microstructures.

Quartz vein samples were classified in the field according to their structural relation. These vein samples (8 mineralized and 5 barren/unmineralized) were prepared as doubly polished thin sections. Small chips of max. $1cm^2$ were examined with a Linkam (LMS600) temperature-controlled microscope stage, combined with an Olympus BX50 microscope, a x100 LWD objective and an attached 16 megapixels Nikon DS-Ri2 camera at the UCC Geomicroscopy Facility. Bi-phase (L+V) fluid inclusions, were analysed for their freezing temperature T_{ice}, the first melt temperature T_{fm} and the final melt temperatures T_m, as well as the homogenisation temperature T_h = liquid + vapour = liquid. Special care was taken to measure primary fluid inclusion assemblages along growth zones of the quartz grains. Secondary inclusion trails and healed areas, as well as necking fluid inclusions were avoided. Within the mineralized veins, primary inclusions were selected, which are genetically related to the copper sulphides (see Appendix B1 and B2). The stage was calibrated using a CO_2 standard (-56.6 °C, Camperio) and a synthetic, doubly distilled H_2O standard (T_m = 0.0 °C, T_h = L + V = L: 374.0 °C, Leoben). The resolution of the used stage system is 0.1°C. The uncertainty of the analyses for this type of

stage is described in detail by Doppler and Bakker (2014) with a maximum standard deviation of ± 0.4 °C. Salinity was calculated as wt% $NaCl_{equiv}$ by using the Excel macro HOKIEFLINCS_H2O-NACL (Steele-MacInnis *et al.* 2012; Bodnar 1993; Atkinson 2002; Bodnar *et al.* 1994; Bodnar 1983).

A historic molybdenite sample (BM.1964,R231) from Mountain Mine (Fig. 3.2) was provided by the National History Museum in London (NHM). The mineralized quartz-molybdenite specimen was collected by Sir Arthur Russell from the Mountain Mine dumps in 1918 (NHM Russell collection). A second molybdenite sample was discovered recently from spoil near Caminches Mine (Fig. 3.2). Small fragments (< 1 cm) were separated from the samples using a micro chisel to avoid major damage and potential rhenium contamination. The samples, which both contain fine-grained molybdenite (< 2 mm), were analysed using reflected light microscopy and fluid inclusion microthermometry (quartz). The samples were used for Re-Os geochronology at Durham University Laboratory for Source Rock and Sulfide Geochemistry and Geochronology. Sample preparation and analysis was undertaken as described in detail by Selby & Creaser (2001) and Li *et al.* (2017). The molybdenite material was isolated from the vein quartz and other minerals with HF. Approximately 10mg of pure molybdenite was loaded into a carius tube with aqua regia (3 ml HCl + 6 ml HNO_3) and a known about of tracer solution (^{185}Re + isotopically normal Os). The carius tube was then sealed and placed in an oven for 24 hrs at 220˚C. The Os and Re isotopically equilibrated sample and tracer solution were extracted from the acid solution using solvent extraction, microdistillation and anion chromatography methods. The purified Re and Os fractions were measured for their isotopic compositions in static mode using a Thermo Scientific Triton mass spectrometer in the Arthur Holmes Laboratory at Durham University. The Re-Os molybdenite model age was calculated with the equation $t = \ln(^{187}Os/^{187}Re + 1)/\lambda$ (Smoliar *et al.* 1996), where λ is the decay constant for $^{187}Re = 1.666 \times 10^{-11}\ a^{-1}$ (Smoliar *et al.* 1996; Selby *et al.* 2007). Uncertainties were calculated with mass spectrometry uncertainty, all analytical sources uncertainties and the decay constant (Table 3.1).

3.5 Results

3.5.1 Field Observations

Host Lithologies

The area north of Mountain Mine is dominated by micaceous siltstones and quartz arenites of the Allihies Sandstone Member (Caha Mountain Formation). The siltstones have a reddish to greyish colour and form beds from 10 cm to several metres thick. The sandstones are red to grey and are generally well sorted. Occasionally, siltstone clasts up to 2 cm were found within the sandstone. Ripple marks and mud cracks occur on the bedding planes. Grey mudstones of the Ballydonegan Slate Member are mainly observed in the southern part of the study area between Mountain Mine and Allihies village.

Both lithologies can display alteration zones adjacent to large (> 0.5 m width) mineralized quartz veins. The colour varies from yellowish-brown to pale yellowish-red, mainly due to the presence of iron hydroxides. These alteration zones are rarely wider than one metre around the mineralized veins but next to the smaller veins (< 10 cm width) they are often absent.

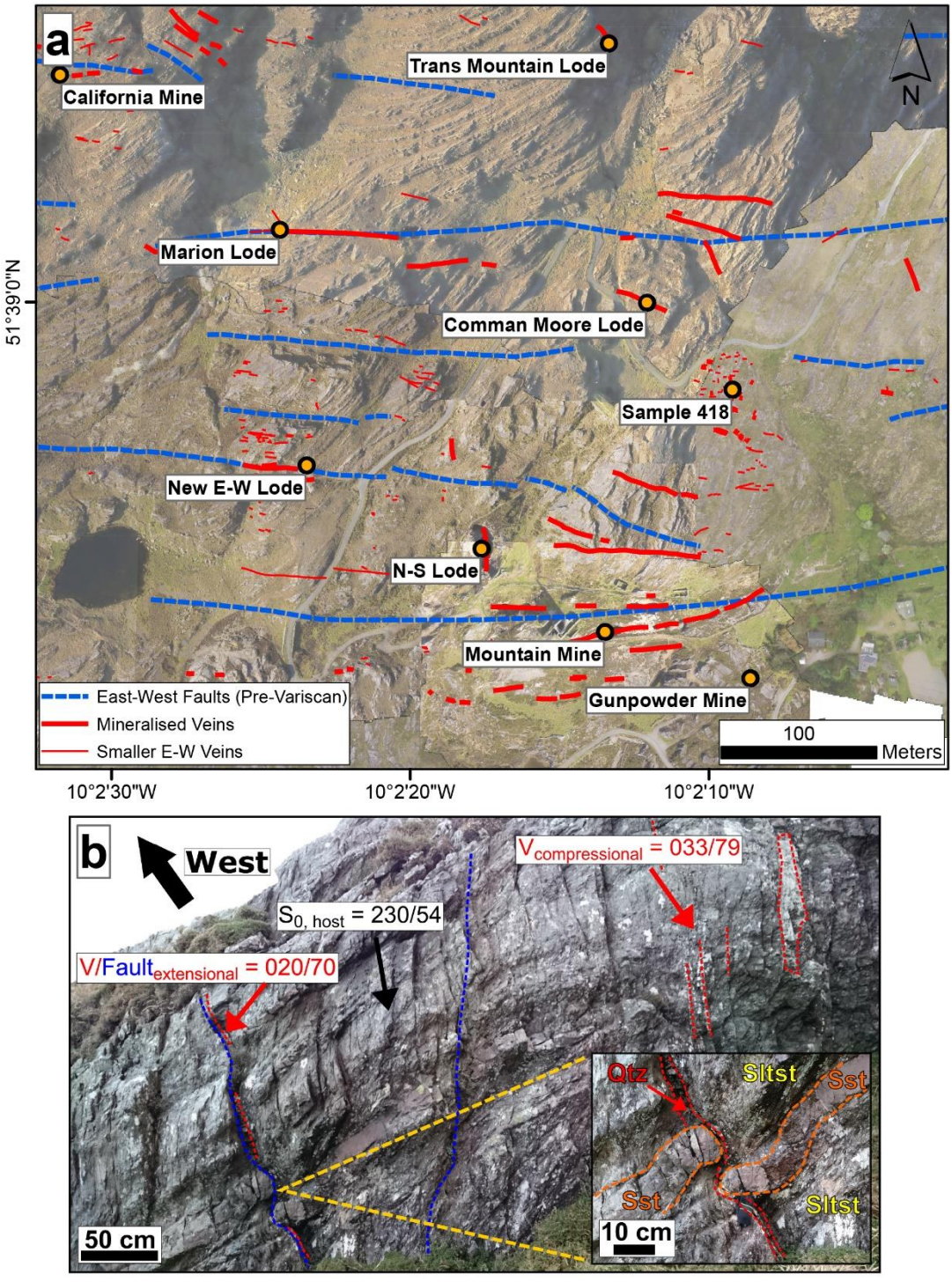


Fig. 3.3a) The major lodes and mineralized veins of the Mountain Mine Area with pre-deformation structures. High-resolution drone maps and Bing™ Satellite Maps (2016), including field analysis and modifications from Reilly (1986). b) Outcrop of pre-Variscan, extensional faults (graben structure) at the western end of Mountain Mine E-W Lode. The southern fault is filled with a quartz-chlorite vein ($V_{extensional}$ = 020/70), which is deformed (syn-Variscan)

by competent sandstone layers (Sst) and incompetent siltstones (Sltst). Syn-Variscan, compressional veins ($V_{compressional}$ = 033/79) occur at the northern part of the outcrop.

Early extensional structures and mineralization

East-West striking, normal faults with a strike-length of 60 to over 1000 m are present near, and at, the historic mine shafts (Fig. 3.3a). Their strike ranges in between 071 and 123 degrees. Due to surface weathering, these faults form natural depressions. Figure 3.3b shows a quartz vein following a steep dipping (70 degrees) normal E-W striking fault SW of Mountain Mine (Fig. 3.3a). This vein is deformed by a subsequent orogenic compression.

Sub-parallel to ESE-WNW striking quartz veins occur up to 35 m from the E-W faults (Fig. 3.3a and Fig. 3.4a). These veins are mineralized and range from centimetre to metre scale in diameter and have a maximum length of over 100 m. Only two vein sets have been observed striking North-South, including the N-S Lode at Mountain Mine (Fig. 3.3a).

Associated with larger quartz veins are a spatially concentrated series of smaller quartz veinlets with an average width of 0.5 to 10 cm and a maximum length of 108 m (Fig. 3.3a). Similar to the larger veins and lodes, these smaller veins have an ESE-WNW strike with a nearly vertical dip (Fig. 3.4b). Major mineral constituents are quartz, fine disseminated chlorite and minor amounts of chalcopyrite.

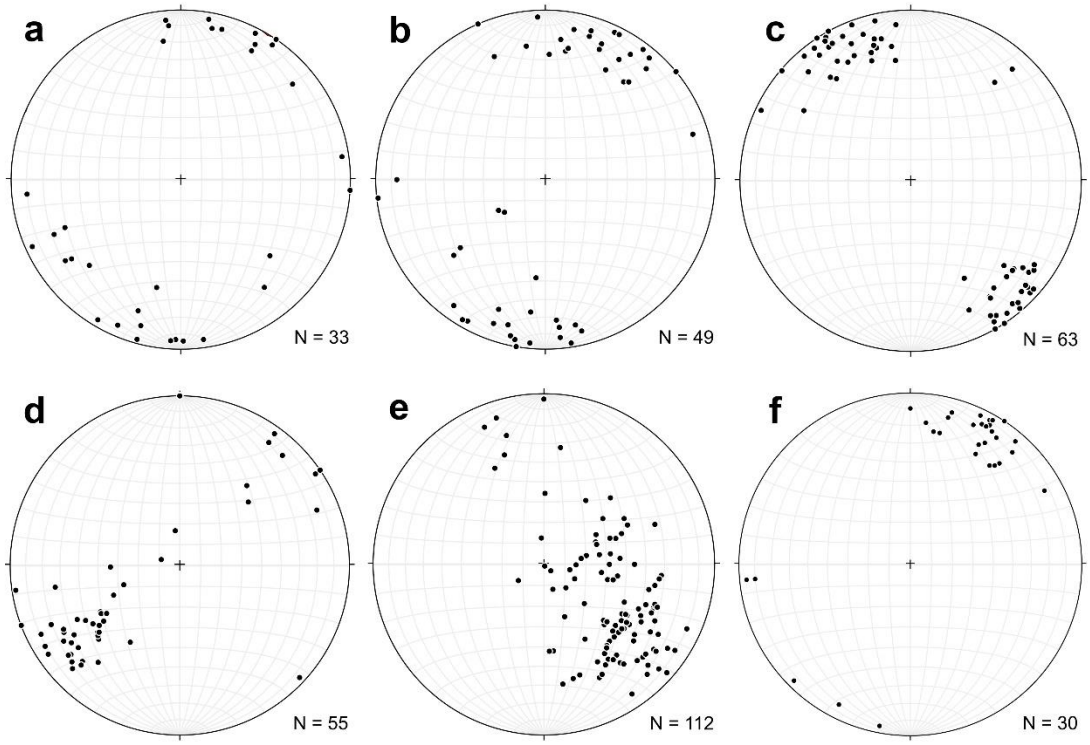


Fig. 3.4) Equal angle stereoplots of structural features of the Allihies Mining District showing the poles according to the measured planar structures (Key: Kamb contours in standard deviation, interval 2, significance level 3; created with Stereonet (Allmendinger et al. 2013, Cardozo and Allmendinger 2013)). a) Mineralized quartz veins. b) Smaller E-W quartz veins. c) Cleavage $S_{1,\ host}$ of the host rock sediments. d) Bedding-cleavage intersection lineations showing steep plunge. e) Bedding of the host rock sediments (Caha Mountain Formation). f) Jointing within the host rock sediments.

Figure 3.5 (and Dig. App.) displays the extent of the underground workings at Mountain Mine, where it is evident that the E-W Lode and the New E-W Lode are connected by the N-S Lode. It is important to note that the E-W Lode extends to the West of N-S Lode while the New E-W Lode extends to the East of N-S Lode. Both extensions pinch out laterally.

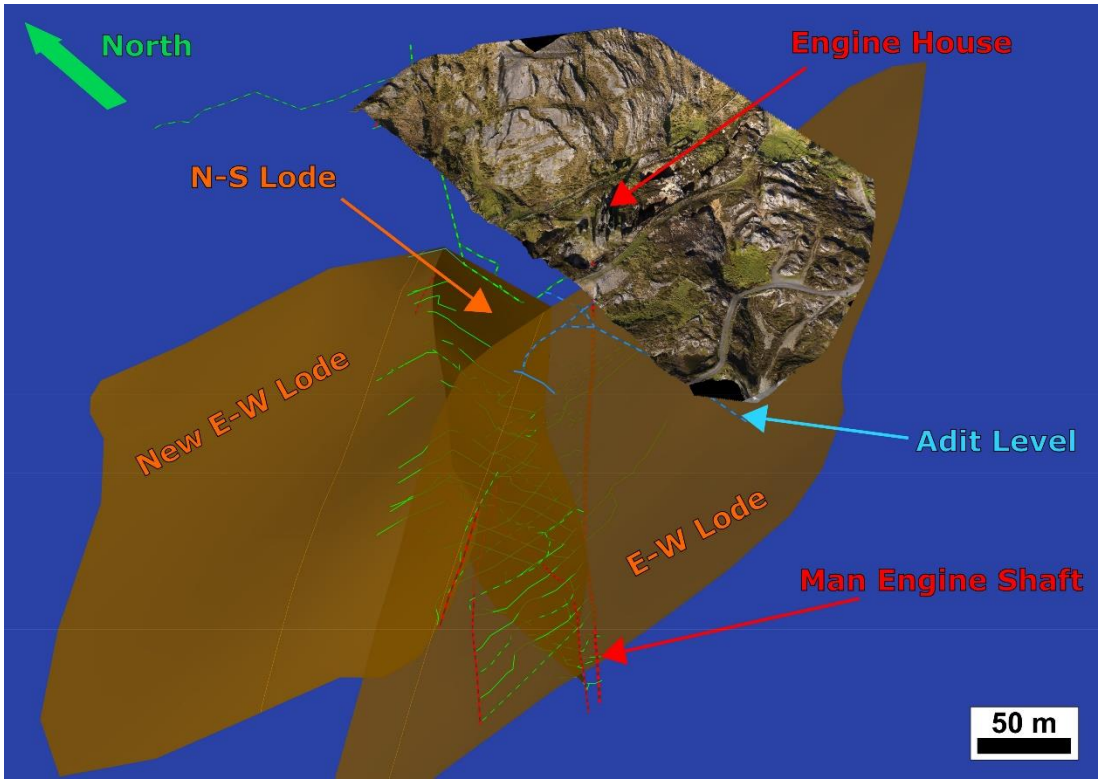


Fig. 3.5) 3D model of the major lodes and the underground workings at Mountain Mine. This model is a combination of a drone photogrammetry model, Bing™ Satellite Maps (2016), metadata for the SRTM digital terrain model (Jarvis et al. 2008) and historic mining plans (Wilson and Powell 1956).

In places, sets of multiple sub-parallel and closely spaced veins form lodes with a maximum surface outcrop of up to 18 m in width and up to 160 m in length (Fig. 3.6). The Marion Lode (Fig. 3.3a and Fig. 3.6) is formed by multiple generations (G1-G3) of E-W striking mineralized and brecciated quartz (G1), mineralized quartz (G2) and sub-horizontal unmineralized thinner quartz (G3). Corrugations on the vein wall of (G1) and rotated vein fragments indicate strike slip movement parallel to the vein orientation (Fig. 3.6).

Mineralization of the large orebodies is dominated by chalcopyrite with minor amounts of bornite and late veinlets of tetrahedrite/tennantite. Aggregates of fine-grained chlorite and late cavity-fill siderite with minor calcite, associated with malachite were found on spoil material from Caminches Mine (Fig. 3.2).

Pockets of clear, vuggy quartz crystals (up to 2 cm) are present in the outcrop of the massive Coom Lode.

At the surface, most of the lodes and the smaller E-W veins do not show any evidence of copper mineralization. Malachite staining occurs only at fresh outcrops of the historical mines. Due to the lack of free carbonate within the sediments, malachite can be completely absent. Traces of reddish goethite staining, as well as extensively altered chalcopyrite can be found about 20 to 40 cm below the surface within the veins. Apparently barren, but mineralized veins were identified by the presence of epimorphs caused by weathered sulphides and the internal reddish staining from iron hydroxides, often visible through the partially translucent quartz as pale red staining.

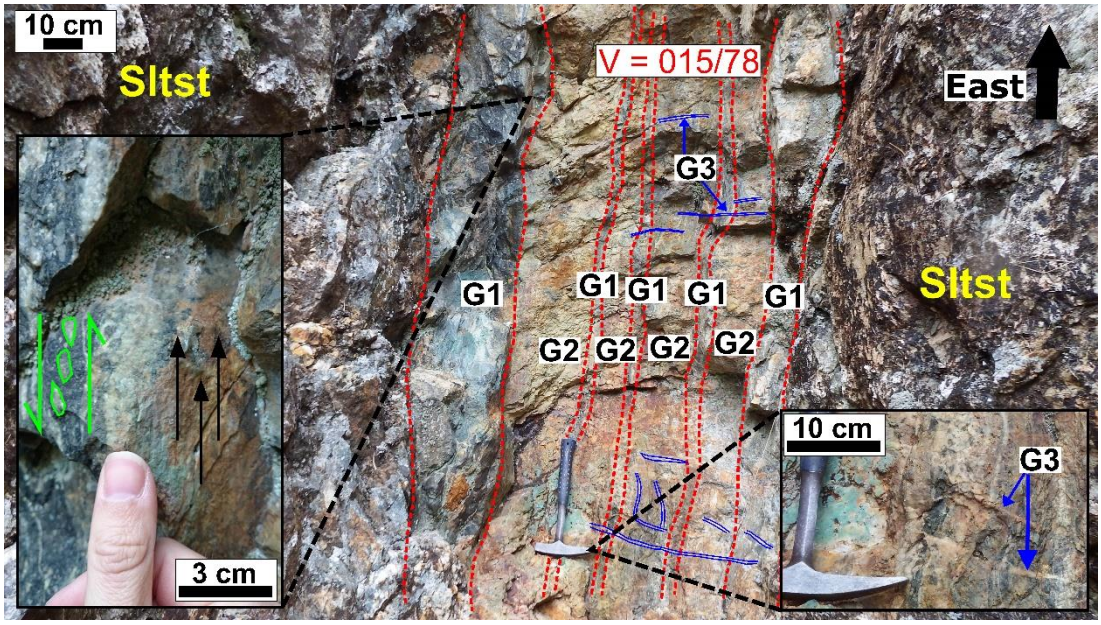


Fig. 3.6) Photographs of pre-Variscan structures observed in the field of the Allihies Mining District: Outcrop at Marion Lode showing 3 different vein generations (G1-G3) in the siltstone (Sltst). The dip direction of the lode is V = 015/78. The magnification inset (left) shows anticlockwise rotated vein clasts and corrugations (black arrows) on the vein surface, which indicate strike slip movement. The magnification (right) shows the 3rd vein generation (G3) cross-cutting the previous generations with a sub-horizontal orientation.

Syn-Compressional structures

Large scale SW-NE trending faults cut the sedimentary succession into elongate blocks up to 550 m lateral length, and result in predominantly sinistral offset of the E-W faults with a maximum dislocation of 17 m observed near the New E-W Lode (Fig. 3.7a). SE-NW to SSE-NNW striking faults (e.g. Cornish Village Fault, Fig. 3.2 and Fig. 3.7a) constrain northern and southern boundaries of the fault blocks. All ESE-WNW trending veins are affected by oblique faulting with lateral sinistral offsets of up to 83 m (Fig. 3.7b and Fig. 3.7c).

Thin beds (max. 30 cm) of the competent sandstones were found boudinaged in between layers of less competent siltstones. Penetrative cleavage is clearly visible within the siltstones, but less distinctive within the sandstones. The cleavage in the slates has a phyllitic texture and a high amount of sericitic, fine crystalline mica. Cleavage $S_{1,\ host}$ has a general SW-NE strike with a sub-vertical dip (Fig. 3.4c). Some of the early quartz veins (e.g. at Great Mountain Mine North and Coom Mine, Fig. 3.7b and Fig. 3.7c) show clear evidence of syn-compressional cleavage development (Fig. 3.8a), S_1 cleavage-refraction in the veins compared to the surrounding siltstones (Fig. 3.8b) and cataclastic deformation (Fig. 3.8c). Smaller E-W veins sometimes display asymmetric folding, cleavage and boudinage.

Second and third order step folds show bedding-S_1-cleavage intersection lineations with a mean plunge of 47 degrees to the southwest (N = 55, Fig. 3.4d). These folds have an asymmetrical step geometry with limbs dipping from the northwest to the southeast with a shallow to vertical angle (Fig. 3.4e). Metre-scale joints observed are generally oriented SE-NW with a sub-vertical dip (Fig. 3.4f).

Other compressional structures (Fig. 3.3b) include saddle reef quartz veins up to one metre wide and 10 cm thick (Fig. 3.8d), and en echelon quartz tension gash arrays in semi-brittle shear zones ranging from 40 cm to several metres in length. These vein types host disseminated chlorite, as well as aggregates of chlorite. Subvertical extension related to subsequent tectonic compression

led to the development of shallow dipping quartz veins within the earlier extensional lodes.

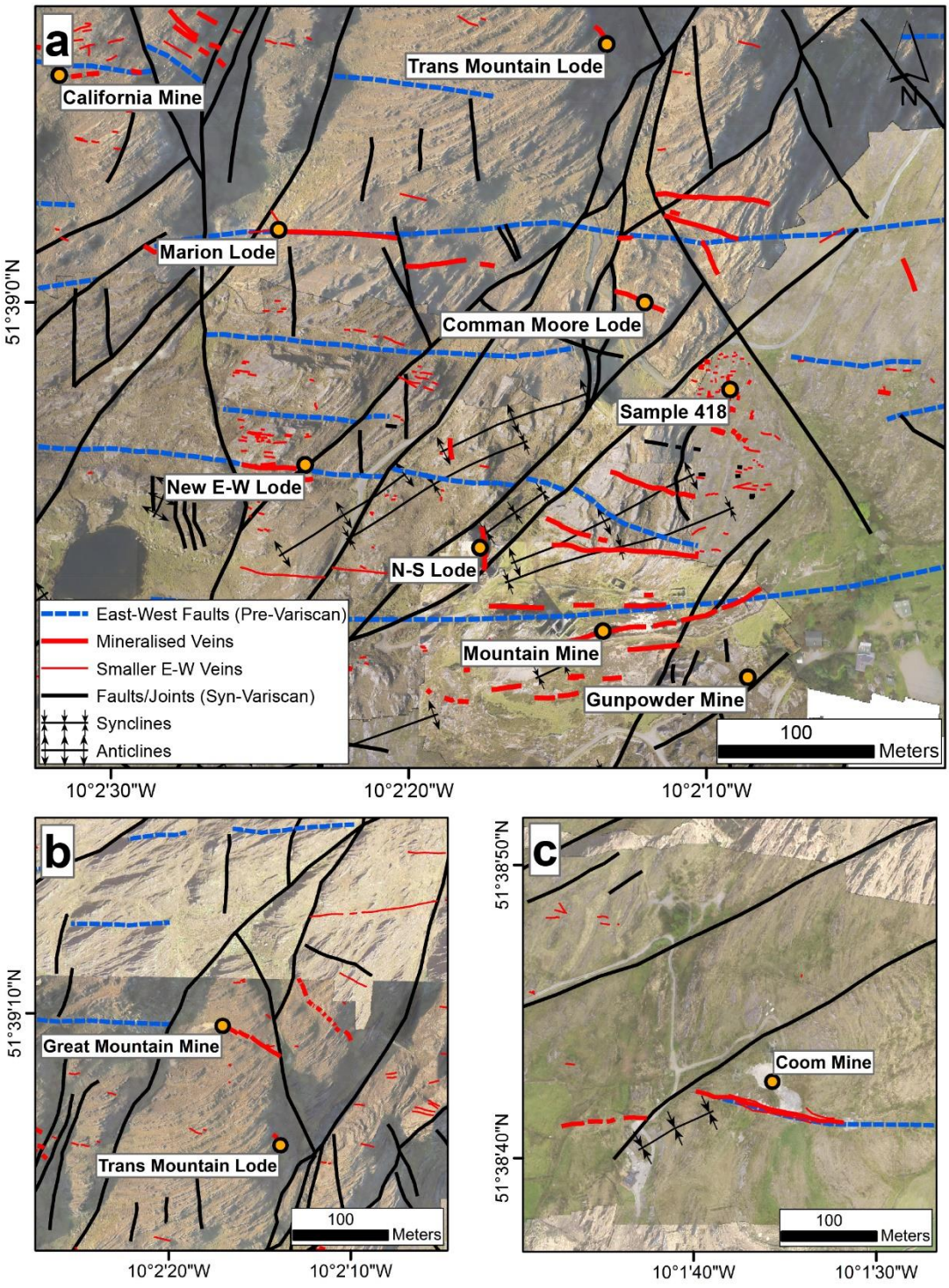


Fig. 3.7) Map with syn-Variscan structures affecting the pre-Variscan faults and veins (drone maps and Bing™ Satellite Maps (2016), including field analysis and modifications from Reilly (1986)). a) The major lodes of the

Mountain Mine Area with pre- and syn-deformation structures. b) Is showing the sinistral faulted lode of Great Mountain Mine (NW of Mountain Mine Area, see Fig. 3.2). c) Sinistral faulting of Coom Lode (ESE of Mountain Mine, see Fig. 3.2).

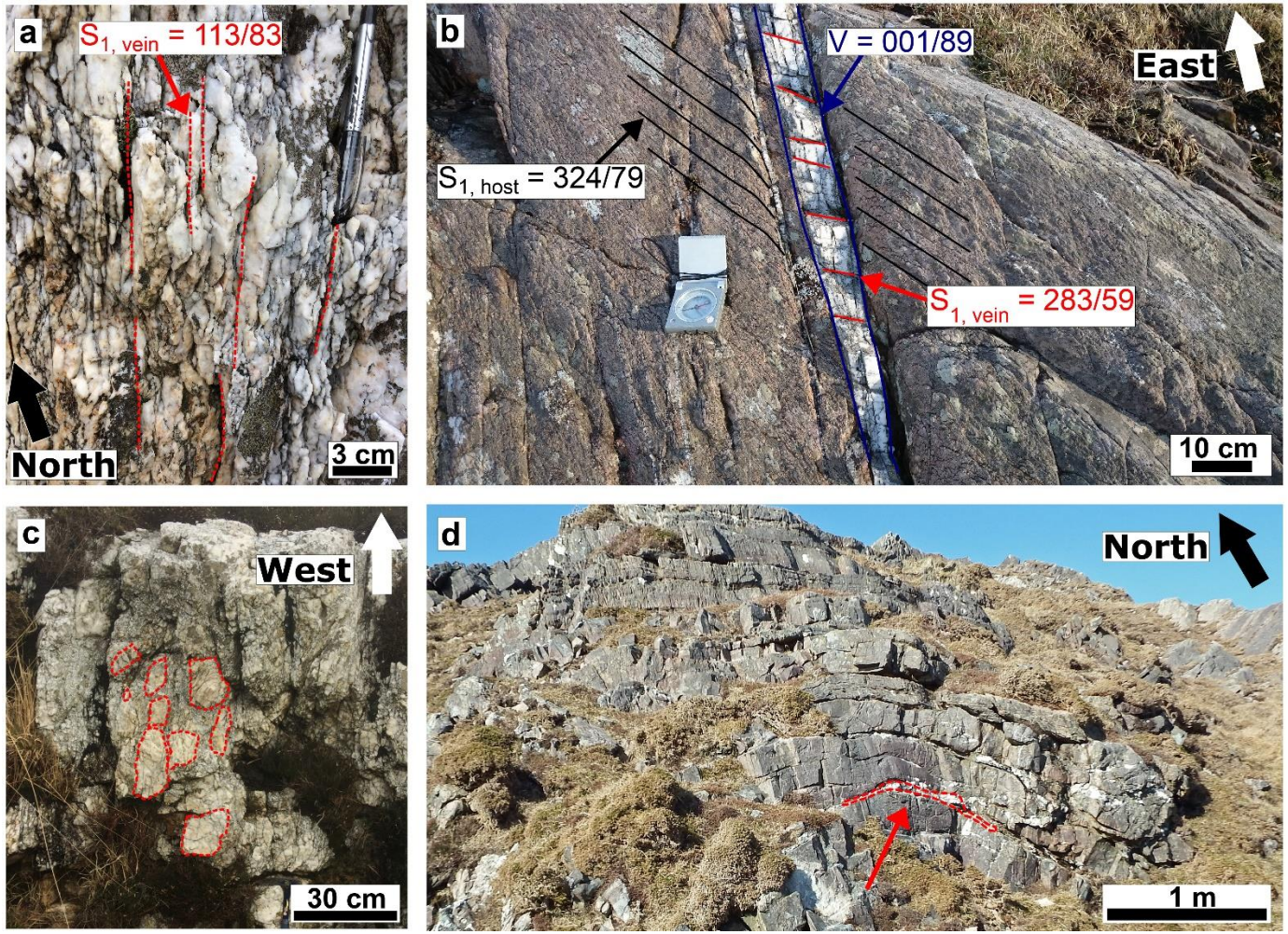


Fig. 3.8) Field observations of the syn-Variscan structures at Allihies. a) Cleavage (dip direction $S_{1, vein}$ = 113/83) within the Northern Lode of Great Mountain Mine. b) Smaller E-W vein north of Mountain Mine displaying the cleavage within the vein ($S_{1, vein}$ = 283/59) and the cleavage of the hosting siltstone $S_{1, host}$ = 324/79 which aligns parallel to the vein orientation V = 001/89. c) Cataclastic deformation at the eastern end of Coom Lode. d) Syn-compressional saddle reef quartz veins occurring at the fold axis of second order folds.

3.5.2 Vein petrography and microstructures

Early extensional E-W veins

Combined reflected and transmitted light microscopy show a coeval paragenesis of elongate blocky quartz and chalcopyrite mineralization within veins (Mountain Mine, Fig. 3.9a). Quartz grains with cogenetic chalcopyrite and bornite with chalcopyrite exsolution lamellae were found in a sample from Mountain Mine spoil. Both minerals are partially surrounded by chalcocite of the same generation. Alteration seams with blue covellite and goethite occur around the sulphides as a result of supergene alteration. Parts of the mineralized veins are cross-cut by later quartz veinlets. Some specimens from Mountain Mine (Gunpowder Mine, Fig. 3.3a) contain quartz-chalcopyrite-tetrahedrite/tennantite veins, which are cross-cut by later tetrahedrite/tennantite-quartz-chalcopyrite veinlets. Minor amounts of specular hematite occur within a sample from Coom Lode (Fig. 3.2). Reflected light microscopy on the historic molybdenite material from Mountain Mine (BM.1964,R231) indicate a syngenetic intergrowth of quartz, molybdenite and minor chalcopyrite (Fig. 3.9b). Figure 3.9c shows the generalised paragenetic sequence of the E-W veins with all minerals observed in this study at the different mines of the Allihies District.

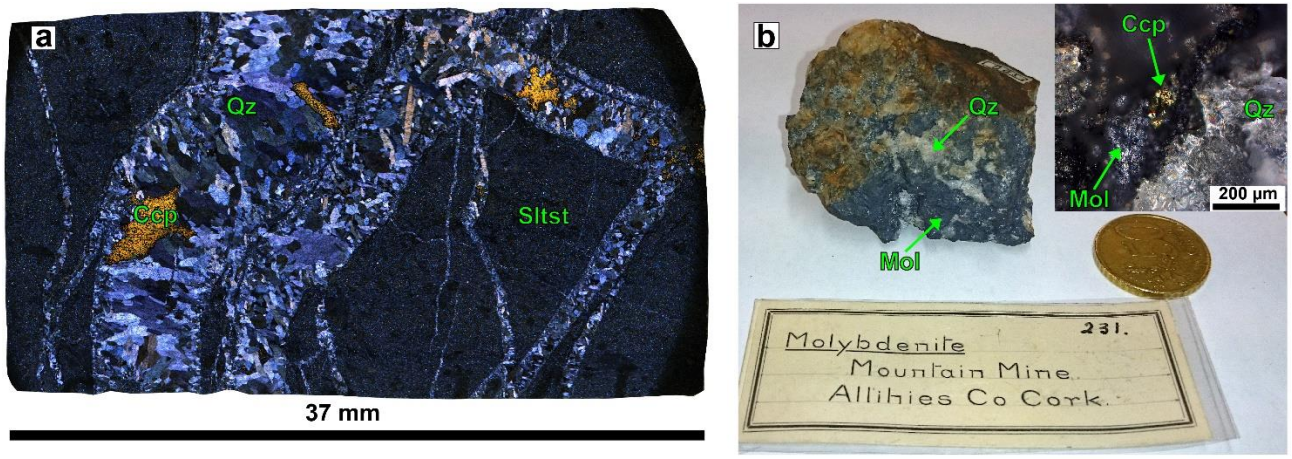


Fig. 3.9) Microphotographs of samples from the Allihies Mining District. a) Mineralized quartz (Qz) veins within fine grained siltstone (Sltst) show syntaxial elongate blocky crystals with cogenetic chalcopyrite (Ccp) (xpl, Mountain Mine Underground). b) Historic quartz (Qz) vein with molybdenite (Mol). The sample was collected by Sir Arthur Russell in 1918 (BM.1964,R231; National History Museum of London). The smaller microscopic image (top right) shows the syngenetic intergrowth of molybdenite (Mol) with chalcopyrite (Ccp) within the quartz (Qz) vein. c) Paragenetic sequence of the pre-Variscan minerals within the quartz veins at the Allihies Mining District.

Syn-Compressional veins

The syn-compressional veins are mainly formed by stretched (Bons *et al.* 2012) to fibrous quartz crystals with sweeping type to no undulous extinction (Trouw *et al.* 2009). The fibrous quartz crystals are perpendicular to the vein walls but can be curved within the vein itself. As there are no clearly visible median zones, these veins are dominated by antitaxial crystal growth (Bons *et al.* 2012).

Compressional deformation of E-W veins

Microstructural examination of oriented, mineralized, E-W striking quartz veins (Sample 418, Fig. 3.3a) show a predominance of syntaxial elongate blocky quartz crystals (Fig. 3.9a and Fig. 3.10, Sample 418_A). The larger crystals in the vein centre have no or sweeping type undulous extinction with lobate contacts due to grain boundary migration (Trouw *et al.* 2009). The smaller crystals at the margin with the host rock show patchy undulous extinction (Trouw *et al.* 2009). WSW to ENE striking, intergranular secondary fluid inclusion trails occur in sample 418_B2 (Fig. 3.10). Vein samples 418_B1 and 418_B3 (Fig. 3.10) show centimetre wide, E-W striking cataclastic zones with anhedral and subhedral microcrystals in between the elongate blocky areas. In the case of vein B3, these cataclastic zones are associated with microfractures. Similar to vein A, the smaller crystals in vein B show a patchy undulous extinction, while the larger elongate blocky crystals show sweeping extinction and have lobate contacts. Sample 418_B1 (Fig. 3.10) shows en echelon microveins with sinistral movement indicators along E-W strikes. In vein 418_B3 intensive brecciation of the elongate blocky crystals is visible with fine grained zones of subhedral crystals and cataclastic seams around microfractures (Fig. 3.10, vein B3 magnified images).

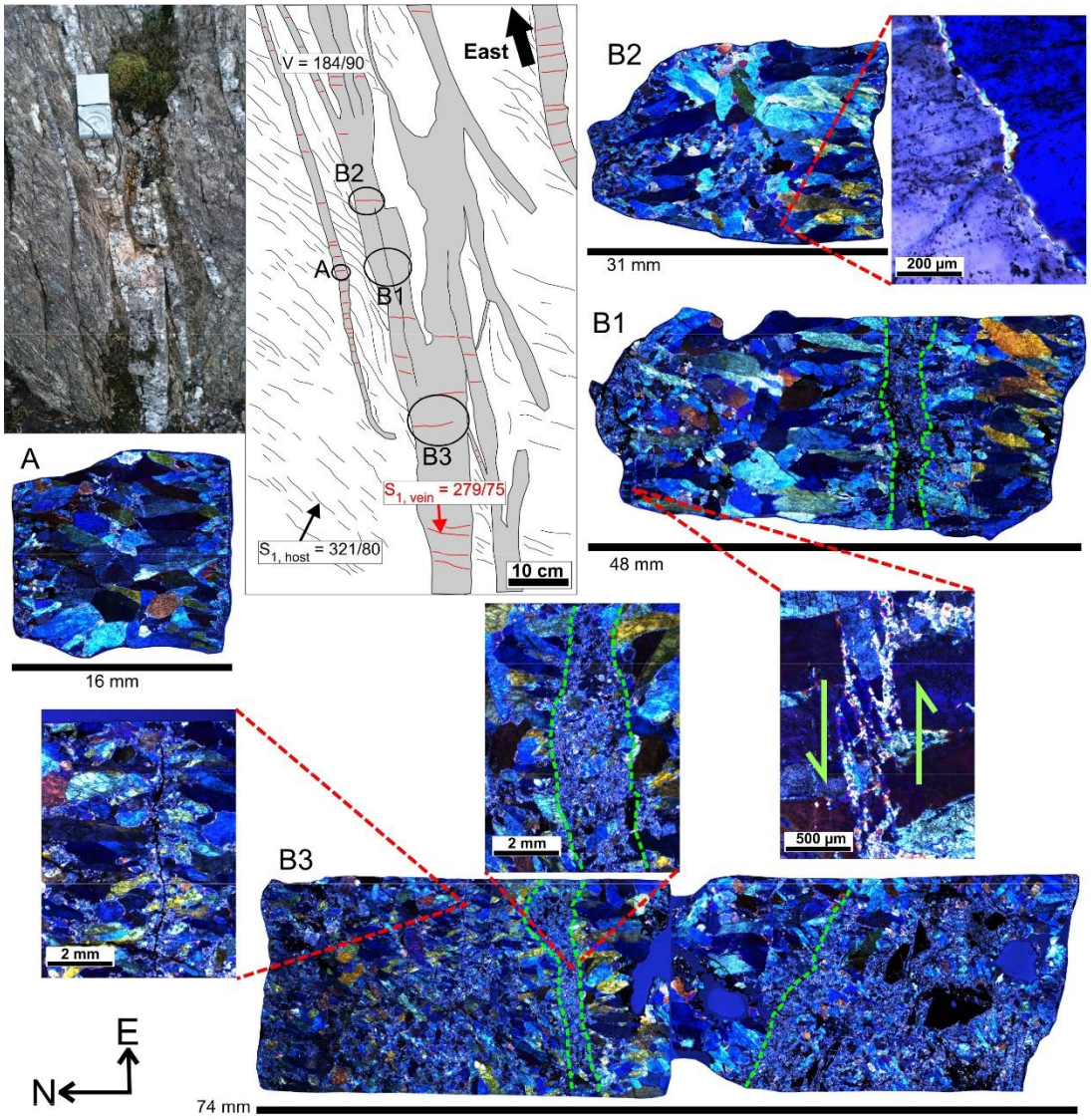


Fig. 3.10) Mineralized E-W veins collected North of Mountain Mine (samples 418). The figure shows the E-W strike of the veins (dip direction V = 184/90), their cleavage $S_{1, vein}$ = 279/75 and the cleavage of the hosting, fine grained siltstone $S_{1, host}$ = 321/80. The false colour microphotographs were captured (xpl) from thin sections (>30 µm) cut perpendicular to the vein cleavage $S_{1, vein}$ = 279/75. Vein A is a syntaxial quartz vein with elongate blocky crystals. Vein B1 shows elongate blocky crystals with a cataclastic zone of smaller, subhedral crystals to the northern vein boundary (the colour change at the southern part of B1 is caused by image stitching effects). The magnification shows N-S striking intergranular secondary fluid inclusion trails. In vein B2, the elongate blocky crystals are cross-cut by a cataclastic zone to the northern grain boundary and one in the middle of the vein. The magnification

shows a micro en echelon vein which indicates sinistral movement. Vein B3 shows intensive brecciation of the elongate blocky crystals.

3.5.3 Fluid inclusion microthermometry

Following the structural field observations, the quartz vein samples for fluid inclusion microthermometry were classified into 11 extensional (Pre-Variscan) E-W veins, and two syn-compressional (Syn-Variscan, saddle reef and en echelon) vein samples (Fig. 3.11 and Appendix B). Eight of the extensional (Pre-Variscan) samples are mainly mineralized with chalcopyrite, as well as minor tetrahedrite/tennantite (Sample JL_AH_367B, Gunpowder Mine, Appendix B), and molybdenite (R231A2, Mountain Mine, Appendix B). Minor amounts of hematite were detected in the vuggy quartz vein sample from Coom Mine (JL_AH_423, Appendix B). Three vein samples do not show any mineralization (but owing to their structural settings they were classified as extensional Pre-Variscan E-W veins). The two syn-compressional (Syn-Variscan) vein samples are unmineralized/barren (Appendix B). All fluid inclusions within the quartz veins show a major liquid (L) phase and a minor vapour (V) phase with various volumes (Appendix B). A CO_2 phase was not detected. Generally, the quartz grains are anhedral to subhedral which prevents the clear identification of individual growth zones. The quartz veins show many secondary and pseudosecondary fluid inclusions along healed fractures. These inclusions were avoided. The primary fluid inclusions (focus of this study) occur as clusters along growth zones and are not related to any fractures (Goldstein and Reynolds 1994, Appendix B). For each sample the primary inclusions were classified into several fluid inclusion assemblages (FIA, Goldstein and Reynolds 1994). The major criteria for the individual assemblages are the volume of the vapour phase at room temperature, the fluid inclusion shape, as well as their petrographical association (growth zones) within the vein sample (Appendix B2). Owing to the complexity of growth zonations within the quartz grains a clear chronological placement of the individual fluid inclusion assemblages (FIA) was not possible.

Extensional E-W veins

Fluid inclusion assemblages in the mineralized, quartz veins, including the historic molybdenite sample, are generally oval to irregular shaped and consist of an undersaturated liquid-rich phase, and a vapour phase between 0.5 and 15 volume percent (Appendix B). Homogenisation temperatures T_h range between 121 and 272 °C (Fig. 3.11a-l, Appendix B). The salinities vary between 3.2 and 25.4 wt% $NaCl_{equiv}$. The fluid inclusion assemblage FIA_367B.1 from the later tetrahedrite/tennantite-quartz-chalcopyrite veinlet from Gunpowder Mine (Fig. 3.11a-l, Appendix B3) shows higher homogenisation temperatures with a maximum of 314 °C and a mean salinity of 13.7 wt% $NaCl_{equiv}$ (n = 4). Some of the fluid inclusions from this veinlet decrepitated at temperatures from around 259 °C. The pockets of vuggy, clear quartz from the Coom lode, which indicate a late formation of the early extensional veins contain unaltered, primary fluid inclusions up to 60 µm (Appendix B) and display assemblages with very high salinities of up to 28.5 wt% $NaCl_{equiv}$ (FIA_423.2) and low homogenisation temperatures with a minimum of 74 °C (FIA_423.3, Fig. 3.11a-l, Appendix B3).

Overall, there is a large variety of fluid inclusion assemblages, whereby the fluids of the E-W mineralized, quartz veins range from moderate salinity and high homogenisation temperatures to high salinities and very low homogenisation temperatures. Similar trends are observed in the small E-W veins which are associated with the mineralized veins (Fig. 3.3a, Fig. 3.8b and Fig. 3.11a-l).

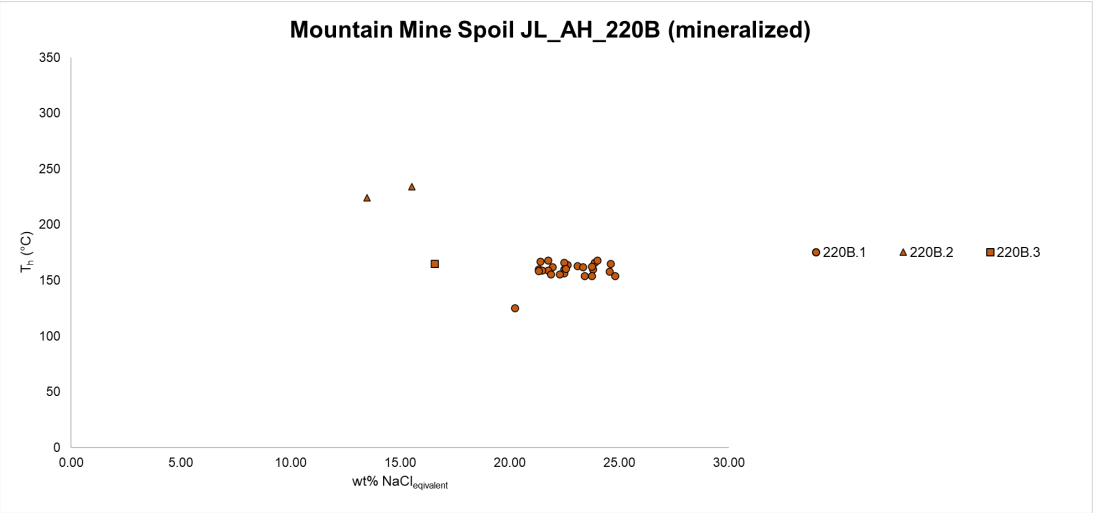
Syn-compressional veins

The fluid inclusions in the syn-compressional quartz veins are mainly elongate and the fluid inclusion assemblages consist of a liquid and a vapour phase with variable volumes between 0.5 and 5 vol.% (Appendix B). The inclusions have an average size of 10 µm (max. 22 µm) and the various assemblages display homogenisation temperatures ranging between 121 and 243 °C

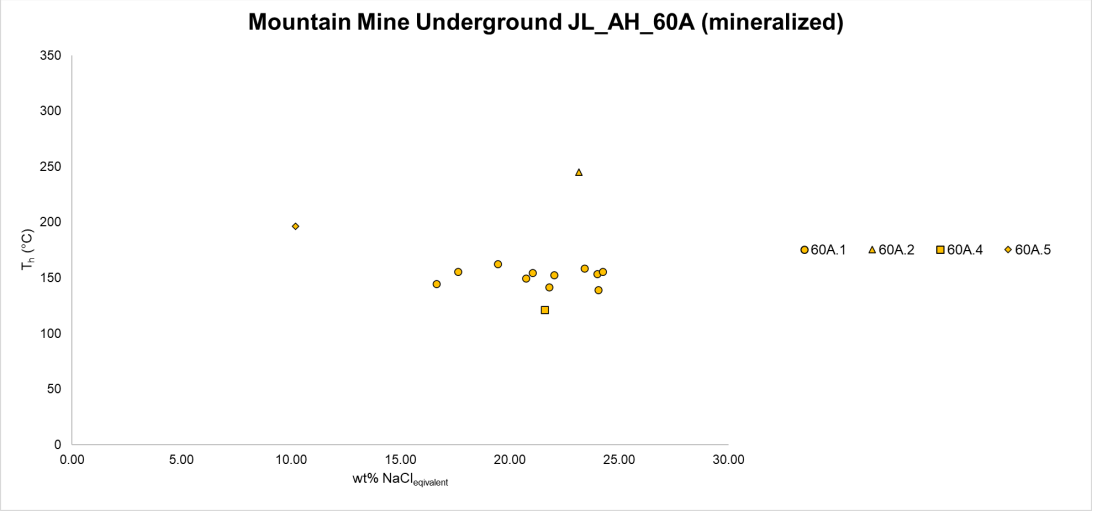
(outlier: 309 °C), and low to moderate salinities between 8.2 and 19.1 wt% $NaCl_{equiv}$ (Fig. 3.11m-o, Appendix B3).

Fig. 3.11) Fluid inclusions from samples of the Allihies District (see Appendix B3 for details). Plot of the salinity wt% $NaCl_{equiv}$ versus the homogenisation temperatures T_h (°C). The different colours show the various locations, and the symbols indicate the individual fluid inclusion assemblages (FIA) within one sample. a-l) Early extensional (Pre-Variscan) vein samples. m-o) Compressional (Syn-Variscan) vein samples.

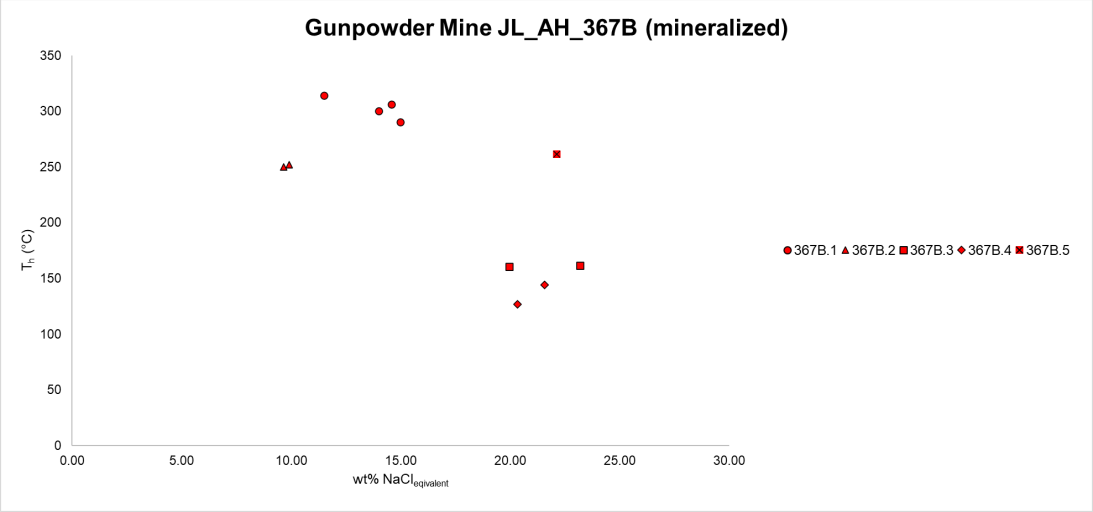
3.11a)



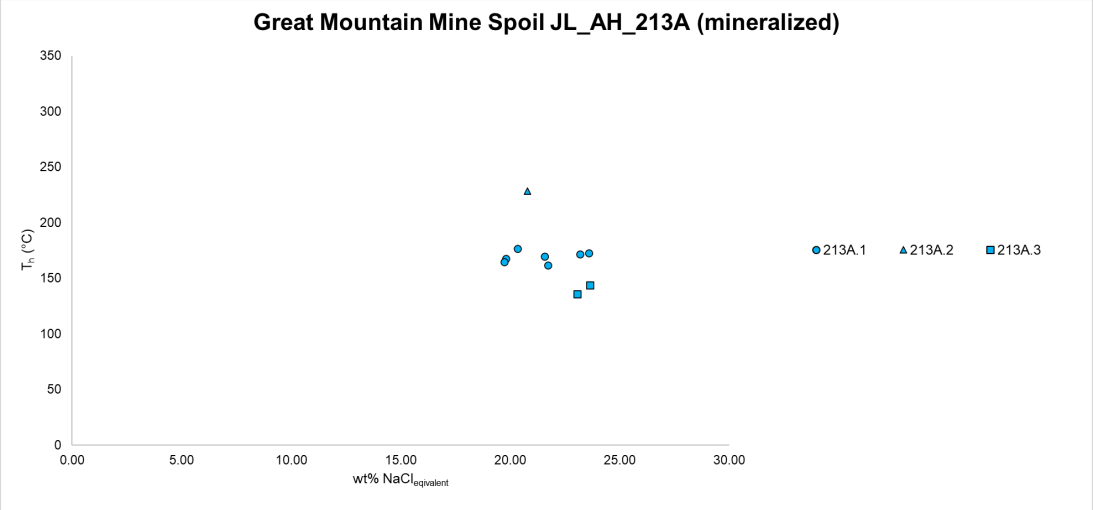
3.11b)



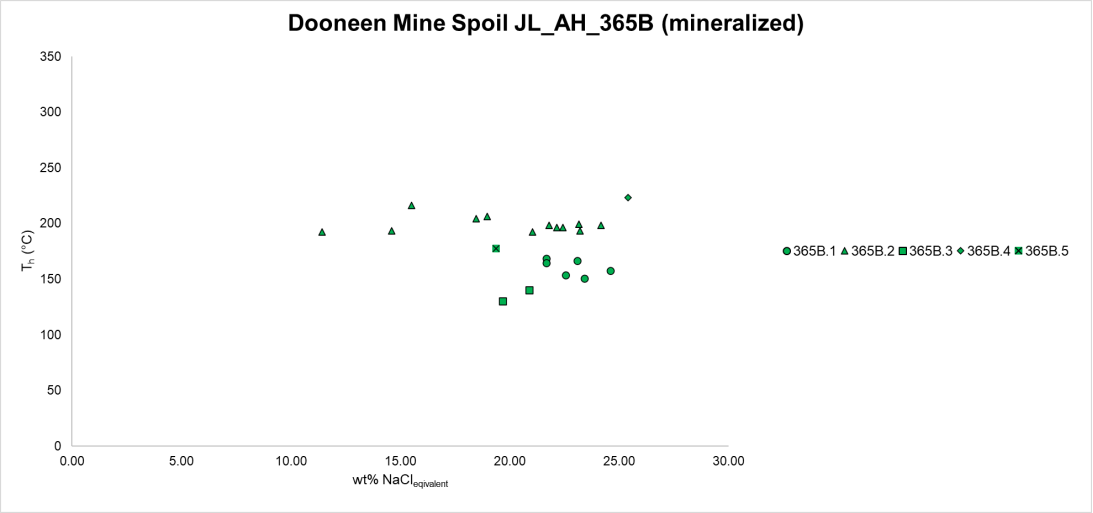
3.11c)



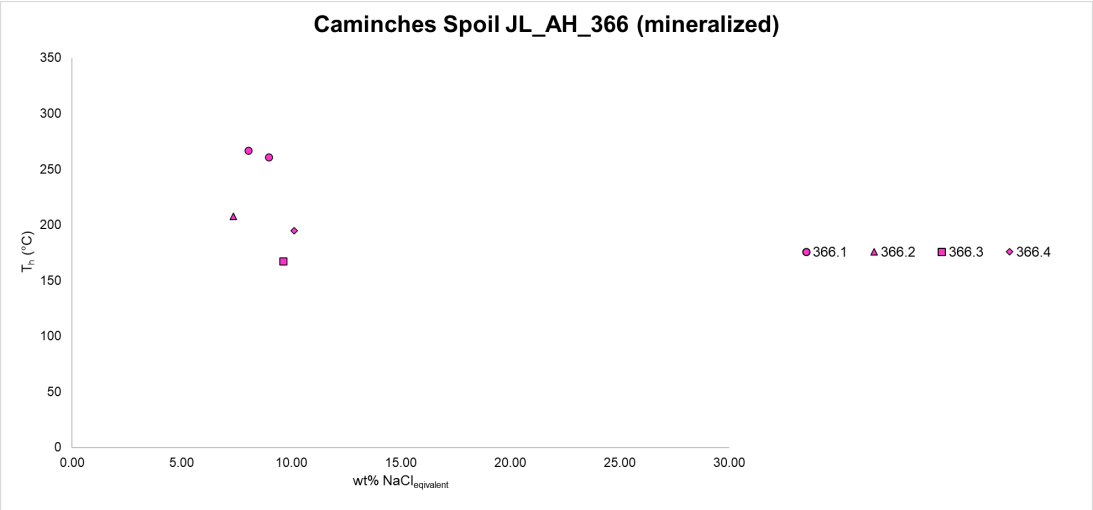
3.11d)



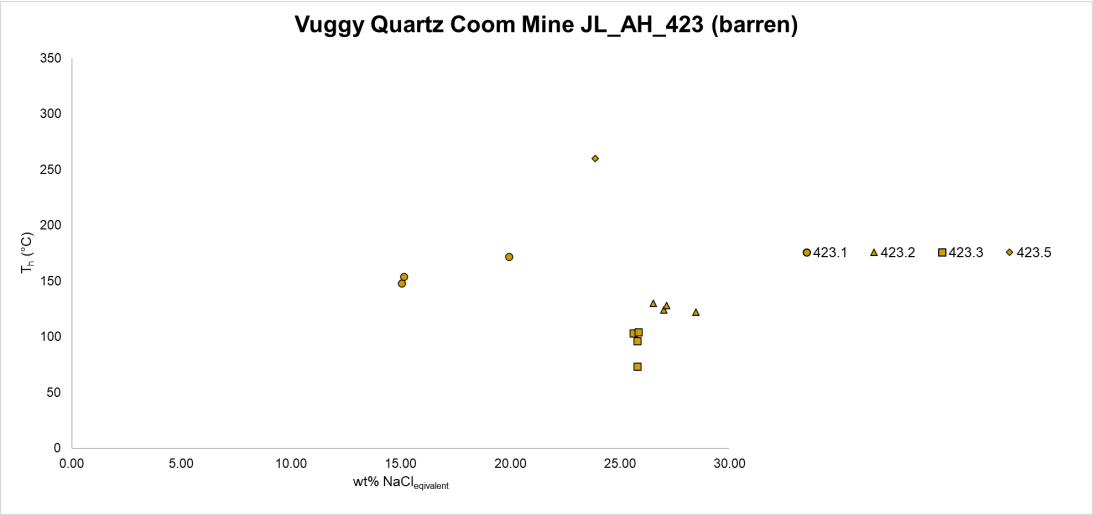
3.11e)



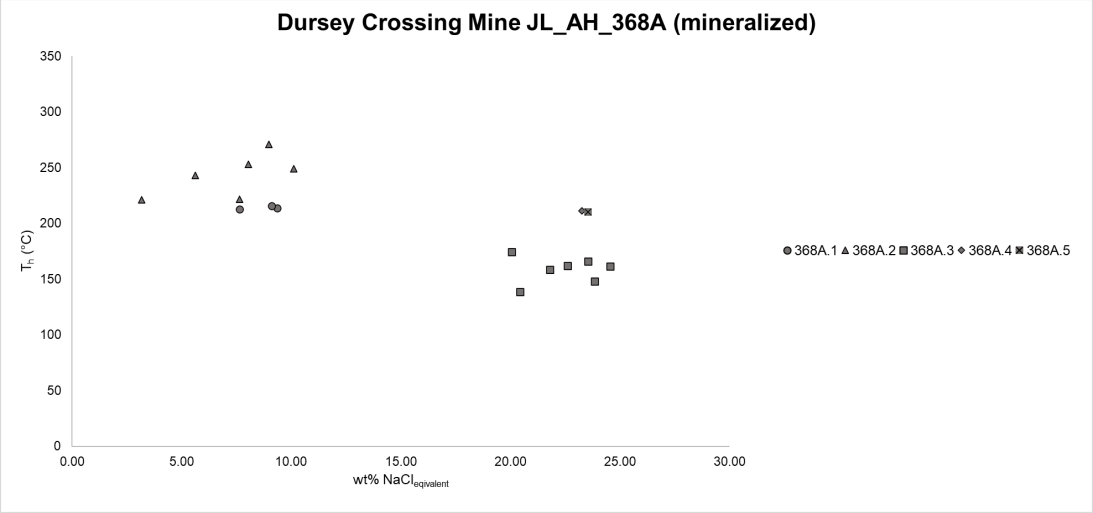
3.11f)



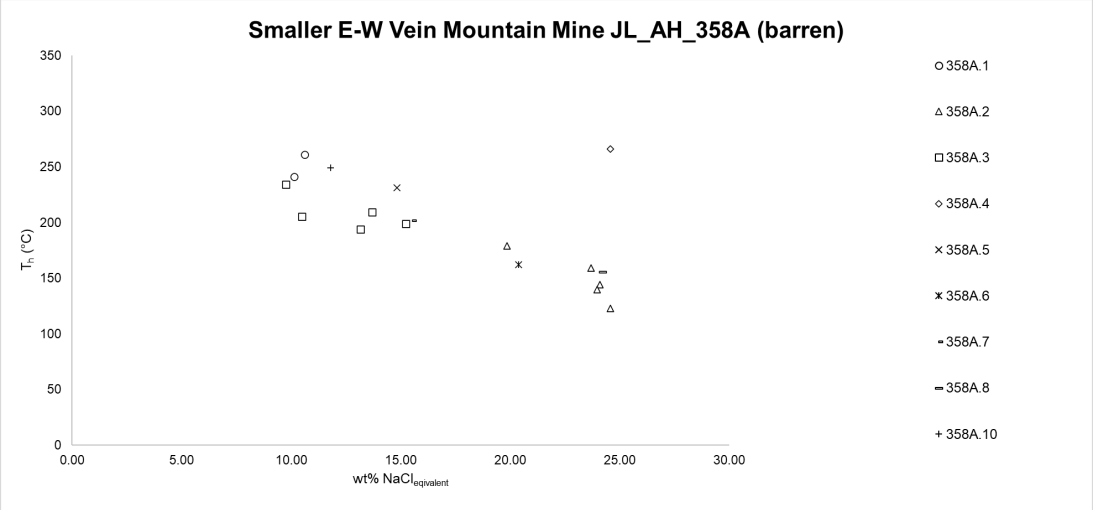
3.11g)



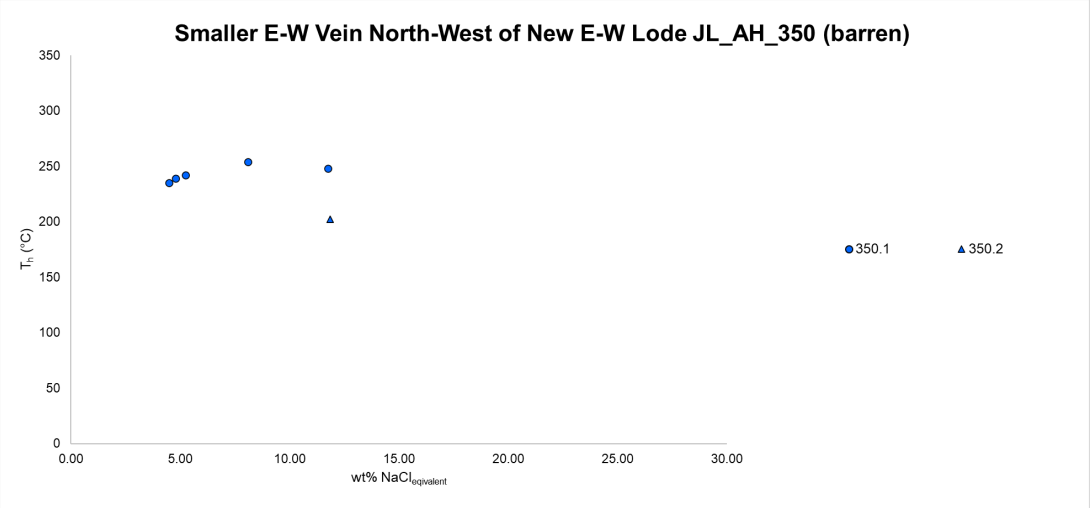
3.11h)



3.11i)



3.11j)


Smaller E-W Vein North-West of New E-W Lode JL_AH_350 (barren)
350
300
250
200
150
100
50
0
T_h (°C)
0.00
5.00
10.00
15.00
20.00
25.00
30.00
wt% $NaCl_{eqivalent}$
350.1
350.2

3.11k)

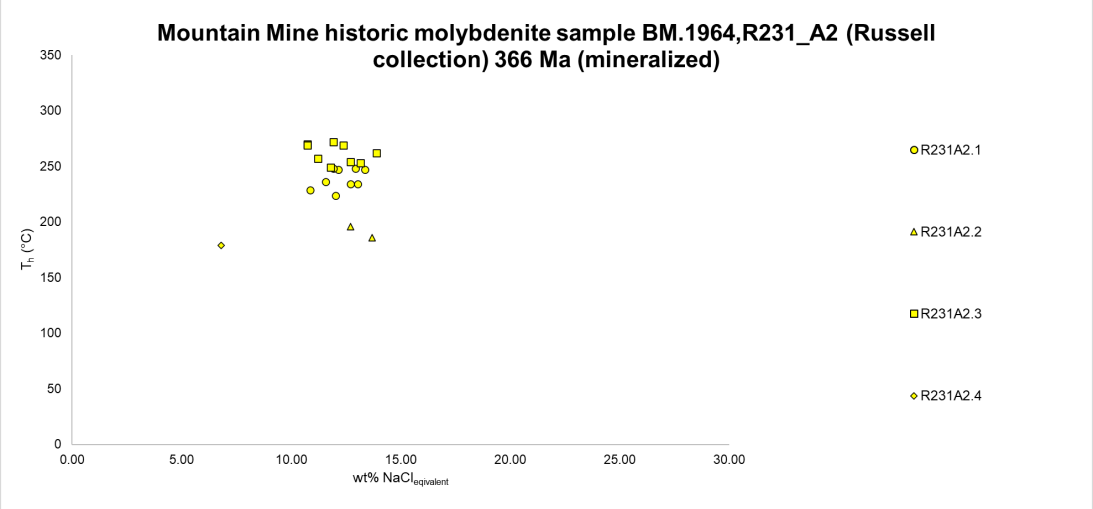
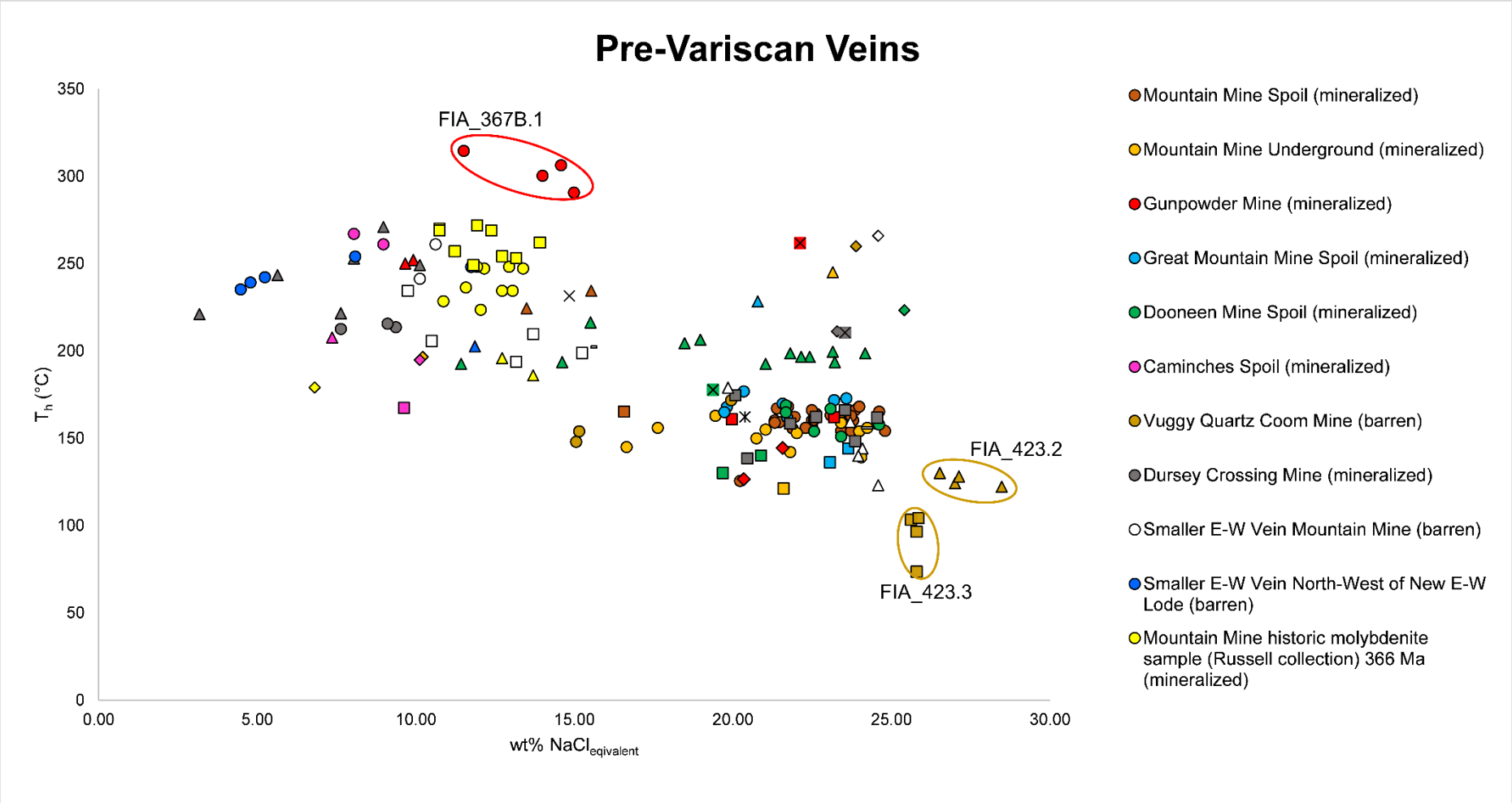
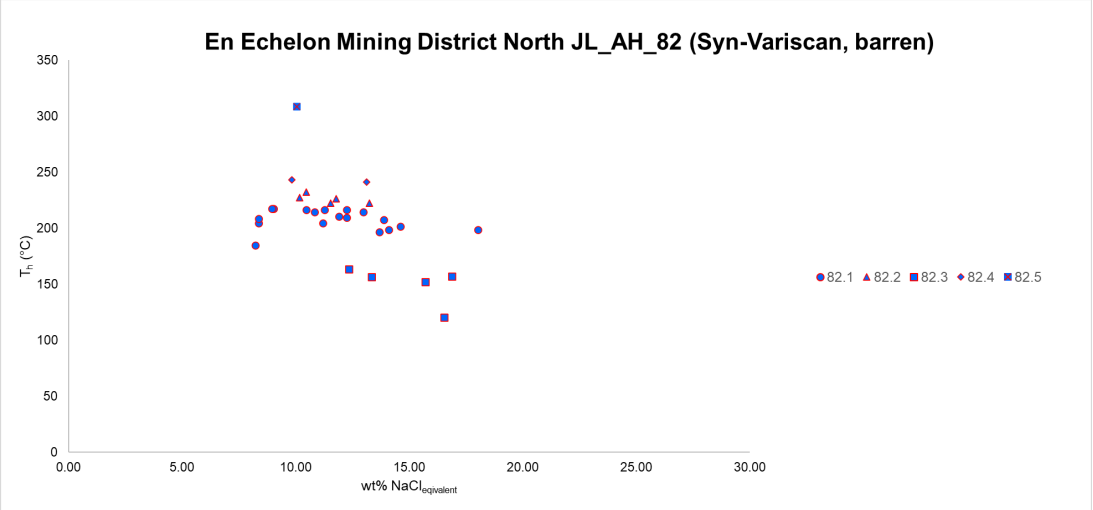

Mountain Mine historic molybdenite sample BM.1964,R231_A2 (Russell collection) 366 Ma (mineralized)
350
300
250
200
150
100
50
0
T_h (°C)
0.00
5.00
10.00
15.00
20.00
25.00
30.00
wt% $NaCl_{eqivalent}$
R231A2.1
R231A2.2
R231A2.3
R231A2.4

Fig. 3.11l)


Pre-Variscan Veins
FIA_367B.1
FIA_423.2
FIA_423.3
T_h (°C)
wt% $NaCl_{eqivalent}$
0
50
100
150
200
250
300
350
0.00
5.00
10.00
15.00
20.00
25.00
30.00
Mountain Mine Spoil (mineralized)
Mountain Mine Underground (mineralized)
Gunpowder Mine (mineralized)
Great Mountain Mine Spoil (mineralized)
Dooneen Mine Spoil (mineralized)
Caminches Spoil (mineralized)
Vuggy Quartz Coom Mine (barren)
Dursey Crossing Mine (mineralized)
Smaller E-W Vein Mountain Mine (barren)
Smaller E-W Vein North-West of New E-W Lode (barren)
Mountain Mine historic molybdenite sample (Russell collection) 366 Ma (mineralized)

3.11m)


En Echelon Mining District North JL_AH_82 (Syn-Variscan, barren)
350
300
250
200
150
100
50
0
T_h (°C)
0.00
5.00
10.00
15.00
20.00
25.00
30.00
wt% $NaCl_{eqivalent}$
82.1
82.2
82.3
82.4
82.5

3.11n)

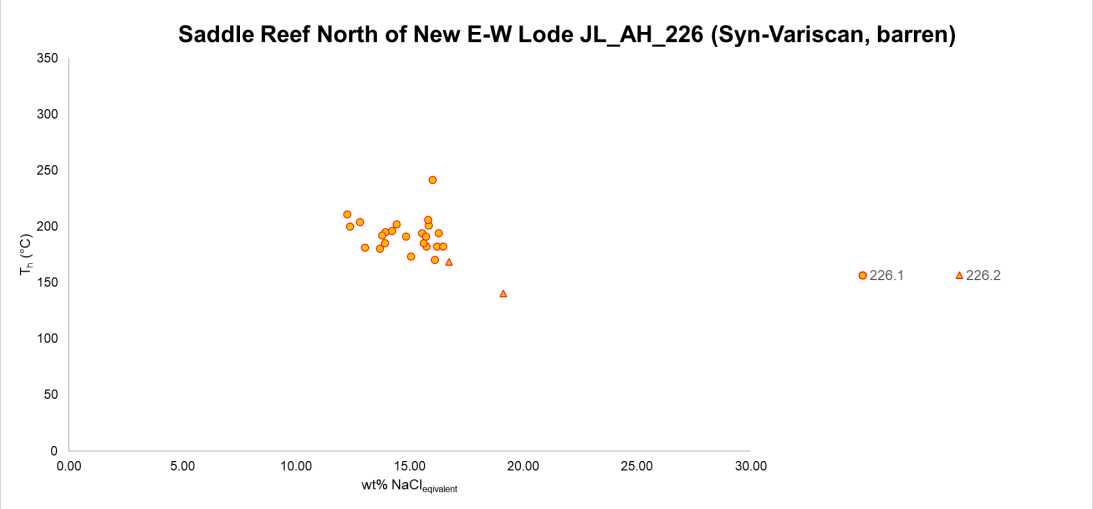
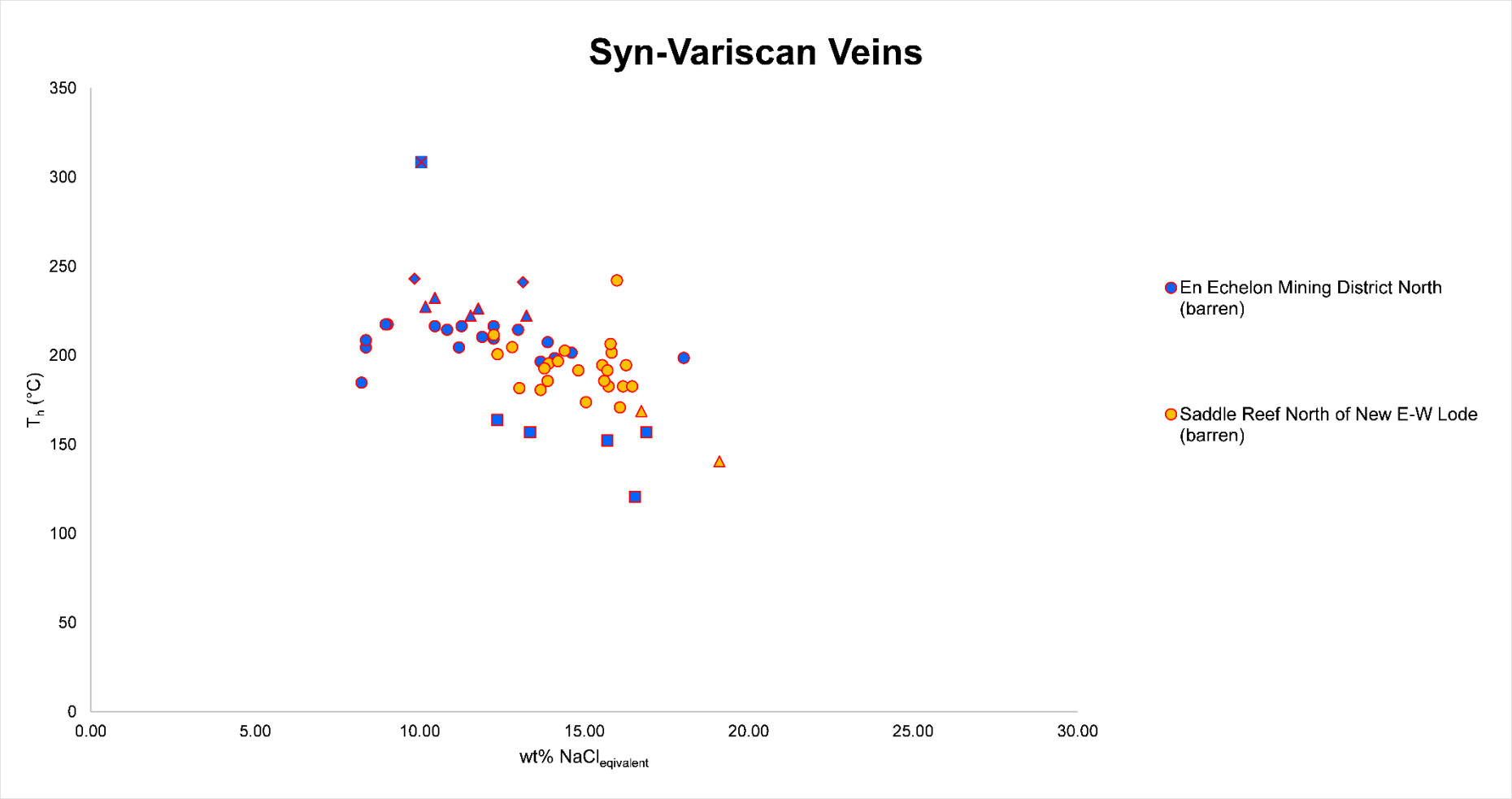

Saddle Reef North of New E-W Lode JL_AH_226 (Syn-Variscan, barren)
350
300
250
200
150
100
50
0
T_h (°C)
0.00
5.00
10.00
15.00
20.00
25.00
30.00
wt% $NaCl_{eqivalent}$
226.1
226.2

Fig. 3.11o)


Syn-Variscan Veins
350
300
250
200
150
100
50
0
T_h (°C)
0.00
5.00
10.00
15.00
20.00
25.00
30.00
wt% $NaCl_{eqivalent}$
En Echelon Mining District North (barren)
Saddle Reef North of New E-W Lode (barren)

3.5.4 Re-Os molybdenite geochronology

The fine grained (grain size < 2 mm) molybdenite sample from Mountain Mine spoil (BM.1964,R231, Fig. 3.9b) possesses 43.9 ± 0.2 ppm Re, 27.6 ± 0.1 ppm ^{187}Re and 169.1 ± 0.8 ppb ^{187}Os. The ^{187}Re-^{187}Os data yield to a model age of 366.4 ± 1.9 Ma for the molybdenite mineralization. The molybdenite sample from Caminches Mine spoil is also fine grained and has 3.83 ± 0.04 ppm Re, 2.41 ± 0.03 ppm ^{187}Re and 14.78 ± 0.16 ppb ^{187}Os. The ^{187}Re-^{187}Os model age is 367.3 ± 5.5 Ma.

Sample	*Sample wt (g)*	*Re (ppm)*	*±2σ*	^{187}Re *(ppm)*	*±2σ*	^{187}*Os (ppb)*	*±2σ*	*Model age (Ma)**	*±2σ*†	*±2σ*‡	*±2σ*§
BM.1964,R231, Mountain Mine	0.010	43.9	0.2	27.6	0.1	169.1	0.8	366.4	0.2	1.5	1.9
Caminches Mine	0.011	3.83	0.04	2.41	0.03	14.78	0.16	367.3	0.2	5.4	5.5

All data blank corrected (Re – 1.9 pg, Os – 0.8 pg with an $^{187}Os/^{188}Os$ of 0.201 ± 0.03)

*Model age calculated using the decay constant $^{187}Re = 1.666 \times 10^{-11}$ a^{-1} (Smoliar *et al.*, 1996; Selby *et al.*, 2007)

†uncertainty including only mass spectrometry uncertainty

‡uncertainty including all sources of analytical uncertainty

§uncertainty including all sources of analytical uncertainty plus decay constant

Table 3.1) Re-Os isotope data and model ages for the molybdenite samples from Allihies Mountain Mine (BM.1964,R231) and Caminches Mine (Fig. 3.2).

3.6 Discussion

Large E-W faults, such as the Coomnacronia-Killarney-Mallow Fault Zone and the Cork-Kenmare Fault Zone (Fig. 3.1, Naylor & Jones 1967; Capewell 1975; Price & Todd 1988; Meere 1995b; Vermeulen *et al.* 2000; Landes *et al.* 2003; MacCarthy 2007; Ennis *et al.* 2015) played an important role in the development of the Munster Basin. These major faults are part of a southwards progressing extensional fault system (Landes *et al.* 2003). Mineralized vein systems follow the same strike as these basin controlling structures (Fig. 3.12a). The E-W faults would have acted as pathways for the mineralising fluids.

Recent sulphur isotope studies on chalcopyrite from the Allihies Mining Area (Spinks *et al.* 2016) show consistent negative $\delta^{34}S$ values (-16.9 to -10.4 ‰). These values imply a biogenic sedimentary origin. This could indicate copper remobilisation from the host sediments into the quartz veins. Another possibility would be a more distant copper source. Meere & Banks (1997) described a basinal sediment infill of over 6 km. As the pre-Variscan, extensional E-W faults can be laterally extensive (e.g. Williams 2000; Landes *et al.* 2003; MacCarthy 2007; Ennis *et al.* 2015; Fig. 3.1), it is possible, that their extension to depth can reach the basement. According to seismic interpretation from Landes *et al.* (2003) a P-wave velocity change in 13 – 14 km depth possibly indicates the termination of the basin controlling, E-W striking Cork-Kenmare Fault Zone (Fig. 3.1). This suggests that some of the major extensional fault zones extend below the basin infill.

The 3D model (Fig. 3.5) displaying the historic underground workings shows that the North-South Lode connects to the East-West Lode and the New East-West Lode at Mountain Mine. Previous workers described this arrangement as a Z-shaped structure of the Mountain Mine Lodes (e.g. Fletcher 1969; Reilly 1986). This is a misleading description, as both the E-W striking lodes extend laterally beyond the N-S Lode before pinching out (Fig. 3.3a and Fig. 3.5) This structure could be interpreted as a transfer fault or breached relay ramp

(Walsh & Watterson 1991; Fossen & Rotevatn 2016) that developed during the early extensional phase.

The smaller E-W striking quartz veins appear to be barren at the surface. Their classification was only possible with the help of the drone and satellite imaging as it is clearly visible on Figure 3.3a, that the smaller E-W striking veins are always aligned parallel to the larger mineralized lodes. It seems that the smaller E-W veins are branches of larger lodes in their immediate proximity. According to this, the smaller E-W veins and the mineralized lodes can be classified together as pre-Variscan early extensional veins. Due to extensive surficial leaching processes mineralized quartz veins could be misinterpreted as barren. Reilly (1986) already mentioned this “apparently barren nature of the outer metre or so” at the Mountain Mine Lodes.

Meere & Banks (1997) sampled an extensional quartz vein (Fig. 3.3b) near Mountain Mine that showed high salinities (Vein 7, 22-27 wt% $NaCl_{equiv}$) and was identified as a post-orogenic extensional vein. For this study, the identical vein from this locality was sampled again and is now classified as an early extensional vein (Smaller E-W Vein Mountain Mine (barren), Fig. 3.11a-l). The assemblages of the pre-Variscan veins cover a quite large field of higher homogenisation temperatures (up to T_h = 271 °C, Fig. 3.11a-l) and low salinities (as low as 3.2 wt% $NaCl_{equiv}$), to very low homogenisation temperatures with a minimum of 74 °C and a high salinity of up to 28.5 wt% $NaCl_{equiv}$. Nevertheless, the individual fluid inclusion assemblages show generally a quite small spread with narrow clusters (Fig. 3.11a-l). Signs of fluid mixing within individual fluid inclusion assemblages were not observed. The wide range in T_h and salinity for the multiple Fluid inclusion assemblages, as well as the observed cross-cutting veins (Fig. 3.6) is interpreted to reflect the complexity of the mineralizing fluids which occurred probably in several pulses with different compositions that show a spatial and temporal variability. A cavity fill of (unmineralized) vuggy quartz crystals within the major mineralized lode at Coom Mine (Fig. 3.2, Fig. 3.11a-l: Vuggy Quartz Coom Mine (barren), and Appendix B2) is interpreted to belong to the pre-Variscan stage and which was generated by progressive fluid cooling and an increase in salinity

concentration at the end of the early vein filling processes. This development could be very localised, as the vuggy quartz occurs in small pockets within the massive Coom Lode.

Even though special care was taken to measure only primary fluid inclusion assemblages from the extensional E-W veins, it needs to be admitted that these pre-Variscan veins suffered syn-Variscan compression with metamorphism to sub-greenschist facies (Meere 1995b). Cleavage formation (Fig. 3.8a + b) indicates a fluid remobilisation which could have led to the formation of late syn-Variscan fluid inclusion assemblages or fluid inclusion leaking within the pre-Variscan E-W veins.

The early E-W veins contain mainly oval shaped inclusions. Their orientation does not indicate any tectonic stress or deformation. The shape is interpreted to demonstrate uniform crystal growth. This shape of the fluid inclusions can be a diagnostic feature in comparison to later compressional quartz veins which show a majority of elongated (high eccentricity) fluid inclusions. This elongation is probably caused by fibrous crystal growth in the Variscan quartz veins.

Due to their high competency, the East-West striking lodes and large quartz veins apparently cross-cut structures, such as bedding, folding and even faulting. These veins, with a width of at least 40 cm, show only very weak or no folding and the compressional features, caused by the Variscan Orogeny, such as tectonic cleavage and folding (e.g. Cooper & Trayner 1986; Ford 1987) can be easily missed and might be a reason why some previous workers (Sheridan 1964; Halliday & Mitchell 1983; Wen *et al.* 1996; Meere & Banks 1997; Spinks *et al.* 2016) interpreted the timing of the mineralized lodes as a syn- to post-Variscan. Variscan compression (Ford 1987) affected the early mineralized veins and is clearly demonstrated by an intensely cleaved lode ($S_{1,\ vein}$) at Great Mountain Mine (Fig. 3.8a), or the cataclastic deformation in the Coom Lode (Fig. 3.8c). Sanderson (1984) identified N-S trending veins on Beara Peninsula as early extension veins with cleavage and mineralization. The early extensional N-S and NW-SE trending veins seem to be more affected by the syn-Variscan compression than the majority of the E-W

trending veins due to the low angle of the vein's strike to the Variscan NNW-SSE maximum principle stress σ_1 (Fig. 3.7b and Fig. 3.8a). Smaller E-W veins display a well-developed Variscan cleavage (Fig. 3.8b) and associated minor folding.

Sinistral faulting of the Great Mountain Mine Lode (Fig. 3.7b) and the Coom Lode (Fig. 3.7c) is also interpreted to be a result of NNW to SSE oriented Variscan compression. Minor sinistral faulting of the E-W Lode of Mountain Mine has been described by Matthews (1964) and Reilly (1986) on the 1400 level.

The saddle reef veins (Fig. 3.8d) are clearly syn-compressional structures and were already described by several authors as syn-Variscan features (e.g. Dolan 1984). A similar genesis is proposed for the en echelon tension gash arrays which are vertical and related to minor shears resulting from the main deformation (Coller 1984). The sub-horizontal veinlets (Fig. 3.6 generation 3) which are present at Marion Lode and cross-cut all previous vein generations are similar to the sub-horizontal veins (from near Mountain Mine) described by Meere (1995a) and are also related to ongoing Variscan compression and associated vertical extension.

Variscan deformation of the early E-W veins has also been identified in the microstructures (Fig. 3.10). The elongate blocky syntaxial veins, belonging to the early extensional structures (mineralizing event, Fig. 3.10, vein 418_A), were later deformed and developed cataclastic zones, microfractures (Fig. 3.10, vein 418_B1 and 418_B3) and micro en echelon veins (vein 418_B2). Sweeping undulosity in larger blocky crystals, with lobate contacts in the vein centre and patchy undulosity in the small grains along the vein rim, indicate a low temperature crystal-plastic deformation (Trouw *et al.* 2009). This is in agreement with Meere (1995a) who identified a micro brecciated zone within a sample from nearby Mountain Mine as a result of Variscan compression normal to the vein wall. The micro fractures with the seams of cataclastic sub-hedral grains show patchy undulous extinction (Fig. 3.10 vein B3) and could be explained by deformation under low-grade sub-greenschist facies metamorphism during the Variscan Orogeny (Meere 1995b). This provided

conditions for a semi-brittle deformation, which caused partially recrystallization and fracturing.

Wen *et al.* (1996) collected syn-Variscan fluid inclusion measurements from Mizen Head with peak temperatures T_h of 300 to 400 °C. These are much higher than the results presented here with approximately 150 to 240 °C for assemblages in the syn-Variscan quartz veins (Fig. 3.11m-o). A possible reason could be the different burial depths between the two locations. Meere & Banks' (1997) results of moderate salinities of 4 to 16 wt% $NaCl_{equiv}$ for syn-Variscan quartz veins fit very well with this study's results of about 8 to 19 wt% $NaCl_{equiv.}$ The characteristic shape of the syn-Variscan fluid inclusions is elongated with a high eccentricity.

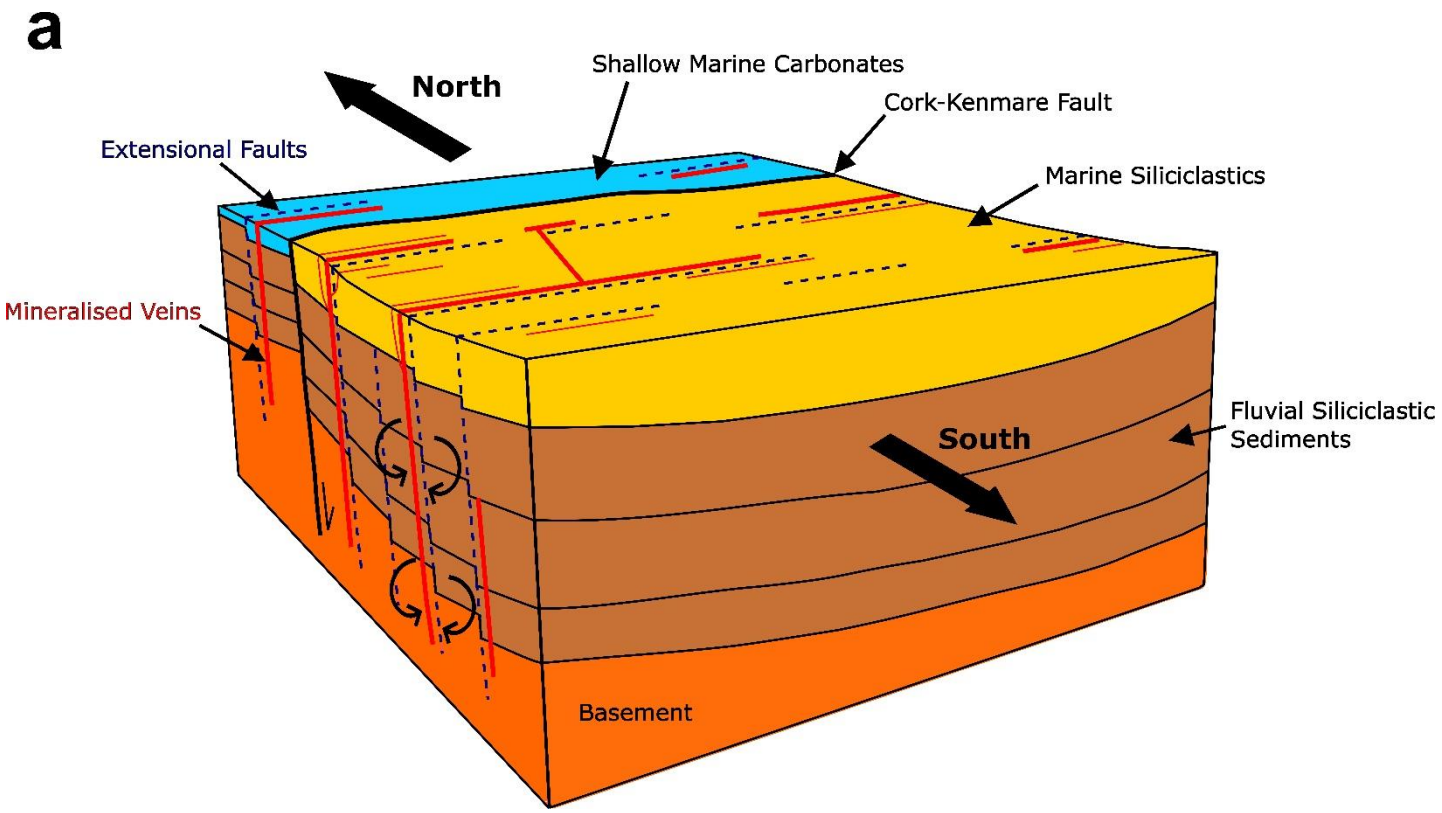
Following the new vein classification of pre-Variscan early extensional veins and syn-Variscan veins, a simplified genetic model of mineralization at Allihies is proposed (Figure 3.12). North-South extension during the development of the Munster Basin and South Munster Basin during the Middle Devonian to early Upper Devonian generated large scale E-W striking extensional faults which provided deep fluid pathways for medium to high saline copper-rich fluids (Fig. 3.12a). These fluids formed the mineralized, mainly E-W striking, and steep dipping quartz veins seen in the Allihies region.

The relatively high homogenisation temperatures recorded from fluid inclusions during this study with T_h values of up to 314 °C (FIA_367B.1, Fig. 3.11a-l) confirm the identification of high geothermal gradients during basin formation (Meere 1995b; Williams 2000). This is caused by extensive rifting processes with crustal thinning and resultant upwelling of the Moho (Williams 2000). According to seismic interpretations (Landes *et al.* 2003) the depth of the Moho can vary between 28 and 33 km. The large amount of basinal infill (Meere & Banks 1997) probably provided an excess of pore fluids which could have led to the extensive quartz vein formation.

The end Carboniferous Variscan Orogeny folded and faulted the basin structures generating silica-rich fluids which precipitated quartz veins into

tension gashes such as saddle reefs, en echelon veins and sub-horizontal veins (Fig. 3.12b).

Fig. 3.12)


a
North
Shallow Marine Carbonates
Cork-Kenmare Fault
Extensional Faults
Marine Siliciclastics
Mineralised Veins
South
Fluvial Siliciclastic
Sediments
Basement

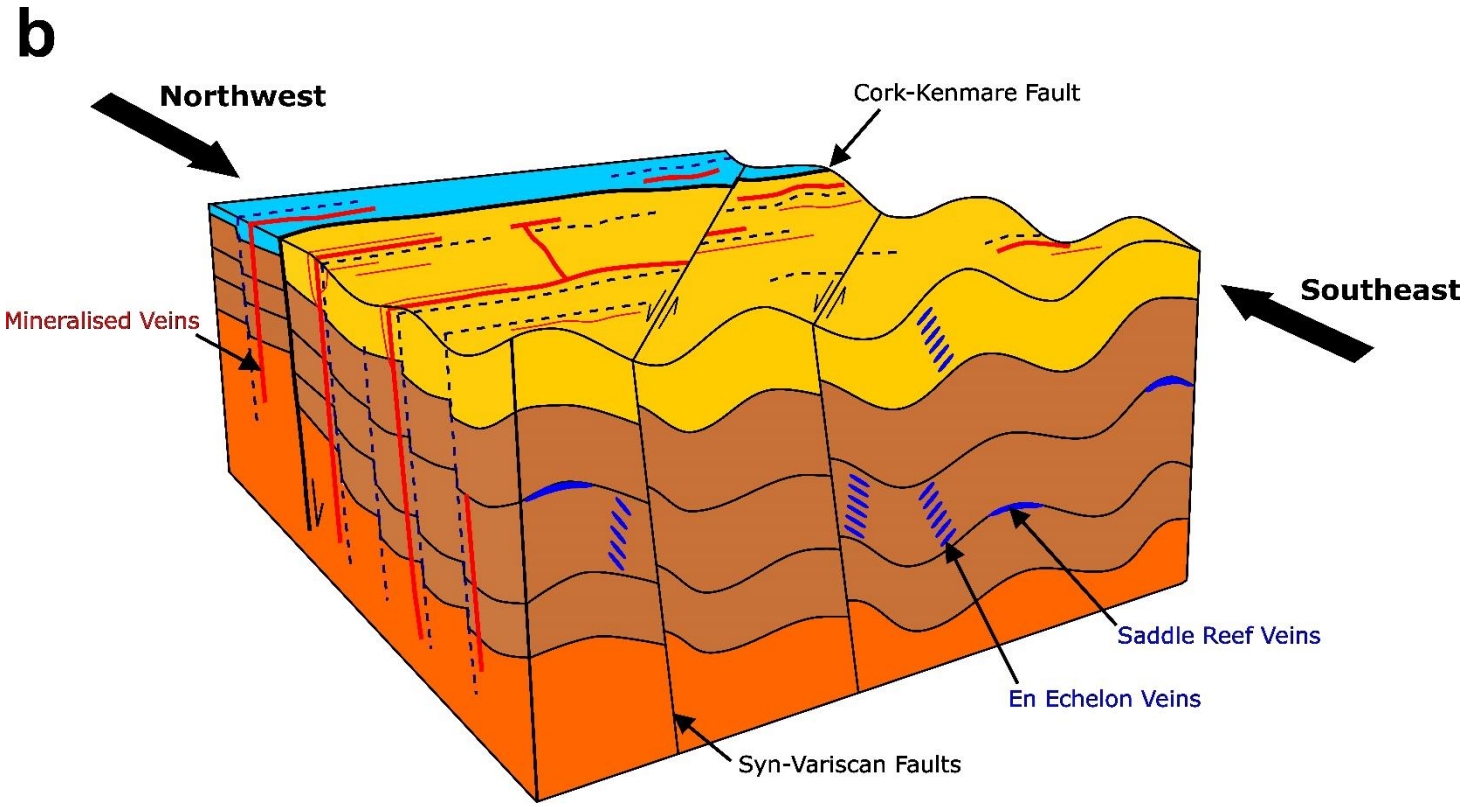


Fig. 3.12) Schematic model of the vein development, mineralization and structural evolution of the Munster Basin and South Munster Basin (not to scale). a) North-South extension listric subsidence and alluvial sedimentation into the Munster and South Munster Basin. Active Extensional Faults, parallel aligned to the Cork-Kenmare Fault, provide fluid pathways for the precipitation of mineralized quartz veins. b) Syn-Variscan compression causes cleavage, folding and faulting of the basin sediments. Cleavage development within early extensional quartz veins and sinistral faulting. Formation of syn-compressional saddle reef and en echelon veins.

3.6.1 Timing of the copper mineralization

Based on Pb/Pb model age measurements on vein hosted copper deposits from Ross Island (Killarney, Kerry), Kinnaird *et al.* (2002) assumed a syn-Variscan vein mineralization between 290 and 270 Ma for the Munster Basin deposits. K-Ar dates (Halliday and Mitchell 1983) from clay minerals which were sampled in Allihies from the wall rock next to the quartz veins produced ages of 290 to 261 Ma for the Mountain Mine Lode and an older age of 321 Ma for an apparently un-mineralized quartz vein. The post-Variscan dates from Allihies are probably caused by a younger alteration of the clay minerals.

The new model, presented in this paper, is supported by molybdenite Re-Os model ages of 367.3 ± 5.5 to 366.4 ± 1.9 Ma (Table 3.1). It can be assumed that molybdenite formation was contemporaneous with the major copper mineralization phase based on the petrographical association of molybdenite and chalcopyrite (Fig. 3.9b) and Reilly's (1986) description of "Molybdenum Mineralization" within the centre of the Main E-W Lode at Mountain Mine.

The Re-Os ages belong to the Famennian Stage (Cohen *et al.* 2019) of the Upper Devonian, suggesting that mineralization was emplaced during basin development and sedimentation which occurred between the Upper Devonian and Lower Carboniferous (MacCarthy 2007). As no visible disseminated copper is known around the Allihies mining area, partial lithification may have already occurred in the adjacent host sediments to provide an impermeable, barrier to the mineralising fluids. On the other hand, all sedimentary copper could have been remobilised into the quartz veins and the sedimentary source was therefore older than the vein mineralization. This would explain the sedimentary sulphur isotope signature described by Spinks *et al.* (2016). The lamprophyric intrusions at Black Ball Head (314.44 ± 1.00 Ma, Quinn *et al.* 2005), dated as coinciding with the Variscan compression (Sanderson 1984; Ford 1987; Meere 1995c) postdate the mineralization.

This new model puts the copper mineralization at Allihies into a similar tectonic setting as the formation of large Zn-Pb deposits at Navan, Lisheen (pyrite Re-Os 346.6 ± 3.0 Ma, Hnatyshin *et al.* 2015) in the Lower Carboniferous to the

north. Similar to this study, the well investigated Zn-Pb deposits, such as Silvermines (334.0 ± 6.1 Ma, Hnatyshin *et al.* 2015) and Tynagh Mine (Irish Midlands, e.g. Kinnaird *et al.* 2002), are related to E-W striking faults, caused by a pre-Variscan North-South extensional phase (e.g. Hitzman 1999). Comparable to Allihies, the Variscan compression of the Irish Midlands deposits had only little effect on mineralization related normal faults of these deposits (Hitzman 1999). Further similarities can be observed with fluid inclusion salinities and homogenisation temperatures (Fig. 3.11a-l). Comparable to the pre-Variscan extensional veins from the Allihies District, the Irish Type Deposits show a range of homogenisation temperatures T_h up to about 240 °C and low salinities (about 10 wt% $NaCl_{equiv}$), to very low homogenisation temperatures with a minimum of about 55 °C and a high salinity of up to 24 wt% $NaCl_{equiv}$ (Wilkinson 2001; Wilkinson 2010; Gleeson & Yardley 2002).

3.7 Conclusions

The Allihies Mining District is dominated by two different quartz veining generations:

(1) Quartz veins with a general E-W strike are associated with early-extensional faults and branch out to smaller E-W striking veins. These veins bear the primary copper mineralization as mainly chalcopyrite, bornite, tetrahedrite/tennantite and molybdenite. The timing of the mineralization is dated by molybdenite Re-Os geochronology of 367.3 ± 5.5 to 366.4 ± 1.9 Ma. The dates coincide with basin development and shortly post-date the early sedimentation sequences during the Upper Devonian. These appear to be directly related to large, basin controlling E-W faults.

Fluid inclusion data suggest multiple fluid pulses with moderate to high salinities and homogenisation temperatures of up to 314 °C.

(2) Syn-Variscan veins occur as saddle reefs and en echelon tension gash shear structures. Sub-horizontal veins cross-cut early extensional structures.

The homogenisation temperature is around 200 °C with moderate salinities.

Drone imaging and aerial photograph interpretation has proven to be very beneficial for the identification of pre-compressional features at the Allihies Mining District.

3.8 Acknowledgements

This publication has emanated from research supported in part by a research grant from Science Foundation Ireland (SFI) under Grant Number 13/RC/2092 and is co-funded under the European Regional Development Fund and by iCRAG industry partners.

SCJ is supported by iCRAG under the Science Foundation Ireland, EU Regional Development Fund and industry partners (13/RC/2092), as well as SFI research grant 16/RP/3849.

The work of KT was funded from the European Union's Horizon 2020 research and innovation program under Marie Skłodowska-Curie grant agreement no. 745945.

The authors are grateful for the assistance from Lingli Zhou (Trinity College Dublin) for the precise geochemical classification of the tennantite/tetrahedrite mineralization. Many thanks to David van Acken (University College Dublin) for the initial geochronology on chalcopyrite which lead to the new perspective and finally to the new discoveries presented in this publication. Thanks to Tadhg O'Sullivan and his colleagues from the Allihies Copper Mine Museum for the historical background knowledge and granting access to the underground workings of Allihies Mountain Mine. Many thanks to Geoff Long (University of Portsmouth) for his support with thin section preparation. Special

thanks to the National History Museum in London (Simon Kocher and Robin Hansen) for providing molybdenite sample material (BM.1964,R231) from the historic Russell collection. Thanks to Kate Kiseeva for providing her recent finding of molybdenite from Caminches Mine.

The Geological Survey Ireland are acknowledged for providing regional data and background information for our 2-D mapping and 3-D modelling efforts. We also thank ARANZGeo/Seequent (Leapfrog3DGeo), Emerson Paradigm (SKUA-GoCAD), Microsoft (Bing Satellite Maps), Mira Geoscience (Mining Suite Plugins), Modri planet d.o.o. (3Dsurvey) and ESRI (ArcGIS) for providing support and academic licenses of software essential to this project.

DS acknowledges the technical support of Antonia Hoffman, Geoff Nowell and Chris Ottley, and the Total Endowment Fund and the CUG Wuhan Dida Fund.

Thanks also to the reviewers Samuel C. Spinks and Eddie Dempsey, as well as to the editor John MacDonald who commented on the earlier version of this manuscript and helped to improve this paper.

3.9 Chapter References

Allmendinger, R.W., Cardozo, N.C. and Fisher, D. 2013. Structural Geology Algorithms: Vectors & Tensors. Cambridge University Press, Cambridge.

Atkinson, Jr. A.B., 2002. A Model for the PTX Properties of H2O–NaCl. MSc thesis, Virginia Tech, Blacksburg, VA.

Blenkinsop, H.G. 1902. Notes on the Berehaven copper mines. Transactions of the Institution of Mining and Metallurgy, 12, 1–7.

Bodnar, R.J. 1983. A method of calculating fluid inclusions volumes based on vapor bubble diameters and P–V–T–X properties of inclusion fluids. Economic Geology, 78, 535–542, https://doi.org/10.2113/gsecongeo.78.3.535

Bodnar, R.J. 1993. Revised equation and table for determining the freezing point depression of H2O–NaCl solutions. Geochimica et Cosmochimica Acta, 57, 683–684, https://doi.org/10.1016/0016-7037(93)90378-A

Bodnar, R.J. and Vityk, M.O. 1994. Interpretation of microthermometric data for H2O–NaCl fluid inclusions. In: Vivo, B.D. and Frezzotti, M.L. (eds) Fluid Inclusions in Minerals, Methods and Applications. Virginia Tech, Blacksburg, VA, 117–130.

Bons, P.D., Elburg, M. and Gomez-Rivas, E. 2012. A review of the formation of tectonic veins and their microstructures. Journal of Structural Geology, 43, 33–62, https://doi.org/10.1016/j.jsg.2012.07.005

Capewell, J. 1975. The Old Red Sandstone Group of Iveragh, Co. Kerry. Proceedings of the Royal Irish Academy, Section B, 75, 155–171.

Cardozo, N. and Allmendinger, R.W. 2013. Spherical projections with OSXStereonet. Computers & Geosciences, 51, 193–205, https://doi.org/10.1016/j.cageo.2012.07.021

Caumon, G., Collon-Drouaillet, P., Le Carlier de Veslud, C., Viseur, S. and Sausse, J. 2009. Surface-based 3-D modeling of geological structures. Mathematical Geosciences, 41, 927–945, https://doi.org/10.1007/s11004-009-9244-2

Cohen, K.M., Harper, D.A.T. and Gibbard, P.L. 2019. ICS International Chronostratigraphic Chart 2019/05. International Commission on Stratigraphy, IUGS. www.stratigraphy.org [last accessed 12 August 2019].

Coller, D.W. 1984. Variscan structures in the Upper Palaeozoic rocks of west central Ireland. Geological Society, London, Special Publications, 14, 185-194, https://doi.org/10.1144/GSL.SP.1984.014.01.18

Cooper, M.A. and Trayner, P.M. 1986. Thrust-surface geometry: implications for thrust-belt evolution and section-balancing techniques. Journal of Structural Geology, 8, 305–312, https://doi.org/10.1016/0191-8141(86)90051-9

Daltry, V.D.C. 1985. A structural, geochemical and mineralogical appraisal of the stratabound ore deposits in western County Cork, Ireland. Ph.D. Thesis, University College Cardiff.

Dolan, J.M. 1984. A structural cross-section through the Carboniferous of northwest Kerry. Irish Journal of Earth Sciences, 95–108.

Doppler, G., Bakker, R.J. 2014. The influence of the α–β phase transition of quartz on fluid inclusions during re-equilibration experiments. Lithos 198–199,14–23.

Ennis, M., Meere, P.A., Timmerman, M.J. and Sudo, M. 2015. Post-Acadian sediment recycling in the Devonian Old Red Sandstone of Southern Ireland. Gondwana Research, 28, 1415–1433, https://doi.org/10.1016/j.gr.2014.10.007

Fletcher, C.I. 1969. The sulphide mineralization in the Allihies region, County Cork, Eire. Ph.D. Dissertation, University of Leicester, 128–129.

Ford, M. 1987. Practical application of the sequential balancing technique: an example from the Irish Variscides. Journal of the Geological Society, London, 144, 885–891, https://doi.org/10.1144/gsjgs.144.6.0885

Fossen, H. and Rotevatn, A. 2016. Fault linkage and relay structures in extensional settings – A review. Earth-Science Reviews, 154, 14–28, https://doi.org/10.1016/j.earscirev.2015.11.014

Gleeson, S.A. and Yardley, B.W.D. 2002. Extensional Veins and Pb–Zn Mineralisation in Basement Rocks: The Role of Penetration of Formation Brines. In: Stober, I. and Bucher, K. (eds) Water–Rock Interaction. Water Science and Technology Library, Vol. 40. Springer, Dordrecht, 189–205.

Goldstein, R.H. and Reynolds, T.J. 1994. Systematics of fluid inclusions in diagenetic minerals. SEPM (Society for Sedimentary Geology), USA

Halliday, A.N. and Mitchell, J.G. 1983. K–Ar ages of clay concentrates from Irish orebodies and their bearing on the timing of mineralisation. Earth and Environmental Science Transactions of the Royal Society of Edinburgh, 74, 1–14, https://doi.org/10.1017/S0263593300009858

Hitzman, M.W. 1999. Extensional faults that localize Irish syndiagenetic Zn–Pb deposits and their reactivation during Variscan compression. Geological Society, London, Special Publications, 155, 233–245, https://doi.org/10.1144/GSL.SP.1999.155.01.17

Hnatyshin, D., Creaser, R.A., Wilkinson, J.J. and Gleeson, S.A. 2015. Re–Os dating of pyrite confirms an early diagenetic onset and extended duration of mineralization in the Irish Zn–Pb ore field. Geology, 43, 143–146, https://doi.org/10.1130/G36296.1

Jarvis, A., Reuter, H.I., Nelson, A. and Guevara, E. 2008. Hole-filled SRTM for the globe Version 4. International Centre for Tropical Agriculture (CIAT), http://srtm.csi.cgiar.org [last accessed 25 July 2017].

Kinnaird, J.A., Ixer, R.A., Barreiro, B. and Nex, P.A. 2002. Contrasting sources for lead in Cu-polymetallic and Zn–Pb mineralisation in Ireland: constraints from lead isotopes. Mineralium Deposita, 37, 495–511, https://doi.org/10.1007/s00126-001-0252-5

Landes, M., O'Reilly, B.M., Readman, P.W., Shannon, P.M. and Prodehl, C. 2003. VARNET-96: three-dimensional upper crustal velocity structure of SW Ireland. Geophysical Journal International, 153, 424–442, https://doi.org/10.1046/j.1365-246X.2003.01911.x

Li, Y., Selby, D., Condon, D. and Tapster, S. 2017. Cyclic Magmatic–Hydrothermal Evolution in Porphyry Systems: High-Precision U–Pb and Re–Os Geochronology Constraints on the Tibetan Qulong Porphyry Cu–Mo Deposit. Economic Geology, 112, 1419–1440, https://doi.org/10.5382/econgeo.2017.4515

MacCarthy, I.A.J. 1990. Alluvial sedimentation patterns in the Munster Basin, Ireland. Sedimentology, 37, 685–712, https://doi.org/10.1111/j.1365-3091.1990.tb00629.x

MacCarthy, I.A.J. 2007. The South Munster Basin of southwest Ireland. Journal of Maps, 3, 149–172, https://doi.org/10.1080/jom.2007.9710835

MacCarthy, I.A.J., Pracht, M. and Sleeman, A.G. 2002. Geology of West Cork, Scale 1:100000, Sheet 24. Geological Survey of Ireland, Dublin.

Matthews, P.F.P. 1964. The Copper Mineralization near Allihies, Co. Cork. M.Sc. Dissertation, Trinity College, Dublin.

Meere, P.A. 1995a. High and low density fluids in a quartz vein from the Irish Variscides. Journal of Structural Geology, 17, 435–446, https://doi.org/10.1016/0191-8141(94)00066-9

Meere, P.A. 1995b. Sub-greenschist facies metamorphism from the Variscides of SW Ireland an early syn-extensional peak thermal event. Journal of the Geological Society, London, 152, 511–521, https://doi.org/10.1144/gsjgs.152.3.0511

Meere, P.A. 1995c. The structural evolution of the western Irish Variscides: an example of obstacle tectonics? Tectonophysics, 246, 97–112, https://doi.org/10.1016/0040-1951(94)00267-D

Meere, P.A. and Banks, D.A. 1997. Upper crustal fluid migration: an example from the Variscides ofSW Ireland. Journal of the Geological Society, London, 154, 975–985, https://doi.org/10.1144/gsjgs.154.6.0975

Naylor, D. and Jones, P.C. 1967. Sedimentation and tectonic setting of the Old Red Sandstone of southwest Ireland. In: Oswald, D. (ed.) International Symposium on the Devonian System (Calgary). Society of Petroleum Geology 2, Calgary, Alberta, 1089–1099.

O'Brien, M.V. 1959. The future of non-ferrous mining in Ireland. In: The Future of Non-Ferrous Mining in Great Britain and Ireland. Institution of Mining and Metallurgy Symposium, 5–26.

O'Brien, W.F. 1987. The dating of the Mt Gabriel-type copper mines of West Cork. Journal of the Cork Historical and Archaeological Society, 92, 50–70.

Pracht, M. 2000. Controls on magmatism in the Munster Basin, SW Ireland. Geological Society, London, Special Publications, 180, 303–317, https://doi.org/10.1144/GSL.SP.2000.180.01.14

Pracht, M. and Kinnaird, J.A. 1995. Mineral chemistry of megacrysts and ultramafic nodules from an undersaturated pipe at Black Ball Head, County Cork. Irish Journal of Earth Sciences, 14, 47–58.

Pracht, M. and Sleeman, A.G. 2002. A geological description of West Cork and adjacent parts of Kerry to accompany the Bedrock Geology, 1:100,000 Scale Map Series, Sheet 24, West Cork. With accompanying contributions by Wright, G. (Groundwater) and Cox, W. (Minerals). Geological Survey of Ireland, Dublin.

Price, C.A. and Todd, S.P. 1988. A model for the development of the Irish Variscides. Journal of the Geological Society, London, 145, 935–939, https://doi.org/10.1144/gsjgs.145.6.0935

Quinn, D., Meere, P.A. and Wartho, J.A. 2005. A chronology of foreland deformation: Ultra-violet laser 40Ar/39Ar dating of syn/late-orogenic intrusions from the Variscides of southwest Ireland. Journal of Structural Geology, 27, 1413–1425, https://doi.org/10.1016/j.jsg.2005.02.003

Reilly, T.A. 1986. A review of vein mineralization in SW County Cork, Ireland. In: Andrew, C.J., Crowe, R.W.A., Finlay, S., Pennell, W.M. and Pyne, J.F. (eds) Geology and Genesis of Mineral Deposits in Ireland. Irish Association for Economic Geology, Dublin, 513–544.

Rogers, J.G. 2002. Regional veining in the Upper Palaeozoic Munster and South Munster Basins, Ireland; the evolution of palaeofluids and palaeofluid flow during basin inversion. Ph.D. Dissertation, University College Cork.

Sanderson, D.J. 1984. Structural variation across the northern margin of the Variscides in NW Europe. Geological Society, London, Special Publications, 14, 149–165, https://doi.org/10.1144/GSL.SP.1984.014.01.15

Selby, D. and Creaser, R.A. 2001. Re–Os geochronology and systematics in molybdenite from the Endako porphyry molybdenum deposit, British Columbia, Canada. Economic Geology, 96, 197–204, https://doi.org/10.2113/gsecongeo.96.1.197

Selby, D., Creaser, R.A., Stein, H.J., Markey, R.J. and Hannah, J.L. 2007. Assessment of the 187Re decay constant by cross calibration of Re–Os molybdenite and U–Pb zircon chronometers in magmatic ore systems. Geochimica et Cosmochimica Acta, 71, 1999–2013, https://doi.org/10.1016/j.gca.2007.01.008

Sheridan, D.J. 1964. The structure and mineralisation of the Mountain Mine area, Allihies, west Co. Cork, Ireland. Scientific Proceedings, Royal Dublin Society, Series A, 2, 21–27.

Smoliar, M.I., Walker, R.J. and Morgan, J.W. 1996. Re–Os ages of group IIA, IIIA, IVA, and IVB iron meteorites. Science, 271, 1099–1102, https://doi.org/10.1126/science.271.5252.1099

Spinks, S.C., Parnell, J., Bellis, D. and Still, J. 2016. Remobilization and mineralization of selenium–tellurium in metamorphosed red beds: Evidence from the Munster Basin, Ireland. Ore Geology Reviews, 72, 114–127, https://doi.org/10.1016/j.oregeorev.2015.07.007

Steele-MacInnis, M., Bodnar, R.J. and Naden, J. 2011. Numerical model to determine the composition of H2O–NaCl–CaCl2 fluid inclusions based on microthermometric and microanalytical data. Geochimica et Cosmochimica Acta, 75, 21–40, https://doi.org/10.1016/j.gca.2010.10.002

Steele-MacInnis, M., Lecumberri-Sanchez, P. and Bodnar, R.J. 2012. Short note: HokieFlincs_H2O-NaCl: A Microsoft Excel spreadsheet for interpreting microthermometric data from fluid inclusions based on the PVTX properties of H2O–NaCl. Computers & Geosciences, 49, 334–337, https://doi.org/10.1016/j.cageo.2012.01.022

Trouw, R.A.J., Passchier, C.W. and Wiersma, D.J. 2009. Crystal-Plastic Deformation, Recovery and Recrystallisation of Quartz. In: Atlas of Mylonites and Related Microstructures. Springer, Berlin, 241–262.

Unknown Author 1919. Historic mining map, Allihies Copper Mines. Geological Survey of Ireland, GSI Goldmine, https://secure.dccae.gov.ie/goldmine/docpage.html?id1=8260590&id2=9553634&id3=9556911 [last accessed 16 July 2017].

Vermeulen, N.J., Shannon, P.M., Masson, F. and Landes, M. 2000. Wide-angle seismic control on the development of the Munster Basin, SW Ireland. Geological Society, London, Special Publications, 180, 223–237, https://doi.org/10.1144/GSL.SP.2000.180.01.11

Walsh, J.J. andWatterson, J. 1991. Geometric and kinematic coherence and scale effects in normal fault systems. Geological Society, London, Special Publications, 56, 193–203, https://doi.org/10.1144/GSL.SP.1991.056.01.13

Wen, N., Boyce, A.J., Fallick, A.E., Ashworth, J.R. and Ixer, R.A. 1996. The genesis of Cu-bearing quartz veins by metamorphic remobilization from stratiform red bed deposits, SW County Cork, Ireland. Mineralogy and Petrology, 57, 73–89, https://doi.org/10.1007/BF01161622

Wilkinson, J.J. 2001. Fluid inclusions in hydrothermal ore deposits. Lithos, 55, 229–272, https://doi.org/10.1016/S0024-4937(00)00047-5

Wilkinson, J.J. 2010. A Review of Fluid Inclusion Constraints on Mineralization in the Irish Ore Field and Implications for the Genesis of Sediment-Hosted Zn–Pb Deposits. Economic Geology, 105, 417–442, https://doi.org/10.2113/gsecongeo.105.2.417

Williams, R.A. 1991. The Berehaven copper mines. British Mining, 42. Northern Mine Research Society, Sheffield.

Williams, E.A. 2000. Flexural cantilever models of extensional subsidence in the Munster Basin (SW Ireland) and Old Red Sandstone fluvial dispersal systems. Geological Society, London, Special Publications, 180, 239–268, https://doi.org/10.1144/GSL.SP.2000.180.01.12

Wilson, W.H. and Powell, S. 1956. Historic mining map, Allihies Copper Mines (Co. Cork), Mountain Mine. Geological Survey of Ireland, GSI Goldmine. https://secure.dccae.gov.ie/goldmine/docpage.html?id1=8264207&id2=24780680&id3=24780686 [last accessed 8 May 2017].

Chapter 4: The Copper Mineralization of West Cork

Status: Ready for Submission

Following the new genetic model of the vein hosted copper mineralization at Allihies (Chapter 3), this paper was produced to set the focus on a larger regional scale. Several localities (mostly historic copper mines) of West Cork were examined to compare and prove the theory of the new “Allihies Model”.

Appendix E1-3: Fluid inclusions measurements of selected locations and historic copper mines from West Cork. Locations are as shown in Fig. 4.3.

Appendix F: Sample locations from West Cork, SW Ireland

Paper title (examples):

The Chrono-Structural Setting of the Copper Deposits in the South Munster Basin, West Cork, Southern Ireland

The Copper Mineralization of West Cork, Southwest Ireland – A Chrono-Structural Study

The Timing of the West Cork Copper Deposits and their Structural Setting in Southwest Ireland

Preliminary author list:

Jürgen Lang, Patrick A. Meere, Richard P. Unitt and David Selby

4.1 Abstract

This study provides a new insight into the genetical and chronological development of the vein hosted copper sulphide mineralization in the Late Palaeozoic Munster Basins of SW Ireland. Field mapping, supported by drone photogrammetry, petrography, microthermometry and geochronology of selected historic mining sites in West Cork reveal elementary data for a reinterpretation of the mineralization processes. Structural investigations define two distinct ore forming episodes: The initial vein precipitation is directly related to syn-basinal, extensional E-W to ENE-WSW striking normal faults. Smaller sediment hosted Cu sulphide occurrences are related to the extensional fault systems. The second mineralization phase occurred during the early stage of the late Carboniferous Variscan compression by reactivation of early extensional, basinal fault systems. Cu mineralization related molybdenite samples from the historical Ballycummisk Mines on Mizen Peninsula produced Re-Os dates from 315.5 ± 1.6 Ma to 311.8 ± 1.6 Ma. This Pennsylvanian (Upper) Carboniferous sulphide emplacement is related to the later, Syn-Variscan compressional mineralization event. The discovery of the two distinct Cu mineralizing events in SW Ireland provides an important contribution to the understanding of the development of the Irish Ore Field including the Pb-Zn Midlands Deposits.

4.2 Introduction

The copper occurrences of SW Ireland have been utilized for over 3500 years (Williams 1991) Bronze Age (O'Brien 1987) sites on the Mizen Peninsula (Figs 4.1 and 4.2) show that the original extraction of Cu ore targeted surficial malachite stained, sediment-hosted mineralization. The heyday of Cu mining in SW Ireland was between 1812 and 1885 when an estimated total of 284,500 tonnes of vein-hosted ore was extracted from Mountain Mine at Allihies, the most productive mine in the area (Fig. 4.2, O'Brien 1959, Williams 1991). Many smaller mines were also active throughout West Cork during the 19th century (Reilly 1986).

During recent decades mining and exploration has mainly focussed on the rich Pb-Zn (+Cu) deposits of the Irish Midlands (e.g. Aldwell 1990; Hitzman 1999; Wilkinson 2001, 2010; Torremans *et al.* 2018 and references therein). The Cu deposits in SW Ireland were described as syn- to post-Variscan (Sheridan 1964; Halliday and Mitchell 1983; Wen *et al.* 1996; Meere and Banks 1997; Spinks *et al.* 2016) suggesting that their genesis was unrelated to the Irish Midlands Deposits. Recent findings by Lang *et al.* (2020) reveal Re-Os dates from mineralization related molybdenite from the Allihies Mining Area of 367.3 ± 5.5 and 366.4 ± 1.9 Ma. This new time frame for mineralization, combined with new structural interpretation (Lang *et al.* 2020), now provides a potential link to the Irish Midland deposits.

This paper focusses on selected localities and historic Cu mines of Munster and South Munster Basins (Figs 4.1 and 4.2) to provide an overview of the genetic links to the Allihies Copper Mines and their potential relationship with the Irish Midlands Deposits.

4.3 Geological Setting

North-south crustal extension between the Middle Devonian and Upper Devonian, led to the development of a large half-graben basin in southern Ireland, the Munster Basin (Naylor & Jones 1967). The east-west trending listric Coomnacronia-Killarney-Mallow Fault Zone marks the northern bounding structure of this intracratonic basin (Fig. 4.1; Naylor & Jones 1967; Capewell 1975; Price & Todd 1988; Meere 1995c; Vermeulen *et al.* 2000; Landes *et al.* 2003; MacCarthy 2007; Ennis *et al.* 2015). Williams (2000) alternatively described the Dingle Bay-Galtee Fault Zone as major margin to the north (Fig. 4.1).

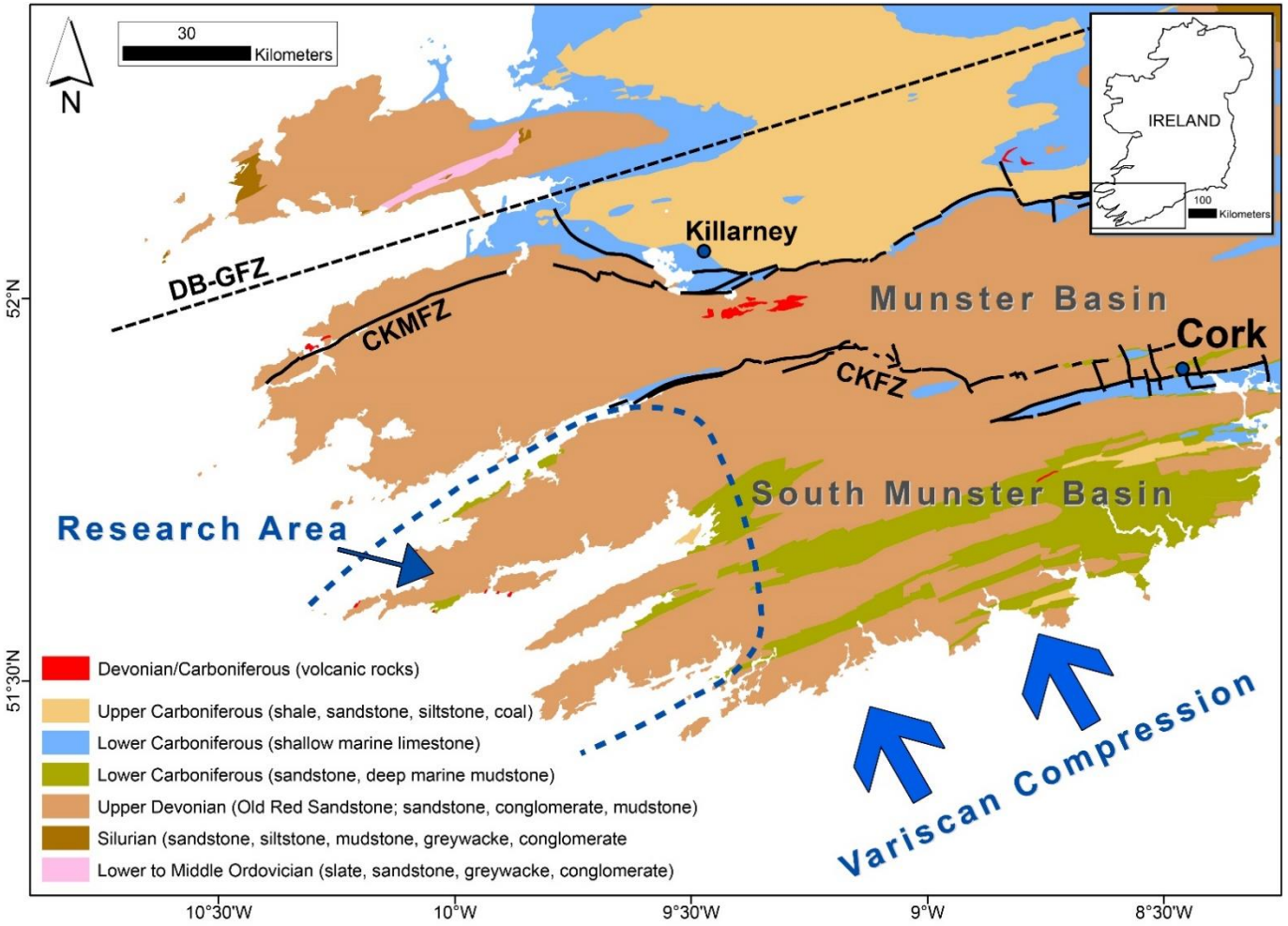


Fig. 4.1) Simplified geological map of the Munster Basin and the South Munster Basin in SW Ireland. The Munster Basin is defined by the Coomnacronia-Killarney-Mallow Fault Zone (CKMFZ) or alternatively by the Dingle Bay-Galtee Fault Zone (DB-GFZ) in the North. The Cork-Kenmare Fault Zone (CKFZ) indicates the rim to the South Munster Sub-Basin. A NNW directed compression indicates the Variscan Orogeny (modified from Sanderson 1984; Williams 2000; MacCarthy et al. 2002; Landes et al. 2003; MacCarthy 2007; Ennis et al. 2015).

The basinal infill is dominated by late Middle to Upper Devonian alluvial and fluvial siliciclastic sediments (Fig. 4.2, MacCarthy 1990). These sediments were mainly transported from the north into the Munster Basin. Detailed stratigraphic nomenclature is described by Williams *et al.* (1989), MacCarthy (1990), Williams (2000), MacCarthy *et al.* (2002) and Pracht & Sleeman (2002, Fig. 4.2a and 4.2b): The siliciclastic Valentia Slate and Bird Hill Formation form the base of the northern basin infill, which are followed by sandstones and siltstones of the Slaheny Formation in the north and the sandstones with interbedded mudstones of the Sherkin Formation to the south (Pracht & Sleeman 2002). Alluvial bedding is formed by sandstones and siltstones of the Caha Mountain, Castlehaven and Gun Point Formations. These formations are summarized to the Upper Old Red Sandstone Facies, which formed a basinal infill of over 6 km (Williams *et al.* 1989, Meere & Banks 1997, Williams 2000). The cross-bedded sandstones of the Toe Head Formation mark a transition zone between the underlying non marine Old Red Sandstone Magna-Facies and the overlain marine Old Head Sandstone Formation (Pracht & Sleeman 2002).

Continuous subsidence and formation of the South Munster Basin was triggered by the east-west trending Cork-Kenmare Fault Zone (CKFZ) at the end of the Devonian (Fig. 4.1, MacCarthy 2007). Seismic interpretations from Landes *et al.* (2003) show a possible depth of 13–14 km for the basin-controlling Cork–Kenmare Fault Zone. The concomitant marine transgression from the south resulted in the accumulation of marine siliciclastics within the South Munster Basin south of the CKFZ and limestones on a more stable platform to the north (Fig. 4.2; MacCarthy 2007).

Fig. 4.2a) *4.2b)*

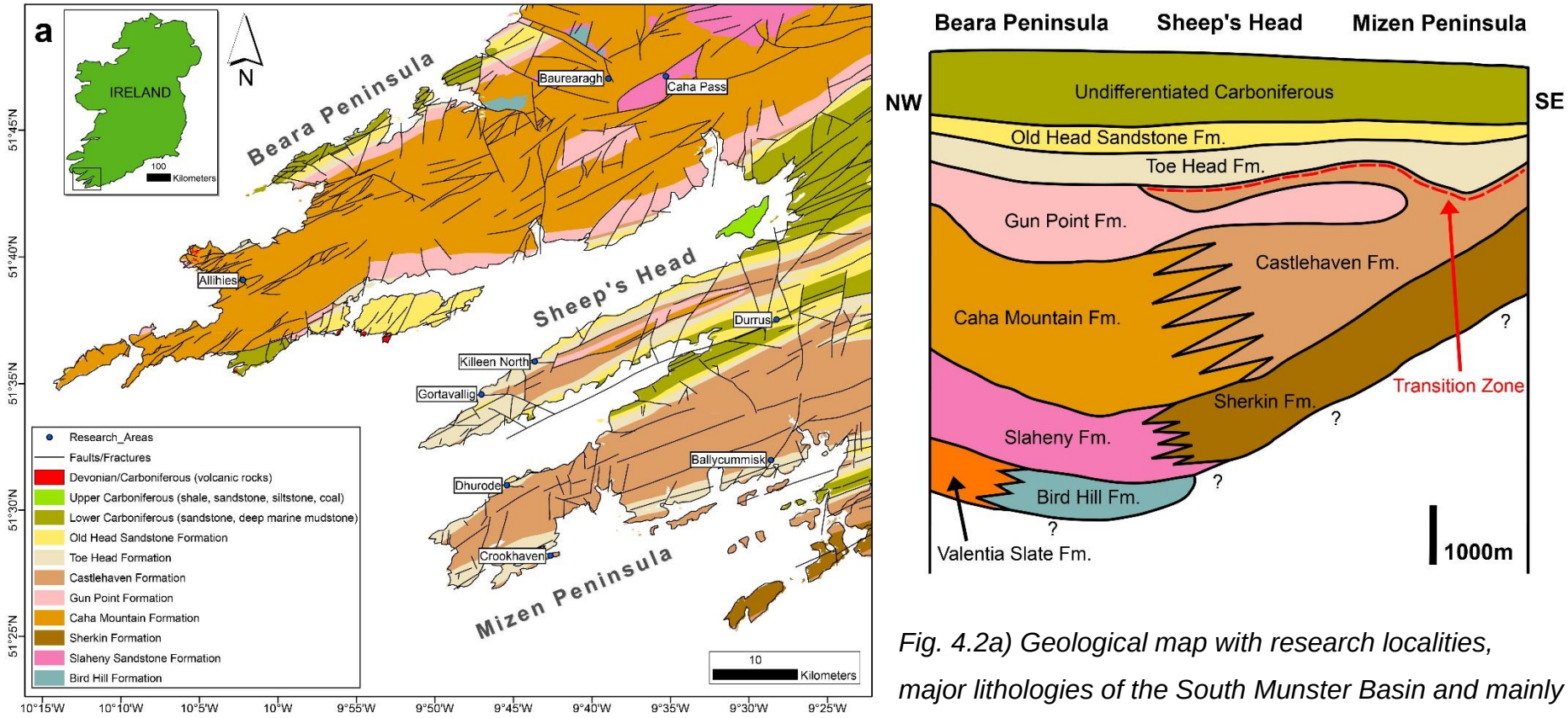


Fig. 4.2a) Geological map with research localities, major lithologies of the South Munster Basin and mainly Variscan NE-SW striking fractures (modified from GSI 2016). b) Simplified profile of the Munster Basin sedimentary formations including the copper hosting transition zone at the top of the Castlehaven Formation (modified from Snodin 1972; MacCarthy 1990; Wen et al. 1996; MacCarthy et al. 2002; Pracht & Sleeman 2002; GSI 2016 and Spinks et al. 2016).

NNW-directed compression (Fig. 4.1) terminated sedimentation towards the end of the Carboniferous and marked the beginning of the Variscan Orogeny (Sanderson 1984; Ford 1987; Meere 1995b; Quinn *et al.* 2005). According to Ar-Ar dates of cleaved and deformed intrusive rocks on Beara Peninsula (Fig. 4.2a, Quinn *et al.* 2005), the initial effect of the Variscan compression started before 314.4 Ma. The orogeny resulted in crustal shortening of over 52 % with the development of a pervasive cleavage, followed by kilometre scale buckling and faulting (Fig. 4.2a, Cooper & Trayner 1986; Ford 1987). The folding and faulting followed a general NE-SW strike (Fig. 4.2a, GSI 2016). High-angle basin-controlling faults were reactivated during compression (Price & Todd 1988). Reverse NE-SW-trending faults, as well as rarer NW-SE-trending strike slip faults are described by Meere (1995c) occurring in the west of the Munster Basin. The sediments underwent metamorphism to sub-greenschist facies (Meere 1995b).

Minor intrusions ranging from dioritic to trachytic occur around Beara Peninsula and the northern Sheep's Head coastline (Boldy 1955, Viswanathiah 1959 and Reilly 1986, Figs. 4.1 and 4.2). These sheet-like intrusions were described by Pracht (2000) as mainly alkali basalts, trachytes and phonolites. Basalts formed high level shallow intrusions during the subsidence phase of the Munster Basin. Ductile deformed, pipe-like lamprophyric intrusions dated at 314.44 ± 1.00 Ma (Ar/Ar phlogopite, Quinn *et al.* 2005) have been found at Black Ball Head (5.6 km south of Allihies, Fig. 4.2) and were formed during the early Variscan compression (Pracht & Kinnaird 1995; Pracht 2000). Undeformed trachytic dykes from White Ball Head (400 m northwest of Black Ball Head) show ages of 296.88 ± 0.60 Ma (Ar/Ar phlogopite), which confine and therefore post-date the Variscan Orogeny (Quinn *et al.* 2005).

The formation of the sediment hosted and vein hosted copper mineralization in SW Ireland has been described by several authors with various interpretations in timing and formation:

4.3.1 Sediment hosted mineralization

According to Snodin (1972) interstitial brines from the marine basin migrated through the uppermost red-bed sediments and produced sulphite with anaerobic bacteria. Wen *et al.* (1996) and Snodin (1972) identified sediment hosted mineralization in stratigraphically bound, reduced green sandstone zones (green beds) within the upper Castlehaven Formation (Fig. 4.2b). The sedimentary Cu occurrences are related to channel sandstones near the base of the Toe Head Formation and within the upper part of the Castlehaven Formation (Reilly 1986, Fig. 4.2). Spinks *et al.* (2016) measured negative $\delta^{34}S$ values at Allihies caused by biogenically-induced reduction within the Old Red Sandstone Facies resulting in syngenetic-diagenetic sulphide mineralization. This copper was mined historically from green sandstones and slates (Fig. 4.3, GSI 2016 & GSI Jetstream 2019).

4.3.2 Vein hosted mineralization

The vein hosted deposits at Crookhaven (Fig. 4.2) have been described as saddle reef tension gashes exposed in an anticlinal (Variscan) core (Duffy 1932 & Reilly 1986). Halliday and Mitchell (1983) dated clay minerals from Allihies (Fig. 4.2), which were sampled from the wall rock next to the quartz veins. The K-Ar dates showed results between 290 and 261 Ma for the Mountain Mine Lode. An older age of 321 Ma was measured for an apparently unmineralized quartz vein (Halliday and Mitchell 1983). In contrary, Sanderson (1984) described N-S trending mineralized veins on Beara Peninsula with strong folding and cleavage, which led to a proposed pre/syn-Variscan age. Faulting and brecciation of mineralized veins occurring at deposits on Mizen Peninsula (Fig. 4.2) has been confirmed by Reilly (1986). For Crookhaven Reilly (1986) considered a late syntectonic mineralization.

According to Wen *et al.* (1996) and Spinks *et al.* (2016) the sediment-hosted sulphides were remobilised into late- or post-Variscan quartz veins. This remobilisation was driven by non-magmatic, metamorphic (Variscan) fluids which were capable of dissolving and reprecipitating the sulphides (Wen *et al.* 1996, Spinks *et al.* 2016). Meere and Banks (1997) described a minor vein formation related to early orogenic compression. Wen *et al.* (1996), Meere and Banks (1997), as well as Spinks *et al.* (2016) interpreted a post-Variscan N-S extension as the major sulphide remobilisation and mineralization event with large quartz vein precipitation along normal faults.

Model age measurements (Pb/Pb) on vein-hosted copper occurrences from Ross Island (Northern Munster Basin at Killarney, Kerry, Fig. 4.1) yield to a syn-Variscan vein mineralization between 290 and 270 Ma (Kinnaird *et al.* 2002). Recent findings (Lang *et al.* 2020) show cleaved and folded N-S and E-W striking mineralized quartz veins at Allihies. Lang *et al.* (2020) distinguished two groups of quartz veins; pre-Variscan mineralized veins, mainly E-W striking, and syn-Variscan veins (generally barren) related to tension gashes and en echelon structures. Some of the pre-Variscan copper lodes where sinistrally off-set by Variscan compressional faults. Vein mineralization related molybdenite Re-Os dates from the Allihies Copper mines show formation ages of 367.3 ± 5.5 to 366.4 ± 1.9 Ma (Lang *et al.* 2020). This is interpreted as mineralization related to basin formation and associated N-S crustal extension (Lang *et al.* 2020).

Mineralization within quartz veins at Allihies (Fig. 4.2) consists of mainly chalcopyrite, tetrahedrite/tennantite, bornite, molybdenite, as well as minor chalcocite (Sheridan 1964, Reilly 1986, Lang *et al.* 2020). Chalcopyrite is described as the dominant Cu ore on Sheep's Head and Mizen Head locations (Fig. 4.2, Snodin 1972). Tennantite-tetrahedrite, as well as euhedral arsenopyrite has been found at Gortavallig and Dhurode Mine (Snodin 1972). The latter also has traces of galena. The mines at Crookhaven show mainly a chalcopyrite-bornite-quartz assemblage (Reilly 1986). Next to the primary Cu ore (chalcopyrite), Snodin (1972) described significant quantities of barite and

specular hematite occurring at Ballycummisk Mine (Fig. 4.2). Fletcher (1969) recognized molybdenite in copper-bearing quartz veins at Ballycummisk, Dhurode and Crookhaven, similar to the Allihies veins.

Fluid inclusion microthermometry measurements of quartz veins from Mizen Peninsula suggest peak-metamorphic conditions of between 300-400 °C (Wen *et al.* 1996). Homogenisation temperatures T_h can be as low as 100 °C (Crookhaven, Wen *et al.* 1996). Meere and Banks (1997) indicated medium to moderate salinities (4-16 wt% $NaCl_{equiv}$) for syn-Variscan quartz veins and high salinities (22-27 wt% $NaCl_{equiv}$) for post-orogenic extensional veins at Allihies. Recent detailed measurements from Allihies copper mines range from moderate salinity and higher homogenisation temperatures (T_h LV-L = <314 °C; >3.2 %$NaCl_{equiv.}$) to high salinities and very low homogenisation temperatures (T_h LV-L = >74 °C; <28.5 %$NaCl_{equiv.}$) for the mineralized Pre-Variscan quartz veins (Lang *et al.* 2020). Syn-Variscan quartz veins (en echelon tension gashes) show low to moderate salinities and T_h values of about 200 °C.

4.4 Methodology

The examined study areas (Fig. 4.3) were selected based on historical importance, and their ability to demonstrate clear structural history. Field mapping in the selected areas focussed primarily on the classification and sampling of mineralized and unmineralized quartz veins, as well as mineralized sedimentary units. Structural measurements and identification of structural field relations between the different veins was utilised for chronological identification. Aerial drone mapping was used to investigate the study areas to contextualise features identified in the field. A DJI Phantom 3 Professional with a 4K, 12.4-megapixel camera was flown at a vertical height of between 10 to 50 m, depending on the surface topography, over a defined area of approximately 30,000 m^2 per flight. The high-resolution images were captured with 60 to 70 % overlap. The geotagged images were processed with the photogrammetry software 3Dsurvey by *Modri planet* to calculate a 3-dimensional (3-D) digital terrain model (DTM) and a 2-D high-resolution

orthorectified photograph, which was georeferenced in ArcGIS and combined with field observations.

Large scale structures identified in the field were traced on open access satellite maps to identify the overall structural pattern (Fig. 4.3; Bing™ Satellite Maps, 2016-2019; Google Maps, 2016-2019; ArcGIS BaseMaps, 2016-2020). Offshore bathymetry data (GSI Infomar, 2017) provided additional bedrock information around Mizen Peninsula (Fig. 4.3). Special care was taken to identify the photolineaments as real geological features and to exclude any manmade lineaments, such as fences, roads and historical mining trails. The geological features have been enhanced by preferential erosion. Glacial erosion and coastal weathering developed trenches and small valleys along natural fault zones which can be distinguished from man-made constructs. The identified structures were ground-truthed at the selected study areas.

Some individual quartz veins were traced on the high-resolution georeferenced drone maps using ArcGIS. The orientation of the large-scale structures (Fig. 4.3) as well as the orientation of the individually traced quartz veins was gathered using the add-in Orientation Analysis Tools for ArcGIS (Kocianova, 2016). The values were calculated by using the mean azimuth of the polyline segments. The rose diagrams were created with Stereonet (Allmendinger *et al.* 2013; Cardozo and Allmendinger 2013)).

The 3-D digital terrain model from Baurearagh (Fig. 4.4a + 4.4b) was used to create a 3-D model of the area to identify its structure. Data entry and 3-D modelling was done using SKUA-GoCAD (Emerson Paradigm) and the Mining Suite plugins of Mira Geoscience, using the discrete smooth interpolator to model the veins (Caumon *et al.* 2009). Data entry and georeferencing was performed in ArcMap (ESRI). Data validation and visualization were carried out with Leapfrog3DGeo (ARANZ Geo Ltd., now Seequent).

Quartz vein samples and ore samples were collected from all of the study areas where available. In-situ samples were taken whenever possible. In some cases, where the historic mine shafts were not accessible or due to the lack of outcrop (Ballycummisk, Fig. 4.3), it was necessary to collect samples from spoil material.

The samples were petrographically analysed as polished blocks and polished thin sections using transmitted and reflected light microscopy. Images were captured using a Leica (DVM2500) digital microscope with an attached VZ700C lens in the Geomicroscopy Facility at University College Cork.

Pre-Variscan and syn-Variscan quartz veins were classified in the field according to their structural genesis. Five mineralized and seven unmineralized (barren) quartz vein samples were prepared as doubly polished thin sections. Small chips of max. 0.5 cm^2 were examined with a Linkam (LMS600) temperature-controlled microscope stage, combined with an Olympus BX50 microscope, a x100 LWD objective and an attached 16 megapixels Nikon DS-Ri2 camera at the UCC Geomicroscopy Facility. Bi-phase (liquid and vapour, L+V) fluid inclusions were analysed for their freezing temperature T_{ice}, the first melt temperature T_{fm} and the final melt temperatures T_m, as well as the homogenisation temperature T_h = liquid + vapour = liquid. Special care was taken to measure only the primary fluid inclusion assemblages related to growth zones of the quartz grains. Necking fluid inclusions, as well as secondary or pseudosecondary inclusions related to healed cracks were avoided. Within the mineralized veins, primary inclusions were selected, which are genetically related to the copper sulphides (Appendix E). The stage was calibrated using a CO_2 standard (-56.6 °C, Camperio) and a synthetic, doubly distilled H_2O standard (T_m = 0.0 °C, T_h = L + V = L: 374.0 °C, Leoben). The stage system has a resolution of 0.1°C. Doppler and Bakker (2014) described an uncertainty for this type of stage in detail with a maximum standard deviation of ± 0.4 °C. Salinity was calculated as wt% $NaCl_{equiv}$ by using the Excel macro HOKIEFLINCS_H2O-NACL (Steele-MacInnis *et al.* 2011; Steele-MacInnis *et al.* 2012; Bodnar 1993; Atkinson 2002; Bodnar *et al.* 1994; Bodnar 1983).

A historic molybdenite sample (BM.1964,R230) from Ballycummisk Mine (Fig. 4.3) was provided by the National History Museum in London (NHM). The mineralized quartz-molybdenite specimen was collected by Sir Arthur Russell from the Ballycummisk dumps in 1907 (NHM Russell collection). A further molybdenite sample was discovered recently on the dumps of Ballycummisk Mine (Table 4.1, JL_BC_525). Small fragments (< 1 cm) were separated from

the samples using a micro chisel to avoid major damage and potential rhenium contamination. Both samples contain fine-grained molybdenite with crystal size smaller than 2 mm. They were both analysed using reflected light microscopy. The recent finding (JL_BC_525) was used for and fluid inclusion microthermometry, as well. Both samples were used for Re-Os geochronology at Durham University Laboratory for Source Rock and Sulfide Geochemistry and Geochronology. Sample preparation and analysis was undertaken as described in detail by Selby & Creaser (2001) and Li *et al.* (2017). The molybdenite material was isolated from the vein quartz and other minerals with HF. Approximately 10mg of pure molybdenite was loaded into a carius tube with aqua regia (3 ml HCl + 6 ml HNO_3) and a known amount of tracer solution (^{185}Re + isotopically normal Os). The carius tube was then sealed and placed in an oven for 24 hrs at 220˚C. The Os and Re isotopically equilibrated sample and tracer solution were extracted from the acid solution using solvent extraction, microdistillation and anion chromatography methods. The purified Re and Os fractions were measured for their isotopic compositions in static mode using a Thermo Scientific Triton mass spectrometer in the Arthur Holmes Laboratory at Durham University. The Re-Os molybdenite model age was calculated with the equation $t = \ln(^{187}Os/^{187}Re + 1)/\lambda$ (Smoliar *et al.* 1996), where λ is the decay constant for $^{187}Re = 1.666 \times 10^{-11}\ a^{-1}$ (Smoliar *et al.* 1996; Selby *et al.* 2007). Uncertainties were calculated with mass spectrometry uncertainty, all analytical sources uncertainties and the decay constant (Table 4.1).

4.5 Results

Large areas of outcropping bedrock, especially on the West Cork peninsulas and south-western coastline greatly facilitates the structural interpretation of satellite imaging data and kilometre scale geological features. This detailed aerial image interpretation is ground truthed for selected localities (Fig. 4.3).

In the northernmost part of the research area, the Beara Peninsula (Fig. 4.1 + 4.3), East-West striking faults and fault systems are identified as negative topographic features (photolineaments) on satellite imaging data (Bing™

Satellite Maps, 2016-2019). Owing to surficial weathering the faults form trenches of about 3 to 40 metres width and up to 8.4 kilometres length (Fig. 4.3). The strike of these E-W faults has a mean direction of 089° (N = 301). Along the coastline the faults often form narrow elongate bays due to erosion. Sometimes, the faults are associated with large (up to several hundred metres) E-W trending quartz veins. Many of these form historically mined copper lodes (GSI Jetstream 2019; Fig. 4.3, e.g. Allihies and north coast of Beara Peninsula). Perpendicular N-S striking faults up to 4.3 km in length are generally not associated with quartz veins, with the exception of Allihies (Fig 3). Owing to their nearly parallel orientation to the Variscan compression the N-S faults show stronger folding than the E-W faults (nearly perpendicular to Variscan stress).

On Sheep's Head Peninsula (Fig. 4.1 + 4.3) the E-W faults have a maximum length of 4.7 km and a mean strike of 089 (N = 63). Similar to the Beara Peninsula the E-W faults are associated with historically mined, mineralized quartz veins (Fig. 4.3, e.g. Gortavallig and Killeen North). N-S to NNE-SSW striking faults with a maximum length of up to 5 kilometres are also present.

The southern part of Mizen Peninsula (Fig. 4.1 + 4.3) is dominated by ENE-WSW striking faults, which belong to the same fault system as the E-W faults on Beara Peninsula and Sheep's Head. These ENE-WSW faults can be followed offshore (GSI Infomar 2017). Their mean strike is 082° (N = 115) and the faults can have a maximum length of 7 km (Fig. 4.3). The north-eastern part of Mizen Peninsula shows more an E-W strike of these faults with max. 4.3 km length and a mean strike of 090° (N = 98). The E-W striking, as well as the ENE-WSW striking faults can sometimes be associated with the historic copper lodes (Fig. 4.3, e.g. Dhurode Mine and Crookhaven Mines). N-S striking faults on Mizen Peninsula have a maximum length of 6.6 km and are generally not associated to mineralized quartz veins.

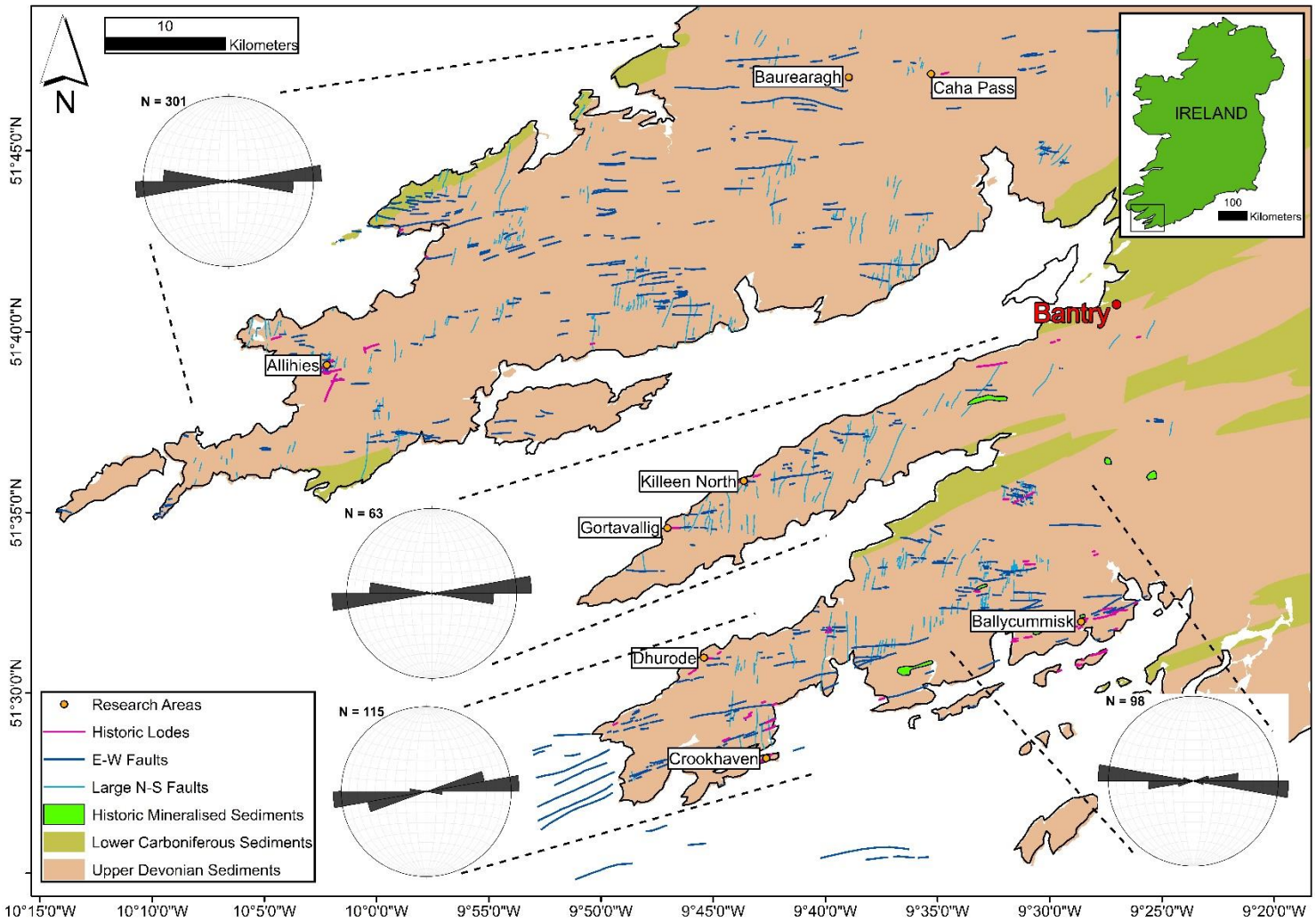


Fig. 4.3) Geological map with research localities, modified after GSI (2016), including satellite image and bathymetry data interpretation (Bing™ Satellite Maps 2016-2019, GSI Infomar 2017) and historical mineralization localities (GSI Jetstream 2019): West Cork peninsulas with outcropping Upper Devonian and Lower Carboniferous sediments. Large scale E-W faults and N-S faults with their relation to historic copper lodes and mineralized sediments. The rose diagrams show the mean orientation of the E-W and ENE-WSW striking faults.

The following localities are used as case studies to study the relationship of the mineralized quartz veins (copper lodes) to the E-W striking, kilometre scale, faults (Fig. 4.3):

4.5.1 Baurearagh

Location and Lithology

The research area is a hill next to the Baurearagh Valley, located in a mountainous area of the Beara Peninsula, about 17.5 kilometres northwest of Bantry (Fig. 4.3). The area was chosen due to the large number of quartz veins that were identified using satellite imaging. There is no record of any copper mineralization or historic mining, but the unusual N-S strike of the quartz veins in this area that required detailed examination. The outcropping rocks are mainly a mica-rich, beige to reddish-brown sandstones (Caha Mountain Formation, GSI 2016) with individual beds up to 1 m thickness.

Pre-Variscan Structures

A major E-W to ENE-WSW striking fault was identified in the northern part of this area (Fig. 4.4a). The fault forms a shallow trench which can be up to 85 metres wide. To the east, the fault forms an E-W oriented trench, as well as apparent N-S striking structures (Fig. 4.4a). A drone photogrammetry 3-dimensional model of this area shows that the topography effect of a relatively shallow (57° to the south, instead of vertical) dipping E-W fault caused the apparent N-S striking features (Fig. 4.4b). Quartz veins up to 40 metres length and 1.5 m in width occur parallel to the E-W striking faults (Fig. 4.4a). Most of the veins occur near the surficial outcropping intersection of the E-W to “N-S” striking faults (Fig. 4.4a + 4.4b). The mean strike of the veins is 085° (N = 457). The largest veins occur at the narrow areas of the E-W faults in the North. Smaller quartz veins can have a random orientation and form hydrofractures with stockwork veining containing brecciated host rock sediment clasts (Fig. 4.4c). The host rock sediments do not show any alteration nearby the quartz veins (Fig. 4.4c).

Variscan Structures

The rocks in the Bauregaragh area show a well-developed tectonic cleavage with a NE-SW to ENE-WSW strike and a nearly vertical dip. A SW to NE striking open, upright syncline occurs along the ridge of the hill (Fig. 4.4a + 4.4b) which is parallel aligned with a minor parasitic anticline. The large syncline forms a pair with a large anticline occurring about 480 m to the southeast (Fig. 4.4a + 4.4b). Variscan conjugate semi brittle shear zones with tension gashes occur across the entire area forming en echelon quartz veins (Fig. 4.4d). The host rock next to the quartz veins does not show any alteration (Fig. 4.4d). Parallel to the fold axes are several NE-SW striking fractures with no or little visible displacement (Fig. 4.4a + 4.4b).

Some pre-Variscan vein structures have developed cleavage parallel to the host rock cleavage as well as varying degrees of folding. Some of these veins also have a minor sinistral offset of about 3-4 cm due to cleavage-parallel faulting. The E-W striking extensional fault in the north (Fig. 4.4a) has associated parallel-aligned extensional quartz veins with widths of up to 60 cm (Fig. 4.4e). One of these veins show a fault surface (116/41) and slickenlines (orientated 32→147) indicating reverse movement of the hanging wall to the NW during compression. Perpendicular to the fault surface stylolites and cleavage are developed within this vein (Fig. 4.4e).

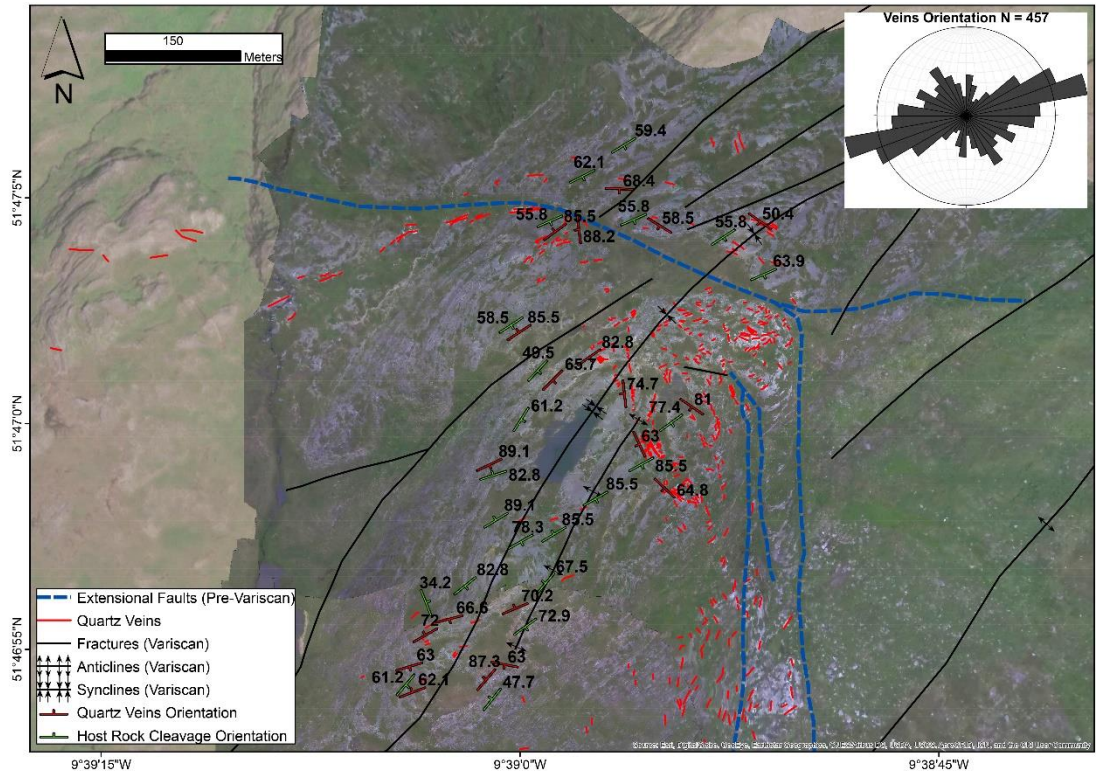
Mineralization and Microstructures

The pre-Variscan quartz veins show high concentrations of chlorite which can form green rims around the host rock sediment clasts (Fig. 4.4c) or as discreet aggregates of up to 4 cm diameter.

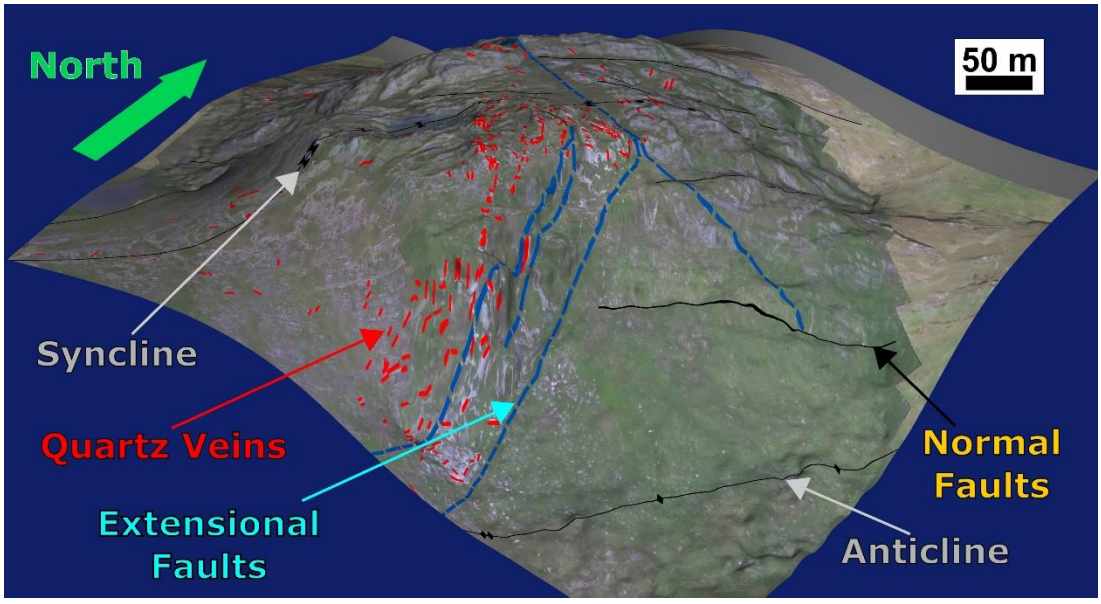
Some of the pre-Variscan quartz veins contain specular hematite. Petrographic analyses reveal that the hematite within the quartz vein is folded and shows deformation twinning (Fig. 4.4f). Within the same sample stylolites can be found in the quartz vein (Fig. 4.4g). The stylolites are lined with goethite. The pre-Variscan quartz veins have generally elongate blocky quartz crystals (Fig. 4.4g).

The Variscan en echelon quartz veins are usually free of chlorite, but they can show minor amounts of iron hydroxides. The quartz crystals can be elongate blocky to stretched elongate blocky.

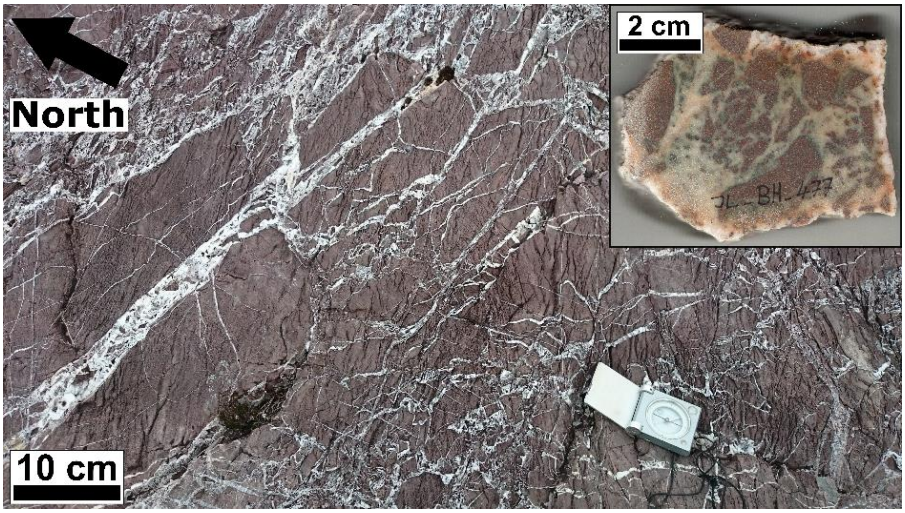
Fig. 4.4a)



4.4b)



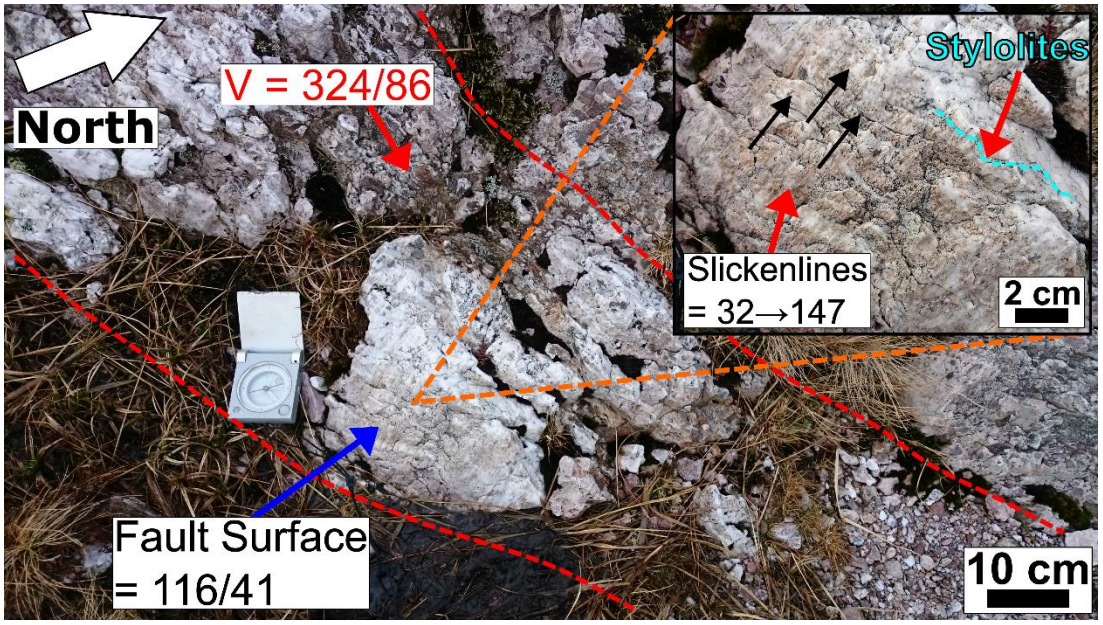
4.4c)


North
2 cm
10 cm

4.4d)


North
10 cm

4.4e)


North
V = 324/86
Stylolites
Slickenlines
= 32→147
2 cm
Fault Surface
= 116/41
10 cm

4.4f) *4.4g)*

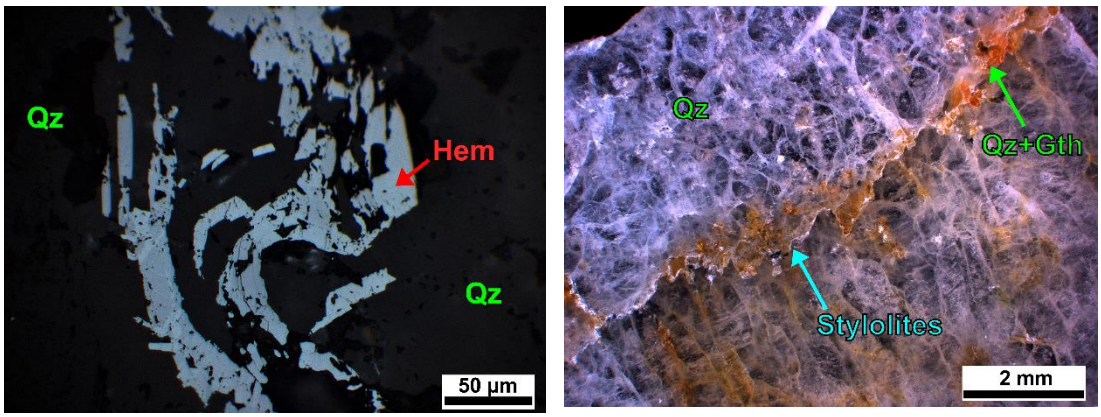


Fig. 4.4) Baurearagh on Beara Peninsula: a) Structural map with detailed drone maps of the research area showing pre-Variscan E-W and N-S faults and quartz veins, as well as compressional NE-SW striking folds and faults. b) 3-dimensional photogrammetry drone model shows the topography effect of the steep dipping E-W striking fault. c) Stockwork quartz veining within the red sandstone; smaller image: quartz vein hydraulic breccia with red sandstone clasts and green chlorite rims. d) Syn-compressional en echelon quartz veins within the cleaved sandstone. e) E-W striking quartz veins showing cleavage, stylolites and slickenlines, which indicate reverse movement of the hanging wall. f) + g) Microphotographs of the Baurearagh mapping area: f) Quartz vein (Qz) with folded specular hematite (Hem) with deformation twinning. g) Quartz vein (Qz) with elongate blocky quartz crystals and stylolites seamed by a mixture of quartz (Qz) and goethite (Gth).

4.5.2 Caha Pass

Location and Lithology

The mapping area is directly located above and around the Turners Rock Tunnel on Caha Pass (road N 71) about 15.2 km northwest of Bantry and 4 km east of Baurearagh on the Beara Peninsula (Fig. 4.3 + 4.5a). The lithology is purple siltstone with occasional symmetrical ripple marks in the southeast of the mapping area (Fig. 4.5a). The area around the tunnel is dominated by greenish grey to beige siltstone (Slaheny Sandstone Formation, GSI 2016).

Pre-Variscan Structures

The N-S oriented tunnel cuts through three major E-W striking faults (Fig. 4.5a). The faults usually form narrow linear topographic depressions with a maximum width of 10 metres. They are associated with E-W striking quartz veins with a maximum length of 37 metres and a width of up to 1 m (Fig. 4.5a). The mean strike of the quartz veins is 089° (N = 48). In the East, the veins form sub-parallel groups of 2 – 40 cm wide massive quartz with occasional vugs with euhedral quartz crystals. In the western part of the area (Fig. 4.5a), the quartz forms a stockwork veining zone (1 m width) with brecciated and weathered host rock sediment clasts. In some cases, the quartz veins have N-S oriented horsetail splays diverging from the large E-W veins. No host rock alteration next to the quartz veins was observed.

Variscan Structures

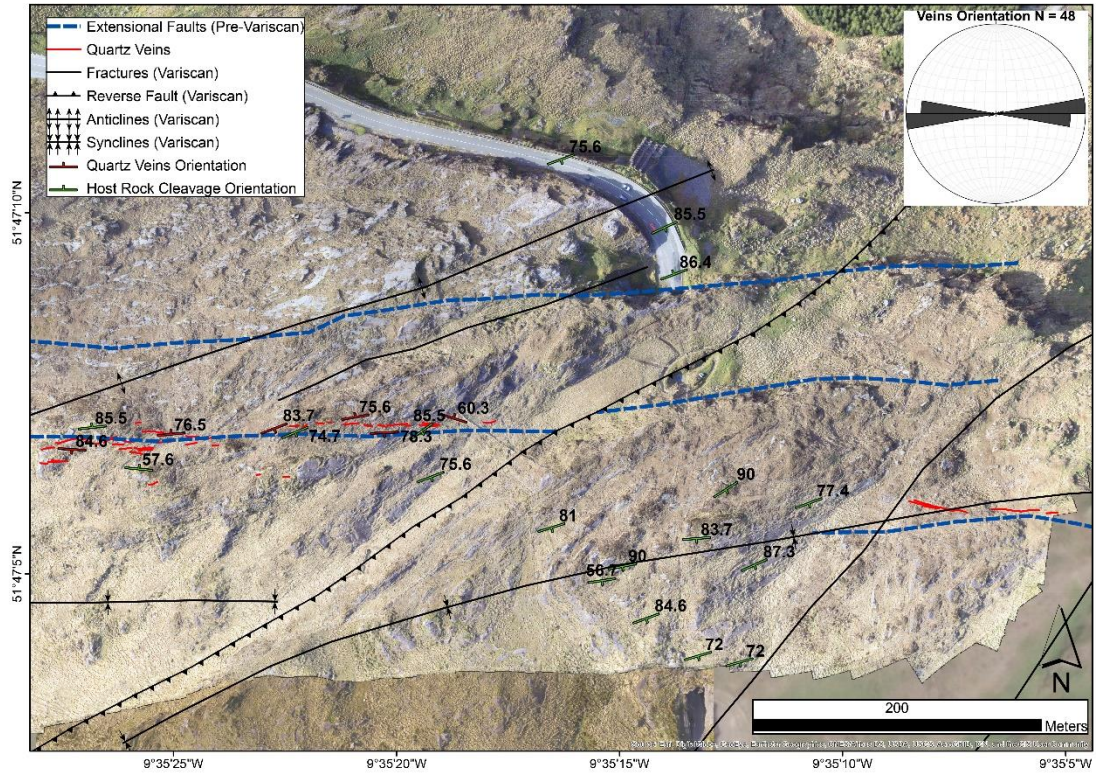
The cleavage of the siltstones shows an overall E-W to NE-SW strike with a steep dip (Fig. 4.5a). A WSW-ENE striking anticline occurs at the northern entrance of the tunnel. About 150 metres to the south is an E-W striking syncline which is apparently faulted dextrally by a NE-SW striking reverse fault (Fig. 4.5a). This reverse fault forms an apparent sinistral offset to one of the E-W striking early faults. Several NE-SW striking fractures occur within a distance of 150 to 225 m from this structure. Host rock cleavage occurs generally sub-parallel to the pre-Variscan E-W striking quartz veins. Pre-Variscan veinlets (< 3 cm) with an N-S strike are folded and show cleavage. Stylolites have been observed within the E-W quartz veins sub-parallel to the host rock cleavage (Fig. 4.5b).

Mineralization and Microstructures

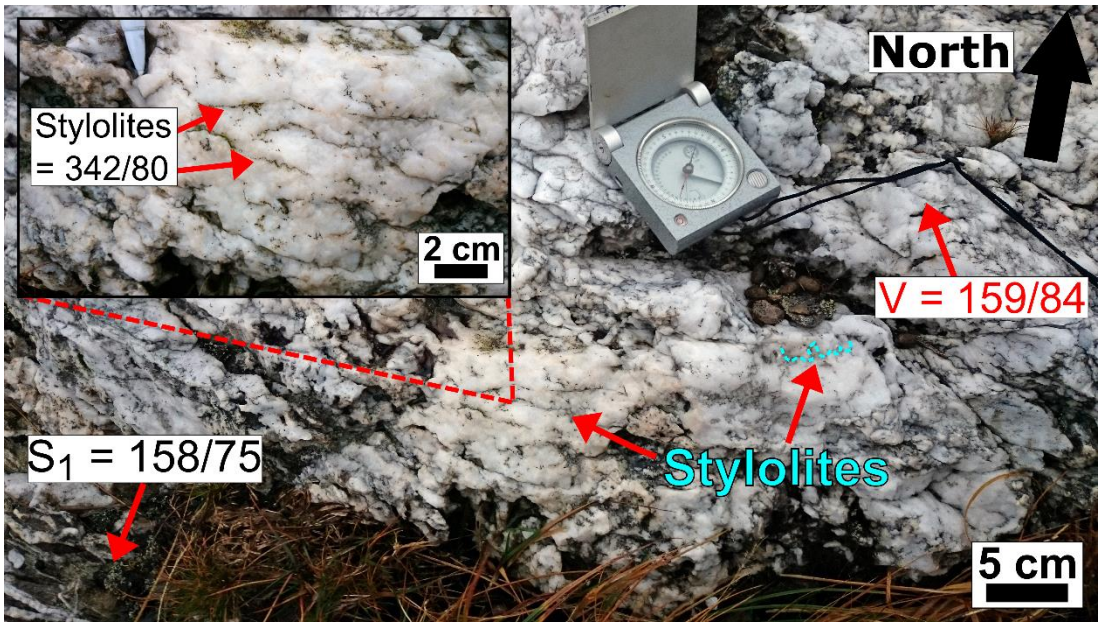
Some of the E-W striking quartz veins are slightly reddish stained by iron hydroxides within the quartz. These veins are highly enriched in green chlorite. Within the tunnel (Fig. 4.5a) a crust of malachite was found on the cleaved siltstone nearby an E-W striking fault. A sample from the quartz veins in the western mapping area (Fig. 4.5a) shows a massive quartz (Fig. 4.5c, earlier generation) with disseminated chlorite, as well as chlorite aggregations with a small amount of malachite. This chlorite-rich quartz vein is crosscut by a later

generation quartz vein. The later quartz generation consists of clear elongate stretched quartz crystals. Both earlier and later quartz veins show stylolites. The chlorite forms seams along the stylolites as an insoluble mineral (Fig. 4.5c).

Fig. 4.5a)



4.5b)



4.5c)

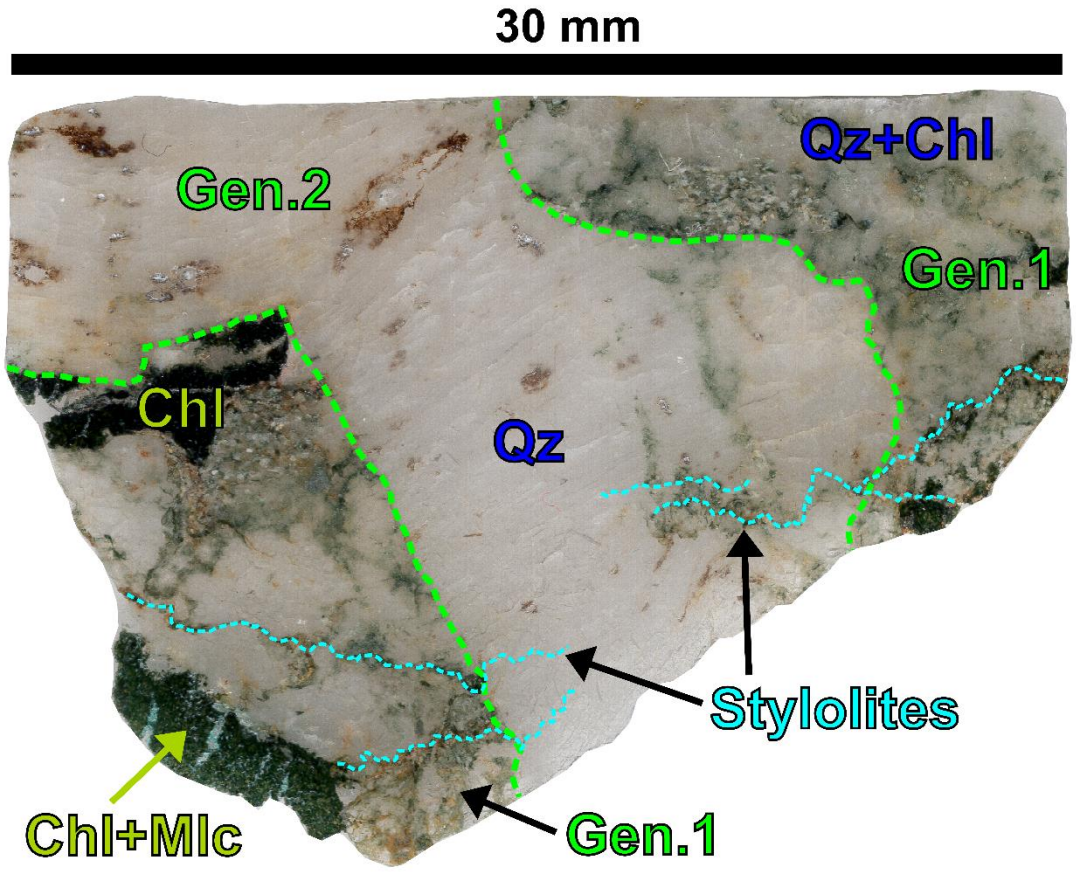


Fig. 4.5) The Caha Pass with the Turners Rock Tunnel on Beara Peninsula: a) Structural map with detailed drone maps of the research area showing pre-Variscan E-W faults and quartz veins, as well as compressional WSW-ENE to E-W striking folds and NE-SW striking faults. b) Pre-Variscan E-W striking quartz vein with syn-compressional stylolites. c) Polished slide from an E-W striking quartz vein (Qz) with an earlier chlorite-rich (Chl) generation (Gen. 1) and minor malachite (Mlc), crosscut by a later generation (Gen. 2) of clear elongate quartz (Qz). Both generations show stylolites.

4.5.3 Gortavallig

Location and Lithology

The historic mines of Gortavallig are located on the northern coast of Sheep's Head Peninsula, approximately 25.5 kilometres Southwest of Bantry (Fig. 4.3). The host lithology belongs to the Toe Head Formation (GSI 2016) with cross-

bedded beige sandstone in the north of the mining area, grey-beige sandstone to the west, and mica-rich siltstone to grey sandy slates around the mine shafts (Fig. 4.6a).

Pre-Variscan Structures

Two major E-W to ENE-WSW striking faults occur at the cliff face in the north and continue inland to the east (Fig. 4.6a). These faults form linear topographical depressions up to 30 m wide. At narrow parts of the depressions, and along the cliff face, mineralized and partly mineralized E-W trending (087° - N = 38) quartz veins up to 1.5 m width and over 35 m length can be found. The generally massive quartz veins show occasional vugs of euhedral quartz crystals (up to 2 cm).

Variscan Structures

The host rock sediments contain a cleavage with a general NE-SW strike and a steep to vertical dip (Fig. 4.6a). A series of NE-SW striking anticlines and synclines occur within a parallel distance of 115 to 350 metres. The limbs of the folds contain a series of semi brittle shear zones within the coarse-grained sandy units which are filled with quartz veins (Fig. 4.6b).

Small N-S trending fractures, with almost no strike-slip movement, occur across the entire mapping area. A kilometre long, NE-SW striking reverse fault is aligned to the fold axes (Figs. 4.6a + 4.6b). Within a historic adit exposed on the cliff face the siltstone footwall shows slickensides with a 54->202 lineation, indicating a NW movement of the hanging wall. This reverse fault generates an apparent sinistral offset of about 118 metres to the pre-Variscan E-W striking fault and associated quartz veins (Fig. 4.6a). About 520 metres southwest of the main shafts an intensively iron stained quartz vein (striking NE-SW) is cut off by a bedding parallel thrust (S_0 = 144/35) adjacent to a minor anticline (Fig. 4.6c). Some of the early E-W striking veins show a tectonic cleavage, minor folding (especially thinner veins with max. 3 cm width), and slickensides. The host rocks next to the larger quartz veins (> 40 cm) show minor bleaching with some localized iron hydroxide concentrations within a distance of max. 50 cm to the veins (Fig. 4.6c).

Mineralization and Microstructures

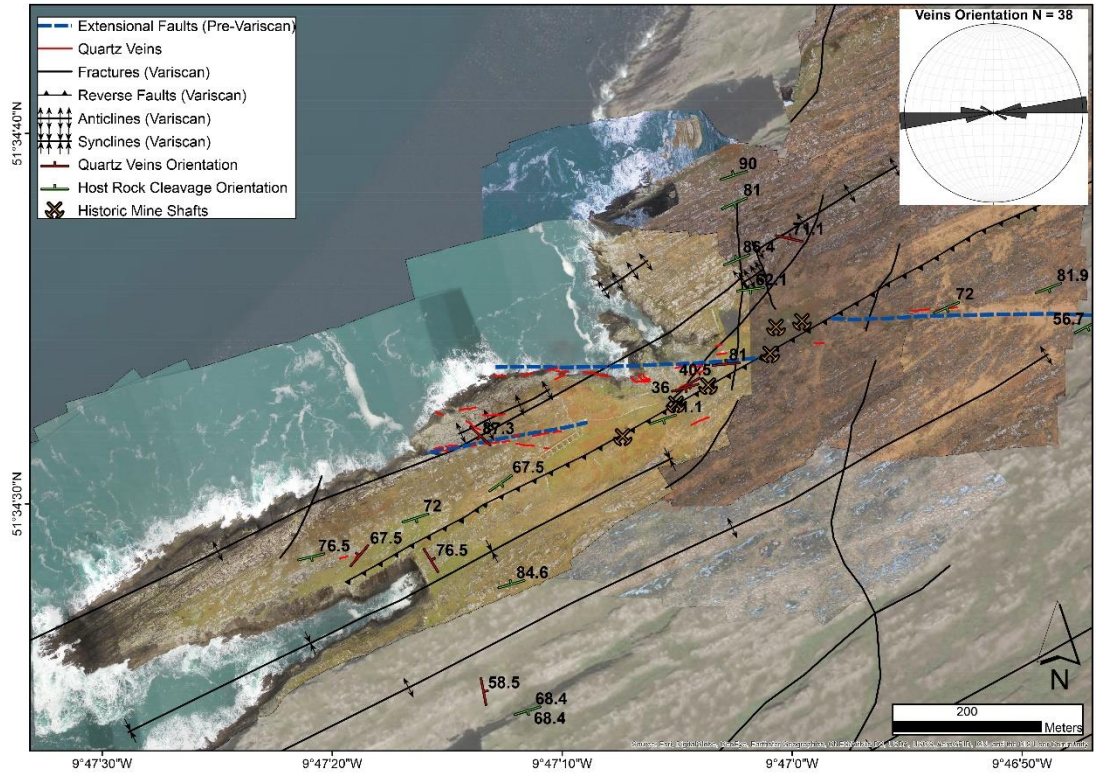
The mineralized veins show intensively red iron hydroxide (goethite) stained zones (Fig. 4.6c). Minor chalcopyrite can be identified in the vein outcrop. Near the major adits, the quartz veins show minor crusts of secondary copper minerals.

Petrographic analyses show quartz veins with cataclasticly deformed arsenopyrite (Fig. 4.6d). The arsenopyrite is euhedral to subhedral and the crystals can have a diameter of up to 1 cm. Syngenetic to the arsenopyrite, small amounts of chalcopyrite can be found. Along the major E-W fault (Fig. 4.6a) several hand specimens with massive pyrite were found. The pyrite is intergrown with smaller amounts of galena (Fig. 4.6e) as well as syngenetic chalcopyrite and tetrahedrite (Fig. 4.6f). An in-situ sample from near the adits shows a mineralized quartz vein (chalcopyrite) within a sandstone (Fig. 4.6g). The vein is in direct contact to a slate which is as well mineralized with chalcopyrite.

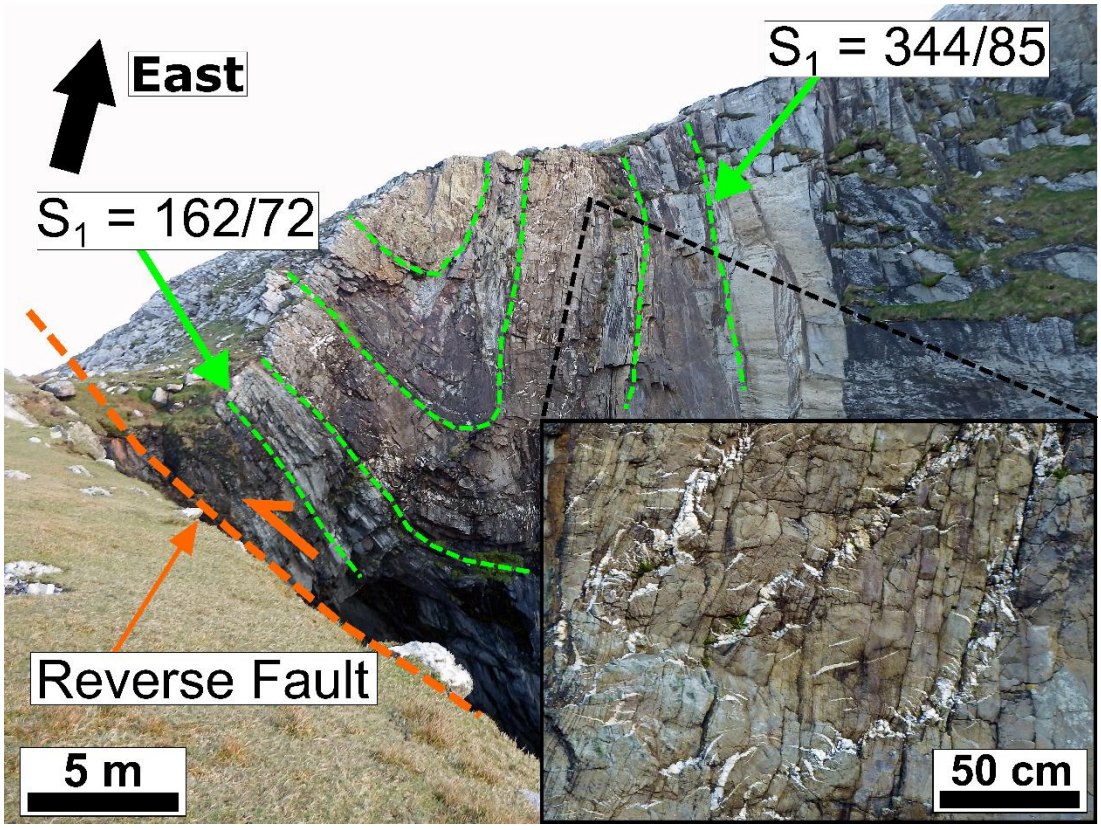
The syn-compressional veins (e.g. en echelon veins) don't show any sign of mineralization. They are mainly formed by clear stretched to fibrous quartz crystals. No host rock alteration next to the compressional veins was observed.

About 7.7 kilometres northeast of Gortavallig are the historical mines of Killeen North (Fig. 4.3). The structural setting is similar to Gortavallig and the mine shafts occur mainly along a large E-W striking fault. A hand specimen of a mineralized conglomerate was collected near an adit. Petrography reveals that some of the former carbonate-rich mudstone conglomerate clasts were replaced by chalcopyrite (Fig. 4.6h-k). The matrix of the conglomerate is siltstone. One of the mineralized clasts shows regular, elongated, cellular structures from a fossilised plant which is mainly chalcopyritized (permineralized in chalcopyrite) with a small amount of tetrahedrite (Fig. 4.6h-k).

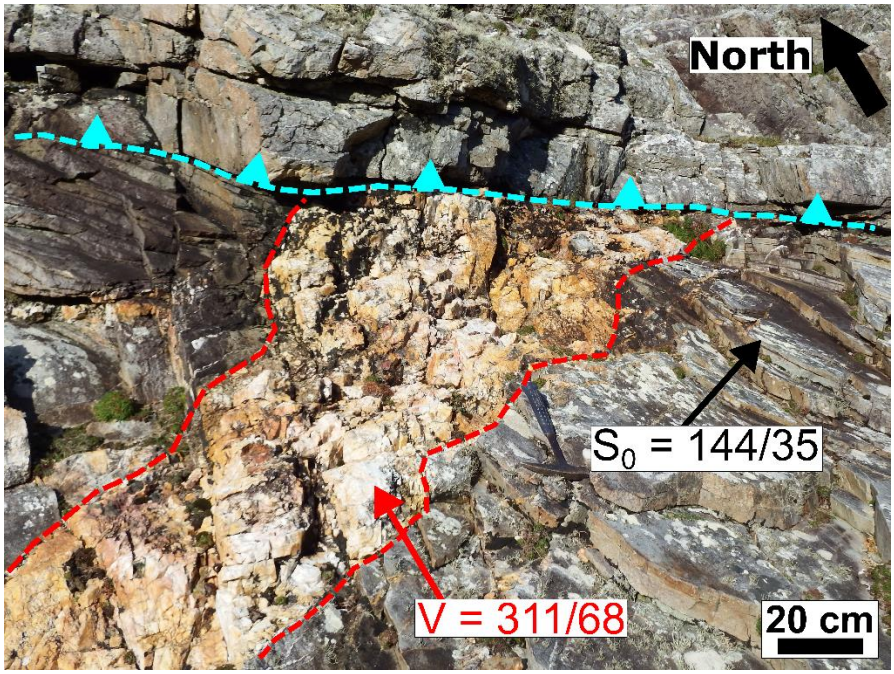
Fig. 4.6a)


Extensional Faults (Pre-Variscan)
Quartz Veins
Fractures (Variscan)
Reverse Faults (Variscan)
Anticlines (Variscan)
Synclines (Variscan)
Quartz Veins Orientation
Host Rock Cleavage Orientation
Historic Mine Shafts
Veins Orientation N = 38
51°34'40"N
51°34'30"N
9°47'30"W
9°47'20"W
9°47'10"W
9°47'0"W
9°46'50"W
90
81
71.1
86.4
82.1
81.9
72
56.7
81
40.5
36
87.3
67.5
72
76.5
67.5
76.5
84.6
58.5
68.4
68.4
N
200
Meters

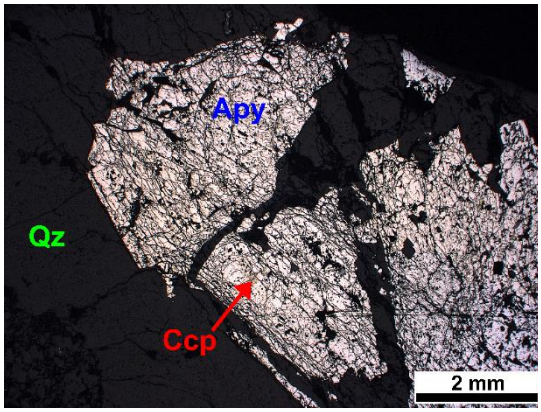
4.6b)


East
S_1 = 344/85
S_1 = 162/72
Reverse Fault
5 m
50 cm

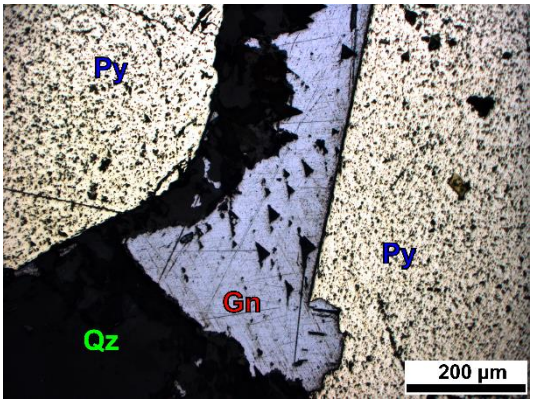
4.6c)



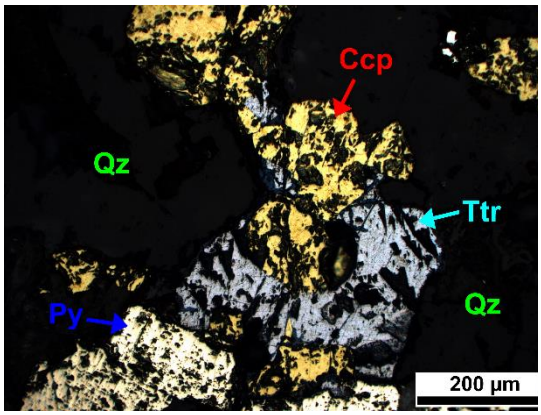
4.6d)



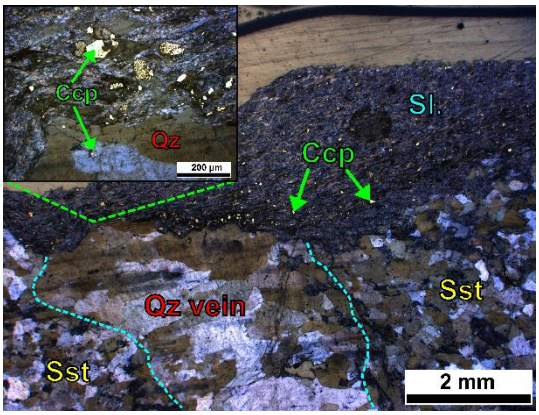
4.6e)



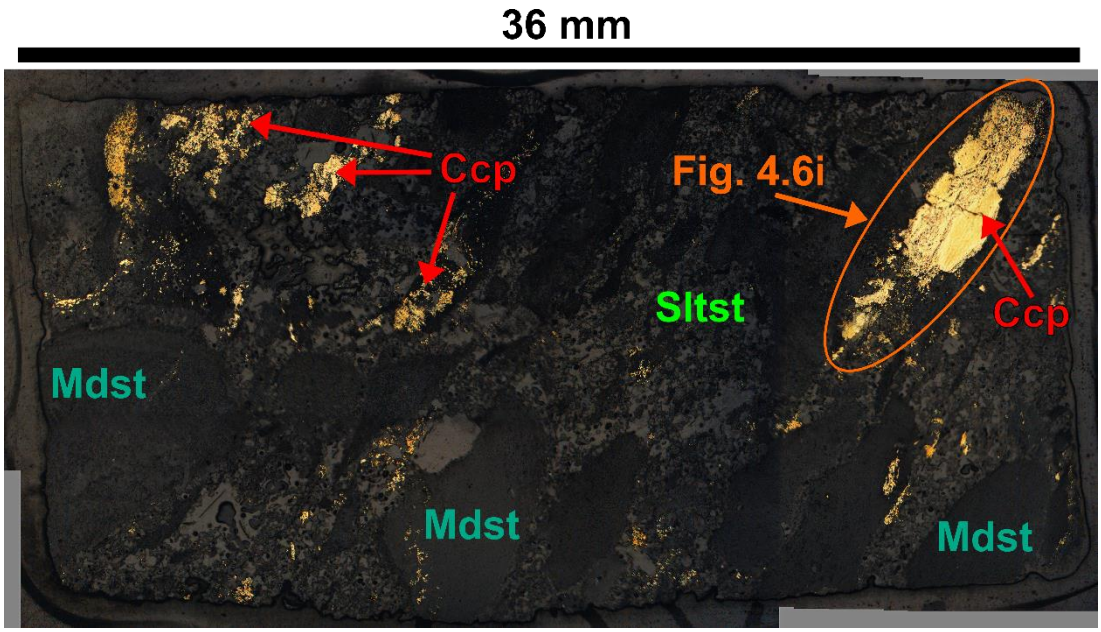
4.6f)



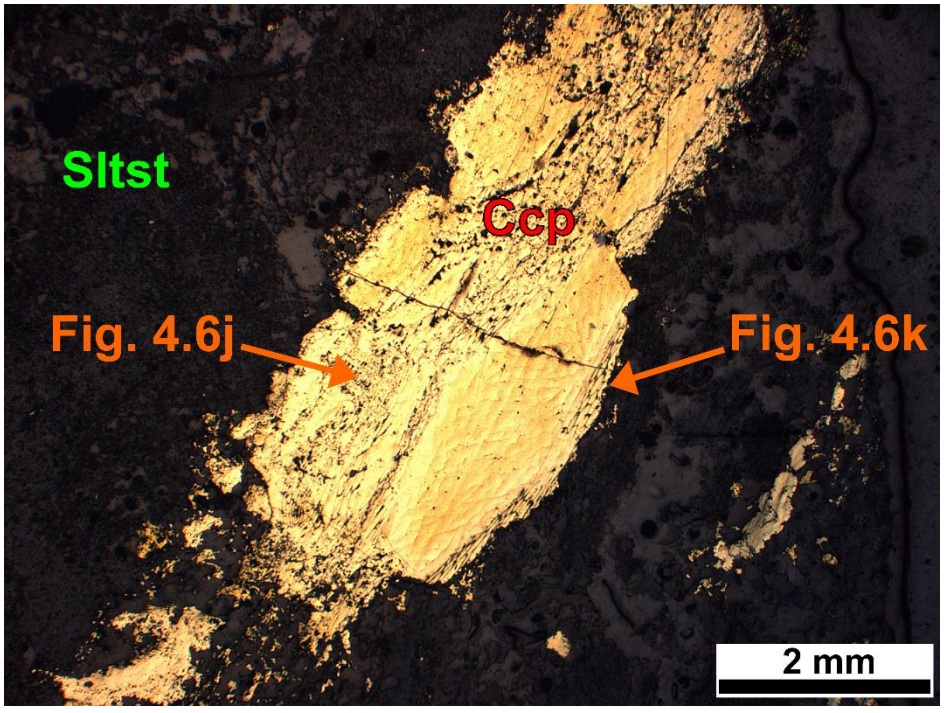
4.6g)



4.6h)


36 mm
Ccp
Fig. 4.6i
Sltst
Ccp
Mdst
Mdst
Mdst

4.6i)


Sltst
Ccp
Fig. 4.6j
Fig. 4.6k
2 mm

4.6j) *4.6k)*

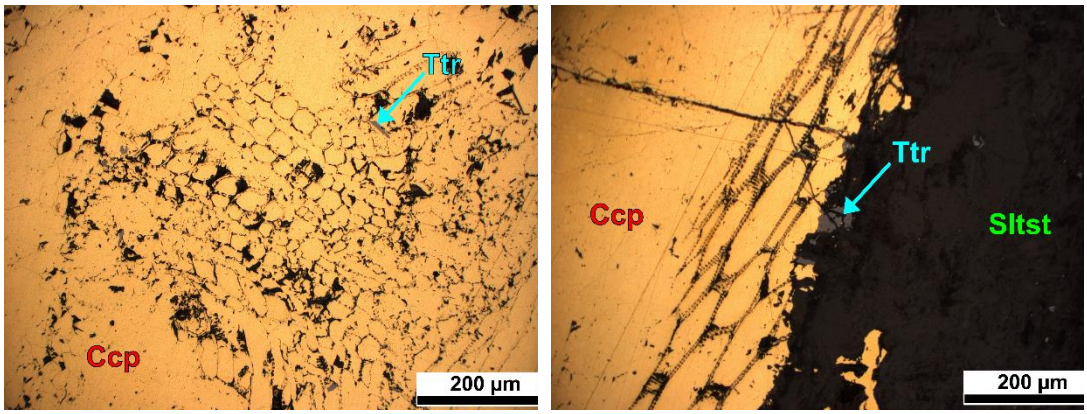


Fig. 4.6) The historic mines of Gortavallig on Sheep's Head: a) Structural map with detailed drone maps of the mining area showing early E-W faults and mineralized veins, as well as compressional NE-SW striking cleavage, folds and faults. b) Field image of NE-SW striking syncline with reverse fault and en echelon veining along the fold limbs. c) Iron-stained quartz vein cut off by bedding parallel thrust. d) – k) Microphotographs of mineralization at Gortavallig Mining Area: d) Cataclastic deformed arsenopyrite (Apy) within quartz (Qz) vein and minor chalcopyrite (Ccp), (reflected light, ppl). e) Massive pyrite (Py) with galena (Gn) and quartz (Qz) vein filling, (reflected light, ppl). f) Quartz vein (Qz) with syngenetic pyrite (Py), chalcopyrite (Ccp) and tetrahedrite (Ttr), (reflected light, ppl). g) Quartz vein (Qz) within sandstone (Sst) next to slate (Sl.). Both quartz vein and slate are mineralized with chalcopyrite (Ccp), (reflected and transmitted light, xpl). h-k) Conglomerate with mudstone (Mdst) and chalcopyritized (Ccp) clasts within siltstone (Sltst) matrix (Killeen North Mine). One of the chalcopyritized (Ccp) clasts shows oval to elongated fossilised plant cells with minor tetrahedrite (Ttr), (reflected light, ppl).

4.5.4 Dhurode

Location and Lithology

The historic copper mine of Dhurode is located on the northern coast of Mizen Peninsula, about 27 kilometres southwest of Bantry (Fig. 4.1 + 4.3). The major lithology in the mining area (Fig. 4.7a) is brownish red to grey, cross-bedded

silty sandstone and sandy siltstone (Toe Head Formation, GSI 2016). A grey to beige silty mudstone occurs at the quarry and the northern mine shafts near the cliff face (Fig. 4.7a, Old Head Sandstone Formation, GSI 2016).

Pre-Variscan Structures

A series of E-W striking extensional faults were identified from detailed drone mapping (Fig. 4.7a). These faults begin at the cliff face and show a strike swing from WNW-ESE in the east to ENE-WSW in the west. Around the historic mine shafts, the faults split up at the coastline and merge again after 200 - 400 m in the West (Fig. 4.7a). This fault zone has a width of up to 119 m. Pre-Variscan quartz veins are rarely visible, due to the amount of vegetation covering the fault zone and can only be identified close to mine shafts (outcrops). These quartz veins strike E-W and can be up to 30 cm wide. They contain small (< 2 cm) weathered host rock clasts. Smaller quartz veins (0.5 – 3 cm) show a random orientation. Bleaching of the host rock was observed within a max. distance of 20 cm to the quartz veins.

Variscan Structures

The Variscan cleavage has a NE-SW strike and a steep to nearly vertical dip generally to the SE, but occasionally to the NW (Fig. 4.7a + 4.7b). An anticline with an axial trace striking WSW-ENE is located about 300 metres northeast of the mining shafts (Fig. 4.7a + 4.7b). A syncline to the north forms an anticline-syncline pair with about 60 m wavelength. Each limb of the anticline is cut by WSW-ENE striking reverse faults forming a triangle zone which is recognised as a WSW-ENE striking topographical depression (Fig. 4.7b). NW-SE, NE-SW and N-S striking fractures occur throughout the area some have minor horizontal displacement. NW-SE striking and steep dipping quartz veins up to 10 cm in width occur within the quarry (Fig. 4.7a). These veins show stretched to fibrous quartz crystals with occasional vugs of euhedral quartz crystals.

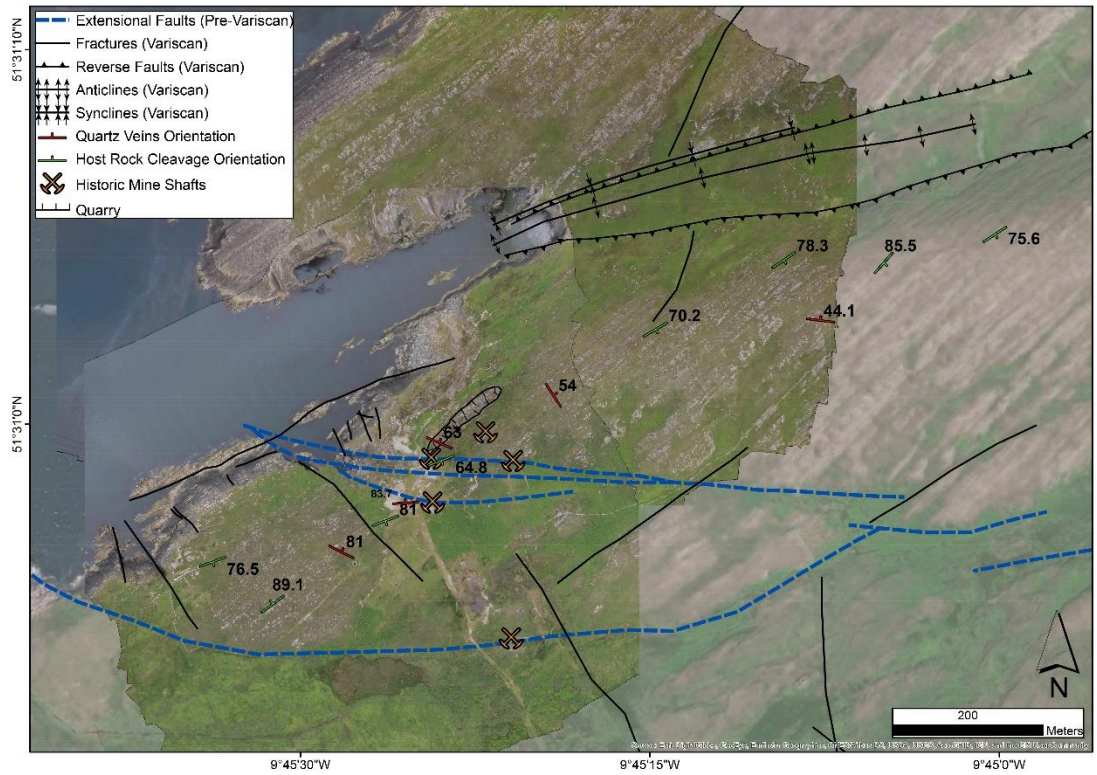
Small pre-Variscan quartz veins display minor folding. Veins show strong internal cleavage, especially when they are orientated perpendicular to the host rock cleavage.

Mineralization and Microstructures

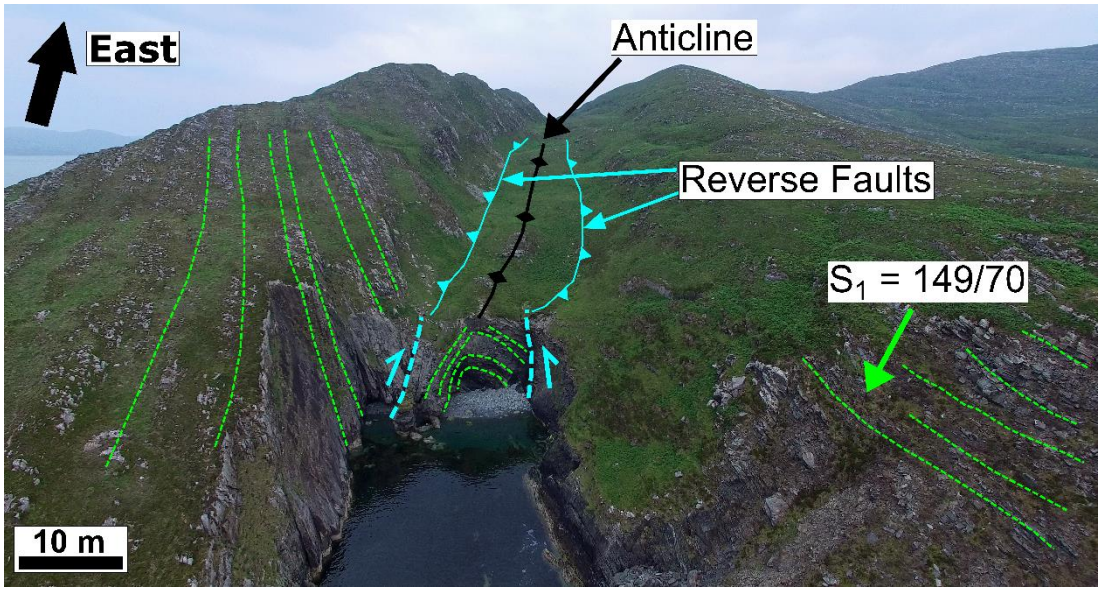
Fibrous quartz veins, containing minor siderite, show intensive iron hydroxide staining within the quarry (Fig. 4.7a). An oriented sample of an E-W striking quartz vein collected near the mine shafts was used for microstructural analysis (Fig. 4.7c, A). The quartz vein macroscopically shows patches of iron staining (altered sulphides). At the northern and southern rim of the vein (B) small (1 - 4 mm) quartz crystals occur, whereas the centre of the vein is dominated by elongate blocky crystals (< 7 mm) with an NE-SW c-axis orientation. While the crystals in the vein centre show a sweeping (Trouw *et al.* 2009) undulous extinction, the crystals at the rim are mainly dominated by patchy undulous extinction. Within the vein is a NNW-SSE striking micro-fault (C) of about 500 µm width which shows partial recrystallization. The elongate blocky crystals show a dextral offset of about 200 µm (D).

The mining tailings contain quartz veins containing predominantly chalcopyrite and arsenopyrite mineralization. Euhedral crystals of arsenopyrite are common. The arsenopyrite (< 3 cm) can occur within the quartz veins, as well as close to the veins within the siltstones. Petrographical analysis (Fig. 4.7d) shows fractured, euhedral arsenopyrite, with syngenetic chalcopyrite and minor syngenetic tetrahedrite.

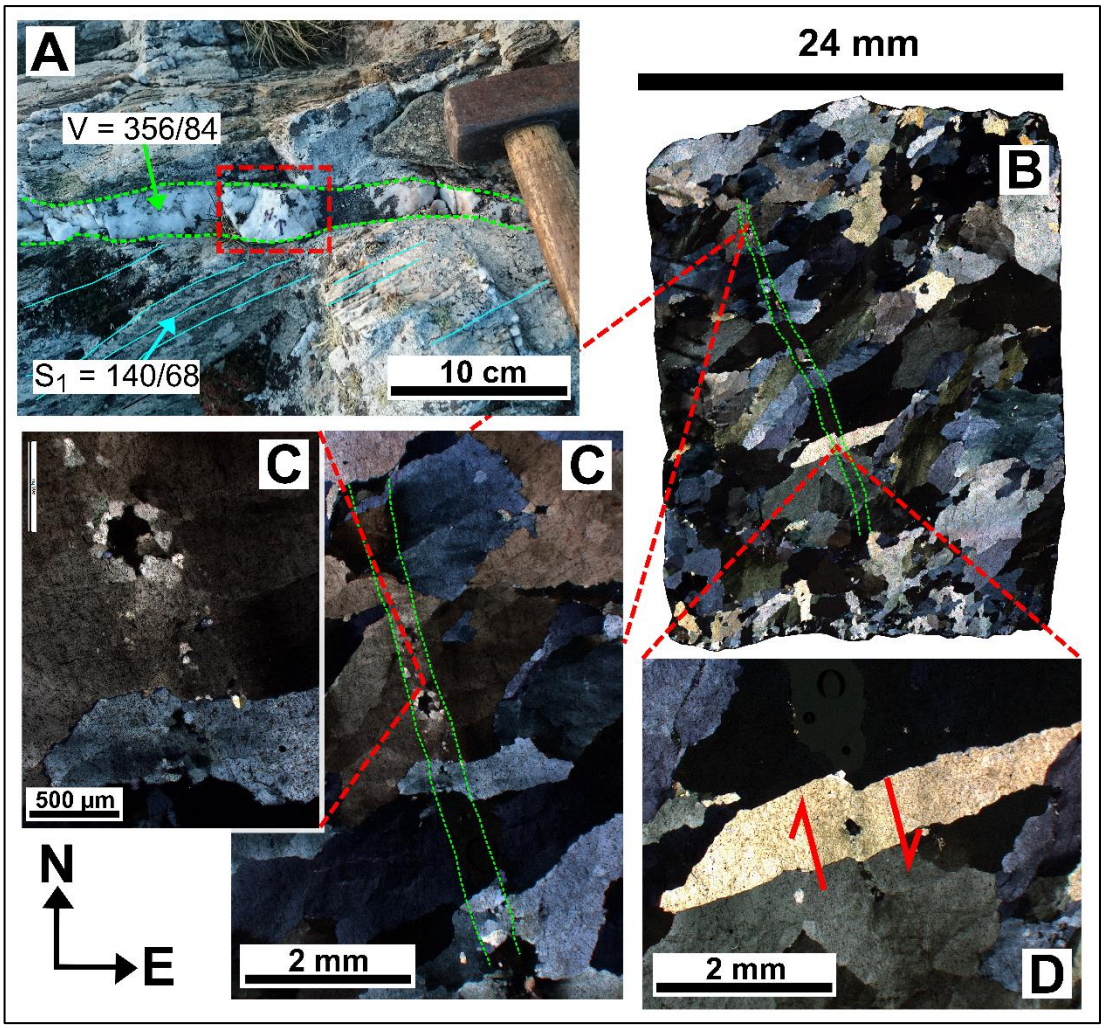
Fig. 4.7a)


Extensional Faults (Pre-Variscan)
Fractures (Variscan)
Reverse Faults (Variscan)
Anticlines (Variscan)
Synclines (Variscan)
Quartz Veins Orientation
Host Rock Cleavage Orientation
Historic Mine Shafts
Quarry
51°31'10"N
51°31'0"N
9°45'30"W
9°45'15"W
9°45'0"W
78.3
85.5
75.6
70.2
44.1
54
63
64.8
63.7
81
81
76.5
89.1
N
200
Meters

4.7b)


East
Anticline
Reverse Faults
S_1 = 149/70
10 m

4.7c)



4.7d)

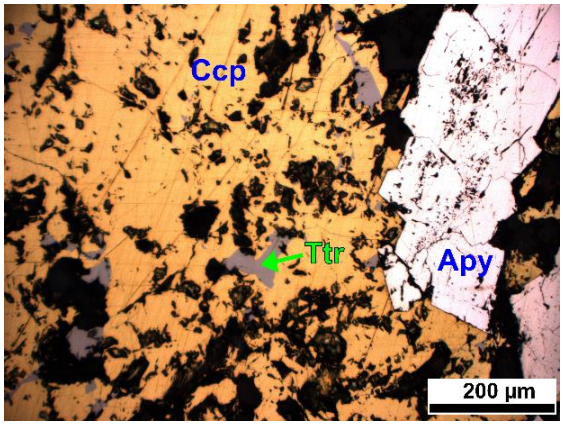


Fig. 4.7) The copper mines of Dhurode on the northern coast of Mizen Peninsula: a) Structural map with detailed drone maps of the research area showing pre-Variscan E-W faults, compressional NE-SW striking cleavage, as well as WSW-ENE oriented folds and faults. b) Aerial drone image of the coastal area at Dhurode showing NE-SW striking host rock cleavage and WSW-ENE striking anticline rimmed by two reverse faults. c) Thin section of oriented, mineralized quartz vein (near

mining shafts, cut perpendicularly to cleavage $S_{1,vein}$*.) showing elongate blocky quartz crystals with undulous extinction and partially recrystallized microfault (transmitted light, xpl). d) Microphotograph of mineralized quartz vein (Dhurode tailings) shows euhedral arsenopyrite (Apy) with syngenetic chalcopyrite (Ccp) and tetrahedrite (Ttr).*

4.5.5 Crookhaven

Location and Lithology

The historic Crookhaven Copper Mines are located at the southern coast of Mizen Peninsula (Fig. 4.1 + 4.3) about 6.2 km SSE of the Dhurode Mines. The lithology (Castlehaven Formation, GSI 2016) varies from greenish-grey mica-rich sandstone in the north of the mapping area (Fig. 4.8a), to grey phyllitic slate in the east and pale white to greenish-grey siltstone along the southern and western coastal outcrops. The siltstone in the central area shows herringbone cross stratification.

Pre-Variscan Structures

A series of NE-SW striking extensional faults can be identified in cliff outcrops (Fig. 4.8a). They generate topographical depressions up to 300 m long and up to 9-metre-wide. Partially mineralized massive quartz veins have developed parallel to these faults. The quartz veins can be up to 30 m long and have a width of up to 50 cm. Several quartz veins together can form lodes of over 400 m length (Fig. 4.8a). The quartz veins have a steep to nearly vertical dip with a mean strike of 075° (N = 680). Along the NE-SW striking quartz veins, splaying horsetail veinlets indicate sinistral extensional movement (Fig. 4.8b). Euhedral quartz crystals of up to 3 cm length can occur within vugs in the massive quartz veins. The siltstone next to the quartz veins shows a pale white to green (chlorite) alteration zone within 50 cm next to the quartz veins (Figs. 4.8c and 4.8d).

Variscan Structures

A pervasive, NE-SW striking, and steeply dipping cleavage is present throughout the mapping area (Fig. 4.8a). Parallel to the cleavage are a series of tight folds with 20 to 30 m wavelengths. The interlimb angle and the wavelength of the folds increases to the south (Fig. 4.8a). The area contains N-S striking joints up to 60 m length and a spacing of 5 to 10 metres (Fig. 4.8a).

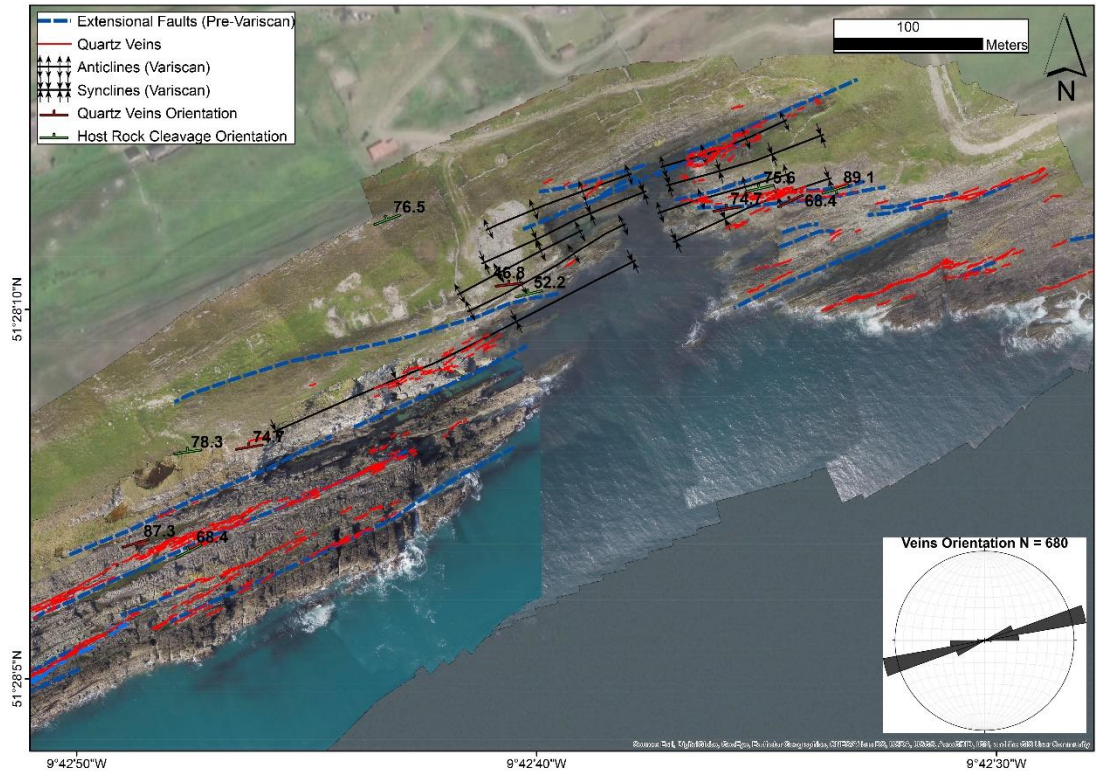
In the north-western part of the area, the pre-Variscan quartz veins show a bi-convex shaped strike (outcrop) formed by folding along the dominant syncline (Fig. 4.8a). Small quartz veinlets with chalcopyrite mineralization and intensive compressional folding occur within the pale-white cleaved siltstone adjacent to one of the major mineralized lodes. (Fig. 4.8c). Splaying horsetail veinlets from the NE-SW striking quartz veins (Fig. 4.8b) show intensive cleavage sub-parallel to the host rock cleavage, as well as minor to intermediate folding.

Mineralization and Microstructures

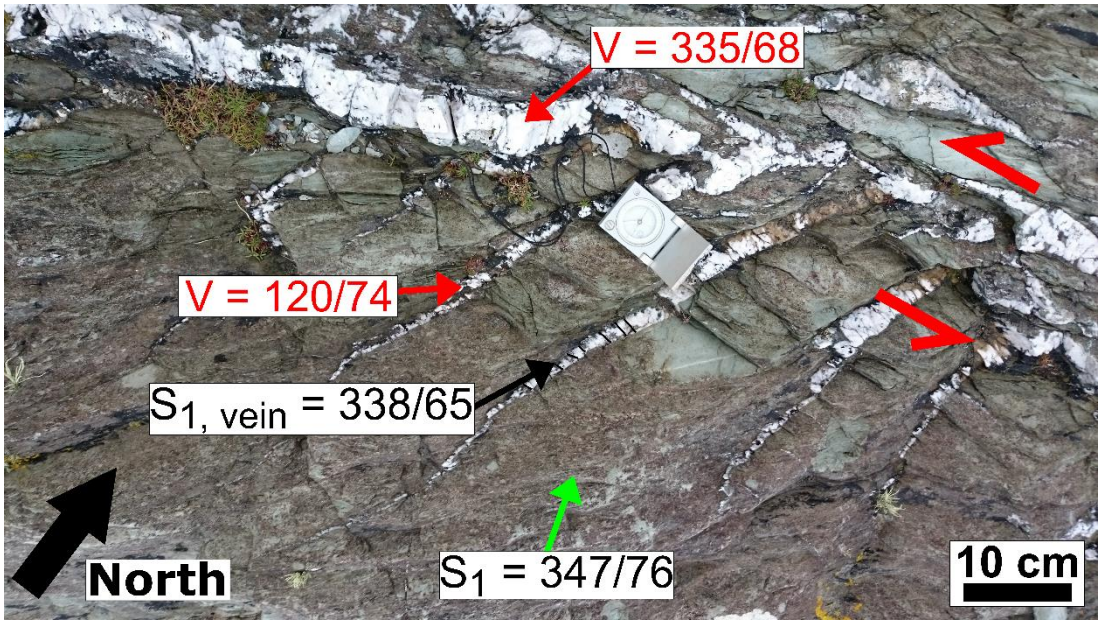
The outcropping NE-SW striking quartz veins commonly contain aggregates of chlorite and minor chalcopyrite (Fig. 4.8c) and barite. Some parts of the veins can be stained with iron hydroxides. Samples were taken from a mineralized quartz vein (Fig. 4.8d), as well as from an adjacent malachite-stained siltstone. Petrographical analyses shows disseminated chalcopyrite within the siltstone (Fig. 4.8d, A) and massive chalcopyrite, partially altered to goethite, within the quartz vein (Fig. 4.8d, B). A polished section of a quartz vein within a sandstone was generated from the Crookhaven tailings (Fig. 4.8e). The quartz vein is mineralized with bornite. Next to this vein is a microfracture with an altered fracture zone formed by fine grained quartz and goethite. A close-up of the altered zone shows cataclastic fractured bornite with minor, syngenetic chalcopyrite. The bornite is intensively altered to chalcocite clasts and minor covellite (Fig. 4.8e). The mineralized quartz veins generally have elongate blocky quartz crystals (Fig. 4.8f) and occasionally contain tectonic stylolites. Goethite and chlorite form concentrations as insoluble minerals along the stylolites. A chalcopyrite quartz vein with fibrous

quartz-siderite bands was found in the tailings (Fig. 4.8g). These bands show deformation kinks of up to 90 degrees.

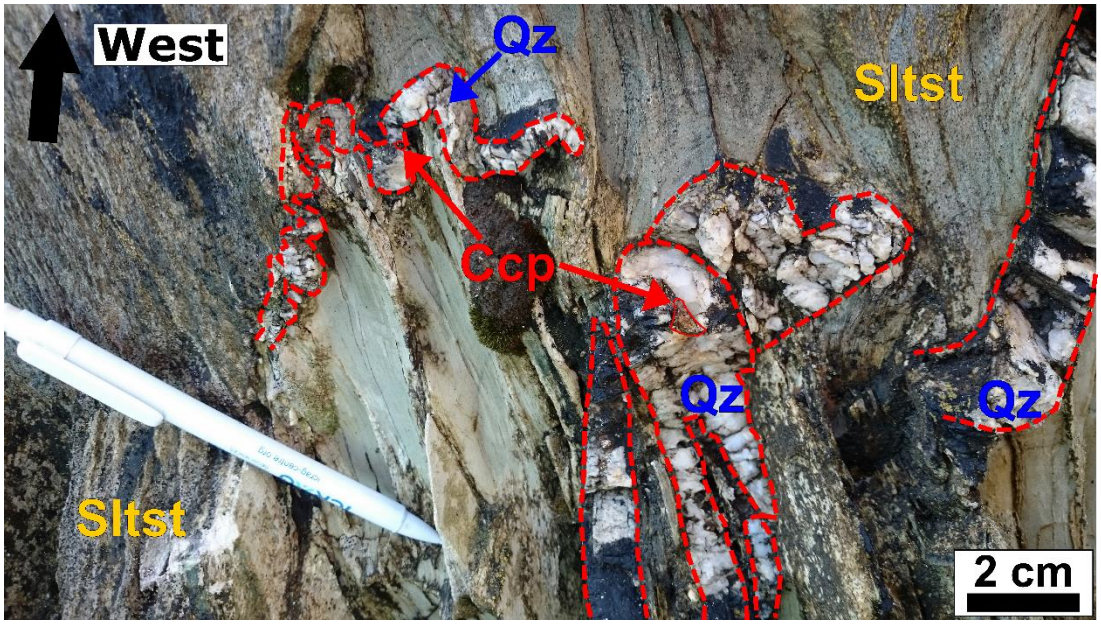
Fig. 4.8a)



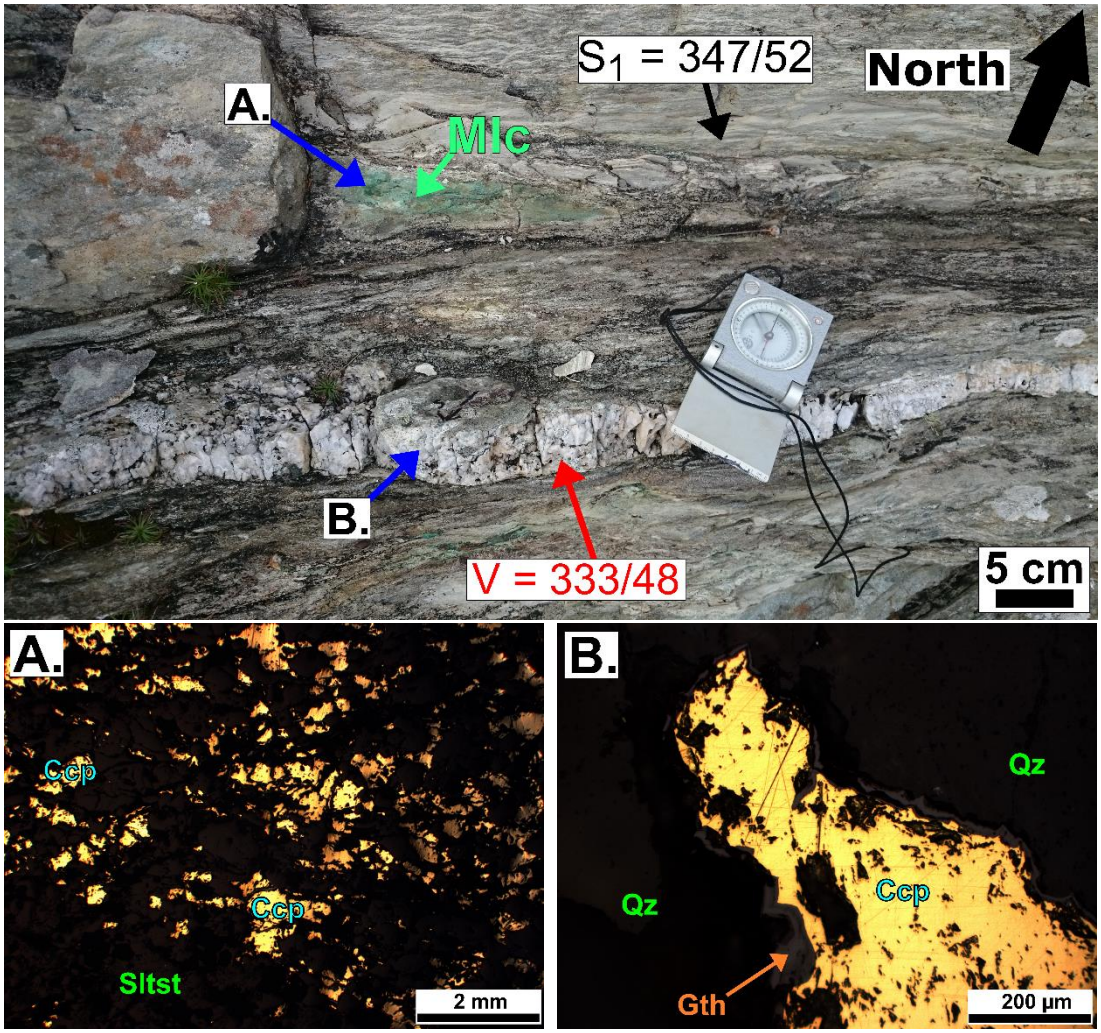
4.8b)



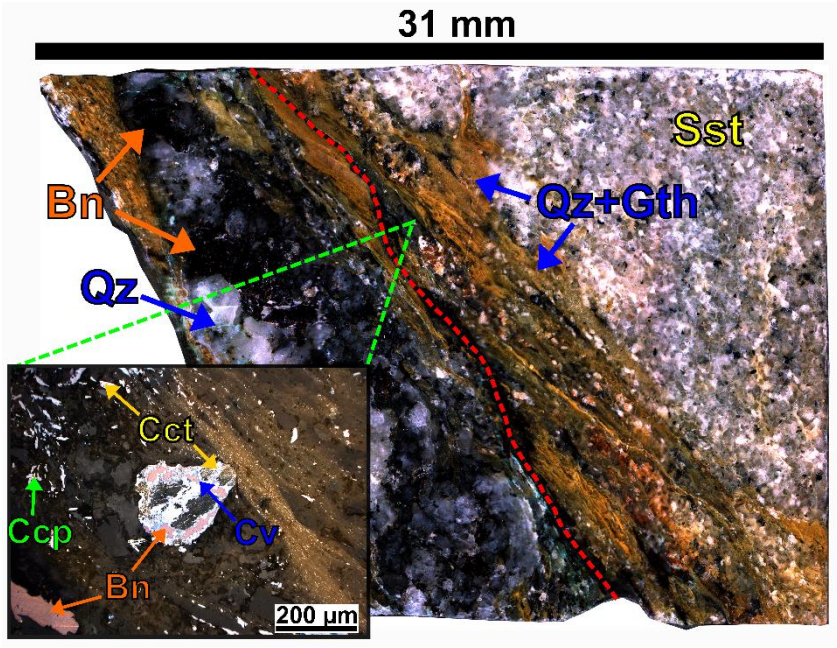
4.8c)


West
Qz
Sltst
Ccp
Qz
Qz
Sltst
2 cm

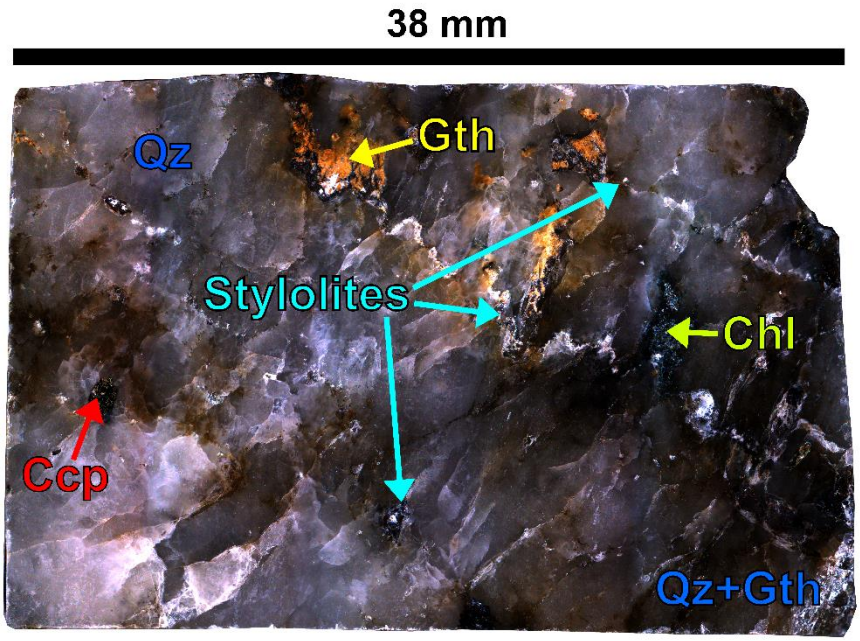
4.8d)


S_1 = 347/52
North
A.
Mic
B.
V = 333/48
5 cm
A.
Ccp
Ccp
Sltst
2 mm
B.
Qz
Qz
Ccp
Gth
200 µm

4.8e)


31 mm
Sst
Bn
Qz+Gth
Qz
Cct
Ccp
Cv
Bn
200 µm

4.8f)


38 mm
Qz
Gth
Stylolites
Chl
Ccp
Qz+Gth

4.8g)

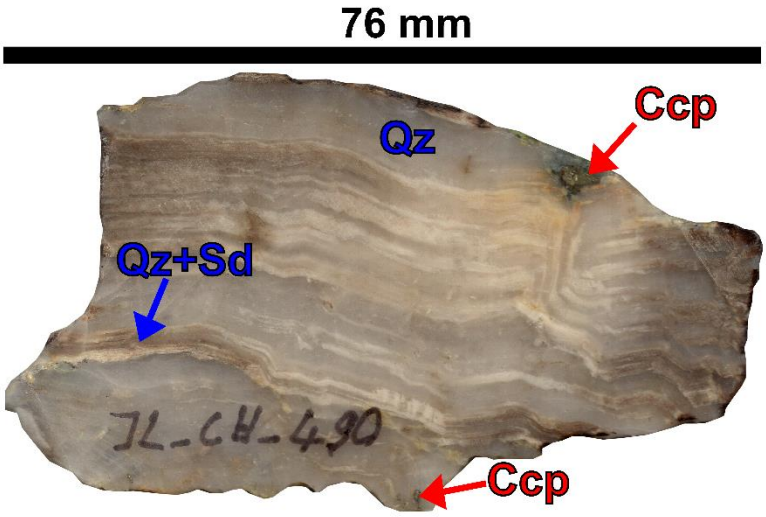


Fig. 4.8) The Crookhaven Copper Mines on the southern coast of Mizen Peninsula: a) Structural map with detailed drone maps of the research area showing pre-Variscan NE-SW striking faults, parallel compressional cleavage, and NE-SW striking folds. b) Splaying horsetail quartz veinlets with vein cleavage sub-parallel to the host rock cleavage. c) Siltstone (Sltst) with folded, mineralized quartz (Qz) veins with chalcopyrite (Ccp). d) Mineralized quartz vein within malachite (Mlc) stained siltstone: The microphotographs show (A) disseminated chalcopyrite (Ccp) within the siltstone (Sltst), as well as (B) massive chalcopyrite (Ccp) with goethite (Gth) alteration within the quartz (Qz) vein (reflected light, ppl). e) Microphotograph of quartz (Qz) vein with bornite (Bn) next to a sandstone (Sst) (reflected light, ppl). The microfracture (red line) is rimmed by quartz (Qz) and goethite (Gth). The close-up image shows cataclastic bornite (Bn) with minor chalcopyrite (Ccp) and chalcocite (Cct) and covellite (Cv) alterations. f) Quartz (Qz) vein with chalcopyrite (Ccp), chlorite (Chl), goethite (Gth) and stylolites (reflected ring light, ppl). g) Fibrous quartz (Qz) vein with parallel siderite (Sd) and minor chalcopyrite (Ccp) (high resolution optical scan).

4.5.6 Ballycummisk

Location and Lithology

The Ballycummisk Copper Mines are located close to the southern coast of Mizen Peninsula (Fig. 4.1 + 4.3). The historic mining area is about 16.5 km South of Bantry and 17.7 km Northwest of Crookhaven (Fig. 4.3). Although, there is no outcropping bedrock, but a hand specimen from the tailings shows a beige, silty sandstone as host rock with intensive pale grey to brownish red alterations. According to GSI (2016, Geological Map) the mining area of Ballycummisk is dominated by the Castlehaven Formation and the Toe Head Formation.

General Structures

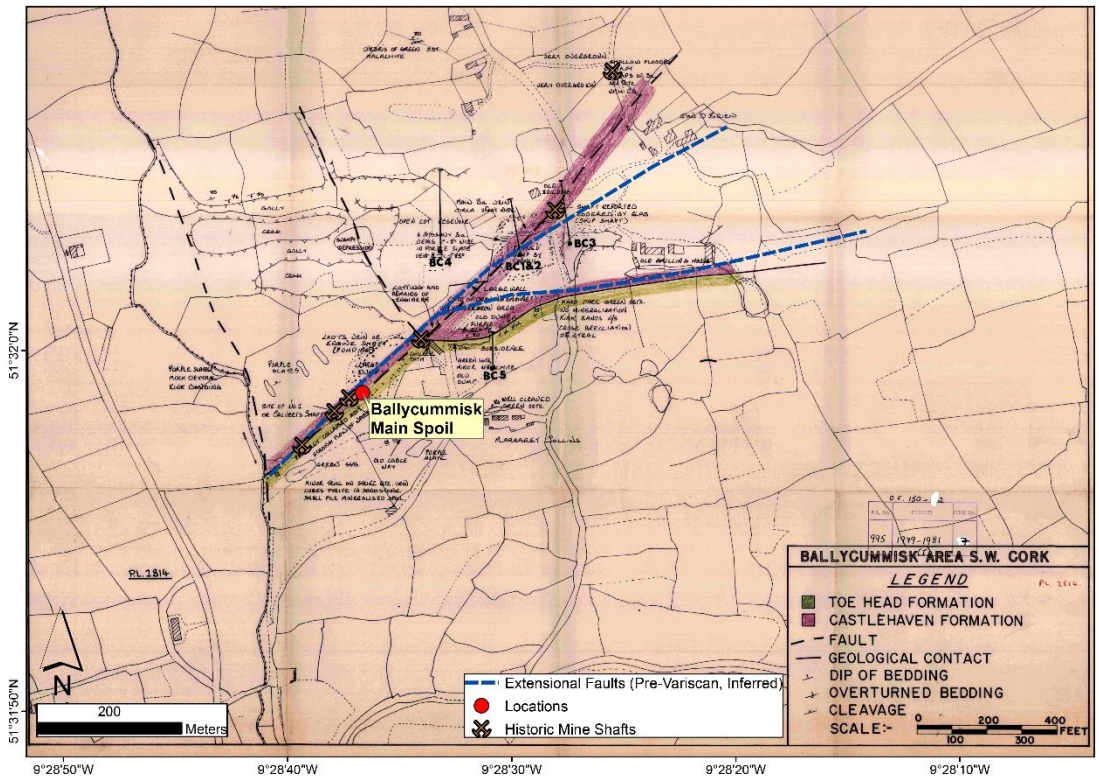
Due to the poor outcrop, any structural and lithological description is inferred by a combination of tailings samples, aerial satellite imaging interpretation of photolineaments, as well as historic mining maps (GSI Jetstream 2019). Two E-W striking faults occur near the major mining shafts (Fig. 4.9a). These faults merge to one E-W oriented fault in the East. A NE-SW striking fault crosscuts the E-W striking structures; most of the mine shafts are located along this NE-SW fault (Fig. 4.9a). A series of NNW-SSE parallel striking faults occur across the entire mining area. These faults appear to be slightly folded (Fig. 4.9a).

Mineralization and Microstructures

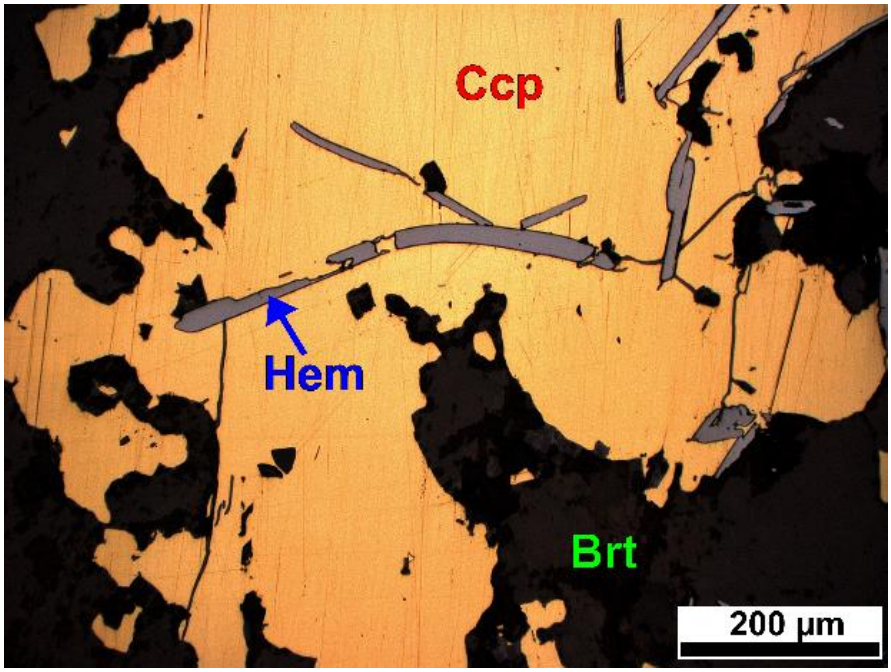
Quartz vein samples from the Ballycummisk main spoil (Fig. 4.9a) show chalcopyrite and tetrahedrite as major copper minerals. The sulphides occur as aggregates, up to several centimetres in diameter or as single euhedral crystals, up to 0.5 cm within the quartz veins. White to red massive, as well as crystalline barite occurs syngenetically with quartz, chalcopyrite and specular hematite. Later generations of barite can be found as colloform reddish layers. The mineralized quartz-barite-chalcopyrite-hematite veins can be cross-cut by late vuggy veins of euhedral barite-quartz with chlorite encrustations. Folded quartz-barite-hematite veins in pale yellow altered mudstone were found as well. Smaller veinlets occur aligned to the cleavage within the mudstone. Other samples show quartz intergrown with euhedral siderite (< 4 cm). Petrographic

analyses display the syngenetic relation between chalcopyrite, barite and specular hematite (Fig. 4.9b). Some of the hematite crystals are partially deformed. A further sample (Fig. 4.9c) shows a quartz vein with intergrown barite zones and goethite alteration. Molybdenite aggregates, as well as disseminated molybdenite which is syngenetically intergrown with chalcopyrite can be found in this sample. The molybdenite from this sample (Fig. 4.9c) was used for Re-Os geochronology (see section on *Molybdenite Re-Os geochronology*). One hand specimen of a quartz vein is mineralized with syngenetic chalcopyrite and fine disseminated syngenetic molybdenite (Fig. 4.9d). The molybdenite forms a residuum along stylolites within the quartz vein. Microscopic analyses show the molybdenite occurring as radial crystals within the quartz vein (Fig. 4.9e). The radial crystalline molybdenite is aggregated and slightly deformed along the stylolitic contact. A hand specimen of a slate (Fig. 4.9f) shows intensive greenish to beige alteration. Perpendicular to the slate cleavage is a strongly folded and cleaved quartz vein. This quartz vein is cross-cut by smaller cleavage-parallel quartz-barite-hematite veins with minor chalcopyrite and malachite mineralization (Fig. 4.9f).

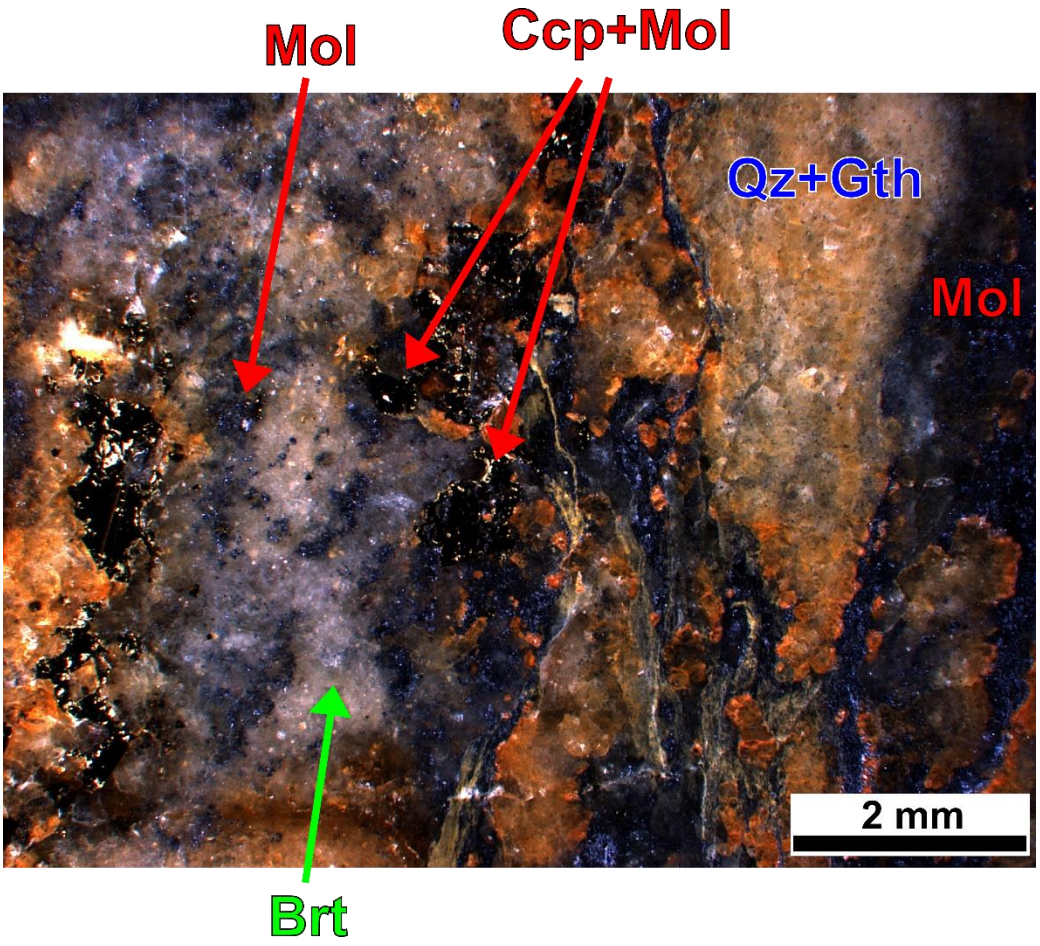
Fig. 4.9a)



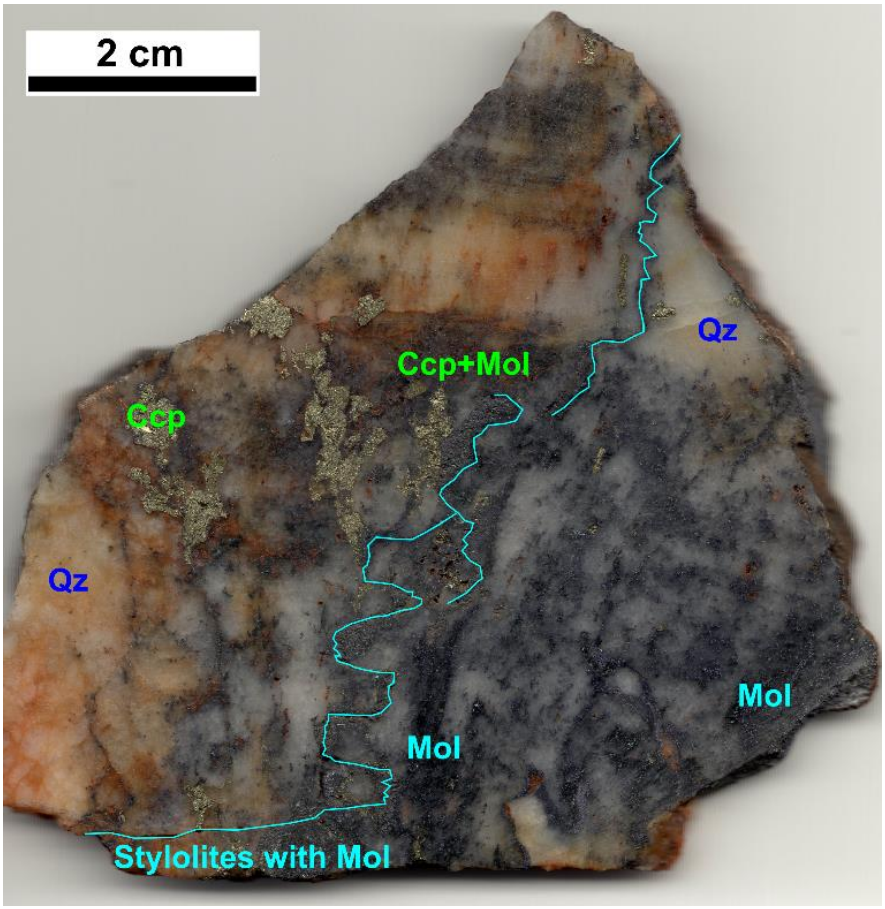
4.9b)



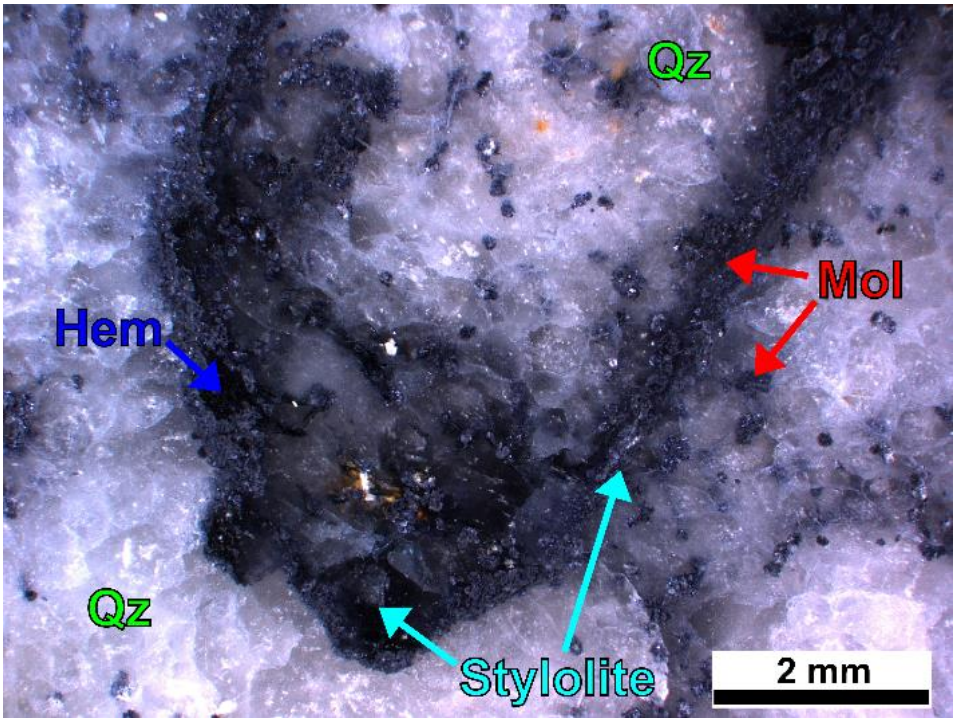
4.9c)



4.9d)


2 cm
Qz
Ccp+Mol
Ccp
Qz
Mol
Mol
Stylolites with Mol

4.9e)


Qz
Mol
Hem
Qz
Stylolite
2 mm

4.9f)

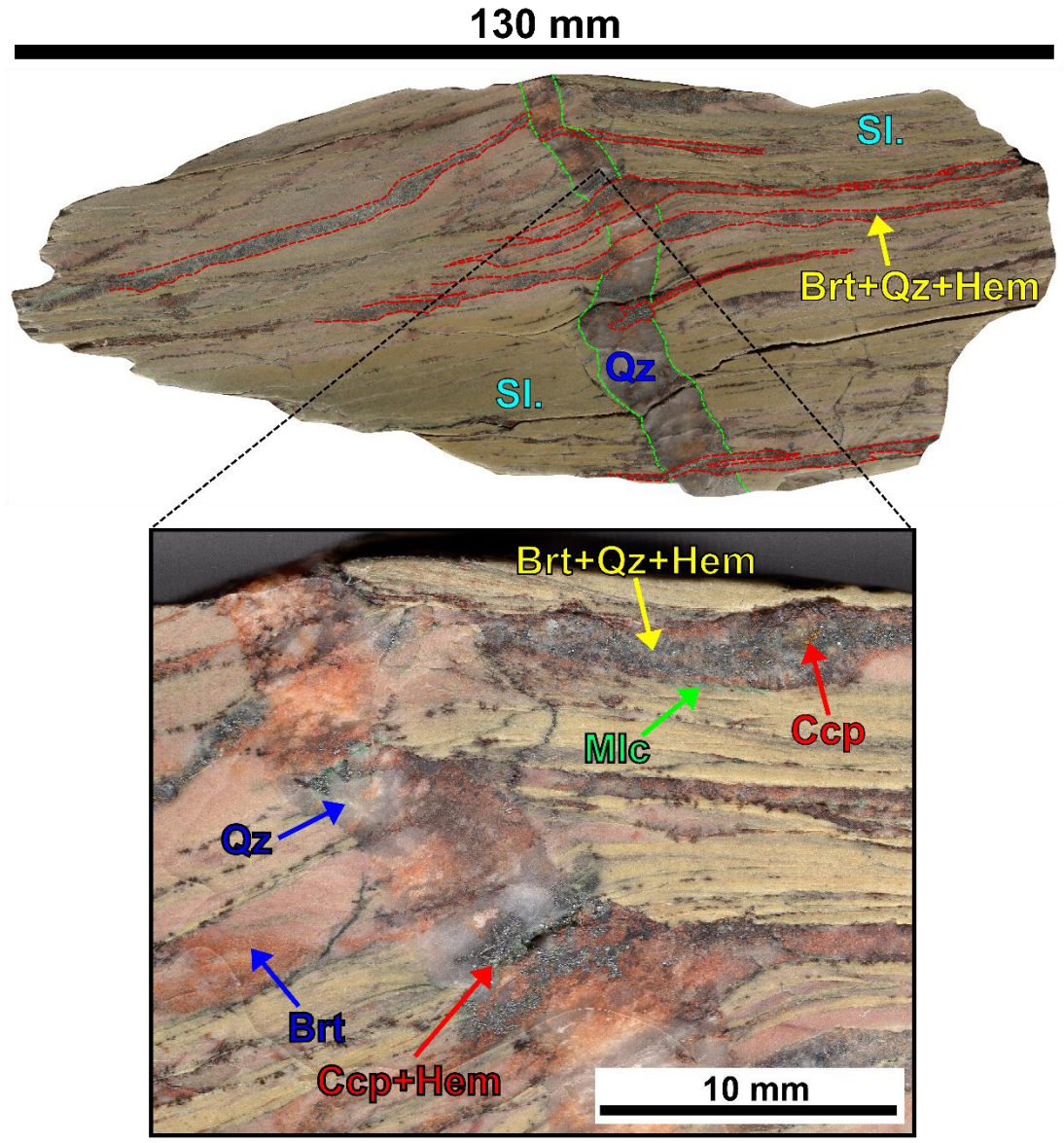


Fig. 4.9) The Ballycummisk Copper Mines near the southern coast of Mizen Peninsula: a) Structural map with inferred structures (modified after Bing™ Satellite Maps 2016-2019, Google Maps 2016-2019, and historic mining maps from GSI Jetstream 2019) showing E-W, SW-NE, and N-S striking faults. b) Microphotograph of tailings sample with barite (Brt), chalcopyrite (Ccp) and deformed, specular hematite (Hem) (reflected light, ppl). c) Microphotograph of quartz-barite vein (Qz, Brt) with syngenetic chalcopyrite (Ccp) and molybdenite (Mol), as well as goethite (Gth) alterations (ring light, ppl). d) High-resolution scan of hand specimen of quartz (Qz) vein with syngenetic chalcopyrite (Ccp) and molybdenite (Mol), as well as molybdenite

aggregations along stylolites. e) Microphotograph of quartz (Qz) vein with disseminated molybdenite (Mol), molybdenite aggregations along stylolites and minor, specular hematite (Hem). f) Greenish altered slate (Sl.) with folded and cleaved quartz vein (Qz) which is cross-cut by cleavage-parallel quartz-barite-hematite veins (Qz, Brt, Hem) with chalcopyrite (Ccp) and malachite (Mlc) mineralization.

Molybdenite Re-Os geochronology

The fine grained (grain size < 2 mm) historic molybdenite sample from the Ballycummisk tailings (BM.1964,R230) possesses 70.7 ± 0.3 ppm Re, 44.4 ± 0.2 ppm ^{187}Re and 231.3 ± 0.7 ppb ^{187}Os. The ratio yields to a model age of 311.8 ± 1.6 Ma for the molybdenite mineralization. The recent molybdenite finding from the Ballycummisk tailings (Fig. 4.9c) has a grain size of < 100 µm. It contains 113.5 ± 0.4 ppm Re, 71.3 ± 0.3 ppm ^{187}Re and 375.9 ± 1.2 ppb ^{187}Os. The ^{187}Re-^{187}Os model age is 315.5 ± 1.6 Ma.

Sample	*Sample wt (g)*	*Re (ppm)*	*±2σ*	^{187}Re *(ppm)*	*±2σ*	^{187}*Os (ppb)*	*±2σ*	*Model age (Ma)**	*±2σ*†	*±2σ*‡	*±2σ*§
BM.1964,R230	0.020	70.7	0.3	44.4	0.2	231.3	0.7	311.8	0.2	1.3	1.6
JL_BC_525	0.022	113.5	0.4	71.3	0.3	375.9	1.2	315.5	0.2	1.3	1.6

All data blank corrected (Re – 1.9 pg, Os – 0.8 pg with an $^{187}Os/^{188}Os$ of 0.201 ± 0.03)

**Model age calculated using the decay constant $^{187}Re = 1.666 \times 10^{-11}\ a^{-1}$ (Smoliar et al., 1996; Selby et al., 2007)*

†uncertainty including only mass spectrometry uncertainty

‡uncertainty including all sources of analytical uncertainty

§uncertainty including all sources of analytical uncertainty plus decay constant

***Table 4.1**. Re-Os isotope data for the molybdenite samples BM.1964,R230 and JL_BC_525 (Fig. 4.9c) from Ballycummisk Mine (Fig. 4.3 + 4.9a).*

4.5.7 Fluid inclusion microthermometry

According to their structural formation, 7 quartz vein samples were classified as pre-Variscan veins (mainly E-W to SW-NE striking, 5 mineralized and 2 unmineralized/barren, Appendix E). Five unmineralized/barren vein samples were classified as syn-Variscan (en echelon tension gashes, Appendix E). All mineralized (pre-Variscan) samples show chalcopyrite as major copper ore (Appendix E2). Minor amounts of syngenetic arsenopyrite (Dhurode Mine, JL_DH_522) and syngenetic molybdenite (Ballycummisk, JL_BC_525Re) occur (Appendix E2). The fluid inclusions of both pre-Variscan and syn-Variscan vein types consist of a 2-phase system with a major liquid (L) and a minor vapour (V) phase (Fig. 4.10a-d, Appendix E). No CO_2 phase was detected. Anhedral to subhedral quartz grains prevented a clear identification of individual growth zones. The measured quartz veins show a large amount of secondary and pseudosecondary fluid inclusion trails along healed fractures. These fractures were avoided. The primary fluid inclusions (target for this study) occur as clusters or separate inclusions along growth zones (Goldstein and Reynolds 1994, Appendix E). Primary fluid inclusion assemblages (FIA) were classified individually for each sample (Appendix E). The classification criteria for the assemblages are the most finely discriminated, petrographically associated group of coeval inclusions. This incorporates the fluid inclusion shape, the volume of the vapour phase at room temperature, and the spatial distribution (growth zones) within the vein sample. The complex growth zonations within the quartz vein samples prevented a temporal placement of the individual fluid inclusion assemblages.

<u>Pre-Variscan E-W veins</u>

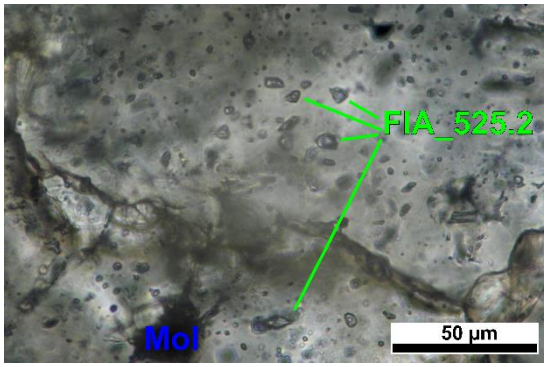
Primary (syn-mineralization) fluid inclusion assemblages in the pre-Variscan, early E-W quartz veins are generally oval to angular shaped (Fig. 4.10a + 4.10b, Appendix E). They consist of an undersaturated liquid-rich phase, and a vapour phase with 0.5 to 20 volume percent. The individual fluid inclusion assemblages (FIA) show generally a quite narrow spread in salinities and homogenisation temperatures for each individual sample location (Appendix

E3, Fig. 4.11a-h). However, between the different sample locations, there is a larger spread in T_h and salinities (Fig. 4.11a-h, Appendix E). The homogenisation temperatures T_h range between 90 and 335 °C. Salinities vary between 5.2 and 22.4 wt.% $NaCl_{equiv}$. The mineralized quartz vein sample from Caha Pass (JL_CP_432E, Fig. 4.3) represents an exemption with fluid inclusion assemblages clustering between 9.2 and 15.3 wt.% $NaCl_{equiv}$ and a T_h range between 125 to 189 °C, as well as showing a more saline FIA (432E.4) with values between 22.3 and 22.4 wt.% $NaCl_{equiv}$ and T_h between 90 and 123 °C (Fig. 4.11a-h, Appendix E3). The mean homogenisation temperature T_h of all fluid inclusion assemblages from the early E-W veins is 211 °C with a mean salinity of 11.2 wt.% $NaCl_{equiv}$ (n = 126).

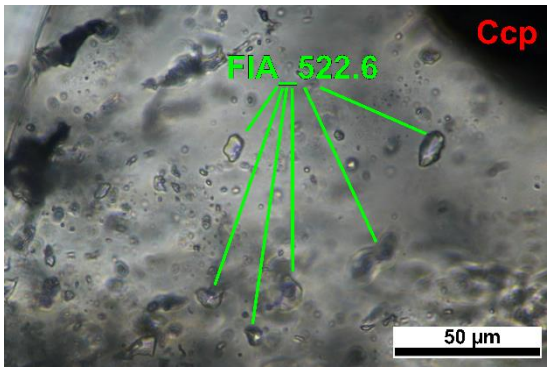
Syn-Variscan veins

Primary fluid inclusions of the compressional, syn-Variscan quartz veins (en echelon, tension gashes) can be elongated (Fig. 4.10c), but also irregular angular shaped (Fig. 4.10d, and Appendix E2). All assemblages consist of a liquid and a vapour phase with 0.1 to 10 vol.% (Appendix E). The homogenisation temperature T_h ranges from 104 to 270 °C with salinities between 4.8 and 16.7 wt.% $NaCl_{equiv}$ (Fig. 4.11i-n, Appendix E3). Syn-compressional vein samples with fibrous veins and vugs with large (< 5 cm), euhedral crystals were collected near Durrus (Fig. 4.3). The euhedral crystals show assemblages with a T_h from 174 to 240 °C, and salinities between 11.8 and 13.4 wt.% $NaCl_{equiv}$ (Fig. 4.11i-n, Appendix E3). A single measurement (outlier) showed a T_h of 101 °C and 10.4 wt.% $NaCl_{equiv}$ salinity (Fig 4.11i-n, Appendix E3). The assemblage 517.1 from Gortavallig (Fig. 4.11i-n, Appendix E3) shows the relatively highest T_h (239 to 271 °C) with low salinities (4.8 to 8.5 wt.% $NaCl_{equiv}$). The mean homogenisation temperature T_h of all Syn-Variscan fluid inclusion assemblages is 178 °C with a mean salinity of 10.2 wt.% $NaCl_{equiv}$ (n = 87).

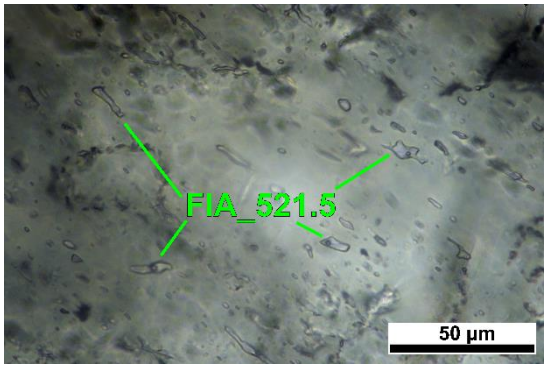
Fig. 4.10a)



4.10b)



4.10c)



4.10d)

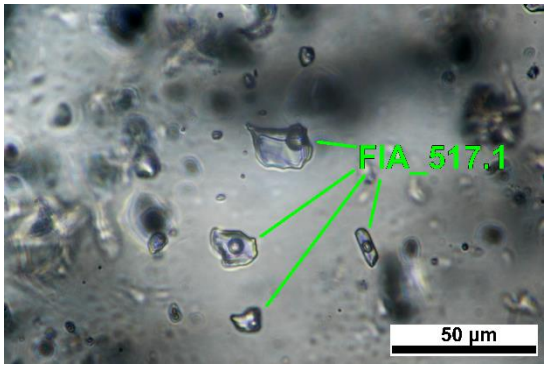
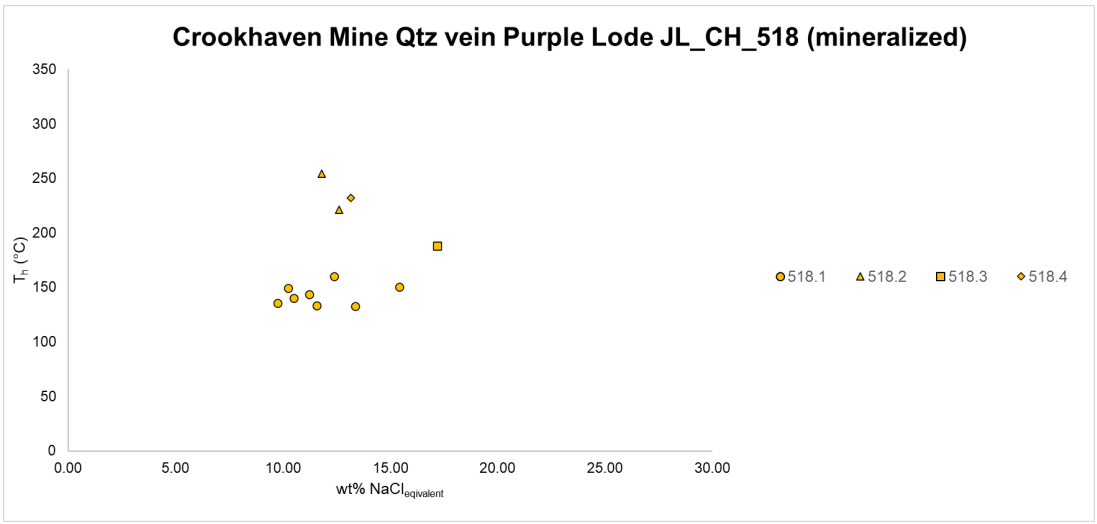
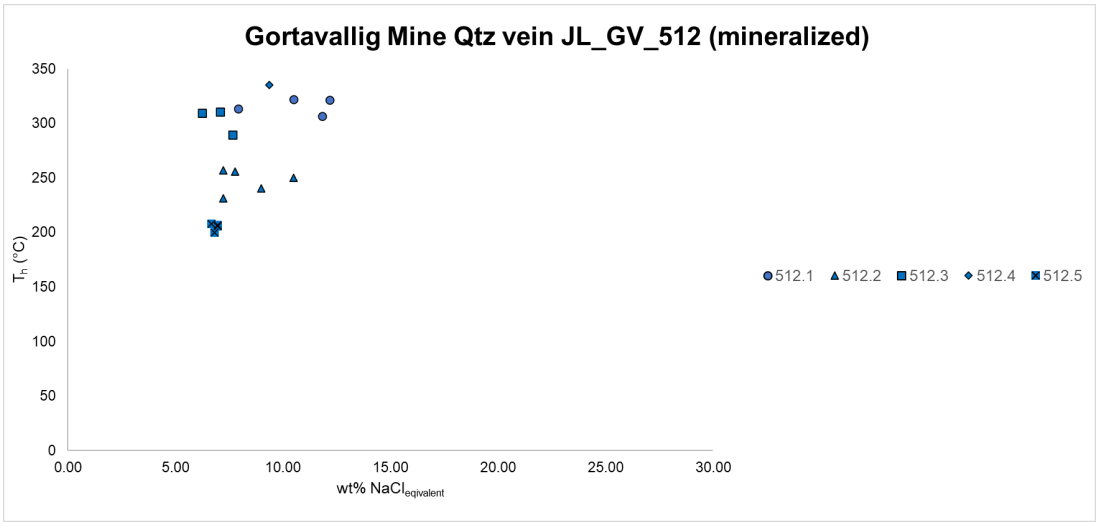


Fig. 4.10) Examples of fluid inclusions assemblages (FIAs) within quartz veins (microphotographs): a) Ballycummisk (pre-Variscan): Oval to angular shaped fluid inclusions with large vapour phase (mineralized vein with molybdenite, Mol). b) Dhurode (pre-Variscan): Mineralized quartz vein with chalcopyrite (Ccp) and oval shaped fluid inclusions with small vapour phase. c) Crookhaven: Elongated fluid inclusions within syn-Variscan quartz vein. d) Gortavallig: Large angular to oval shaped fluid inclusions from syn-Variscan quartz vein. See Appendix E2 for further FIAs.

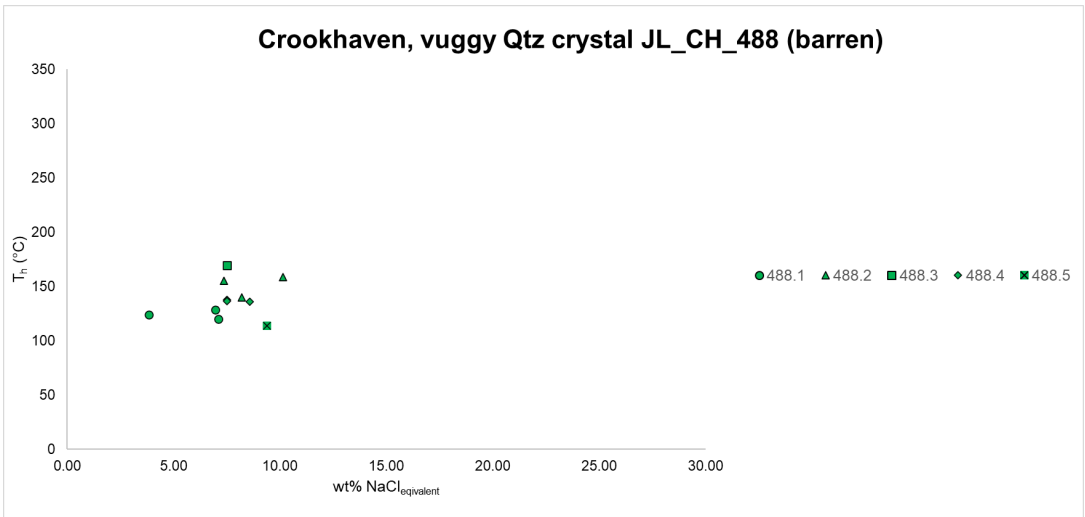
Fig. 4.11a)



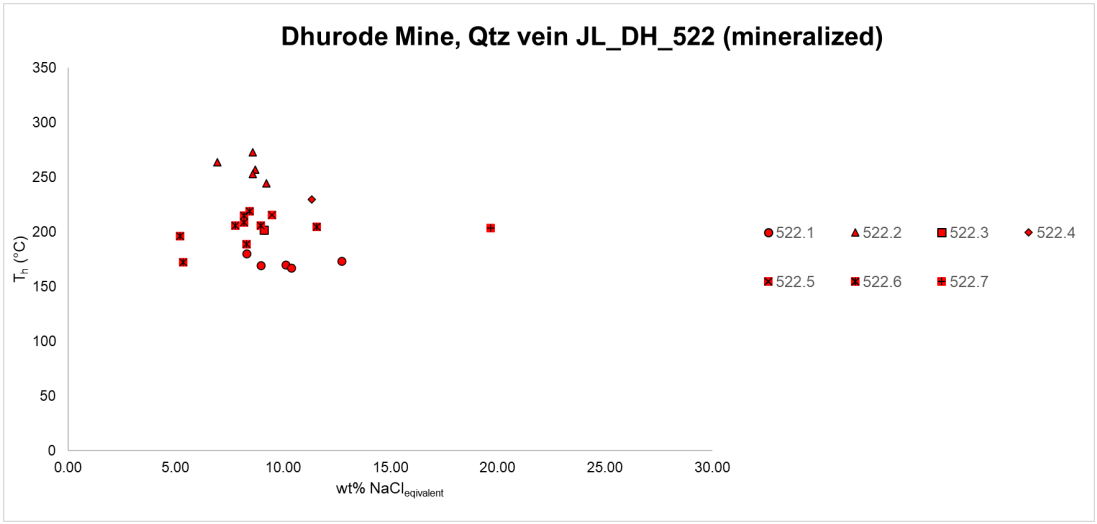
4.11b)



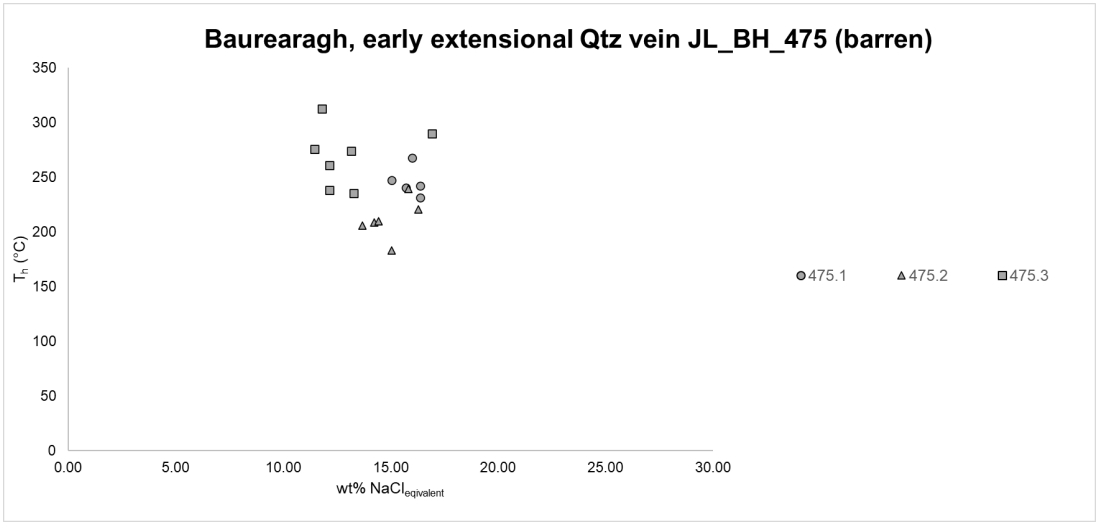
4.11c)



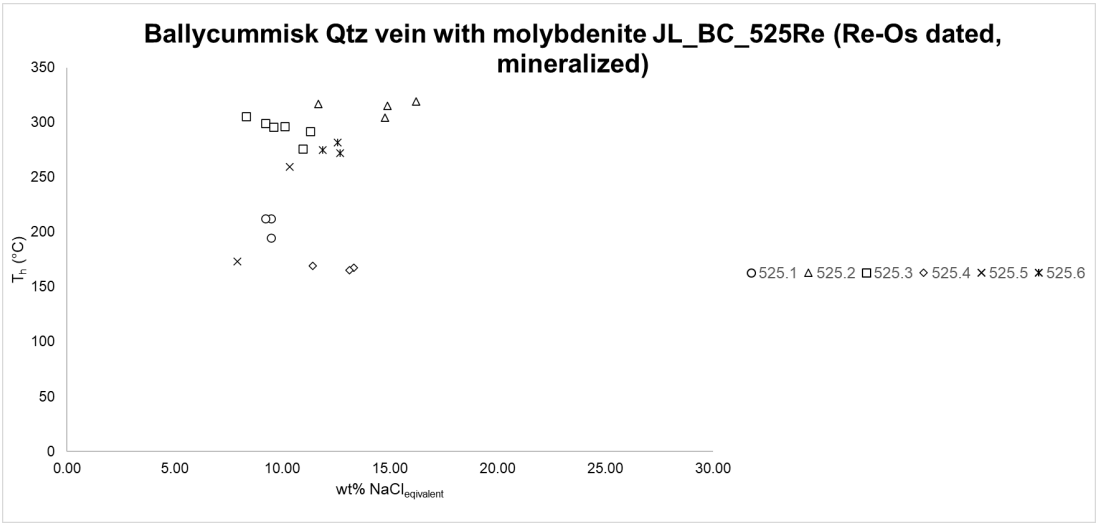
4.11d)



4.11e)



4.11f)



4.11g)

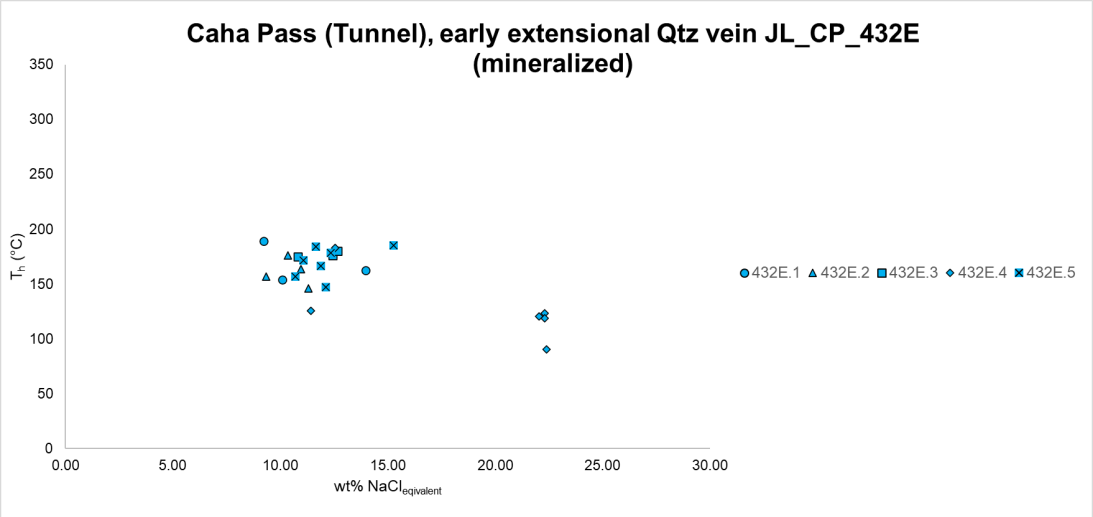
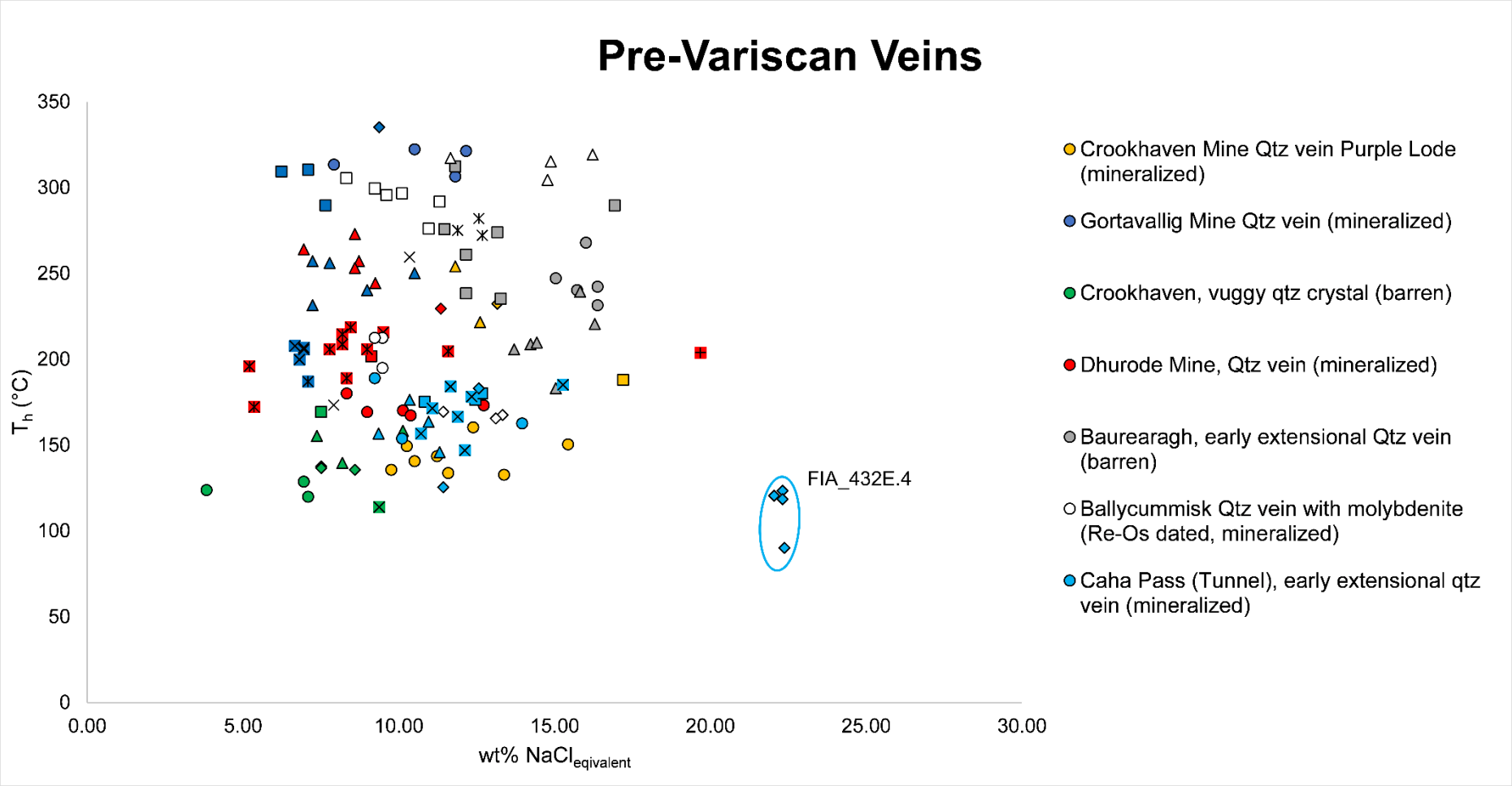
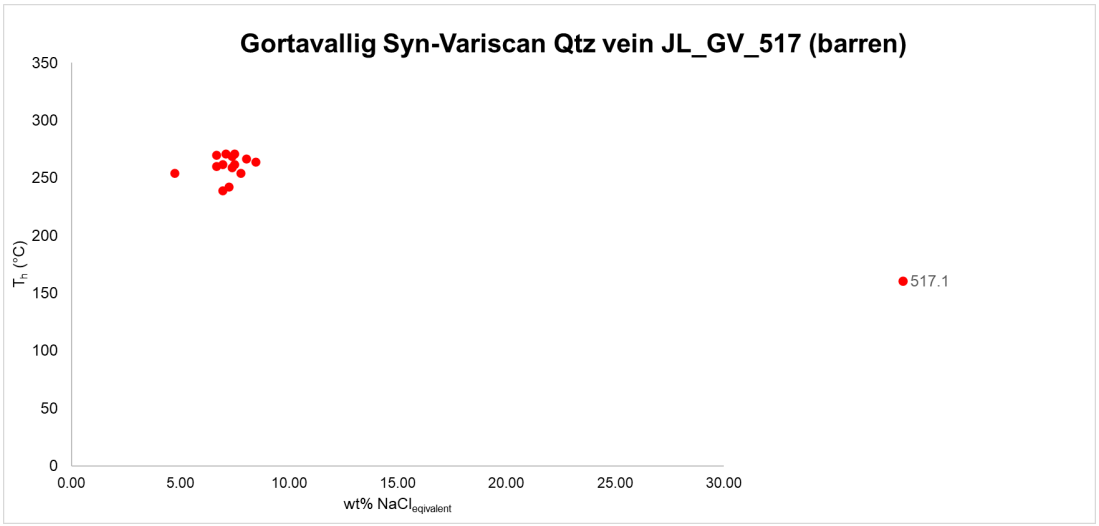

Caha Pass (Tunnel), early extensional Qtz vein JL_CP_432E (mineralized)
350
300
250
200
150
100
50
0
T_h (°C)
0.00
5.00
10.00
15.00
20.00
25.00
30.00
wt% $NaCl_{eqivalent}$
432E.1
432E.2
432E.3
432E.4
432E.5

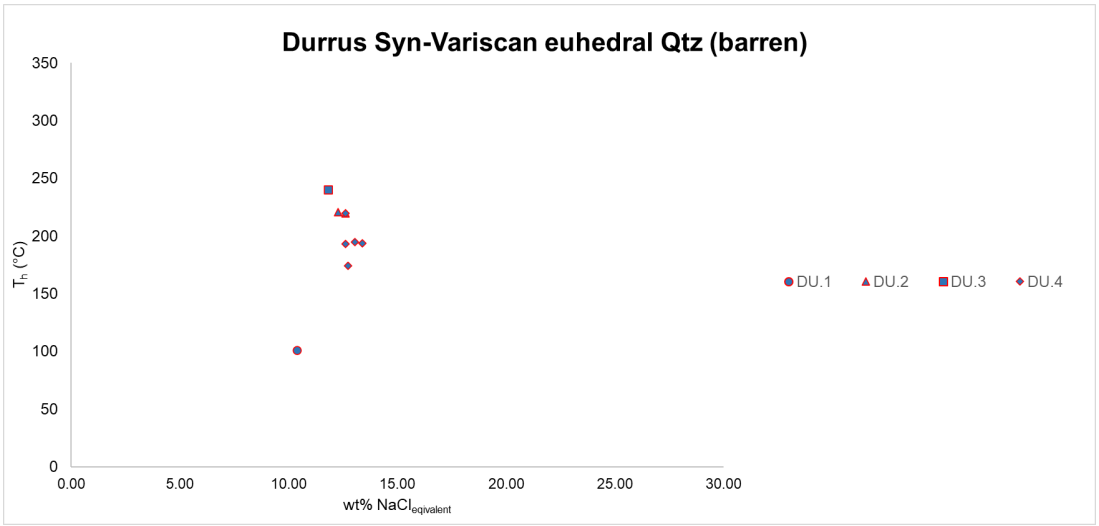
Fig. 4.11h)


Pre-Variscan Veins
350
300
250
200
150
100
50
0
T_h (°C)
0.00
5.00
10.00
15.00
20.00
25.00
30.00
wt% $NaCl_{eqivalent}$
FIA_432E.4
Crookhaven Mine Qtz vein Purple Lode (mineralized)
Gortavallig Mine Qtz vein (mineralized)
Crookhaven, vuggy qtz crystal (barren)
Dhurode Mine, Qtz vein (mineralized)
Baurearagh, early extensional Qtz vein (barren)
Ballycummisk Qtz vein with molybdenite (Re-Os dated, mineralized)
Caha Pass (Tunnel), early extensional qtz vein (mineralized)

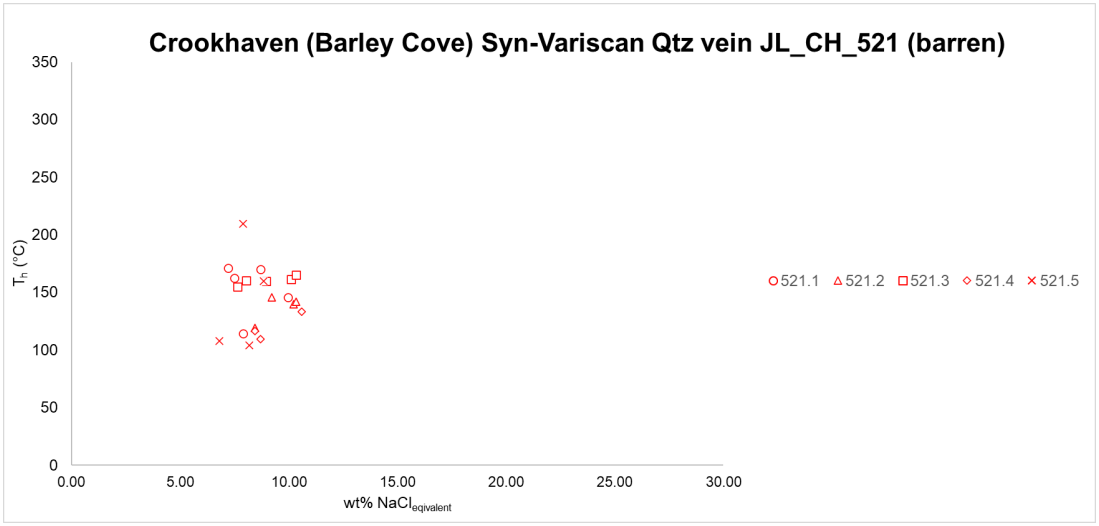
4.11i)



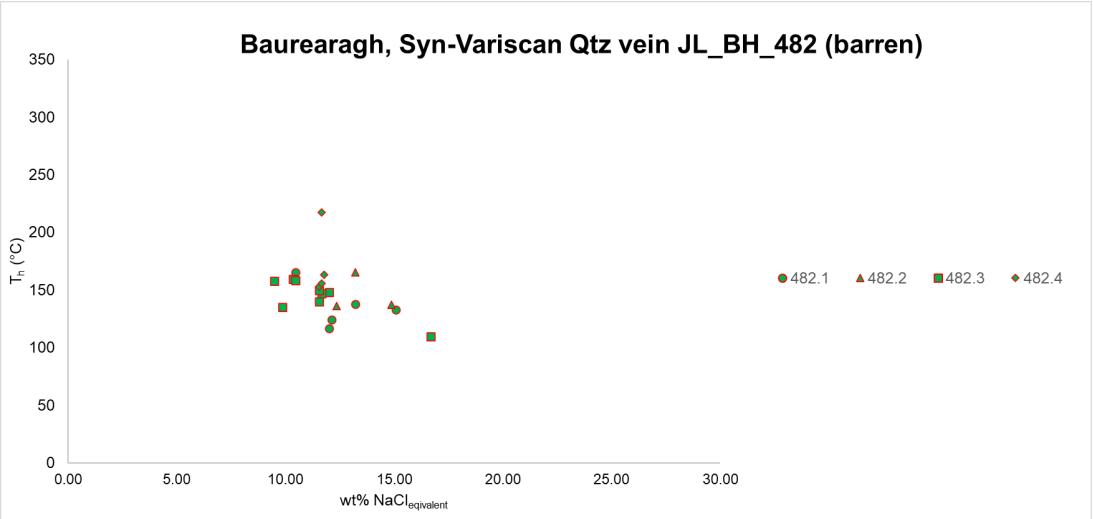
4.11j)



4.11k)



4.11l)


Baurearagh, Syn-Variscan Qtz vein JL_BH_482 (barren)
350
300
250
200
150
100
50
0
T_h (°C)
0.00
5.00
10.00
15.00
20.00
25.00
30.00
wt% $NaCl_{eqivalent}$
482.1
482.2
482.3
482.4

4.11m)

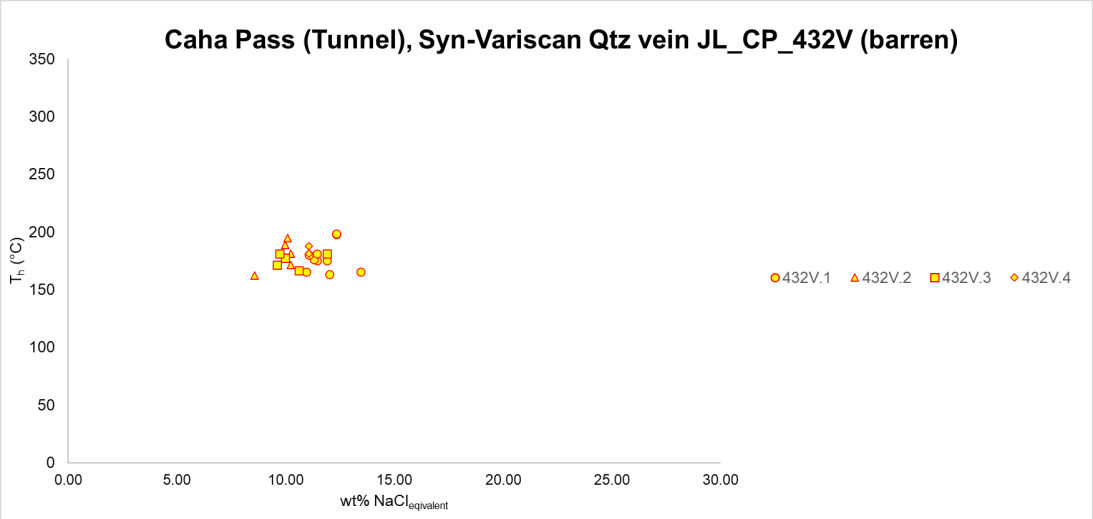

Caha Pass (Tunnel), Syn-Variscan Qtz vein JL_CP_432V (barren)
350
300
250
200
150
100
50
0
T_h (°C)
0.00
5.00
10.00
15.00
20.00
25.00
30.00
wt% $NaCl_{eqivalent}$
432V.1
432V.2
432V.3
432V.4

Fig. 4.11n)

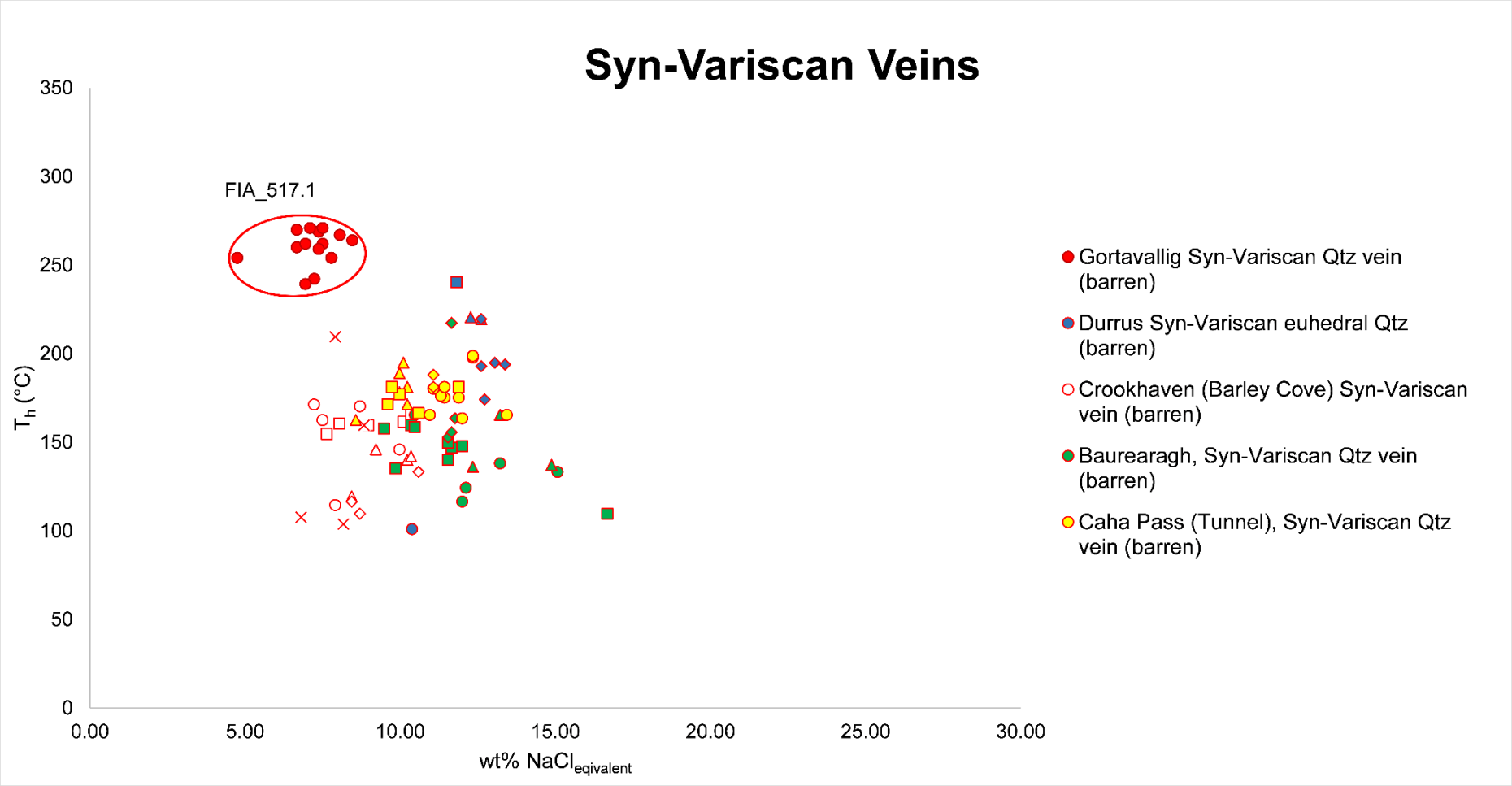

Syn-Variscan Veins
FIA_517.1
350
300
250
200
150
100
50
0
T_h (°C)
0.00
5.00
10.00
15.00
20.00
25.00
30.00
wt% $NaCl_{eqivalent}$
Gortavallig Syn-Variscan Qtz vein (barren)
Durrus Syn-Variscan euhedral Qtz (barren)
Crookhaven (Barley Cove) Syn-Variscan vein (barren)
Baurearagh, Syn-Variscan Qtz vein (barren)
Caha Pass (Tunnel), Syn-Variscan Qtz vein (barren)

Fig. 4.11) Fluid inclusions measurements from the selected research areas in West Cork (Fig. 4.3): Plot of the salinity wt% $NaCl_{equiv}$ versus the homogenisation temperatures T_h (°C). The different colours show the various locations, and the symbols indicate the individual fluid inclusion assemblages (FIA) within one sample (see Appendix E for details). a-h) Early extensional (Pre-Variscan) vein samples. i-n) Compressional (Syn-Variscan) vein samples.

4.6 Discussion

4.6.1 Basinal kinematics and fluid flow – A basinal crustal N-S extension provides E-W to ENE-WSW fluid pathways

The current study demonstrates that ore mineralization in SW Ireland shares a common structural regime to that described at Allihies on Beara Peninsula (Fig. 4.2, Lang *et al.* 2020). The kilometre scale E-W to ENE-WSW striking normal faults (Fig. 4.3) are part of the fault system that includes the basin controlling Coomnacronia-Killarney-Mallow Fault Zone and the Cork-Kenmare Fault Zone (Fig. 4.1; Naylor and Jones 1967; Capewell 1975; Price and Todd 1988; Meere 1995b; Vermeulen *et al.* 2000; Landes *et al.* 2003; MacCarthy 2007; Ennis *et al.* 2015; Lang *et al.* 2020). The large lateral extent of these faults onshore, as well as offshore (Fig. 4.3) suggest a deep-reaching fault system caused by crustal extension (Fig. 4.12a, Naylor & Jones 1967). This corresponds with seismic interpretation from Landes *et al.* (2003) who determined a possible 13-14 km depth for the Cork-Kenmare Fault Zone. Nevertheless, it is not clear if all of these extensional faults reached the basement (Fig. 4.12a). According to Williams *et al.* (1989) and Williams (2000) the E-W basinal faults show a steep dip to the South at Beara Peninsula and Sheep's Head (Fig. 4.12a+b); however, at Mizen Peninsula antithetic intrabasinal northwards dipping faults were inferred. The faults show an E-W strike at Beara Peninsula, Sheep's Head and northern Mizen Peninsula (Fig. 4.3), which rotates to an ENE-WSW strike on the south-western part of Mizen

Peninsula. This rotation could be caused by a minor tectonic anticlockwise plate rotation during the basinal extension phase. Alternatively, an oroclinal swing during the Variscan compression (Pastor-Galán *et al.* 2015) resulted in the rotated fault strike. Historically mined copper lodes (Fig. 4.3, GSI Jetstream 2019) are related to these basin forming structures and their strike coincides with the regional orientation of these faults on the various West Cork peninsulas. Only a few historic copper lodes follow the kilometre scale N-S to NNE-SSW striking faults (Fig. 4.3). As one example Lang *et al.* (2020) described the large N-S lode at Mountain Mine, Allihies as a possible transfer fault or breached relay ramp (Walsh and Watterson 1991; Fossen and Rotevatn 2016). The large extent of these N-S faults can be explained by major cross-strike faults (Morley 1995) which are part of an extensional transfer fault system and can cut across multiple fault blocks. Later compression of the E-W and N-S faults indicates a Variscan orogenic overprint which consequently confirms their pre-Variscan formation. Sanderson (1984) noted N-S striking mineralized quartz veins on Beara Peninsula with strong folding and cleavage, which were interpreted as early extension veins. The predominant E-W orientation of mineralized lodes (Fig. 4.3) in comparison to less abundant N-S lodes can be explained by the space formation for fluid pathways. An N-S oriented crustal extension provides more spacing along the E-W striking normal faults compared to the shear zones along the N-S trending transfer faults.

On a local scale we see structures (Figs. 4.4a, 4.5a, 4.6a, 4.7a, 4.8a, 4.9a), which show evidence for E-W to ENE-WSW striking extensional faults which are associated with meter-scale, steep dipping quartz veins and mineralized copper lodes. The major normal faults and their associated large quartz veins at Baurearagh (Fig. 4.4a) present an unusual apparent N-S strike which doesn't fit into the general E-W/SW-NE striking extensional structural pattern. 3D drone photogrammetry modelling (Fig. 4.4b) shows that the apparent N-S strike is caused by a relatively shallow (57°, instead of vertical) southwards dipping E-W striking fault combined with high topographical erosion. This topographical effect should not be misinterpreted with the nearly vertical dipping breached relays/transfer faults from Allihies (Lang *et al.* 2020). The

shallow dip of this specific fault at Baurearagh represents a coincidence in the uniform structural E-W striking pattern. This proves the overall tectonic kinematics of the Munster Basin formation: A pre-Variscan N-S crustal extension formed E-W/SW-NE striking extensional faults which provided the fluid pathways for the primary copper mineralization.

Stockwork-veining at Baurearagh (Fig. 4.4c) and hydraulic breccia with host rock sediment clasts within the quartz veins (Baurearagh, Fig. 4.4c and Caha Pass) indicate intensive hydrofracturing during pre-Variscan vein formation (Fig. 4.12a). The extensional phase caused a crustal thinning (Williams 2000), which resulted in a low lithostatic vs. hydrostatic ratio, which then again caused probably a rapid ascend of fluids in mobile hydrofractures (Bons 2001). These mobile hydrofractures can explain the large-scale vein precipitation. Large quartz veins are mainly concentrated into narrow zones (8 – 11 metres) of the outcrop adjacent to the extensional faults (e.g. Fig. 4.4a + 4.6a). This is probably caused by an increased fluid concentration. The parallel aligned quartz veins next to the extensional faults represent sealed weakness zones in the host rock sediments. The extensional faults, which provide the fluid pathways themselves were probably active for a longer time period which made them susceptible for surficial erosion. As a result, the extensional faults appear as eroded trenches in the topography. As shown at the Main E-W Lode from Mountain Mine at Allihies (Reilly 1986), these extensional faults can bear quite large quartz (+Cu) veins in further (uneroded) depth.

Fig. 4.12a)

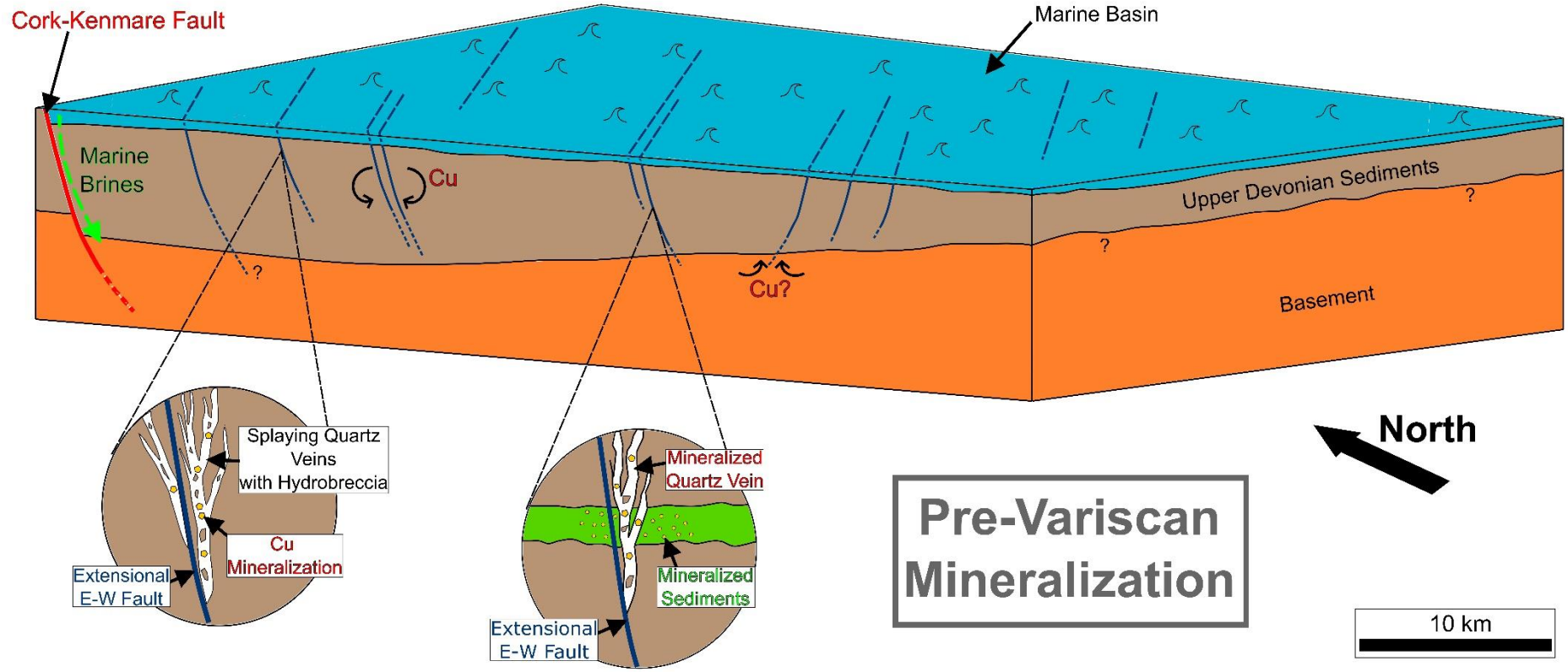

Cork-Kenmare Fault
Marine Basin
Marine
Brines
Cu
Cu?
Upper Devonian Sediments
Basement
?
Splaying Quartz
Veins
with Hydrobreccia
Cu
Mineralization
Extensional
E-W Fault
Mineralized
Quartz Vein
Mineralized
Sediments
Extensional
E-W Fault
North
Pre-Variscan
Mineralization
10 km

Fig. 4.12b)

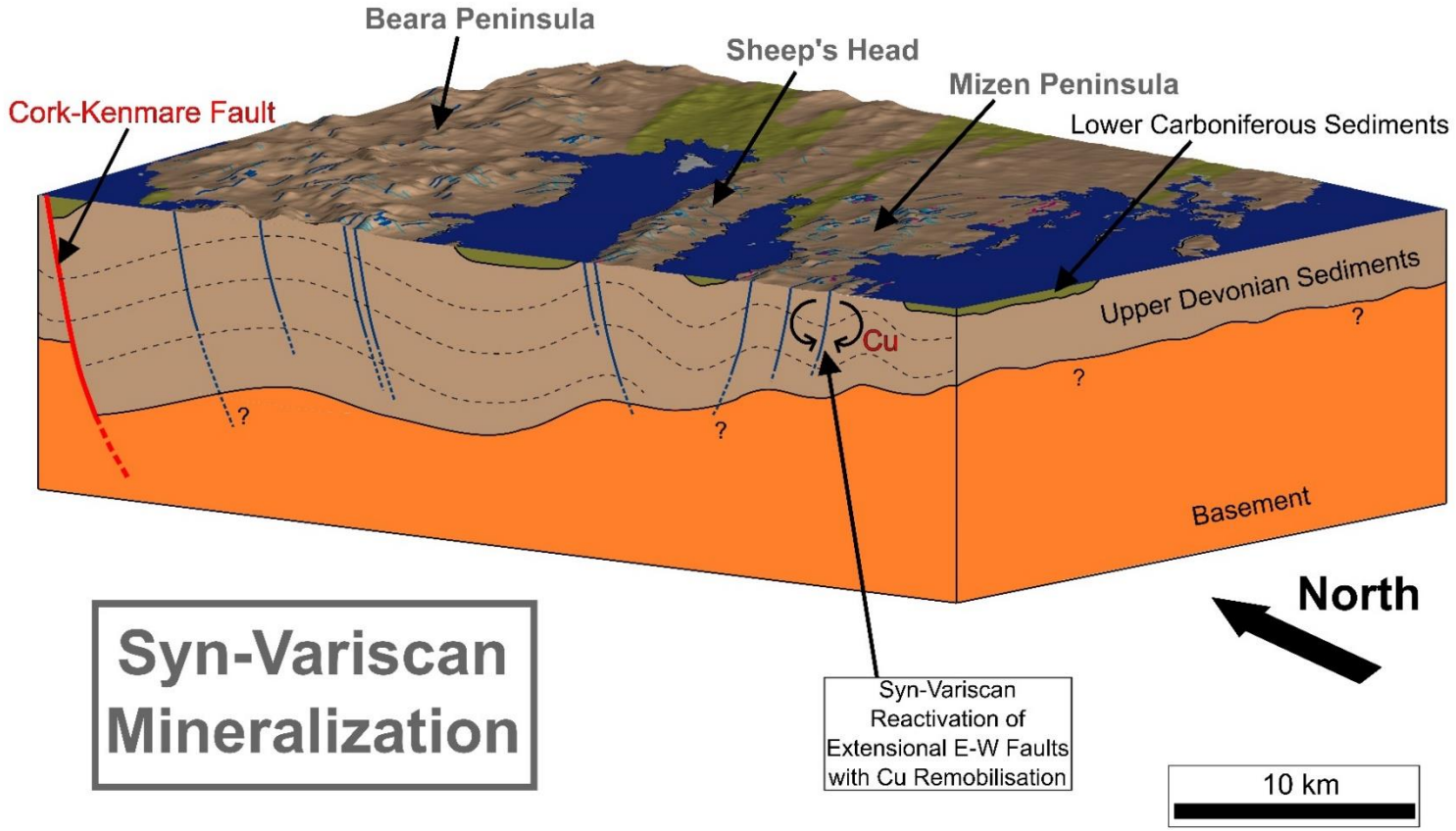


Fig. 4.12) Block model of the South Munster Basin in West Cork (including adaptions after Williams, 2000, Landes et al., 2003 and SRTM digital terrain model from Jarvis et al. 2008). a) The basinal E-W faults follow the strike of the major Cork-Kenmare Fault in the North. The E-W faults form the fluid pathways for the mineralized quartz veins which can be associated with sediment hosted copper beds. b) A reactivation of these E-W faults during the Variscan Compression and crustal shortening can remobilise basin related copper mineralization.

4.6.2 Regional and microscopic evidence for a pre- and syn-Variscan mineralization

Some of the E-W/ENE-WSW striking faults with the associated mineralized quartz veins show metre-scale folding (e.g. NW of Crookhaven, Fig. 4.8a). In some places, the faults and veins have an apparent sinistral lateral offset of up to 118 metres (reverse faults e.g. Caha Pass, Fig. 4.5a and Gortavallig, Fig. 4.6a). Folding as well as the offset (reverse faults) is caused by an NNW-directed Variscan compression (e.g. Sanderson 1984). Hence, a pre-Variscan genesis of the E-W structures can be determined. A historic mine map (GSI 1863) describes the underground workings of Gortavallig. At the eastern end of the adits the copper lode is described as “suddenly cut off” which basically marks the reverse fault (Fig. 4.6a) caused by Variscan (post-mineralization) compression. Sinistral faulting of mineralized E-W veins has been described by Reilly (1986) occurring at Allihies and Mizen Peninsula (East) copper mines (Fig. 4.3). The cut-off vein at Gortavallig West (Fig. 4.6c) represents a local-scale example of early mineralized structures impacted by a Variscan thrust fault. Syn-Variscan quartz veins were described at Allihies (Lang *et al.* 2020) as generally small-scaled (< 1 m) en echelon tension gashes in semi brittle shear zones. They can be found in all examined areas and occur within local shear fractures (Fig. 4.4d) and meso-scale folds (Fig. 4.6b). Generally, these syn-Variscan veins appear to be unmineralized. The WSW-ENE striking triangle zone at Dhurode (Figs. 4.7a + 4.7b) represents a Variscan feature. Even though the associated faults extend over several hundred metres no mineralization related to these structures has been observed. Similar structures can be found at Gortavallig (Fig. 4.6a) where the SW-NE striking Syn-Variscan reverse fault shows no mineralization. Slickenlines found on E-W striking extensional quartz veins at Baureagh (Fig. 4.4e) indicate a NW directed movement with fault reactivation during Variscan compression. Reilly (1986) describes the major copper mineralization from Crookhaven (Fig. 4.3) occurring predominantly within saddle reef structures along the fold axis of a Variscan anticline. A reasoned argument is that the Cu mineralization was remobilised from the early extensional veins into the saddle reefs during compression. Syn-Variscan structures (folds, faults and cleavage) at the

southern coast of Mizen Peninsula (especially Crookhaven and Ballycummisk) are aligned parallel to the ENE-WSW strike of the early extensional basin structures (Figs. 4.3, 4.8a and 4.9a). This parallel alignment of extensional and compressional features in the South could have caused a reactivation of deep-reaching fault systems with fluid remobilisation during the Variscan compression (Fig. 4.12b). The fluid conditions for such a copper remobilisation are discussed in the section below (section 4.6.5).

Microstructures and small-scale field observations support the theory of basin related extensional mineralization with a Variscan overprint. At Crookhaven the SW-NE striking quartz veins with splaying horsetail veinlets (Fig. 4.8b) indicate a local sinistral extensional movement (Fig. 4.3 + 4.8b). Several study localities from West Cork show cleavage within mineralization related E-W and ENE-WSW quartz veins (e.g. Figs 4.8b and 4.8c). This veining cleavage represents a syn-compressional overprint. Similar to Allihies (Lang *et al.* 2020) a low angle of the vein's strike related to the Variscan NNW–SSE maximum principal stress σ1 forms the most distinct vein cleavage. Stylolites within the pre-Variscan quartz veins and mineralized lodes are very common (Figs 4.4e, 4.5b, 4.5c, 4.8f, 4.9d, 4.9e) and represent a weak form of cleavage (Alvarez *et al.* 1978) caused by pressure solution. Figure 4.4e and 4.5b show that the stylolites are oriented normal to the NNW-SSE Variscan compression. Occasionally, the stylolites are rimmed by insoluble goethite (Fig. 4.8f) or molybdenite (Ballycummisk, Figs 4.9d + 4.9e). The goethite could be a remnant from altered sulphides within the quartz veins. Tectonism induced molybdenite stylolites have been described by Gaba (1990) and Lawley *et al.* (2013) occurring within other quartz vein related deposits. According to Lawley *et al.* (2013) the sawtooth pattern of stylolite-like veins proposes a stress-induced solution transfer.

The oriented sample of the mineralization related E-W striking quartz vein from Dhurode (Fig. 4.7c) has sweeping to patchy undulous extinction indicating a low-temperature crystal-plastic deformation (Trouw *et al.* 2009). The NNW-SSE striking microfault with partial recrystallization suggests low-grade sub-grain rotation during deformation (Fig. 4.7c: C+D, Trouw *et al.* 2009). The cataclastic fractured arsenopyrite from Dhurode (Fig. 4.6d), the microfracture

with altered bornite from Crookhaven (Fig. 4.8e) and the partially deformed hematite within the chalcopyrite from Ballycummisk (Fig. 4.9b) represent a post-mineralization semi-brittle deformation. Snodin (1972) described deformed chalcopyrite from the major quartz-sulphide veins e.g. Dhurode and Ballycummisk (Fig. 4.3) as clear evidence of intense deformation. This is in agreement with Meere (1995a, 1995b) who postulated a low-grade sub-greenschist-facies metamorphism during the Variscan Orogeny which caused an overprint to the major Cu mineralization at Allihies (Lang *et al.* 2020).

Syn-Variscan quartz veins are generally small scale (<1 m) and form stretched to fibrous antitaxial quartz fillings within tension gashes (Figs. 4.4d + 4.6b). The crystals are typically formed during a continuous crack-seal event (Bons *et al.* 2012). The mineralized sample from Crookhaven with fibrous kinked quartz and siderite crystals (Fig. 4.8g) also represents a continuous crack-seal event (Bons *et al.* 2012) generated by progressive deformation during the Variscan orogeny. The elongated to stretched quartz crystals from Caha Pass (Fig. 4.5c, Gen. 2) were possibly formed during the early Variscan compression, as they contain minor stylolites. The cleaved slate sample from Ballycummisk with the cross-cutting vein generations (Fig. 4.9f) represents an early, pre-compressional quartz precipitation, as well as a syn-compressional barite-quartz-hematite-chalcopyrite mineralization. This late mineralization took place after the major Variscan cleavage formation (Cooper & Trayner 1986; Ford 1987, see section 4.6.5). From these observations it can be summarised that the second copper vein mineralization happened at the beginning of the Variscan Orogeny, and these veins were deformed by ongoing compression.

4.6.3 Fluid inclusions microthermometry of the pre-Variscan and syn-Variscan quartz veins

The fluid inclusion homogenisation temperatures and salinities from the pre-Variscan E-W veins (Fig. 4.11a-h) display a range of T_h = 90° to 335 °C and 3.8 to 22.4 wt.% $NaCl_{equiv.}$ These values correspond with values observed at Allihies (Lang *et al.* 2020) which display the range of T_h between 74° to 271°C

and salinities from 3.2 to 28.5 wt.% $NaCl_{equiv}$. The assemblages from the individual localities in West Cork were generally formed under quite similar T_h and salinity conditions (Fig. 4.11a-h, Appendix E3). Indeed, the different sample localities between each other show a wider spread in T_h and salinity (Fig. 4.11a-h, Appendix E3). This reflects the various and complex conditions with multiple fluid pulses which led to the primary mineralization in the Munster Basin. No sign of fluid mixing was recorded. Previous measurements from Dhurode, Crookhaven and Ballycummisk (Fig. 4.3, Wen *et al.* 1996) show T_h ranging between 100° and 348°C. Relatively high homogenisation temperatures (Fig. 4.11a-h) are probably caused by crustal thinning during the extensional phase resulting high geothermal gradients with upwelling of the Moho (Meere 1995b; Williams 2000). Meere and Banks (1997) described comparable values, but also showed a quartz vein from Allihies which has higher salinities (22-27 wt.% $NaCl_{equiv}$) than the results from this study (max. 22.4 wt.% $NaCl_{equiv}$). The high saline values were described by Lang *et al.* (2020) as localized assemblages from end members of a cooling fluid system occurring at the end of the primary mineralization phase. It needs to be noted that all these measured pre-Variscan vein samples from the Munster Basin suffered a metamorphism up to sub-greenschist facies during syn-Variscan compression (Meere 1995b). Cleavage formation (e.g. Fig. 4.8b), folding (Fig. 4.4f, 4.8c) and stylolitisation (Fig. 4.4e, 4.4g, 4.5b, 4.9d, 4.9e) show evidence that fluid remobilisation has occurred. This could have caused a syn-Variscan alteration of the pre-Variscan fluid inclusions. Nevertheless, the carefully selected inclusions do not show any sign of deformation or leaking (Appendix E2). The oval shaped inclusions are interpreted as negative crystal features with no sign of external stress deformation and the high competency of the massive quartz lodes has protected most of the internal pre-Variscan vein structures.

Fluid inclusion assemblages in syn-Variscan samples from this study have a much narrower homogenisation temperature and salinity range (T_h = 101 to 270 °C and 4.8 to 16.7 wt.% $NaCl_{equiv}$) than those from the pre-Variscan veins (Fig. 4.11i-n, Appendix E3). Lang *et al.* (2020) presented similar syn-Variscan homogenization temperatures from Allihies ranging between 121 and 243°C.

The span of salinities from this study (West Cork) is slightly lower (4.8 to 16.7 wt.% $NaCl_{equiv}$) than the values measured at Allihies (8.2 and 19.1 wt% $NaCl_{equiv}$, Lang *et al.* 2020). In general, the syn-Variscan inclusions are less saline and show slightly cooler homogenisation temperatures than the pre-Variscan inclusions. The two different vein types show only a partial overlap (Fig. 4.11).

Both vein types (pre-Variscan and syn-Variscan) display a regional variation occurring between the sample localities (Fig. 4.11a-h and 4.11i-n). This could suggest that a similar fluid source generated both mineral systems. Lower salinity and narrower T_h ranges imply evolving fluid pulses over time. The occurrences of siderite (Fig. 4.8g) and barite (Fig. 4.9b, 4.9c, 4.9f) at Crookhaven and Ballycummisk indicate that there are additional phases in the H_2O-NaCl fluid system. These are most likely $CaCl_2$ and $BaCl_2$. The H_2O–NaCl–$CaCl_2$-$BaCl_2$ system infers an early marine brine signature (Meere and Banks 1997).

4.6.4 Magmatism and mineralization

The measured molybdenite Re-Os model ages of 315.5 ± 1.6 Ma and 311.8 ± 1.6 Ma from Ballycummisk (Fig. 4.3, Table 4.1) coincide with the lamprophyric intrusions dated at 314.44 ± 1.00 Ma (Ar/Ar phlogopite, Quinn *et al.* 2005) from Black Ball Head near Allihies. These intrusions were formed during the early Variscan compression (Pracht & Kinnaird 1995; Pracht 2000). Coe (1959), Charlesworth (1963), Murphy (1960), and Fletcher (1969) presumed a magmatic intrusion as being the source for the sulphide mineralization. Nevertheless, no magmatic intrusion was dated in the time frame of the primary, pre-Variscan mineralization between 367.3 ± 5.5 and 366.4 ± 1.9 Ma (Allihies, Lang *et al.* 2020). None of the examined mineralized quartz veins in this study was directly or indirectly locally linked to a magmatic intrusion. Spinks *et al.* (2016) presented negative $\delta^{34}S_{CDT}$ values (-16.9 to -10.4 ‰) for chalcopyrite from Allihies. Wen *et al.* (1996) showed mostly negative $\delta^{34}S_{CDT}$ values (-21.0 to +5.1 ‰) for vein- and stratiform-disseminated deposits from West Cork. These negative values represent a bacteriogenic reduction of

sulphur within the sediments and are evident for a sedimentary, non-magmatic fluid source. Higher fluid inclusion homogenisation temperatures of up to 335 °C from Gortavallig or Ballycummisk Mines (Fig. 4.11) represent high geothermal gradients during basin formation (Meere 1995b, Williams 2000) with crustal thinning and upwelling of the Moho (Williams 2000).

4.6.5 Timing of the copper emplacement and previous mineralization models

Based on the predominantly negative $\delta^{34}S_{CDT}$ values from Allihies (vein-hosted chalcopyrite: -16.9 to -10.4 ‰) and West Cork (vein- and stratiform-disseminated chalcopyrite: -21.0 to +5.1 ‰) Spinks *et al.* (2016) and Wen *et al.* (1996) presumed a sedimentary, bacteriogenic reduced fluid source for the copper mineralization. They assumed that an originally stratiform syngenetic-diagenetic sulphide mineralization was remobilised by metamorphic fluids into quartz veins at different stages of the Variscan Orogeny: According to Meere and Banks minor vein formation is related to the early Variscan compression. The three studies by Wen *et al.* (1996), Meere and Banks (1997), as well as Spinks *et al.* (2016) defined the major vein mineralization/remobilisation during the post-Variscan N-S oriented relaxation event.

The demonstrated outcome of this study, as well as recent structural observations from Lang *et al.* (2020) show that the major E-W to ENE-WSW vein-hosted Cu mineralization is related to early basinal extension and pre-dates the Variscan Orogeny. This early mineralization is followed by a second syn-compressional event. In the following paragraph we discuss the geochronological evidence which proves a new time-setting of the mineralizing phases:

The copper deposits from Allihies (Fig. 4.3) show an age between 367.3 ± 5.5 and 366.4 ± 1.9 Ma (Re-Os, Lang *et al.* 2020) and are described as syn-basinal mineralization during the Famennian Stage (Cohen *et al.* 2019) of the Upper Devonian. The second episode of Cu-vein formation is related to the early compressional phase at Ballycummisk (Fig. 4.3) between 315.5 ± 1.6 Ma and 311.8 ± 1.6 Ma (molybdenite Re-Os model ages, Table 4.1) belonging to the

Bashkirian to Moscovian Stage (Cohen *et al.* 2019) of the Pennsylvanian (Upper) Carboniferous. The molybdenite stylolitisation (Figs. 4.9d + 4.9e) indicates that the samples suffered compressional deformation. According to Stein *et al.* (2001) the molybdenite still represents the primary mineralization, as the Re-Os chronometer is resistant to high-grade metamorphism and deformation. As the dated molybdenite is syngenetically intergrown with chalcopyrite (Fig. 4.9c), it can be assumed that the Re-Os ages represent the major Cu emplacement at Ballycummisk. Quinn *et al.* (2005) postulated that the initial effect of the Variscan compression with cleavage formation started before 314.4 Ma which proves that the compressional mineralization was emplaced at the beginning of the Variscan Orogeny.

This newly classified time-setting of a syn-basinal and an early Variscan mineralization phase contradicts the previous mineralization models which presumed a post-Variscan emplacement by metamorphic fluids (Wen *et al.* 1996, Meere and Banks 1997, Spinks *et al.* 2016). The less developed to absent host rock alteration nearby the mineralized quartz veins (Figs. 4.4c, 4.4d, 4.8c, 4.8d) can be explained by a consolidated sediment with low permeability. The Caha Mountain Formation, for example, which hosts the large Allihies copper lodes was overlain by several hundred meters or even up to several kilometres of basinal sediments during the vein precipitation (e.g. Gun Point Formation: 300 m to 2500 m, Fig. 4.2b, Pracht & Sleeman 2002). This caused an advanced super mature diagenetic stage with only slight porosity left (Montañez & Crossey 2017). The bacteriogenic reduced fluid (negative $\delta^{34}S_{CDT}$ values, Wen *et al.* 1996, Spinks *et al.* 2016) did form the vein hosted copper mineralization possibly simultaneously together with the sediment-hosted sulphide emplacement (e.g. Crookhaven, Fig. 4.8d).

A sulphide remobilisation as described by Wen *et al.* (1996) and Spinks *et al.* (2016) did not occur during a post-Variscan relaxation event. As mentioned before, the early Variscan Cu mineralization at Ballycummisk took place *after* the major Variscan cleavage formation (Fig. 4.9f, Cooper & Trayner 1986; Ford 1987), but still at the beginning of the Variscan Orogeny. The cleavage formation provided a fractures within the pre-Variscan basinal mineralized quartz veins (e.g. Fig. 4.9f). These cleavage related pathways allowed a

sulphide remobilisation by low-grade sub-greenschist-facies metamorphic fluids (Meere 1995a, 1995b). As we know from the fluid inclusion studies (Fig. 4.11i-n) the mean homogenisation temperature T_h of all measured Syn-Variscan veins is 178 °C with a mean salinity of 10.2 wt.% NaCl equivalent (n = 87). Under these conditions the solubility of metals in hydrothermal fluids which are in equilibrium with chalcopyrite is about 0.01 ppm (Fig. 4.13, Fontboté *et al.* 2017). A low pH increases the metal solubility (Fontboté *et al.* 2017). As described by Spinks *et al.* (2016) the metamorphic fluids were responsible for remobilising both sulphur and metals. The relatively low solubility of 0.01 ppm metals (e.g. copper) requires a sulphide-rich source (e.g. early pre-Variscan veins) and/or a high fluid flow under low pH conditions. The early Variscan reactivation of pre-Variscan mineralized basinal fault systems provided an immediately adjacent sampling and sulphide remobilisation from the early into the late Cu-vein systems over a very short distance. Both mineralization generations show therefore a highly proximal emplacement.

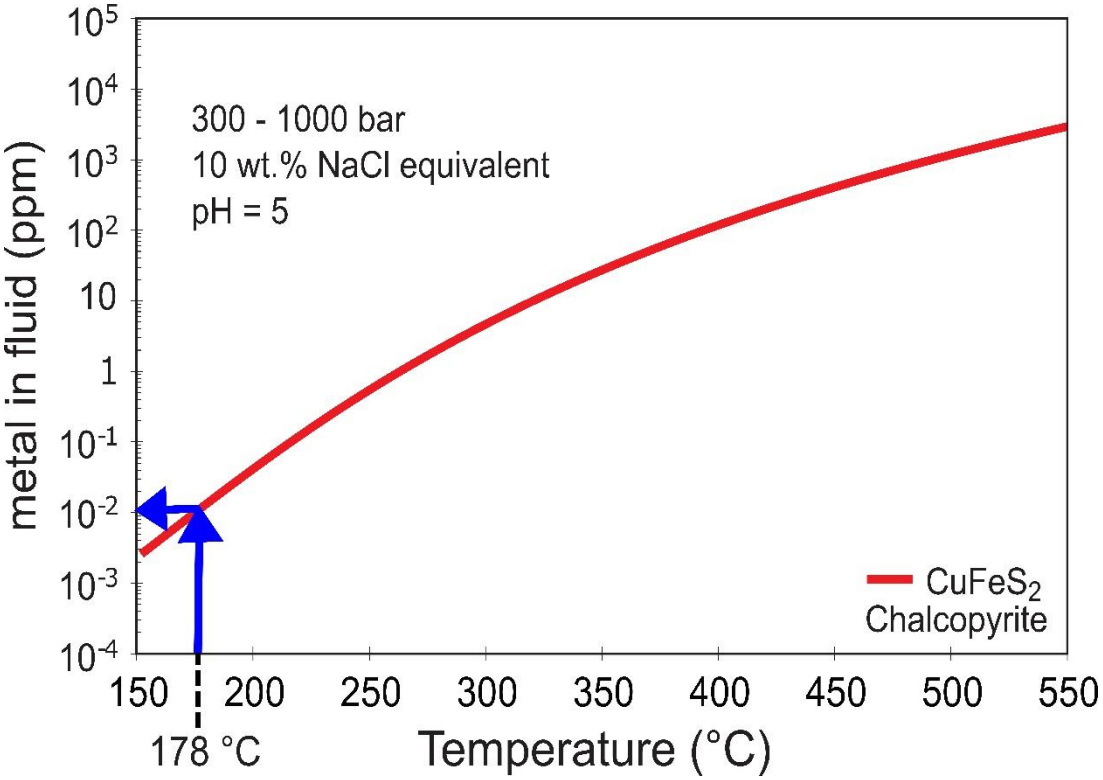


Fig. 4.13) Solubility of metals in hydrothermal fluids (modified from Fontboté et al. 2017).

4.6.6 Sediment-hosted stratiform copper (SSC) deposits and exploration potential

Sediment-hosted stratigraphically bound copper mineralization within the Munster Basin was described by Snodin (1972) and Wen *et al.* (1996). The disseminated copper mineralization occurs in reduced green sandstone zones (green beds, transition zone) within the upper Castlehaven Formation just below the nonreddish Toe Head Formation (see Fig. 4.2b). The typical SSC deposits, such as the Permian Kupferschiefer in Germany and Poland and the Zambian Central African Copperbelt have a sedimentary basin architecture with continental siliciclastic sedimentary rocks (red beds) which are overlain by nonreddish siltstones, sandstones, carbonates and/or shales, known as reduced graybeds (e.g. Kirkam 1989, Hitzman *et al.* 2005, Brown 2014 and references herein). In SSC deposits the reduced graybeds form a stratiform thin-layered host rock for the sulphide mineralization (Hitzman *et al.* 2005). The observations of this study show that the vein hosted copper deposits of West Cork are predominantly hosted within sandstone and siltstone formations of the oxidized Upper Devonian siliciclastic sediments (Fig. 4.12a). These formations belong to the Upper Old Red Sandstone Facies (Williams *et al.* 1989). Only with regard to the host lithology of an SSC type deposit the copper mineralization of the Muster Basin in West Cork could be classified as a Redbed-Type Copper Deposit which is generally hosted by the oxidized red bed sequence and not by the reduced graybeds (Brown 2014). Examples are Dzhezkazgan in Kazakhstan and Lisbon Valley in Utah (Brown 2014, Hitzman *et al.* 2005). The copper mineralization in SSC deposits is often related to organic matter; for example, pyritized plant debris is replaced by copper sulphides (e.g. Cumberland Basin of Nova Scotia, Brown 2014). The cellular permineralized plant fossil from Killeen North (Figs. 4.3 + 4.6h-k) is a nice example for this sediment hosted copper mineralization. The sample was found next to a historically mined E-W lode. Therefore, it is suspected that this Cu fossilisation is in direct relation to the pre-Variscan basinal vein mineralization. Cu- and S-rich fluids possibly percolated from the extensional faults into the highly porous host rock conglomerates and replaced the organic

cellular material by redox reaction (e.g. Berner 1984). Comparable to this is the occurrence of disseminated chalcopyrite within an organic-rich slate next to a mineralized quartz vein from Gortavallig (Fig. 4.6g). The mineralized siltstone next to the chalcopyrite-rich quartz vein from Crookhaven (Fig. 4.8d) provides a similar example. Apart from these examples the sulphide mineralization of the examined localities is mainly hosted within the quartz veins. This is not typical for a sediment-hosted stratiform copper deposit. Vein-style mineralization can occur for example at the Kupferschiefer Deposit in Poland/Germany or at Coates Lake Deposit in Canada but is generally subordinate and the veins are rather described as veinlets (<1 to 15 cm, Hitzman *et al.* 2005, Milton *et al.* 2017). The examined deposits of West Cork could be named as vein hosted Redbed-Type SSC deposits.

The reason for the mainly vein hosted concentration of the West Cork copper deposits was already discussed in the previous paragraph which involved a diagenetically consolidated host rock during vein formation. This has a strong implication for potential mineral exploration in the West Cork area: The copper sulphides are mainly hosted in proximal relation to E-W and WSW-ENE basin-controlled extensional fault systems, as well as to their syn-Variscan re-activated pendants. Disseminated sediment-hosted sulphide mineralization is subordinate and always related to the basinal fault systems.

4.6.7 Comparison with Zn-Pb Deposits of the Irish Midlands

The Cu mineralization in the SW Ireland was compared with the large Zn-Pb deposits of the Irish Midlands. Pyrite Re-Os dates reveal an age of 346.6 ± 3.0 Ma at Lisheen and 334.0 ± 6.1 Ma at Silvermines (Hnatyshin *et al.* 2015). This postdates the mineralization at Allihies (367.3 ± 5.5 and 366.4 ± 1.9 Ma) but predates the ages from Ballycummisk (315.5 ± 1.6 Ma and 311.8 ± 1.6 Ma). Similarities of the examined localities in West Cork to the Irish Midlands can be observed in the geostructural genesis and kinematics of the deposits. Comparable to the observations in this study, Silvermines and Tynagh Mine are related to E-W striking normal faults, caused by a pre-Variscan N-S extensional phase (e.g. Kinnaird *et al.* 2002, Hitzman 1999). In contrary to the

mainly siliciclastic (Upper Devonian) hosted West Cork deposits Navan, Lisheen, Galmoy, Silvermines and Tynagh are hosted within the Lower Carboniferous carbonates next to the E-W and SW-NE faults (e.g. Gleeson and Yardley 2002, and Everett *et al.* 1999b). Late Carboniferous Variscan reactivation of normal faults and the formation of transpressional faults in the Irish Midlands (Coller, 1984; Johnston *et al.*, 1996; Hitzman, 1999; Kyne *et al.*, 2017, Torremans *et al.* 2018) can be compared with the reactivated fault at Baurearagh (Fig. 4.4e), the compressional mineralized quartz vein from Crookhaven (Fig. 4.8g) and the early Variscan mineralized veins from Ballycummisk (Fig. 4.9f).

Fluid inclusion measurements from the Irish Type Deposits show a range of up to about 240°C for homogenisation temperature and low salinities (about 10 wt% $NaCl_{equiv}$), to very low T_h values with a minimum of about 55°C and a high salinity of up to 24 wt% $NaCl_{equiv}$ (Wilkinson 2001, 2010; Gleeson and Yardley 2002). Banks (2002) assumed from chloride and Br concentrations (crush + leach studies), that the main ore fluid from Tynagh and Silvermines was seawater that had evaporated until the salinity was between 12 and 18 wt%. Measurements from pre-Variscan E-W veins of West Cork (Fig. 4.11a-h) indicate comparable values, but homogenisation temperatures T_h can get hotter with up to 335 °C and the salinity can show even lower concentrations with 5.2 wt% $NaCl_{equiv}$.

4.7 Conclusions

Copper mineralization in West Cork is predominantly related to extensional E-W to ENE-WSW striking basin structures, which form pathways for deep sourcing metal-rich fluids (Fig. 4.12). The ore is often hosted within large meter- to tens of meters-scale quartz veins with occasional high-pressure hydraulic brecciation and stockwork veining. Sediment-hosted mineralization related to the extensional basin structures is also present. All E-W quartz veins and extensional structures show a Variscan compressional overprint (folding, cleavage, stylolitisation, brecciation), whereby a reverse reactivation of the extensional fractures is possible and Cu mineralization was emplaced during

early compressional phase (Fig. 4.12). Pre-Variscan, mineralizing fluid inclusion assemblages show multiple fluid pulses with homogenisation temperatures T_h from 90 to 335 °C (Fig. 4.11a-h). Salinities vary between 3.8 and 22.4 wt% $NaCl_{equiv}$. Syn-Variscan quartz veins show also multiple pulses with T_h ranges from 101 to 270 °C and with salinities between 4.8 and 16.7 wt% $NaCl_{equiv}$. There is no evidence for a magmatic driven fluid source.

The timing of Cu mineralization (molybdenite Re-Os) reveals two distinct episodes from syn-basinal formation at Allihies between 367.3 ± 5.5 and 366.4 ± 1.9 Ma (Fig. 4.3, Lang *et al.* 2020), to an early compressional phase at Ballycummisk between 315.5 ± 1.6 Ma and 311.8 ± 1.6 Ma.

The basin architecture of the West Cork copper mineralization shows genetic links to the Redbed-Type SSC deposits and a structural kinematic similarity to the Zn-Pb deposits of the Irish Midlands.

4.8 Acknowledgements

This publication has emanated from research supported in part by a research grant from Science Foundation Ireland (SFI) under Grant Number 13/RC/2092 and is co-funded under the European Regional Development Fund and by iCRAG industry partners.

The authors are grateful for the field, laboratory and software assistance from Ronan Hennessy (University College Cork). Many thanks to the local residents from Crookhaven Peninsula for granting access to the historic mining sites. Special thanks to the National History Museum in London (Simon Kocher and Robin Hansen) for providing molybdenite sample material (BM.1964,R230) from the historic Russell collection.

The Geological Survey Ireland are acknowledged for providing regional data and background information for our 2-D mapping and 3-D modelling efforts. We also thank ARANZGeo/Seequent (Leapfrog3DGeo), Emerson Paradigm (SKUA-GoCAD), Microsoft (Bing Satellite Maps, 2016-2019), Google Maps (2016-2019), Mira Geoscience (Mining Suite Plugins), Modri planet d.o.o.

(3Dsurvey) and ESRI (ArcGIS) for providing support and academic licenses of software essential to this project.

DS acknowledges the technical support of Antonia Hoffman, Geoff Nowell and Chris Ottley, and the Total Endowment Fund and the CUG Wuhan Dida Fund.

4.9 Chapter References

Aldwell, C.R. 1990. Some examples of mining in Ireland and its impact on the environment. Environmental Geology and Water Sciences, 15(2), 145–157, doi:10.1007/bf01705103

Allmendinger, R.W., Cardozo, N.C. and Fisher, D. 2013. Structural Geology Algorithms: Vectors & Tensors. Cambridge University Press, Cambridge.
Atkinson, Jr. A.B., 2002. A Model for the PTX Properties of H2O–NaCl. MSc thesis, Virginia Tech, Blacksburg, VA.

Alvarez, W., Engelder, T., and Geiser, P.A. 1978. Classification of solution cleavage in pelagic limestones. Geology, 6(5), 263-266. https://doi.org/10.1130/0091-7613(1978)6<263:COSCIP>2.0.CO;2

Atkinson, Jr. A.B. 2002. A Model for the PTX Properties of H2O–NaCl. MSc thesis, Virginia Tech, Blacksburg, VA.

Banks, D.A., Boyce, A.J. and Samson, I.M. 2002. Constraints on the origins of fluids forming Irish Zn-Pb-Ba deposits: Evidence from the composition of fluid inclusions. Economic Geology and the Bulletin of the Society of Economic Geologists, 97(3), pp. 471-480.

Berner, R.A. 1984. Sedimentary pyrite formation: An update. Geochimica et Cosmochimica Acta, 48(4), 605-615, https://doi.org/10.1016/0016-7037(84)90089-9.

Bodnar, R.J. 1983. A method of calculating fluid inclusions volumes based on vapor bubble diameters and P–V–T–X properties of inclusion fluids. Economic Geology, 78, 535–542, https://doi.org/10.2113/gsecongeo.78.3.535

Bodnar, R.J. 1993. Revised equation and table for determining the freezing point depression of H2O–NaCl solutions. Geochimica et Cosmochimica Acta, 57, 683–684, https://doi.org/10.1016/0016-7037(93)90378-A

Bodnar, R.J. and Vityk, M.O. 1994. Interpretation of microthermometric data for H2O–NaCl fluid inclusions. In: Vivo, B.D. and Frezzotti, M.L. (eds) Fluid Inclusions in Minerals, Methods and Applications. Virginia Tech, Blacksburg, VA, 117–130.

Boldy, G.D.J. 1955. The Petrology of the Igneous rocks near Castletownbere, West Co. Cork and their relationship with the Armorican Orogenesis in S.W. England. Unpublished M.Sc. Thesis. Trinity College, Dublin.

Bons, P. 2001. The formation of large quartz veins by rapid ascent of fluids in mobile hydrofractures. Tectonophysics, 336, 1-17, https://doi.org/10.1016/S0040-1951(01)00090-7.

Bons, P.D., Elburg, M. and Gomez-Rivas, E. 2012. A review of the formation of tectonic veins and their microstructures. Journal of Structural Geology, 43, 33–62, https://doi.org/10.1016/j.jsg.2012.07.005

Brown, A.C. 2014. Low-Temperature Sediment-Hosted Copper Deposits. Editors: Heinrich, D., Holland, Karl, Turekian, K., Treatise on Geochemistry (Second Edition), Elsevier, 251-271. https://doi.org/10.1016/B978-0-08-095975-7.01110-4

Capewell, J. 1975. The Old Red Sandstone Group of Iveragh, Co. Kerry. Proceedings of the Royal Irish Academy, Section B, 75, 155–171. Cardozo, N. and Allmendinger, R.W. 2013. Spherical projections with OSXStereonet. Computers & Geosciences, 51, 193–205, https://doi.org/10.1016/j.cageo.2012.07.021

Cardozo, N. and Allmendinger, R. W. 2013. Spherical projections with OSXStereonet: Computers & Geosciences, 51(0), 193-205, https://doi.org/10.1016/j.cageo.2012.07.021

Caumon, G., Collon-Drouaillet, P., Le Carlier de Veslud, C., Viseur, S. and Sausse, J. 2009. Surface-based 3-D modeling of geological structures. Mathematical Geosciences, 41, 927–945, https://doi.org/10.1007/s11004-009-9244-2

Cohen, K.M., Harper, D.A.T. and Gibbard, P.L. 2019. ICS International Chronostratigraphic Chart 2019/05. International Commission on Stratigraphy, IUGS. www.stratigraphy.org [last accessed 12 August 2019].

Coller, D.W. 1984. Variscan structures in the Upper Palaeozoic rocks of west central Ireland. Geological Society, London, Special Publications, 14, 185–194, https://doi.org/10.1144/GSL.SP.1984.014.01.18

Cooper, M.A. and Trayner, P.M. 1986. Thrust-surface geometry: implications for thrust-belt evolution and section-balancing techniques. Journal of Structural Geology, 8, 305–312, https://doi.org/10.1016/0191-8141(86)90051-9

Doppler, G., Bakker, R.J. 2014. The influence of the α–β phase transition of quartz on fluid inclusions during re-equilibration experiments. Lithos 198–199,14–23.

Duffy, T.J. 1932. Copper Deposits in Southwest Ireland. Unpublished report and field sheets. Geol. Surv. Ireland.

Ennis, M., Meere, P.A., Timmerman, M.J. and Sudo, M. 2015. Post-Acadian sediment recycling in the Devonian Old Red Sandstone of Southern Ireland. Gondwana Research, 28, 1415–1433, https://doi.org/10.1016/j.gr.2014.10.007

Everett, C.E., Wilkinson, J.J. and Rye, D.M. 1999b. Fracture-controlled fluid flow in the Lower Palaeozoic basement rocks of Ireland: Implications for the genesis of Irish-type Zn-Pb deposits. In: McCaffrey, K.J.W., Lonergan, L. & Wilkinson, J.J. (eds.) Fractures, Fluid Flow and Mineralization. Geol. Soc. Spec. Pub., 155, 247-276.

Fletcher, C.I. 1969. The sulphide mineralization in the Allihies region, County Cork, Eire. Ph.D. Dissertation, University of Leicester, 128–129.

Fontboté, L., Kouzmanov, K., Chiaradia, M., Pokrovski, G.S. 2017. Sulfide Minerals in Hydrothermal Deposits. Elements 13 (2), 97–103. https://doi.org/10.2113/gselements.13.2.97

Ford, M. 1987. Practical application of the sequential balancing technique: an example from the Irish Variscides. Journal of the Geological Society, London, 144, 885–891, https://doi.org/10.1144/gsjgs.144.6.0885

Fossen, H. and Rotevatn, A. 2016. Fault linkage and relay structures in extensional settings – A review. Earth-Science Reviews, 154, 14–28, https://doi.org/10.1016/j.earscirev.2015.11.014

Gaba, R.G. 1990. Stockwork Molybdenite in the Mission Ridge Pluton: A new Exploration Target in the Bridge River Mining Camp* (92J/16). British Columbia Geological Survey Branch, Geological Fieldwork IYR9, Paper 1990-1

Gleeson, S.A. and Yardley, B.W.D. 2002. Extensional Veins and Pb–Zn Mineralisation in Basement Rocks: The Role of Penetration of Formation Brines. In: Stober, I. and Bucher, K. (eds) Water–Rock Interaction. Water Science and Technology Library, Vol. 40. Springer, Dordrecht, 189–205.

Geological Survey of Ireland, GSI, unknown author 1863. Gortavallig Mine, Horizontal Plan. GSI Goldmine, https://secure.dccae.gov.ie/goldmine/docpage.html?id1=8260692&id2=9553735&id3=9557012 [last accessed 17 May 2020]

Geological Survey of Ireland, GSI 2016. Bedrock 100k (scale 1:100,000), Bedrock Geology, Coordinate System: Irish Transverse Mercator / ITM. https://www.gsi.ie/en-ie/data-and-maps/Pages/Bedrock.aspx# [last accessed 20/04/2020]

Geological Survey of Ireland, GSI Infomar 2017. Bathymetry - South West - bylrsw10m. INFOMAR INSS 10m Bathymetry & LIDAR WGS84 projection. Ireland. LAT (lowest astronomical tide). https://www.infomar.ie/data/ [last accessed 20/04/2020]

Geological Survey of Ireland, GSI Jetstream 2019. Historical Maps of Copper Deposits in SW Ireland. https://jetstream.gsi.ie [last accessed 08/03/2019]

Goldstein, R.H. and Reynolds, T.J. 1994. Systematics of fluid inclusions in diagenetic minerals. SEPM (Society for Sedimentary Geology), USA

Halliday, A.N. and Mitchell, J.G. 1983. K–Ar ages of clay concentrates from Irish orebodies and their bearing on the timing of mineralisation. Earth and Environmental Science Transactions of the Royal Society of Edinburgh, 74, 1–14, https://doi.org/10.1017/S0263593300009858

Hitzman, M.W. 1999. Extensional faults that localize Irish syndiagenetic Zn–Pb deposits and their reactivation during Variscan compression. Geological Society, London, Special Publications, 155, 233–245, https://doi.org/10.1144/GSL.SP.1999.155.01.17

Hitzman, M.W., Kirkham, R., Broughton, D., Thorson, J., and Selley, D. 2005. The sediment hosted stratiform copper ore system. In: Hedenquist, J.W., Thompson, J.F.H., Goldfarb, R.J., and Richards, J.P. (eds.). Economic Geology 100th Anniversary Volume 1905–2005, 609–642. Littleton, CO: Society of Economic Geologists, Inc.

Hnatyshin, D., Creaser, R.A., Wilkinson, J.J. and Gleeson, S.A. 2015. Re–Os dating of pyrite confirms an early diagenetic onset and extended duration of mineralization in the Irish Zn–Pb ore field. Geology, 43, 143–146, https://doi.org/10.1130/G36296.1

Jarvis, A., Reuter, H.I., Nelson, A. and Guevara, E. 2008. Hole-filled SRTM for the globe Version 4. International Centre for Tropical Agriculture (CIAT), http://srtm.csi.cgiar.org [last accessed 25 July 2017].

Johnston, J.D., Coller, D., Millar, G., and Critchley, M.F. 1996. Basement structural controls on Carboniferous-hosted base metal mineral deposits in Ireland: Geological Society, London, Special Publication, 107, 1-21.

Kinnaird, J.A., Ixer, R.A., Barreiro, B. and Nex, P.A. 2002. Contrasting sources for lead in Cu-polymetallic and Zn–Pb mineralisation in Ireland: constraints from lead isotopes. Mineralium Deposita, 37, 495–511, https://doi.org/10.1007/s00126-001-0252-5

Kirkham, R.V. 1989. Distribution, setting and genesis of sediment-hosted stratiform copper deposits. In: Boyle, R.W., Brown, A.C., Jefferson, C.W., Jowett, E.C., and Kirkham, R.V. (eds.), Sediment-Hosted Stratiform Copper Deposits, Geological Association of Canada Special Paper 36, 3–38. Ottawa: Geological Association of Canada.

Kocianova, L. 2016. Orientation Analysis Tools for ArcGIS. OATools. https://is.muni.cz/www/lenka.koc/prvnistrana.html [last access: 07/04/2020]

Kyne, R., Torremans, K., Güven, J., Doyle, R., Walsh, J. 2017. 3-D Modeling of the Lisheen and Silvermines Deposits, County Tipperary, Ireland: Insights into Structural Controls on the Formation of Irish Zn-Pb Deposits. Economic Geology, 114 (1), 93-116, https://doi.org/10.5382/econgeo.2019.4621

Landes, M., O'Reilly, B.M., Readman, P.W., Shannon, P.M. and Prodehl, C. 2003. VARNET-96: three-dimensional upper crustal velocity structure of SW Ireland. Geophysical Journal International, 153, 424–442, https://doi.org/10.1046/j.1365-246X.2003.01911.x

Lang, J., Meere, P. A., Unitt, R. P., Johnson, S. C., Solferino, G., Torremans, K., Selby, D. and Kyne, R. 2020. The Vein Hosted Copper Deposits of the Allihies Mining Area, Southwest Ireland – A New Structural and Chronological Evaluation. Journal of the Geological Society, jgs2019–154, https://doi:10.1144/jgs2019-154

Lawley, C., Selby, D. and Imber, J. 2013. Re-Os Molybdenite, Pyrite, and Chalcopyrite Geochronology, Lupa Goldfield, Southwestern Tanzania: Tracing Metallogenic Time Scales at Midcrustal Shear Zones Hosting Orogenic Au Deposits. Economic Geology, 108, 1591-1613, https://doi.org/10.2113/econgeo.108.7.1591

Li, Y., Selby, D., Condon, D. and Tapster, S. 2017. Cyclic Magmatic–Hydrothermal Evolution in Porphyry Systems: High-Precision U–Pb and Re–Os Geochronology Constraints on the Tibetan Qulong Porphyry Cu–Mo Deposit. Economic Geology, 112, 1419–1440, https://doi.org/10.5382/econgeo.2017.4515

MacCarthy, I.A.J. 1990. Alluvial sedimentation patterns in the Munster Basin, Ireland. Sedimentology, 37, 685–712, https://doi.org/10.1111/j.1365-3091.1990.tb00629.x

MacCarthy, I.A.J. 2007. The South Munster Basin of southwest Ireland. Journal of Maps, 3, 149–172, https://doi.org/10.1080/jom.2007.9710835

MacCarthy, I.A.J., Pracht, M. and Sleeman, A.G. 2002. Geology of West Cork, Scale 1:100000, Sheet 24. Geological Survey of Ireland, Dublin.

Meere, P.A. 1995a. High and low density fluids in a quartz vein from the Irish Variscides. Journal of Structural Geology, 17, 435–446, https://doi.org/10.1016/0191-8141(94)00066-9

Meere, P.A. 1995b. Sub-greenschist facies metamorphism from the Variscides of SW Ireland an early syn-extensional peak thermal event. Journal of the Geological Society, London, 152, 511–521, https://doi.org/10.1144/gsjgs.152.3.0511

Meere, P.A. 1995c. The structural evolution of the western Irish Variscides: an example of obstacle tectonics? Tectonophysics, 246, 97–112, https://doi.org/10.1016/0040-1951(94)00267-D

Meere, P.A. and Banks, D.A. 1997. Upper crustal fluid migration: an example from the Variscides ofSW Ireland. Journal of the Geological Society, London, 154, 975–985, https://doi.org/10.1144/gsjgs.154.6.0975

Milton, J.E., Hickey, K.A., Gleeson, S.A., Falck, H., Allaz, J. 2017. In Situ Monazite Dating of Sediment-Hosted Stratiform Copper Mineralization in the Redstone Copper Belt, Northwest Territories, Canada: Cupriferous Fluid Flow Late in the Evolution of a Neoproterozoic Sedimentary Basin. Economic Geology, 112 (7), 1773–1806. https://doi.org/10.5382/econgeo.2017.4529

Montañez, I. P., & Crossey, L. J. 2017. Diagenesis. Encyclopedia of Engineering Geology, 1–11. https://doi.org/10.1007/978-3-319-39193-9_35-1

Morley, C.K. 1995. Developments in the structural geology of rifts over the last decade and their impact on hydrocarbon exploration. Geological Society, London, Special Publications, 80, 1-32, https://doi.org/10.1144/GSL.SP.1995.080.01.01

Naylor, D. and Jones, P.C. 1967. Sedimentation and tectonic setting of the Old Red Sandstone of southwest Ireland. In: Oswald, D. (ed.) International Symposium on the Devonian System (Calgary). Society of Petroleum Geology 2, Calgary, Alberta, 1089–1099.

O'Brien, M.V. 1959. The future of non-ferrous mining in Ireland. In: The Future of Non-Ferrous Mining in Great Britain and Ireland. Institution of Mining and Metallurgy Symposium, 5–26.

O'Brien, W.F. 1987. The dating of the Mt Gabriel-type copper mines of West Cork. Journal of the Cork Historical and Archaeological Society, 92, 50–70.

Pastor-Galán, D., Ursem, B., Meere, P.A., Langereis, C. 2015. Extending the Cantabrian Orocline to two continents (from Gondwana to Laurussia). Paleomagnetism from South Ireland. Earth and Planetary Science Letters, 432, 223-231, https://doi.org/10.1016/j.epsl.2015.10.019

Pracht, M. 2000. Controls on magmatism in the Munster Basin, SW Ireland. Geological Society, London, Special Publications, 180, 303–317, https://doi.org/10.1144/GSL.SP.2000.180.01.14

Pracht, M. and Kinnaird, J.A. 1995. Mineral chemistry of megacrysts and ultramafic nodules from an undersaturated pipe at Black Ball Head, County Cork. Irish Journal of Earth Sciences, 14, 47–58.

Pracht, M. and Sleeman, A.G. 2002. A geological description of West Cork and adjacent parts of Kerry to accompany the Bedrock Geology, 1:100,000 Scale Map Series, Sheet 24, West Cork. With accompanying contributions by Wright G (Groundwater) and CoxW (Minerals). Geological Survey of Ireland, Dublin.

Price, C.A. and Todd, S.P. 1988. A model for the development of the Irish Variscides. Journal of the Geological Society, London, 145, 935–939, https://doi.org/10.1144/gsjgs.145.6.0935

Quinn, D., Meere, P.A. and Wartho, J.A. 2005. A chronology of foreland deformation: Ultra-violet laser 40Ar/39Ar dating of syn/late-orogenic intrusions from the Variscides of southwest Ireland. Journal of Structural Geology, 27, 1413–1425, https://doi.org/10.1016/j.jsg.2005.02.003

Reilly, T.A. 1986. A review of vein mineralization in SW County Cork, Ireland. In: Andrew, C.J., Crowe, R.W.A., Finlay, S., Pennell, W.M. and Pyne, J.F. (eds) Geology and Genesis of Mineral Deposits in Ireland. Irish Association for Economic Geology, Dublin, 513–544.

Sanderson, D.J. 1984. Structural variation across the northern margin of the Variscides in NW Europe. Geological Society, London, Special Publications, 14, 149–165, https://doi.org/10.1144/GSL.SP.1984.014.01.15

Selby, D. and Creaser, R.A. 2001. Re–Os geochronology and systematics in molybdenite from the Endako porphyry molybdenum deposit, British Columbia, Canada. Economic Geology, 96, 197–204, https://doi.org/10.2113/gsecongeo.96.1.197

Selby, D., Creaser, R.A., Stein, H.J., Markey, R.J. and Hannah, J.L. 2007. Assessment of the 187Re decay constant by cross calibration of Re–Os molybdenite and U–Pb zircon chronometers in magmatic ore systems. Geochimica et Cosmochimica Acta, 71, 1999–2013, https://doi.org/10.1016/j.gca.2007.01.008

Sheridan, D.J. 1964. The structure and mineralisation of the Mountain Mine area, Allihies, west Co. Cork, Ireland. Scientific Proceedings, Royal Dublin Society, Series A, 2, 21–27.

Smoliar, M.I., Walker, R.J. and Morgan, J.W. 1996. Re–Os ages of group IIA, IIIA, IVA, and IVB iron meteorites. Science, 271, 1099–1102, https://doi.org/10.1126/science.271.5252.1099

Snodin, S.R. 1972. Copper and other mineralisation in the Upper Palaeozoic strata of south-west Cork, Ireland, and related areas. Unpublished Ph.D. Thesis. University of Leicester.

Spinks, S.C., Parnell, J., Bellis, D. and Still, J. 2016. Remobilization and mineralization of selenium–tellurium in metamorphosed red beds: Evidence from the Munster Basin, Ireland. Ore Geology Reviews, 72, 114–127, https://doi.org/10.1016/j.oregeorev.2015.07.007

Steele-MacInnis, M., Bodnar, R.J. and Naden, J. 2011. Numerical model to determine the composition of H2O–NaCl–CaCl2 fluid inclusions based on microthermometric and microanalytical data. Geochimica et Cosmochimica Acta, 75, 21–40, https://doi.org/10.1016/j.gca.2010.10.002

Steele-MacInnis, M., Lecumberri-Sanchez, P. and Bodnar, R.J. 2012. Short note: HokieFlincs_H2O-NaCl: A Microsoft Excel spreadsheet for interpreting microthermometric data from fluid inclusions based on the PVTX properties of H2O–NaCl. Computers & Geosciences, 49, 334–337, https://doi.org/10.1016/j.cageo.2012.01.022

Stein, H.J., Markey, R.J., Morgan, J.W., Hannah, J.L. and Scherstén, A. 2001. The remarkable Re-Os chronometer in molybdenite: How and why it works. Terra Nova, 13, 479-486. https://doi.org/10.1046/j.1365-3121.2001.00395.x

Torremans, K., Kyne, R., Doyle, R., Güven, J.F., Walsh, J.J. 2018. Controls on Metal Distributions at the Lisheen and Silvermines Deposits: Insights into Fluid Flow Pathways in Irish-Type Zn-Pb Deposits. Economic Geology 113 (7), 1455-1477. https://doi.org/10.5382/econgeo.2018.4598

Trouw, R.A.J., Passchier, C.W. and Wiersma, D.J. 2009. Crystal-Plastic Deformation, Recovery and Recrystallisation of Quartz. In: Atlas of Mylonites and Related Microstructures. Springer, Berlin, 241–262.

Vermeulen, N.J., Shannon, P.M., Masson, F. and Landes, M. 2000. Wide-angle seismic control on the development of the Munster Basin, SW Ireland. Geological Society, London, Special Publications, 180, 223–237, https://doi.org/10.1144/GSL.SP.2000.180.01.11
Viswanathiah, M.N. 1959. Geology and Mineralisation around Allihies – Castletownbere Area. Co. Cork, Ireland. Unpublished Ph.D. Thesis, London University.

Walsh, J.J. and Watterson, J. 1991. Geometric and kinematic coherence and scale effects in normal fault systems. Geological Society, London, Special Publications, 56, 193–203, https://doi.org/10.1144/GSL.SP.1991.056.01.13

Wen, N., Boyce, A.J., Fallick, A.E., Ashworth, J.R. and Ixer, R.A. 1996. The genesis of Cu-bearing quartz veins by metamorphic remobilization from stratiform red bed deposits, SW County Cork, Ireland. Mineralogy and Petrology, 57, 73–89, https://doi.org/10.1007/BF01161622

Wilkinson, J.J. 2001. Fluid inclusions in hydrothermal ore deposits. Lithos, 55, 229–272, https://doi.org/10.1016/S0024-4937(00)00047-5

Wilkinson, J.J. 2010. A Review of Fluid Inclusion Constraints on Mineralization in the Irish Ore Field and Implications for the Genesis of Sediment-Hosted Zn–Pb Deposits. Economic Geology, 105, 417–442, https://doi.org/10.2113/gsecongeo.105.2.417

Williams, R.A. 1991. The Berehaven copper mines. British Mining, 42. Northern Mine Research Society, Sheffield.

Williams, E.A., Bamford, M.L.F., Cooper, M.A., Edwards, H.E., Ford, M., Grant, G.G., MacCarthy, I.A.J., McAfee, A.M., and O'Sullivan, M.J., 1989. Tectonic controls and sedimentary response in the Devonian-Carboniferous Munster and South Munster basins, south-west Ireland. In: R.S. Arthurson, P. Gutteridge and S.C. Nolan (Editors), Role of Tectonics in Devonian and Carboniferous Sedimentation in the British Isles. Spec. Publ. Yorkshire Geol. Soc., 6, 123-141.

Williams, E.A. 2000. Flexural cantilever models of extensional subsidence in the Munster Basin (SW Ireland) and Old Red Sandstone fluvial dispersal systems. Geological Society, London, Special Publications, 180, 239–268, https://doi.org/10.1144/GSL.SP.2000.180.01.12

Chapter 5: Synthesis

This thesis provides a new view onto the mineral deposits in SW Ireland, their similarities to the sediment-hosted stratiform copper (SSC) mineralization, and their importance to the entire Irish Ore Field. The presented outcome is supported by additional geochemical data:

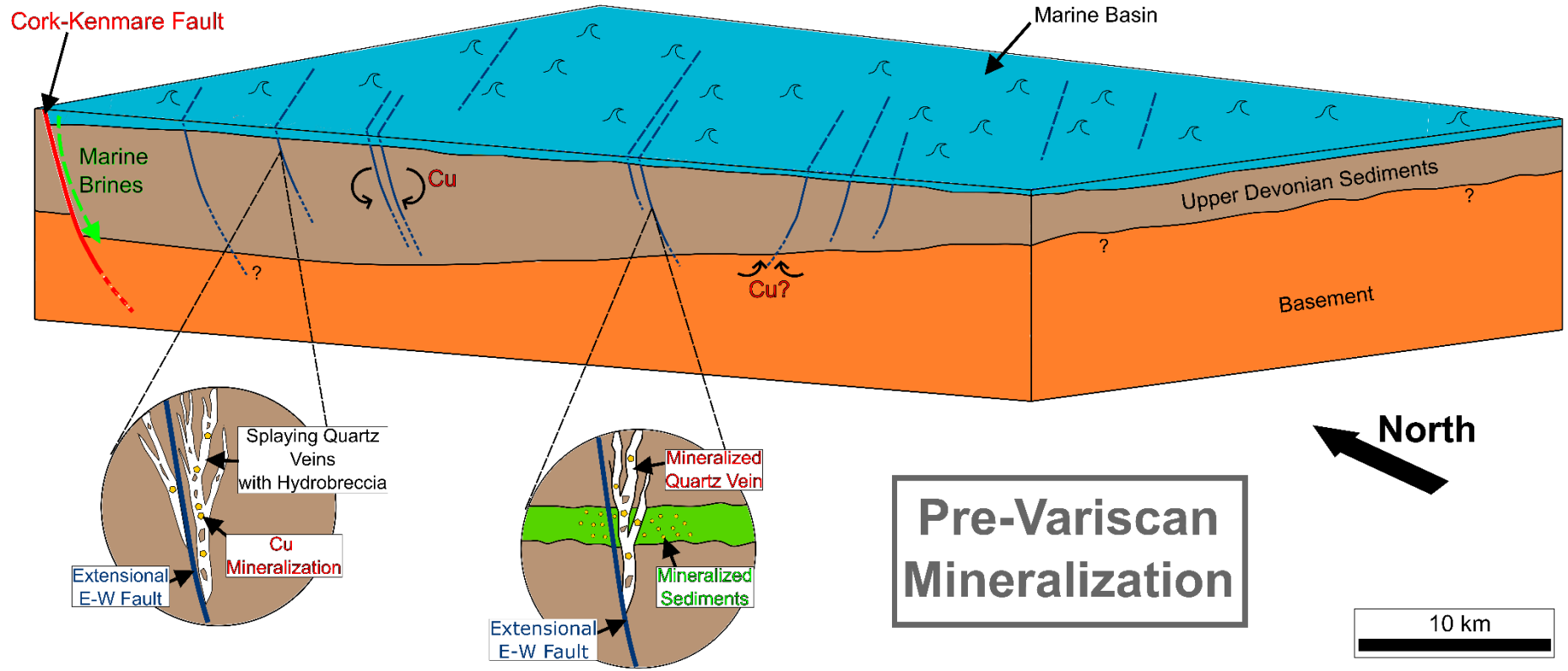
Appendix H – Stable Isotope Geochemistry on quartz-chalcopyrite veins from the Allihies Mining Area, showing $\delta^{34}S_{CDT}$ value, $\delta^{18}O_{SMOW}$ value and δD_{SMOW} value analysis.

Appendix I – LA-ICP-MS trace element analysis on mineralized samples from the historic copper mines in West Cork.

The mineralization model described in Chapter 3 (Fig. 3.12a + 3.12b) for the selected copper deposit at Allihies as an example was confirmed for the entire Munster and South Munster Basins (Chapter 4, Fig. 4.12a + 4.12b, West Cork and Appendix G, e.g. Fig. G.1, Caherdaniel Behaghane). This new model outlines two distinct mineralization events (Fig. 4.12a + 4.12b):

- The pre-Variscan, basinal, early mineralization; sulphide bearing quartz veins are directly related to extensional E-W to ENE-WSW striking normal faults as fluid pathways (feeder zones).
- The syn-Variscan, compressional, late mineralization; quartz veins with sulphides occur along saddle reefs and reactivated pre-Variscan extensional faults.

Fig. 4.12a)


Cork-Kenmare Fault
Marine Basin
Marine
Brines
Cu
Upper Devonian Sediments
?
?
?
Cu?
Basement
Splaying Quartz
Veins
with Hydrobreccia
Cu
Mineralization
Extensional
E-W Fault
Mineralized
Quartz Vein
Mineralized
Sediments
Extensional
E-W Fault
North
Pre-Variscan
Mineralization
10 km

4.12b)

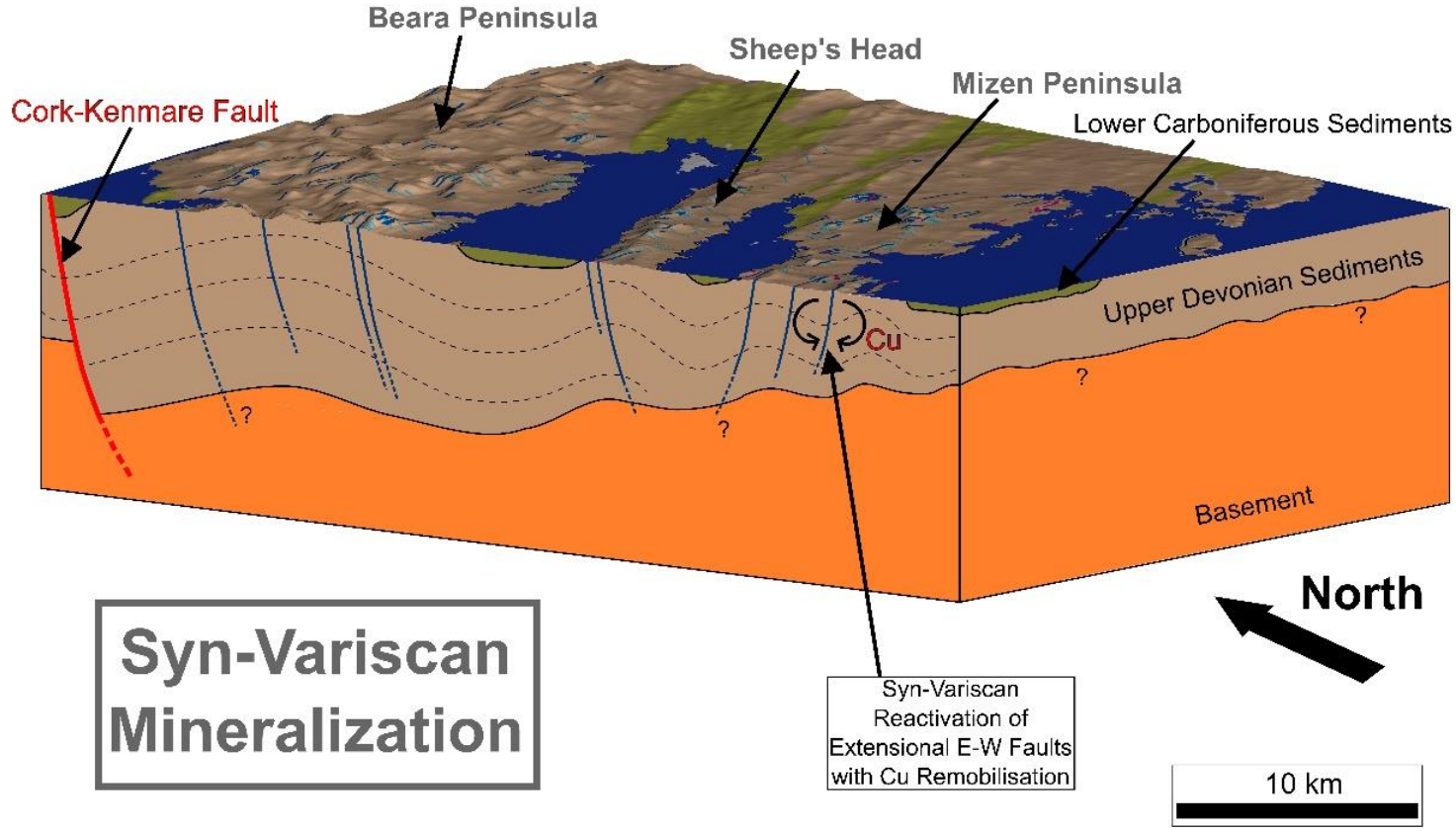


Fig. 4.12) Block model of the South Munster Basin in West Cork (including adaptions after Williams 2000, Landes et al. 2003 and SRTM digital terrain model from Jarvis et al. 2008). a) The basinal E-W faults follow the strike of the major Cork-Kenmare Fault in the North. The E-W faults form the fluid pathways for the mineralized quartz veins which can be associated with sediment hosted copper beds. b) A reactivation of these E-W faults during the Variscan Compression and crustal shortening can remobilise basin related copper mineralization.

5.1 Geomorphology, Supergene Leaching and Historical Exploration – An important key for the new model

A fundamental basis for the understanding of the new genetic model is the geomorphological appearance of the deposits and their outcrops in SW Ireland. As showed in Chapter 3, most of the mineralized quartz veins suffered intensive supergene leaching. It is quite common that the outcropping veins do not have any sign of mineralization. Occasionally, there are only rare remnants of altered chalcopyrite to goethite, and even rarer, due to the lack of carbonates, there are sparse secondary copper minerals (malachite). In general, most of the mineralized quartz veins have a white, “pure” surficial appearance with no mineral component other than chlorite and occasional hematite. Altered minerals or fresh sulphides can be found at a depth of 20 cm or deeper. Reilly (1986) already mentioned this “apparently barren nature of the outer metre or so” at the Mountain Mine Lodes from Allihies. The quite thorough sulphide leaching can be explained by the pre-Variscan nature of the mineralized veins which show intensive syn-Variscan cleavage and fracturing, and therefore provided fluid pathways for the leaching meteoric water.

Logically, the inverse conclusion explains why most of the historic copper findings and former mining sites of West Cork are located directly at or nearby the coastline (Fig. 5.1, GSI Mineral Localities 2016). Coastal erosion provides “fresher” outcrops to the E-W extensional faults and their related mineralized quartz veins. The saline seawater, plus minor carbonate from the host rock or the seawater itself formed crusts of secondary copper mineralization. These “malachite stained” cliff faces could be easily spotted from the sea (Blenkinsop 1902; Reilly 1986). Figure 5.1 shows that most of the historical copper findings are related to the mapped E-W to ENE-WSW extensional faults.

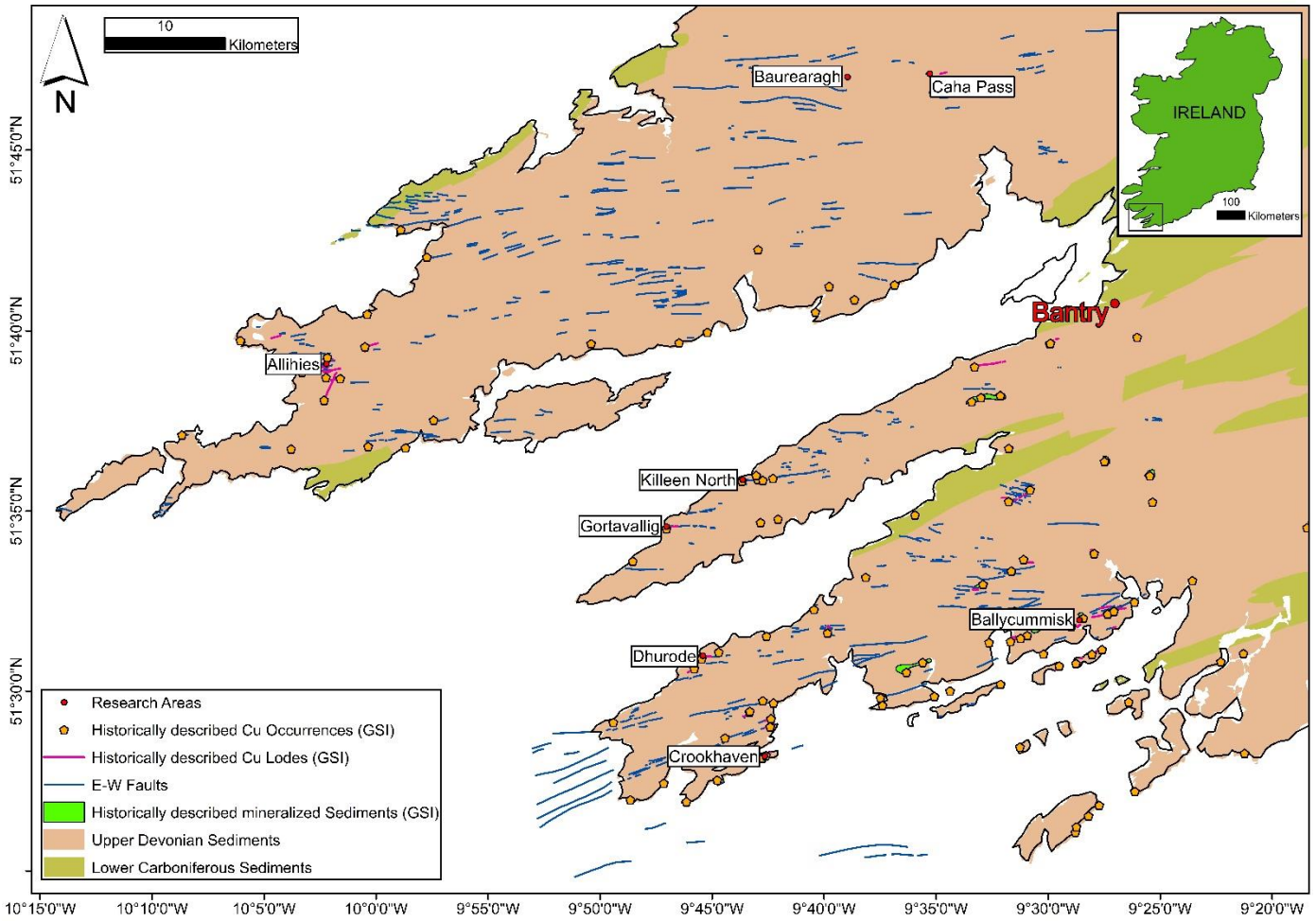


Fig. 5.1) Map of West Cork showing the major research areas with the E-W extensional faults (see Chapter 4) and the historically documented Cu lodes and smaller Cu findings (modified from GSI 2016; GSI Mineral Localities 2016; GSI Jetstream 2019).

5.2 Structural Evolution and Re-Os Geochronology

An interesting observation is that the copper mineralization in the north of the research area (Allihies, Gortavallig) is mainly hosted within the pre-Variscan, extensional quartz veins. The syn-Variscan compressional quartz veins are generally barren. However, the deposits along the southern coastline of Mizen Peninsula (Crookhaven, Ballycummisk) show both pre-Variscan and syn-Variscan mineralization.

An explanation for this fact can be the strike of the mineralization related extensional faults. They rotate from straight E-W in the northern research areas (Beara Peninsula, Sheep's Head, northern Mizen Peninsula) to an ENE-WSW strike in the south (southern Mizen Peninsula, Figs. 4.3 + 5.1). Splaying extensional faults at Goleen (Appendix G, Fig. G.5a), as well as splaying horsetail quartz veinlets from Crookhaven (both southern Mizen Peninsula, Chapter 4, Fig. 4.8b) indicate a rotation of the syn-basinal extension direction σ_3 from N-S to NNW-SSE. The ENE-WSW strike of the extensional faults coincides with the compressional strike of the syn-Variscan structures (folds, faults, cleavage). Hence, a reactivation of the southern extensional faults and reutilization of initial fluid pathways was rather likely and more developed than further north, which caused syn-Variscan mineralization or remobilisation (Chapter 4).

Based on the Re-Os geochronology of this study there were identified at least two different vein mineralization ages within a wide span of over 50 Ma during the Munster Basin history. The Allihies vein formation occurred relatively early (367.3 ± 5.5 to 366.4 ± 1.9 Ma, Chapter 3) and was emplaced during basin development and sedimentation between the Upper Devonian and Lower Carboniferous (MacCarthy 2007). The syn-Variscan Ballycummisk mineralization was dated at 315.5 ± 1.6 Ma to 311.8 ± 1.6 Ma (Chapter 4). Reverse movement (Variscan Orogeny) started at the end of the Carboniferous (Sanderson 1984; Ford 1987; Meere 1995b; Quinn *et al.* 2005). According to Quinn *et al.* (2005) the initial effect of the Variscan compression commenced well before 314.4 Ma with folding and cleavage formation. The

Ballycummisk mineralization was emplaced in a very short geological time frame after that (315.5 ± 1.6 Ma to 311.8 ± 1.6 Ma, Chapter 4). It is unclear what happened in between the two major mineralization events. Geochemical (and reliable) dating of Cu deposits located geographically (Fig. 5.1) between the older Allihies and younger Ballycummisk deposits would be required. The major target areas would be the Gortavallig Mines on Sheep's Head (Fig. 5.1) and the Dhurode Mines at the northern coast of Mizen Peninsula.

Several attempts were made to measure Re-Os dates from Allihies (chalcopyrite) (with David van Acken, University College Dublin); Gortavallig (chalcopyrite), Dhurode (chalcopyrite, arsenopyrite) and Crookhaven (chalcopyrite) (with Dave Selby, Durham University, UK). Unfortunately, the initially measured Re abundance within all samples was too low and heterogenous so that it was not possible to produce a meaningful data set. Nevertheless, various concentrations of Mo traces measured within selected chalcopyrite samples by LA-ICP-MS (Appendix I, Allihies, Gortavallig, Killeen North, Ballycummisk) indicate the presence of molybdenite micro inclusions (D. van Acken, pers. comm. 2018/2019, and e.g. George *et al.* 2018, Cook *et al.* 2016). According to Fletcher 1969 molybdenite has been recognized at Dhurode and Crookhaven. A small sample of syngenetic molybdenite would be sufficient to produce reliable Re-Os dates. Despite an intensive search no molybdenite material was found at Gortavallig, Dhurode or Crookhaven for this study.

5.3 Intrusion related Mineralization?

Several authors postulated a buried magmatic intrusion as the source for the sulphide mineralization (Coe 1959, Charlesworth 1963, Murphy 1960, Fletcher 1969). Murphy (1960) described a negative gravity anomaly south of Killarney (north of Allihies, Fig. 5.1). Meere 1995c inferred an igneous intrusive in the basement below the east Iveragh area (north of Allihies, Fig. 5.1) causing an obstacle effect during the Variscan compression. Higher fluid inclusion homogenisation temperatures of up to 314 °C at Allihies (Chapter 3) and up to

335 °C at Gortavallig Mine (Chapter 4) are generated by high geothermal gradients during basin formation (Meere 1995b, Williams 2000) and extensive rifting processes with crustal thinning and upwelling of the Moho (Williams 2000). Therefore, an intrusion as possible heat source is not necessary. This corresponds with measurements from Spinks *et al.* (2016), which show consistent negative $\delta^{34}S_{CDT}$ values (-16.9 to -10.4 ‰) for chalcopyrite from Allihies. Wen *et al.* (1996) presented wide-ranging and mostly negative $\delta^{34}S_{CDT}$ values (-21.0 to +5.1 ‰) for vein- and stratiform-disseminated deposits from West Cork (supporting measurements from Allihies, see Appendix H). Both Wen *et al.* (1996) and Spinks *et al.* (2016) assume that the negative $\delta^{34}S$ values were caused by a bacteriogenic reduction of sulphur within the sediments. This is evident for a sedimentary, non-magmatic fluid source.

5.4 The Copper Mineralization in SW Ireland – A Sediment-Hosted Stratiform Copper Ore System?

One of the key points of this study is to determine whether the copper mineralization in the Munster Basins can be classified as typical sediment-hosted stratiform copper (SSC) deposit. As in the example of the well-known Permian Kupferschiefer deposits in Germany and Poland and the Zambian Central African Copperbelt (Fig. 2.1) SSC deposits show a typical sedimentary basin architecture (e.g. Kirkam 1989, Hitzman *et al.* 2005, Brown 2014 and references herein): Oxidized, hematite-bearing, continental siliciclastic sedimentary rocks (red beds) form an unconformable fill on the basement. This red bed sequence is typically overlain by nonreddish siltstones, sandstones, carbonates and/or shales, which are known as reduced graybeds (e.g. Brown 2014). In the Munster Basin oxidized siliciclastics developed by alluvial depositions are assigned to the Upper Old Red Sandstone magnafacies, which formed a basinal infill of over 6 km (Fig. 2.3b, Fig. 5.2, Williams *et al.* 1989, Meere & Banks 1997, Williams 2000). Sandstones of the Toe Head Formation mark a transition zone between the underlying oxidized non marine

Old Red Sandstones and the overlain nonreddish marine Old Head Sandstone Formation (Pracht & Sleeman 2002). Besides the siliciclastics within the South Munster Basin shelf limestones occur on a more stable platform to the north (Fig. 2.2; MacCarthy 2007).

Fig. 2.3b)

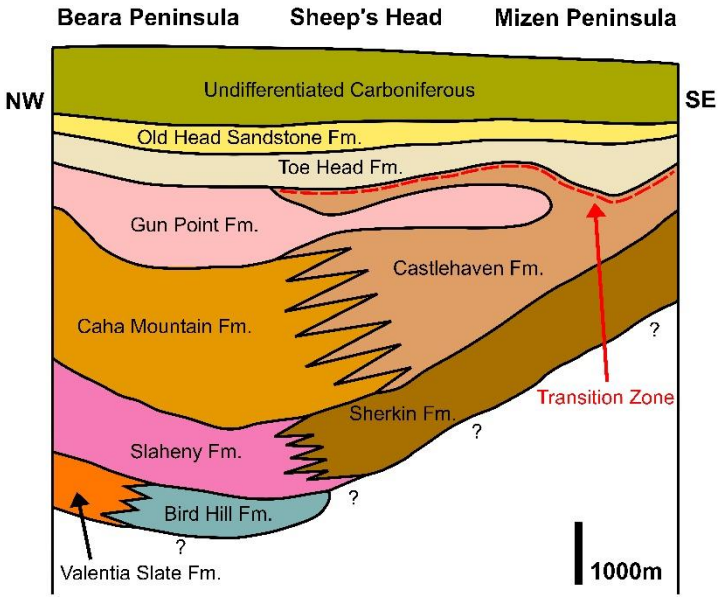


Fig. 5.2)

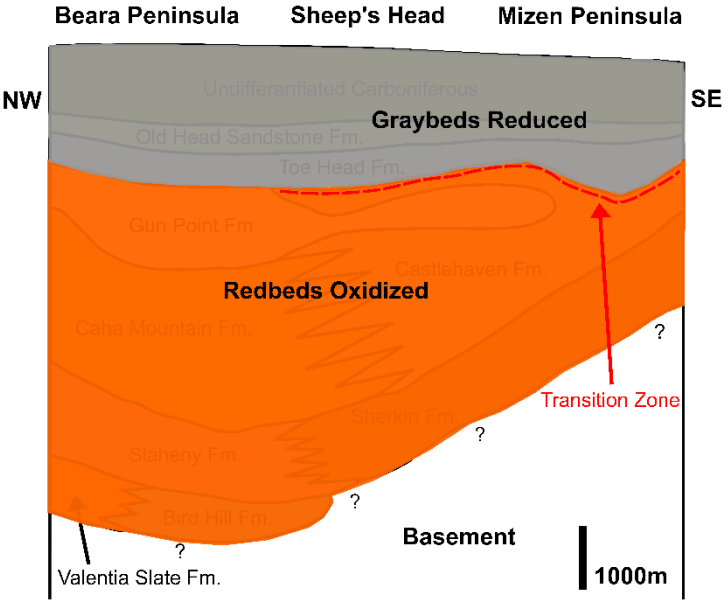


Fig. 2.3b) Simplified profile of the Munster Basin sedimentary formations including the copper hosting transition zone at the top of the Castlehaven Formation (modified from Snodin 1972; MacCarthy 1990; Wen et al. 1996; MacCarthy et al. 2002; Pracht & Sleeman 2002; GSI 2016 and Spinks et al. 2016). Fig. 5.2) Modification of Fig. 2.3b (and references herein) showing a

simplified model of the Munster Basin as an SSC deposit with oxidized red beds and reduced graybeds (Hitzman et al. 2005, Brown 2014).

A general characterization of SSC deposits are the relatively thin sulphide bearing zones which are peneconcordant with the lithological layering (Hitzman *et al.* 2005). In the Munster Basin Snodin (1972) and Wen *et al.* (1996) described sediment hosted mineralization in stratigraphically bound, reduced green sandstone zones (green beds) within the upper Castlehaven Formation just below the nonreddish Toe Head Formation transition zone (see Fig. 2.3b). The green to grey sandstone lithologies form beds with < 3 m thickness and have Cu grades of up to 6.4 wt% (Snodin 1972). These deposits were historically mined on Sheep's Head and Mizen Peninsula (Fig. 2.2c, e.g. Wen *et al.* 1996 and GSI Jetstream 2019).

The lithological genesis of the sediment hosted copper mineralization in the Munster Basins shows evidence for a typical SSC deposit. Nevertheless, this study, as well as previous authors (e.g. Snodin 1972, Wen *et al.* 1996) show that a large amount of the copper ore is not hosted within stratiform sedimentary beds. Most of the historical mines followed mineralized copper lodes which were formed by up to tens of meter wide and several hundreds of meters long quartz vein systems (e.g. Reilly 1986). The examined localities from this study only show very minor disseminated sediment hosted Cu occurrences at Gortavallig Mine (within slate, Fig. 4.6g) and Crookhaven Mine (within siltstone, Fig. 4.8g). Most of the copper ore is hosted within quartz veins directly related to or part of basin controlling extensional E-W to ENE-WSW normal faults with a nearly vertical dip. These fault systems crosscut the stratigraphic layers of the Munster Basin sediments (Fig. 4.12). Vein hosted copper mineralization is also described in the Kupferschiefer deposit (Fig. 2.1) with late-stage, structurally controlled, but economically unimportant "Rücken-Type" veins which are associated with basin wide Alpine tectonism (Vaughan *et al.* 1989, Wodzicki and Piestrzynski 1994, Kucha 2003). At Coates Lake, Northwest Territories, Canada bedding-parallel veins were described to host a minor component of the Cu mineralization (Milton *et al.* 2017).

The copper mineralization in the Zambian Copper Belt (Fig. 2.1) is related to a syn-sedimentary, sub-basins generating master fault system, which was reactivated during inversion deformation (Lefebvre 1989 Selley *et al.* 2005). According to McGowan *et al.* (2003) mineralizing fluids migrated along earlier extensional structures, as well as later compressional structures and were therefore able to reach high in the sedimentary sequence. Re-Os geochronology from the Zambian Copper Belt established a protracted multi-stage mineralization period (Barra *et al.* 2004). This coincides with the extensional, pre-Variscan and compressional, syn-Variscan mineralization phases from of the Munster Basin.

The large (> 0.5 m width) mineralized copper lodes/vein systems of SW Ireland show iron hydroxide alteration (goethite) zones which are rarely wider than one metre around the mineralized veins, while with the smaller veins (< 10 cm width) these are often absent (Chapter 3 and 4). This indicates consolidated host rock sediments with an absent porosity during mineralization and vein formation. The diagenesis and sealing of the basin sediments must have already been in an advanced state. Observations from the Paradox Basin, Utah (Thorson 2004) and the Zambian Copperbelt (Selley *et al.* 2005) show that the mineralization can range to very late, or even post-diagenetic time frame of the sedimentary rocks. According to Hitzman *et al.* (2005) the fluid permeability for late or post-diagenetic mineralization must be provided by dissolution or tectonism. In the Munster Basin this tectonic permeability is provided by the dominant presence of the basin controlling extensional faults, as well as their reactivation during Variscan compression. Stockwork veining at Baurearagh (Chapter 4) as well as hydrobrecciation indicates an elevated hydrostatic pressure (Bons 2001) which provided an increased fluid flow. Observations on fluid contents and permeabilities within modern basins (Hanor 1987, Garven and Raffensberger 1997) support this mineralization model.

A critical observation in the basin history of SW Ireland is the relatively early vein precipitation of the Allihies Cu lodes with 367.3 ± 5.5 to 366.4 ± 1.9 Ma (Chapter 3, Fig. 5.3). During this time at the end of the Devonian the east-west

trending Cork-Kenmare Fault Zone (CKFZ) has triggered the marine transgression (MacCarthy 2007). It is not clear which amount of the reducing marine siliciclastics and limestones (in the north, MacCarthy 2007) were already accumulated during contemporaneous vein precipitation (Fig. 4.12a). The vein Cu mineralization in SW Ireland is mainly hosted within the oxidized red bed sequence. Brown (2014) described this SSC sub-type as Redbed-Type Copper deposits. These deposit types are hosted by redbed sequences without any regional or basin-scale reducing graybeds. Generally, these deposits are economically less important owing to their limited dimension of the mineralized zones (Brown 2014). The most important localities are Dzhezkazgan in Kazakhstan (22 Mt Cu), Corocoro in Boliva (0.5 Mt Cu) and Lisbon Valley in Utah (0.6 Mt Cu) (Fig. 2.1, Brown 2014, Hitzman *et al.* 2005) The Redbed-Type Copper deposits show a mineral paragenesis which includes copper sulphides, minor galena and sphalerite (Brown 2014). Further metals can be silver, uranium, vanadium, molybdenum, mercury and selenium (Brown 2014). This is in accordance with the mineral paragenesis found in SW Ireland (e.g. galena from Gortavallig, Fig. 4.6e, and molybdenite from Allihies and Ballycummisk, Fig. 3.9 and Fig. 4.9), as well as the increased traces of selenium from Allihies (Spinks *et al.* 2016, Appendix I). The petro-stratigraphic formation of the Munster Basin represents clear indicators for an SSC type deposit. A major difference to the typical SSC deposits is that the majority of the copper mineralization in the study area is not stratiform sedimentary hosted. The copper is hosted within quartz veins which are crosscutting the layers of the red bed sediments.

5.4.1 Metal Sources and Fluid Flow

In SSC deposits metals were generally transported by low- to moderate temperature (50 – 400 °C) aqueous fluids with moderate to high salinities of variable compositions and the metal source was mainly the red-bed sequence (Rose 1976, Haynes 1986a, Susura *et al.* 1986, Kirkham 1989, Brown 2001, Hitzman *et al.* 2005). The measured fluid inclusions from this study (Fig. 3.11 and Fig. 4.11) show similar ranges of moderate saline – moderate

homogenisation temperatures to highly saline – low homogenisation temperatures. The Old Red Sandstone sediments of the Munster Basins are suitable as a possible metal source. The basinal sediment infill of over 6 km depth (Meere and Banks 1997) provides enough detrital material to function as copper source. According to Brown (2014) diagenetic pore waters can leach copper from labile minerals (e.g. pyroxenes, amphiboles, biotite, feldspars, magnetite) which are present in immature basin sediments. Large amounts of K-feldspar within the Munster Basin red bed sediments were identified by Meere *et al.* (2019).

Quite surprisingly for the Munster Basins is the absence of any evaporitic layers. In SSC deposits, these evaporites are likely the source of sulphur and high-salinity brines, which are capable of leaching metals from the redbeds (Hitzman *et al.* 2005). A strong sea water Br/Cl signature from quartz vein fluid inclusions from Allihies measured by Meere & Banks (1997) indicates an early marine brine which perculated into the underlying sediments during South Munster Basin formation. This marine influx could have been caused by an early marine transgression during the Upper Devonian (MacCarthy 2007), which coincides with the Upper Devonian mineralization Re-Os dates from Allihies (Chapter 3, Fig. 4.12a). The large lateral extent of the pre-Variscan extensional faults onshore, as well as offshore (Chapter 4) suggest a deep-reaching fault system (Naylor & Jones 1967). The basin controlling structures, such as the Coomnacronia-Killarney-Mallow Fault Zone and the Cork-Kenmare Fault Zone (with a possible depth of 13-14 km, Landes *et al.* 2003) can reach into the basement rocks. These faults are most likely to provide a downward directed fluid flow with marine brines which can leach copper from the red bed basin sediments, as well as the underlying basement rocks (Fig. 4.12a).

Negative $\delta^{34}S_{CDT}$ values (−16.9 to −10.4 ‰) for mineralized quartz veins from Allihies (chalcopyrite, Spinks *et al.* 2016) and for vein- and stratiform-disseminated deposits from West Cork (- 21.0 to + 5.1 ‰, Wen *et al.* 1996) were interpreted as a mineralization trap from bacterial sulfate reduction. Altogether, the pre-Variscan extensional fault systems function as fluid

pathways across the basement and diagenetically consolidated stratiform sedimentary layers, as well as vein hosted mineralization trap. These faults and fluid pathways were reactivated during the early Variscan compression.

5.4.2 Exploration Guidelines

In recent times, the exploration mining industry raised interest again in the historically mined copper deposits in SW Ireland. Sediment-hosted stratiform copper deposits were the major target of the exploration activity. However, this study provides strong evidence that the majority of the copper mineralization is vein-hosted and not stratiform-hosted. The late to post-diagenetic copper emplacement leads to some specific advice:

A very basic, but essential guideline for copper exploration in the Munster Basin is “finding the early extensional E-W to ENE-WSW fault systems”. These fault systems are interpreted as fluid pathways and traps for the copper mineralization. The highest concentration of Cu should generally occur at or close by these fault systems. In West Cork and on Iveragh Peninsula the early E-W to ENE-WSW fault systems can be easily mapped by using high resolution satellite images. Surficial erosion marks the faults as negative topographic features (trenches) of about 3 to 40 metres width and up to 8.4 kilometres length. Associated and parallel aligned to these fault systems are the mineralized quartz veins from centimetre size to several meter sized copper lodes. Generally, all veins are completely barren at the surface (10 cm to 1 m depth) owing to intensive supergene leaching. The absence of carbonates prevents most of the secondary Cu mineralization. Alteration zones are less developed or nearly absent and can therefore not be used as exploration aid. Smaller incrustations of secondary copper minerals can occur along the coastline. The copper concentrations within the quartz veins are irregularly distributed. These facts require further geophysical measurements (geomagnetics, gravimetry) as well as exploration drilling along the faults. Arrays of smaller quartz veins can point to larger copper lodes in the depth (e.g. Reilly 1986). The large extend of the extensional fault systems indicates

a deep reaching vein formation. Rarely, the copper lodes can show a syn-compressional (mostly sinistral) offset in metre to few tens of metre scale. Most of the prospective vein- and fault systems show a nearly vertical dip which would require deep underground mining. Sediment-hosted stratiform disseminated copper mineralization can occasionally occur in porous, reduced greenbeds (e.g. Wen *et al.* 1996). This mineralization is linked to the E-W to ENE-WSW fault systems (feeder zones). Nevertheless, owing to the late-diagenetic mineralization most of the copper ore is probably hosted within the quartz veins. The actual GSI structural map (GSI 2016, Bedrock 100k) does not show all of the E-W to ENE-WSW faults. In the southern part of Mizen Peninsula the extensional faults coincide with the compressional (syn-Variscan) ENE-WSW faults (reactivation of feeder zones) and are suitable for syn-Variscan vein-hosted mineralization. Selenium anomalies within mineralized quartz veins from Allihies mining area (Spinks *et al.* 2016 and Appendix I) should be reconsidered for potential selenium deposits.

5.5 Copper Mineralization in SW Ireland and their Relation to the Irish Orefield (Irish Midlands Zn-Pb Deposits)

This study reveals four crucial Re-Os mineralization ages, which provide a fundamental contribution to our comprehension of the formation of the Irish Orefield in the widest sense. In comparison to the well-known Zn-Pb deposits of the central Irish Ore Field Allihies represents a relatively early mineralization (367.3 ± 5.5 to 366.4 ± 1.9 Ma, Chapter 3, Fig. 5.3). About 54 km NE of Allihies, just a few kilometres north of the Munster Basin, is the stratabound Cu-Pb-Zn deposit of Muckross (Fig. 5.3, Kinnaird *et al.* 2002). Muckross is hosted within Lower Carboniferous (Tournaisian) limestone and yields a Pb/Pb age of about 360 ± 15 Ma (Fig. 5.3, Kinnaird *et al.* 2002). This Pb/Pb age broadly coincides with the Re-Os age from Allihies of this study. Other well-known deposits of the Irish Midlands show similar or slightly later mineralization ages (Fig. 5.3): Similar to this study Hnatyshin *et al.* (2015) used the Re-Os dating technique on pyrite (this study molybdenite) and presented an age of 346.6 ± 3.0 Ma for

Lisheen, and 334.0 ± 6.1 Ma for Silvermines. A Rb-Sr measurement of sphalerite from Silvermines yields to an earlier age of 360 ± 5.2 Ma (Schneider *et al.* 2007). A K-Ar age (clay concentrates) of 366 ± 11 Ma was presented for Navan by Halliday and Mitchell (1983). Symons *et al.* (2002) used palaeomagnetic studies at Navan and deducted 327 ± 3 Ma as the youngest possible emplacement. U/Pb (340 ± 20 Ma) and Pb/Pb (359 ± 26 Ma) whole-rock measurements from Gortdrum were presented by Duane *et al.* (1986). It has to be mentioned that the Re-Os chronometer (Silvermines, Lisheen, Allihies, Ballycummisk) is remarkably robust against deformation and metamorphism (Stein *et al.* 2001). Other dating methods may show distortion after metamorphic, even greenschist facies overprinting and deformation (Rb/Sr: Hradetzky and Lippolt 1993; K-Ar, Ar-Ar: e.g. Kelley 2002; Pb/Pb: e.g. Babinski *et al.* 1999). These distortion effects could have occurred during the syn-Variscan compression (e.g. Meere 1995b).

Nevertheless, the examples show that the Allihies mineralization broadly fits into the general pre-Variscan, syn-basinal time frame of the major Irish Midlands Zn-Pb deposits. However, the much later formation of the Ballycummisk mineralization (315.5 ± 1.6 Ma to 311.8 ± 1.6 Ma, Chapter 4) represents a syn-Variscan emplacement. Kinnaird *et al.* (2002) recognized two phases of mineralization in southern Ireland: one during Carboniferous basin extension and one during Variscan compression. Pb/Pb ages from Crow Island and Ross Island (next to Muckross, Fig. 5.3) suggest syn-Variscan ages between 290 and 270 Ma (Kinnaird *et al.* 2002). According to Quinn *et al.* (2005) the Variscan compression in SW Ireland terminated before 296 Ma. This sets the Crow Island and Ross Island mineralization into a post-Variscan, relaxation time frame. Chalcopyrite-tennantite mineralization from Ross Island occurs along pressure solution cleavage planes caused by the Variscan deformation (Kinnaird *et al.* 2002). This structural relation can be compared with the hand specimen from Ballycummisk (Chapter 4, Fig. 9f) which shows cleavage-parallel quartz-barite-hematite-chalcopyrite veinlets. In addition to this, several authors described the Late Carboniferous Variscan reactivation of normal faults and the formation of transpressional faults in the Irish Midlands deposits (Chapter 4, Coller 1984, Johnston *et al.* 1996, Hitzman 1999; Kyne

et al. 2017, Torremans *et al.* 2018). Besides the early Variscan mineralized veins from Ballycummisk (Chapter 4, Fig. 4.9f), a reactivated fault was found at Baurearagh (Beara Peninsula, Chapter 4, Fig. 4.4e) and compressional mineralized quartz veins occur at Crookhaven (Mizen Head, Fig. 4.8g).

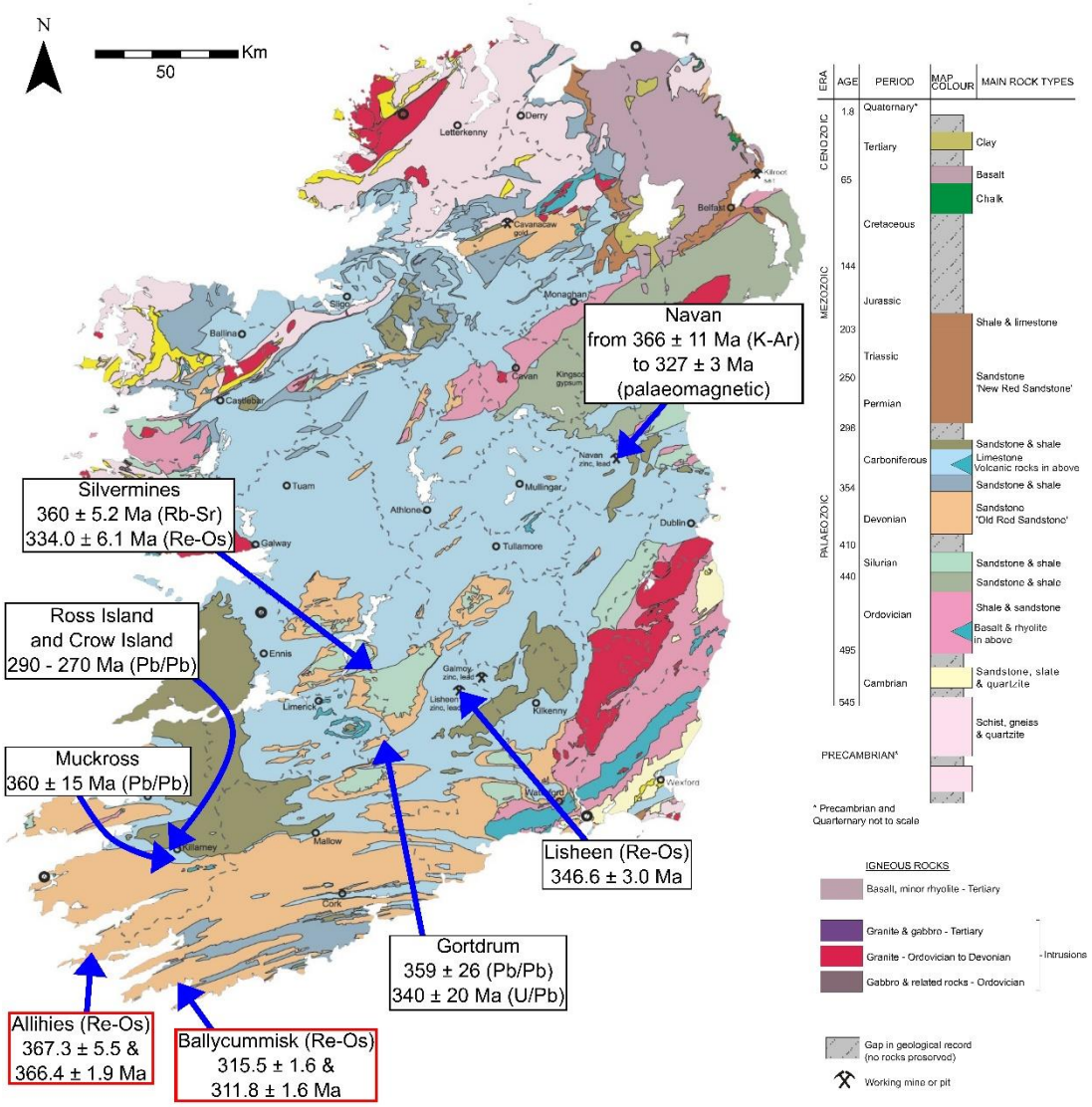


Fig. 5.3) Geological map of Ireland with a selection of the geochronological dated Zn-Pb deposits and the Re-Os dating results of this study for the Cu mineralization in SW Ireland (modified from Geological Survey of Ireland 2004 with data from Kinnaird et al. 2002, Hnatyshin et al. 2015, Schneider et al. 2007, Halliday and Mitchell 1983, Symons et al. 2002 and Duane et al. 1986).

Wilkinson (2003) described the principal geological features of the Irish Zn-Pb-(Ag-Ba) deposits. The following list presents the similarities and differences between the Cu deposits of SW Ireland (this thesis) and the criteria after Wilkinson (2003):

- *"Hosted by non-argillaceous carbonates within mixed carbonate-siliciclastic succession." (Wilkinson 2003)*

+ The Cu deposits of SW Ireland are located within the Munster and South Munster Basins. Therefore, the major host rock lithologies belong to the Old Red Sandstone (red beds) Facies with mainly siliciclastic sediments (Chapter 3, Chapter 4, Fig. 4.2).

- *"Spatial association of orebodies with syn-sedimentary faults (normally within hanging wall)." (Wilkinson 2003)*

+ The primary mineralization in SW Ireland is related to extensional E-W to ENE-WSW striking basinal faults. The Re-Os ages from Allihies (Chapter 3) belong to the Famennian Stage (Cohen *et al.* 2019) of the Upper Devonian, suggesting that mineralization was emplaced during basin development and syn-sedimentation which occurred between the Upper Devonian and Lower Carboniferous (MacCarthy 2007).

- *"Ore formation during diagenesis." (Wilkinson 2003)*

+ Spinks *et al.* (2016) measured negative $\delta^{34}S$ values at Allihies caused by biogenically-induced reduction within the Old Red Sandstone Facies resulting in syngenetic-diagenetic sulphide mineralization. The little to no host rock alteration nearby the mineralized quartz veins indicates an advanced or post-diagenetic ore precipitation.

- *"Orebodies comprise single or multiple lenses with generally stratiform but strictly stratabound morphology." (Wilkinson 2003)*

+ The major sulphide mineralization in SW Ireland is vein hosted within massive quartz lodes. Sediment hosted Cu can occur within reduced green sandstone zones (green beds) of the upper Castlehaven Formation (Chapter 4, Fig. 4.2b, Wen *et al.* 1996 and Snodin 1972). Minor sediment hosted Cu mineralization was found in association with the mineralized quartz veins and the E-W extensional faults within various lithologies (Chapter 4: Gortavallig – slate, Fig. 4.6g; Killeen North – conglomerate, Fig. 4.6h; Crookhaven – siltstone, Fig. 4.8d).

- *"Orebodies dominated by massive sulphide well-developed lateral metal zonation." (Wilkinson 2003)*

+ No general zonation was observed in SW Ireland. Sulphides generally occur distributed within syngenetic quartz vein mineralization (Chapter 3 and Chapter 4). Multiple vein generations are present (Chapter 3 and Chapter 4).

- *"Sulphur source dominantly of bacteriogenic origin ($\delta^{34}S$ = -15 ± 10)." (Wilkinson 2003)*

+ The sulphur isotope values of the vein hosted chalcopyrite from Allihies represent relatively low values. Wen *et al.* (1996) and Spinks *et al.* (2016) assume that the negative $\delta^{34}S$ values were caused by a bacteriogenic sedimentary source. The low values from Allihies (vein hosted chalcopyrite) are confirmed by own measurements (from -15.5 to -12.0 ‰ $\delta^{34}S_{CDT}$, Appendix H).

- *"Barite is a common minor and locally major constituent." (Wilkinson 2003)*

+ In this study barite was found at Crookhaven (Mizen Peninsula, Chapter 4), Ballycummisk (Mizen Peninsula, Chapter 4) and Seven Heads (South Cork, Appendix G). Major barite mineralization was historically mined at Derryginagh (West Cork near Bantry, Reilly 1986) and Mount

Corin on Mizen Peninsula (e.g. Derreennalomane, GSI Mineral Localities 2016).

- *"Orefluid temperatures in the range 100-240 °C." (Wilkinson 2003)*

+ The general homogenisation temperature from Allihies, West Cork and the Irish Midlands Deposits is mainly around 200° C (Chapter 3 and 4). However, Allihies can show higher homogenisation temperatures of up to 314 °C, and vein samples from other West Cork deposits have a maximum T_h of 335 °C.

- *The salinity of the Irish Midlands deposits ranges between 4 and 28 wt% with a major moderate salinity between 8 and 19 wt% (Wilkinson 2010).*

+ Allihies (3.2 to 25.4 wt% $NaCl_{equiv}$) and West Cork deposits (5.2 to 22.4 wt.% $NaCl_{equivalent}$) show similar values of moderate to high salinities (Fig. 3.11 and Fig. 4.11).

Simplified, it can be said that the vein hosted copper mineralization in SW Ireland has many common characteristics with the Irish Midlands Zn-Pb Deposits. The major differences are:

- The host lithologies: the siliciclastic red bed sediments from the Munster Basin are generally non-reactive and the fluids precipitate the mineralization along the faults as concentrated quartz veins. The carbonate lithologies of the Waulsortian Limestones which dominate the Irish Midlands provide a stratiform reactive host for the mineralizing fluids (e.g. Wilkinson 2003).
- Timing of the deposit formation: Just comparing the robust Re-Os chronometer the Allihies Cu deposits are nearly 20 Ma older than mineralization dates from Lisheen Mine (Hnatyshin *et al.* 2015, Fig. 5.3). For Re-Os models from Silvermines there is even a difference of over 30 Ma (Hnatyshin *et al.* 2015, Fig. 5.3).

- The fluid inclusion properties of the SW Ireland mineralization vs. the Irish Midlands Deposits are quite similar, but the fluids of SW Ireland can be up to 55° C hotter.
- The sulphide mineralogy of the Irish Midlands Deposits is mainly dominated by sphalerite, galena, pyrite and minor chalcopyrite (e.g. Wilkinson 2003). In contrast, the sulphides of the SW Ireland deposits are generally chalcopyrite, tetrahedrite/tennantite, and minor bornite.

5.6 Possibly linked Fluid Systems

Even though there is a large time span between the Allihies Cu mineralization, the Irish Midlands Zn-Pb deposits and the Ballycummisk Re-Os dates, there is a strong kinematic linkage in between their structural formation. In relation to SSC deposits previous studies showed a protracted period of multiple mineralization phases (Barra *et al.* 2004). In the Kupferschiefer for example the deposit formation was formed over a broad time range from diagenetic, to epigenetic, to syn-orogenetic Alpine uplift (Kulig *et al.* 1994, Michalik 1997, Bechtel *et al.* 1999, Hitzman *et al.* 2005). SSC deposits from the Central African Copperbelt show evidence of multiple episodes of mineralization up to 300 Ma (McGowan *et al.* 2003, Selley *et al.* 2005, McGowan *et al.* 2006, El Desouky *et al.* 2008, Muchez *et al.* 2008, El Desouky *et al.* 2009, Muchez *et al.* 2010, Sillitoe *et al.* 2010, Muchez *et al.* 2015, Milton *et al.* 2017). Seeing the Munster Basin as an open fluid system with multiple mineralization phases a possible link can be drawn to the fluid systems of the Irish Midlands Deposits.

The higher fluid temperatures of the SW Ireland Copper Deposits could be the reason for the various metal distribution seen in these deposits. According to Large (1992) (and Robb 2005) the Cu solubility within hydrothermal fluids is lower than the solubility of Zn and Pb depending on the fluid temperature (and pH, salinity). This means that the higher temperature fluids of SW Ireland can already precipitate Cu mineralization while Zn and Pb are still in solution and emplace in shallower depths with cooler fluid temperatures. This corresponds with the model from Hitzman (1999) who described a reverse movement with

the inherent uplift of the Munster Basin sediments in SW Ireland which caused the loss of any possible deposits due to erosion. Possible Zn-Pb deposits in SW Ireland would have been emplaced in upper lithologies and are simply eroded. Kinnaird *et al.* (2002) presented a different model whereby the various ore assemblages (between SW Ireland and the Irish Midlands) are related to the variable presence of the red bed sediment facies (Cu source). While there are several kilometres of red bed sediments in the south-west, the Irish Midlands deposits on the contrary, are underlain by Lower Palaeozoic greywackes with little intervening red beds (Kinnaird *et al.* 2002). The results of this study support Kinnaird's model, as the mineralizing fluids show a strong sedimentary isotopes signature (Spinks *et al.* 2016, Appendix H).

A model from Everett *et al.* (2003) (and references herein) describes a general fluid flow from the south through the red bed sediments of the Munster Basin (below the Lower Carboniferous sea) into the north and the Irish Midlands Basin with the basin margin fault zones and normal faults as fluid pathways. Fluid recharge was provided by local, partially evaporated seawater descending into the basement (Everett *et al.* 2003). Everett *et al.* (2003) combined this fluid flow model (from south to north) with the idea of a gravity-driven meteoric water fluid flow induced by the developing Hercynian (Variscan) mountain range in the south (Hitzman and Beaty, 1996). According to the results of this thesis Everett's fluid flow model can be possible with the minor changes that the fluid flow already started in the Upper Devonian (Allihies 367.3 ± 5.5 to 366.4 ± 1.9 Ma, Chapter 3) and mineralization also occurred along intra-basinal, syn-sedimentary, extensional Munster Basin faults. Gravity-driven fluid flow (Hitzman and Beaty, 1996) could be related to the syn-Variscan mineralization of the Late Carboniferous (Ballycummisk 315.5 ± 1.6 Ma to 311.8 ± 1.6 Ma, Chapter 4). In this sense, it is possible to see the Cu mineralization of SW Ireland as being linked to the entire Irish Ore Field system with an initial metal emplacement into the Munster Basin sediments during the Upper Devonian.

5.7 Chapter References

Auclair, G. & Fouquet, Y. 1987. Distribution of Selenium in High-Temperature Hydrothermal Sulfide Deposits at 13 degree North, East Pacific Rise. Canadian Mineralogist. 25, 577-587.

Babinski, M., Van Schmus, W.R., Chemale, F. 1999. Pb–Pb dating and Pb isotope geochemistry of Neoproterozoic carbonate rocks from the São Francisco basin, Brazil: implications for the mobility of Pb isotopes during tectonism and metamorphism. Chemical Geology, 160, 3, 175-199. https://doi.org/10.1016/S0009-2541(99)00067-4

Barra, F., Broughton, D., Ruiz, J., and Hitzman, M. 2004 Multi-stage mineralization in the Zambian Copperbelt based on Re-Os isotope constraints [abs.]: Geological Society of America Abstracts with Program, v. 36, no. 5, p. 516.

Bechtel, A., Elliot, W.C., Wampler, J.M., and Oszczepalski, S. 1999. Clay mineralogy, crystallinity, and K-Ar ages of illites within the Polish Zechstein basin: Implications for the age of Kupferschiefer mineralization. Economic Geology, 94, 261–272.

Blenkinsop, H.G. 1902. Notes on the Berehaven copper mines. Transactions of the Institution of Mining and Metallurgy, 12, 1-7.

Bons, P. 2001. The formation of large quartz veins by rapid ascent of fluids in mobile hydrofractures. Tectonophysics, 336, 1-17. https://doi.org/10.1016/S0040-1951(01)00090-7

Brown, A.C. 2001. Redbeds: Source of metals for sediment-hosted stratiform copper, sandstone copper, sandstone lead, and sandstone uranium-vanadium deposits: Geological Association of Canada Geotext 4, 121–133.

Brown, A.C. 2014. Low-Temperature Sediment-Hosted Copper Deposits. Editors: Heinrich, D., Holland, Karl, Turekian, K., Treatise on Geochemistry (Second Edition), Elsevier, 251-271. https://doi.org/10.1016/B978-0-08-095975-7.01110-4

Charlesworth, J.K. 1963. Historical Geology of Ireland. Oliver and Boyd, 565 p.

Coe, K. 1959. Intrusion breccia of Dunmore, Co. Donegal. Geol. Mag., 96, 172-173.

Cohen, K.M., Harper, D.A.T. and Gibbard, P.L. 2019. ICS International Chronostratigraphic Chart 2019/05. International Commission on Stratigraphy, IUGS. www.stratigraphy.org [last accessed 12 August 2019].

Coller, D.W. 1984. Variscan structures in the Upper Palaeozoic rocks of west central Ireland. Geological Society, London, Special Publications, 14, 185–194. https://doi.org/10.1144/GSL.SP.1984.014.01.18

Cook, N., Ciobanu, C.L., George, L., Zhu, Z.-Y., Wade, B., Ehrig, K. 2016. Trace Element Analysis of Minerals in Magmatic-Hydrothermal Ores by Laser Ablation Inductively-Coupled Plasma Mass Spectrometry: Approaches and Opportunities. Minerals, 6, 111, https://doi.org/10.3390/min6040111

Duane, M.J., Welke, H.J., Allsopp, H.L. 1986. U–Pb age for some base metal sulphide deposits in Ireland: genetic implications for Mississippi Valley-type mineralization. Geology 14, 477–480.

El Desouky, H.A., Muchez, P., and Cailteux, J. 2009. Two Cu–Co sulfide phases and contrasting fluid systems in the Katanga Copperbelt, Democratic Republic of Congo. Ore Geology Reviews, 36, 315–332.

El Desouky, H.A., Muchez, P., Dewaele, S., Boutwood, A., and Tyler, R. 2008. Postorogenic origin of the stratiform Cu mineralization at Lufukwe, Lufilian foreland, Democratic Republic of Congo: Economic Geology, 103, 555–582.

Everett, C.E., Rye, D.M. and Ellam, R.M. 2003. Source or Sink? An assessment of Role of the Old Red Sandstone in the Genesis of the Irish Zn-Pb Deposits. Economic Geology, 98(1), 31-50. https://doi.org/10.2113/gsecongeo.98.1.31

Fay, D., Kramers, G., Zhang, C., McGrath, D., Grennan, E. 2007. Soil Geochemical Atlas of Ireland. Teagasc and Environmental Protection Agency, Dublin.

Fletcher, C.I. 1969. The sulphide mineralization in the Allihies region, County Cork, Eire. Ph.D. Dissertation, University of Leicester, 128–129.

Ford, M. 1987. Practical application of the sequential balancing technique: an example from the Irish Variscides. Journal of the Geological Society, London, 144, 885–891, https://doi.org/10.1144/gsjgs.144.6.0885

Garven, G., and Raffensperger, J.P. 1997. Hydrogeology and geochemistry of ore genesis in sedimentary basins, in Barnes, H.L., ed., Geochemistry of hydrothermal ore deposits: New York, Wiley, 125–189.

Geological Survey of Ireland, GSI 2016. Bedrock 100k (scale 1:100,000), Bedrock Geology, Coordinate System: Irish Transverse Mercator / ITM. https://www.gsi.ie/en-ie/data-and-maps/Pages/Bedrock.aspx# [last accessed 20/04/2020]

Geological Survey of Ireland, GSI 2016. Mineral Localities (scale 1:100,000), Coordinate System: Irish National Grid / ING. https://www.gsi.ie/en-ie/data-and-maps/Pages/Minerals.aspx#MinLocs [last accessed 17/01/2021]

Geological Survey of Ireland, GSI Jetstream 2019. Historical Maps of Copper Deposits in SW Ireland. https://jetstream.gsi.ie [last accessed 08/03/2019]

George, L.L., Cook, N., Crowe, B., & Ciobanu, C. 2018. Trace elements in hydrothermal chalcopyrite. Mineralogical Magazine, 82(1), 59-88, https://doi.org/10.1180/minmag.2017.081.021

Gleeson, S.A. and Yardley, B.W.D. 2002. Extensional Veins and Pb–Zn Mineralisation in Basement Rocks: The Role of Penetration of Formation Brines. In: Stober, I. and Bucher, K. (eds) Water–Rock Interaction. Water Science and Technology Library, Vol. 40. Springer, Dordrecht, 189–205.

Halliday, A.N. and Mitchell, J.G. 1983. K–Ar ages of clay concentrates from Irish orebodies and their bearing on the timing of mineralisation. Earth and Environmental Science Transactions of the Royal Society of Edinburgh, 74, 1–14, https://doi.org/10.1017/S0263593300009858

Hanor, J.S. 1987. Origin and migration of subsurface sedimentary brines: Society of Economic Paleontologists and Mineralogists Short Course 21, p. 247.

Haynes, D.W. 1986a. Stratiform copper deposits hosted by low-energy sediments. I. Timing of sulfide precipitation—an hypothesis. Economic Geology, 81, 250–265.

Hitzman, M.W. 1999. Extensional faults that localize Irish syndiagenetic Zn–Pb deposits and their reactivation during Variscan compression. Geological Society, London, Special Publications, 155, 233–245, https://doi.org/10.1144/GSL.SP.1999.155.01.17

Hitzman, M.W., and Beaty, D.W. 1996. The Irish Zn-Pb-(Ba) orefield, in Sangster, D.F., ed., Carbonate-hosted lead-zinc deposits: Society of Economic Geologists, Special Publication 4, 112-143.

Hitzman, M.W., Kirkham, R., Broughton, D., Thorson, J., and Selley, D. 2005. The sediment hosted stratiform copper ore system. In: Hedenquist, J.W., Thompson, J.F.H., Goldfarb, R.J., and Richards, J.P. (eds.). Economic Geology 100th Anniversary Volume 1905–2005, 609–642. Littleton, CO: Society of Economic Geologists, Inc.

Hnatyshin, D., Creaser, R.A., Wilkinson, J.J. and Gleeson, S.A. 2015. Re–Os dating of pyrite confirms an early diagenetic onset and extended duration of mineralization in the Irish Zn–Pb ore field. Geology, 43, 143–146, https://doi.org/10.1130/G36296.1

Hradetzky, H. and Lippolt, H.J. 1993. Generation and distortion of Rb/Sr whole-rock isochrons - effects of metamorphism and alteration. European Journal of Mineralogy, 5, 1175-1194. DOI: 10.1127/ejm/5/6/1175

Jarvis, A., Reuter, H.I., Nelson, A. and Guevara, E. 2008. Hole-filled SRTM for the globe Version 4. International Centre for Tropical Agriculture (CIAT), http://srtm.csi.cgiar.org [last accessed 25 July 2017].

Johnston, J.D., Coller, D., Millar, G., and Critchley, M.F. 1996. Basement structural controls on Carboniferous-hosted base metal mineral deposits in Ireland: Geological Society, London, Special Publication, 107, 1-21.

Kelley, S. 2002. K-Ar and Ar-Ar dating. Reviews in Mineralogy and Geochemistry, 47, 785-818.

Kinnaird, J.A., Ixer, R.A., Barreiro, B. and Nex, P.A. 2002. Contrasting sources for lead in Cu-polymetallic and Zn–Pb mineralisation in Ireland: constraints from lead isotopes. Mineralium Deposita, 37, 495–511, https://doi.org/10.1007/s00126-001-0252-5

Kirkham, R.V. 1989. Distribution, setting and genesis of sediment-hosted stratiform copper deposits. In: Boyle, R.W., Brown, A.C., Jefferson, C.W., Jowett, E.C., and Kirkham, R.V. (eds.), Sediment-Hosted Stratiform Copper Deposits, Geological Association of Canada Special Paper 36, 3–38. Ottawa: Geological Association of Canada.

Kucha, H. 2003. Geology, mineralogy and geochemistry of the Kupferschiefer, Poland. In: Kelly, J.G., Andrew, C.J., Ashton, J.H., Boland, M.B., Earls, G., Fusciardi, L., and Stanley, G., eds., Europe's major base metal deposits: Dublin, Irish Association for Economic Geology, 215–238.

Kulig, E., Pye, A., and Michalik, M. 1994. Authigenic clay minerals in upper part of Rotliegendes sandstones in North-Sudetic depression: Polskie Towarzystwo Mineralogiczne-Prace Specjalna, 5, 124–125 (in Polish).

Kyne, R., Torremans, K., Güven, J., Doyle, R., Walsh, J. 2017. 3-D Modeling of the Lisheen and Silvermines Deposits, County Tipperary, Ireland: Insights into Structural Controls on the Formation of Irish Zn-Pb Deposits. Economic Geology, 114 (1), 93-116, https://doi.org/10.5382/econgeo.2019.4621

Landes, M., O'Reilly, B.M., Readman, P.W., Shannon, P.M. and Prodehl, C. 2003. VARNET-96: three-dimensional upper crustal velocity structure of SW Ireland. Geophysical Journal International, 153, 424–442, https://doi.org/10.1046/j.1365-246X.2003.01911.x

Large, R.R., 1992. Australian volcanic-hosted massive sulfide deposits: features, styles and genetic models. Economic Geology, 87, 471-510.

Lefebvre, J.J. 1989. Les gisements stratiformes en roche sedimentaire d'Europe centrale (Kupferschiefer) et de la ceinture cuprifere du Zaire et de Zambie: Annales de la Société Géologique de Belgique, 112, 121–135.

MacCarthy, I.A.J. 1990. Alluvial sedimentation patterns in the Munster Basin, Ireland. Sedimentology, 37, 685–712, https://doi.org/10.1111/j.1365-3091.1990.tb00629.x

MacCarthy, I.A.J. 2007. The South Munster Basin of southwest Ireland. Journal of Maps, 3, 149–172, https://doi.org/10.1080/jom.2007.9710835

MacCarthy, I.A.J., Pracht, M. and Sleeman, A.G. 2002. Geology of West Cork, Scale 1:100000, Sheet 24. Geological Survey of Ireland, Dublin.

McGowan, R.R., Roberts, S., and Boyce, A.J. 2006. Origin of the Nchanga copper-cobalt deposits of the Zambian Copperbelt. Mineralium Deposita, 40, 617–638.

McGowan, R.R., Roberts, S., Foster, R.P., Boyce, A.J., and Coller, D. 2003. Origin of the copper-cobalt deposits of the Zambian Copperbelt: An epigenetic view from Nchanga: Geology, 31, 497–500.

Meere, P.A. 1995b. Sub-greenschist facies metamorphism from the Variscides of SW Ireland an early syn-extensional peak thermal event. Journal of the Geological Society, London, 152, 511–521, https://doi.org/10.1144/gsjgs.152.3.0511

Meere, P.A. 1995c. The structural evolution of the western Irish Variscides: an example of obstacle tectonics? Tectonophysics, 246, 97–112, https://doi.org/10.1016/0040-1951(94)00267-D

Meere, P.A. and Banks, D.A. 1997. Upper crustal fluid migration: an example from the Variscides of SW Ireland. Journal of the Geological Society, London, 154, 975–985, https://doi.org/10.1144/gsjgs.154.6.0975

Meere, P.A., Higgs, K., O'Sullivan, M., Lim, A., Hennessy, R., Unitt, R.P., and Johnson, S.C. 2019. The Geology of Skellig Michael – finally revealed. Irish Geology Research meeting, University College Dublin.

Michalik, M. 1997. Chlorine containing illites, copper chlorides and other chlorine bearing minerals in the Fore-Sudetic copper deposits (Poland). In: Papunen, H., ed., Mineral deposits, research and exploration—where do they meet?: Rotterdam, Balkema, 543–546.

Milton, J.E., Hickey, K.A., Gleeson, S.A., Falck, H., Allaz, J. 2017. In Situ Monazite Dating of Sediment-Hosted Stratiform Copper Mineralization in the Redstone Copper Belt, Northwest Territories, Canada: Cupriferous Fluid Flow Late in the Evolution of a Neoproterozoic Sedimentary Basin. Economic Geology, 112 (7), 1773–1806.
https://doi.org/10.5382/econgeo.2017.4529

Muchez, P., Andre-Mayer, A.S., El Desouky, H.A., and Reisberg, L. 2015. Diagenetic origin of the stratiform Cu-Co deposit at Kamoto in the Central African Copperbelt. Mineralium Deposita, 50, 437–447.

Muchez, P., Brems, D., Clara, E., De Cleyn, A., Lammens, L., Boyce, A., De Muynck, D., Mukumba, W., and Sikazwe, O. 2010. Evolution of Cu-Co mineralizing fluids at Nkana mine, Central African Copperbelt, Zambia. Journal of African Earth Sciences, 58, 457–474.

Muchez, P., Vanderhaeghen, P., El Desouky, H., Schneider, J., Boyce, A., Dewaele, S., and Cailteux, J. 2008. Anhydrite pseudomorphs and the origin of stratiform Cu-Co ores in the Katangan Copperbelt (Democratic Republic of Congo). Mineralium Deposita, 43, 575–589.

Murphy, T. 1960. Gravity Anomaly Maps of Ireland, Sheet 5 - south-west. Communications of the Dublin Institute for Advanced Studies, Geophysical Bulletin no. 18.

Naylor, D. and Jones, P.C. 1967. Sedimentation and tectonic setting of the Old Red Sandstone of southwest Ireland. In: Oswald, D. (ed.) International Symposium on the Devonian System (Calgary). Society of Petroleum Geology 2, Calgary, Alberta, 1089–1099.

Pracht, M. and Sleeman, A.G. 2002. A geological description of West Cork and adjacent parts of Kerry to accompany the Bedrock Geology, 1:100,000 Scale Map Series, Sheet 24, West Cork. With accompanying contributions by Wright, G. (Groundwater) and Cox, W. (Minerals). Geological Survey of Ireland, Dublin.

Quinn, D., Meere, P.A. and Wartho, J.A. 2005. A chronology of foreland deformation: Ultra-violet laser 40Ar/39Ar dating of syn/late-orogenic intrusions from the Variscides of southwest Ireland. Journal of Structural Geology, 27, 1413–1425, https://doi.org/10.1016/j.jsg.2005.02.003

Reilly, T.A. 1986. A review of vein mineralization in SW County Cork, Ireland. In: Andrew, C.J., Crowe, R.W.A., Finlay, S., Pennell, W.M. and Pyne, J.F. (eds) Geology and Genesis of Mineral Deposits in Ireland. Irish Association for Economic Geology, Dublin, 513–544.

Robb, L. 2005. Introduction to ore forming processes. Blackwell ScienceLtd. Blackwell Publishing.

Sanderson, D.J. 1984. Structural variation across the northern margin of the Variscides in NW Europe. Geological Society, London, Special Publications, 14, 149–165, https://doi.org/10.1144/GSL.SP.1984.014.01.15

Rose, A.W. 1976. The effect of cuprous chloride complexes in the origin of red bed copper and related deposits: Economic Geology, 71, 1036–1048.

Schneider, J., Quadt, A.V., Wilkinson, J.J., Boyce, A.J. and Andrew, C.J. 2007. Age of Silvermines Irish-type Zn-Pb deposit from direct Rb-Sr dating of sphalerite. In Digging deeper: Proceedings of the Ninth Biennial SGA meeting: Dublin, Ireland, Irish Association for Economic Geology, 373-376.

Selley, D., Broughton, D., Scott, R., Hitzman, M., Bull, S., Large, R., McGoldrick, P., Croaker, M., Pollington, N., and Barra, F. 2005. A new look at the geology of the Zambian Copperbelt Economic Geology 100Th Anniversary Volume, 965–1000.

Sillitoe, R.H., Perello, J., and Garcia, A. 2010. Sulfide-bearing veinlets throughout the stratiform mineralization of the Central African Copperbelt: Temporal and genetic implications. Economic Geology, 105, 1361–1368.

Snodin, S.R. 1972. Copper and other mineralisation in the Upper Palaeozoic strata of south-west Cork, Ireland, and related areas. Unpublished Ph.D. Thesis. University of Leicester.

Spinks, S.C., Parnell, J., Bellis, D. and Still, J. 2016. Remobilization and mineralization of selenium–tellurium in metamorphosed red beds: Evidence from the Munster Basin, Ireland. Ore Geology Reviews, 72, 114–127, https://doi.org/10.1016/j.oregeorev.2015.07.007

Stein, H.J., Markey, R.J., Morgan, J.W., Hannah, J.L. and Scherstén, A. 2001. The remarkable Re-Os chronometer in molybdenite: How and why it works. Terra Nova, 13, 479-486. https://doi.org/10.1046/j.1365-3121.2001.00395.x

Susura, B.B., Glybovsky, V.O., and Kislitsin, A.V. 1986. Red-colored terrigenous sediments specific copper-forming systems, in Friedrich, G.G. *et al.*, eds. Geology and metallogeny of copper deposits: Berlin, Springer-Verlag, 504–512.

Symons, D.T.A., Smethurst, M.T. and Ashton, J.H. 2002. Paleomagnetism of the Navan Zn-Pb deposit, Ireland. Economic Geology, 97, 997-1012.

Thorson, J.P. 2004. Paradox basin sandstone-hosted copper deposits generated by two episodes of basinal fluid expulsion [abs.]: Geological Society of America Abstracts with Program, v. 36, no. 5, p. 517.

Torremans, K., Kyne, R., Doyle, R., Güven, J.F., Walsh, J.J. 2018. Controls on Metal Distributions at the Lisheen and Silvermines Deposits: Insights into Fluid Flow Pathways in Irish-Type Zn-Pb Deposits. Economic Geology 113 (7), 1455-1477. https://doi.org/10.5382/econgeo.2018.4598
Van Acken, D. 2018/2019. Personal communication. University College Dublin.

Vaughan, D.J., Sweeney, M., Diedel, F.R., and Haranczyk, C. 1989. The Kupferschiefer: An overview with an appraisal of the different types of mineralization. Economic Geology 84, 1003–1027.

Wen, N., Boyce, A.J., Fallick, A.E., Ashworth, J.R. and Ixer, R.A. 1996. The genesis of Cu-bearing quartz veins by metamorphic remobilization from stratiform red bed deposits, SW County Cork, Ireland. Mineralogy and Petrology, 57, 73–89, https://doi.org/10.1007/BF01161622

Wilkinson, J.J. 2003. On diagenesis, dolomitisation and mineralisation in the Irish Zn-Pb orefield. Miner Deposita 38, 968–983. https://doi.org/10.1007/s00126-003-0387-7

Wilkinson, J.J. 2010. A Review of Fluid Inclusion Constraints on Mineralization in the Irish Ore Field and Implications for the Genesis of Sediment-Hosted Zn-Pb Deposits. Economic Geology, 105 (2), 417–442. https://doi.org/10.2113/gsecongeo.105.2.417

Williams, E.A. 2000. Flexural cantilever models of extensional subsidence in the Munster Basin (SW Ireland) and Old Red Sandstone fluvial dispersal systems. Geological Society, London, Special Publications, 180, 239–268. https://doi.org/10.1144/GSL.SP.2000.180.01.12

Williams, E.A., Bamford, M.L.F., Cooper, M.A., Edwards, H.E., Ford, M., Grant, G.G., MacCarthy, I.A.J., McAfee, A.M., and O'Sullivan, M.J., 1989. Tectonic controls and sedimentary response in the Devonian-Carboniferous Munster and South Munster basins, south-west Ireland. In: R.S. Arthurson, P. Gutteridge and S.C. Nolan (Editors), Role of Tectonics in Devonian and Carboniferous Sedimentation in the British Isles. Spec. Publ. Yorkshire Geol. Soc., 6, 123-141.

Wodzicki, A. and Piestrzynski, A. 1994. An ore genetic model for the Lubin-Sieroszowice mining district, Poland. Mineralium Deposita 29, 30–43.

Chapter 6: Summary of Conclusions

The copper mineralization of the Munster and South Munster Basins in SW Ireland is generally hosted by two distinct quartz veining generations - Pre-Variscan and Syn-Variscan:

- Meter- to tens of meters-scale quartz veins are related to early-extensional E-W to ENE-WSW striking, basin controlling normal faults. These quartz veins are hosted within the Upper Devonian sediments. The most dominant veining type is massive quartz with a thickness of 20 cm to 2 m. Zones of smaller (< 2 cm) parallel aligned quartz veins (Allihies, Beara Peninsula), hydraulic brecciation (Caherdaniel, Iveragh Peninsula; Bauréaragh and Goleen, Mizen Peninsula), as well as stockwork veining (Bauréaragh, Beara Peninsula) can occur. All of these early vein types show Variscan deformation (folding, faulting, stylolitisation, cleavage) to a variable degree. The quartz veins bear the primary copper mineralization as mainly chalcopyrite, tetrahedrite/tennantite, minor bornite and chalcocite. Further syngenetic sulphides are arsenopyrite and molybdenite. Gangue minerals (besides quartz) are siderite, chlorite, barite and minor calcite. This early mineralization was formed syn-basinal during the Upper Devonian sequence. Vein hosted molybdenite samples from Allihies (Beara Peninsula) show a Re-Os age of 367.3 ± 5.5 to 366.4 ± 1.9 Ma. Fluid inclusion measurements show multiple mineralization pulses with homogenisation temperatures T_h range from 90 to 335 °C. Salinities vary between 3.2 and 25.4 wt% $NaCl_{equiv}$.

  Less developed to absent host rock alteration nearby the mineralized quartz veins is caused by an advanced diagenetic stage of the basin sediments during vein formation. Minor localized sediment-hosted mineralization related to the extensional basin structures can occur within localized porous host sedimentary rocks. The majority of the copper mineralisation is hosted within the quartz veins.

- Syn-Variscan veins occur as saddle reefs and en echelon tension gash shear structures. In general, these vein types are unmineralized, but in the South on Mizen Peninsula a reverse reactivation of the early extensional fractures is possible and Cu mineralization was emplaced during early compressional phase. Sub-horizontal veins crosscut early extensional structures. Saddle reef mineralization is present at Crookhaven and large copper lodes occur at Ballycummisk. Cu mineralization is chalcopyrite, tetrahedrite/tennantite, bornite and minor chalcocite. Barite, siderite, chlorite molybdenite and hematite belong to the typical paragenesis.

  Re-Os molybdenite from Ballycummisk reveals a mineralization during the early compressional phase between 315.5 ± 1.6 Ma and 311.8 ± 1.6 Ma.

  Syn-Variscan fluids from quartz veins show multiple hydrothermal pulses with T_h ranging from 101 to 270 °C and salinities between 4.8 and 16.7 wt% $NaCl_{equiv}$.

  A remobilisation from pre-Variscan veins into syn-Variscan veins can occur in re-activated extensional fault systems within a proximal distance.

The higher temperatures might be related to an increased geothermal gradient, caused by crustal thinning. An intrusive body as a heat source is not necessary. Negative stable isotopes values from Allihies with $\delta^{34}S_{CDT}$ (-15.5 to -12.0 ‰, chalcopyrite, Appendix H) indicate a sedimentary to metamorphic fluid source. The Munster Basin sediments are the possible source for the primary copper mineralization. An early marine transgression during the Upper Devonian combined with large basin controlling structures provided a fluid flow with marine brines which leached copper from the red bed basin sediments, as well as the underlying basement rocks.

The petro-stratigraphic basin architecture of the Munster Basin shows indicators for a sediment-hosted stratiform copper ore system (SSC). These similarities can be related to an SSC sub-type deposit – A Redbed-Type

copper deposit. The major difference of the SW Ireland copper mineralization to the typical SSC deposits is that most of the copper mineralization in the study area is not stratiform sedimentary hosted. Large quartz veins are the host for the copper sulphides. These veins vertically crosscut the layers of the red bed sediments.

Comparisons of the principal geological features of the Irish Zn-Pb-(Ag-Ba) deposits with the copper mineralization in SW Ireland reveal similarities in the structural kinematic evolution and fluid characteristics. These deposit types show a broadly temporally linked mineralization emplacement. The major differences are the host rock lithologies with siliciclastic (chemically non-reactive) red bed sediments in SW Ireland and carbonate-rich (chemically reactive) Waulsortian limestones in the Irish Midlands. Due to extensive rifting and crustal thinning the vein hosted mineralization in SW Ireland can show up to 55 °C hotter fluids compared to the Irish Midlands deposits. Summarizing the results, genetic models and interpretations of this thesis, the Cu mineralization of SW Ireland can be seen as a connected part of the entire Irish Ore Field system.

Appendix A: Field Data (Chapter 1)

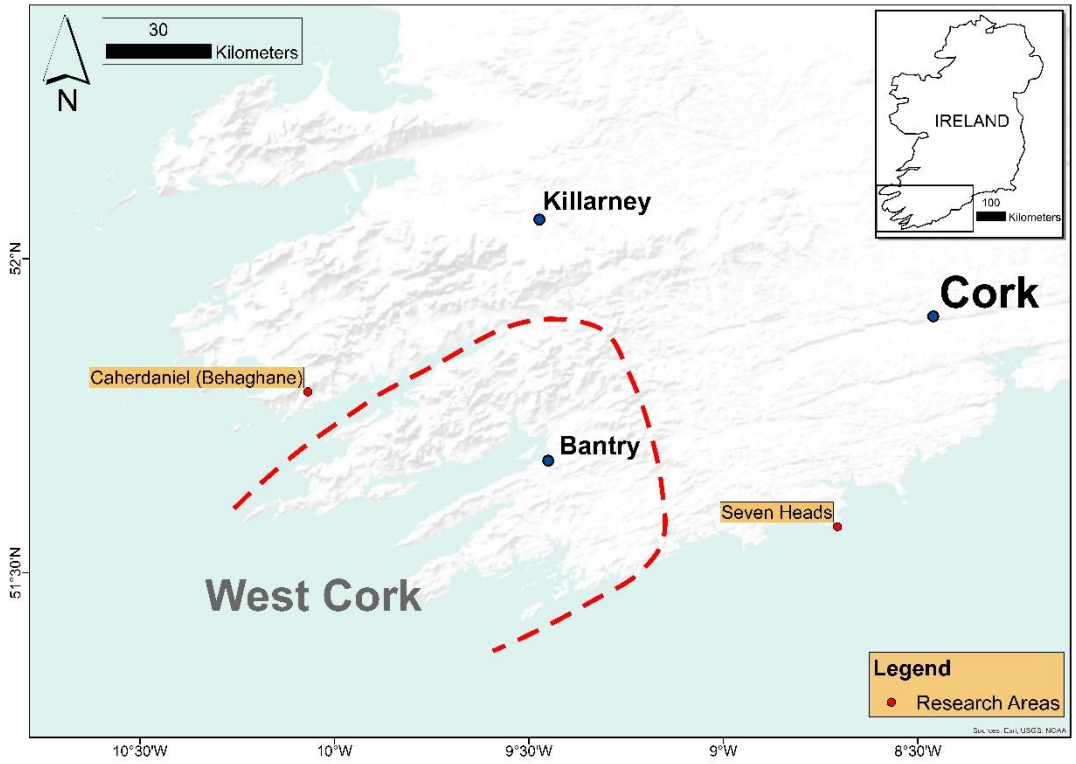
The detailed field notes from all examined locations (Figs. 1.1a and 1.1b, Chapter 1) are attached to this thesis as an Excel file with multiple sheets:

Appendix_A_Field_Data_Thesis_JLang.xlsx

These sheets include all of the collected structural measurements.

The produced high-resolution field maps from these locations are available as individual PDF files in the separate folder **Appendix J.**

Fig. 1.1a)



1.1b)

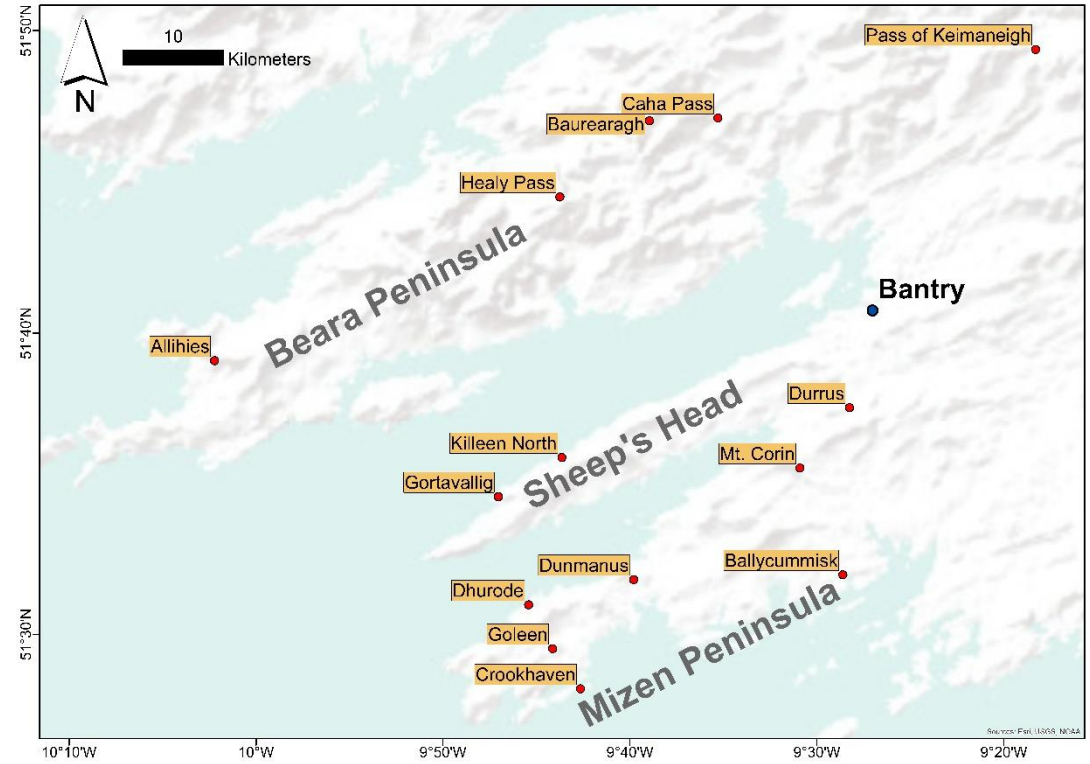


Fig. 1.1a+b, Chapter 1) Overview of the research areas and the examined copper mines in SW Ireland.

Appendix B.1-3 + C + D (Chapter 3)

These Appendices belong to the published paper (Chapter 3) *The Vein Hosted Copper Deposits of the Allihies Mining Area, Southwest Ireland – A New Structural and Chronological Evaluation.* Published in the Journal of the Geological Society (2020),177(4):671.

Publication DOI: https://doi.org/10.1144/jgs2019-154

A previous version of Appendix A and Appendix B, inclusive a video file with the 3D model of the major lodes and the underground workings at Mountain Mine are available as published supplementary data under the following link (last accessed: 08/01/2021):

https://doi.org/10.6084/m9.figshare.c.4875015.v1

Update:

The following version of Appendix B includes revisions and extensions regarding the fluid inclusion assemblages (FIA).

Appendix C shows selected sample locations of the Allihies Copper Mining District.

Appendix D includes supporting petrographical images from representative samples of the Allihies Mining District.

(last update: 12/12/2021)

Appendix B.1 (Chapter 3)

Fluid inclusions measurements of the Allihies Copper Mining District. Locations are as shown in Fig. 3.2 and 3.7:

Fluid Inclusion Measurements of the Allihies Copper Mining District (Supplementary material, Lang *et al.*, University College Cork, Ireland)
Date:
12/12/2021

pressure estimate 6.7km with 2.7g/cm3 (after Meere and Banks, 1997)

about 1800 bar

Standardised with CO_2 Standard (Camperio): T_m = -56.6°C and doubly distilled H_2O Standard (Leoben): T_m = 0.0°C and T_h = 374.0°C

Sample	Chip	FI Number	T_{ice} (°C)	$T_{first\ melt}$ (°C)	T_m (°C)	T_h (°C)	T_m (standardised) (°C)	T_h (standardised) (°C)	$T_{first\ melt}$ (standardised) (°C)	Fluid Inclusion Assemblages (FIA)	diameter in µm	phases	estimated volume of vapour phase in vol. %	primary or secondary inclusion	wt% $NaCl_{equivalent}$ (calculated with Steele-MacInnis *et al.*, 2012)	$T_{trapped}$ (6.7 km depth/1800 bar); calculated with Steele-MacInnis (2012), after Meere and Banks (1997)	comment	location
220B	4	4.1	-61		-23.4	167	-22.2	166		220B.1	4	L+V	5	primary	23.86	249	mineralized	Mountain Mine Spoil
220B	4	4.2	-63		-23.6	169	-22.4	168		220B.1	5	L+V	5	primary	23.98	251	mineralized	Mountain Mine Spoil
220B	4	4.3	-65	-23.3	-21.5	165	-20.4	164	-22.1	220B.1	5	L+V	5	primary	22.62	246	mineralized	Mountain Mine Spoil
220B	4	4.4	-65	-22.5	-21.3	167	-20.2	166	-21.4	220B.1	2	L+V	5	primary	22.49	249	mineralized	Mountain Mine Spoil
220B	4	4.7			-24.5	159	-23.3	158		220B.1	3	L+V	5	primary	24.55	239	mineralized	Mountain Mine Spoil
220B	4	4.8	-73	-25.4	-23.3	161	-22.1	160	-24.2	220B.1	4	L+V	5	primary	23.79	241	mineralized	Mountain Mine Spoil
220B	4	4.9		-24.4	-22.2	164	-21.1	163	-23.2	220B.1	3	L+V	10	primary	23.09	245	mineralized	Mountain Mine Spoil
220B	6	6.1		-26.3	-24.6	166	-23.4	165	-25.1	220B.1	5	L+V	5	primary	24.61	247	mineralized	Mountain Mine Spoil
220B	1	1.5	-66	-23.7	-20.5	163	-19.4	162	-22.5	220B.1	13	L+V	5	primary	21.95	244	mineralized	Mountain Mine Spoil
220B	1	1.6	-76	-25.9	-22.6	163	-21.5	162	-24.7	220B.1	10	L+V	3	primary	23.35	244	mineralized	Mountain Mine Spoil

220B	1	1.7	-68	-26.4	-20.2	160	-19.1	159	-25.2	220B.1	7	L+V	5	primary	21.74	240	mineralized	Mountain Mine Spoil
220B	1	1.8	-72		-21.3	161	-20.2	160		220B.1	11	L+V	5	primary	22.49	241	mineralized	Mountain Mine Spoil
220B	1	1.9	-59	-23.4	-20.2	169	-19.1	168	-22.2	220B.1	6	L+V	5	primary	21.74	251	mineralized	Mountain Mine Spoil
220B	1	1.10	-58	-26.2	-10.6	226	-9.6	224	-25.0	220B.2	8	L+V	5	primary	13.49	334	mineralized	Mountain Mine Spoil
220B	1	1.11	-60		-12.6	236	-11.6	234		220B.2	10	L+V	5	primary	15.53	344	mineralized	Mountain Mine Spoil
220B	1	1.12	-54		-22.7	155	-21.6	154		220B.1	11	L+V	6	primary	23.41	234	mineralized	Mountain Mine Spoil
220B	1	1.13	-64		-19.7	168	-18.6	167		220B.1	9	L+V	5	primary	21.39	250	mineralized	Mountain Mine Spoil
220B	1	1.14	-61	-25.2	-23.2	164	-22.0	163	-24.0	220B.1	13	L+V	5	primary	23.73	244	mineralized	Mountain Mine Spoil
220B	1	1.15	-61		-13.7	166	-12.7	165		220B.3	12	L+V	2	primary	16.57	250	mineralized	Mountain Mine Spoil
220B	1	1.16			-23.2	155	-22.0	154		220B.1	7	L+V	5	primary	23.73	234	mineralized	Mountain Mine Spoil
220B	1	1.17	-66		-18.1	126	-17.0	126		220B.1	12	L+V	5	primary	20.23	199	mineralized	Mountain Mine Spoil
220B	1	1.18	-70	-24.1	-19.6	161	-18.5	160	-22.9	220B.1	12	L+V	5	primary	21.32	241	mineralized	Mountain Mine Spoil
220B	1	1.19	-68	-24.4	-19.8	160	-18.7	159	-23.2	220B.1	7	L+V	2	primary	21.46	240	mineralized	Mountain Mine Spoil
220B	1	1.20	-76	-24.4	-20.4	157	-19.3	156	-23.2	220B.1	4	L+V	5	primary	21.88	236	mineralized	Mountain Mine Spoil
220B	1	1.21	-67	-24.5	-21.3	158	-20.2	157	-23.3	220B.1	8	L+V	5	primary	22.49	237	mineralized	Mountain Mine Spoil
220B	1	1.22	-61		-21.4	161	-20.3	161		220B.1	10	L+V	5	primary	22.56	242	mineralized	Mountain Mine Spoil
220B	1	1.23	-79	-25.5	-24.9	155	-23.7	154	-24.3	220B.1	3	L+V	5	primary	24.79	234	mineralized	Mountain Mine Spoil
220B	1	1.24	-73		-21.0	157	-19.9	156		220B.1	8	L+V	2	primary	22.29	236	mineralized	Mountain Mine Spoil
220B	1	1.25	-68		-19.6	160	-18.5	159		220B.1	7	L+V	2	primary	21.32	240	mineralized	Mountain Mine Spoil
60A	1	1.1	-57	-27.9	-23.0	140	-22.5	139	-27.4	60A.1	10	L+V	2	primary	24.05	215	mineralized	Mountain Mine Underground
60A	1	1.2	-61		-22.9	155	-22.4	154		60A.1	5	L+V	1	primary	23.98	233	mineralized	Mountain Mine Underground
60A	1	1.3	-58		-22.0	160	-21.6	159		60A.1	6	L+V	1	primary	23.41	240	mineralized	Mountain Mine

																		Underground
60A	2	2.2	-44	-25.7	-21.6	247	-21.2	245	-25.2	60A.2	18	L+V	10	primary	23.15	350	mineralized	Mountain Mine Underground
60A	4	4.1	-55		-23.3	157	-22.8	156		60A.1	5	L+V	2	primary	24.24	236	mineralized	Mountain Mine Underground
60A	4	4.2	-54	-20.5	-10.8	222	-10.5	220	-20.1	60A.3	7	L+V	1	pseudo secondary	14.41	327	mineralized	Mountain Mine Underground
60A	5	5.2	-57	-36.0	-19.9	154	-19.5	153	-35.4	60A.1	12	L+V	0.5	primary	22.01	232	mineralized	Mountain Mine Underground
60A	5	5.3	-63	-37.0	-19.6	143	-19.2	142	-36.4	60A.1	8	L+V	1	primary	21.81	219	mineralized	Mountain Mine Underground
60A	5	5.4			-19.3	122	-18.9	121		60A.4	5	L+V	2	primary	21.60	193	mineralized	Mountain Mine Underground
60A	5	5.5	-58	-26.0	-13.1	146	-12.7	145	-25.5	60A.1	7	L+V	1	primary	16.65	225	mineralized	Mountain Mine Underground
60A	5	5.6	-62	-38.0	-16.4	164	-16.0	163	-37.4	60A.1	7	L+V	1	primary	19.45	246	mineralized	Mountain Mine Underground
60A	5	5.7			-14.2	157	-13.8	156		60A.1	4	L+V	2	primary	17.63	238	mineralized	Mountain Mine Underground
60A	5	5.8	-57	-34.0	-18.5	156	-18.1	155	-33.4	60A.1	12	L+V	1	primary	21.03	235	mineralized	Mountain Mine Underground
60A	5	5.9	-62	-32.0	-18.1	151	-17.7	150	-31.5	60A.1	11	L+V	1	primary	20.74	229	mineralized	Mountain Mine Underground
60A	5	5.10	-50	-28.0	-7.1	198	-6.8	197	-27.5	60A.5	10	L+V	5	primary later assemblage	10.22	300	mineralized	Mountain Mine Underground

367B	1	1.1	-44	-16.2	-11.1	309	-10.6	306	-15.7	367B.1	11	L+V	10	primary	14.58	450	mineralized	Gunpowder Mine
367B	2	2.1	-41		-7.0	254	-6.6	252		367B.2	14	L+V	5	primary	9.92	379	mineralized	Gunpowder Mine
367B	2	2.2	-34	-16.6	-6.8	252	-6.4	250	-16.1	367B.2	13	L+V	5	primary	9.67	376	mineralized	Gunpowder Mine
367B	3	3.1	-44	-16.4	-8.3	317	-7.8	314	-15.9	367B.1	6	L+V	5	primary	11.51	470	mineralized	Gunpowder Mine
367B	4	4.1	-51	-23.8	-21.8	163	-21.2	162	-23.2	367B.3	4	L+V	5	primary	23.19	243	mineralized	Gunpowder Mine
367B	4	4.2	-50		-11.5	293	-11.0	291		367B.1	5	L+V	10	primary	14.99	426	mineralized	Gunpowder Mine
367B	5	5.1	-56		-17.2	162	-16.7	161		367B.3	10	L+V	4	primary	19.96	243	mineralized	Gunpowder Mine
367B	8	8.1	-58	-25.0	-19.4	146	-18.8	144	-24.4	367B.4	8	L+V	0.5	primary (early)	21.57	222	mineralized	Gunpowder Mine
367B	8	8.2	-55	-25.2	-17.7	128	-17.2	127	-24.6	367B.4	12	L+V	1	primary (early)	20.35	200	mineralized	Gunpowder Mine
367B	8	8.4	-68	-26.8	-20.2	265	-19.6	262	-26.1	367B.5	13	L+V	2	primary (late) necking !	22.12	374	mineralized	Gunpowder Mine
367B	9	9.1	-41	-21.4	-10.5	304	-10.1	300	-20.8	367B.1	9	L+V	12	primary	14.00	442	mineralized	Gunpowder Mine
213A	1	1.1	-58	-24.8	-19.6	163	-19.0	162	-24.2	213A.1	5	L+V	1	primary	21.71	244	mineralized	Great Mountain Mine Spoil
213A	1	1.2	-57	-25.5	-17.7	178	-17.2	177	-24.9	213A.1	10	L+V	2	primary	20.34	263	mineralized	Great Mountain Mine Spoil
213A	1	1.3	-56	-25.4	-17.0	169	-16.5	168	-24.8	213A.1	11	L+V	2	primary	19.81	252	mineralized	Great Mountain Mine Spoil
213A	1	1.4	-64	-25.3	-19.4	171	-18.8	170	-24.7	213A.1	10	L+V	2	primary	21.57	254	mineralized	Great Mountain Mine Spoil
213A	1	1.5	-61	-27.5	-16.9	166	-16.4	165	-26.9	213A.1	9	L+V	1	primary	19.73	248	mineralized	Great Mountain Mine Spoil
213A	1	1.6	-42	-27.2	-18.3	230	-17.8	228	-26.6	213A.2	8	L+V	5	primary	20.78	330	mineralized	Great Mountain Mine Spoil
213A	2	2.2	-67		-21.6	137	-21.0	136		213A.3	8	L+V	2	primary	23.06	211	mineralized	Great Mountain Mine Spoil
213A	2	2.3	-64	-28.1	-21.8	173	-21.2	172	-27.5	213A.1	11	L+V	2	primary	23.19	256	mineralized	Great Mountain Mine Spoil

213A	2	2.4	-70		-22.4	174	-21.8	173		213A.1	10	L+V	2	primary	23.58	257	mineralized	Great Mountain Mine Spoil
213A	2	2.5	-70	-25.1	-22.5	145	-21.9	144	-24.5	213A.3	10	L+V	1	primary	23.64	221	mineralized	Great Mountain Mine Spoil
365B	1	1.2	-61	-30.0	-22.0	152	-21.6	151	-29.5	365B.1	8	L+V	1	primary assemblage 1	23.41	230	mineralized	Dooneen Mine Spoil
365B	1	1.3	-62	-33.0	-23.9	159	-23.4	158	-32.5	365B.1	7	L+V	1	primary assemblage 1	24.61	238	mineralized	Dooneen Mine Spoil
365B	1	1.4	-50		-25.2	225	-24.7	223		365B.4	3	L+V	3	primary assemblage 1	25.41	321	mineralized	Dooneen Mine Spoil
365B	2	2.1	-41	-29.7	-21.6	201	-21.2	199	-29.2	365B.2	6	L+V	2	primary assemblage 2	23.15	291	mineralized	Dooneen Mine Spoil
365B	2	2.2	-51	-28.8	-20.5	198	-20.1	197	-28.3	365B.2	6	L+V	3	primary assemblage 2	22.42	287	mineralized	Dooneen Mine Spoil
365B	2	2.4	-61		-21.7	195	-21.3	194		365B.2	6	L+V	2	primary assemblage 2	23.22	283	mineralized	Dooneen Mine Spoil
365B	2	2.5	-52		-23.2	200	-22.7	198		365B.2	5	L+V	3	primary assemblage 2	24.17	289	mineralized	Dooneen Mine Spoil
365B	2	2.6	-62		-11.0	195	-10.7	194		365B.2	12	L+V	2	primary assemblage 2	14.62	290	mineralized	Dooneen Mine Spoil
365B	2	2.7	-53		-16.3	179	-15.9	178		365B.5	16	L+V	1	primary assemblage 2	19.37	265	mineralized	Dooneen Mine Spoil
365B	2	2.8	-60	-25.3	-19.6	200	-19.2	198	-24.8	365B.2	13	L+V	2	primary assemblage 2	21.81	290	mineralized	Dooneen Mine Spoil
365B	2	2.9	-54		-20.1	198	-19.7	197		365B.2	7	L+V	2	primary assemblage 2	22.15	287	mineralized	Dooneen Mine Spoil
365B	2	2.10	-64	-30.0	-8.1	194	-7.8	193	-29.5	365B.2	5	L+V	1	primary assemblage 2	11.43	293	mineralized	Dooneen Mine Spoil
365B	2	2.11	-75		-21.5	168	-21.1	167		365B.1	5	L+V	1	primary assemblage 1	23.09	249	mineralized	Dooneen Mine Spoil
365B	2	2.12	-75		-20.7	155	-20.3	154		365B.1	4	L+V	2	primary assemblage 1	22.56	233	mineralized	Dooneen Mine Spoil

365B	3	3.1	-59		-16.7	131	-16.3	130		365B.3	4	L+V	1	primary assemblage 1	19.68	204	mineralized	Dooneen Mine Spoil
365B	3	3.2	-54		-18.3	141	-17.9	140		365B.3	4	L+V	2	primary assemblage 1	20.89	216	mineralized	Dooneen Mine Spoil
365B	3	3.3	-55		-19.4	170	-19.0	169		365B.1	12	L+V	2	primary assemblage 2	21.67	252	mineralized	Dooneen Mine Spoil
365B	3	3.4	-64	-31.0	-22.9	166	-22.4	165	-30.5	365B.1	10	L+V	2	primary assemblage 2	23.98	247	mineralized	Dooneen Mine Spoil
365B	3	3.5	-56		-15.8	208	-15.4	206		365B.2	8	L+V	2	primary assemblage 2	18.97	302	mineralized	Dooneen Mine Spoil
365B	3	3.6	-50	-32.9	-18.5	194	-18.1	193	-32.4	365B.2	12	L+V	6	primary assemblage 2	21.03	283	mineralized	Dooneen Mine Spoil
365B	3	3.7			-11.9	218	-11.5	216		365B.2	6	L+V	2	primary assemblage 2	15.51	320	mineralized	Dooneen Mine Spoil
365B	3	3.8	-57	-19.1	-15.2	206	-14.8	204	-18.7	365B.2	9	L+V	3	primary assemblage 2	18.48	300	mineralized	Dooneen Mine Spoil
366	1	1.1	-38	-12.7	-6.1	269	-5.1	267	-11.7	366.1	14	L+V	5	primary	8.05	404	mineralized	Caminches Spoil
366	1	1.2	-58	-23.3	-5.6	209	-4.6	208	-22.1	366.2	10	L+V	5	primary	7.36	320	mineralized	Caminches Spoil
366	2	2.1	-41	-18.3	-7.3	168	-6.3	167	-17.2	366.3	14	L+V	2	primary	9.63	263	mineralized	Caminches Spoil
366	2	2.3	-52	-19.5	-7.7	196	-6.7	195	-18.4	366.4	7	L+V	1	primary	10.13	298	mineralized	Caminches Spoil
366	2	2.4	-46	-20.6	-6.8	263	-5.8	261	-19.5	366.1	11	L+V	5	primary	8.98	394	mineralized	Caminches Spoil
423	3	3.2	-47		-11.5	155	-11.2	154		423.1	18	L+V	0.5	primary	15.15	237	barren	Vuggy Quartz Coom Mine
423	3	3.3	-51	-39.0	-11.4	149	-11.1	148	-38.4	423.1	13	L+V	1	primary	15.06	230	barren	Vuggy Quartz Coom Mine
423	4	4.1	-48	-32.0	-10.1	186	-9.8	185	-31.5	423.4	60	L+V	2	primary necking	13.72	279	barren	Vuggy Quartz Coom Mine
423	5	5.4	-44		-22.7	262	-22.3	260		423.5	7	L+V	3	primary	23.88	369	barren	Vuggy Quartz

																		Coom Mine
423	7	7.1	-59	-27.3	-17.0	173	-16.6	172	-26.8	423.1	13	L+V	1	primary	19.94	257	barren	Vuggy Quartz Coom Mine
423	1	1.1	-77	-30.9	-27.0	131	-26.5	130	-30.4	423.2	19	L+V	1	primary	26.52	205	barren	Vuggy Quartz Coom Mine
423	1	1.2	-80		-27.8	125	-27.3	124		423.2	17	L+V	1	primary	27.01	198	barren	Vuggy Quartz Coom Mine
423	1	1.4	-74	-29.7	-28.0	129	-27.5	128	-29.2	423.2	8	L+V	1	primary	27.13	203	barren	Vuggy Quartz Coom Mine
423	1	1.5	-75	-36.0	-30.2	123	-29.7	122	-35.5	423.2	12	L+V	0.5	primary	28.48	197	barren	Vuggy Quartz Coom Mine
423	3	3.1	-87	-38.0	-25.5	104	-25.1	103	-37.5	423.3	7	L+V	0.1	primary	25.61	173	barren	Vuggy Quartz Coom Mine
423	5	5.1	-76	-36.0	-25.8	74	-25.4	74	-35.5	423.3	33	L+V	0.5	primary	25.80	138	barren	Vuggy Quartz Coom Mine
423	5	5.2	-75	-36.8	-25.8	97	-25.4	96	-36.3	423.3	39	L+V	2	primary	25.80	165	barren	Vuggy Quartz Coom Mine
423	5	5.3	-80	-35.8	-25.9	105	-25.5	104	-35.3	423.3	35	L+V	0.5	primary	25.86	174	barren	Vuggy Quartz Coom Mine
368A	1	1.3	-42	-9.4	-7.1	215	-6.1	214	-8.4	368A.1	10	L+V	5	primary	9.37	325	mineralized	Dursey Crossing Mine
368A	1	1.4	-54	-9.0	-5.8	214	-4.8	213	-8.0	368A.1	10	L+V	5	primary	7.64	327	mineralized	Dursey Crossing Mine
368A	1	1.5	-56		-6.9	217	-5.9	216		368A.1	8	L+V	5	primary	9.11	328	mineralized	Dursey Crossing Mine
368A	1	1.6	-55	-7.6	-6.1	255	-5.1	253	-6.6	368A.2	7	L+V	5	primary	8.05	383	mineralized	Dursey Crossing Mine

368A	1	1.7	-56	-7.2	-2.8	223	-1.9	221	-6.2	368A.2	10	L+V	5	primary	3.18	343	mineralized	Dursey Crossing Mine
368A	1	1.9	-46	-9.7	-7.7	251	-6.7	249	-8.7	368A.2	9	L+V	5	primary	10.13	374	mineralized	Dursey Crossing Mine
368A	2	2.2	-60	-24.8	-20.3	159	-19.2	158	-23.6	368A.3	7	L+V	5	primary	21.81	239	mineralized	Dursey Crossing Mine
368A	2	2.3	-63	-23.9	-17.9	176	-16.8	175	-22.7	368A.3	13	L+V	5	primary	20.08	260	mineralized	Dursey Crossing Mine
368A	2	2.4	-64		-23.4	149	-22.2	148		368A.3	12	L+V	5	primary	23.86	227	mineralized	Dursey Crossing Mine
368A	2	2.5	-59	-24.9	-18.4	139	-17.3	138	-23.7	368A.3	10	L+V	5	primary	20.45	214	mineralized	Dursey Crossing Mine
368A	2	2.6	-76		-22.5	213	-21.4	211		368A.4	6	L+V	2	primary	23.28	306	mineralized	Dursey Crossing Mine
368A	2	2.7	-67		-21.5	163	-20.4	162		368A.3	9	L+V	2	primary	22.62	244	mineralized	Dursey Crossing Mine
368A	2	2.8	-66		-22.9	167	-21.8	166		368A.3	6	L+V	2	primary	23.54	249	mineralized	Dursey Crossing Mine
368A	2	2.9	-53	-28.4	-22.9	212	-21.8	210	-27.2	368A.5	12	L+V	5	primary	23.54	305	mineralized	Dursey Crossing Mine
368A	3	3.2	-74		-24.5	163	-23.3	162		368A.3	3	L+V	2	primary	24.55	243	mineralized	Dursey Crossing Mine
368A	3	3.3	-49	-8.9	-5.8	223	-4.8	221	-7.9	368A.2	12	L+V	5	primary	7.64	339	mineralized	Dursey Crossing Mine
368A	3	3.4	-45	-10.8	-6.8	273	-5.8	271	-9.8	368A.2	11	L+V	5	primary	8.98	409	mineralized	Dursey Crossing Mine
368A	3	3.5	-41		-4.4	245	-3.5	243		368A.2	11	L+V	5	primary	5.64	373	mineralized	Dursey Crossing Mine
358A	1	1.1	-42	-22.0	-8.1	263	-7.1	261	-20.9	358A.1	8	L+V	5	primary	10.62	391	barren	Smaller E-W Vein Mountain Mine
358A	1	1.2	-66	-21.1	-17.6	180	-16.5	179	-20.0	358A.2	9	L+V	2	primary	19.85	266	barren	Smaller E-W Vein

																		Mountain Mine
358A	2	2.1	-46	-23.1	-8.0	207	-7.0	206	-22.0	358A.3	5	L+V	5	primary	10.50	312	barren	Smaller E-W Vein Mountain Mine
358A	2	2.2	-49	-14.5	-10.8	211	-9.8	210	-13.4	358A.3	6	L+V	5	primary	13.71	313	barren	Smaller E-W Vein Mountain Mine
358A	2	2.4	-55	-24.6	-10.3	195	-9.3	194	-23.4	358A.3	11	L+V	5	primary	13.17	292	barren	Smaller E-W Vein Mountain Mine
358A	2	2.5	-51		-7.7	243	-6.7	241		358A.1	9	L+V	5	primary	10.13	363	barren	Smaller E-W Vein Mountain Mine
358A	2	2.7	-51	-23.7	-7.4	236	-6.4	234	-22.5	358A.3	10	L+V	5	primary	9.75	354	barren	Smaller E-W Vein Mountain Mine
358A	2	2.8	-59	-24.3	-12.3	200	-11.3	199	-23.1	358A.3	6	L+V	2	primary	15.24	296	barren	Smaller E-W Vein Mountain Mine
358A	1	1.3	-64	-21.5	-11.9	233	-10.9	231	-20.4	358A.5	4	L+V	5	secondary	14.84	341	barren	Smaller E-W Vein Mountain Mine
358A	2	2.3	-65	-25.6	-18.3	163	-17.2	162	-24.4	358A.6	14	L+V	5	secondary	20.38	244	barren	Smaller E-W Vein Mountain Mine
358A	2	2.9	-55		-12.6	204	-11.6	202		358A.7	7	L+V	1	secondary	15.53	300	barren	Smaller E-W Vein Mountain Mine
358A	3	3.1	-63	-25.8	-24.0	157	-22.8	156	-24.6	358A.8	9	L+V	2	secondary	24.23	236	barren	Smaller E-W Vein Mountain Mine
358A	3	3.2	-64	-26.7	-22.8	220	-21.7	218	-25.5	358A.9	9	L+V	2	secondary	23.47	315	barren	Smaller E-W Vein Mountain Mine
358A	3	3.3	-53	-22.3	-9.1	251	-8.1	249	-21.2	358A.10	10	L+V	3	secondary	11.82	371	barren	Smaller E-W Vein Mountain Mine

358A	3	3.4	-69		-24.4	176	-23.2	175		358A.8	8	L+V	1	secondary	24.48	260	barren	Smaller E-W Vein Mountain Mine
358A	5	5.1	-66	-36.0	-23.2	145	-22.6	144	-35.3	358A.2	8	L+V	2	primary	24.09	221	barren	Smaller E-W Vein Mountain Mine
358A	5	5.2	-86	-29.0	-23.0	141	-22.4	140	-28.4	358A.2	6	L+V	4	primary	23.96	216	barren	Smaller E-W Vein Mountain Mine
358A	5	5.3	-78		-24.0	124	-23.4	123		358A.2	4	L+V	1	primary	24.59	196	barren	Smaller E-W Vein Mountain Mine
358A	5	5.4	-69		-22.6	160	-22.0	159		358A.2	13	L+V	2	primary	23.71	240	barren	Smaller E-W Vein Mountain Mine
358A	5	5.6	-38		-24.0	268	-23.4	266		358A.4	5	L+V	5	primary	24.59	376	barren	Smaller E-W Vein Mountain Mine
350	1	1.2	-44		-5.6	256	-5.2	254		350.1	10	L+V	5	primary	8.09	385	barren	Smaller E-W Vein North-West of New E-W Lode
350	1	1.3	-55		-8.5	250	-8.0	248		350.1	10	L+V	5	primary	11.74	370	barren	Smaller E-W Vein North-West of New E-W Lode
350	2	2.1	-47		-8.6	204	-8.1	203		350.2	9	L+V	5	primary	11.86	306	barren	Smaller E-W Vein North-West of New E-W Lode
350	2	2.2	-36		-3.6	244	-3.2	242		350.1	3	L+V	5	primary	5.24	372	barren	Smaller E-W Vein North-West of New E-W Lode
350	3	3.1	-36		-3.3	241	-2.9	239		350.1	6	L+V	5	primary	4.79	368	barren	Smaller E-W Vein

																		North-West of New E-W Lode
350	3	3.2	-37		-3.1	237	-2.7	235		350.1	6	L+V	5	primary	4.48	362	barren	Smaller E-W Vein North-West of New E-W Lode
82	2	2.1	-46	-23.0	-13.5	158	-13.0	157	-22.4	82.3	6	L+V	5	primary	16.89	240	barren	En Echelon Mining District North (Syn-Variscan)
82	2	2.2	-44	-13.4	-5.8	206	-5.4	204	-12.9	82.1	10	L+V	5	primary	8.36	314	barren	En Echelon Mining District North (Syn-Variscan)
82	2	2.3	-42		-8.1	218	-7.6	216		82.1	10	L+V	5	primary	11.27	326	barren	En Echelon Mining District North (Syn-Variscan)
82	2	2.4	-53		-14.8	200	-14.3	199		82.1	6	L+V	3	primary	18.03	293	barren	En Echelon Mining District North (Syn-Variscan)
82	2	2.5	-54	-12.9	-9.6	216	-9.1	214	-12.4	82.1	4	L+V	5	primary	12.99	321	barren	En Echelon Mining District North (Syn-Variscan)
82	2	2.6	-44		-6.3	219	-5.9	217		82.1	11	L+V	5	primary	9.03	331	barren	En Echelon Mining District North

																		(Syn-Variscan)
82	2	2.7	-45		-7.2	229	-6.8	227		82.2	13	L+V	5	primary	10.18	343	barren	En Echelon Mining District North (Syn-Variscan)
82	3	3.1	-39	-13.1	-5.8	210	-5.4	208	-12.6	82.1	12	L+V	3	primary	8.36	320	barren	En Echelon Mining District North (Syn-Variscan)
82	3	3.2			-7.1	311	-6.7	309		82.5	8	L+V	5	primary	10.05	464	barren	En Echelon Mining District North (Syn-Variscan)
82	3	3.3	-41	-12.3	-5.7	186	-5.3	185	-11.8	82.1	5	L+V	1	primary	8.23	288	barren	En Echelon Mining District North (Syn-Variscan)
82	4	4.1	-38	-12.6	-8.8	211	-8.5	209	-12.2	82.1	14	L+V	1	primary	12.25	315	barren	En Echelon Mining District North (Syn-Variscan)
82	4	4.2	-42	-14.8	-8.5	212	-8.2	210	-14.4	82.1	13	L+V	1	primary	11.90	317	barren	En Echelon Mining District North (Syn-Variscan)
82	4	4.3	-43	-16.2	-8.2	224	-7.9	222	-15.8	82.2	10	L+V	1	primary	11.55	334	barren	En Echelon Mining District North

																		(Syn-Variscan)
82	4	4.4	-44	-14.7	-10.3	209	-10.0	207	-14.3	82.1	8	L+V	1	primary	13.89	310	barren	En Echelon Mining District North (Syn-Variscan)
82	4	4.5	-48	-15.1	-8.4	228	-8.1	226	-14.7	82.2	13	L+V	2	primary	11.78	339	barren	En Echelon Mining District North (Syn-Variscan)
82	5	5.1	-43	-14.8	-10.5	200	-10.2	198	-14.4	82.1	4	L+V	2	primary	14.10	297	barren	En Echelon Mining District North (Syn-Variscan)
82	5	5.2	-46	-14.5	-11.0	203	-10.7	201	-14.1	82.1	10	L+V	0.5	primary	14.62	301	barren	En Echelon Mining District North (Syn-Variscan)
82	5	5.3	-48	-14.5	-10.1	198	-9.8	197	-14.1	82.1	7	L+V	0.5	primary	13.68	295	barren	En Echelon Mining District North (Syn-Variscan)
82	6	6.1	-38		-7.3	234	-7.0	232		82.2	15	L+V	6	primary	10.47	349	barren	En Echelon Mining District North (Syn-Variscan)
82	6	6.2	-38		-7.9	206	-7.6	204		82.1	15	L+V	6	primary	11.19	310	barren	En Echelon Mining District North

																		(Syn-Variscan)
82	6	6.3	-38	-21.0	-8.8	218	-8.5	216	-20.6	82.1	15	L+V	4	primary	12.25	324	barren	En Echelon Mining District North (Syn-Variscan)
82	7	7.2	-50	-17.0	-8.9	165	-8.6	164	-16.6	82.3	13	L+V	1	primary	12.36	254	barren	En Echelon Mining District North (Syn-Variscan)
82	8	8.2	-44	-14.2	-9.8	158	-9.5	157	-13.8	82.3	7	L+V	0.5	primary	13.36	243	barren	En Echelon Mining District North (Syn-Variscan)
82	9	9.1	-39	-19.3	-9.7	224	-9.4	222	-18.9	82.2	12	L+V	1	primary	13.25	331	barren	En Echelon Mining District North (Syn-Variscan)
82	10	10.1	-41	-15.7	-7.6	216	-7.3	214	-15.3	82.1	16	L+V	1	primary	10.83	324	barren	En Echelon Mining District North (Syn-Variscan)
82	10	10.2	-46	-18.8	-7.3	218	-7.0	216	-18.4	82.1	22	L+V	3	primary	10.47	327	barren	En Echelon Mining District North (Syn-Variscan)
82	11	11.1	-44	-23.0	-6.8	245	-6.5	243	-22.5	82.4	8	L+V	1	primary	9.84	366	barren	En Echelon Mining District North

																		(Syn-Variscan)
82	11	11.2	-53	-18.1	-9.6	243	-9.3	241	-17.7	82.4	14	L+V	1	primary	13.14	358	barren	En Echelon Mining District North (Syn-Variscan)
82	11	11.3		-18.6	-6.2	220	-5.8	217	-18.1	82.1	14	L+V	1	primary	8.97	331	barren	En Echelon Mining District North (Syn-Variscan)
82	13	13.1	-46		-12.2	154	-11.7	152		82.3	13	L+V	1	primary	15.70	235	barren	En Echelon Mining District North (Syn-Variscan)
82	13	13.2	-50	-23.0	-13.1	122	-12.6	121	-22.4	82.3	22	L+V	1	primary	16.55	194	barren	En Echelon Mining District North (Syn-Variscan)
226	2	2.1	-46		-12.1	184	-11.8	183		226.1	7	L+V	1	primary	15.74	274	barren	Saddle Reef North of New E-W Lode (Syn-Variscan)
226	2	2.2			-10.3	197	-10.0	196		226.1	3	L+V	3	primary	13.93	294	barren	Saddle Reef North of New E-W Lode (Syn-Variscan)
226	2	2.3	-57		-11.9	196	-11.6	195		226.1	3	L+V	3	primary	15.55	290	barren	Saddle Reef North of New E-W Lode (Syn-Variscan)
226	2	2.4			-12.2	203	-11.9	201		226.1	3	L+V	2	primary	15.84	299	barren	Saddle Reef North

																		of New E-W Lode (Syn-Variscan)
226	2	2.5	-58	-16.0	-11.4	175	-11.1	174	-15.6	226.1	7	L+V	2	primary	15.06	263	barren	Saddle Reef North of New E-W Lode (Syn-Variscan)
226	3	3.1	-45	-17.0	-10.3	187	-10.0	186	-16.6	226.1	10	L+V	1	primary	13.89	280	barren	Saddle Reef North of New E-W Lode (Syn-Variscan)
226	3	3.2	-57	-19.0	-12.6	184	-12.2	183	-18.6	226.1	12	L+V	2	primary	16.18	274	barren	Saddle Reef North of New E-W Lode (Syn-Variscan)
226	3	3.3	-58	-20.0	-12.5	172	-12.1	171	-19.6	226.1	11	L+V	0.5	primary	16.09	258	barren	Saddle Reef North of New E-W Lode (Syn-Variscan)
226	3	3.4	-55		-11.2	193	-10.9	192		226.1	12	L+V	1	primary	14.82	287	barren	Saddle Reef North of New E-W Lode (Syn-Variscan)
226	3	3.5	-55		-12.0	187	-11.6	186		226.1	12	L+V	1	primary	15.61	278	barren	Saddle Reef North of New E-W Lode (Syn-Variscan)
226	3	3.6	-52	-21.0	-9.5	183	-9.2	182	-20.6	226.1	20	L+V	1	primary	13.03	276	barren	Saddle Reef North of New E-W Lode (Syn-Variscan)
226	3	3.7	-55	-33.0	-10.1	182	-9.8	181	-32.5	226.1	8	L+V	1	primary	13.68	274	barren	Saddle Reef North of New E-W Lode

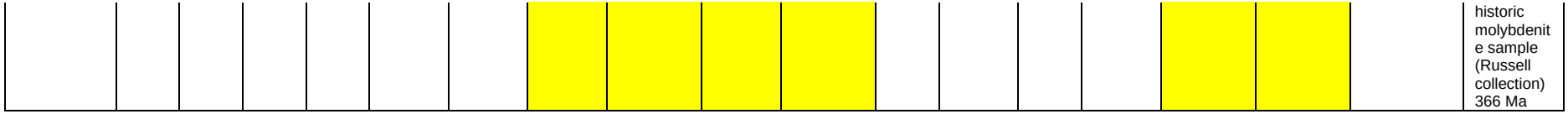
																		(Syn-Variscan)
226	3	3.8	-57	-22.0	-12.9	184	-12.5	183	-21.6	226.1	7	L+V	2	primary	16.46	273	barren	Saddle Reef North of New E-W Lode (Syn-Variscan)
226	3	3.9			-12.2	208	-11.8	206		226.1	8	L+V	2	primary	15.80	306	barren	Saddle Reef North of New E-W Lode (Syn-Variscan)
226	5	5.2	-49	-16.0	-13.2	170	-12.8	169	-15.6	226.2	5	L+V	1	primary	16.74	255	barren	Saddle Reef North of New E-W Lode (Syn-Variscan)
226	5	5.3			-12.1	193	-11.7	192		226.1	3	L+V	2	primary	15.71	286	barren	Saddle Reef North of New E-W Lode (Syn-Variscan)
226	5	5.4	-55	-26.0	-12.4	244	-12.0	242	-25.5	226.1	13	L+V	2	primary	16.00	355	barren	Saddle Reef North of New E-W Lode (Syn-Variscan)
226	5	5.5	-55		-12.7	196	-12.3	195		226.1	14	L+V	2	primary	16.28	289	barren	Saddle Reef North of New E-W Lode (Syn-Variscan)
226	6	6.1	-45		-10.3	195	-9.9	193		226.1	5	L+V	0.5	primary	13.79	290	barren	Saddle Reef North of New E-W Lode (Syn-Variscan)
226	7	7.1	-45		-10.9	205	-10.5	203		226.1	11	L+V	1	primary	14.41	302	barren	Saddle Reef North of New E-W Lode (Syn-Variscan)

226	7	7.2	-45		-16.1	142	-15.6	140		226.2	6	L+V	0.5	primary	19.11	217	barren	Saddle Reef North of New E-W Lode (Syn-Variscan)
226	7	7.3		-21.6	-10.7	199	-10.3	197	-21.0	226.1	10	L+V	1	primary	14.21	295	barren	Saddle Reef North of New E-W Lode (Syn-Variscan)
226	7	7.4		-19.3	-9.0	203	-8.6	201	-18.7	226.1	4	L+V	1	primary	12.37	303	barren	Saddle Reef North of New E-W Lode (Syn-Variscan)
226	7	7.5	-52		-8.9	214	-8.5	211		226.1	4	L+V	1	primary	12.26	318	barren	Saddle Reef North of New E-W Lode (Syn-Variscan)
226	7	7.6			-9.4	207	-9.0	205		226.1	11	L+V	1	primary	12.82	307	barren	Saddle Reef North of New E-W Lode (Syn-Variscan)
R231A2	1	1.1	-39	-13.0	-9.3	198	-8.9	196	-12.5	R231A2.2	8	L+V	1	primary	12.72	296	mineralized	Mountain Mine historic molybdenite sample (Russell collection) 366 Ma
R231A2	1	1.2	-43	-14.1	-10.2	188	-9.8	186	-13.6	R231A2.2	5	L+V	0.5	primary	13.70	281	mineralized	Mountain Mine historic molybdenite sample (Russell collection) 366 Ma
R231A2	1	1.3	-42	-14.5	-9.6	237	-9.2	234	-14.0	R231A2.1	7	L+V	2	primary	13.06	348	mineralized	Mountain Mine historic molybdenit

																		e sample (Russell collection) 366 Ma
R231A2	1	1.4	-41	-20.2	-9.3	237	-8.9	234	-19.7	R231A2.1	5	L+V	2	primary	12.72	349	mineralized	Mountain Mine historic molybdenite sample (Russell collection) 366 Ma
R231A2	1	1.5	-41	-11.2	-4.6	181	-4.3	179	-10.8	R231A2.4	4	L+V	10	primary	6.81	283	mineralized	Mountain Mine historic molybdenite sample (Russell collection) 366 Ma
R231A2	1	1.6	-33	-15.0	-9.7	256	-9.3	253	-14.5	R231A2.3	4	L+V	15	primary	13.16	375	mineralized	Mountain Mine historic molybdenite sample (Russell collection) 366 Ma
R231A2	2	2.1	-42	-13.9	-8.5	252	-8.1	249	-13.4	R231A2.3	10	L+V	10	primary	11.82	371	mineralized	Mountain Mine historic molybdenite sample (Russell collection) 366 Ma
R231A2	2	2.2	-43	-21.2	-8.0	260	-7.6	257	-20.6	R231A2.3	6	L+V	10	primary	11.23	384	mineralized	Mountain Mine historic molybdenite sample (Russell collection) 366 Ma
R231A2	2	2.3	-41	-18.8	-8.3	239	-7.9	236	-18.3	R231A2.1	3	L+V	5	primary	11.58	353	mineralized	Mountain Mine historic molybdenite sample (Russell

																		collection) 366 Ma
R231A2	2	2.4	-41	-18.1	-8.8	250	-8.4	247	-17.6	R231A2.1	5	L+V	5	primary	12.16	368	mineralized	Mountain Mine historic molybdenite sample (Russell collection) 366 Ma
R231A2	2	2.5	-42	-21.8	-9.3	257	-8.9	254	-21.2	R231A2.3	6	L+V	15	primary	12.72	377	mineralized	Mountain Mine historic molybdenite sample (Russell collection) 366 Ma
R231A2	2	2.6	-34	-21.8	-10.4	265	-10.0	262	-21.2	R231A2.3	6	L+V	10	primary	13.91	386	mineralized	Mountain Mine historic molybdenite sample (Russell collection) 366 Ma
R231A2	3	3.1	-42	-23.4	-9.9	250	-9.5	247	-22.8	R231A2.1	9	L+V	2	primary	13.38	366	mineralized	Mountain Mine historic molybdenite sample (Russell collection) 366 Ma
R231A2	3	3.2	-43	-23.9	-8.6	251	-8.2	248	-23.3	R231A2.1	11	L+V	5	primary	11.93	370	mineralized	Mountain Mine historic molybdenite sample (Russell collection) 366 Ma
R231A2	3	3.3	-44	-21.0	-9.5	251	-9.1	248	-20.4	R231A2.1	10	L+V	5	primary	12.95	368	mineralized	Mountain Mine historic molybdenite sample (Russell collection) 366 Ma

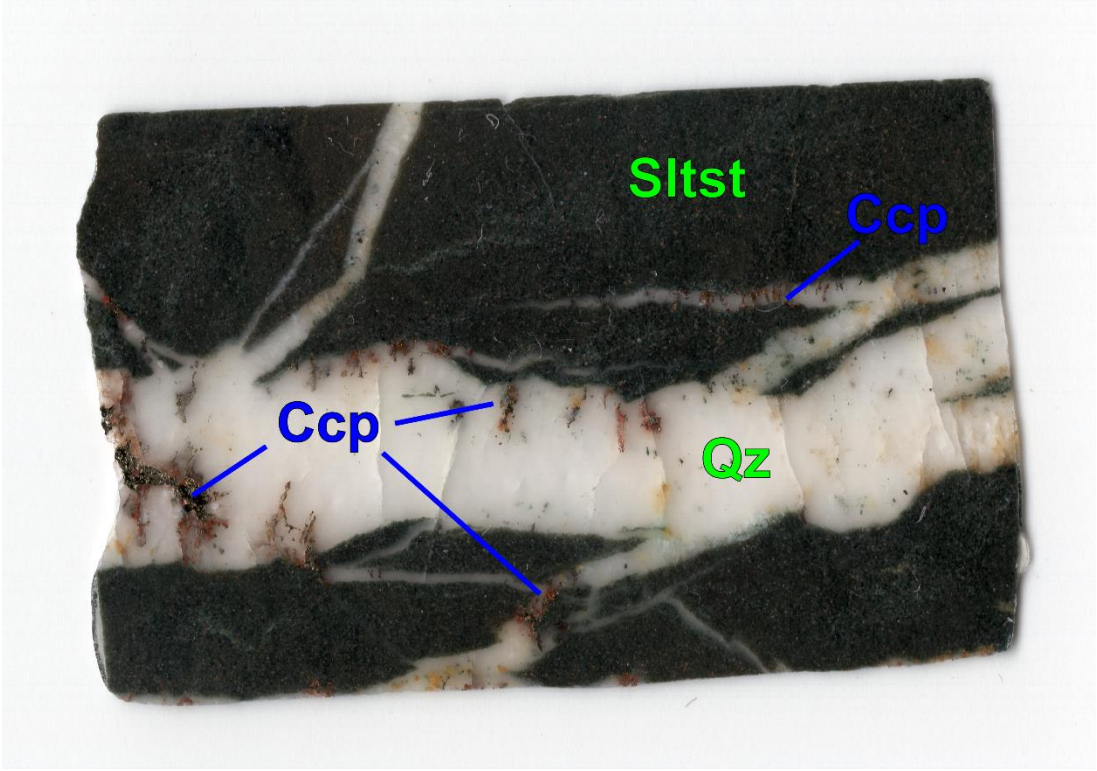
R231A2	4	4.1	-41	-20.9	-8.6	275	-8.2	272	-20.3	R231A2.3	12	L+V	5	primary	11.93	404	mineralized	Mountain Mine historic molybdenite sample (Russell collection) 366 Ma
R231A2	4	4.2	-41		-9.0	272	-8.6	269		R231A2.3	8	L+V	10	primary	12.39	399	mineralized	Mountain Mine historic molybdenite sample (Russell collection) 366 Ma
R231A2	5	5.1	-46	-21.8	-7.6	273	-7.2	270	-21.2	R231A2.3	6	L+V	5	primary	10.75	404	mineralized	Mountain Mine historic molybdenite sample (Russell collection) 366 Ma
R231A2	5	5.2	-43	-20.3	-7.6		-7.2		-19.8	R231A2.3	11	L+V	6	primary	10.75		mineralized	Mountain Mine historic molybdenite sample (Russell collection) 366 Ma
R231A2	5	5.3	-43	-19.9	-8.7	226	-8.3	223	-19.4	R231A2.1	6	L+V	5	primary	12.05	335	mineralized	Mountain Mine historic molybdenite sample (Russell collection) 366 Ma
R231A2	6	6.1	-43	-22.1	-8.5	272	-8.1	269	-21.5	R231A2.3	5	L+V	10	primary	11.82	400	mineralized	Mountain Mine historic molybdenite sample (Russell collection) 366 Ma
R231A2	6	6.2	-46		-7.7	231	-7.3	228		R231A2.1	4	L+V	2	primary	10.87	343	mineralized	Mountain Mine

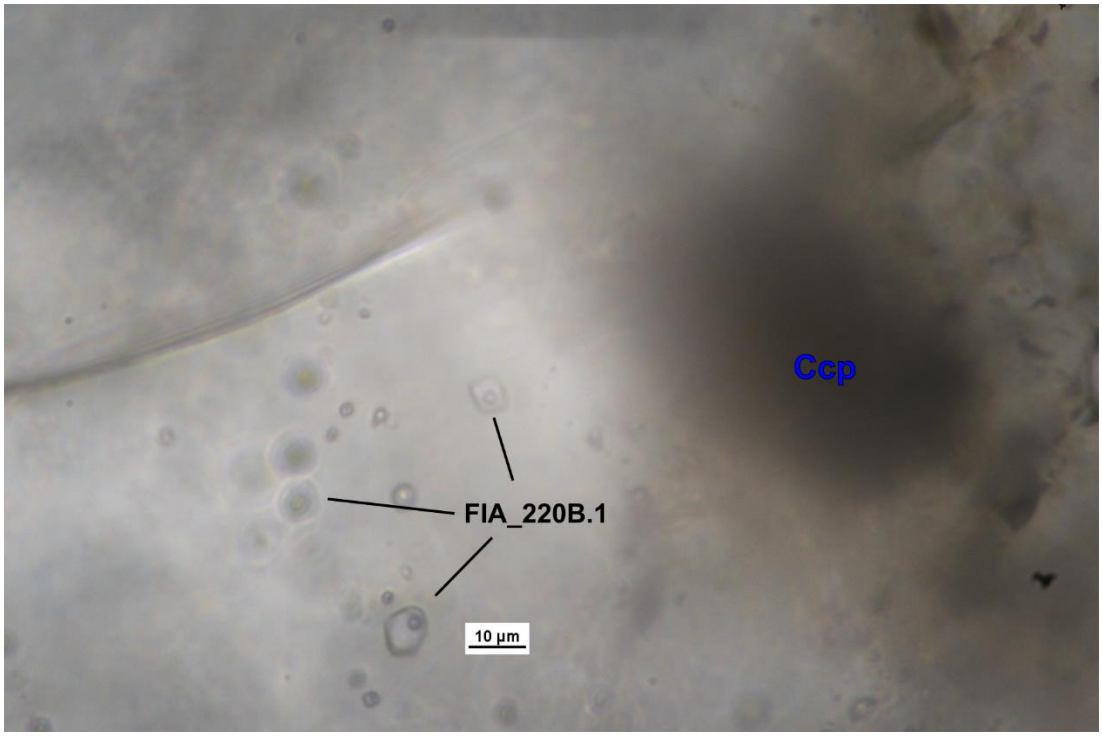

historic molybdenite sample (Russell collection) 366 Ma

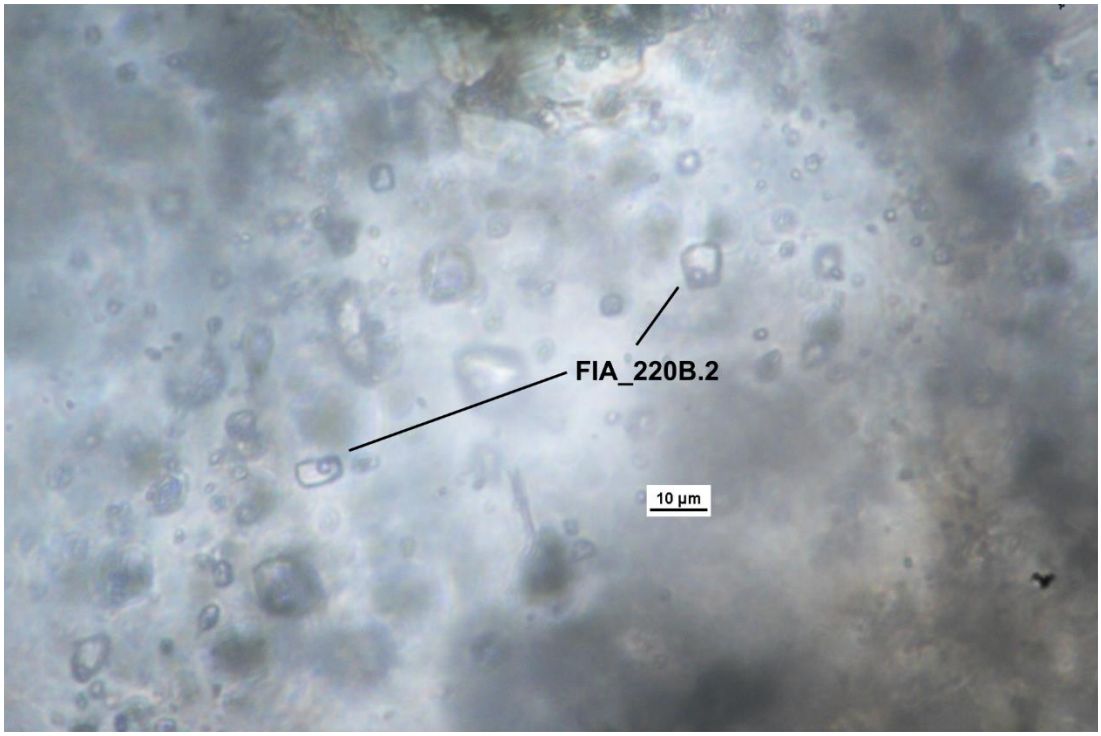
Appendix B.2 (Chapter 3)

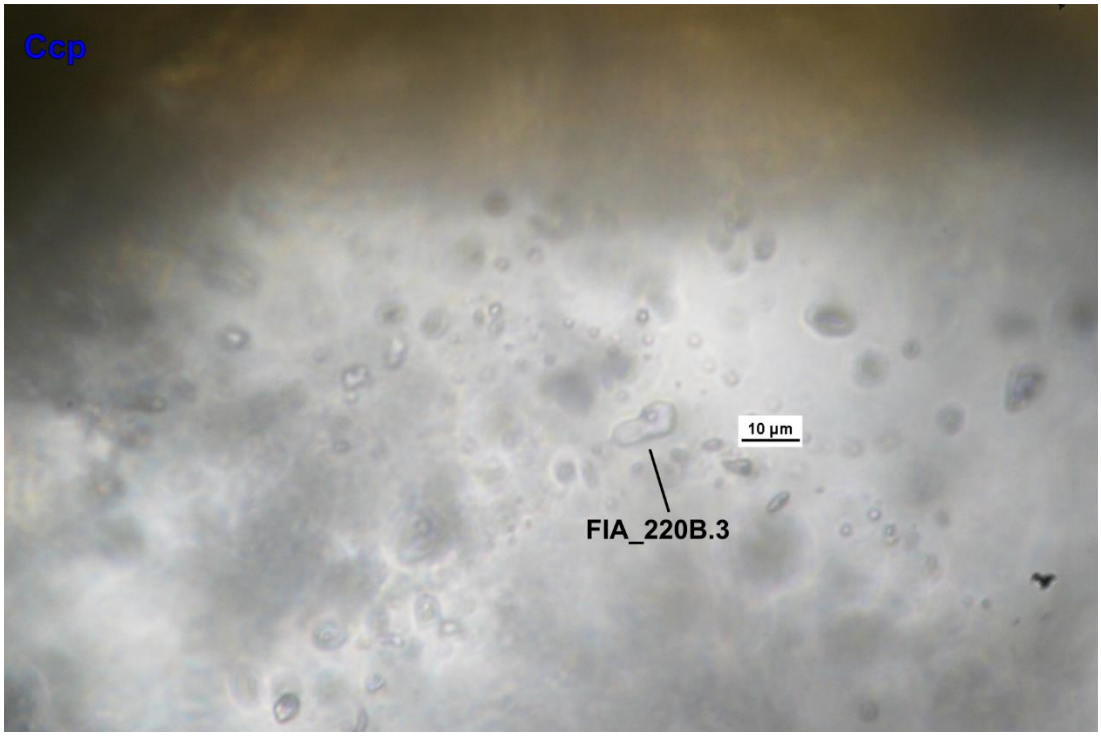
Fluid inclusions assemblages of the Allihies Copper Mining District. The following slide scans and microphotographs (transmitted light) show representative examples of the measured fluid inclusion assemblages (FIA, Appendix B1).

Sample **JL_AH_220B** (scanned slide, width of slide 46 mm, transmitted light images):

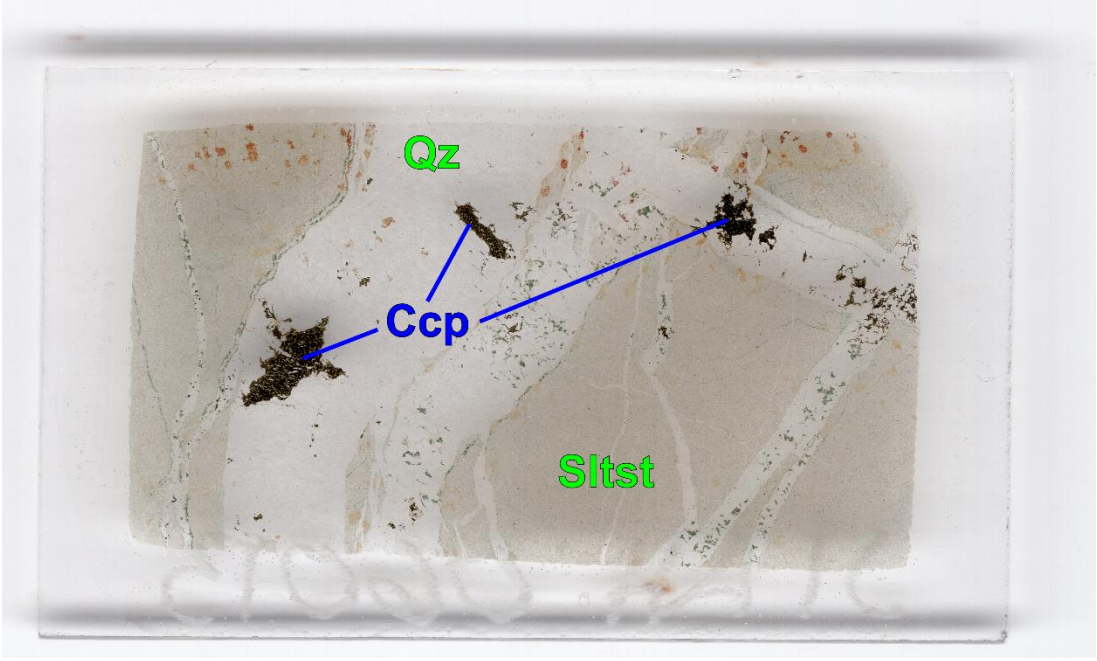


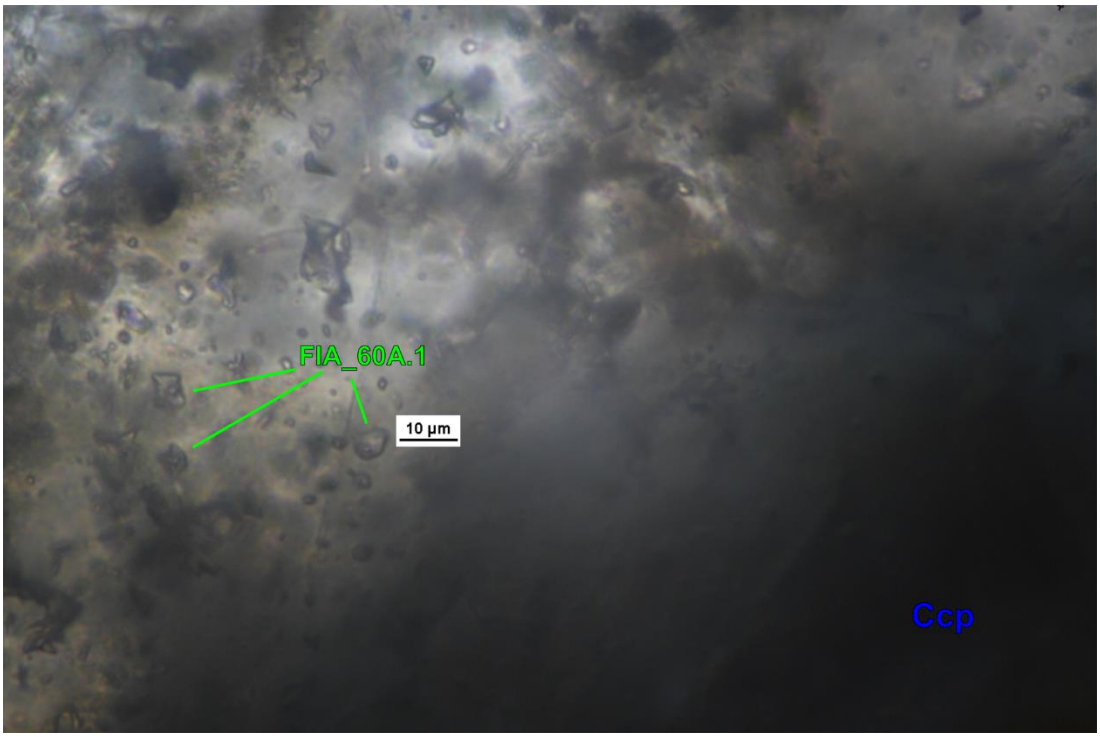


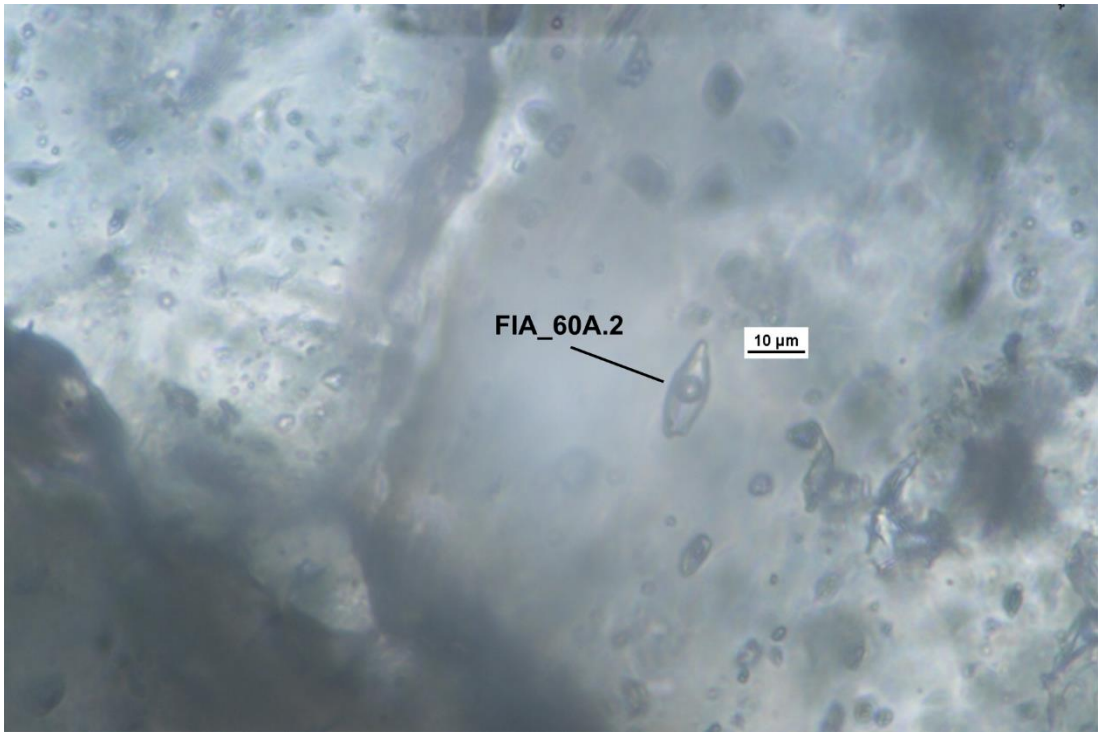

FIA_220B.2
10 µm

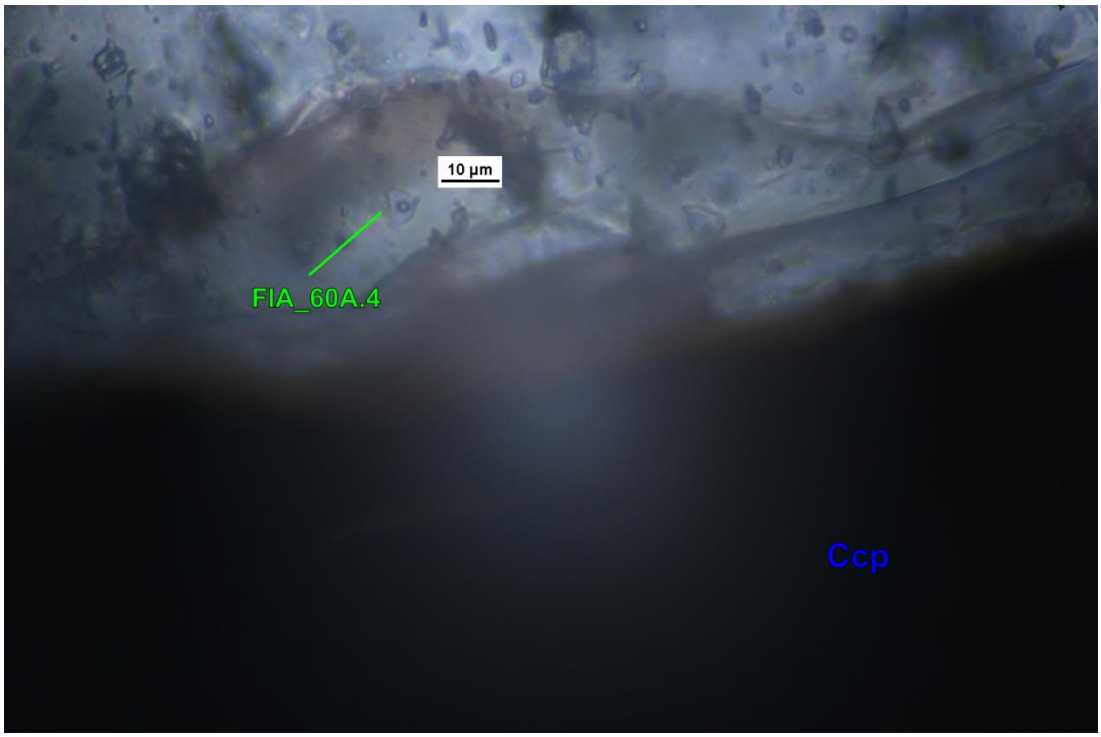

Ccp
10 µm
FIA_220B.3

Sample **JL_AH_60B (JL_AH_60A)** (scanned slide, width of slide 46 mm, transmitted light images):

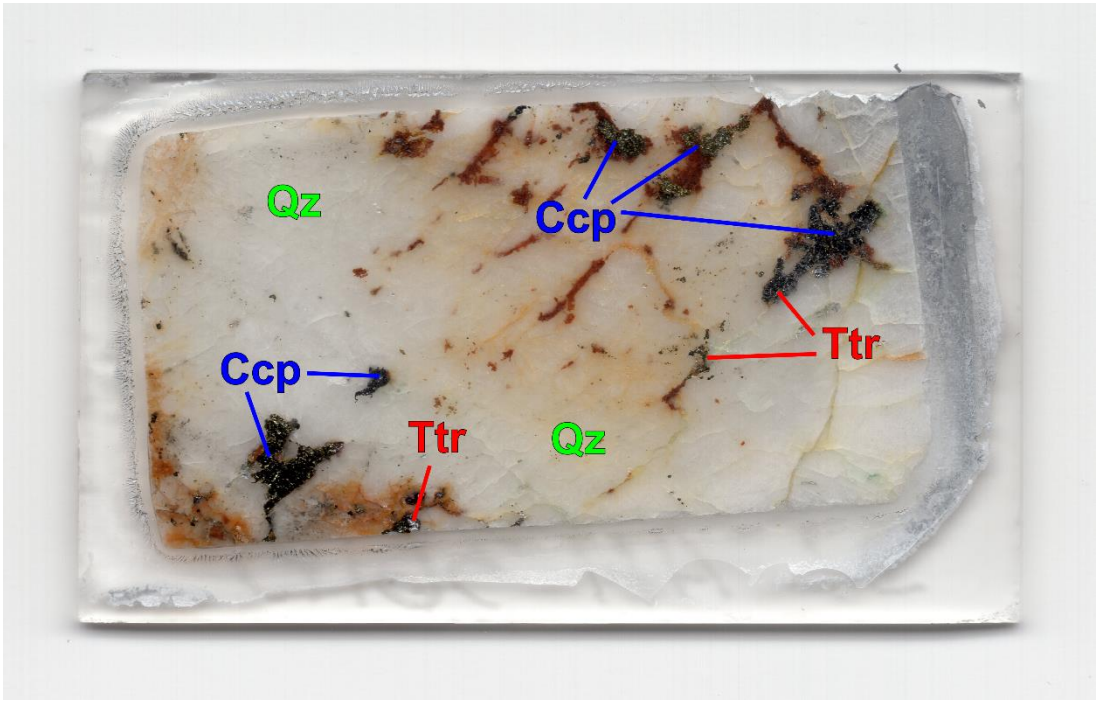


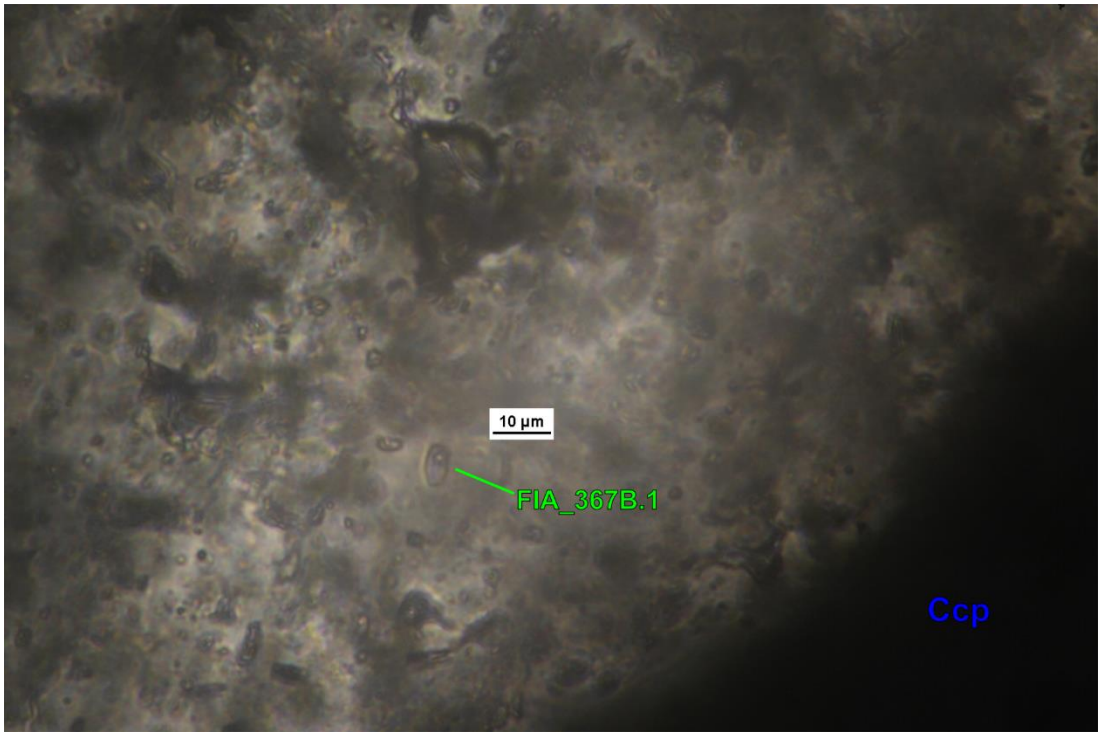


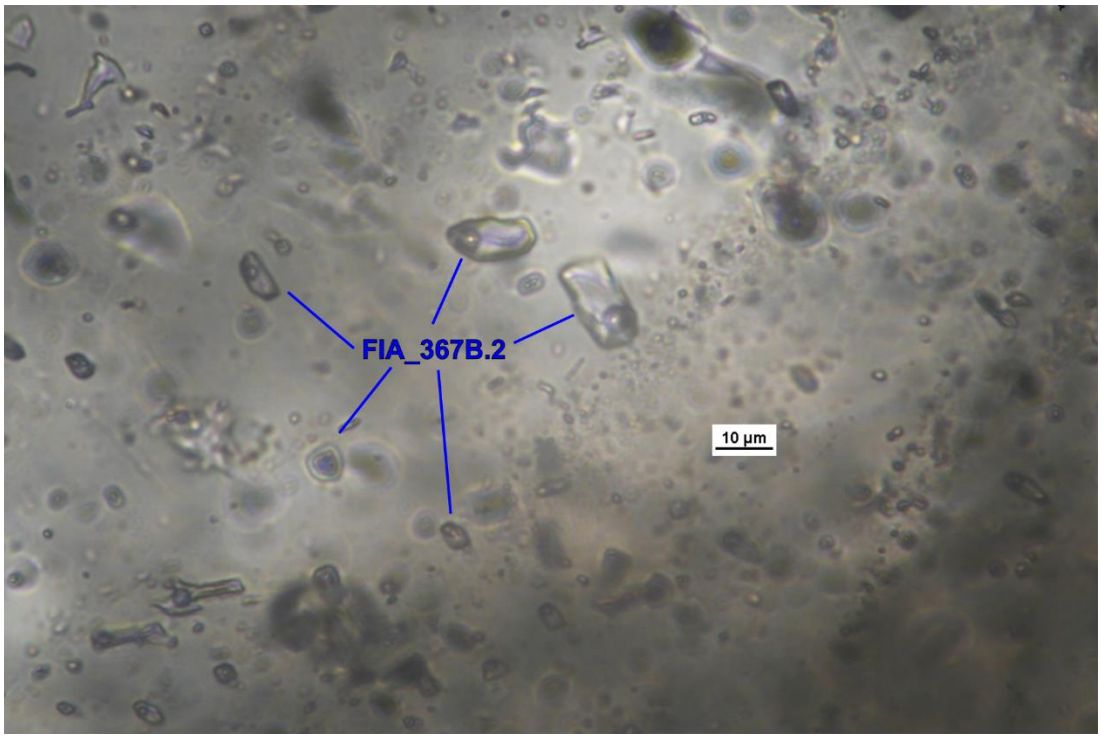

FIA_60A.2
10 µm

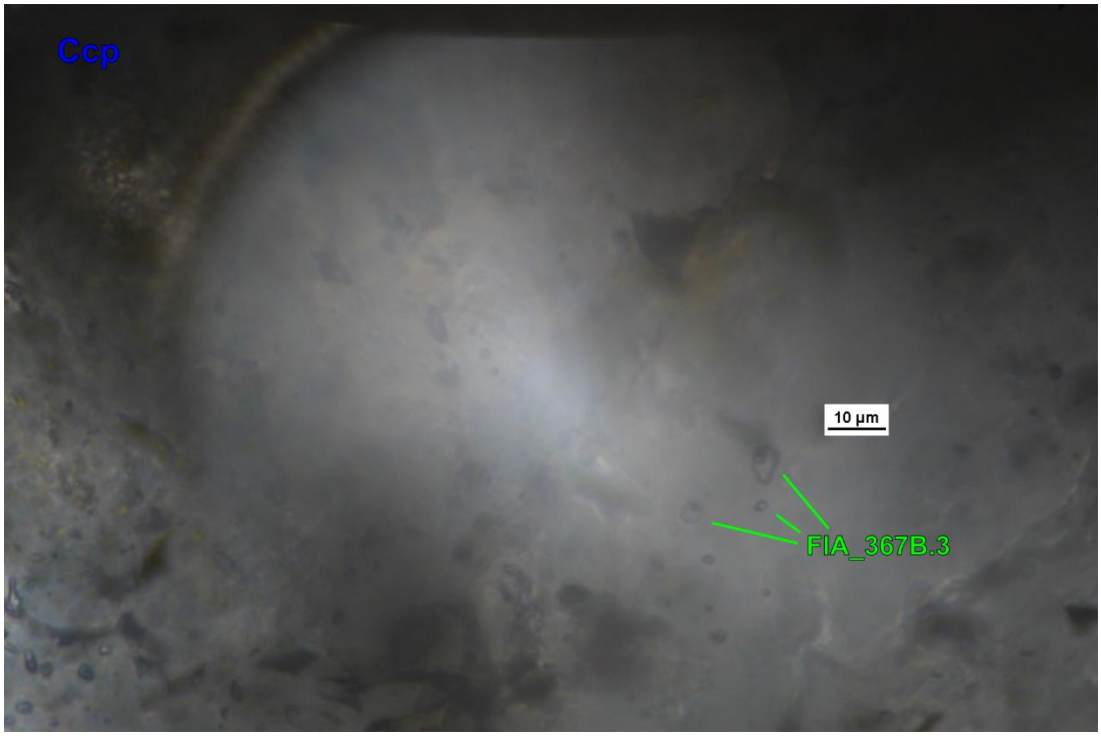

10 µm
FIA_60A.4
Ccp

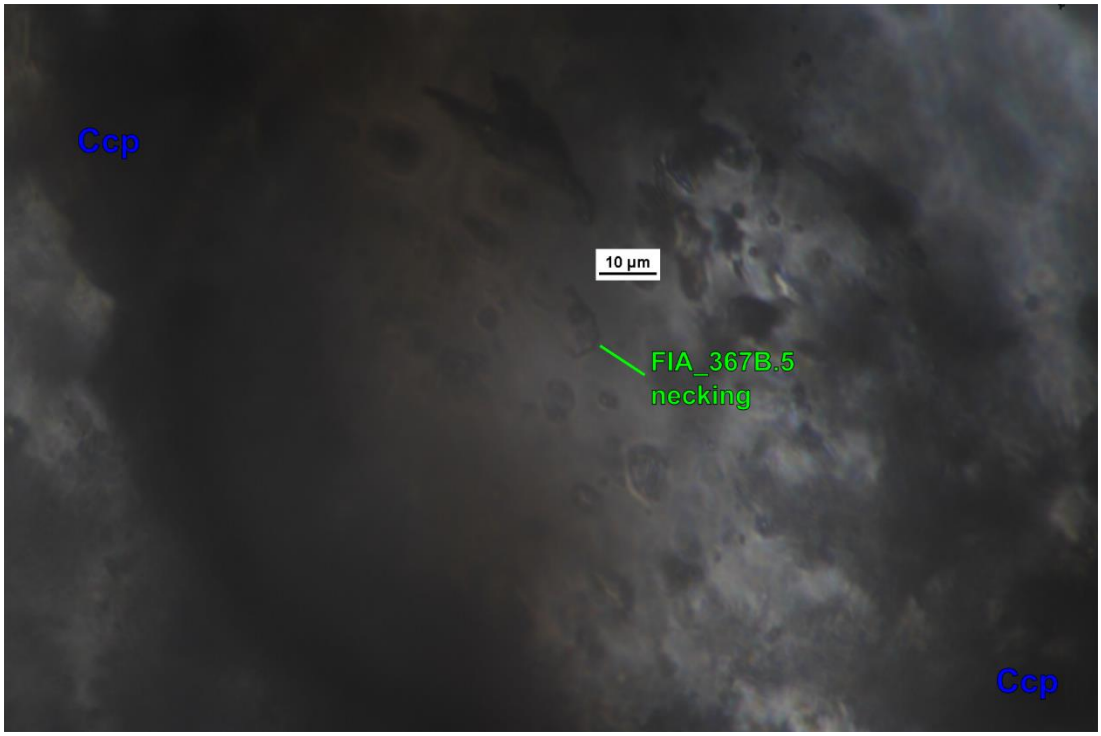
Sample **JL_AH_367B** (scanned slide, width of slide 46 mm, transmitted light images):



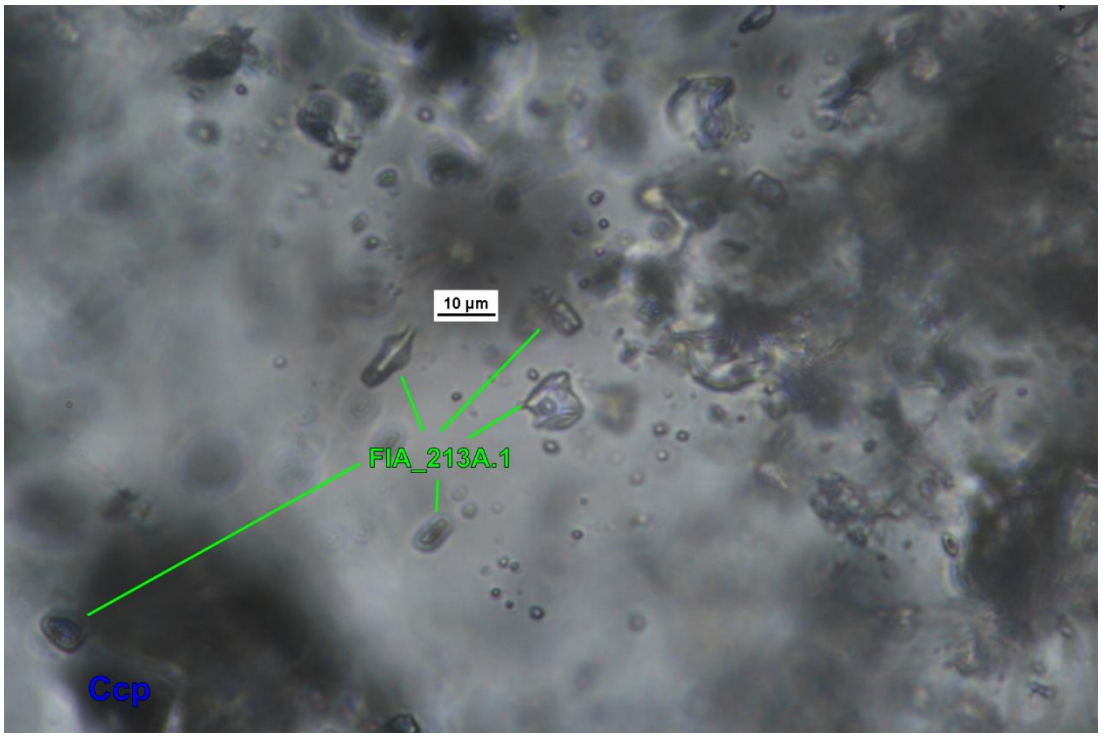


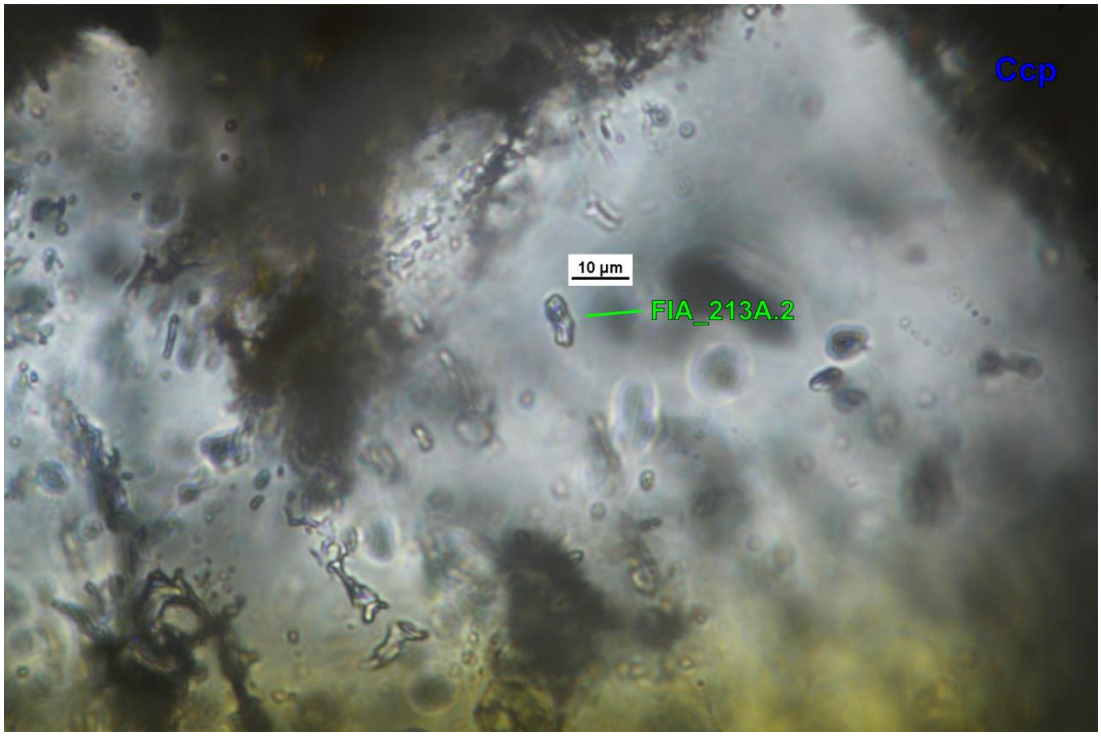

FIA_367B.2
10 µm

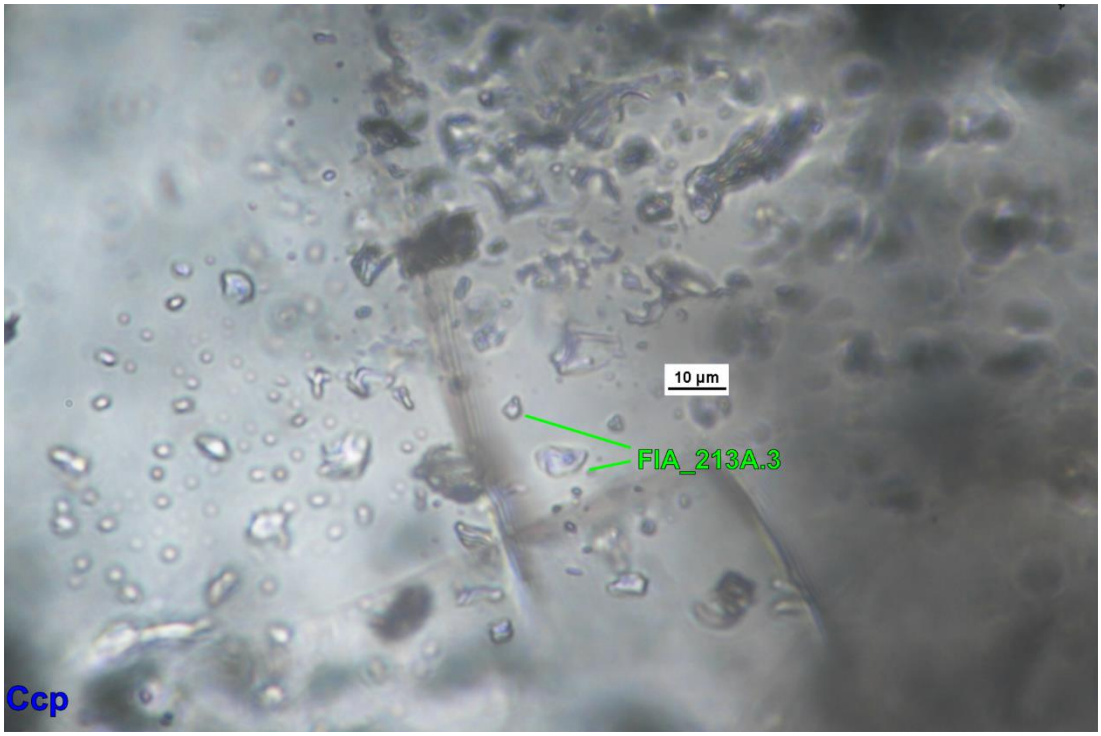

Ccp
10 µm
FIA_367B.3



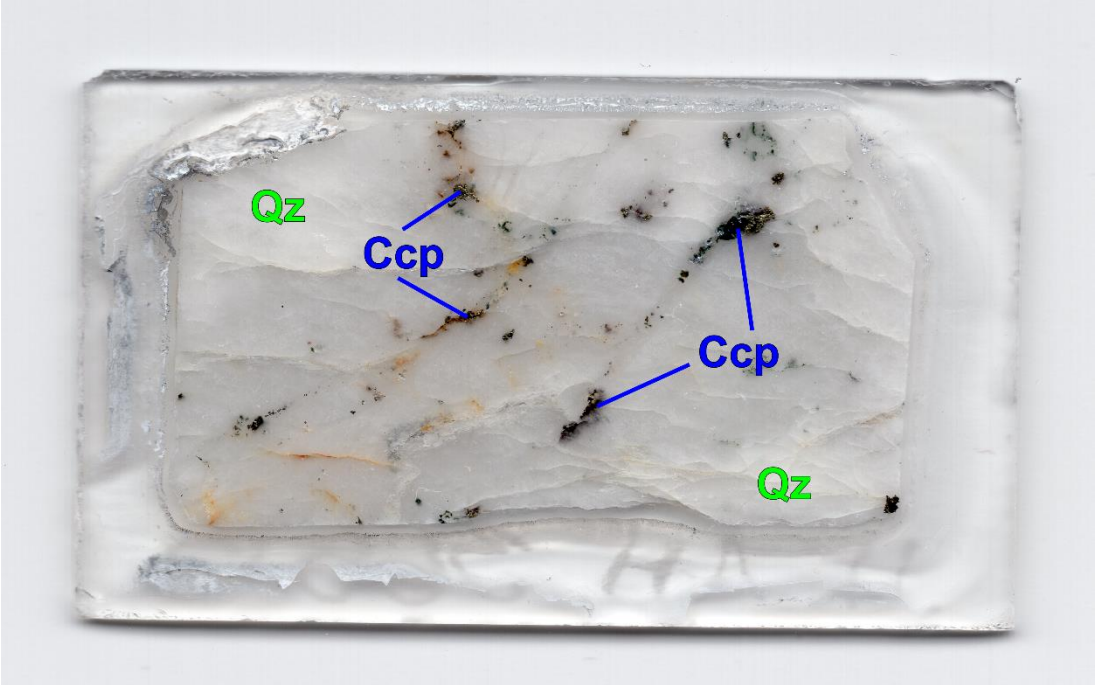
Sample **JL_AH_213A** (transmitted light images):

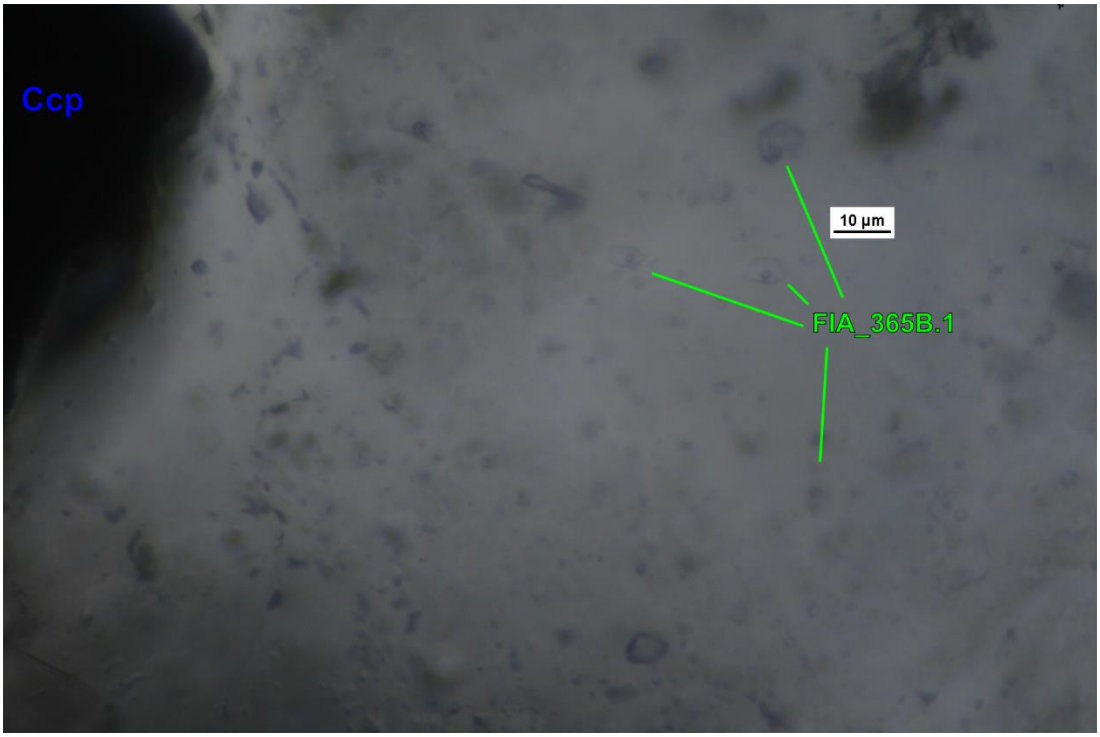



Ccp
10 µm
FIA_213A.2

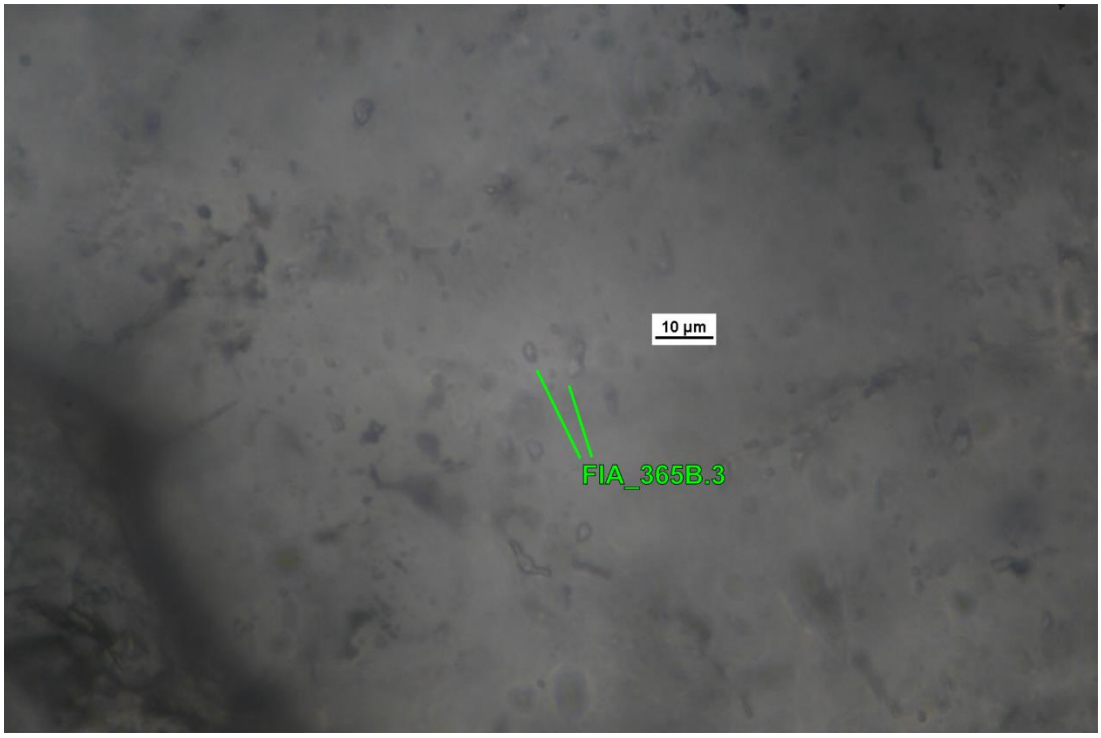

10 µm
FIA_213A.3
Ccp

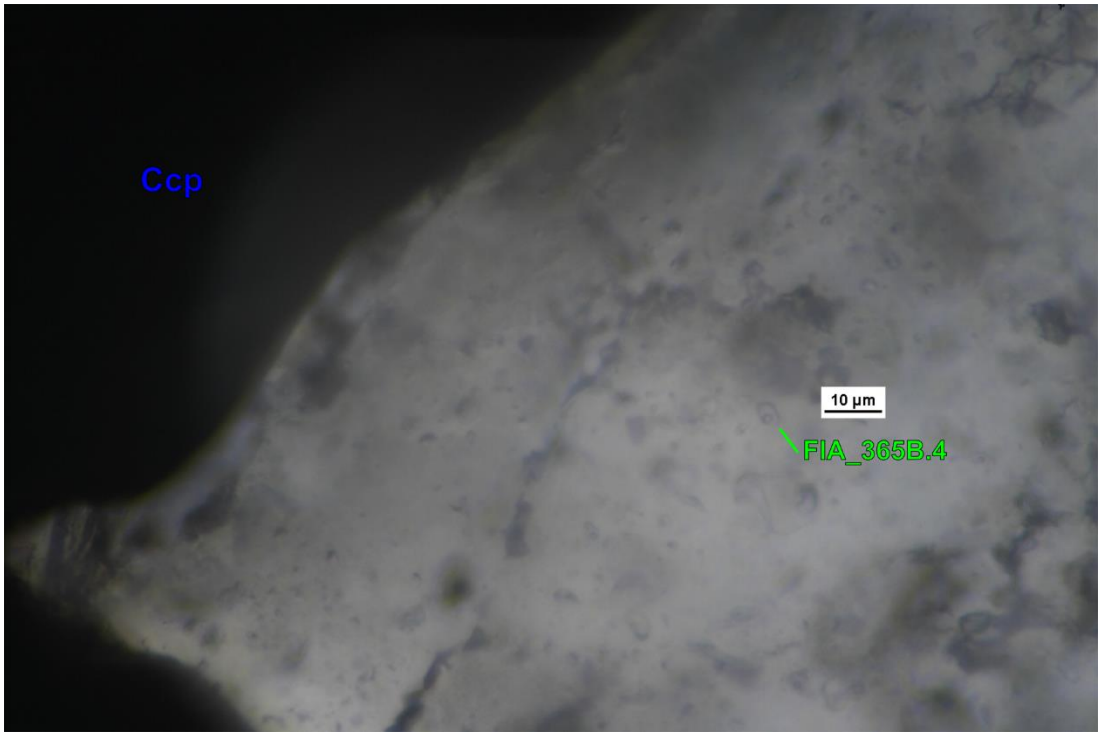
Sample **JL_AH_365B** (scanned slide, width of slide 46 mm, transmitted light images):



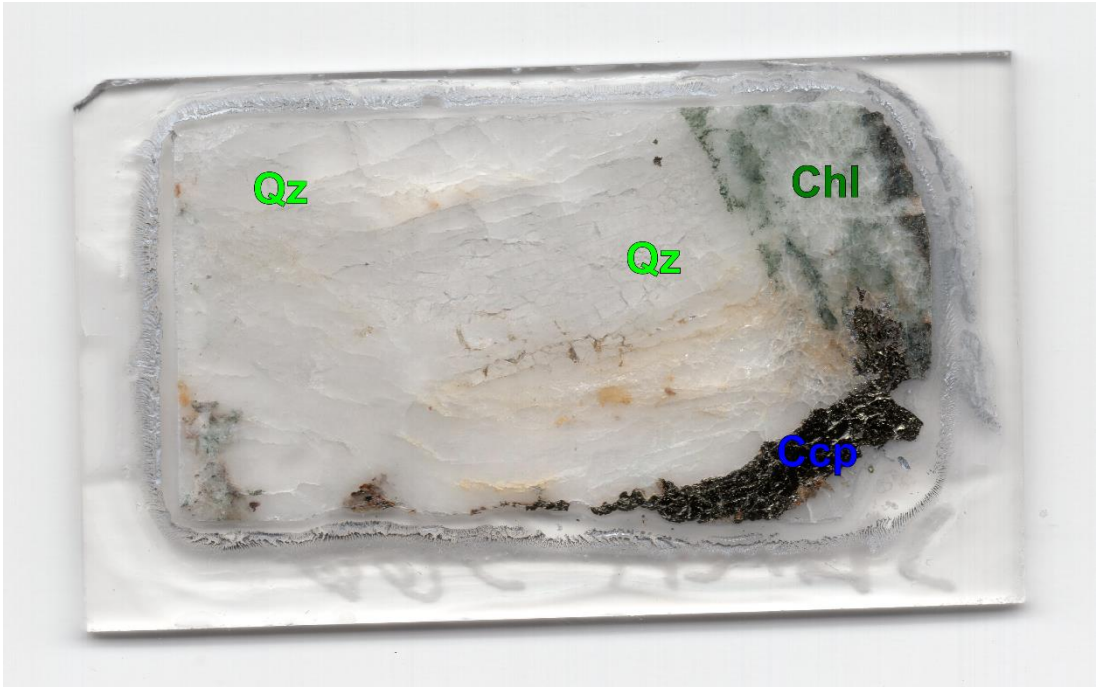


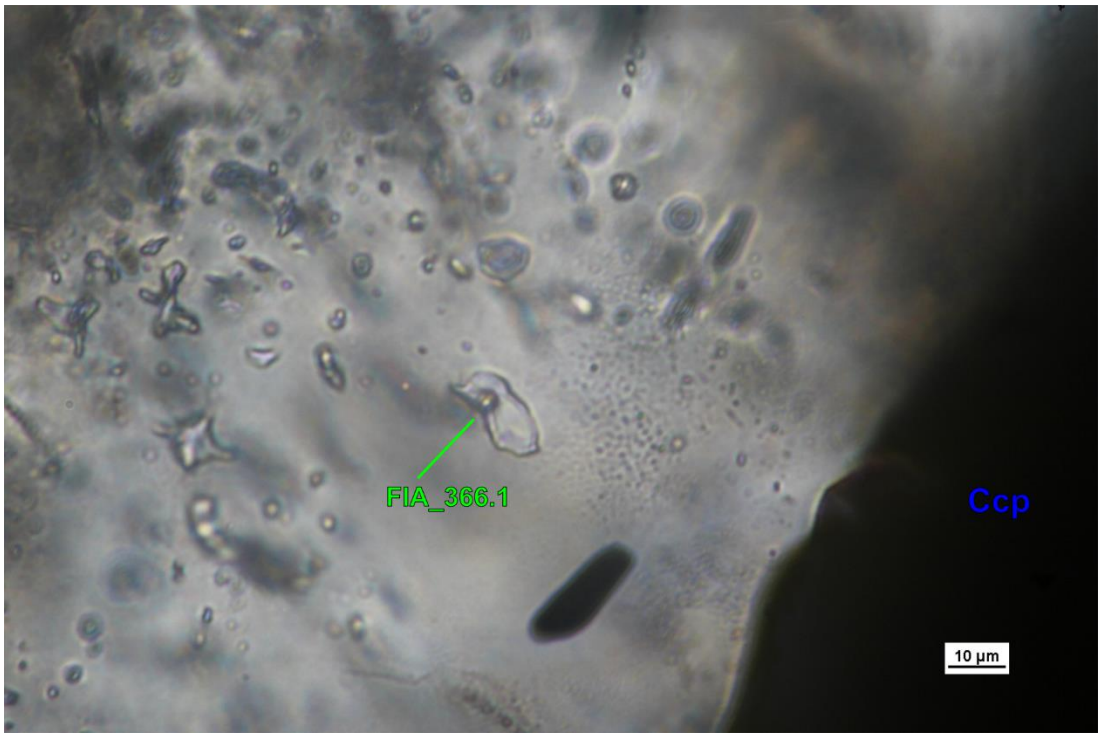

Ccp
10 µm
FIA_365B.2

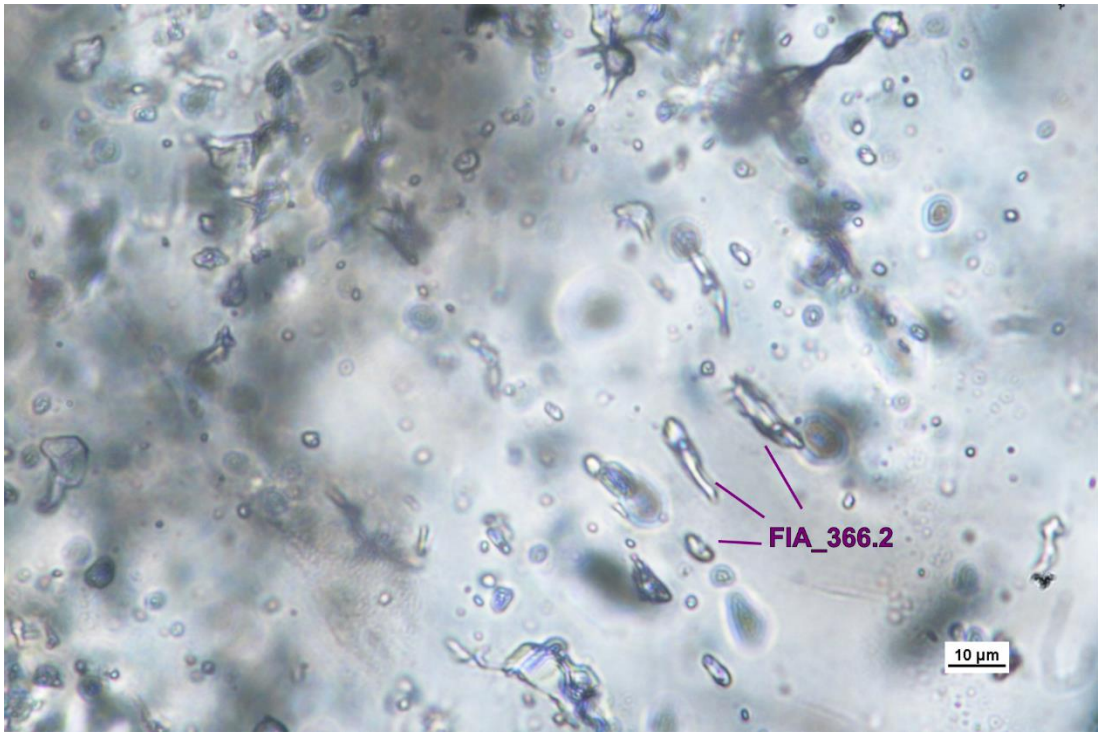

10 µm
FIA_365B.3

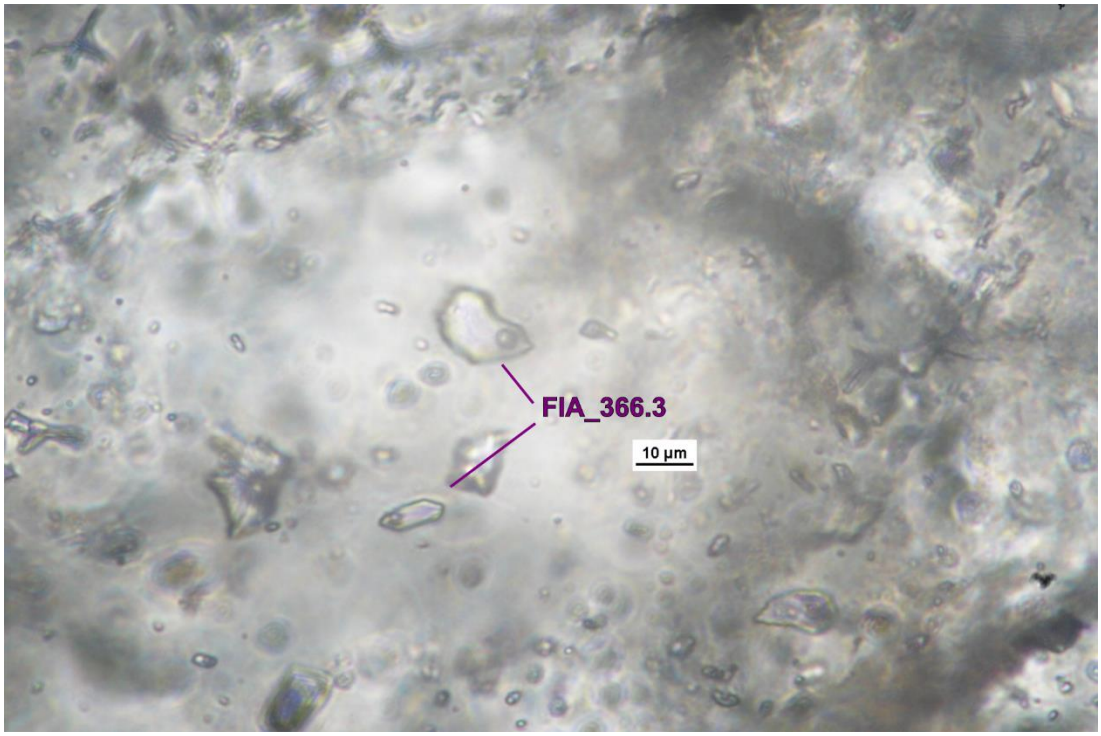


Sample **JL_AH_366** (scanned slide, width of slide 46 mm, transmitted light images):

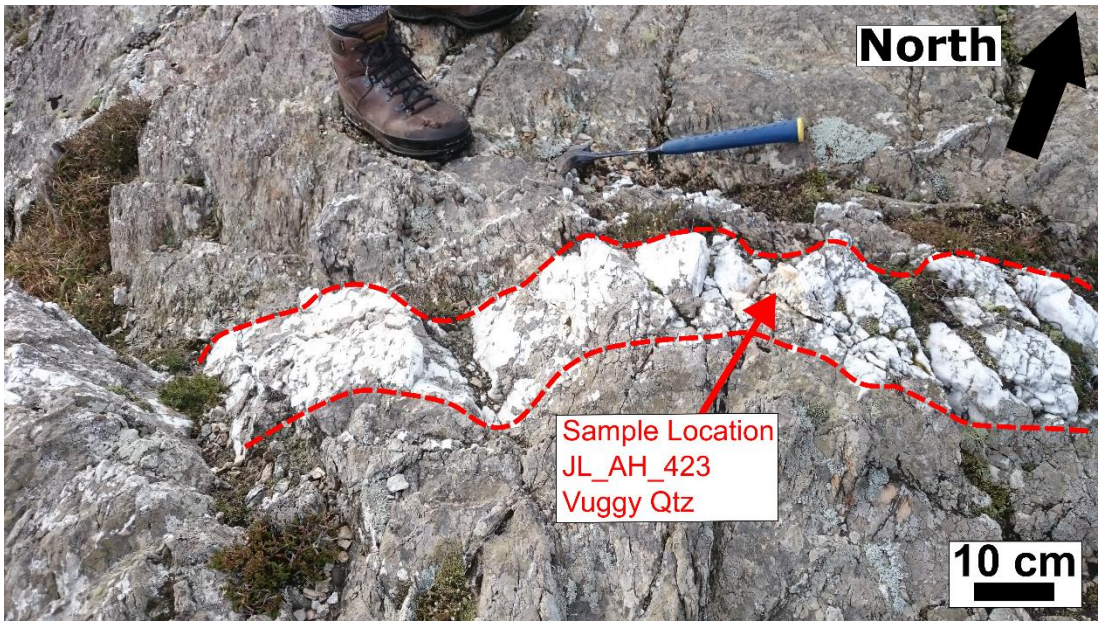



FIA_366.1
Ccp
10 µm

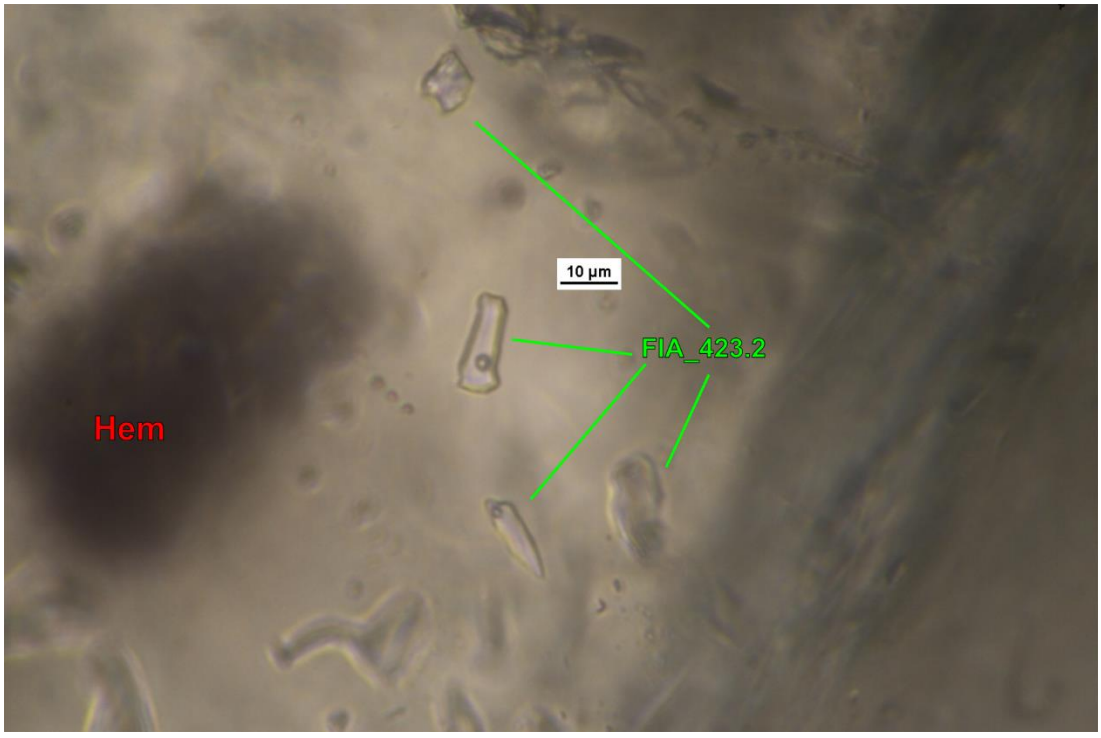

FIA_366.2
10 µm

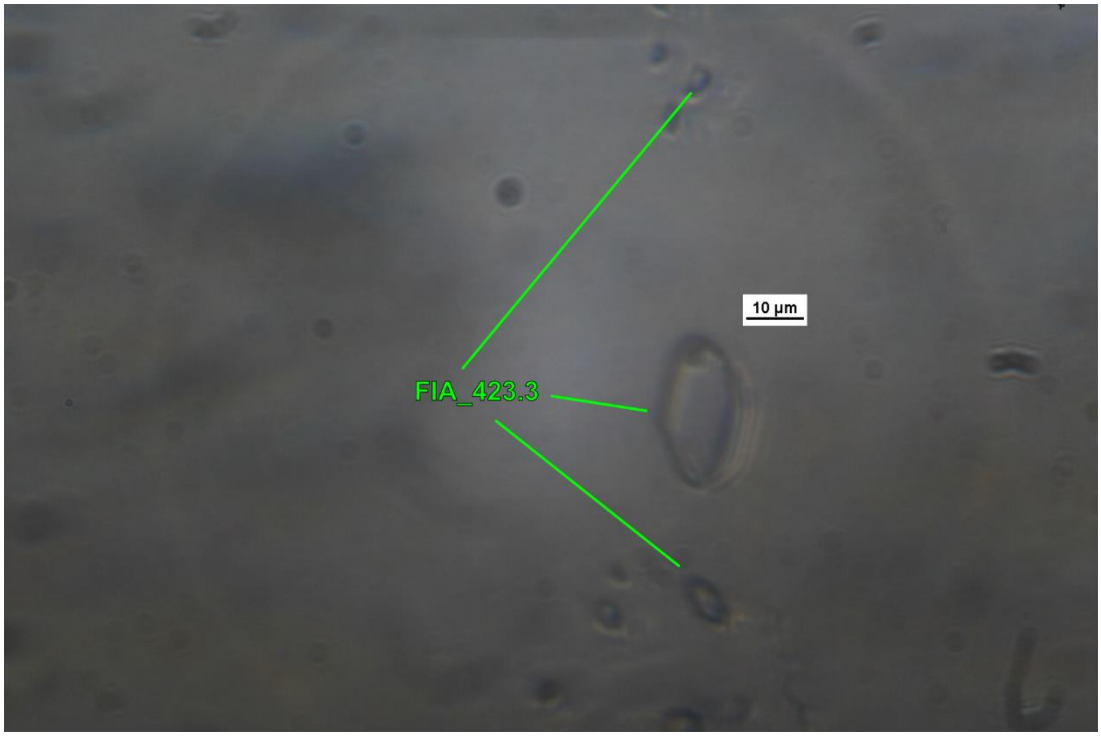


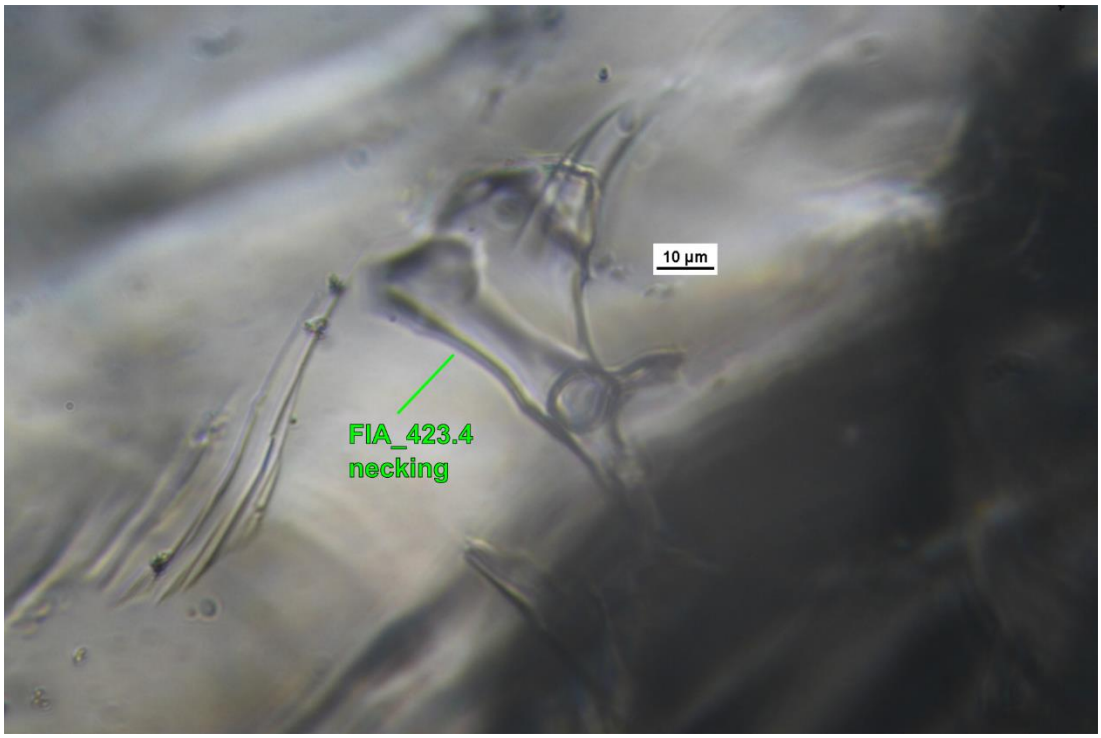
Sample **JL_AH_423** from large quartz vein (related to Coom Lode). Vuggy euhedral quartz crystals (< 0.5 cm) were used directly within the heating-cooling stage, transmitted light images):

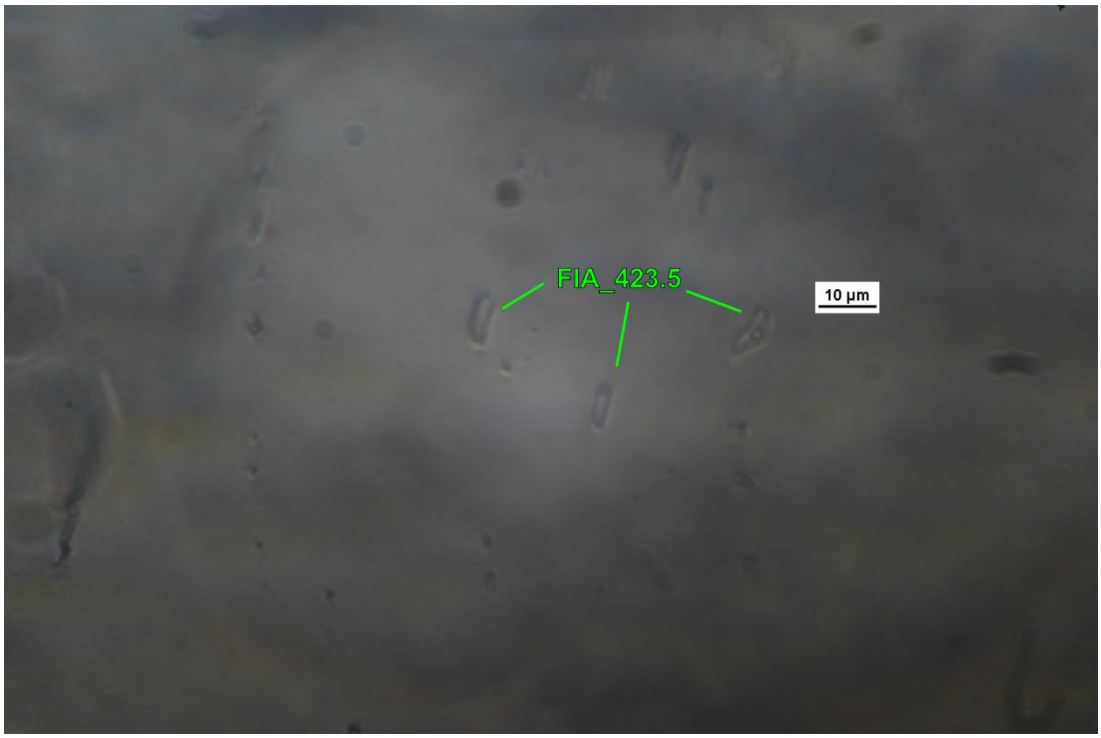



euhedral
vuggy Qz

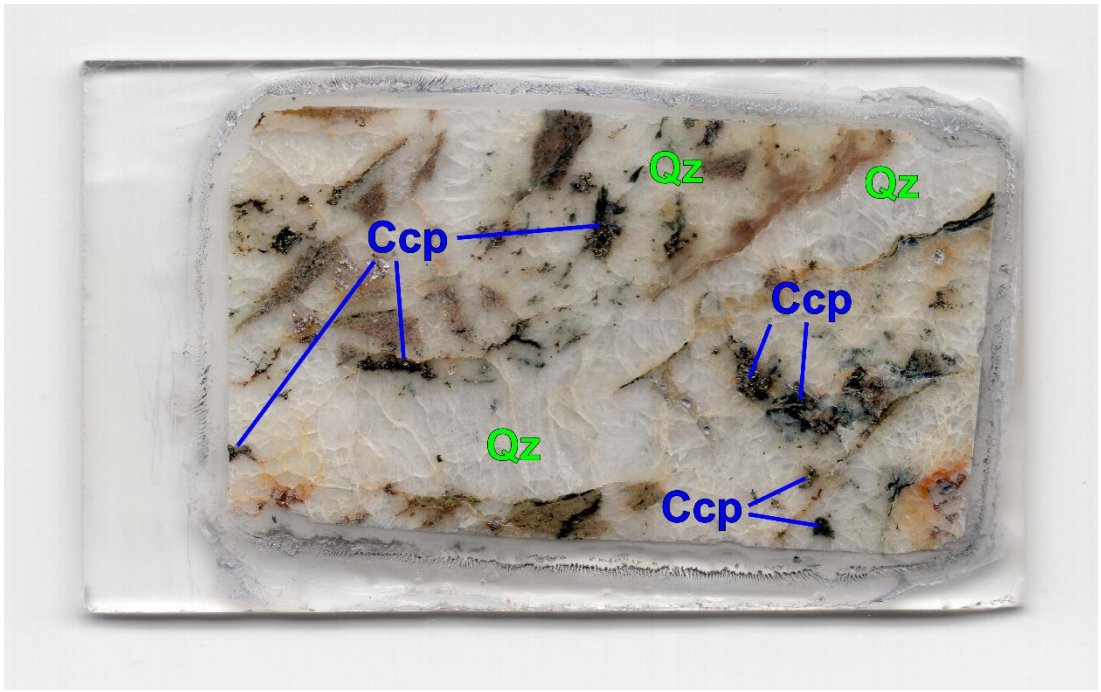

10 µm
FIA_423.2
Hem

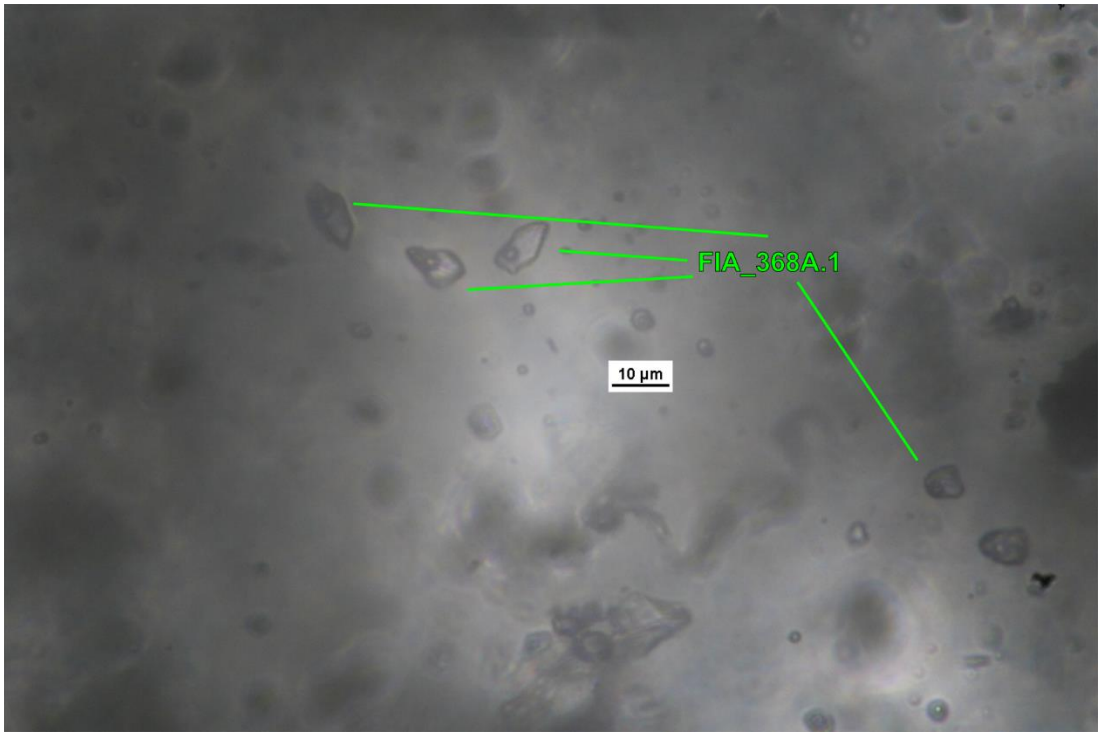

10 µm
FIA_423.3

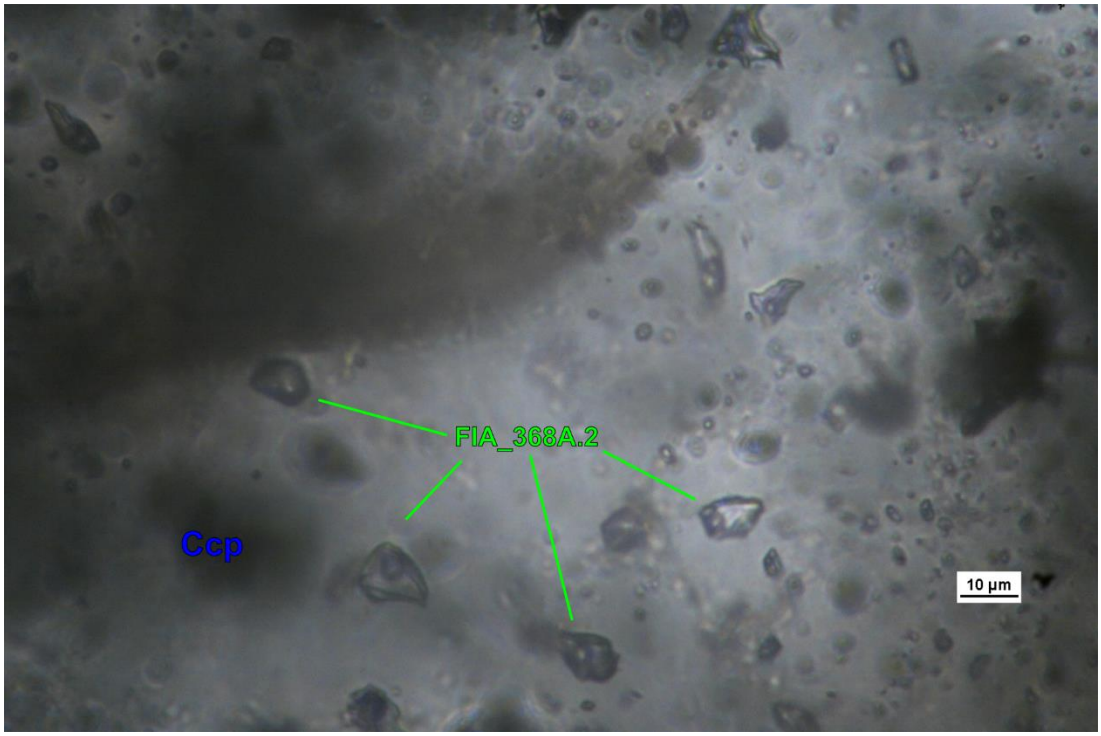

10 µm
FIA_423.4
necking

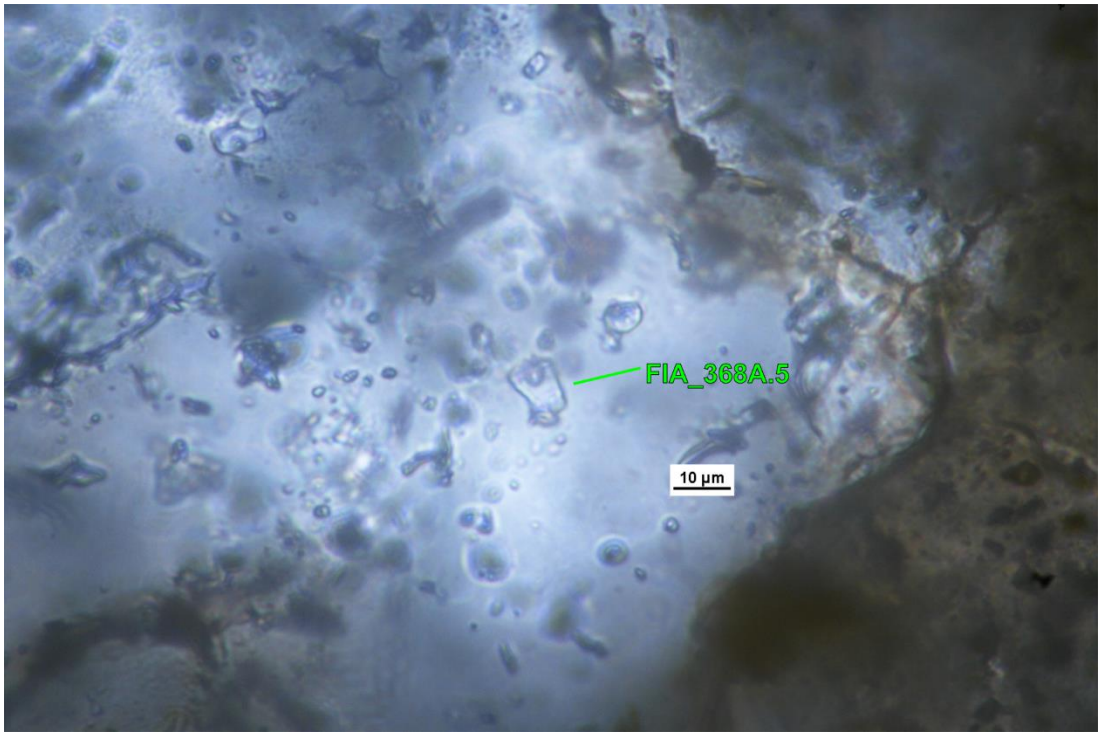


Sample **JL_AH_368A** (scanned slide, width of slide 46 mm, transmitted light images):

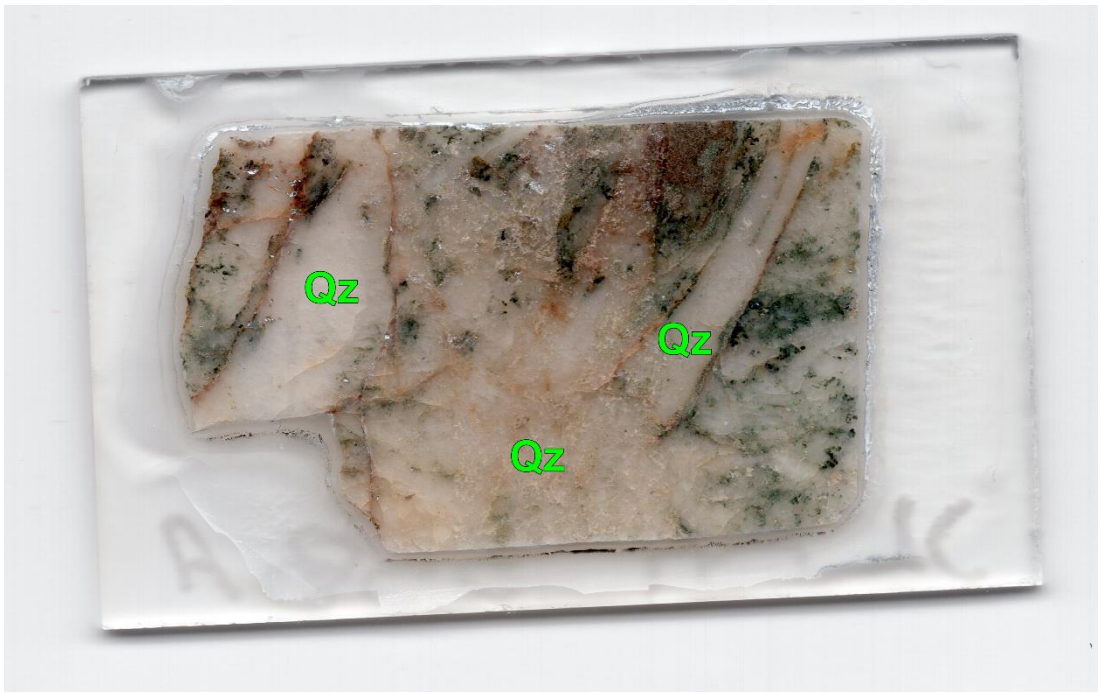


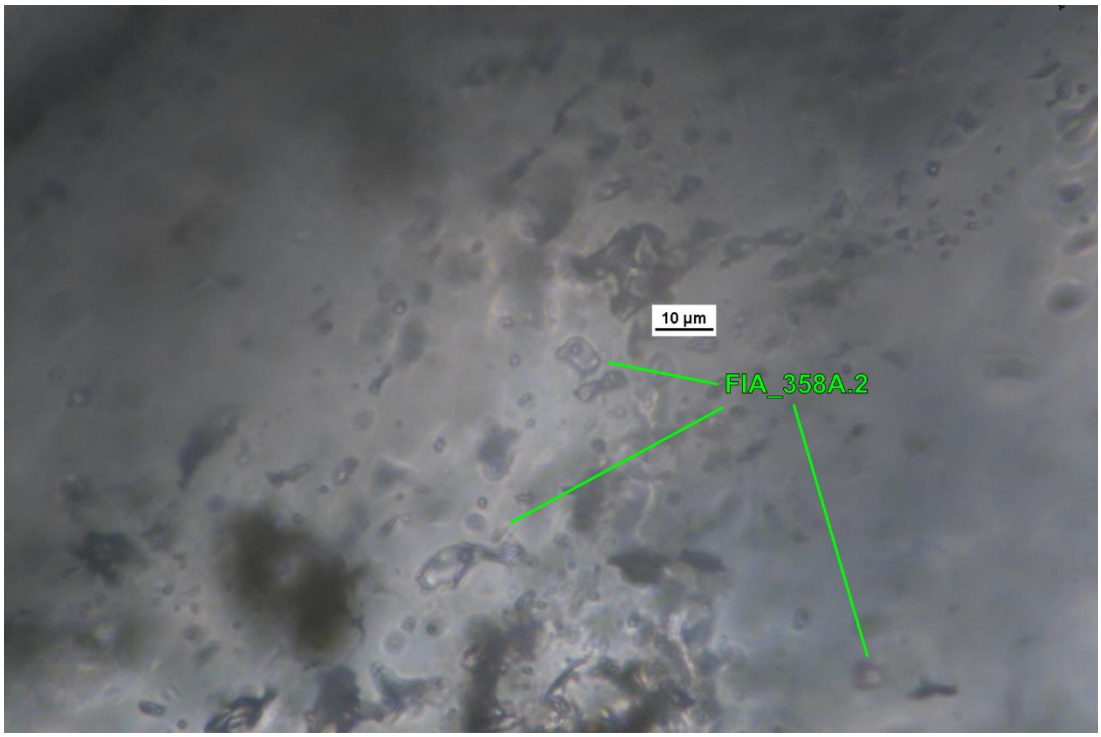

FIA_368A.1
10 µm

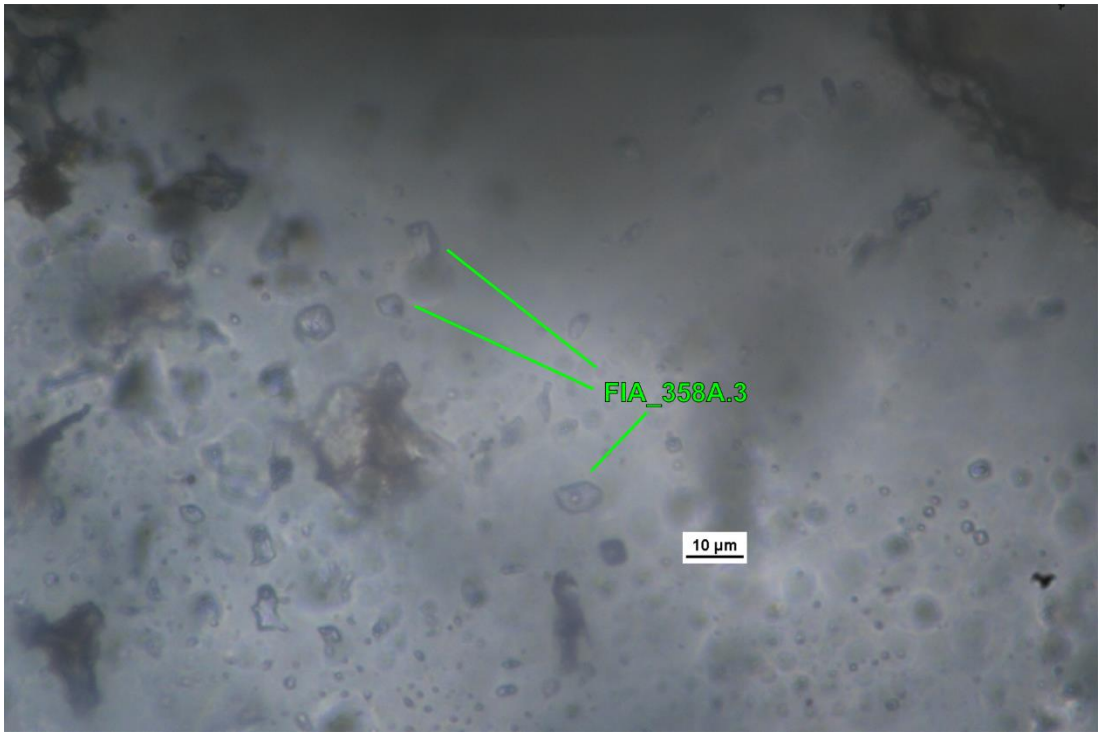

FIA_368A.2
Ccp
10 µm

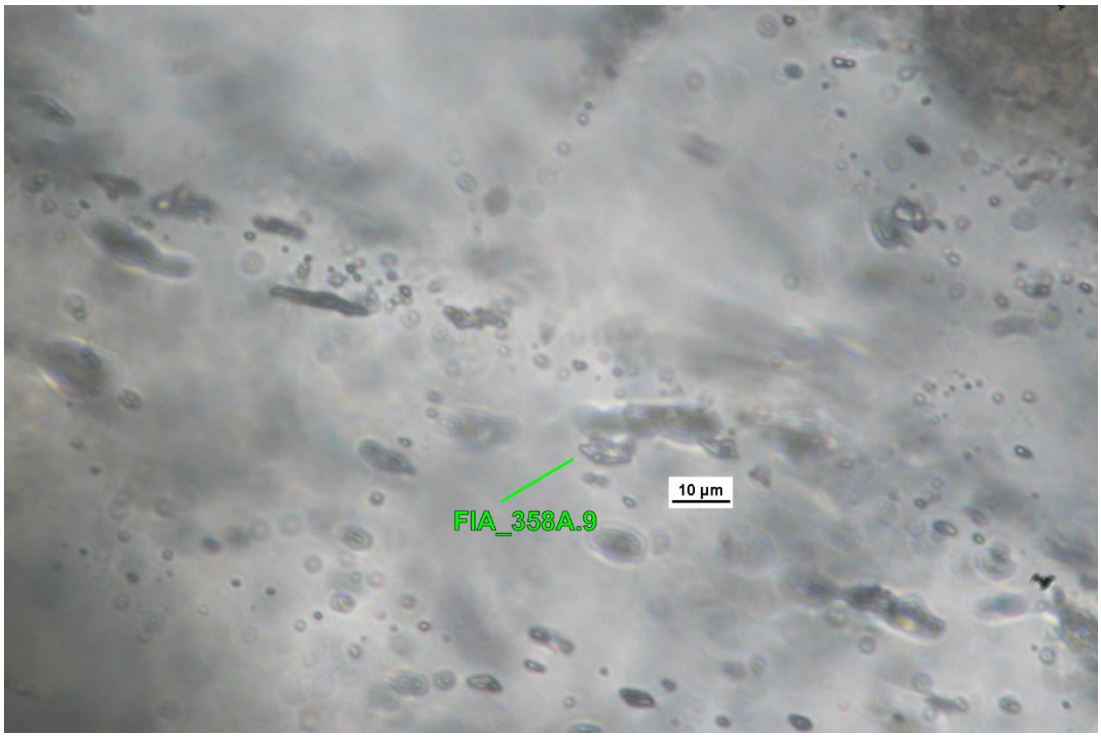


Sample **JL_AH_358A** (scanned slide, width of slide 46 mm, transmitted light images):

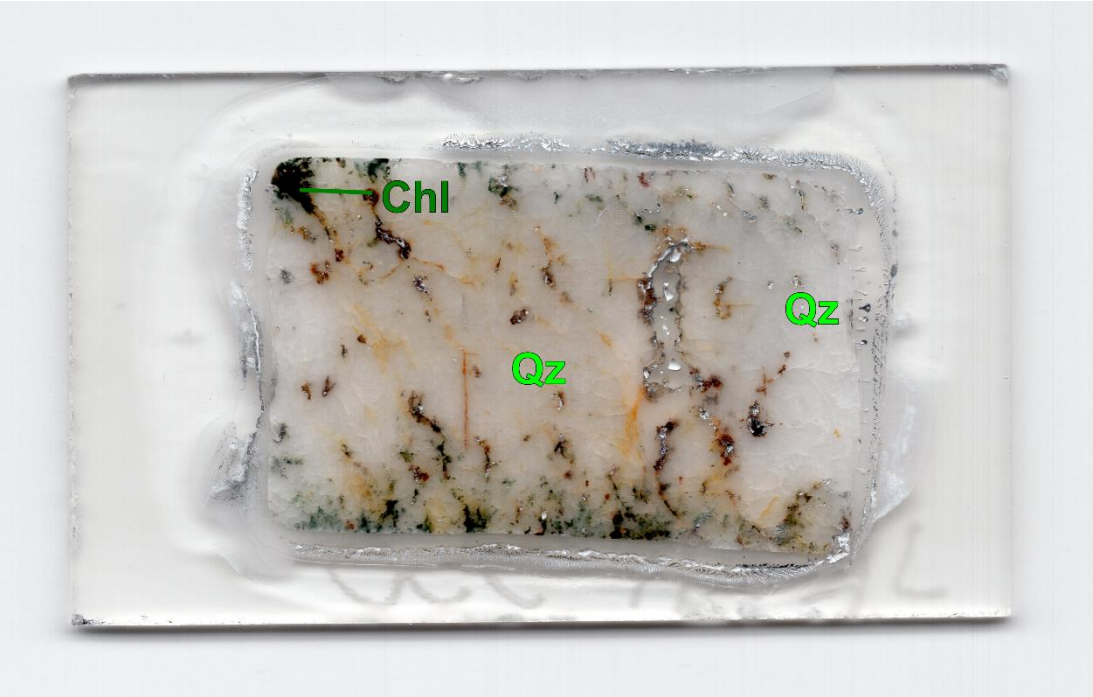


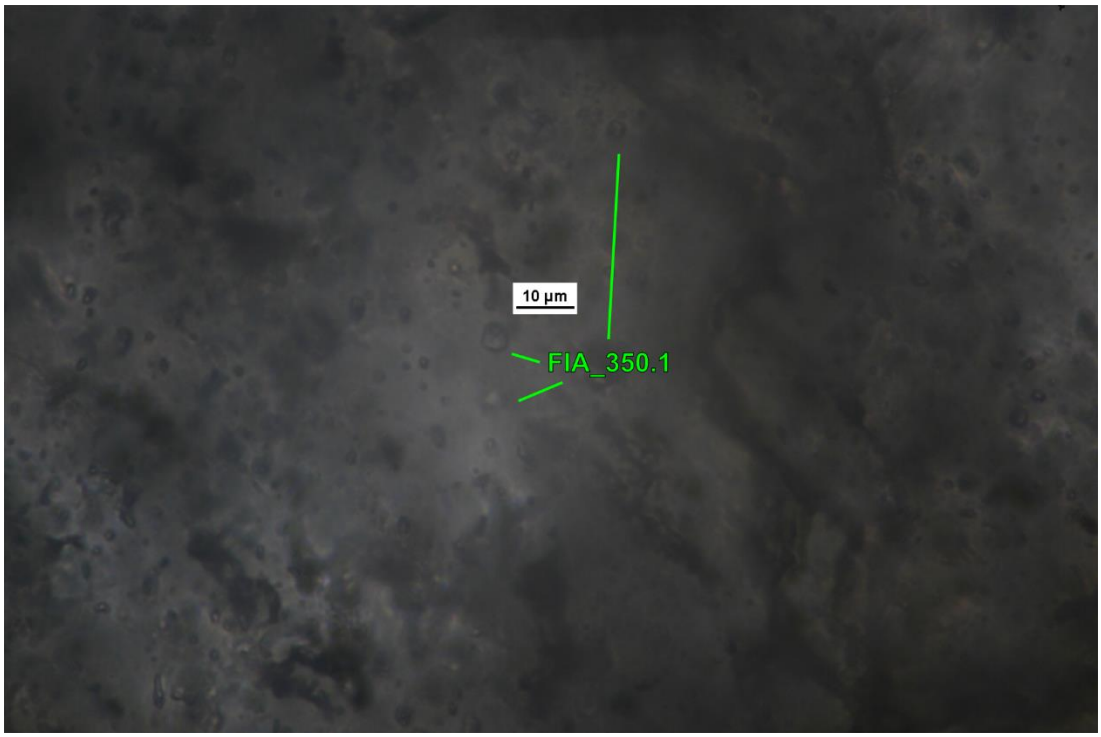

10 µm
FIA_358A.2


FIA_358A.3
10 µm

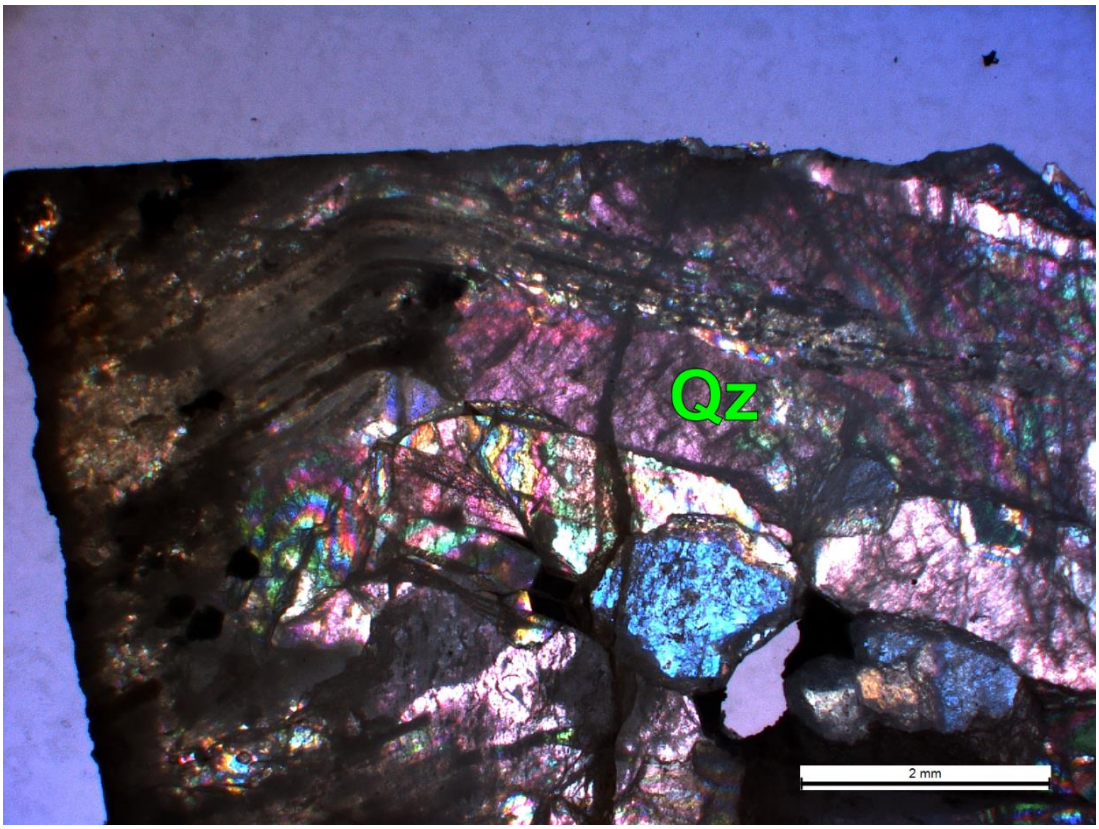

FIA_358A.9
10 µm

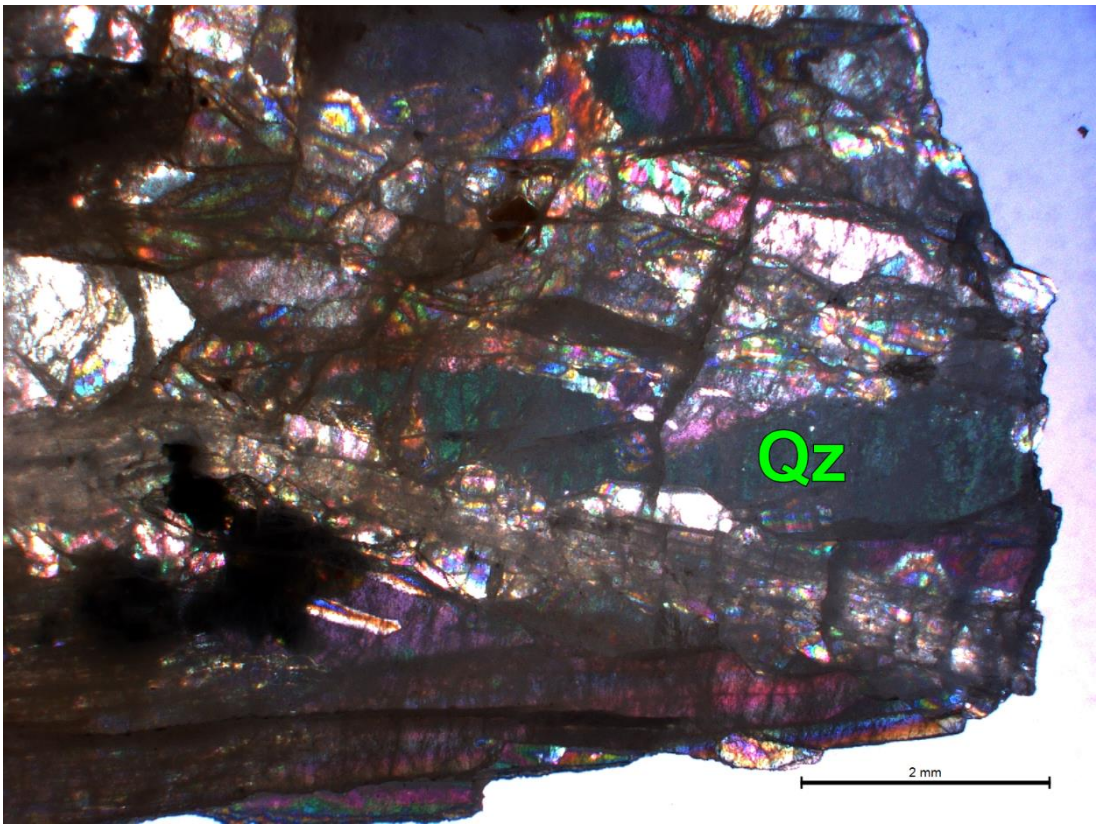
Sample **JL_AH_350** (scanned slide, width of slide 46 mm, transmitted light images):

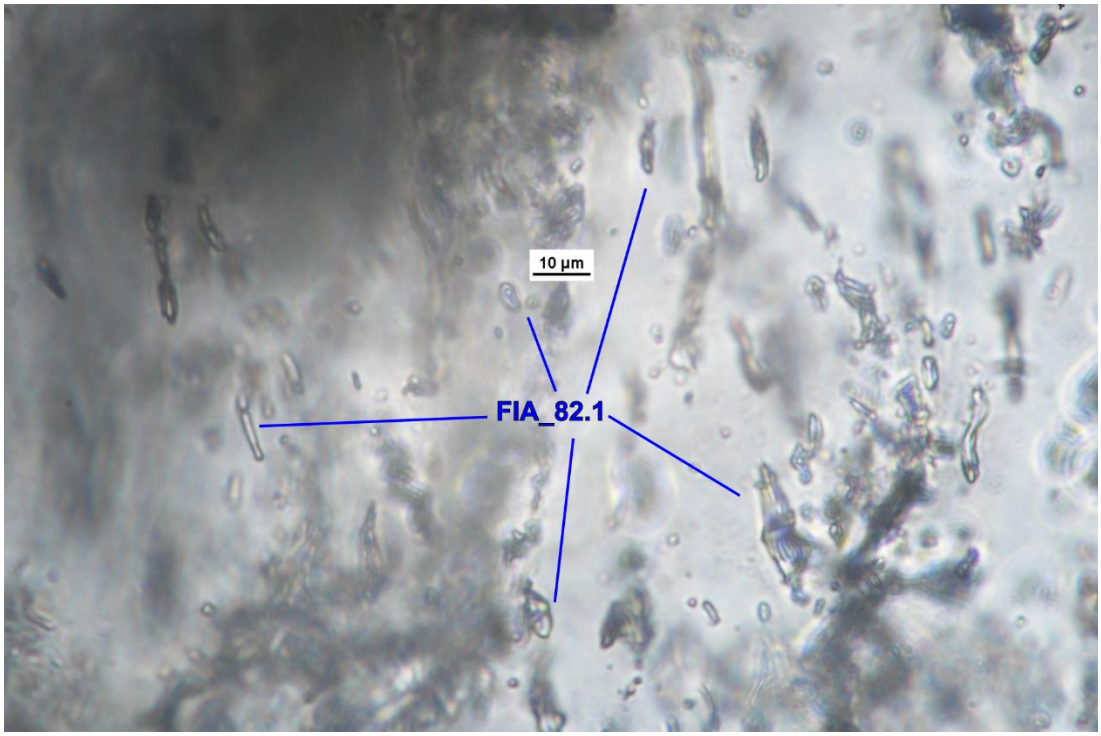


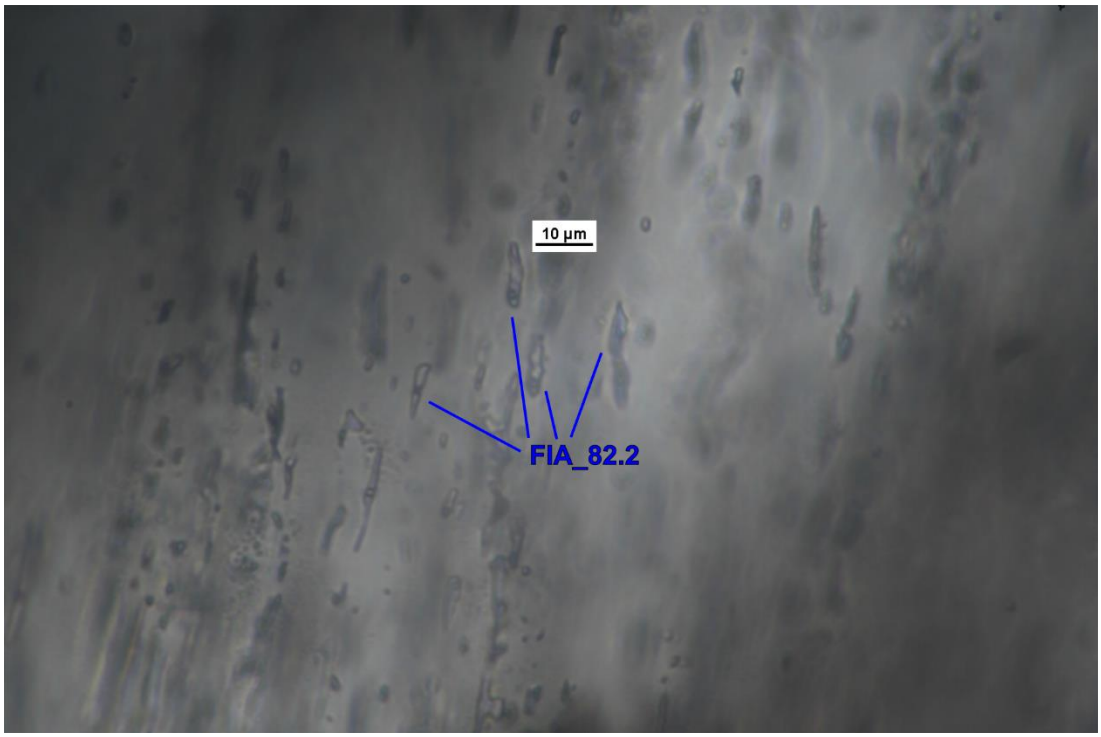


Sample **JL_AH_82** (microscopic images, x pol, and transmitted light images):

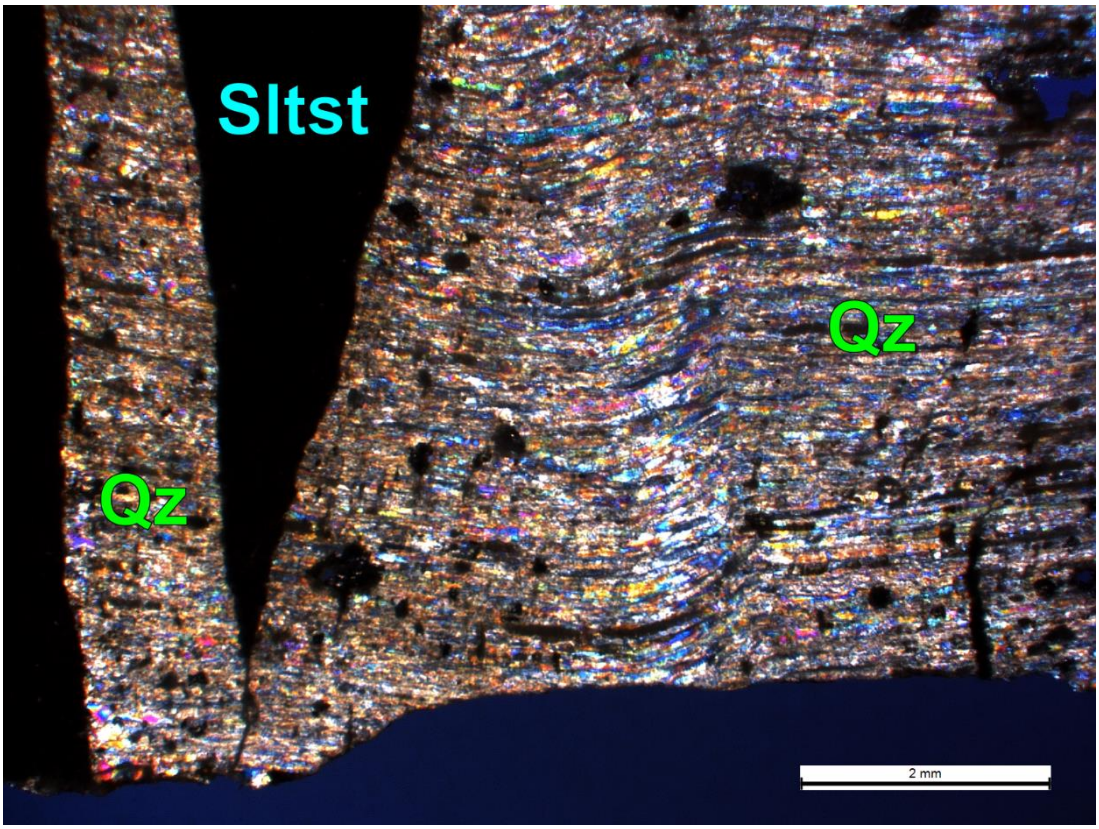


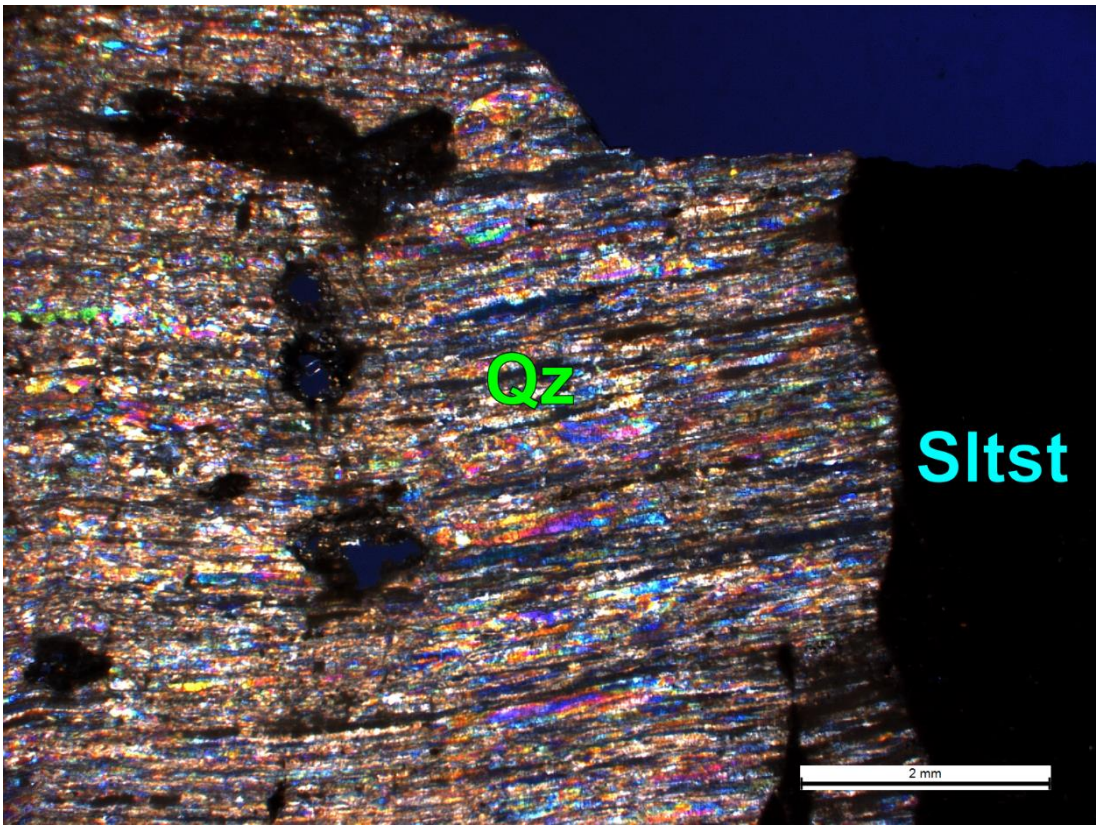


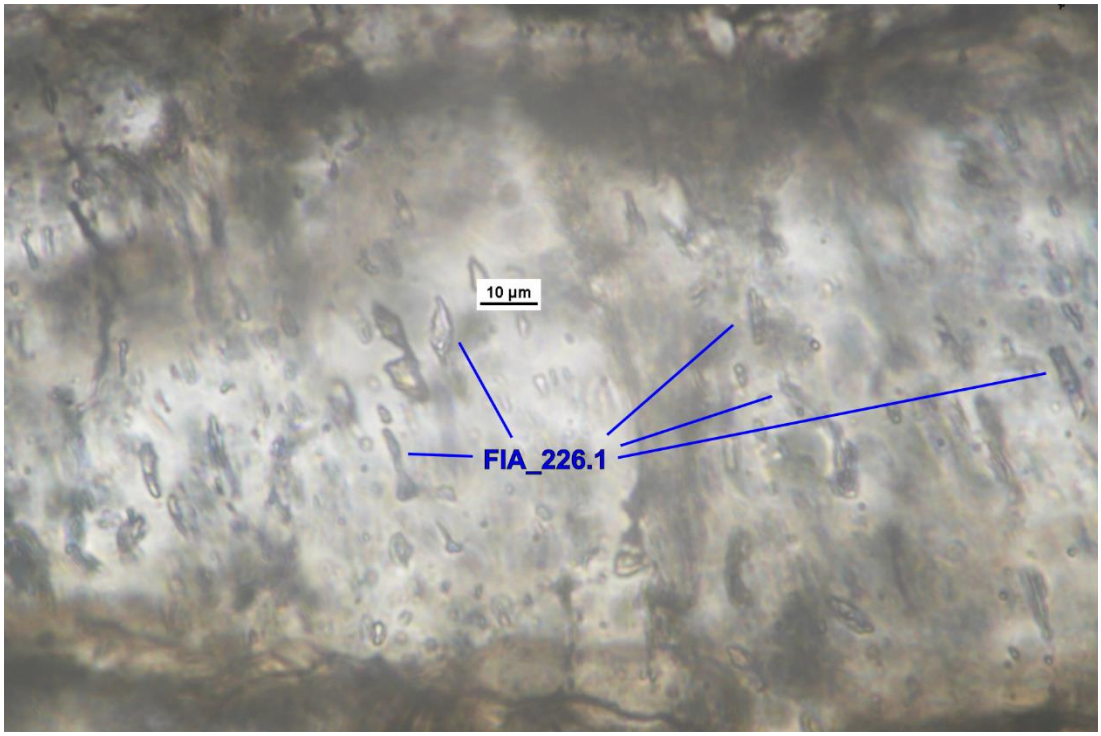

10 µm
FIA_82.1

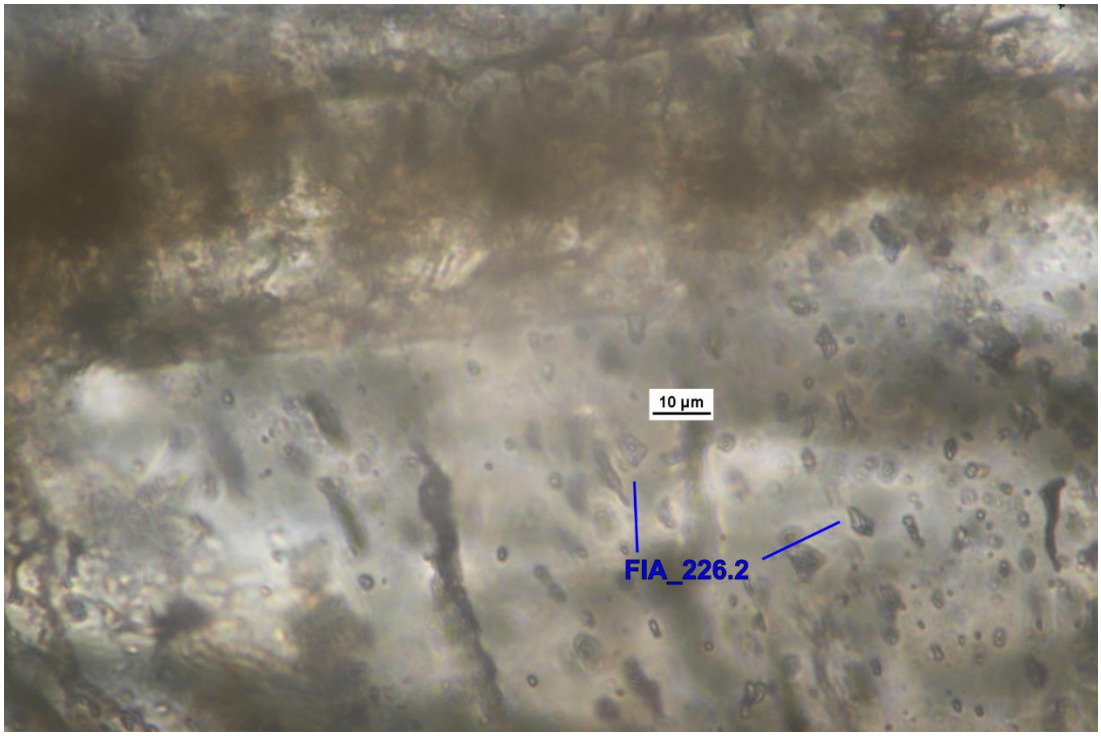

10 µm
FIA_82.2

Sample **JL_AH_226** (microscopic images, x pol, and transmitted light images):

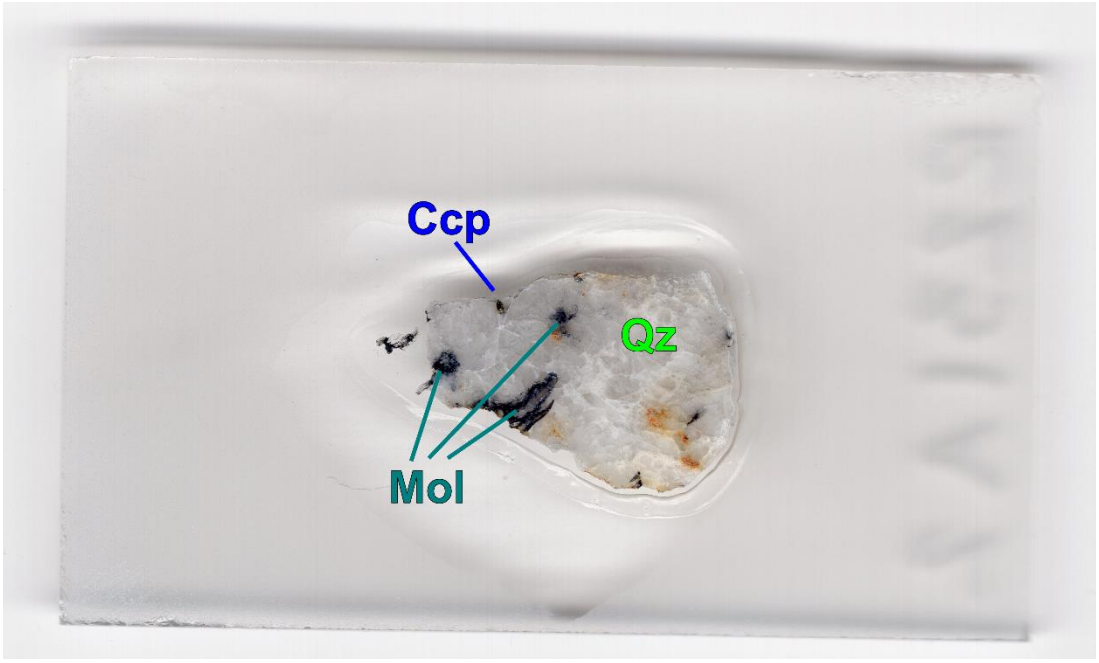


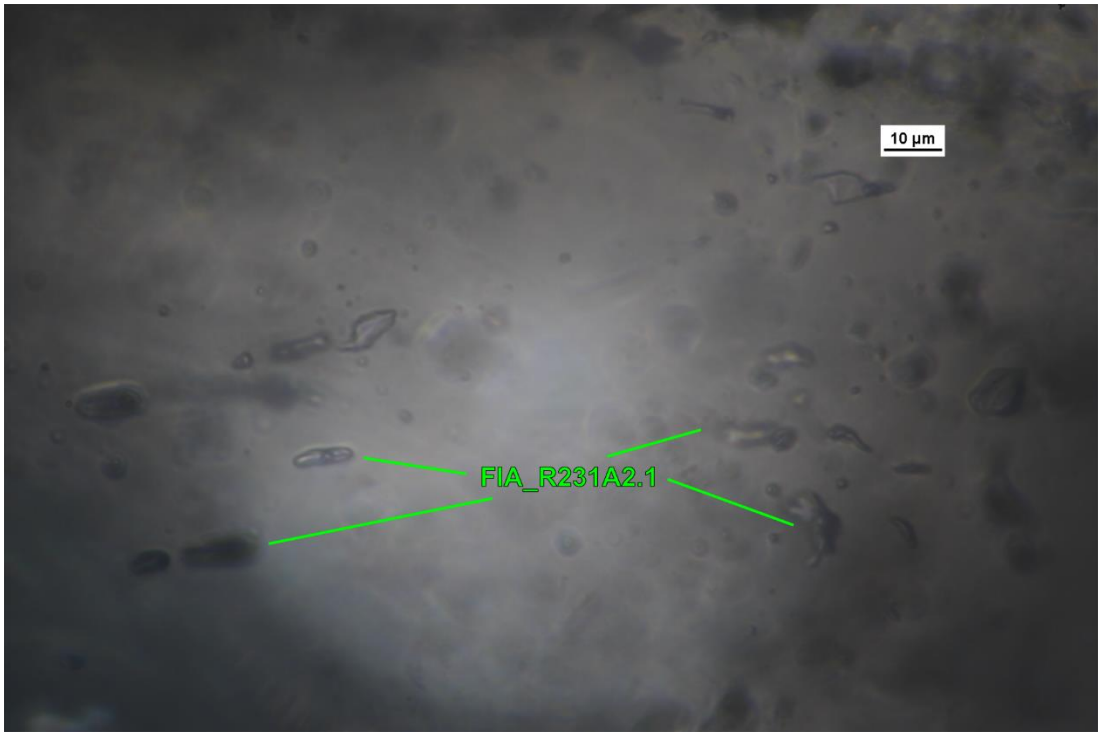


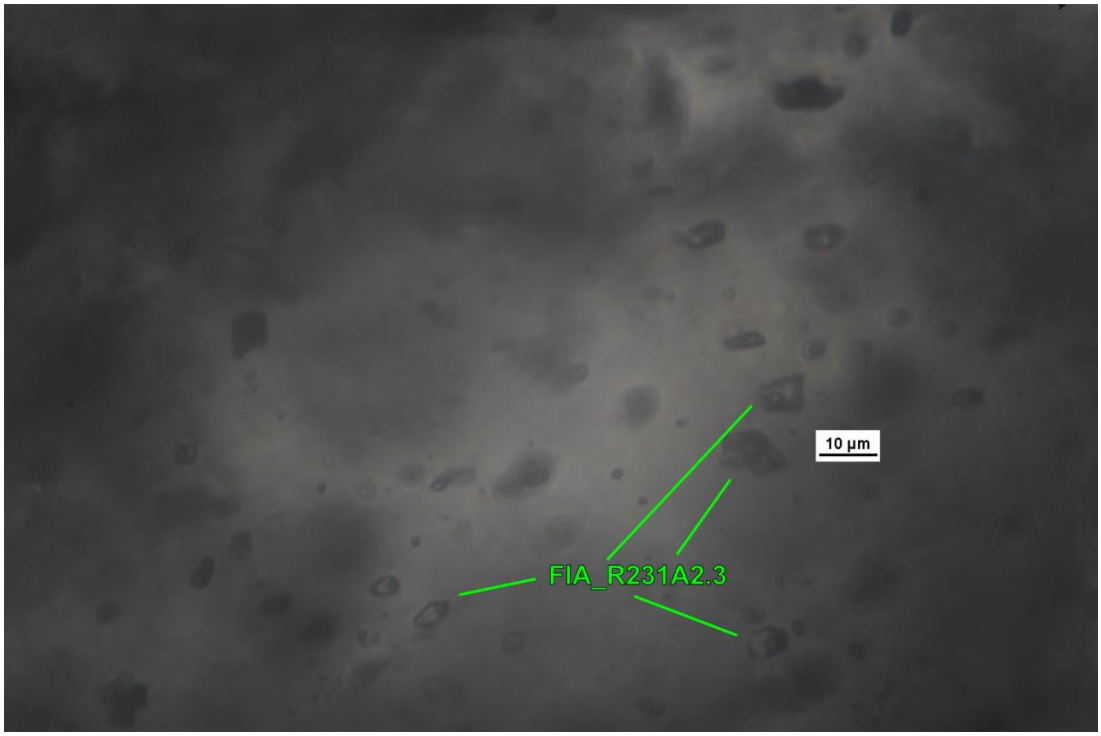

10 µm
FIA_226.1


10 µm
FIA_226.2

Sample **BM.1964,R231** (scanned slide, width of slide 46 mm, transmitted light images):

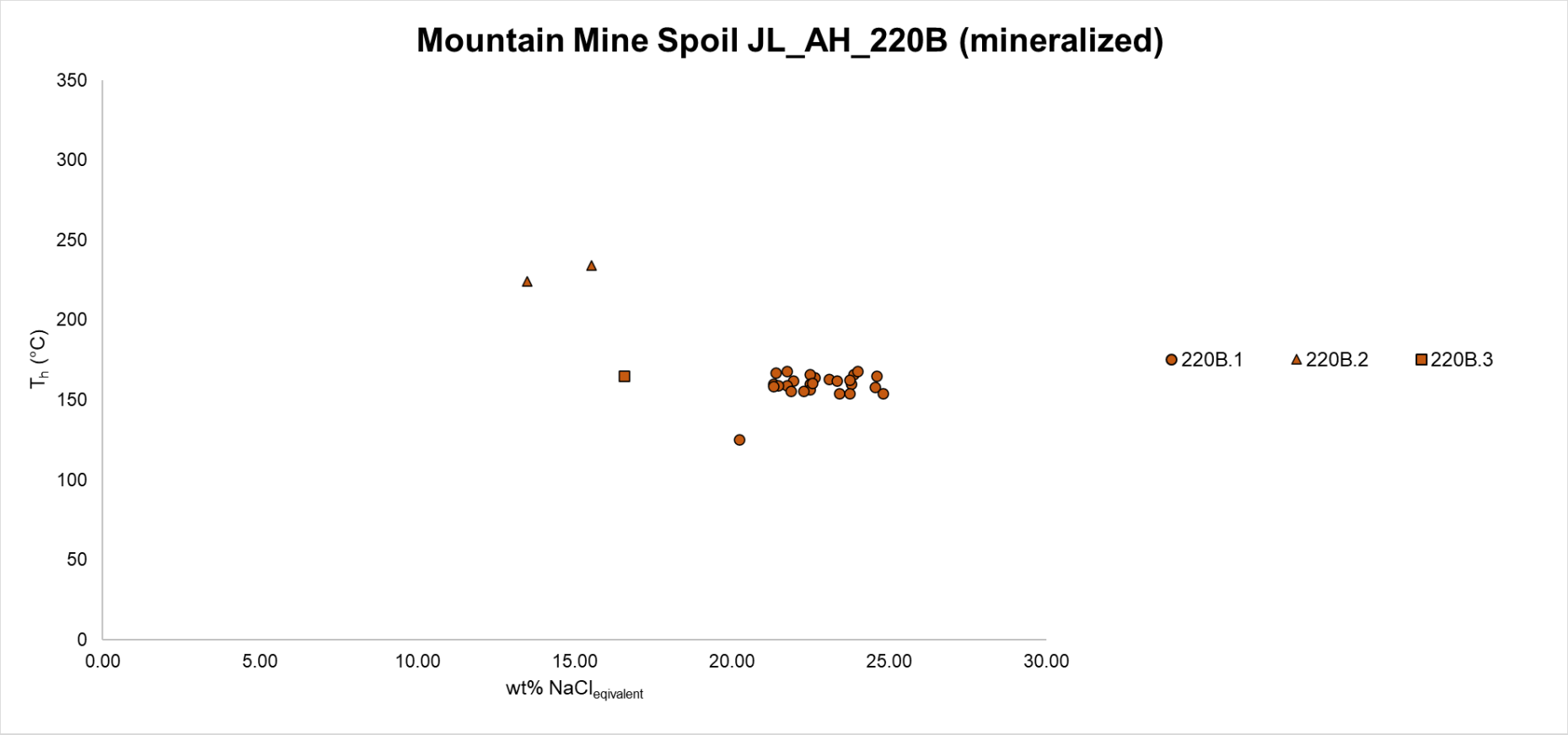


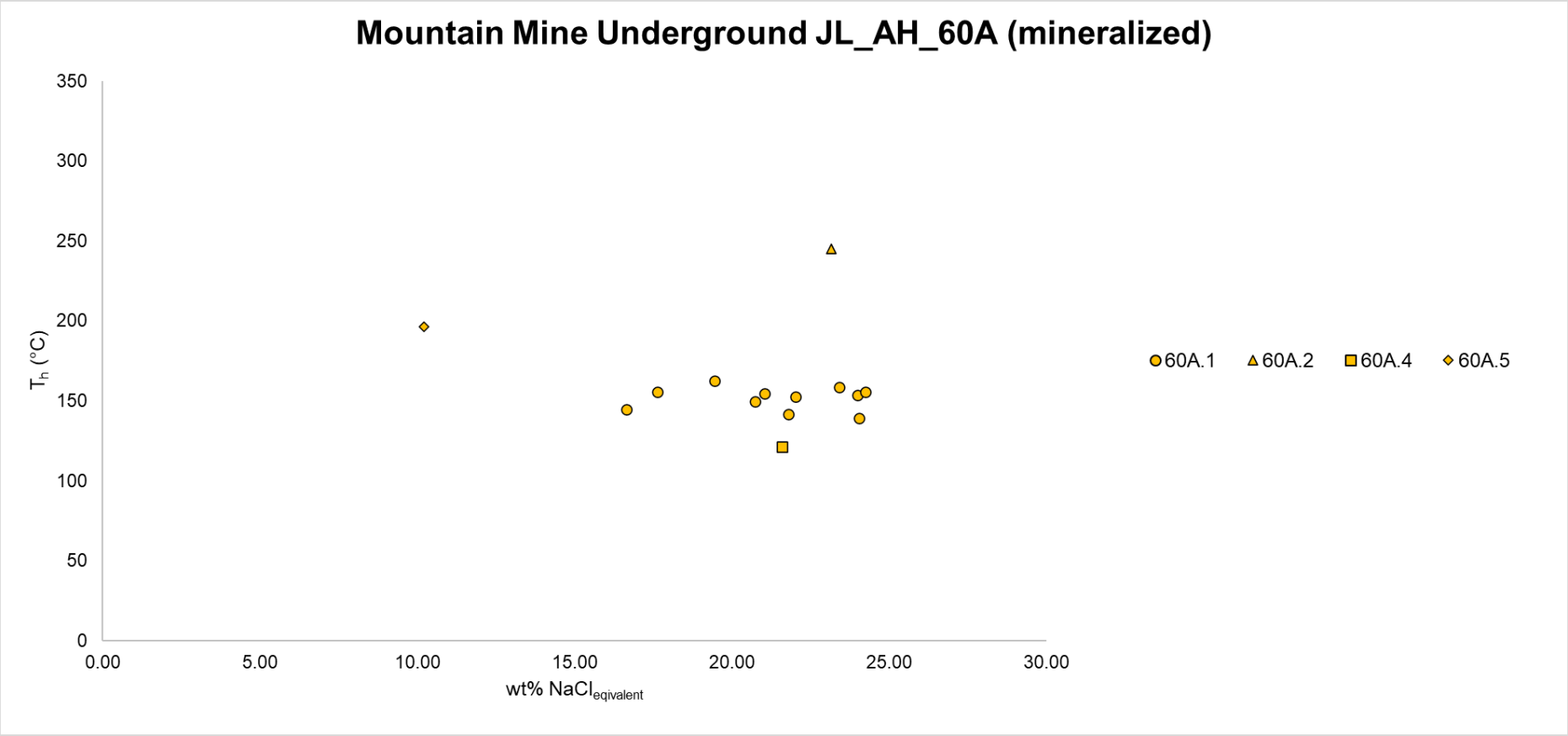


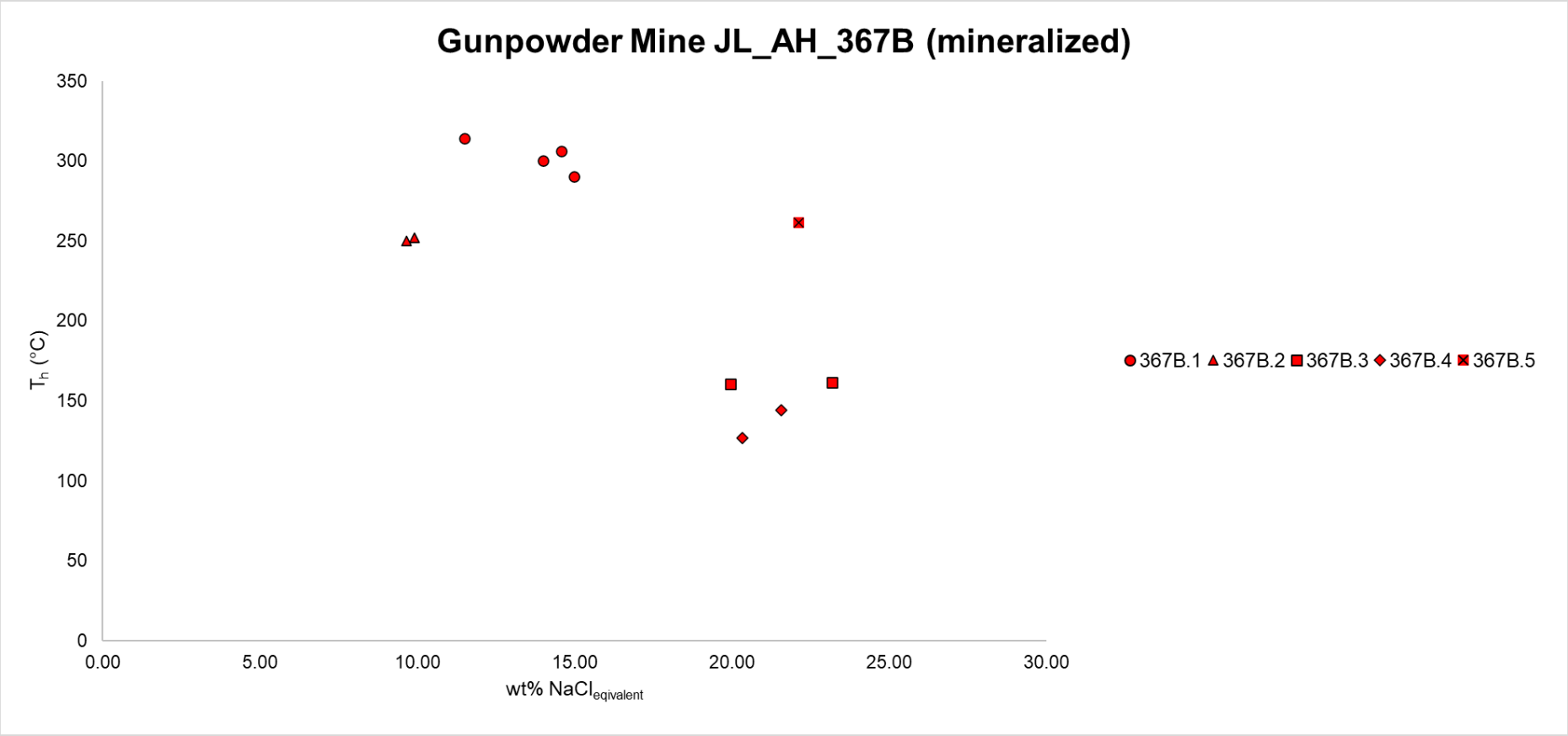

10 µm
FIA_R231A2.3

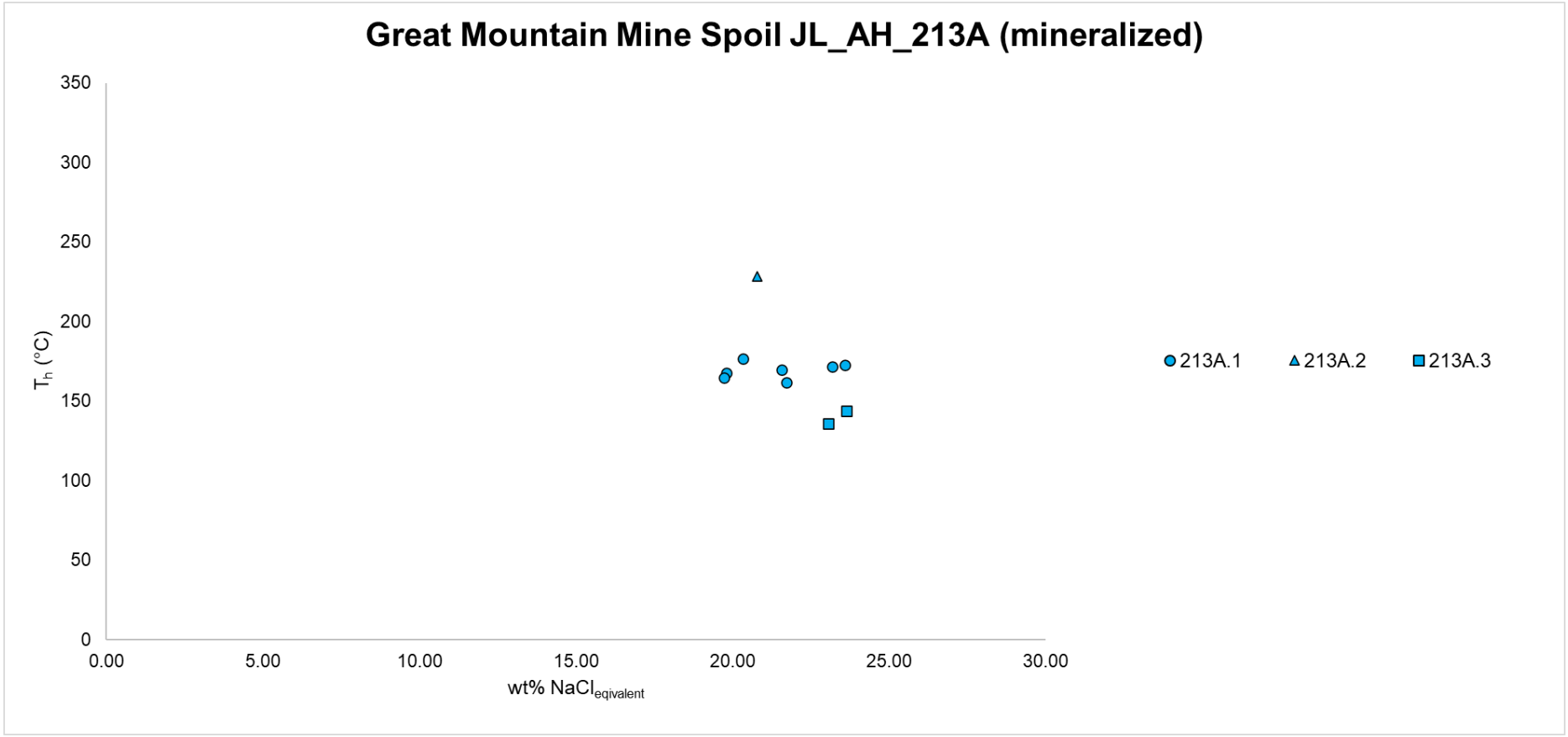
Appendix B.3 (Chapter 3)

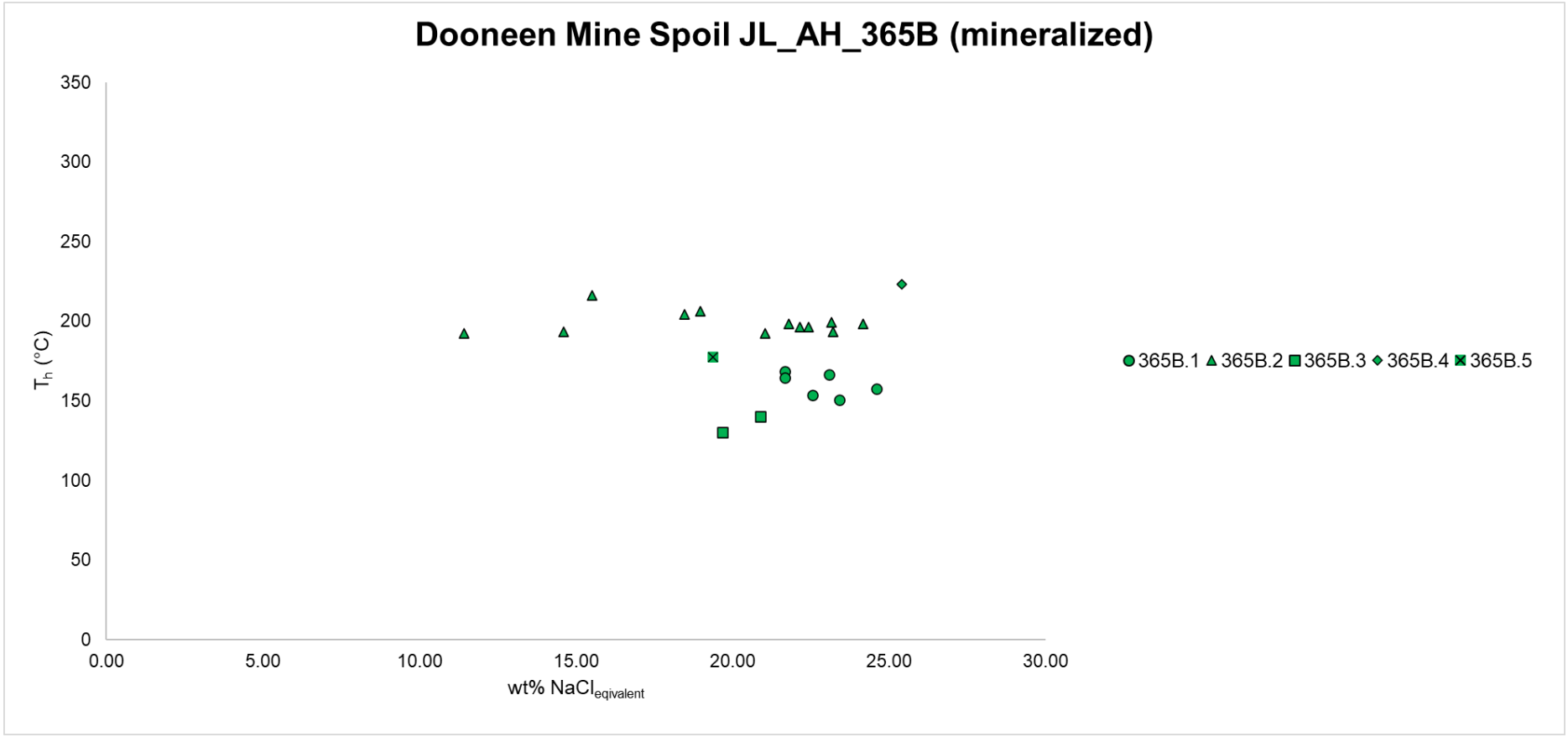
The following graphs show the individual sample plots (salinities wt% $NaCl_{equiv}$ versus homogenisation temperatures T_h (°C)) of the fluid inclusion assemblages (FIA_XXX, Appendix B2) from the Allihies Mining District. See figures 3.11a and 3.11b.

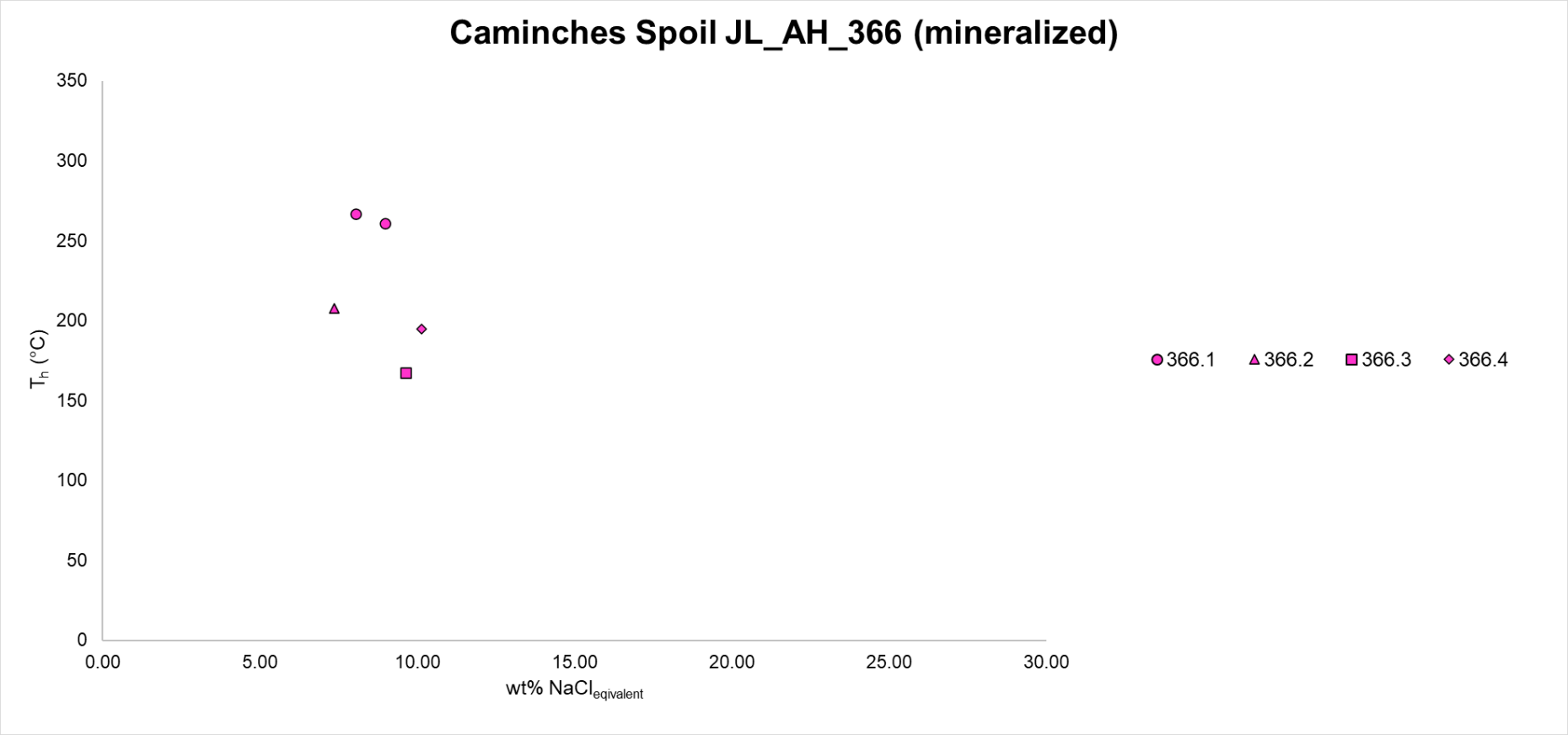

Mountain Mine Spoil JL_AH_220B (mineralized)
350
300
250
200
150
100
50
0
T_h (°C)
0.00
5.00
10.00
15.00
20.00
25.00
30.00
wt% $NaCl_{eqivalent}$
220B.1
220B.2
220B.3

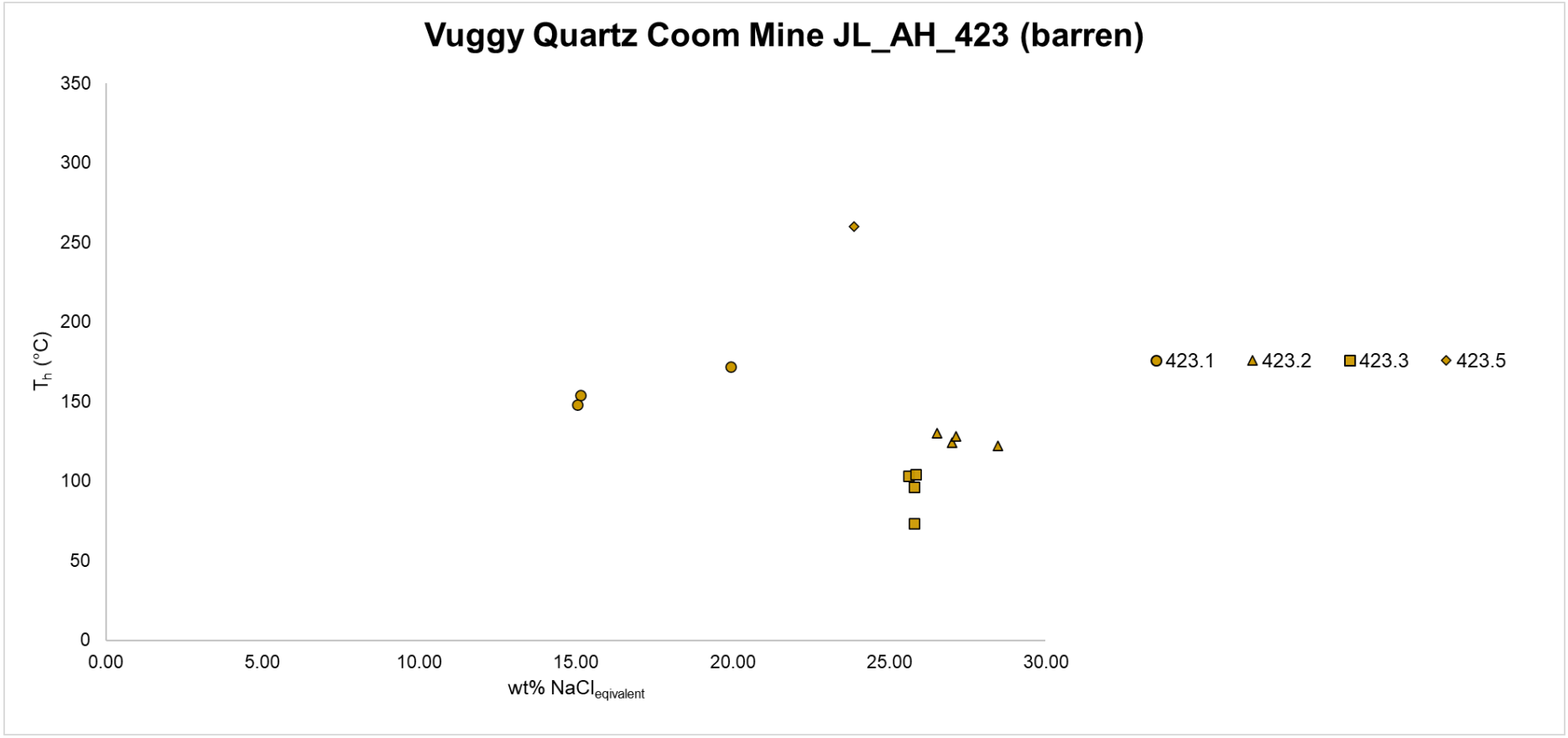

Mountain Mine Underground JL_AH_60A (mineralized)
350
300
250
200
150
100
50
0
T_h (°C)
0.00
5.00
10.00
15.00
20.00
25.00
30.00
wt% $NaCl_{eqivalent}$
60A.1
60A.2
60A.4
60A.5

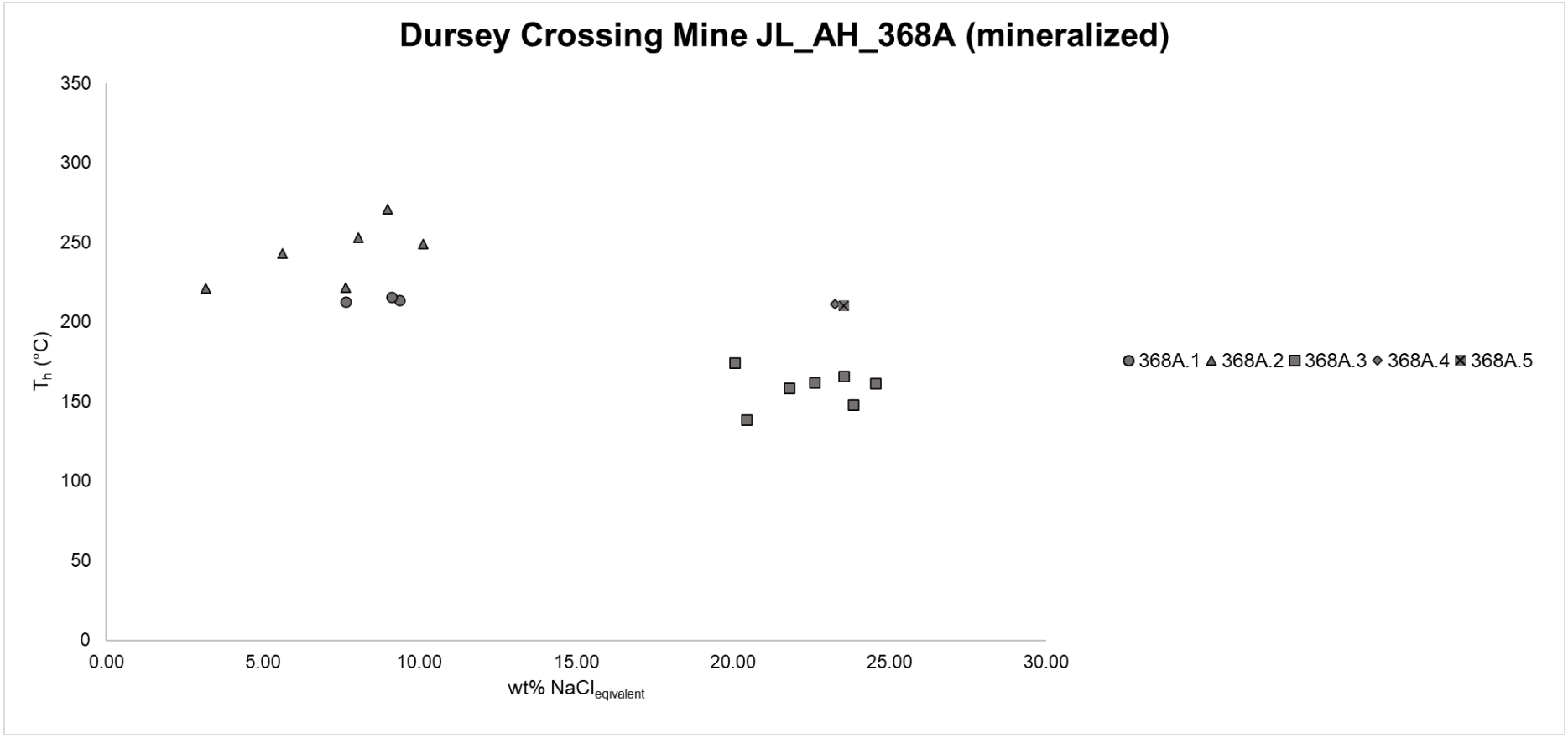

Gunpowder Mine JL_AH_367B (mineralized)
350
300
250
200
150
100
50
0
T_h (°C)
0.00
5.00
10.00
15.00
20.00
25.00
30.00
wt% $NaCl_{eqivalent}$
367B.1
367B.2
367B.3
367B.4
367B.5

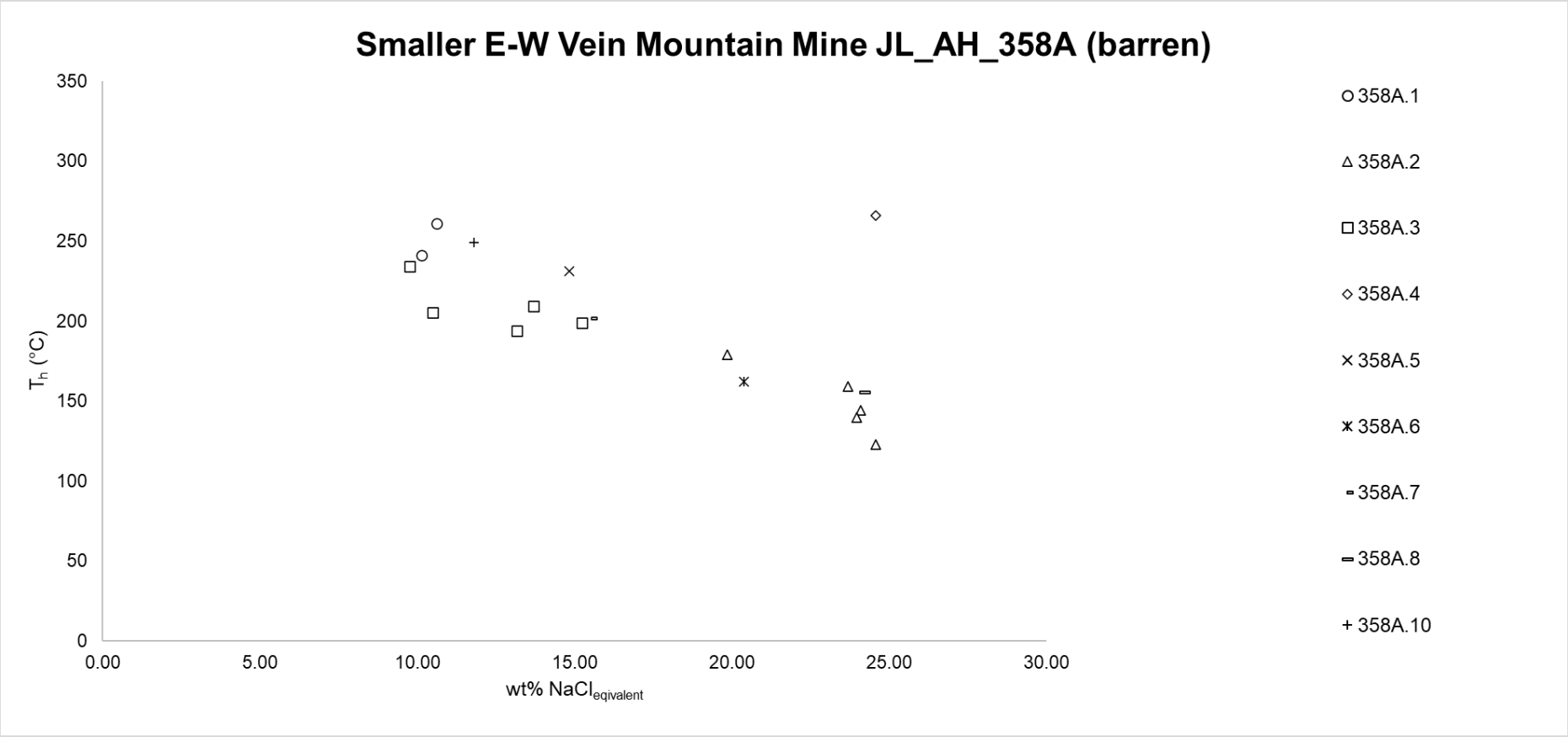

Great Mountain Mine Spoil JL_AH_213A (mineralized)
350
300
250
200
150
100
50
0
T_h (°C)
0.00
5.00
10.00
15.00
20.00
25.00
30.00
wt% $NaCl_{eqivalent}$
213A.1
213A.2
213A.3

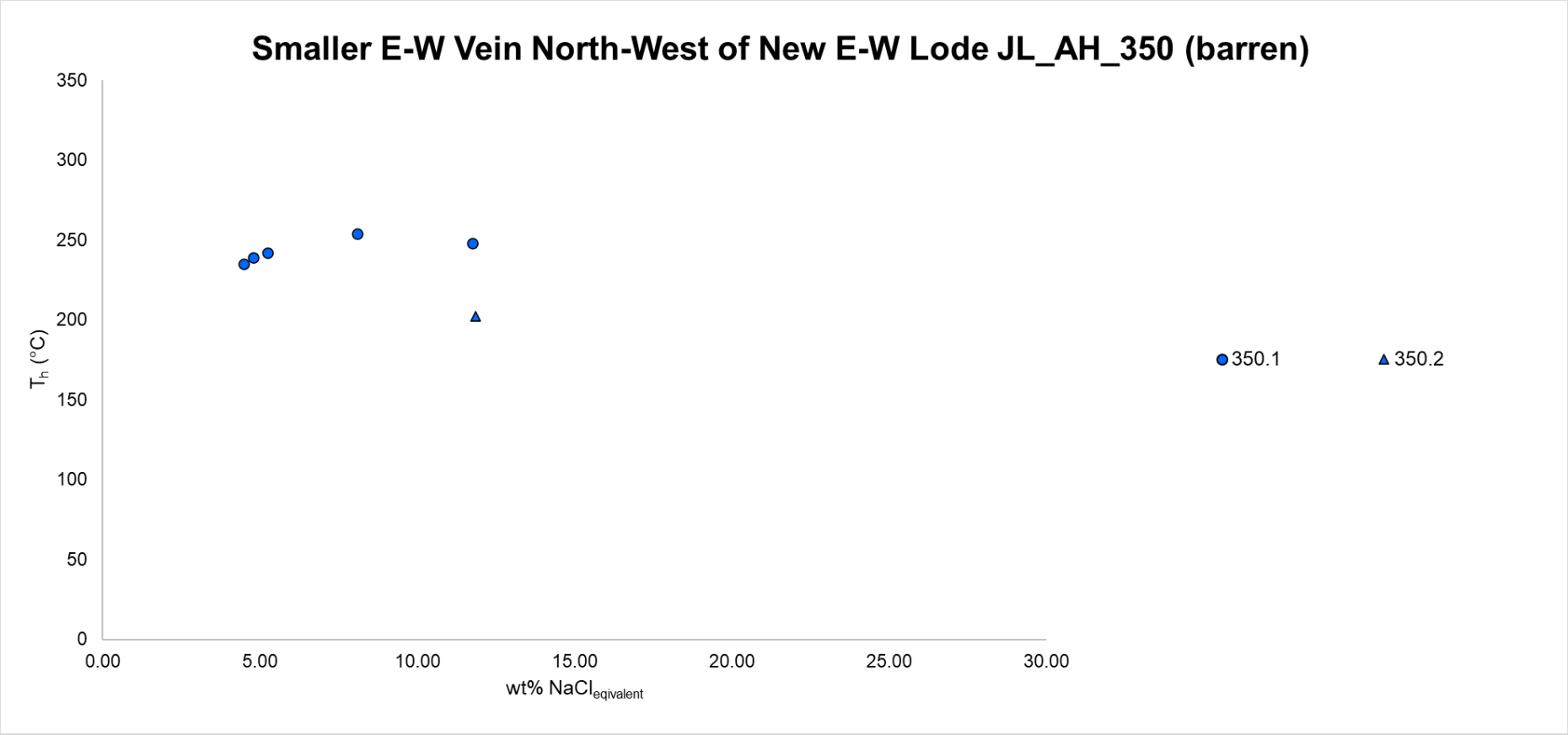

Dooneen Mine Spoil JL_AH_365B (mineralized)
350
300
250
200
150
100
50
0
T_h (°C)
0.00
5.00
10.00
15.00
20.00
25.00
30.00
wt% $NaCl_{eqivalent}$
365B.1
365B.2
365B.3
365B.4
365B.5

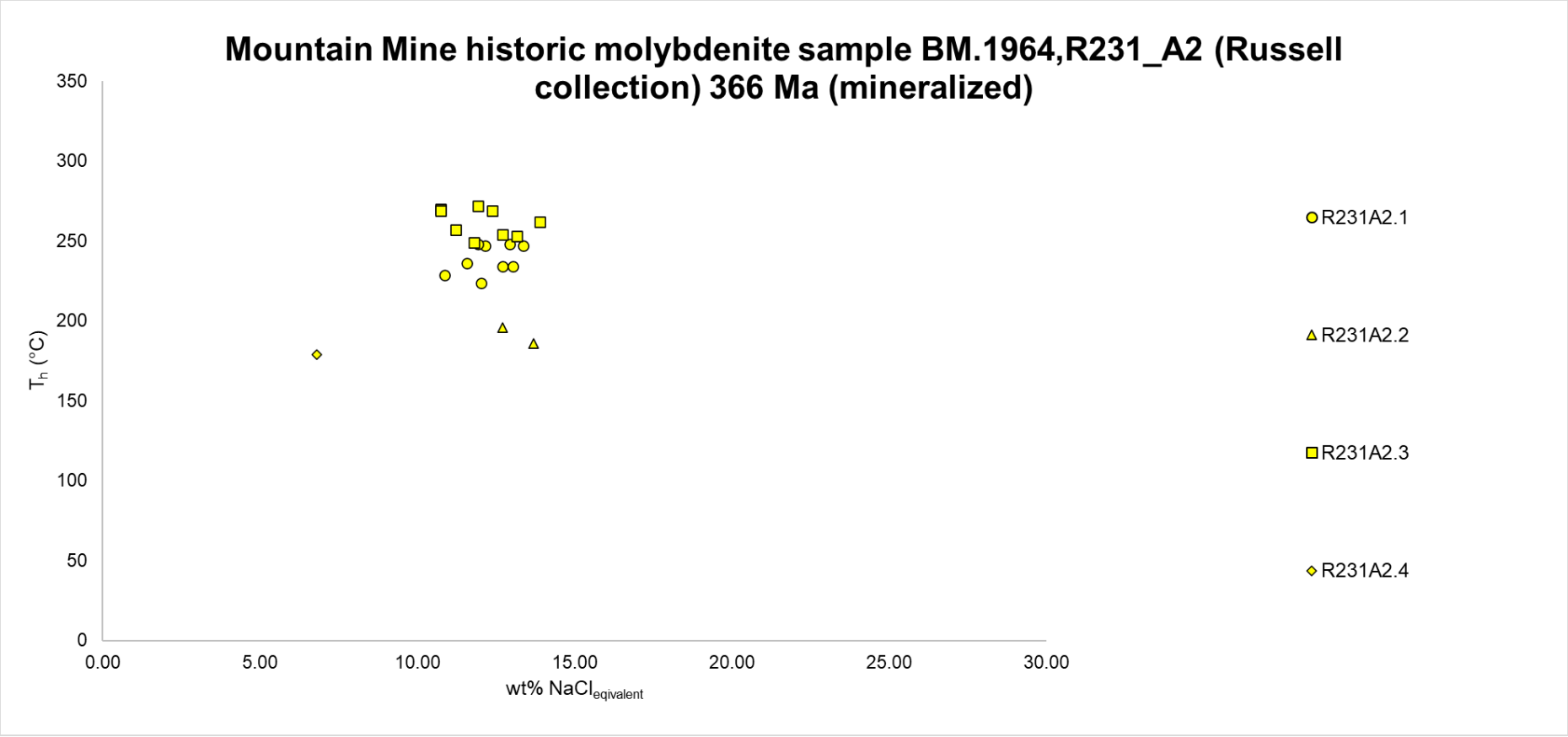

Caminches Spoil JL_AH_366 (mineralized)
350
300
250
200
150
100
50
0
T_h (°C)
0.00
5.00
10.00
15.00
20.00
25.00
30.00
wt% $NaCl_{eqivalent}$
366.1
366.2
366.3
366.4

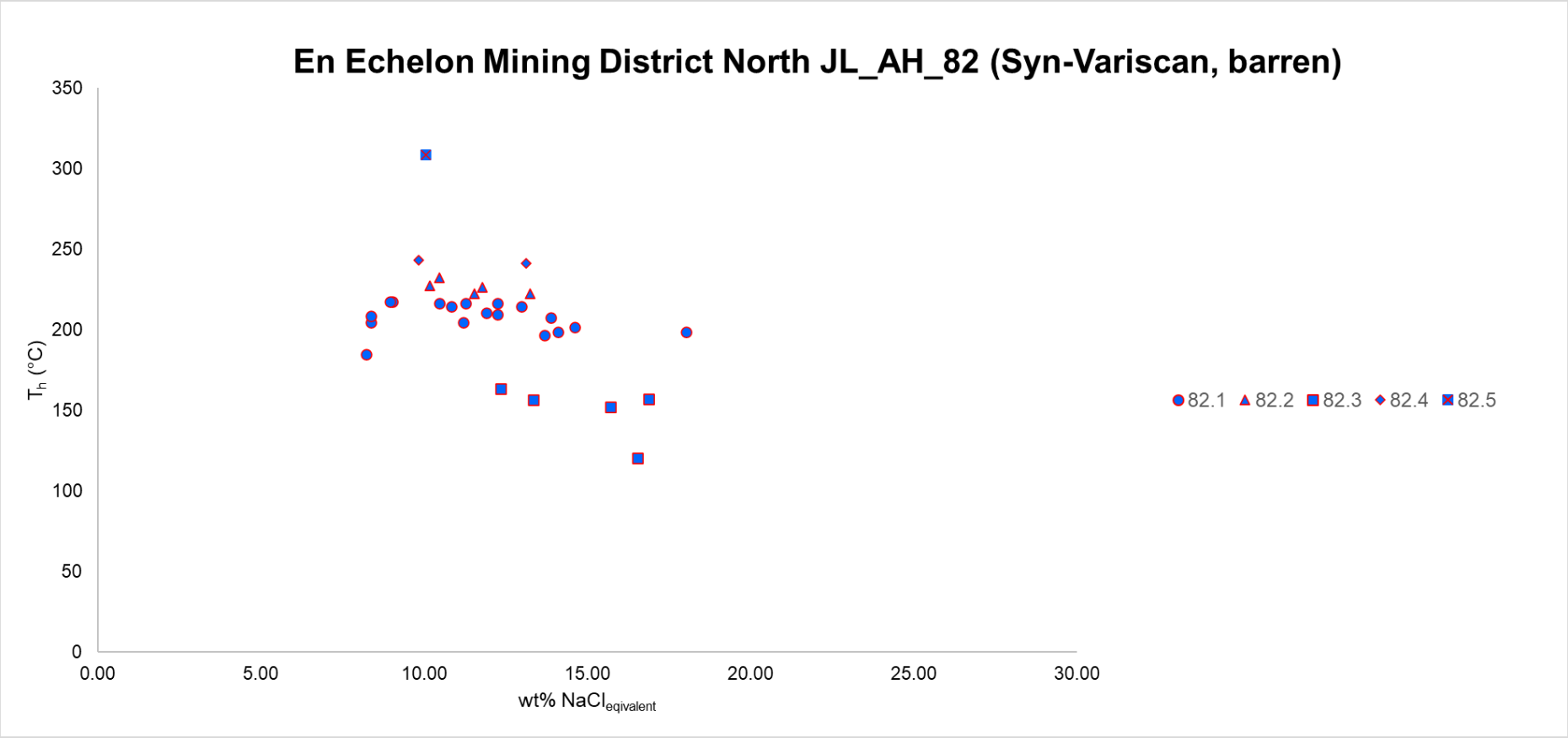

Vuggy Quartz Coom Mine JL_AH_423 (barren)
350
300
250
200
150
100
50
0
T_h (°C)
0.00
5.00
10.00
15.00
20.00
25.00
30.00
wt% $NaCl_{eqivalent}$
423.1
423.2
423.3
423.5

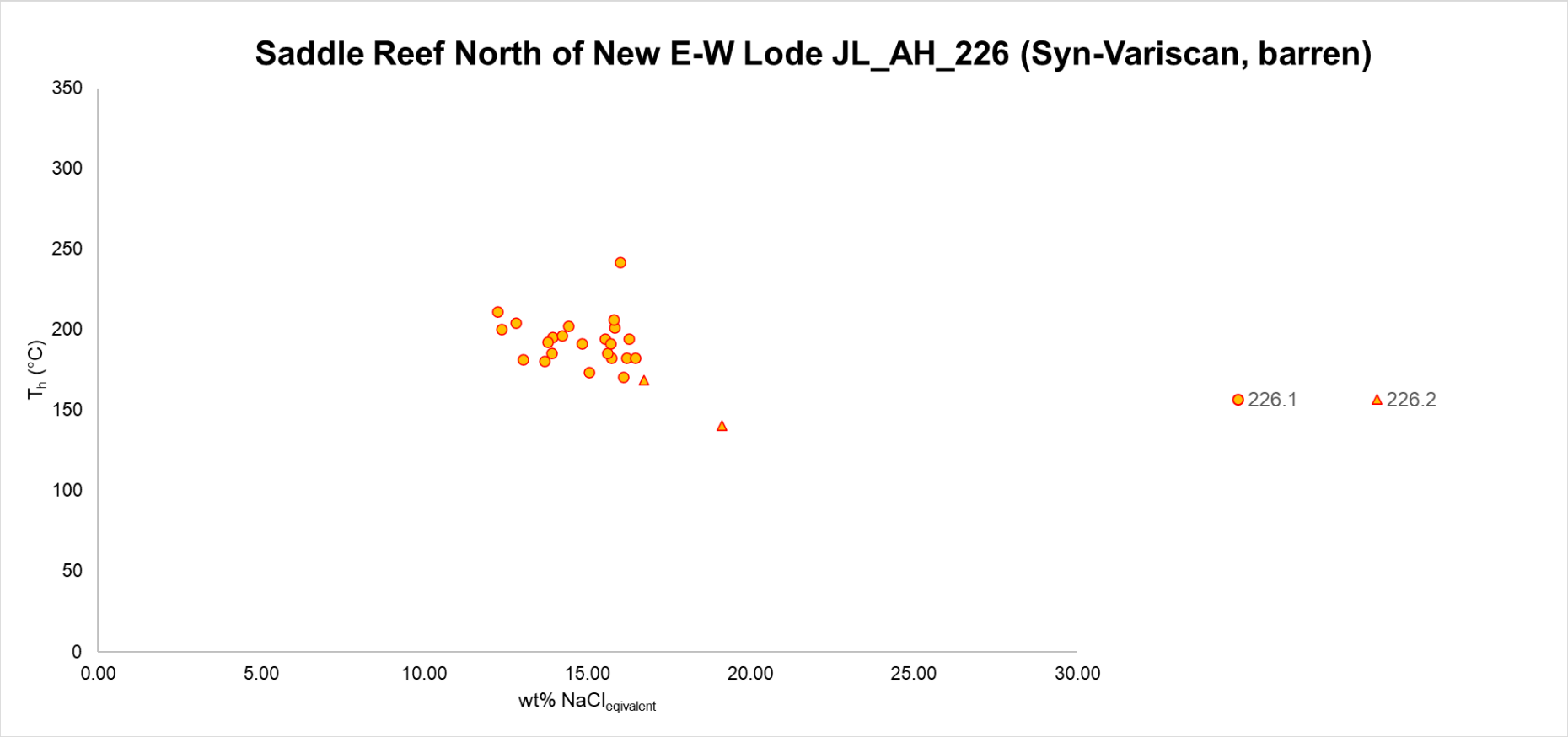

Dursey Crossing Mine JL_AH_368A (mineralized)
350
300
250
200
150
100
50
0
T_h (°C)
0.00
5.00
10.00
15.00
20.00
25.00
30.00
wt% $NaCl_{eqivalent}$
368A.1
368A.2
368A.3
368A.4
368A.5


Smaller E-W Vein Mountain Mine JL_AH_358A (barren)
350
300
250
200
150
100
50
0
T_h (°C)
0.00
5.00
10.00
15.00
20.00
25.00
30.00
wt% $NaCl_{eqivalent}$
358A.1
358A.2
358A.3
358A.4
358A.5
358A.6
358A.7
358A.8
358A.10


Smaller E-W Vein North-West of New E-W Lode JL_AH_350 (barren)
350
300
250
200
150
100
50
0
T_h (°C)
0.00
5.00
10.00
15.00
20.00
25.00
30.00
wt% $NaCl_{eqivalent}$
350.1
350.2


Mountain Mine historic molybdenite sample BM.1964,R231_A2 (Russell collection) 366 Ma (mineralized)
350
300
250
200
150
100
50
0
T_h (°C)
0.00
5.00
10.00
15.00
20.00
25.00
30.00
wt% $NaCl_{eqivalent}$
R231A2.1
R231A2.2
R231A2.3
R231A2.4


En Echelon Mining District North JL_AH_82 (Syn-Variscan, barren)
350
300
250
200
150
100
50
0
T_h (°C)
0.00
5.00
10.00
15.00
20.00
25.00
30.00
wt% $NaCl_{eqivalent}$
82.1
82.2
82.3
82.4
82.5


Saddle Reef North of New E-W Lode JL_AH_226 (Syn-Variscan, barren)
350
300
250
200
150
100
50
0
T_h (°C)
0.00
5.00
10.00
15.00
20.00
25.00
30.00
wt% $NaCl_{eqivalent}$
226.1
226.2

Appendix C (Chapter 3)

Sample locations of the Allihies Copper Mining District (Supplementary material, Lang *et al.* (2020), University College Cork, Ireland):

Geographic Coordinate System:	GCS_WGS_1984
Datum:	D_WGS_1984
Prime Meridian:	Greenwich
Angular Unit:	Degree

Date: 04/09/2019

Sample/Location	Lat (°N)	Long (°E)	Location Name/Description	Comments
JL_AH_60	51.647103	-10.037573	Mountain Mine Underground (E-W Lode)	No GPS underground. The adit entrance is as noted
JL_AH_82	51.652252	-10.034820	En echelon Mining District North (Syn-Variscan)	
JL_AH_213	51.652663	-10.038394	Great Mountain Mine Spoil	
JL_AH_220	51.646068	-10.037864	Mountain Mine Spoil	
JL_AH_226	51.649900	-10.040085	Saddle reef North of New E-W Lode (Syn-Variscan)	
JL_AH_350	51.649310	-10.040410	Smaller E-W vein North-West of New E-W Lode	
JL_AH_358	51.648477	-10.039141	Smaller E-W Vein Mountain Mine	
JL_AH_365	51.648064	-10.055819	Dooneen Mine spoil	
JL_AH_366	51.645713	-10.030508	Caminches Mine spoil	
JL_AH_367	51.647532	-10.036469	Gunpowder Mine (Mountain Mine E-W Lode)	No GPS underground. The adit entrance is as noted
JL_AH_368	51.614517	-10.065739	Dursey Crossing Mine	No GPS underground. The adit entrance is as noted

JL_AH_418	51.649546	-10.035926	North of Mountain Mine E-W Lode	
JL_AH_423	51.645104	-10.027172	Vuggy quartz Coom Mine	
BM.1964,R231	51.646068	-10.037864	Mountain Mine historic molybdenite sample (Russell collection) 366 Ma	No coordinates available, but sample was collected probably close to JL_AH_220 by Sir Arthur Russell (National History Museum London)
Marion Lode	51.650425	-10.040898	Multiple vein generations	
Great Mountain Mine	51.652877	-10.036687	Cleaved vein/lode	
Coom Mine	51.644916	-10.026508	Cataclasis within quartz lode	
Coom Mine	51.644991	-10.026458	Folded vein	
Cleaved small vein	51.649670	-10.035958	Small E-W Veins North of Mountain Mine	

Appendix D (Chapter 3)

The following figures show supporting petrographical images from representative samples of the Allihies Mining District. Please refer to Fig. 3.1 and Fig. 3.2, as well as Appendix C for sample localities.

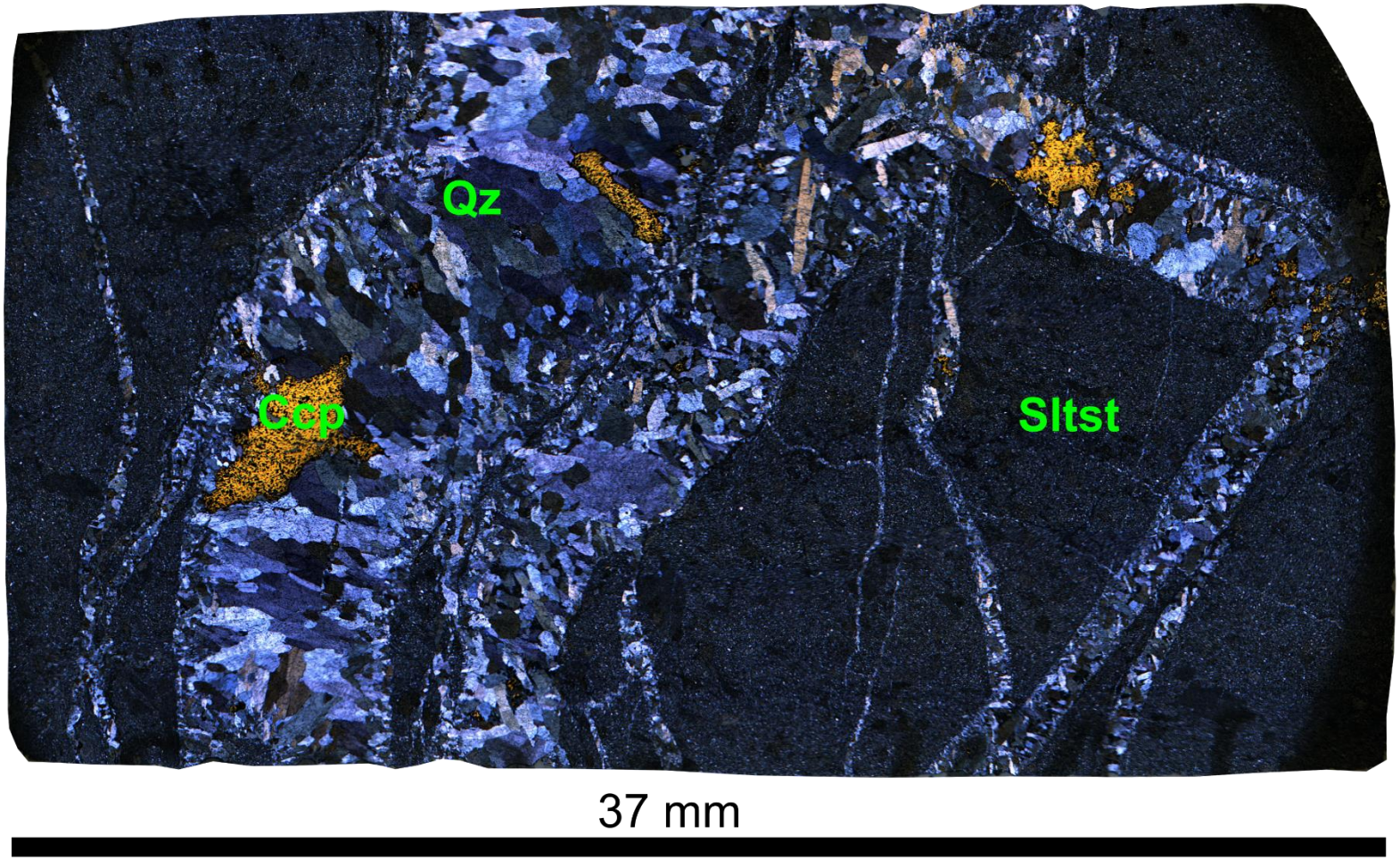


Fig. D.1) Sample JL_AH_60 Mountain Mine Underground: *Microphotograph of mineralized quartz (Qz) veins within fine grained siltstone (Sltst) show syntaxial elongate blocky crystals with cogenetic chalcopyrite (Ccp) (xpl, transmitted and reflected light).*

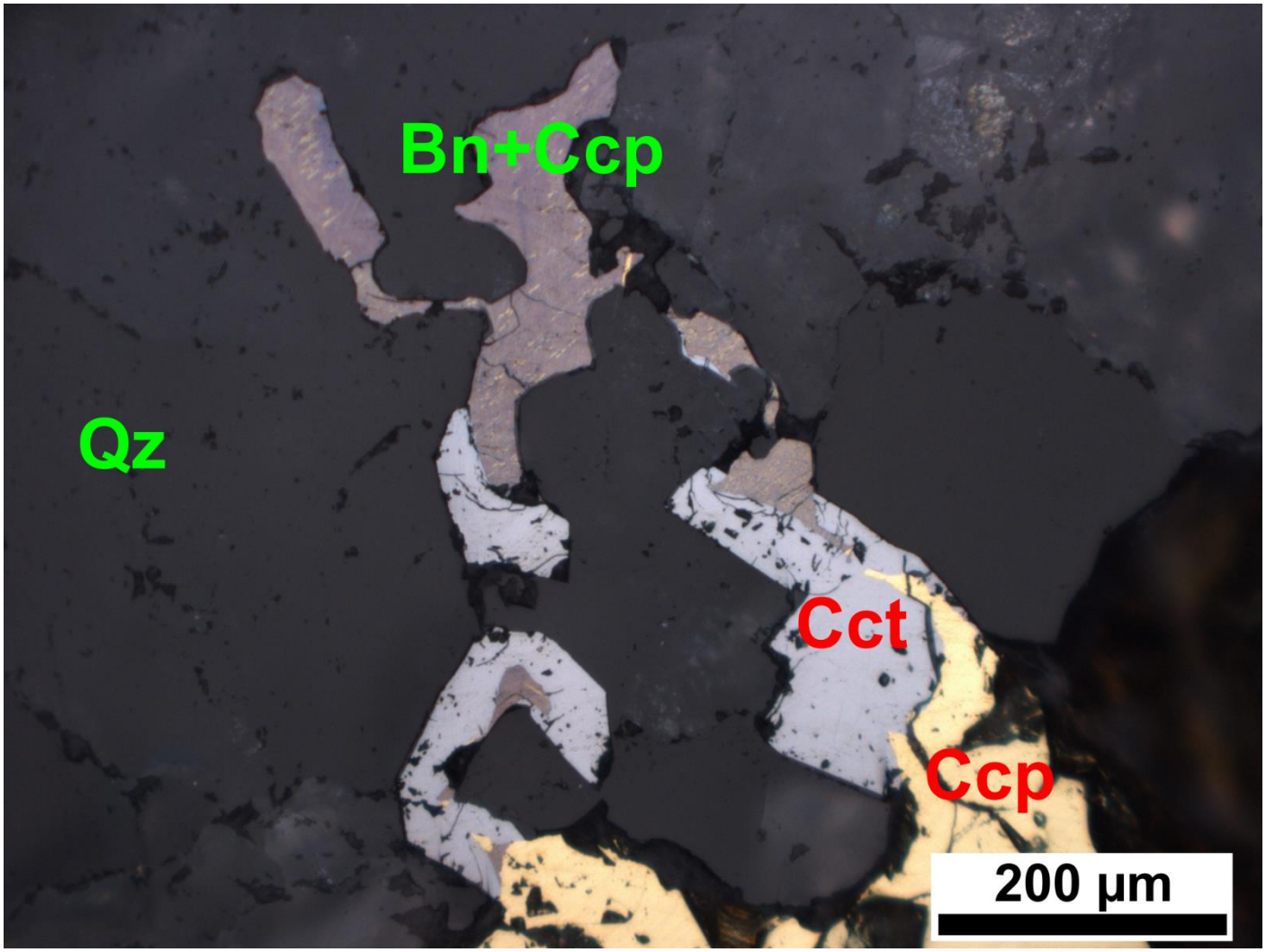


Fig. D.2) Sample JL_AH_220 Mountain Mine Spoil: *Microphotograph of quartz vein (Qz) with cogenetic chalcopyrite (Ccp) and bornite (Bn) with chalcopyrite exsolution lamellae. Both sulphides are surrounded by chalcocite (Cct) (ppl, reflected light).*

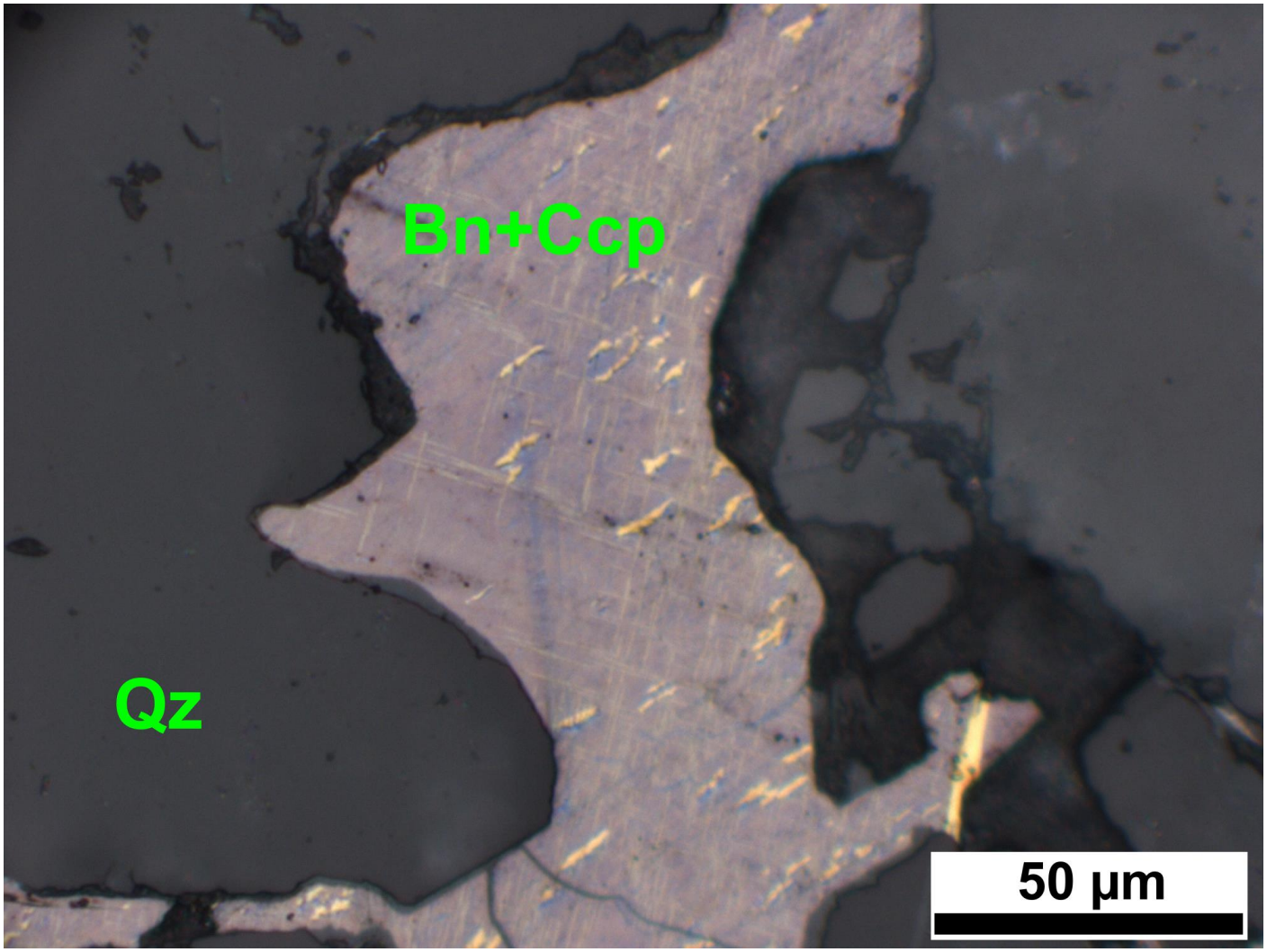


Fig. D.3) Sample JL_AH_220 Mountain Mine Spoil: *Microphotograph, magnification of quartz vein (Qz) with bornite (Bn) with chalcopyrite (Ccp) exsolution lamellae. (ppl, reflected light).*

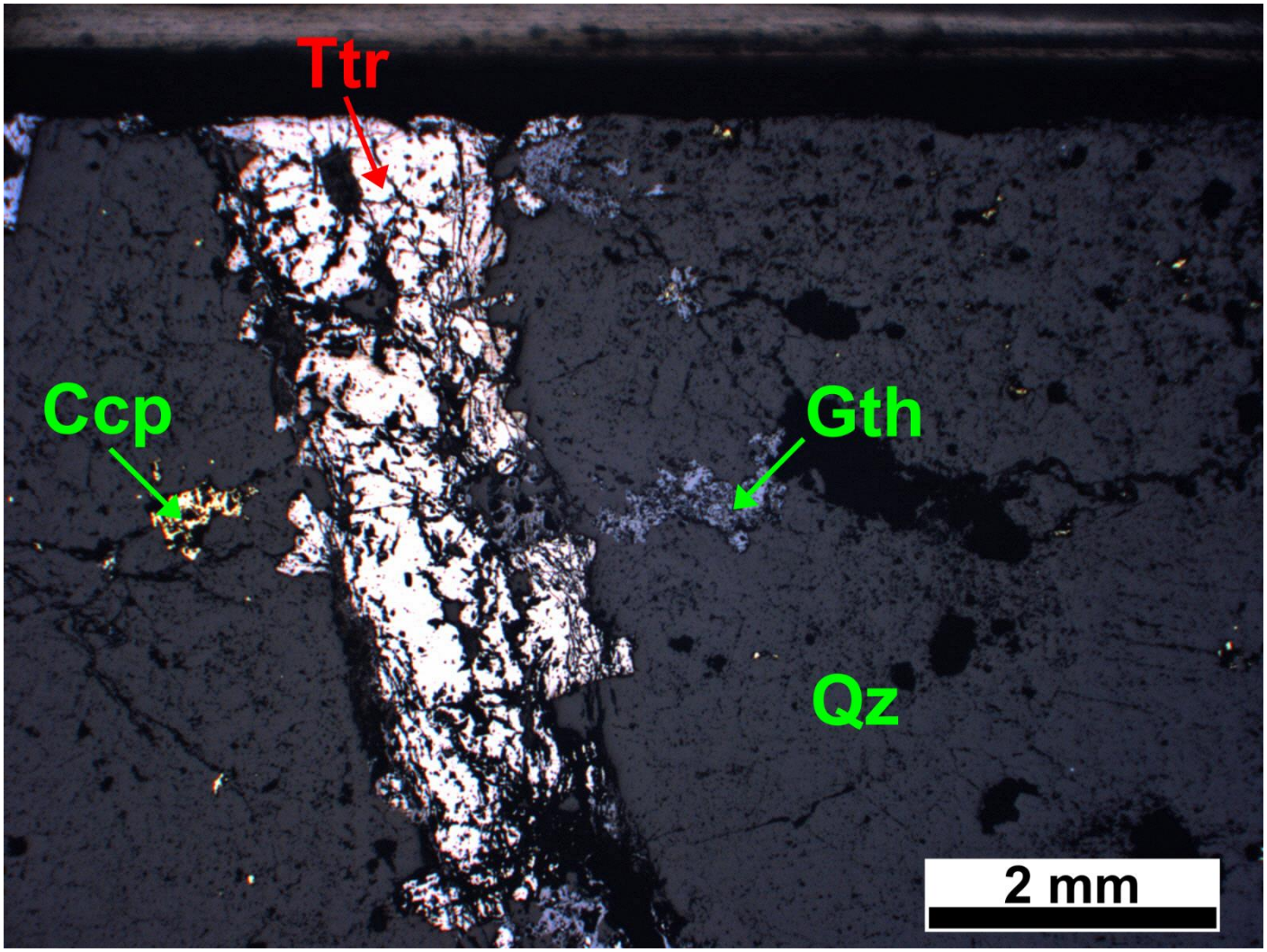


Fig. D.4) Sample JL_AH_367 Mountain Mine - Gunpowder Mine:
A tetrahedrite/tennantite veinlet (Ttr) is cross-cutting a quartz vein (Qz) with chalcopyrite (Ccp) and tetrahedrite/tennantite (Ttr). Rims of goethite (Gth) occur near the sulphides (ppl, reflected light).

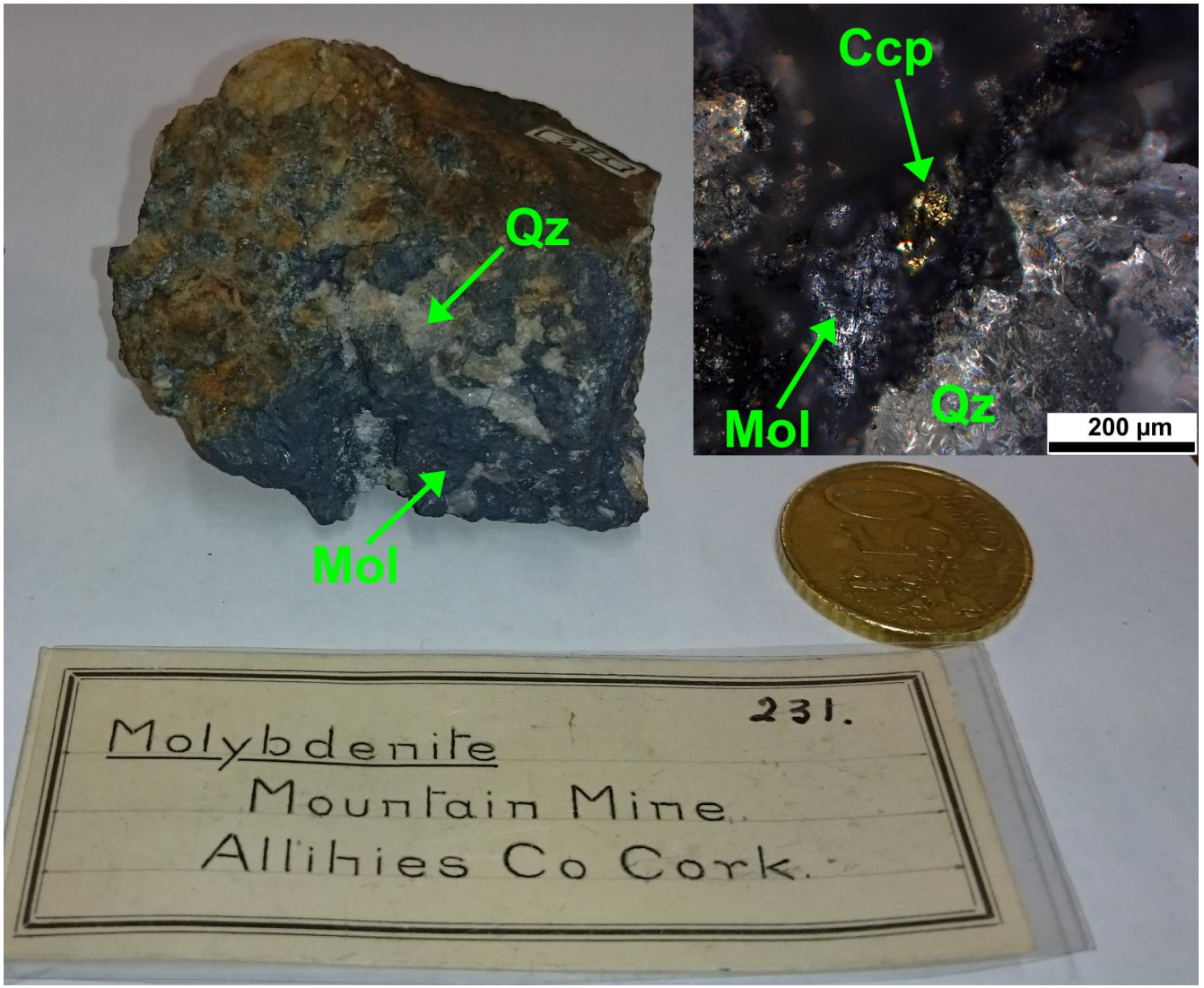


Fig. D.5) Sample BM.1964,R231 Mountain Mine:
Historic quartz (Qz) vein with molybdenite (Mol). The sample was collected by Sir Arthur Russell in 1918 (BM.1964,R231; National History Museum of London). The smaller microscopic image (top right) shows the syngenetic intergrowth of molybdenite (Mol) with chalcopyrite (Ccp) within the quartz (Qz) vein.

Appendix E.1 (Chapter 4)

Fluid inclusions measurements of selected locations and historic copper mines from West Cork. Locations are as shown in Fig. 4.3 and Appendix F:

Fluid Inclusion Measurements West Cork, SW Ireland

12/12/2021

pressure estimate 6.7km with 2.7g/cm3 (after Meere and Banks, 1997)

about 1800 bar

Standardised with CO_2 Standard (Camperio): T_m = -56.6°C and doubly distilled H_2O Standard (Leoben): T_m = 0.0°C and T_h = 374.0°C

Sample	Chip	FI Number	T_{ice} (°C)	$T_{first\ melt}$ (°C)	T_m (°C)	T_h (°C)	T_m (standardised) (°C)	T_h (standardised) (°C)	$T_{first\ melt}$ (standardised) (°C)	Fluid Inclusion Assemblages (FIA)	diameter in µm	phases	estimated volume of vapour phase in vol. %	primary or secondary inclusion	wt% $NaCl_{eativalent}$ (calculated with Steele-MacInnis *et al.*, 2012)	$T_{trapped}$ (6.7 km depth/1800 bar); calculated with Steele-MacInnis (2012), after Meere and Banks (1997)	comment	location
JL_CH_518	2	2.1	-36	-24.4	-11.9	152	-11.5	150	-23.8	518.1	5	L+V	1	primary	15.43	233	mineralized	Crookhaven Mine mineralized Qtz vein Purple Lode
JL_CH_518	2	2.2	-36	-22.9	-9.9	134	-9.5	133	-22.3	518.1	3	L+V	1	primary	13.38	212	mineralized	Crookhaven Mine mineralized Qtz vein Purple Lode
JL_CH_518	2	2.3	-38	-36.1	-13.8	190	-13.3	188	-35.4	518.3	6	L+V	2	primary	17.20	280	mineralized	Crookhaven Mine mineralized Qtz vein Purple Lode
JL_CH_518	3	3.1	-34	-23.4	-9.2	224	-8.8	222	-22.8	518.2	6	L+V	0.5	primary	12.61	331	mineralized	Crookhaven Mine mineralized

																		Qtz vein Purple Lode
JL_CH_518	4	4.1	-35	-22.1	-9.7	235	-9.3	232	-21.5	518.4	8	L+V	2	primary	13.16	345	mineralized	Crookhaven Mine mineralized Qtz vein Purple Lode
JL_CH_518	4	4.2	-35	-21.2	-8.5	257	-8.1	254	-20.6	518.2	6	L+V	0.5	primary	11.82	378	mineralized	Crookhaven Mine mineralized Qtz vein Purple Lode
JL_CH_518	5	5.1	-38	-20.9	-7.2	151	-6.8	149	-20.3	518.1	8	L+V	1	primary	10.26	238	mineralized	Crookhaven Mine mineralized Qtz vein Purple Lode
JL_CH_518	6	6.1	-41	-21.7	-9.0	162	-8.6	160	-21.1	518.1	7	L+V	1	primary	12.39	249	mineralized	Crookhaven Mine mineralized Qtz vein Purple Lode
JL_CH_518	6	6.2	-38	-20.9	-8.3	135	-7.9	134	-20.3	518.1	9	L+V	1	primary	11.58	216	mineralized	Crookhaven Mine mineralized Qtz vein Purple Lode
JL_CH_518	6	6.3	-40	-21.5	-6.8	137	-6.4	136	-20.9	518.1	8	L+V	1	primary	9.76	221	mineralized	Crookhaven Mine mineralized Qtz vein Purple Lode
JL_CH_518	6	6.4	-42		-8.0	145	-7.6	143	0.3	518.1	7	L+V	0.5	primary	11.23	229	mineralized	Crookhaven Mine mineralized Qtz vein Purple Lode
JL_CH_518	6	6.5	-38	-22.3	-7.4	142	-7.0	141	-21.7	518.1	9	L+V	0.5	primary	10.50	227	mineralized	Crookhaven Mine mineralized Qtz vein Purple Lode
JL_GV_512	1	1.1	-39	-25.9	-8.8	325	-8.4	321	-25.3	512.1	7	L+V	15	primary	12.16	479	mineralized	Gortavallig Mine mineralized Qtz vein
JL_GV_512	1	1.2	-41	-24.2	-8.5	310	-8.1	306	-23.6	512.1	5	L+V	15	primary	11.82	457	mineralized	Gortavallig Mine mineralized Qtz vein

JL_GV_512	1	1.3	-40	-23.7	-7.4	326	-7.0	322	-23.1	512.1	7	L+V	10	primary	10.50	485	mineralized	Gortavallig Mine mineralized Qtz vein
JL_GV_512	2	2.1	-39	-20.2	-4.9	234	-4.5	231	-19.7	512.2	7	L+V	5	primary	7.23	353	mineralized	Gortavallig Mine mineralized Qtz vein
JL_GV_512	2	2.2	-40	-11.4	-6.2	243	-5.8	240	-11.0	512.2	7	L+V	5	primary	8.99	363	mineralized	Gortavallig Mine mineralized Qtz vein
JL_GV_512	2	2.3	-34	-15.9	-5.3	259	-4.9	256	-15.4	512.2	7	L+V	5	primary	7.78	388	mineralized	Gortavallig Mine mineralized Qtz vein
JL_GV_512	2	2.4	-33		-7.4	253	-7.0	250	0.3	512.2	7	L+V	10	primary	10.50	375	mineralized	Gortavallig Mine mineralized Qtz vein
JL_GV_512	3	3.1	-41	-22.4	-4.8	314	-4.4	310	-21.8	512.3	5	L+V	10	primary	7.09	475	mineralized	Gortavallig Mine mineralized Qtz vein
JL_GV_512	3	3.2	-37	-19.3	-4.2	313	-3.9	309	-18.8	512.3	6	L+V	10	primary	6.24	476	mineralized	Gortavallig Mine mineralized Qtz vein
JL_GV_512	3	3.3	-41	-20.5	-5.2	293	-4.8	290	-20.0	512.3	5	L+V	10	primary	7.65	440	mineralized	Gortavallig Mine mineralized Qtz vein
JL_GV_512	3	3.4	-35	-17.2	-6.5	339	-6.1	335	-16.7	512.4	5	L+V	20	primary	9.37	509	mineralized	Gortavallig Mine mineralized Qtz vein
JL_GV_512	4	4.1	-37	-23.2	-4.7	209	-4.3	207	-22.6	512.5	10	L+V	2	primary	6.95	319	mineralized	Gortavallig Mine mineralized Qtz vein
JL_GV_512	4	4.2	-40	-22.7	-4.5	210	-4.2	208	-22.1	512.5	8	L+V	0.5	primary	6.67	321	mineralized	Gortavallig Mine mineralized Qtz vein
JL_GV_512	4	4.3	-37	-24.4	-4.7	208	-4.3	206	-23.8	512.5	6	L+V	1	primary	6.95	318	mineralized	Gortavallig Mine mineralized Qtz vein
JL_GV_512	4	4.4	-38	-24.1	-4.6	202	-4.3	200	-23.5	512.5	4	L+V	2	primary	6.81	310	mineralized	Gortavallig Mine

																		mineralized Qtz vein
JL_GV_512	4	4.5	-36	-22.6	-4.8	189	-4.4	187	-22.0	512.6	2	L+V	5	primary	7.09	293	mineralized	Gortavallig Mine mineralized Qtz vein
JL_GV_512	5	5.1	-39	-21.8	-4.9	260	-4.5	257	-21.2	512.2	8	L+V	5	primary	7.23	391	mineralized	Gortavallig Mine mineralized Qtz vein
JL_GV_512	5	5.2	-39	-22.8	-5.4	317	-5.0	313	-22.2	512.1	18	L+V	5	primary	7.92	478	mineralized	Gortavallig Mine mineralized Qtz vein
JL_GV_517	1	1.1	-38	-20.1	-5.3	257	-4.9	254	-19.6	517.1	20	L+V	10	primary	7.78	386	barren	Gortavallig Syn-Variscan Qtz vein
JL_GV_517	1	1.2	-38	-23.0	-3.2	257	-2.9	254	-22.4	517.1	15	L+V	10	primary	4.75	390	barren	Gortavallig Syn-Variscan Qtz vein
JL_GV_517	1	1.3	-39	-18.8	-4.5	273	-4.2	270	-18.3	517.1	12	L+V	10	primary	6.67	411	barren	Gortavallig Syn-Variscan Qtz vein
JL_GV_517	1	1.4	-37	-20.3	-4.5	263	-4.2	260	-19.8	517.1	6	L+V	5	primary	6.67	396	barren	Gortavallig Syn-Variscan Qtz vein
JL_GV_517	2	2.1	-38	-20.9	-4.7	265	-4.3	262	-20.3	517.1	13	L+V	5	primary	6.95	399	barren	Gortavallig Syn-Variscan Qtz vein
JL_GV_517	2	2.2	-39	-21.5	-4.9	245	-4.5	242	-20.9	517.1	23	L+V	10	primary	7.23	369	barren	Gortavallig Syn-Variscan Qtz vein
JL_GV_517	3	3.1	-39	-20.2	-5.1	265	-4.7	262	-19.7	517.1	15	L+V	10	primary	7.51	398	barren	Gortavallig Syn-Variscan Qtz vein
JL_GV_517	3	3.2	-37	-19.4	-4.7	242	-4.3	239	-18.9	517.1	10	L+V	10	primary	6.95	365	barren	Gortavallig Syn-Variscan Qtz vein
JL_GV_517	3	3.3	-39		-5.8	267	-5.4	264	0.3	517.1	5	L+V	10	primary	8.46	399	barren	Gortavallig Syn-Variscan Qtz vein
JL_GV_517	3	3.4	-38	-19.6	-5.5	270	-5.1	267	-19.1	517.1	14	L+V	5	primary	8.06	404	barren	Gortavallig Syn-Variscan Qtz vein
JL_GV_517	3	3.5	-38	-19.6	-5.0	272	-4.6	269	-19.1	517.1	25	L+V	5	primary	7.37	408	barren	Gortavallig Syn-Variscan Qtz vein

JL_GV_517	4	4.1	-40	-19.1	-5.1	274	-4.7	271	-18.6	517.1	13	L+V	3	primary	7.51	411	barren	Gortavallig Syn-Variscan Qtz vein
JL_GV_517	4	4.2	-39	-20.4	-4.8	274	-4.4	271	-19.9	517.1	12	L+V	5	primary	7.09	412	barren	Gortavallig Syn-Variscan Qtz vein
JL_GV_517	4	4.3	-40	-19.8	-5.0	262	-4.6	259	-19.3	517.1	6	L+V	5	primary	7.37	394	barren	Gortavallig Syn-Variscan Qtz vein
JL_CH_488	1	1.1	-48	-36.4	-4.8	121	-4.4	120	-35.7	488.1	13	L+V	1	primary	7.09	206	barren	Crookhaven, vuggy qtz crystal
JL_CH_488	1	1.2	-49	-28.5	-4.7	130	-4.3	129	-27.9	488.1	21	L+V	0.5	primary	6.95	218	barren	Crookhaven, vuggy qtz crystal
JL_CH_488	1	1.3	-50	-29.3	-2.6	125	-2.3	124	-28.6	488.1	10	L+V	0.1	primary	3.83	218	barren	Crookhaven, vuggy qtz crystal
JL_CH_488	2	2.1	-51	-29.7	-6.5	115	-6.1	114	-29.0	488.5	2	L+V	5	primary	9.37	195	barren	Crookhaven, vuggy qtz crystal
JL_CH_488	3	3.1	-41	-25.5	-7.1	160	-6.7	158	-24.9	488.2	23	L+V	5	primary	10.13	250	barren	Crookhaven, vuggy qtz crystal
JL_CH_488	3	3.2	-42	-25.2	-5.6	141	-5.2	140	-24.6	488.2	12	L+V	1	primary	8.19	229	barren	Crookhaven, vuggy qtz crystal
JL_CH_488	3	3.3	-40	-24.3	-5.0	157	-4.6	155	-23.7	488.2	13	L+V	1	primary	7.37	251	barren	Crookhaven, vuggy qtz crystal
JL_CH_488	3	3.4	-41	-26.2	-5.1	171	-4.7	169	-25.6	488.3	8	L+V	2	primary	7.51	268	barren	Crookhaven, vuggy qtz crystal
JL_CH_488	3	3.5	-44	-25.9	-5.1	139	-4.7	138	-25.3	488.4	9	L+V	1	primary	7.51	228	barren	Crookhaven, vuggy qtz crystal
JL_CH_488	3	3.6	-52	-25.5	-5.9	137	-5.5	136	-24.9	488.4	4	L+V	5	primary	8.59	223	barren	Crookhaven, vuggy qtz crystal
JL_CH_488	3	3.7	-46	-25.4	-5.1	138	-4.7	137	-24.8	488.4	14	L+V	1	primary	7.51	227	barren	Crookhaven, vuggy qtz crystal
Durrus crystals	1	1.1	-46	-29.8	-7.3	102	-6.9	101	-29.1	DU.1		L+V		primary	10.38	177	barren	Euhedral, single crystals, no thin section, Syn-Variscan
Durrus crystals	2	2.1	-48	-25.0	-9.2	222	-8.8	220	-24.4	DU.2		L+V		primary	12.61	328	barren	Euhedral, single

																		crystals, no thin section, Syn-Variscan
Durrus crystals	2	2.2	-63	-29.0	-8.9	223	-8.5	221	-28.3	DU.2		L+V		primary	12.28	330	barren	Euhedral, single crystals, no thin section, Syn-Variscan
Durrus crystals	3	3.1	-61	-24.0	-8.5	243	-8.1	240	-23.4	DU.3		L+V		primary	11.82	359	barren	Euhedral, single crystals, no thin section, Syn-Variscan
Durrus crystals	4	4.1	-51	-26.6	-9.3	176	-8.9	174	-26.0	DU.4		L+V		primary	12.72	267	barren	Euhedral, single crystals, no thin section, Syn-Variscan
Durrus crystals	4	4.2	-50	-26.6	-9.6	197	-9.2	195	-26.0	DU.4		L+V		primary	13.06	294	barren	Euhedral, single crystals, no thin section, Syn-Variscan
Durrus crystals	4	4.3	-49	-25.4	-9.2	195	-8.8	193	-24.8	DU.4		L+V		primary	12.61	292	barren	Euhedral, single crystals, no thin section, Syn-Variscan
Durrus crystals	4	4.4	-65	-25.9	-9.2	222	-8.8	220	-25.3	DU.4		L+V		primary	12.61	328	barren	Euhedral, single crystals, no thin section, Syn-Variscan
Durrus crystals	4	4.5	-64	-26.4	-9.9	196	-9.5	194	-25.8	DU.4		L+V		primary	13.38	292	barren	Euhedral, single crystals, no thin section, Syn-Variscan
JL_DH_522	1	1.1	-39	-21.9	-9.3	175	-8.9	173	-21.3	522.1	7	L+V	2	primary	12.72	265	mineralized	Dhurode Mine, mineralized Qtz vein
JL_DH_522	1	1.2	-39	-20.4	-6.2	171	-5.8	169	-19.9	522.1	3	L+V	2	primary	8.99	266	mineralized	Dhurode Mine, mineralized Qtz vein
JL_DH_522	1	1.3	-41	-21.8	-7.1	172	-6.7	170	-21.2	522.1	4	L+V	2	primary	10.13	265	mineralized	Dhurode Mine, mineralized Qtz vein

JL_DH_522	1	1.4	-41	-21.2	-7.3	169	-6.9	167	-20.6	522.1	6	L+V	2	primary	10.38	261	mineralized	Dhurode Mine, mineralized Qtz vein
JL_DH_522	1	1.5	-39	-21.4	-5.7	182	-5.3	180	-20.8	522.1	5	L+V	2	primary	8.33	281	mineralized	Dhurode Mine, mineralized Qtz vein
JL_DH_522	2	2.1	-40	-18.2	-5.9	276	-5.5	273	-17.7	522.2	8	L+V	3	primary	8.59	412	mineralized	Dhurode Mine, mineralized Qtz vein
JL_DH_522	2	2.2	-39	-17.8	-6.4	247	-6.0	244	-17.3	522.2	7	L+V	5	primary	9.25	369	mineralized	Dhurode Mine, mineralized Qtz vein
JL_DH_522	2	2.3	-39	-24.9	-6.0	260	-5.6	257	-24.3	522.2	13	L+V	5	primary	8.72	388	mineralized	Dhurode Mine, mineralized Qtz vein
JL_DH_522	2	2.4	-40	-18.2	-5.9	256	-5.5	253	-17.7	522.2	12	L+V	3	primary	8.59	383	mineralized	Dhurode Mine, mineralized Qtz vein
JL_DH_522	2	2.5	-40	-24.5	-6.3	204	-5.9	202	-23.9	522.3	14	L+V	3	primary	9.12	309	mineralized	Dhurode Mine, mineralized Qtz vein
JL_DH_522	2	2.6	-40	-18.6	-4.7	267	-4.3	264	-18.1	522.2	5	L+V	5	primary	6.95	402	mineralized	Dhurode Mine, mineralized Qtz vein
JL_DH_522	2	2.7	-37	-24.8	-8.1	232	-7.7	229	-24.2	522.4	10	L+V	5	primary	11.35	344	mineralized	Dhurode Mine, mineralized Qtz vein
JL_DH_522	2	2.8	-39	-21.1	-6.6	218	-6.2	216	-20.5	522.5	4	L+V	3	primary	9.50	328	mineralized	Dhurode Mine, mineralized Qtz vein
JL_DH_522	3	3.1	-35	-18.8	-3.5	198	-3.2	196	-18.3	522.6	10	L+V	1	primary	5.21	307	mineralized	Dhurode Mine, mineralized Qtz vein
JL_DH_522	3	3.2	-38	-18.2	-3.6	174	-3.3	172	-17.7	522.6	3	L+V	1	primary	5.36	276	mineralized	Dhurode Mine, mineralized Qtz vein
JL_DH_522	3	3.3	-40	-28.1	-6.2	208	-5.8	206	-27.5	522.6	14	L+V	5	primary	8.99	315	mineralized	Dhurode Mine,

																		mineralized Qtz vein
JL_DH_522	3	3.4	-34	-28.8	-8.3	207	-7.9	205	-28.2	522.6	18	L+V	2	primary	11.58	309	mineralized	Dhurode Mine, mineralized Qtz vein
JL_DH_522	3	3.5	-40	-29.7	-5.3	208	-4.9	206	-29.0	522.6	10	L+V	2	primary	7.78	317	mineralized	Dhurode Mine, mineralized Qtz vein
JL_DH_522	3	3.6	-46	-31.3	-16.8	206	-16.3	204	-30.6	522.7	13	L+V	0.5	primary	19.68	298	mineralized	Dhurode Mine, mineralized Qtz vein
JL_DH_522	4	4.1	-42	-15.6	-5.6	211	-5.2	209	-15.1	522.6	13	L+V	2	primary	8.19	320	mineralized	Dhurode Mine, mineralized Qtz vein
JL_DH_522	4	4.2	-43	-24.6	-5.8	221	-5.4	219	-24.0	522.6	5	L+V	2	primary	8.46	334	mineralized	Dhurode Mine, mineralized Qtz vein
JL_DH_522	4	4.3	-42	-17.4	-5.7	191	-5.3	189	-16.9	522.6	8	L+V	2	primary	8.33	293	mineralized	Dhurode Mine, mineralized Qtz vein
JL_DH_522	4	4.4	-42	-21.6	-5.6	217	-5.2	215	-21.0	522.6	3	L+V	5	primary	8.19	328	mineralized	Dhurode Mine, mineralized Qtz vein
JL_BH_475	1	1.1	-48	-27.0	-12.9	245	-12.4	242	-26.4	475.1	8	L+V	1	primary	16.38	354	barren	Baurearagh, early extensional Qtz vein
JL_BH_475	1	1.2	-47	-26.2	-12.9	234	-12.4	231	-25.6	475.1	9	L+V	1	primary	16.38	339	barren	Baurearagh, early extensional Qtz vein
JL_BH_475	1	1.3	-47	-21.0	-12.2	243	-11.8	240	-20.4	475.1	7	L+V	2	primary	15.72	352	barren	Baurearagh, early extensional Qtz vein
JL_BH_475	1	1.4	-52	-23.5	-11.5	250	-11.1	247	-22.9	475.1	11	L+V	5	primary	15.04	363	barren	Baurearagh, early extensional Qtz vein
JL_BH_475	1	1.5	-49	-33.4	-12.5	271	-12.1	268	-32.7	475.1	15	L+V	5	primary	16.01	391	barren	Baurearagh, early extensional Qtz vein

JL_BH_475	2	2.1	-46	-23.6	-10.7	211	-10.3	209	-23.0	475.2	14	L+V	5	primary	14.23	311	barren	Baurearagh, early extensional Qtz vein
JL_BH_475	2	2.2	-49	-25.3	-10.9	212	-10.5	210	-24.7	475.2	10	L+V	1	primary	14.43	312	barren	Baurearagh, early extensional Qtz vein
JL_BH_475	2	2.3	-48	-26.1	-11.5	185	-11.1	183	-25.5	475.2	10	L+V	2	primary	15.04	275	barren	Baurearagh, early extensional Qtz vein
JL_BH_475	2	2.4	-49	-24.9	-12.3	242	-11.9	239	-24.3	475.2	9	L+V	2	primary	15.82	351	barren	Baurearagh, early extensional Qtz vein
JL_BH_475	2	2.5	-49	-26.1	-12.8	223	-12.3	221	-25.5	475.2	2	L+V	2	primary	16.29	324	barren	Baurearagh, early extensional Qtz vein
JL_BH_475	2	2.6	-46	-23.8	-10.2	208	-9.8	206	-23.2	475.2	4	L+V	2	primary	13.70	308	barren	Baurearagh, early extensional Qtz vein
JL_BH_475	3	3.1	-46	-26.9	-9.7	277	-9.3	274	-26.3	475.3	10	L+V	5	primary	13.16	405	barren	Baurearagh, early extensional Qtz vein
JL_BH_475	3	3.2	-44	-29.3	-8.8	264	-8.4	261	-28.6	475.3	10	L+V	1	primary	12.16	388	barren	Baurearagh, early extensional Qtz vein
JL_BH_475	3	3.3	-45	-22.9	-9.8	238	-9.4	235	-22.3	475.3	2	L+V	1	primary	13.27	349	barren	Baurearagh, early extensional Qtz vein
JL_BH_475	3	3.4	-44	-27.4	-8.5	316	-8.1	312	-26.8	475.3	17	L+V	2	primary	11.82	466	barren	Baurearagh, early extensional Qtz vein
JL_BH_475	3	3.5	-49	-25.3	-13.5	293	-13.0	290	-24.7	475.3	10	L+V	2	primary	16.93	421	barren	Baurearagh, early extensional Qtz vein
JL_BH_475	3	3.6	-46	-26.0	-8.8	241	-8.4	238	-25.4	475.3	2	L+V	2	primary	12.16	355	barren	Baurearagh, early extensional Qtz vein
JL_BH_475	3	3.7	-45	-23.3	-8.2	279	-7.8	276	-22.7	475.3	3	L+V	1	primary	11.47	411	barren	Baurearagh, early

																		extensional Qtz vein
JL_CH_521	1	1.1	-39	-19.0	-4.9	166	-4.7	163	-18.5	521.1	10	L+V	5	primary	7.50	260	barren	Crookhaven (Barley Cove) Syn-Variscan vein
JL_CH_521	1	1.2	-40	-22.3	-6.8	149	-6.6	146	-21.8	521.1	12	L+V	2	primary	9.98	234	barren	Crookhaven (Barley Cove) Syn-Variscan vein
JL_CH_521	1	1.3	-39	-23.0	-4.7	175	-4.5	171	-22.5	521.1	8	L+V	2	primary	7.23	272	barren	Crookhaven (Barley Cove) Syn-Variscan vein
JL_CH_521	1	1.4	-38	-28.7	-5.2	117	-5.0	115	-28.0	521.1	13	L+V	0.5	primary	7.91	198	barren	Crookhaven (Barley Cove) Syn-Variscan vein
JL_CH_521	1	1.5	-37	-28.0	-5.8	174	-5.6	170	-27.3	521.1	6	L+V	2	primary	8.71	268	barren	Crookhaven (Barley Cove) Syn-Variscan vein
JL_CH_521	2	2.1	-41	-23.7	-7.0	143	-6.8	140	-23.1	521.2	10	L+V	2	primary	10.23	226	barren	Crookhaven (Barley Cove) Syn-Variscan vein
JL_CH_521	2	2.2	-40	-20.5	-5.6	122	-5.4	119	-20.0	521.2	6	L+V	0.1	primary	8.44	203	barren	Crookhaven (Barley Cove) Syn-Variscan vein
JL_CH_521	2	2.3	-39	-17.7	-7.1	145	-6.9	142	-17.3	521.2	7	L+V	0.5	primary	10.35	229	barren	Crookhaven (Barley Cove) Syn-Variscan vein
JL_CH_521	2	2.4	-40	-20.7	-6.2	149	-6.0	146	-20.2	521.2	6	L+V	0.5	primary	9.22	235	barren	Crookhaven (Barley Cove) Syn-Variscan vein
JL_CH_521	3	3.1	-37	-19.6	-6.9	165	-6.7	162	-19.1	521.3	11	L+V	2	primary	10.10	254	barren	Crookhaven (Barley Cove) Syn-Variscan vein
JL_CH_521	3	3.2	-38	-13.2	-6.0	163	-5.8	160	-12.9	521.3	9	L+V	1	primary	8.97	254	barren	Crookhaven (Barley Cove) Syn-Variscan vein
JL_CH_521	3	3.3	-38	-12.3	-5.3	164	-5.1	161	-12.0	521.3	6	L+V	0.5	primary	8.04	256	barren	Crookhaven (Barley Cove) Syn-Variscan vein

JL_CH_521	3	3.4	-37	-14.6	-5.0	158	-4.8	155	-14.2	521.3	13	L+V	5	primary	7.64	249	barren	Crookhaven (Barley Cove) Syn-Variscan vein
JL_CH_521	3	3.5	-41	-13.7	-7.1	169	-6.9	165	-13.4	521.3	10	L+V	2	primary	10.35	259	barren	Crookhaven (Barley Cove) Syn-Variscan vein
JL_CH_521	4	4.1	-41	-21.8	-7.3	136	-7.1	133	-21.3	521.4	10	L+V	1	primary	10.59	217	barren	Crookhaven (Barley Cove) Syn-Variscan vein
JL_CH_521	4	4.2	-39	-14.6	-5.6	119	-5.4	117	-14.2	521.4	13	L+V	1	primary	8.44	200	barren	Crookhaven (Barley Cove) Syn-Variscan vein
JL_CH_521	4	4.3	-41	-16.4	-5.8	112	-5.6	110	-16.0	521.4	13	L+V	0.5	primary	8.71	191	barren	Crookhaven (Barley Cove) Syn-Variscan vein
JL_CH_521	5	5.1	-39	-23.3	-5.2	214	-5.0	210	-22.7	521.5	13	L+V	2	primary	7.91	322	barren	Crookhaven (Barley Cove) Syn-Variscan vein
JL_CH_521	5	5.2	-37	-25.1	-5.9	163	-5.7	160	-24.5	521.5	10	L+V	1	primary	8.84	254	barren	Crookhaven (Barley Cove) Syn-Variscan vein
JL_CH_521	5	5.3	-37	-23.8	-4.4	110	-4.2	108	-23.2	521.5	14	L+V	0.5	primary	6.81	192	barren	Crookhaven (Barley Cove) Syn-Variscan vein
JL_CH_521	5	5.4	-37	-23.0	-5.4	106	-5.2	104	-22.5	521.5	13	L+V	1	primary	8.18	185	barren	Crookhaven (Barley Cove) Syn-Variscan vein
JL_BC_525 Re	1	1.1	-41	-19.8	-6.4	217	-6.2	212	-19.3	525.1	4	L+V	4	primary	9.48	323	mineralized	Ballycummisk, mineralized qtz vein with molybdenite (Re-Os dated)
JL_BC_525 Re	1	1.2	-41	-18.6	-6.4	199	-6.2	195	-18.1	525.1	5	L+V	2	primary	9.48	299	mineralized	Ballycummisk, mineralized qtz vein with molybdenite (Re-Os dated)

JL_BC_525 Re	1	1.3	-42	-20.3	-6.2	217	-6.0	212	-19.8	525.1	6	L+V	5	primary	9.22	324	mineralized	Ballycummis k, mineralized qtz vein with molybdenite (Re-Os dated)
JL_BC_525 Re	2	2.1	-49	-21.0	-8.2	324	-8.0	317	-20.5	525.2	4	L+V	15	primary	11.66	474	mineralized	Ballycummis k, mineralized qtz vein with molybdenite (Re-Os dated)
JL_BC_525 Re	2	2.2	-46	-23.2	-12.6	326	-12.3	319	-22.7	525.2	7	L+V	20	primary	16.22	466	mineralized	Ballycummis k, mineralized qtz vein with molybdenite (Re-Os dated)
JL_BC_525 Re	2	2.3	-47	-19.8	-11.1	311	-10.8	304	-19.3	525.2	4	L+V	6	primary	14.78	447	mineralized	Ballycummis k, mineralized qtz vein with molybdenite (Re-Os dated)
JL_BC_525 Re	2	2.4	-47	-16.1	-11.2	322	-10.9	315	-15.7	525.2	6	L+V	10	primary	14.88	463	mineralized	Ballycummis k, mineralized qtz vein with molybdenite (Re-Os dated)
JL_BC_525 Re	3	3.1	-44	-18.5	-6.2	306	-6.0	300	-18.1	525.3	14	L+V	6	primary	9.22	452	mineralized	Ballycummis k, mineralized qtz vein with molybdenite (Re-Os dated)
JL_BC_525 Re	3	3.2	-44	-18.5	-6.9	303	-6.7	297	-18.1	525.3	3	L+V	5	primary	10.10	445	mineralized	Ballycummis k, mineralized qtz vein with molybdenite (Re-Os dated)

JL_BC_525 Re	3	3.3	-42	-20.5	-5.5	312	-5.3	305	-20.0	525.3	3	L+V	10	primary	8.31	464	mineralized	Ballycummis k, mineralized qtz vein with molybdenite (Re-Os dated)
JL_BC_525 Re	3	3.4	-43	-18.3	-7.6	282	-7.4	276	-17.9	525.3	8	L+V	5	primary	10.95	412	mineralized	Ballycummis k, mineralized qtz vein with molybdenite (Re-Os dated)
JL_BC_525 Re	3	3.5	-43	-23.7	-7.9	298	-7.7	292	-23.1	525.3	7	L+V	7	primary	11.31	435	mineralized	Ballycummis k, mineralized qtz vein with molybdenite (Re-Os dated)
JL_BC_525 Re	3	3.6	-39	-18.2	-6.5	302	-6.3	296	-17.8	525.3	4	L+V	10	primary	9.61	445	mineralized	Ballycummis k, mineralized qtz vein with molybdenite (Re-Os dated)
JL_BC_525 Re	4	4.1	-44	-14.8	-9.7	171	-9.4	167	-14.4	525.4	10	L+V	1	primary	13.33	257	mineralized	Ballycummis k, mineralized qtz vein with molybdenite (Re-Os dated)
JL_BC_525 Re	4	4.2	-43	-12.5	-9.5	169	-9.2	165	-12.2	525.4	4	L+V	1	primary	13.11	255	mineralized	Ballycummis k, mineralized qtz vein with molybdenite (Re-Os dated)
JL_BC_525 Re	4	4.3	-41	-12.3	-8.0	173	-7.8	169	-12.0	525.4	3	L+V	1	primary	11.43	262	mineralized	Ballycummis k, mineralized qtz vein with molybdenite (Re-Os dated)

JL_BC_525 Re	5	5.1	-40	-19.0	-5.2	177	-5.0	173	-18.5	525.5	2	L+V	2	primary	7.91	273	mineralized	Ballycummis k, mineralized qtz vein with molybdenite (Re-Os dated)
JL_BC_525 Re	5	5.2	-38	-22.8	-7.1	265	-6.9	259	-22.3	525.5	3	L+V	5	primary	10.35	389	mineralized	Ballycummis k, mineralized qtz vein with molybdenite (Re-Os dated)
JL_BC_525 Re	6	6.1	-49	-14.5	-8.4	281	-8.2	275	-14.1	525.6	3	L+V	10	primary	11.89	409	mineralized	Ballycummis k, mineralized qtz vein with molybdenite (Re-Os dated)
JL_BC_525 Re	6	6.2	-37	-14.3	-9.1	278	-8.8	272	-13.9	525.6	2	L+V	10	primary	12.68	403	mineralized	Ballycummis k, mineralized qtz vein with molybdenite (Re-Os dated)
JL_BC_525 Re	6	6.3	-44	-14.8	-9.0	288	-8.8	282	-14.4	525.6	4	L+V	10	primary	12.57	418	mineralized	Ballycummis k, mineralized qtz vein with molybdenite (Re-Os dated)
JL_BH_482	1	1.1	-46	-32.9	-11.4	136	-11.1	133	-32.1	482.1	8	L+V	1	primary	15.07	211	barren	Baurearagh, Syn-Variscan qtz vein
JL_BH_482	1	1.2	-49	-19.8	-9.6	141	-9.3	138	-19.3	482.1	4	L+V	1	primary	13.22	219	barren	Baurearagh, Syn-Variscan qtz vein
JL_BH_482	1	1.3	-41	-17.4	-7.2	169	-7.0	165	-17.0	482.1	9	L+V	1	primary	10.47	259	barren	Baurearagh, Syn-Variscan qtz vein
JL_BH_482	1	1.4	-41	-13.9	-8.5	119	-8.3	117	-13.5	482.1	3	L+V	0.5	primary	12.00	194	barren	Baurearagh, Syn-Variscan qtz vein
JL_BH_482	1	1.5	-43	-22.3	-8.6	127	-8.4	124	-21.8	482.1	4	L+V	2	primary	12.12	204	barren	Baurearagh, Syn-Variscan qtz vein

JL_BH_482	2	2.1	-63	-20.2	-11.2	140	-10.9	137	-19.7	482.2	6	L+V	1	primary	14.88	216	barren	Baurearagh, Syn-Variscan qtz vein
JL_BH_482	2	2.2	-47	-17.6	-9.6	169	-9.3	165	-17.2	482.2	12	L+V	1	primary	13.22	255	barren	Baurearagh, Syn-Variscan qtz vein
JL_BH_482	2	2.3	-58	-18.6	-8.8	139	-8.6	136	-18.1	482.2	5	L+V	1	primary	12.34	218	barren	Baurearagh, Syn-Variscan qtz vein
JL_BH_482	3	3.1	-44	-32.5	-6.4	161	-6.2	158	-31.8	482.3	8	L+V	1	primary	9.48	250	barren	Baurearagh, Syn-Variscan qtz vein
JL_BH_482	3	3.2	-43	-33.1	-7.1	163	-6.9	160	-32.3	482.3	8	L+V	1	primary	10.35	251	barren	Baurearagh, Syn-Variscan qtz vein
JL_BH_482	3	3.3	-43	-28.2	-8.1	143	-7.9	140	-27.5	482.3	14	L+V	1	primary	11.54	224	barren	Baurearagh, Syn-Variscan qtz vein
JL_BH_482	3	3.4	-54	-41.3	-13.1	112	-12.8	110	-40.4	482.3	10	L+V	0.5	primary	16.68	181	barren	Baurearagh, Syn-Variscan qtz vein
JL_BH_482	3	3.5	-38	-34.1	-8.5	151	-8.3	148	-33.3	482.3	15	L+V	1	primary	12.00	234	barren	Baurearagh, Syn-Variscan qtz vein
JL_BH_482	3	3.6	-37	-46.2	-6.7	138	-6.5	135	-45.2	482.3	18	L+V	1	primary	9.86	221	barren	Baurearagh, Syn-Variscan qtz vein
JL_BH_482	3	3.7	-37	-19.6	-8.2	150	-8.0	147	-19.1	482.3	10	L+V	0.5	primary	11.66	233	barren	Baurearagh, Syn-Variscan qtz vein
JL_BH_482	3	3.8	-37	-23.0	-7.2	162	-7.0	159	-22.5	482.3	16	L+V	1	primary	10.47	250	barren	Baurearagh, Syn-Variscan qtz vein
JL_BH_482	3	3.9	-49	-22.9	-8.1	153	-7.9	150	-22.4	482.3	5	L+V	1	primary	11.54	237	barren	Baurearagh, Syn-Variscan qtz vein
JL_BH_482	4	4.1	-37	-17.8	-8.2	222	-8.0	217	-17.4	482.4	22	L+V	5	primary	11.66	327	barren	Baurearagh, Syn-Variscan qtz vein
JL_BH_482	4	4.2	-39	-25.3	-8.1	156	-7.9	153	-24.7	482.4	16	L+V	2	primary	11.54	241	barren	Baurearagh, Syn-Variscan qtz vein
JL_BH_482	4	4.3	-36	-23.0	-8.3	167	-8.1	164	-22.5	482.4	12	L+V	1	primary	11.77	254	barren	Baurearagh, Syn-Variscan qtz vein
JL_BH_482	4	4.4	-36	-23.0	-8.2	159	-8.0	156	-22.5	482.4	7	L+V	2	primary	11.66	244	barren	Baurearagh, Syn-Variscan qtz vein

JL_CP_432E	1	1.1	-41	-23.3	-6.2	193	-6.0	189	-22.7	432E.1	7	L+V	2	primary	9.22	292	mineralized	Caha Pass (Tunnel), early extensional qtz vein
JL_CP_432E	1	1.2	-42	-13.4	-6.9	157	-6.7	154	-13.1	432E.1	3	L+V	1	primary	10.10	244	mineralized	Caha Pass (Tunnel), early extensional qtz vein
JL_CP_432E	1	1.3	-40	-22.3	-10.3	166	-10.0	163	-21.8	432E.1	4	L+V	1	primary	13.96	250	mineralized	Caha Pass (Tunnel), early extensional qtz vein
JL_CP_432E	2	2.1	-41	-21.1	-7.1	180	-6.9	176	-20.6	432E.2	6	L+V	2	primary	10.35	273	mineralized	Caha Pass (Tunnel), early extensional qtz vein
JL_CP_432E	2	2.2	-36	-23.2	-7.9	149	-7.7	146	-22.7	432E.2	7	L+V	2	primary	11.31	232	mineralized	Caha Pass (Tunnel), early extensional qtz vein
JL_CP_432E	2	2.3	-42	-19.6	-7.6	167	-7.4	164	-19.1	432E.2	5	L+V	1	primary	10.95	255	mineralized	Caha Pass (Tunnel), early extensional qtz vein
JL_CP_432E	2	2.4	-39	-22.4	-6.3	160	-6.1	157	-21.9	432E.2	4	L+V	2	primary	9.35	249	mineralized	Caha Pass (Tunnel), early extensional qtz vein
JL_CP_432E	3	3.1	-42	-21.8	-8.9	180	-8.7	176	-21.3	432E.3	12	L+V	2	primary	12.45	270	mineralized	Caha Pass (Tunnel), early extensional qtz vein
JL_CP_432E	3	3.2	-43	-22.2	-9.1	184	-8.8	180	-21.7	432E.3	9	L+V	1	primary	12.68	275	mineralized	Caha Pass (Tunnel), early extensional qtz vein
JL_CP_432E	3	3.3	-42	-18.0	-7.5	179	-7.3	175	-17.6	432E.3	16	L+V	3	primary	10.84	271	mineralized	Caha Pass (Tunnel), early extensional qtz vein

JL_CP_432E	4	4.1	-65	-31.5	-20.4	126	-19.9	123	-30.8	432E.4	10	L+V	2	primary	22.31	196	mineralized	Caha Pass (Tunnel), early extensional qtz vein
JL_CP_432E	4	4.2	-65	-39.1	-20.4	121	-19.9	118	-38.2	432E.4	3	L+V	1	primary	22.31	190	mineralized	Caha Pass (Tunnel), early extensional qtz vein
JL_CP_432E	4	4.3	-46	-24.8	-9.0	187	-8.8	183	-24.2	432E.4	8	L+V	3	primary	12.57	279	mineralized	Caha Pass (Tunnel), early extensional qtz vein
JL_CP_432E	4	4.4	-69	-24.0	-20.5	92	-20.0	90	-23.4	432E.4	10	L+V	1	primary	22.38	156	mineralized	Caha Pass (Tunnel), early extensional qtz vein
JL_CP_432E	4	4.5	-62	-24.8	-20.0	123	-19.5	120	-24.2	432E.4	5	L+V	1	primary	22.05	192	mineralized	Caha Pass (Tunnel), early extensional qtz vein
JL_CP_432E	4	4.6	-45	-23.6	-8.0	128	-7.8	125	-23.0	432E.4	8	L+V	1	primary	11.43	206	mineralized	Caha Pass (Tunnel), early extensional qtz vein
JL_CP_432E	5	5.1	-41	-19.3	-7.4	160	-7.2	157	-18.8	432E.5	5	L+V	1	primary	10.72	247	mineralized	Caha Pass (Tunnel), early extensional qtz vein
JL_CP_432E	5	5.2	-41	-22.8	-7.7	175	-7.5	171	-22.3	432E.5	6	L+V	2	primary	11.07	266	mineralized	Caha Pass (Tunnel), early extensional qtz vein
JL_CP_432E	5	5.3	-40	-20.4	-8.8	182	-8.6	178	-19.9	432E.5	7	L+V	1	primary	12.34	273	mineralized	Caha Pass (Tunnel), early extensional qtz vein
JL_CP_432E	5	5.4	-40	-22.5	-8.2	188	-8.0	184	-22.0	432E.5	4	L+V	2	primary	11.66	281	mineralized	Caha Pass (Tunnel), early extensional qtz vein

JL_CP_432E	5	5.5	-44	-22.4	-8.4	170	-8.2	166	-21.9	432E.5	5	L+V	2	primary	11.89	258	mineralized	Caha Pass (Tunnel), early extensional qtz vein
JL_CP_432E	5	5.6	-44	-20.9	-8.6	150	-8.4	147	-20.4	432E.5	4	L+V	1	primary	12.12	232	mineralized	Caha Pass (Tunnel), early extensional qtz vein
JL_CP_432E	5	5.7	-45	-21.6	-11.6	189	-11.3	185	-21.1	432E.5	5	L+V	1	primary	15.27	278	mineralized	Caha Pass (Tunnel), early extensional qtz vein
JL_CP_432V	1	1.1	-41	-22.4	-8.0	179	-7.8	175	-21.9	432V.1	10	L+V	1	primary	11.43	270	barren	Caha Pass (Tunnel), Syn-Variscan qtz vein
JL_CP_432V	1	1.2	-40	-23.3	-7.9	180	-7.7	176	-22.7	432V.1	9	L+V	1	primary	11.31	272	barren	Caha Pass (Tunnel), Syn-Variscan qtz vein
JL_CP_432V	1	1.3	-39	-22.8	-8.4	179	-8.2	175	-22.3	432V.1	13	L+V	2	primary	11.89	269	barren	Caha Pass (Tunnel), Syn-Variscan qtz vein
JL_CP_432V	1	1.4	-43	-23.9	-9.8	169	-9.5	165	-23.3	432V.1	5	L+V	2	primary	13.44	254	barren	Caha Pass (Tunnel), Syn-Variscan qtz vein
JL_CP_432V	1	1.5	-34	-22.4	-8.5	167	-8.3	164	-21.9	432V.1	19	L+V	3	primary	12.00	254	barren	Caha Pass (Tunnel), Syn-Variscan qtz vein
JL_CP_432V	1	1.6	-42	-21.5	-7.6	169	-7.4	165	-21.0	432V.1	4	L+V	0.5	primary	10.95	258	barren	Caha Pass (Tunnel), Syn-Variscan qtz vein
JL_CP_432V	1	1.7	-38	-22.6	-8.0	185	-7.8	181	-22.1	432V.1	15	L+V	3	primary	11.43	278	barren	Caha Pass (Tunnel), Syn-Variscan qtz vein
JL_CP_432V	1	1.8	-43	-24.8	-8.8	202	-8.6	198	-24.2	432V.1	6	L+V	5	primary	12.34	299	barren	Caha Pass (Tunnel), Syn-Variscan qtz vein
JL_CP_432V	1	1.9	-43	-23.4	-8.8	203	-8.6	199	-22.8	432V.1	12	L+V	5	primary	12.34	300	barren	Caha Pass (Tunnel),

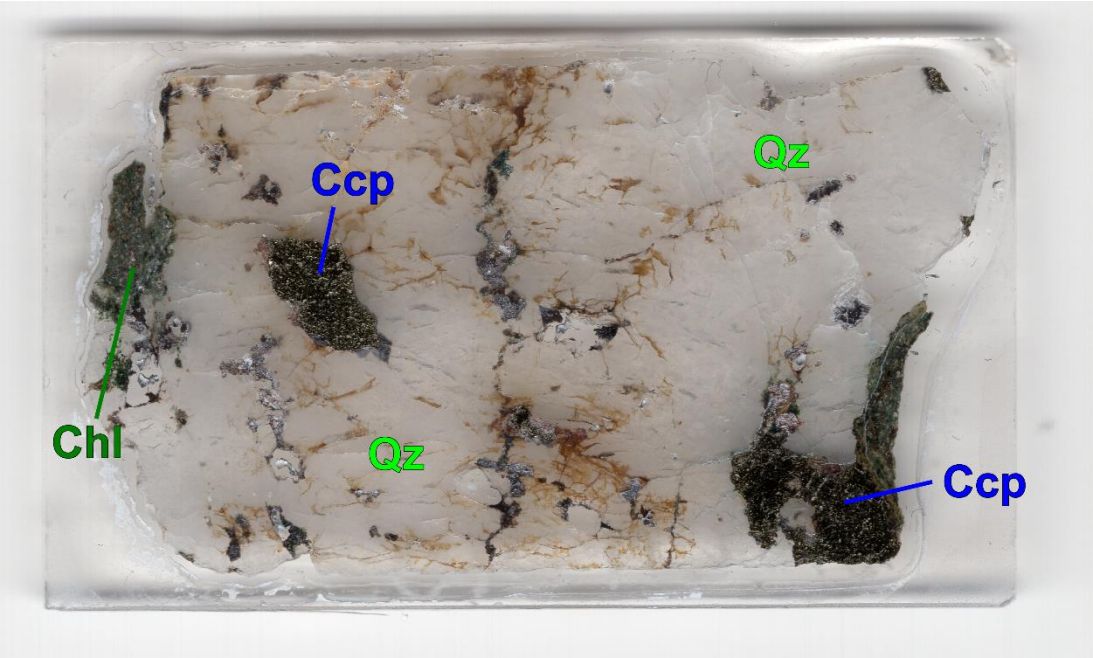
																		Syn-Variscan qtz vein
JL_CP_432V	1	1.10	-41	-23.8	-7.7	184	-7.5	180	-23.2	432V.1	4	L+V	1	primary	11.07	277	barren	Caha Pass (Tunnel), Syn-Variscan qtz vein
JL_CP_432V	2	2.1	-42	-21.8	-7.0	175	-6.8	171	-21.3	432V.2	7	L+V	1	primary	10.23	267	barren	Caha Pass (Tunnel), Syn-Variscan qtz vein
JL_CP_432V	2	2.2	-42	-22.5	-6.8	193	-6.6	189	-22.0	432V.2	6	L+V	1	primary	9.98	291	barren	Caha Pass (Tunnel), Syn-Variscan qtz vein
JL_CP_432V	2	2.3	-39	-21.5	-5.7	166	-5.5	163	-21.0	432V.2	16	L+V	5	primary	8.57	258	barren	Caha Pass (Tunnel), Syn-Variscan qtz vein
JL_CP_432V	2	2.4	-42	-23.0	-6.9	199	-6.7	195	-22.5	432V.2	6	L+V	5	primary	10.10	298	barren	Caha Pass (Tunnel), Syn-Variscan qtz vein
JL_CP_432V	2	2.5	-41	-26.0	-7.0	185	-6.8	181	-25.4	432V.2	12	L+V	3	primary	10.23	280	barren	Caha Pass (Tunnel), Syn-Variscan qtz vein
JL_CP_432V	2	2.6	-41	-22.1	-6.8	182	-6.6	178	-21.6	432V.2	4	L+V	5	primary	9.98	276	barren	Caha Pass (Tunnel), Syn-Variscan qtz vein
JL_CP_432V	3	3.1	-37	-31.8	-7.3	170	-7.1	166	-31.1	432V.3	13	L+V	3	primary	10.59	260	barren	Caha Pass (Tunnel), Syn-Variscan qtz vein
JL_CP_432V	3	3.2	-42	-21.9	-8.4	185	-8.2	181	-21.4	432V.3	5	L+V	10	primary	11.89	277	barren	Caha Pass (Tunnel), Syn-Variscan qtz vein
JL_CP_432V	3	3.3	-41	-25.7	-6.5	175	-6.3	171	-25.1	432V.3	7	L+V	1	primary	9.61	268	barren	Caha Pass (Tunnel), Syn-Variscan qtz vein
JL_CP_432V	3	3.4	-41	-24.2	-6.8	181	-6.6	177	-23.6	432V.3	8	L+V	5	primary	9.98	275	barren	Caha Pass (Tunnel), Syn-Variscan qtz vein
JL_CP_432V	3	3.5	-39	-24.6	-6.6	185	-6.4	181	-24.0	432V.3	13	L+V	5	primary	9.73	281	barren	Caha Pass (Tunnel), Syn-Variscan qtz vein

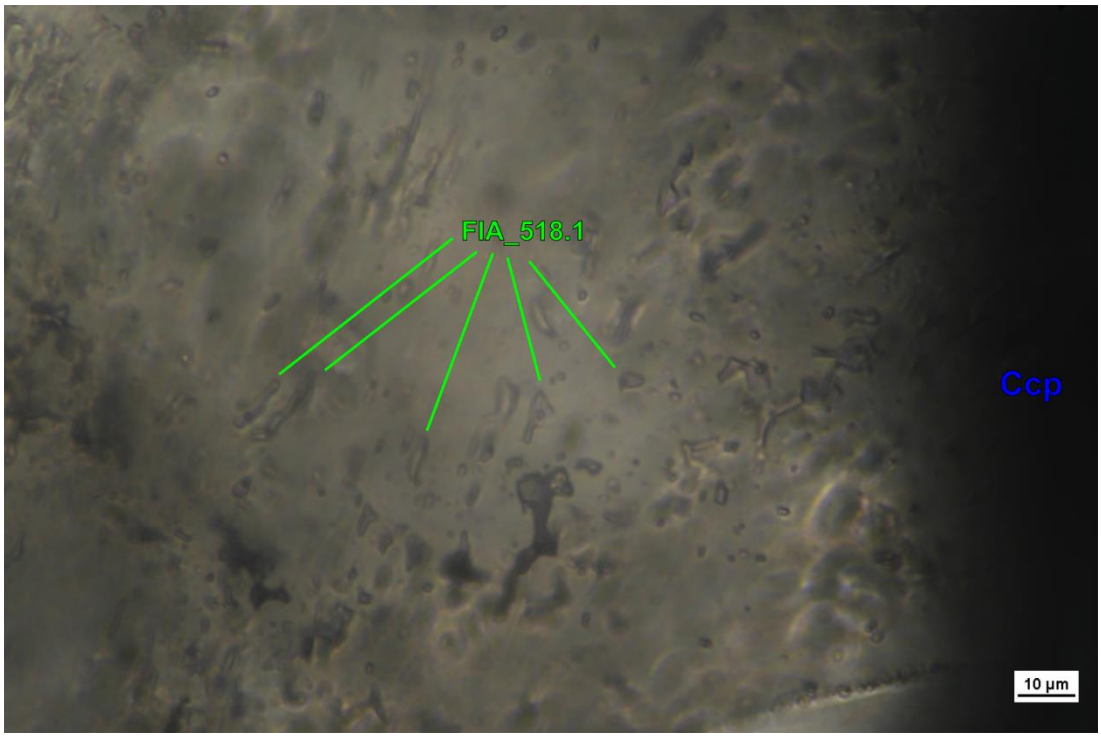
JL_CP_432V	4	4.1	-41	-21.2	-7.7	185	-7.5	181	-20.7	432V.4	14	L+V	3	primary	11.07	278	barren	Caha Pass (Tunnel), Syn-Variscan qtz vein
JL_CP_432V	4	4.2	-44	-25.6	-7.7	192	-7.5	188	-25.0	432V.4	9	L+V	1	primary	11.07	288	barren	Caha Pass (Tunnel), Syn-Variscan qtz vein

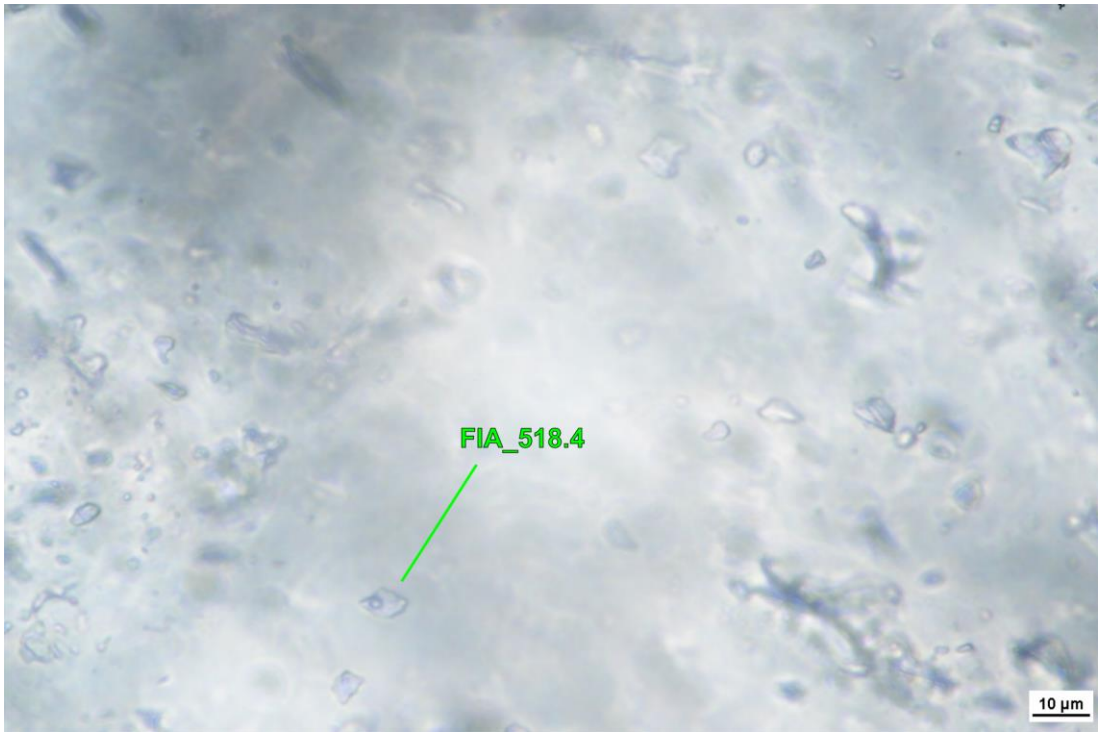
Appendix E.2 (Chapter 4)

Fluid inclusions assemblages of the West Cork Copper Deposits. The following slide scans and microphotographs (transmitted light) show representative examples of the measured fluid inclusion assemblages (FIA, Appendix E1).

Sample **JL_CH_518** (scanned slide, width of slide 46 mm, transmitted light images):

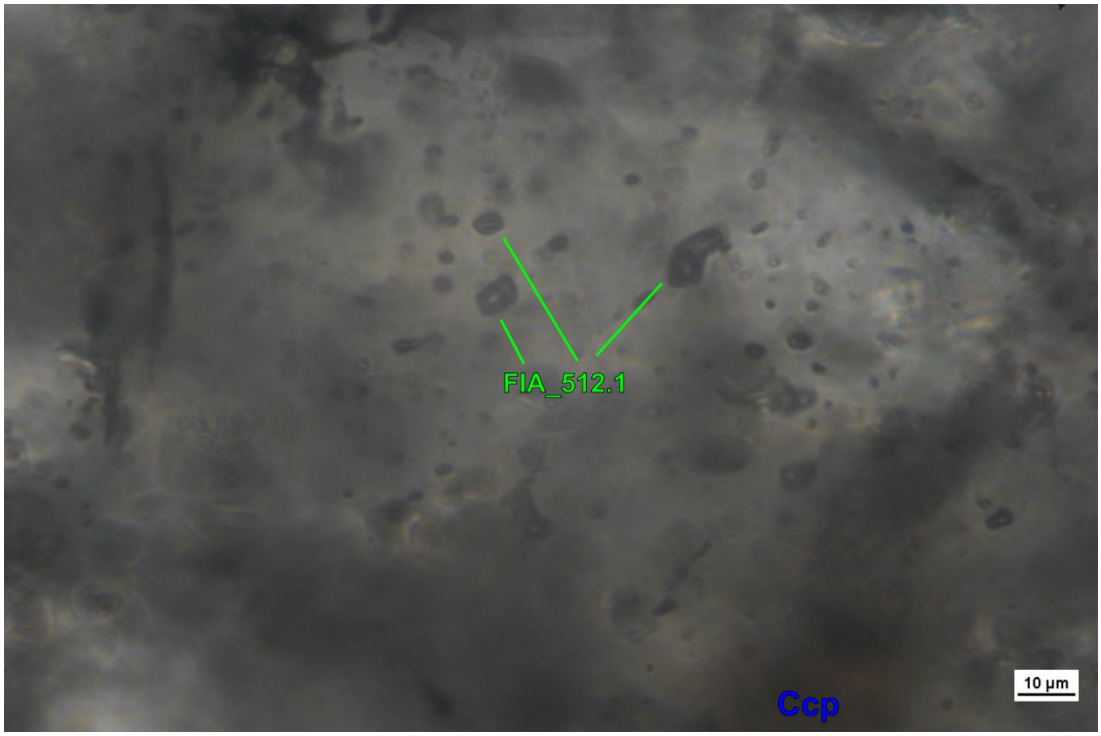


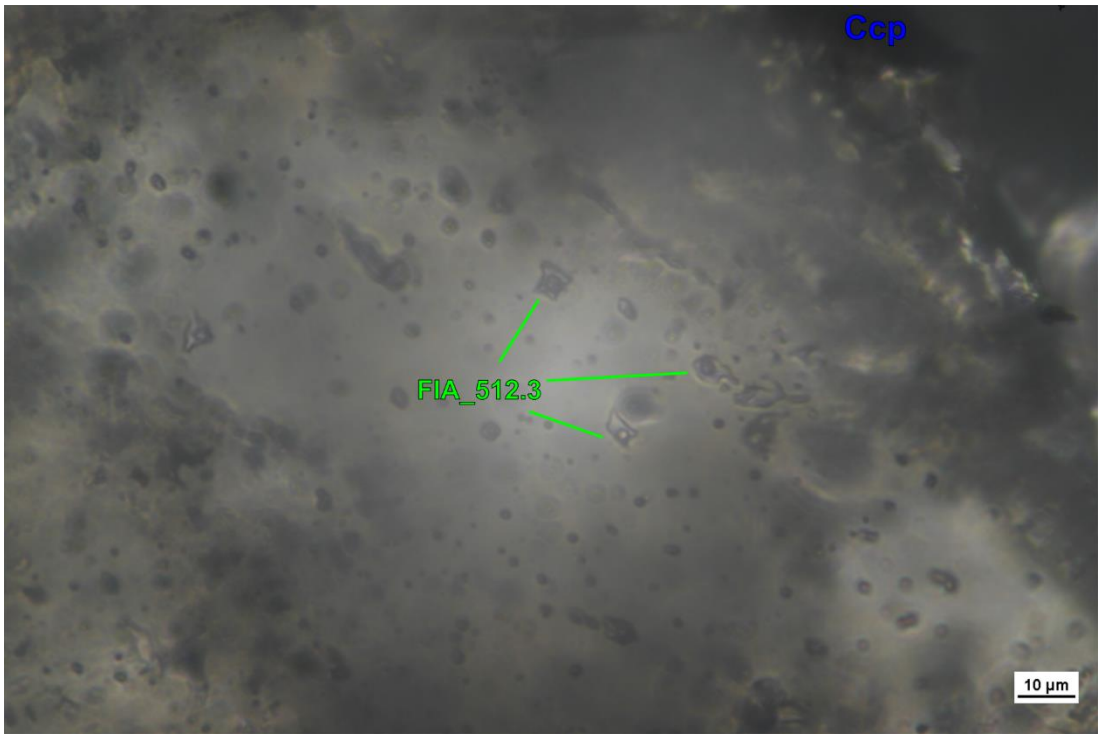


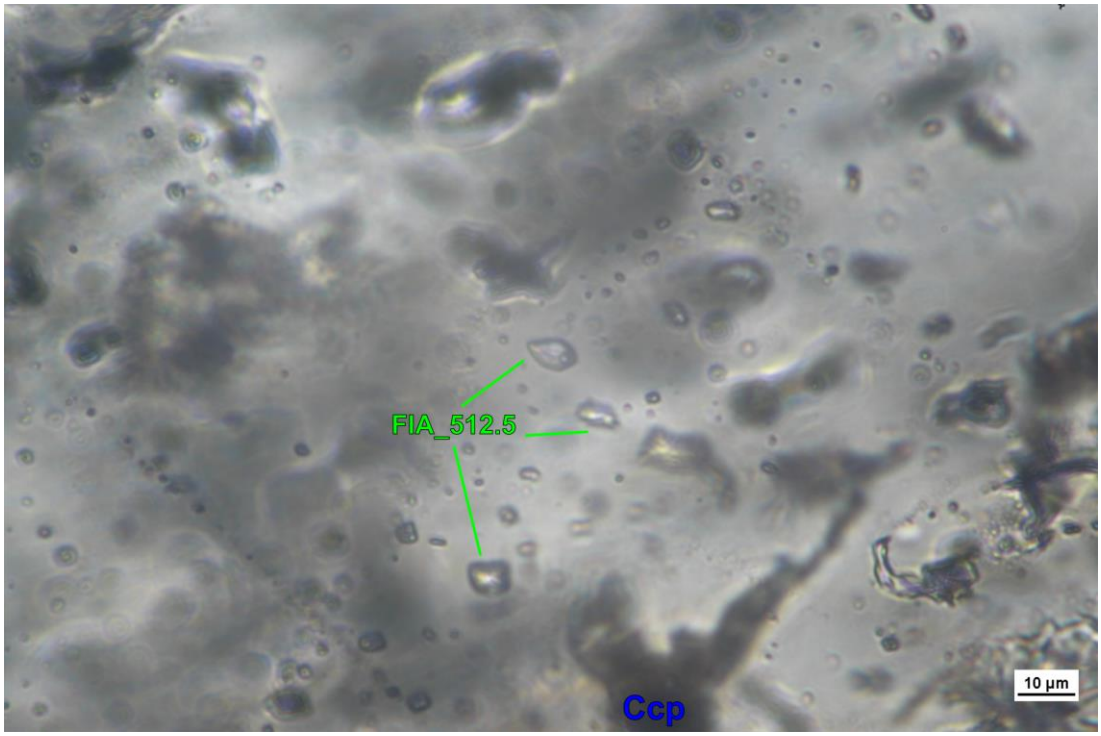


Sample **JL_GV_512** (scanned slide, width of slide 46 mm, transmitted light images):

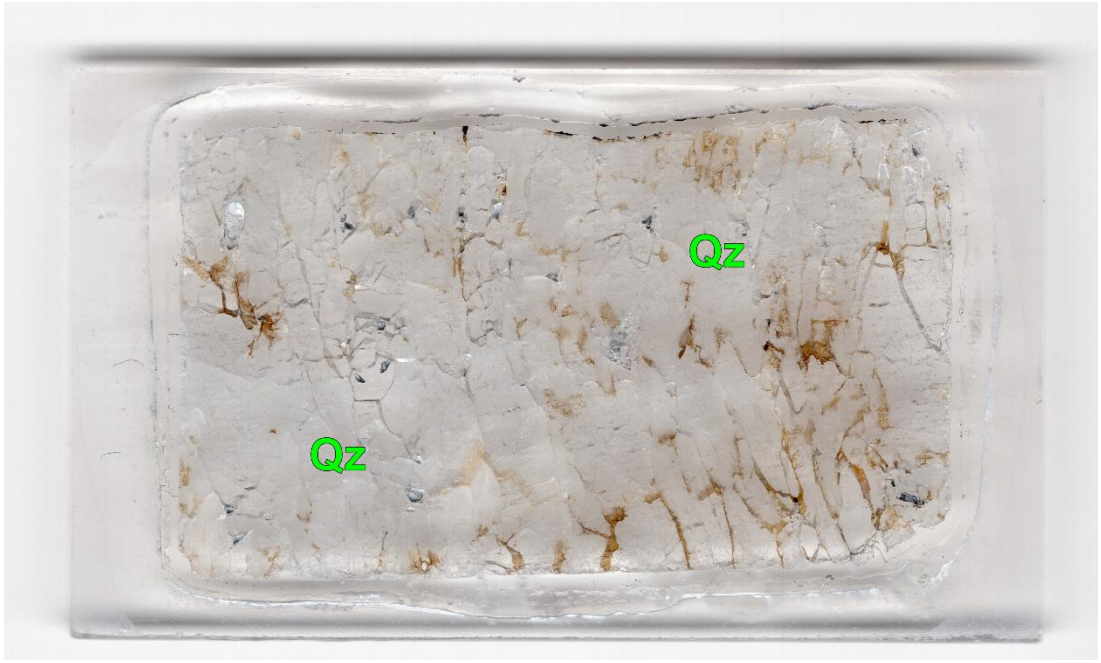


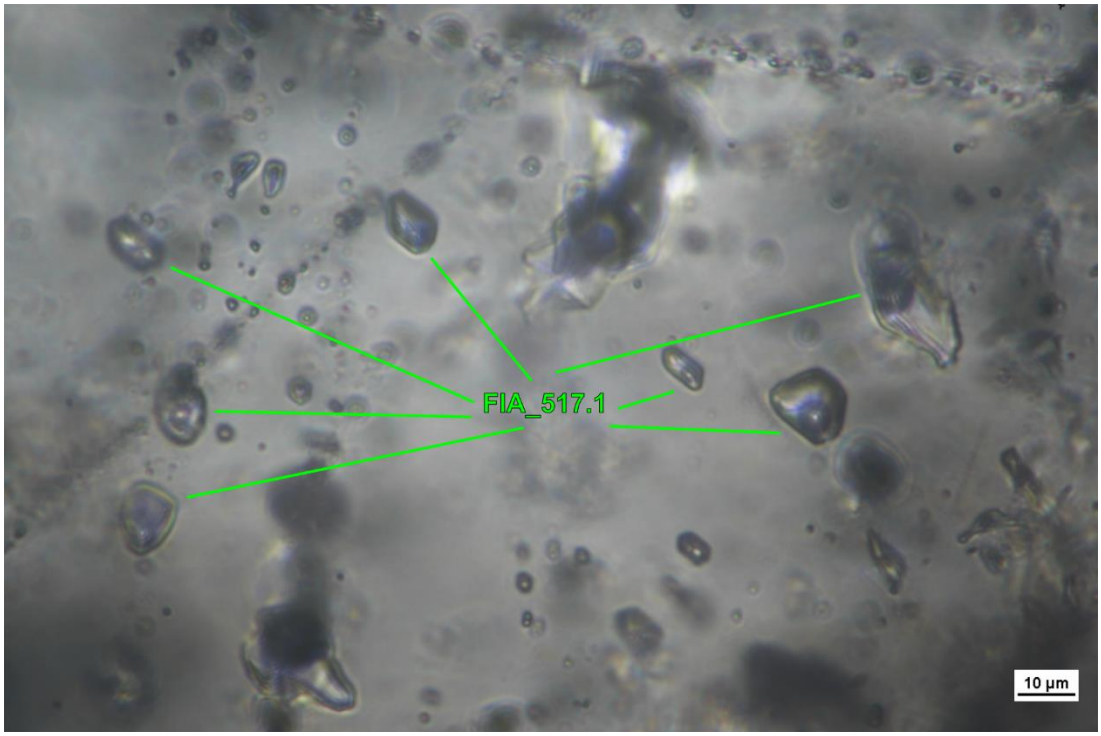

FIA_512.1
Ccp
10 µm


Ccp
FIA_512.3
10 µm



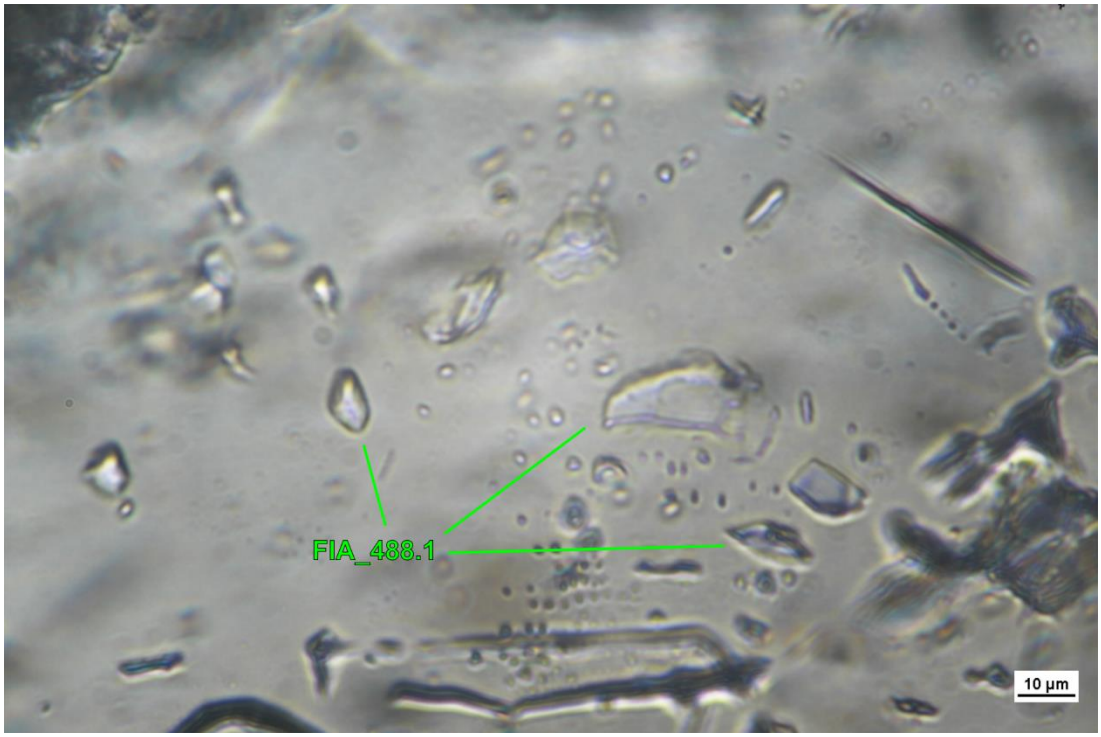
Sample **JL_GV_517** (scanned slide, width of slide 46 mm, transmitted light images):

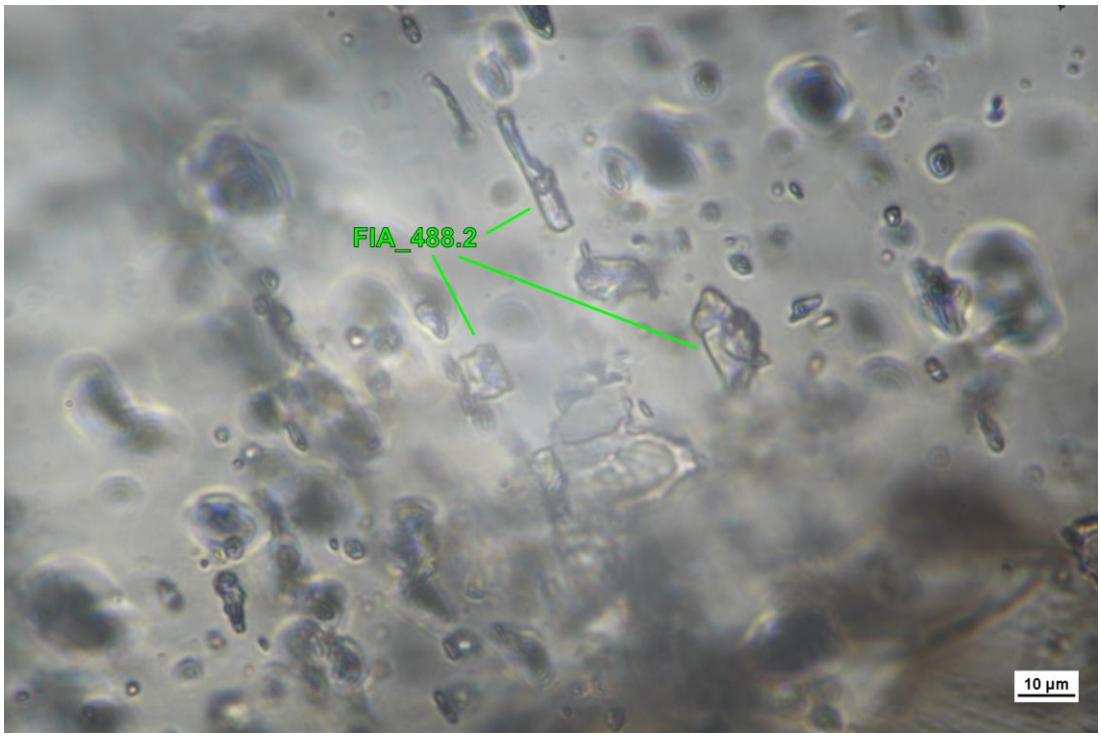




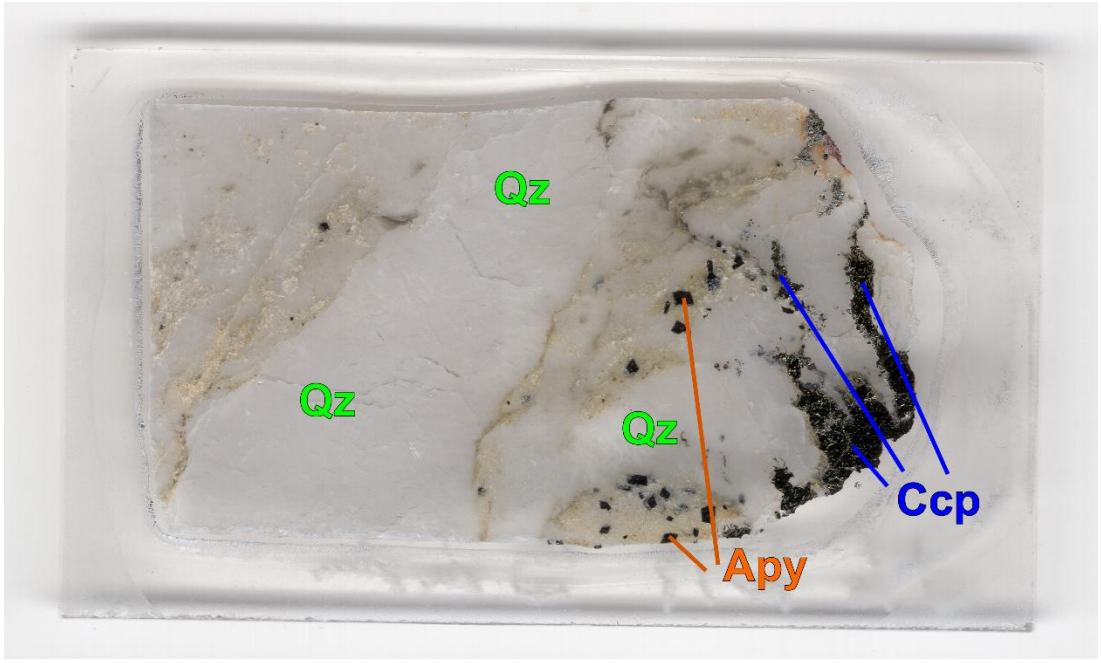
Sample **JL_CH_488** (scanned slide, width of slide 46 mm, transmitted light images):

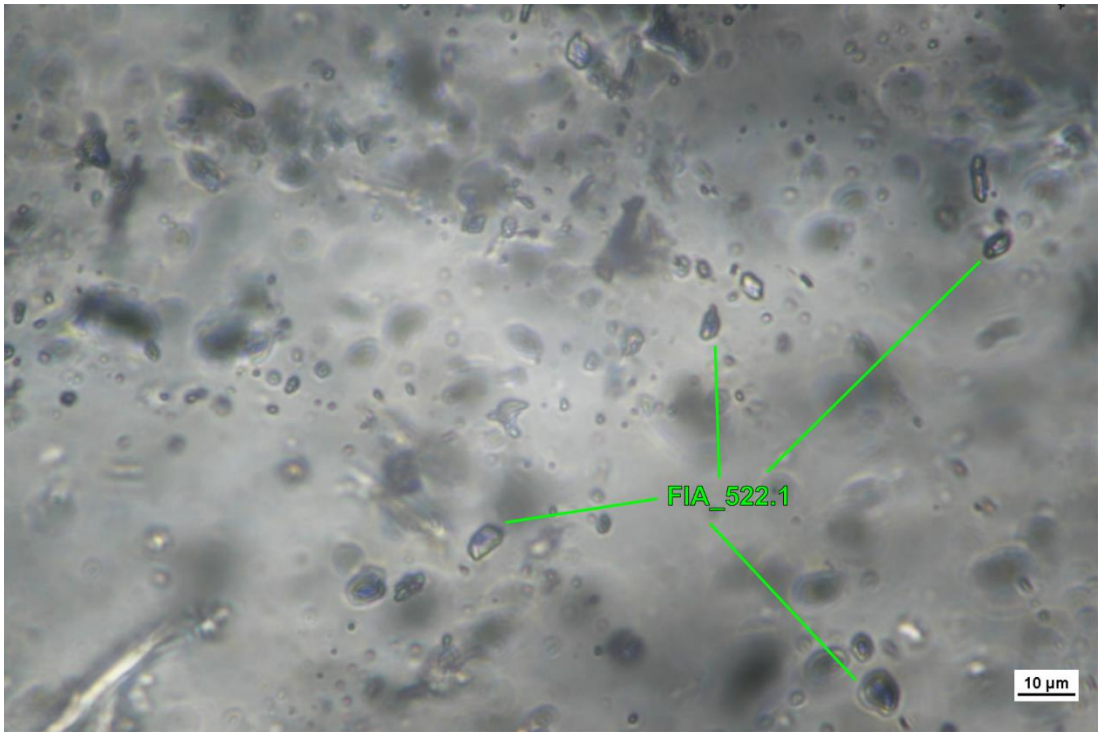


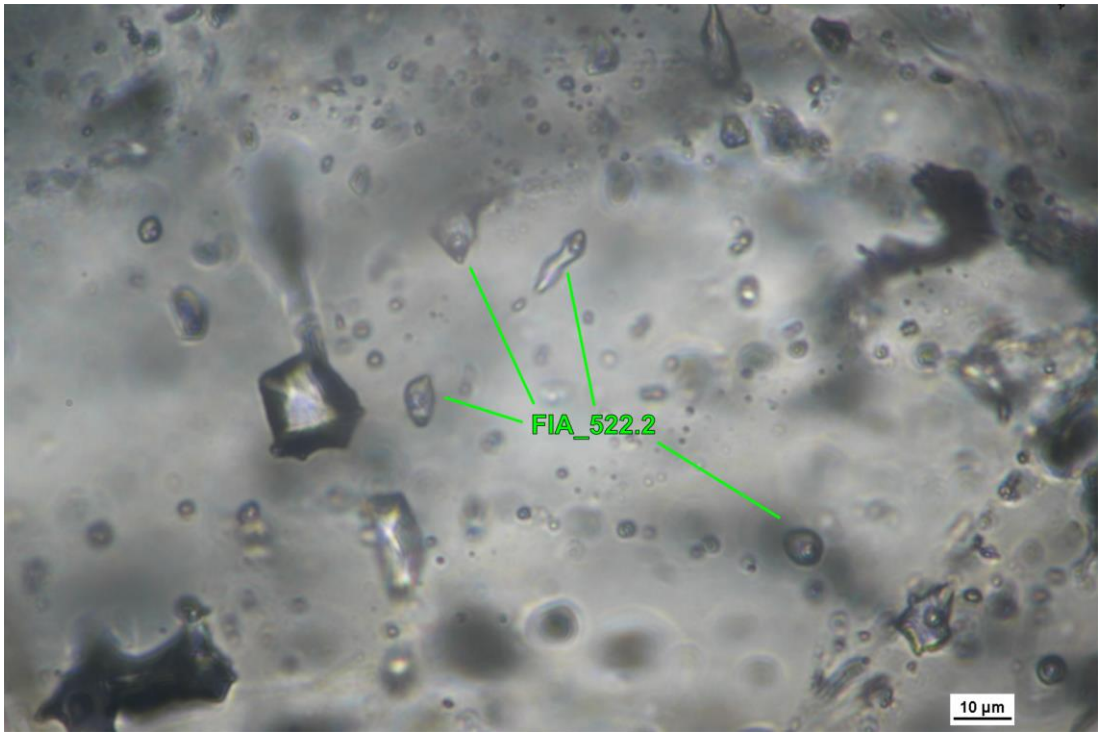

FIA_488.1
10 µm

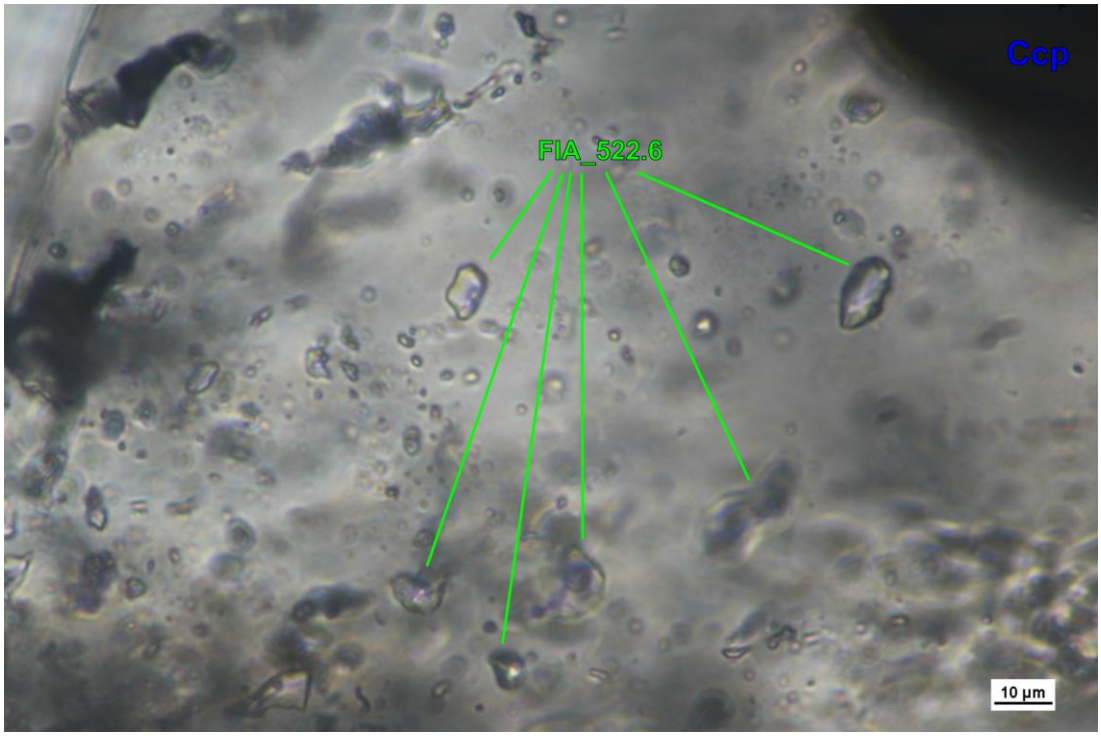

FIA_488.2
10 µm

Sample **JL_DH_522** (scanned slide, width of slide 46 mm, transmitted light images):



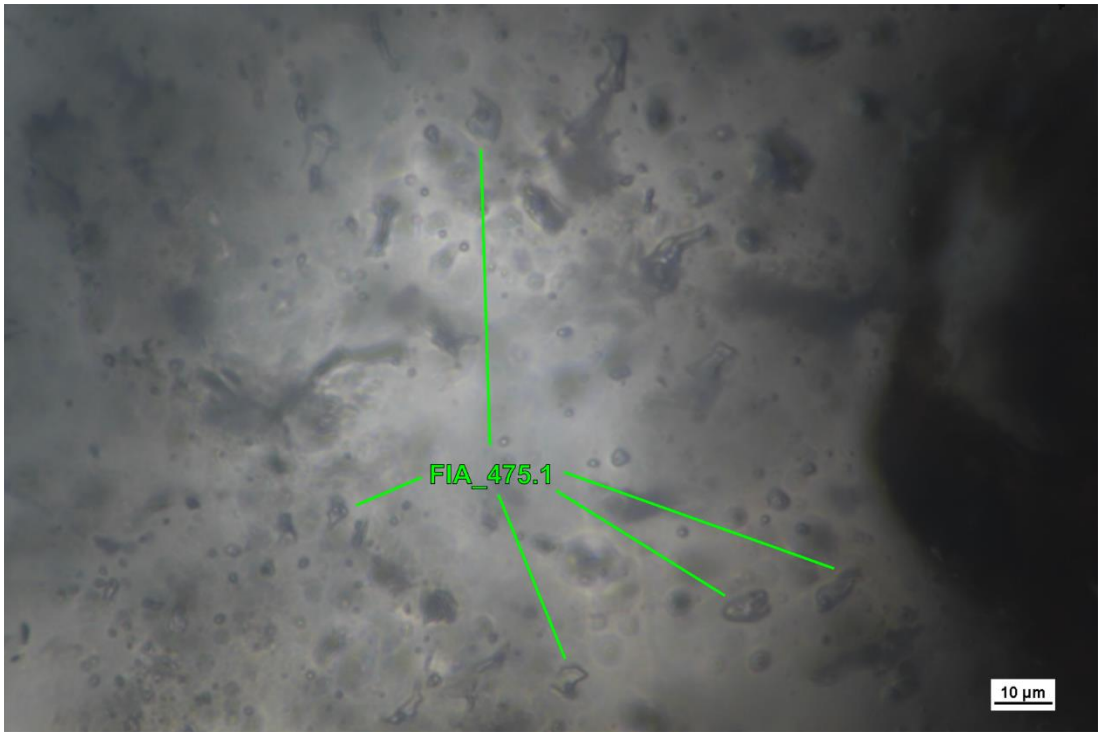


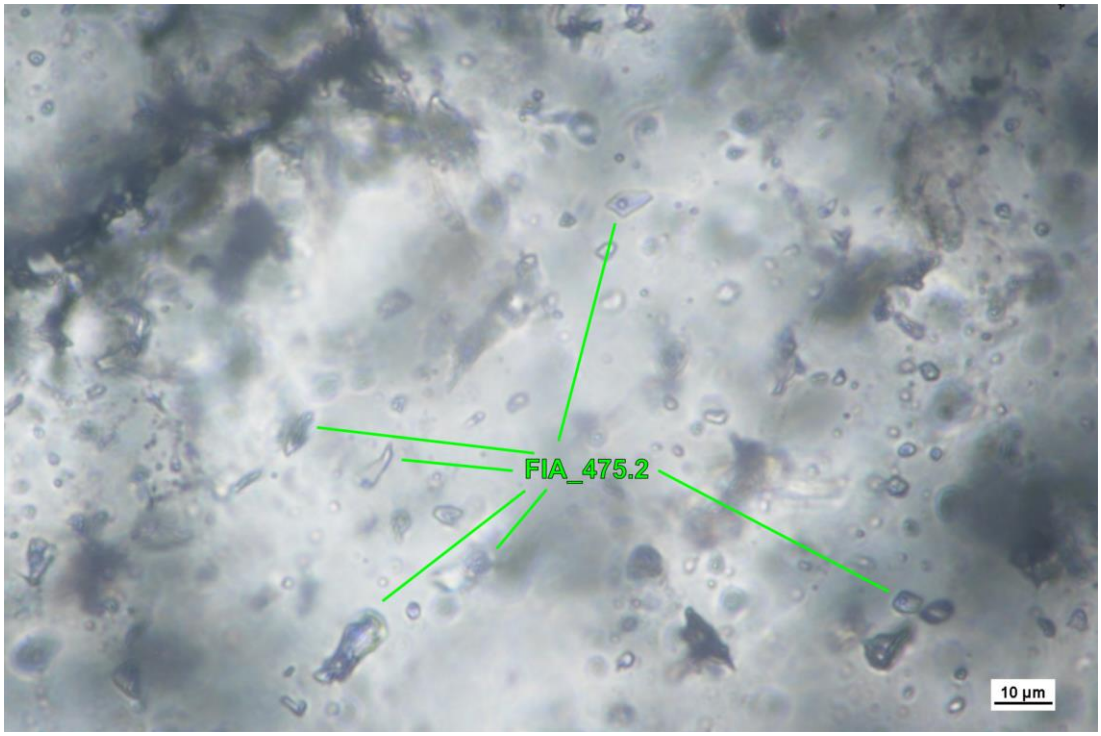

FIA_522.2
10 µm

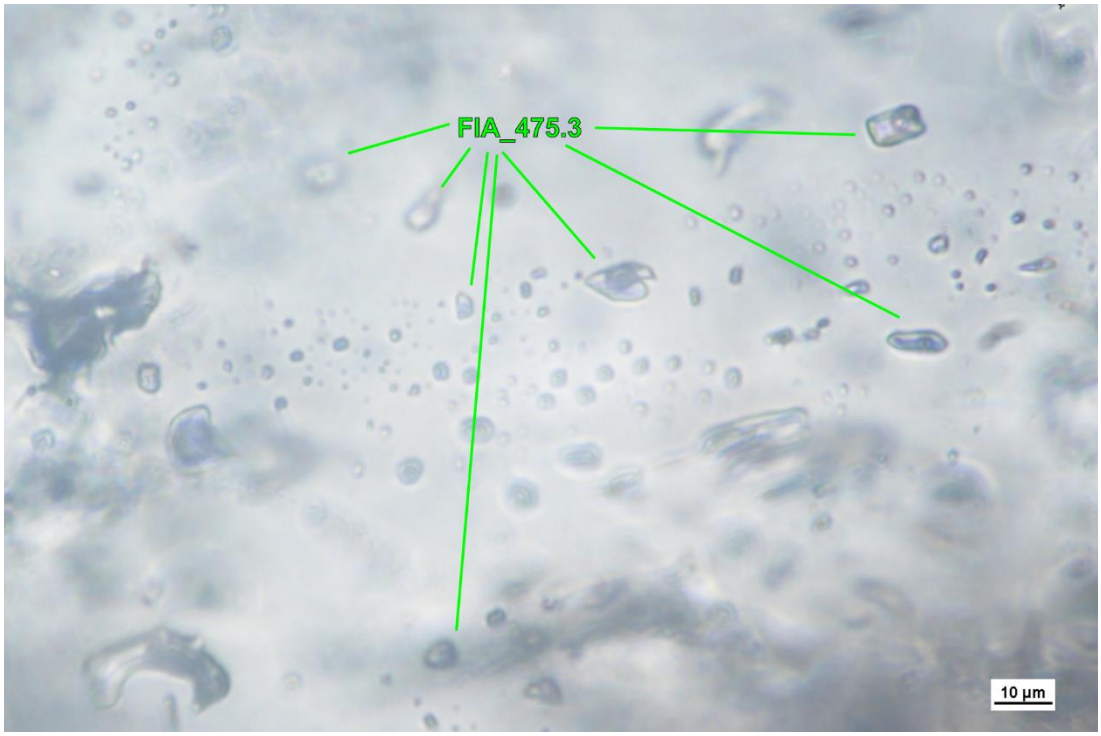

Ccp
FIA_522.6
10 µm

Sample **JL_BH_475** (scanned slide, width of slide 46 mm, transmitted light images):



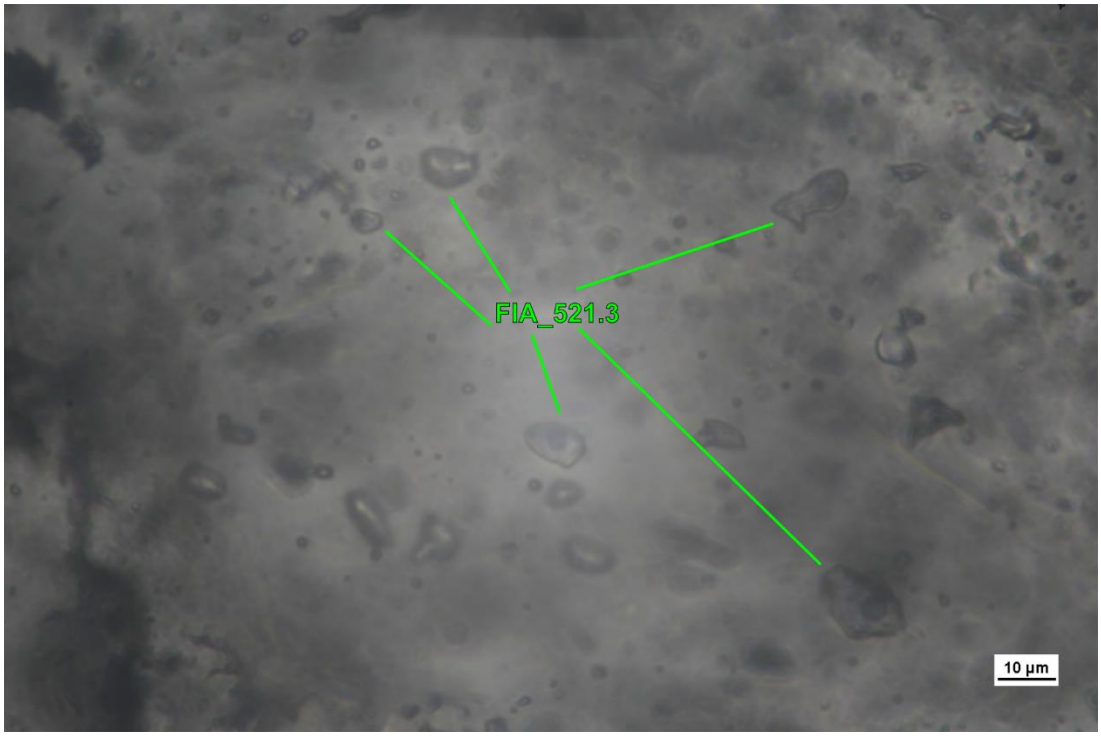


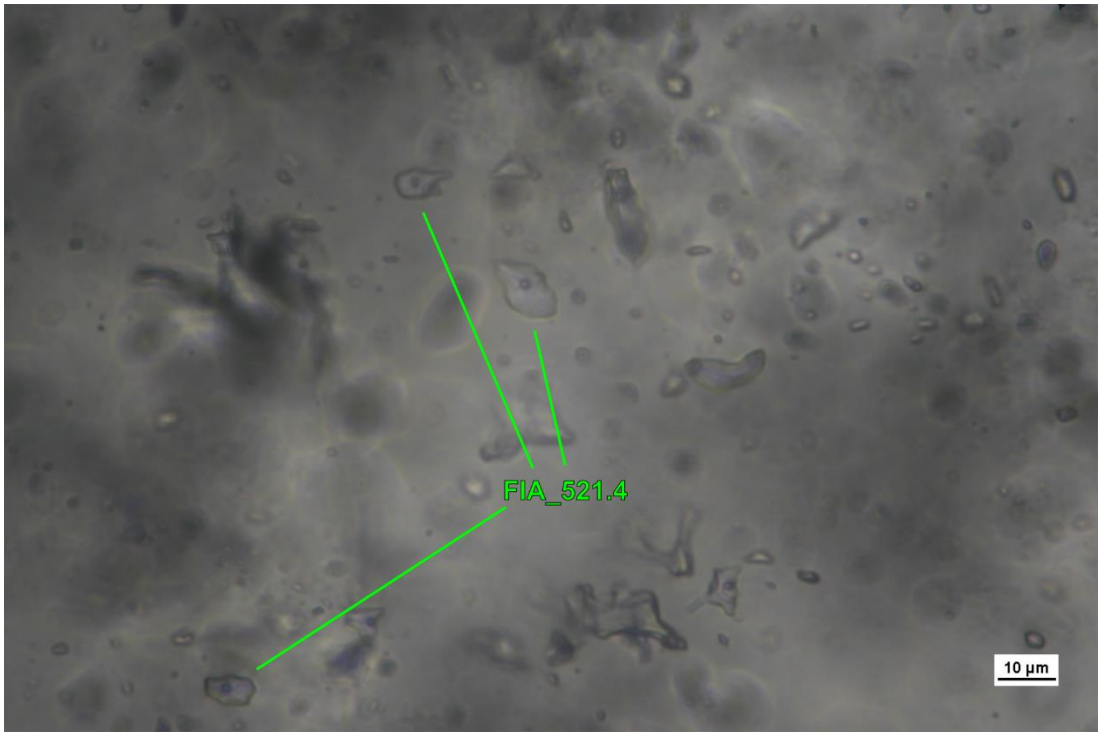

FIA_475.2
10 µm

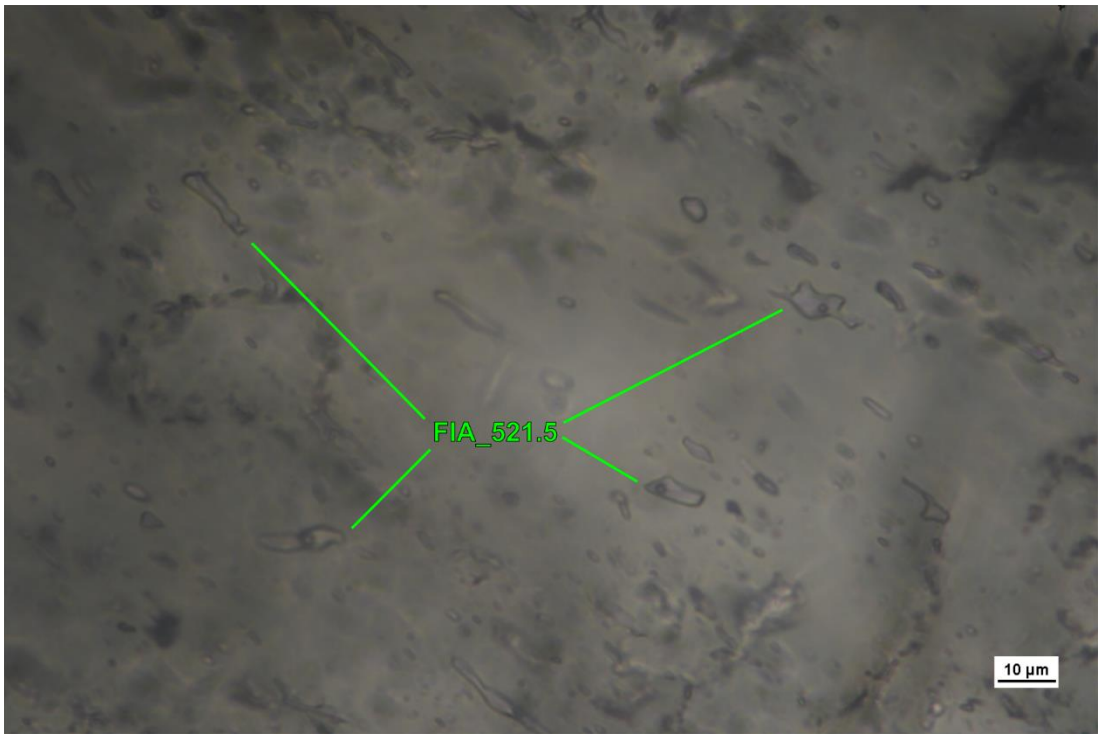

FIA_475.3
10 µm

Sample **JL_CH_521** (scanned slide, width of slide 46 mm, transmitted light images):

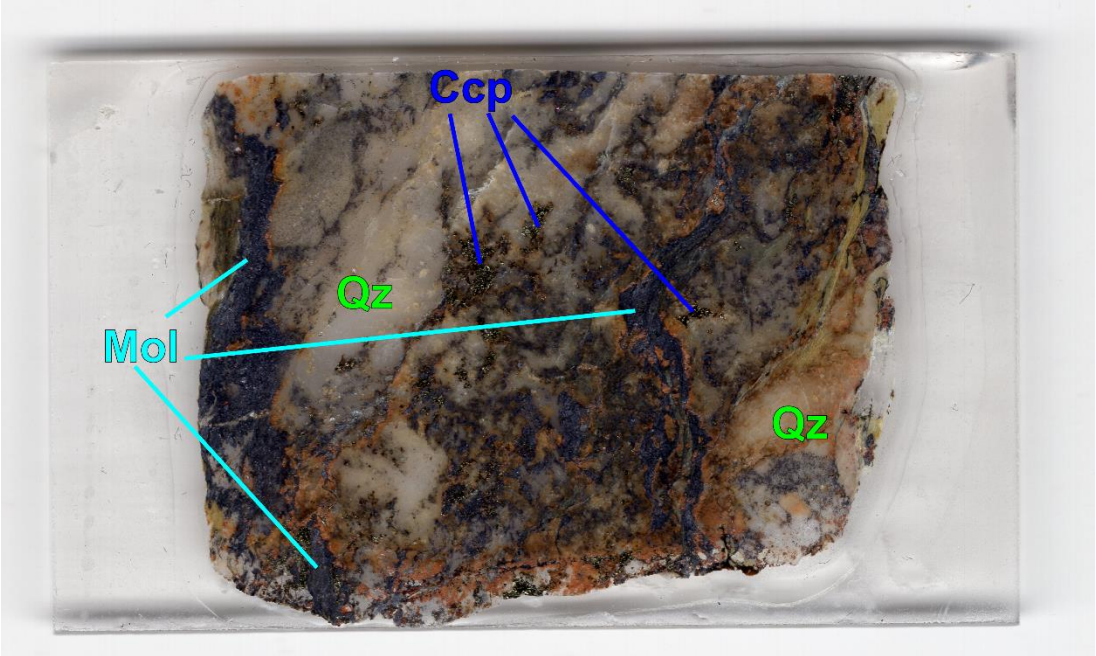


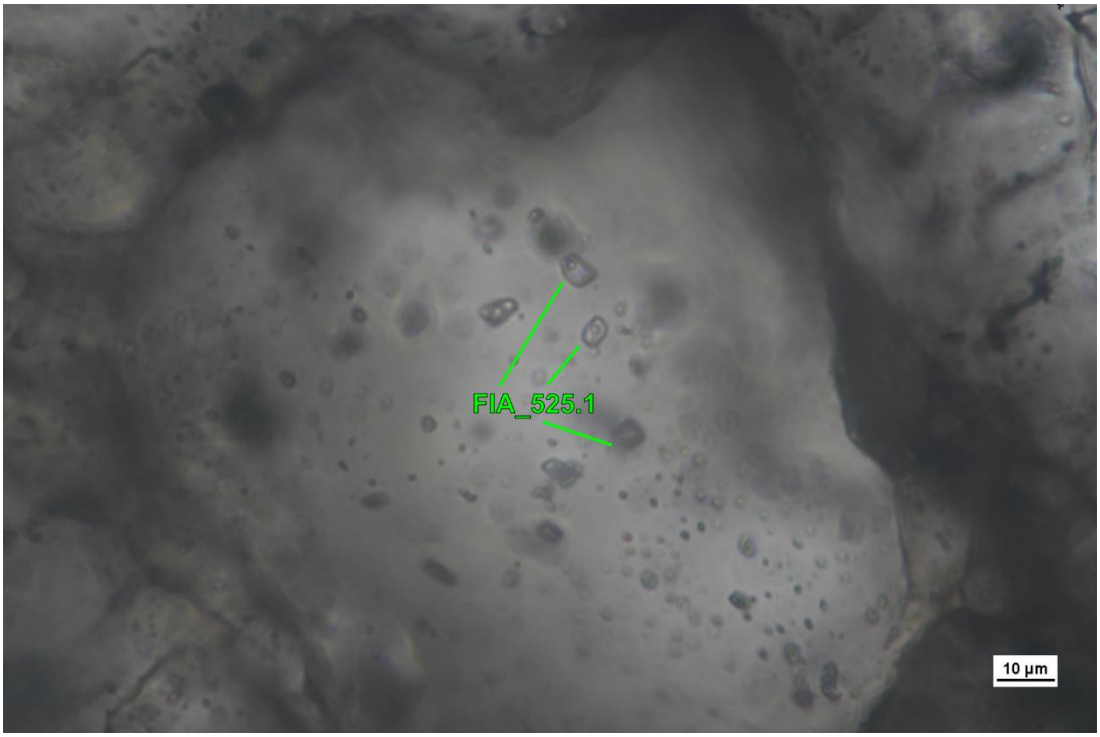


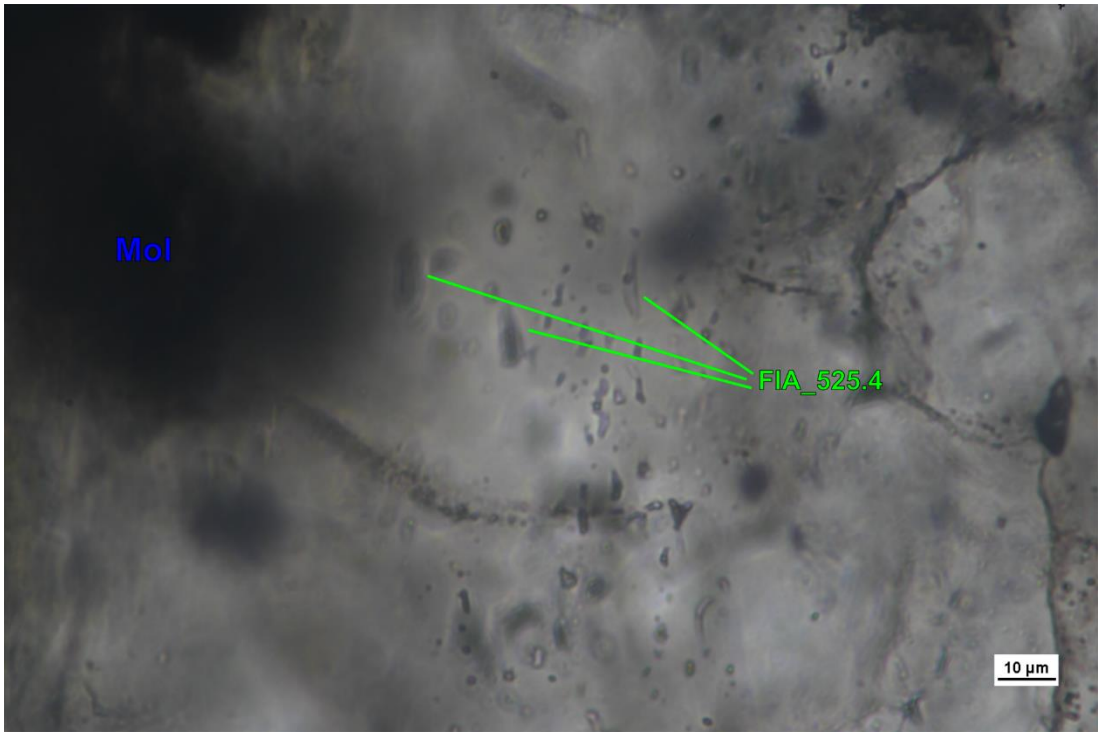

FIA_521.4
10 µm

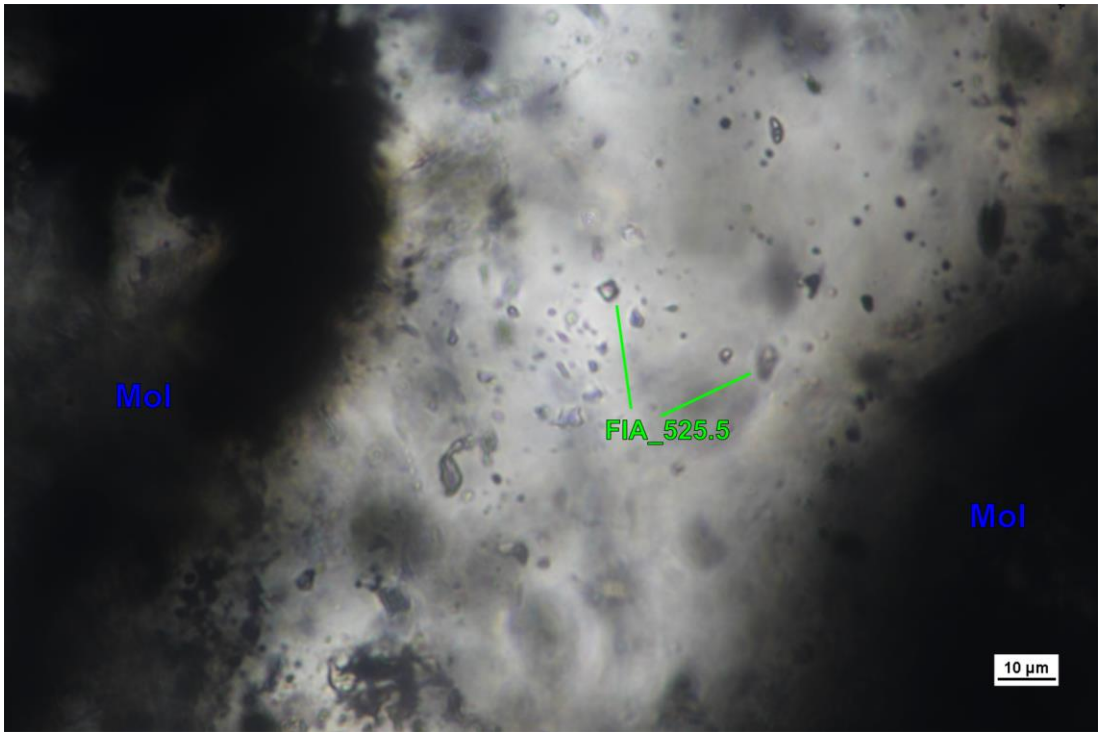

FIA_521.5
10 µm

Sample **JL_BC_525Re** (scanned slide, width of slide 46 mm, transmitted light images):

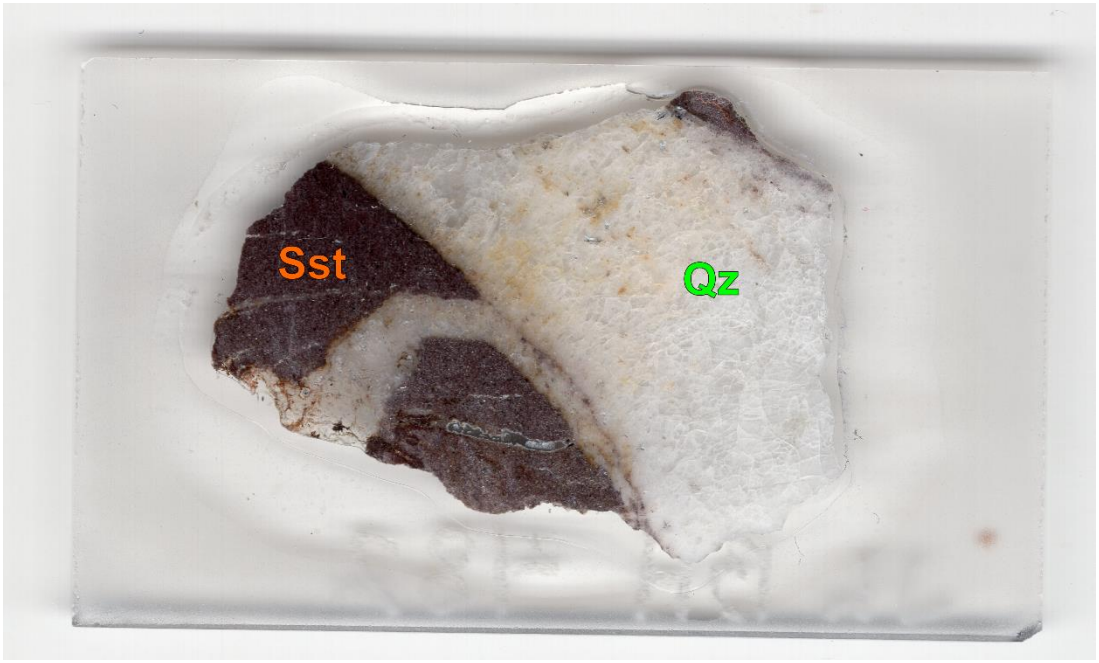


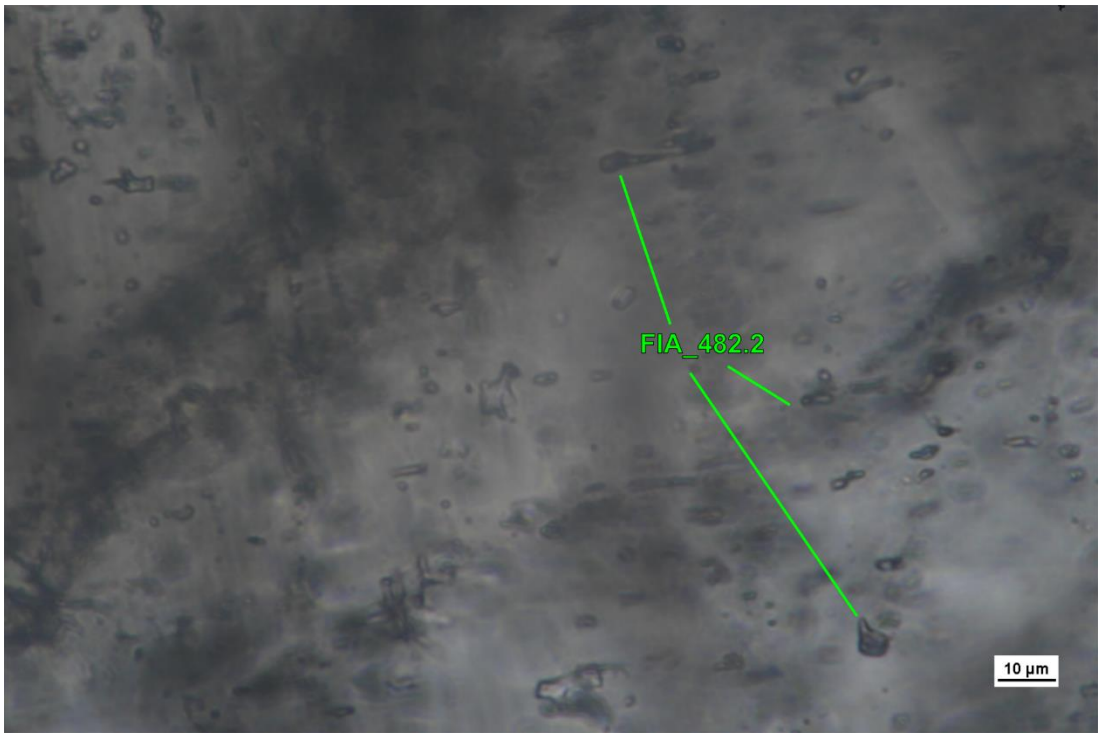


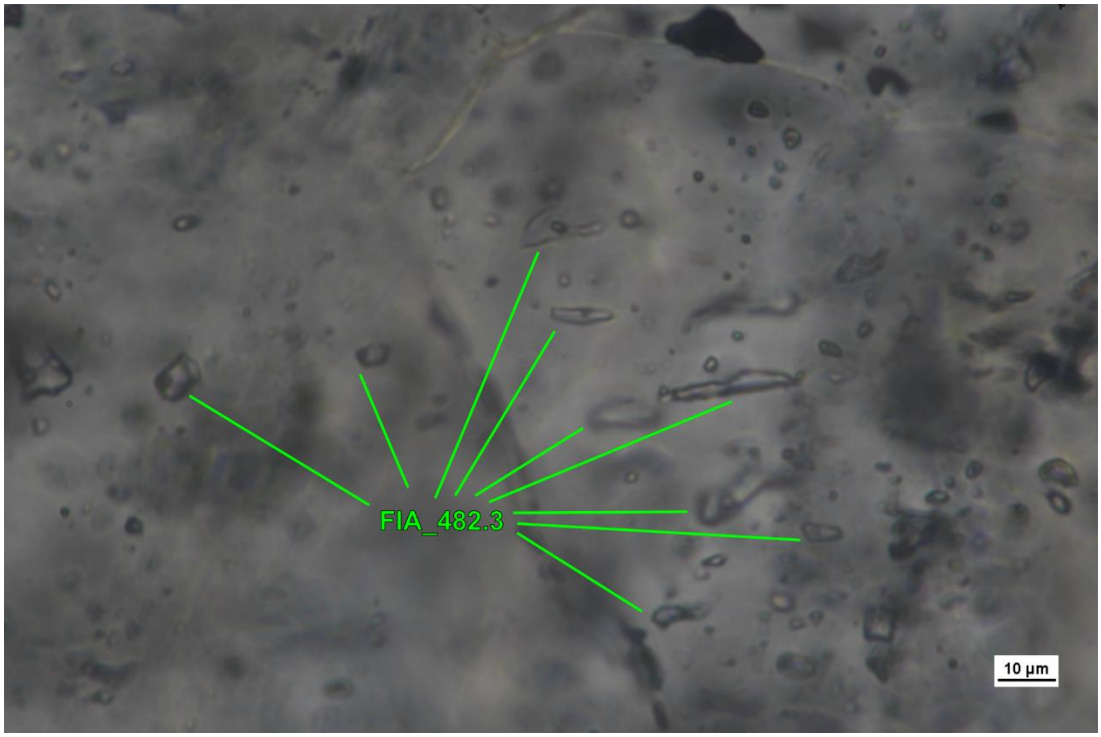

Mol
FIA_525.4
10 µm


Mol
FIA_525.5
Mol
10 µm

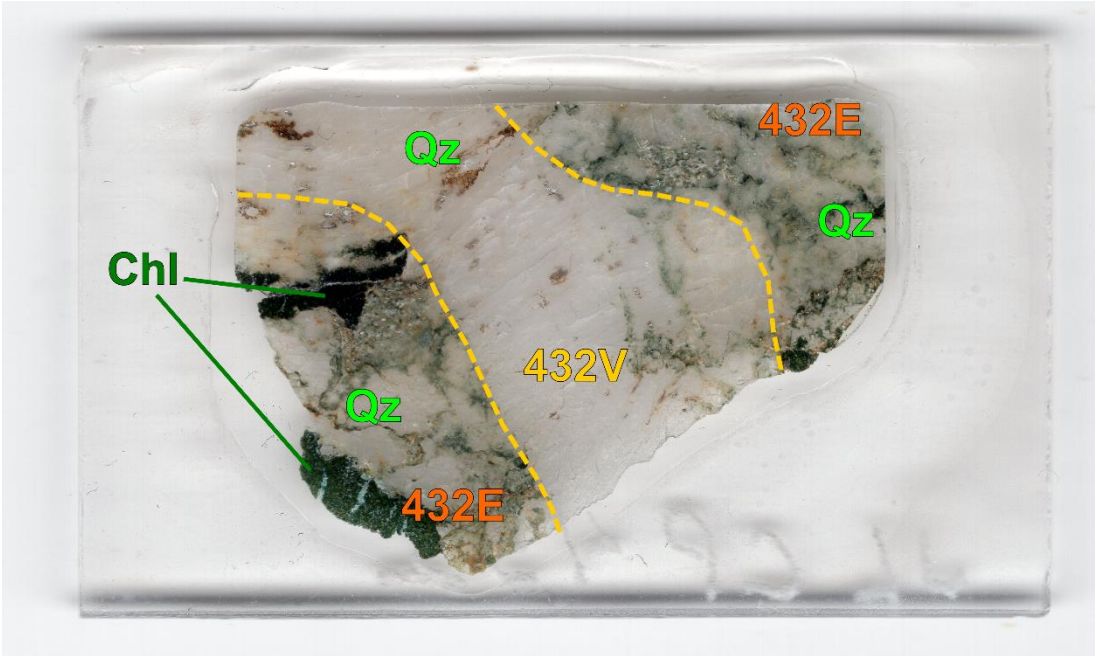
Sample **JL_BH_482** (scanned slide, width of slide 46 mm, transmitted light images):

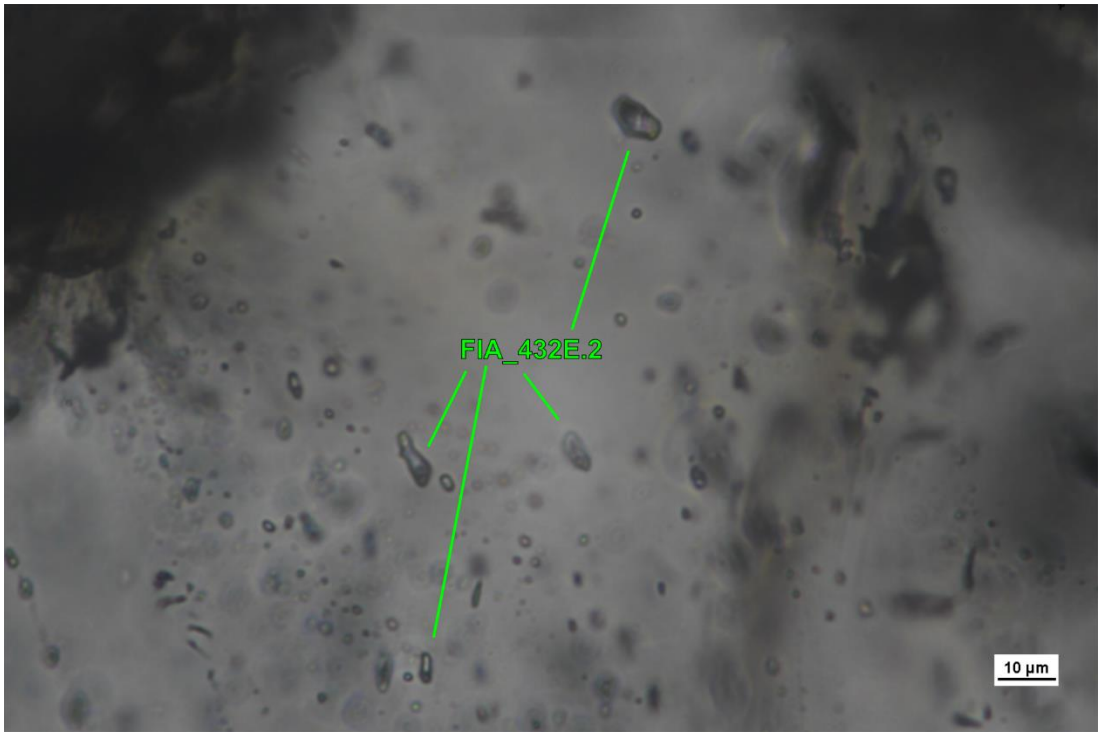


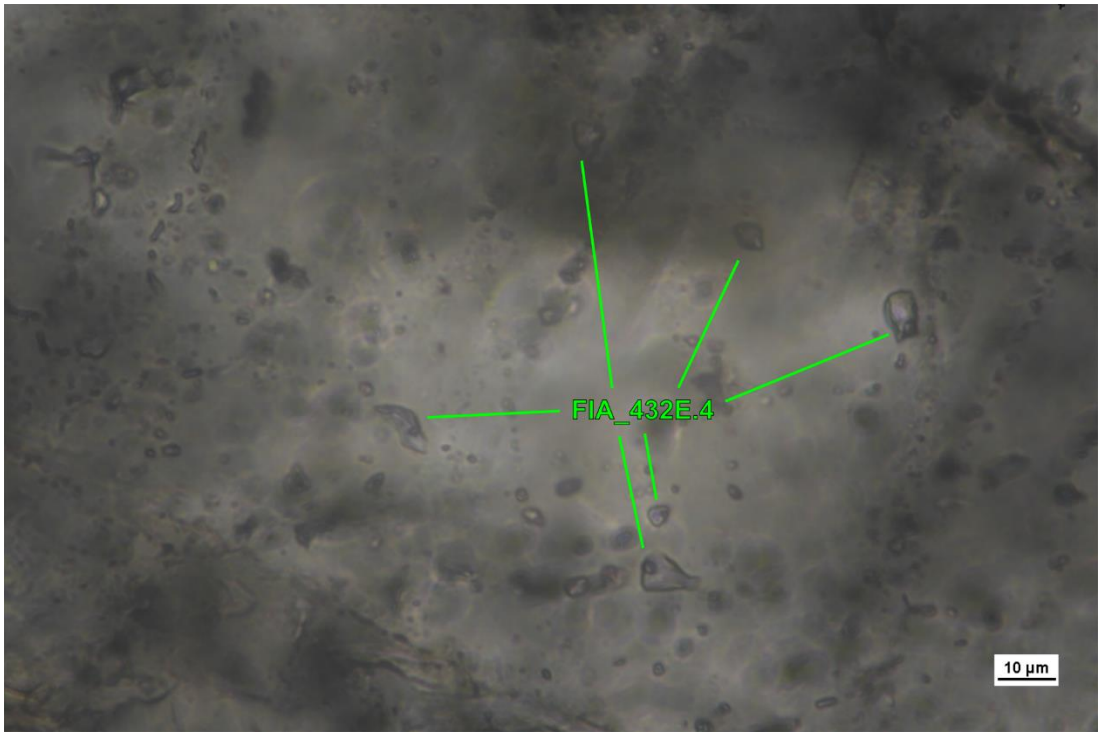


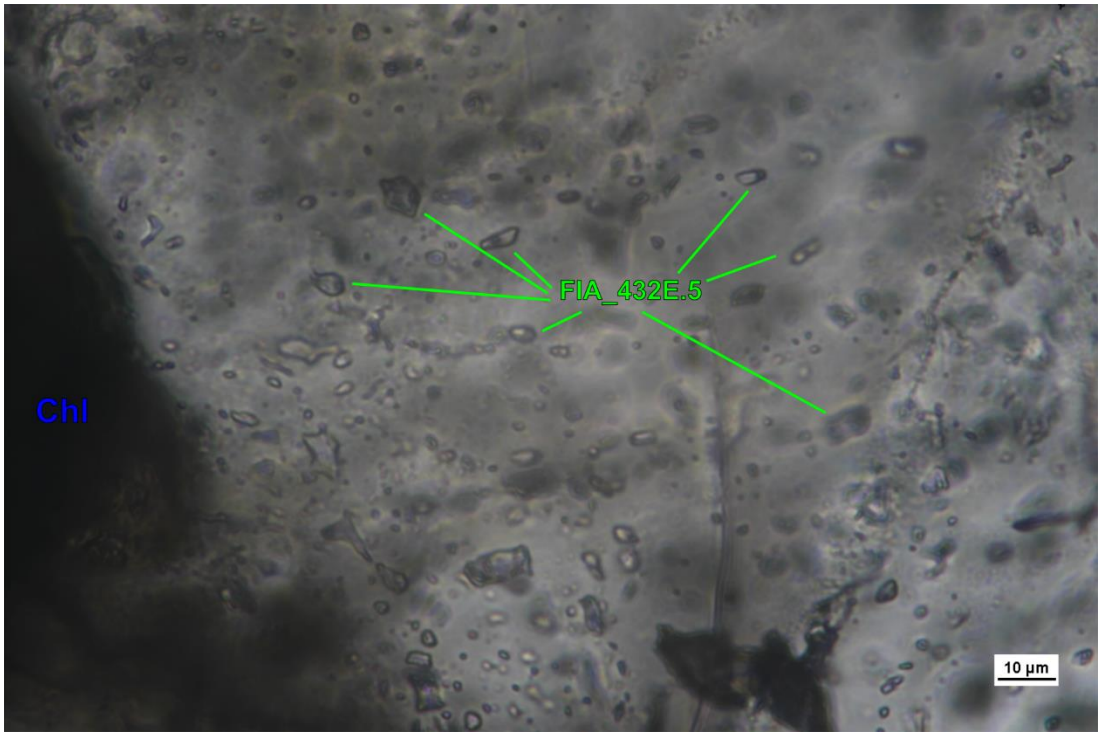


Sample **JL_CP_432E** (scanned slide, width of slide 46 mm, transmitted light images):

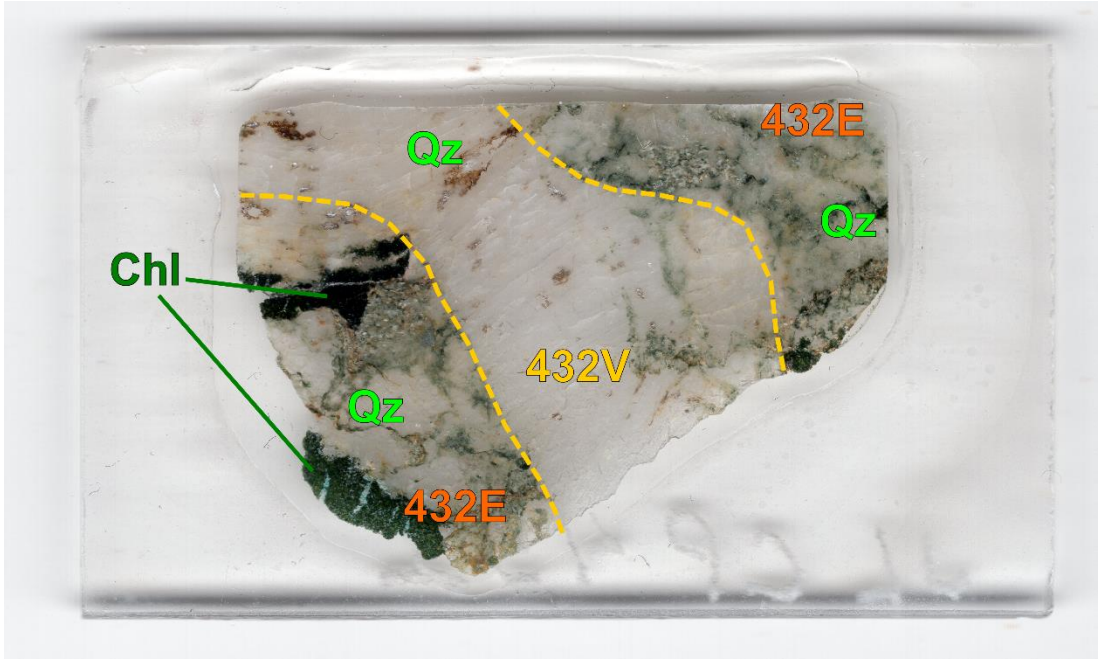


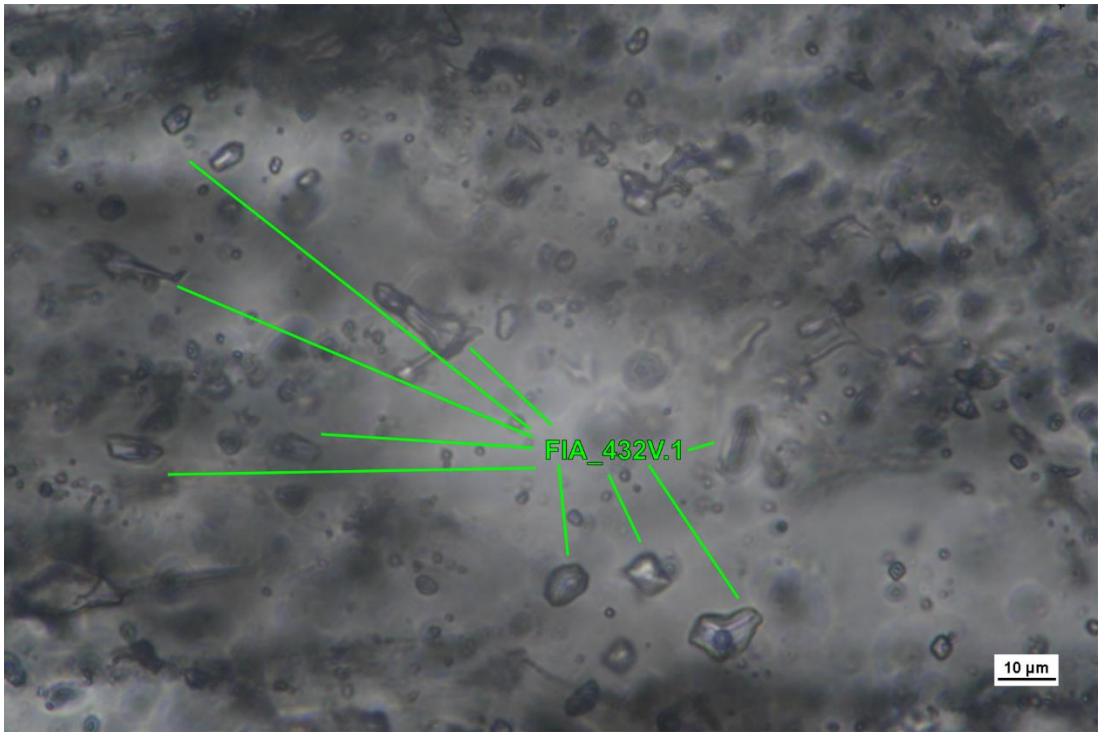

FIA_432E.2
10 µm

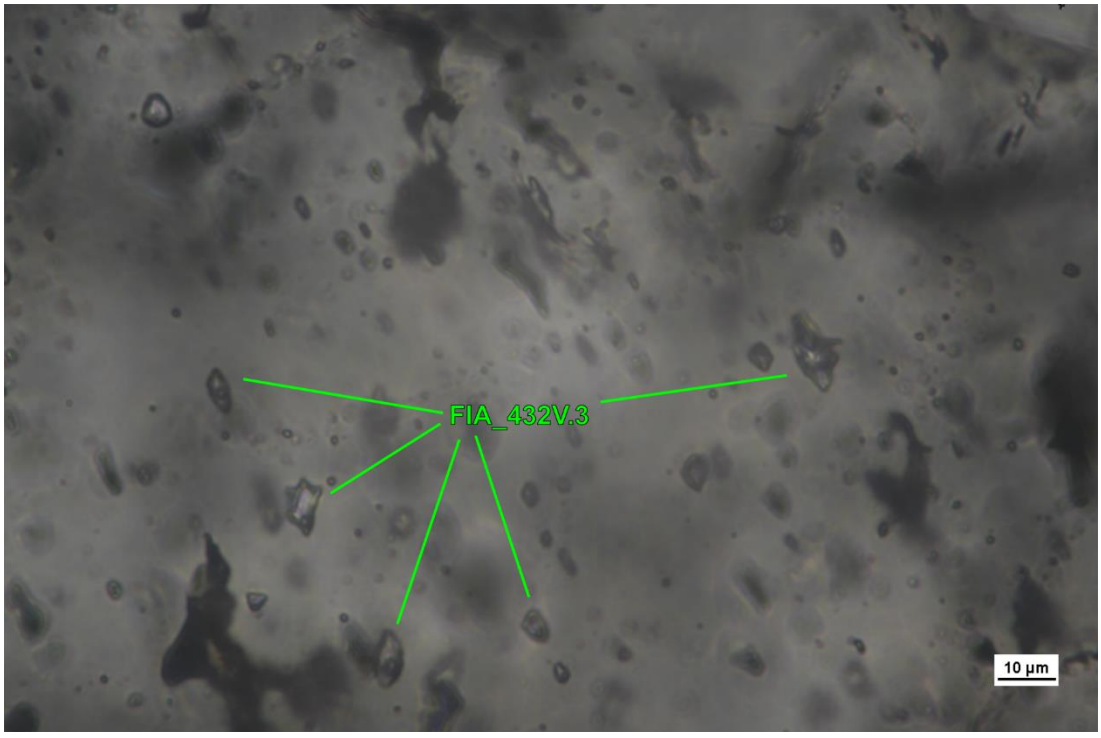

FIA_432E.4
10 µm



Sample **JL_CP_432V** (scanned slide, width of slide 46 mm, transmitted light images):

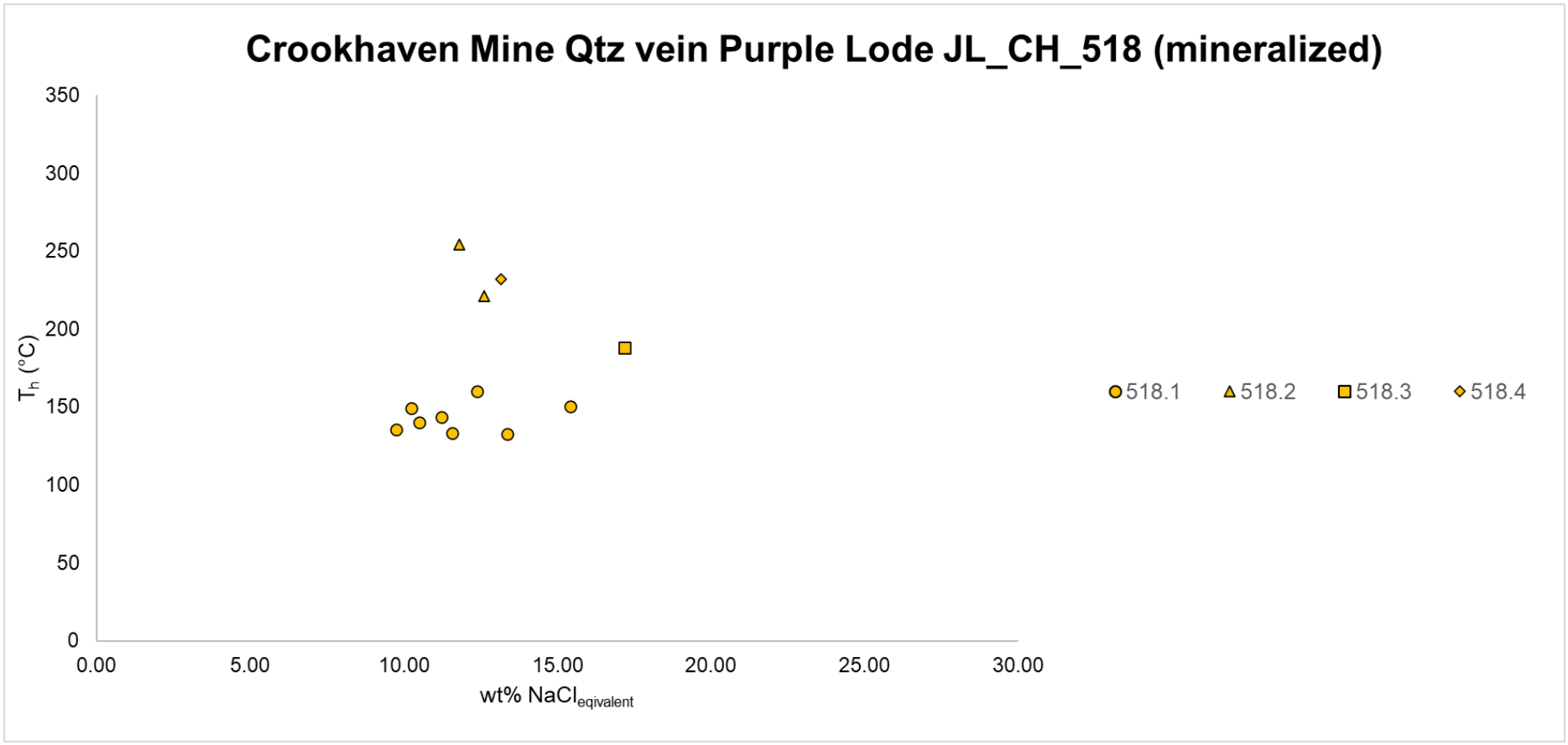


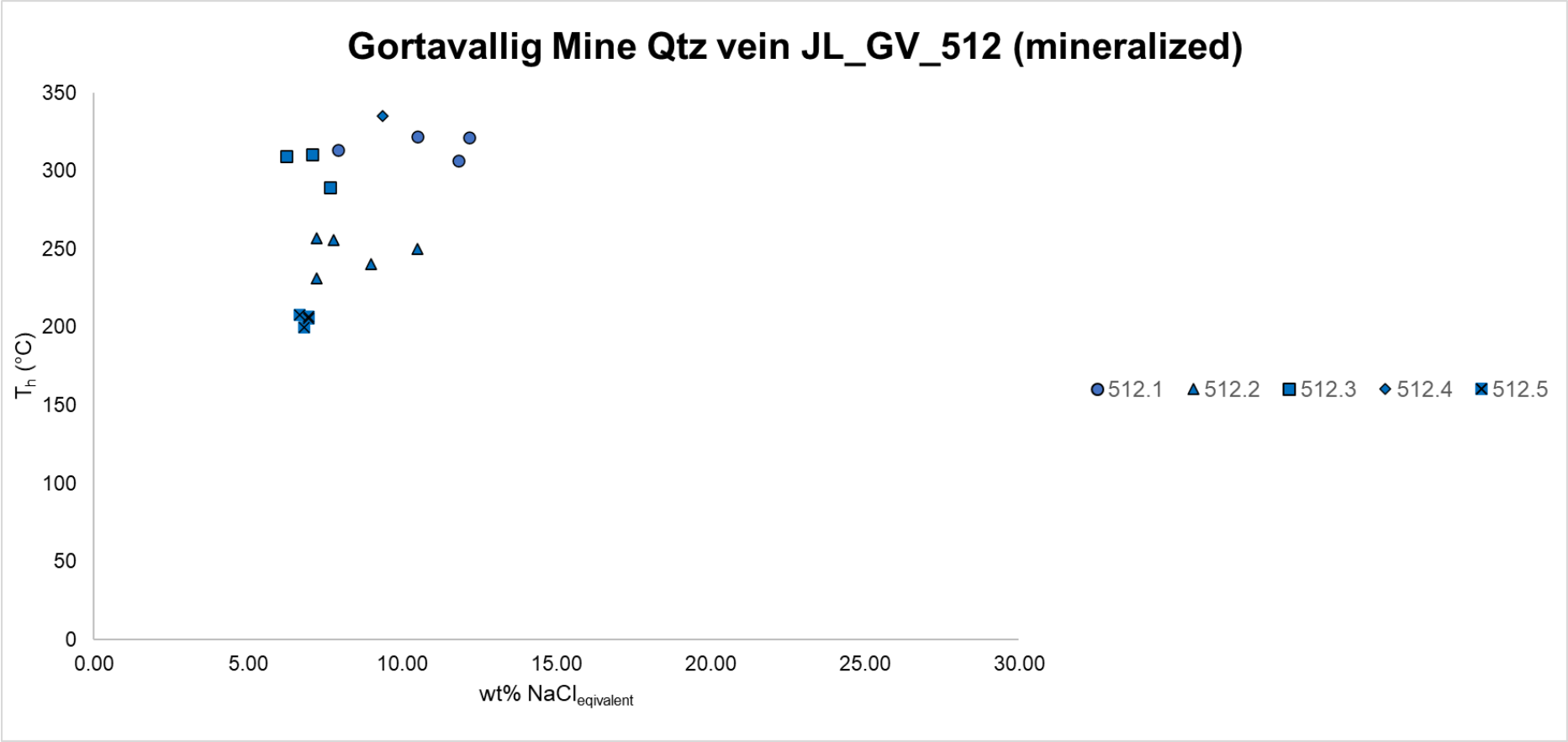

FIA_432V.1
10 µm

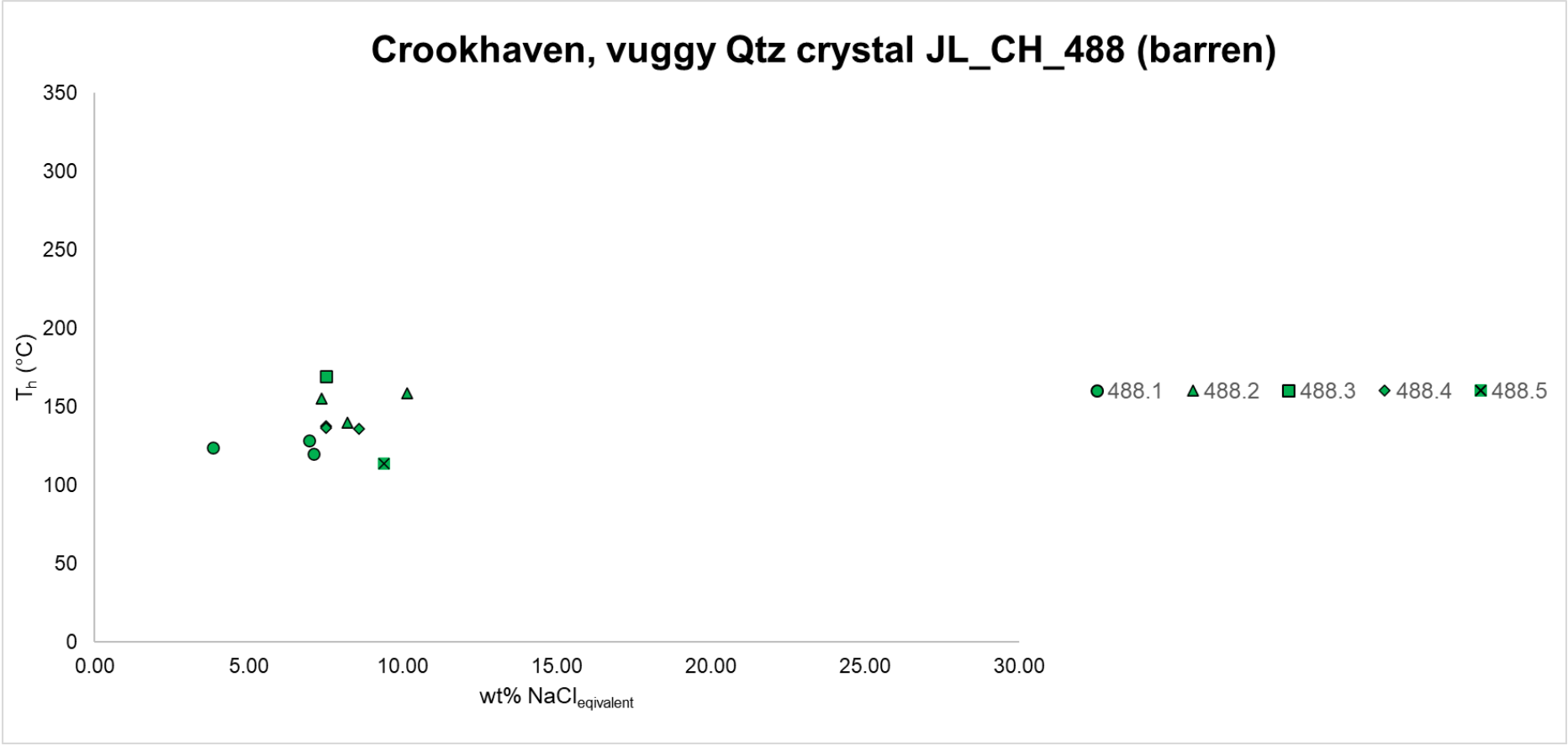

FIA_432V.3
10 µm

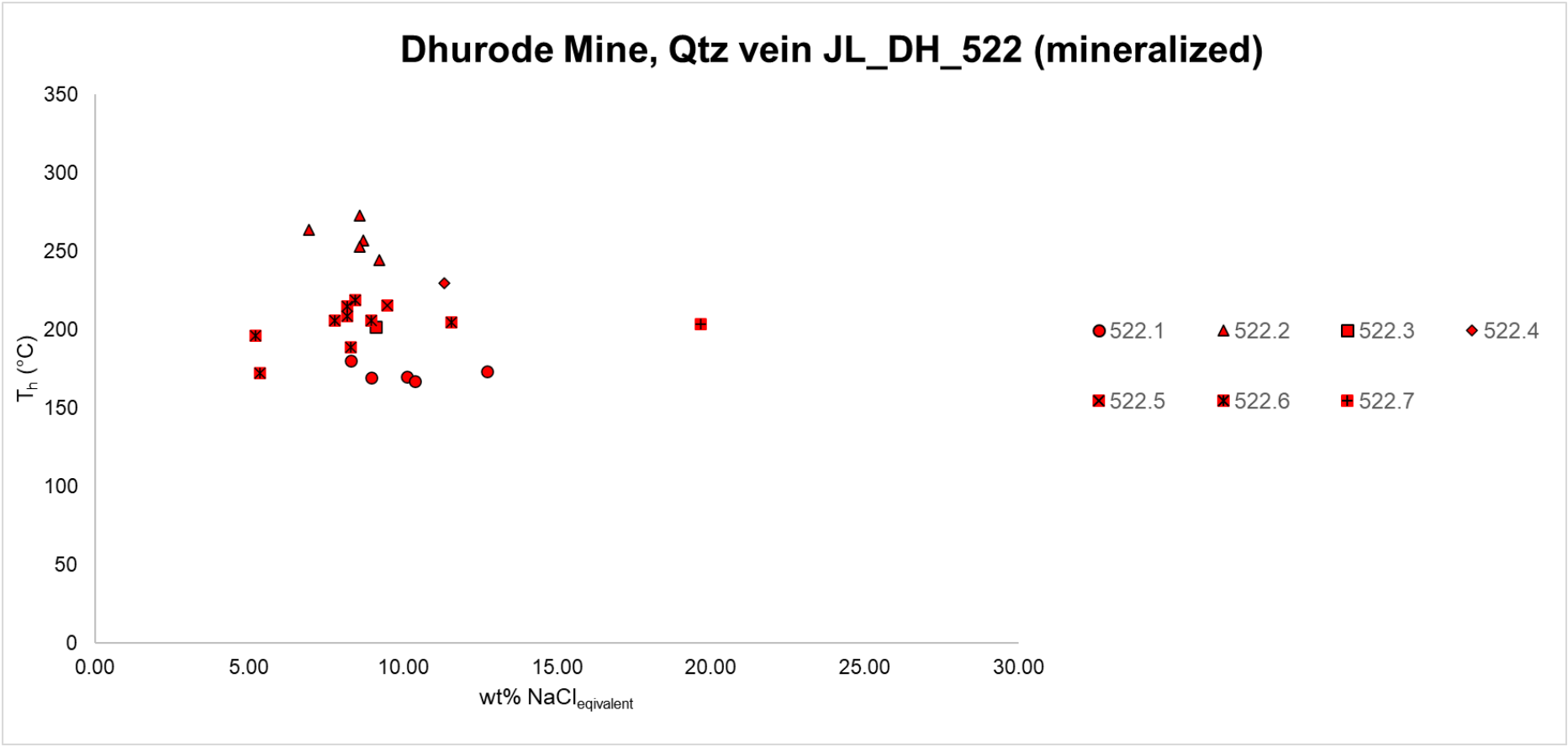
Appendix E.3 (Chapter 4)

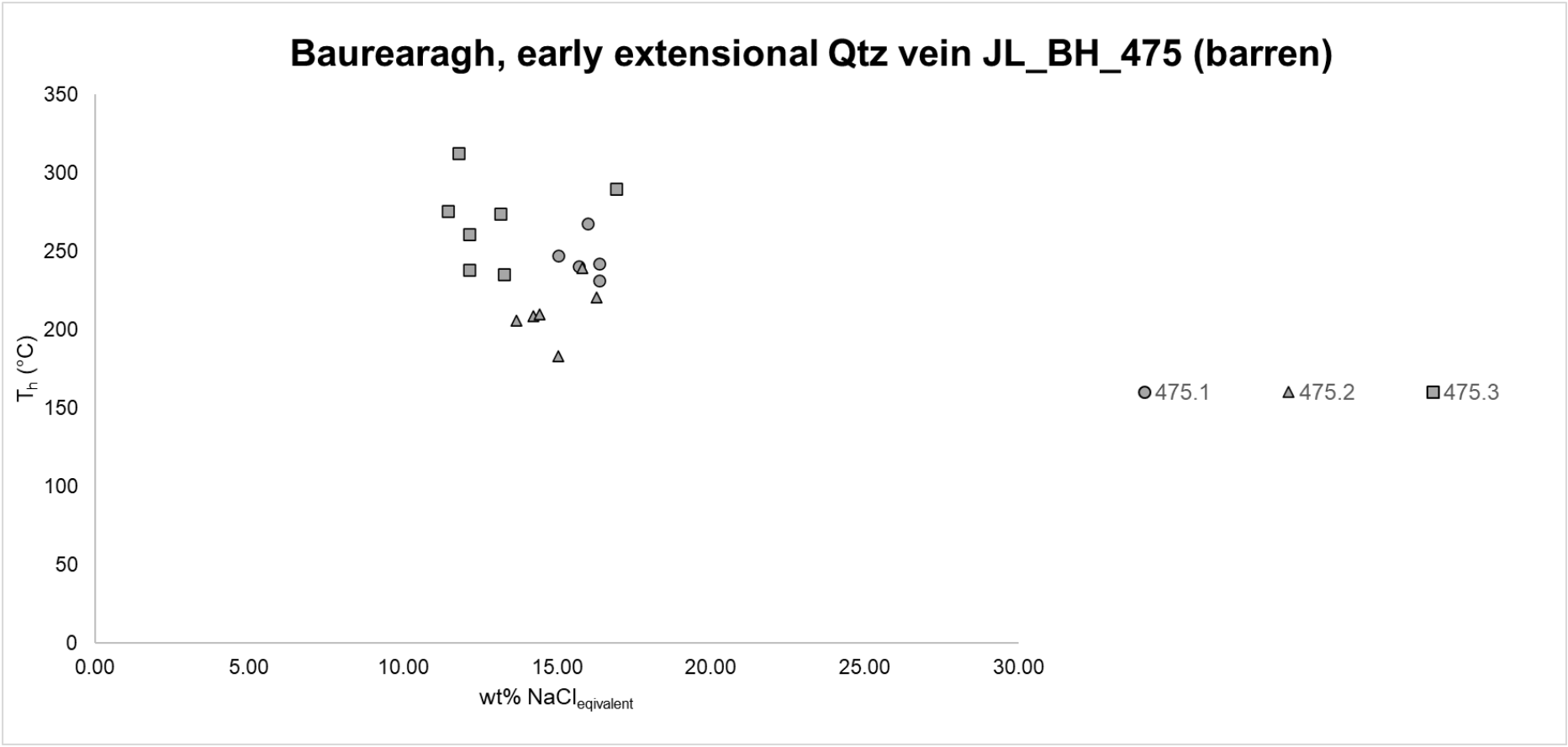
The following graphs show the individual sample plots (salinities wt% $NaCl_{equiv}$ versus homogenisation temperatures T_h (°C)) of the fluid inclusion assemblages (FIA_XXX, Appendix E2) from West Cork Copper Deposits. See figures 4.11a and 4.11b.

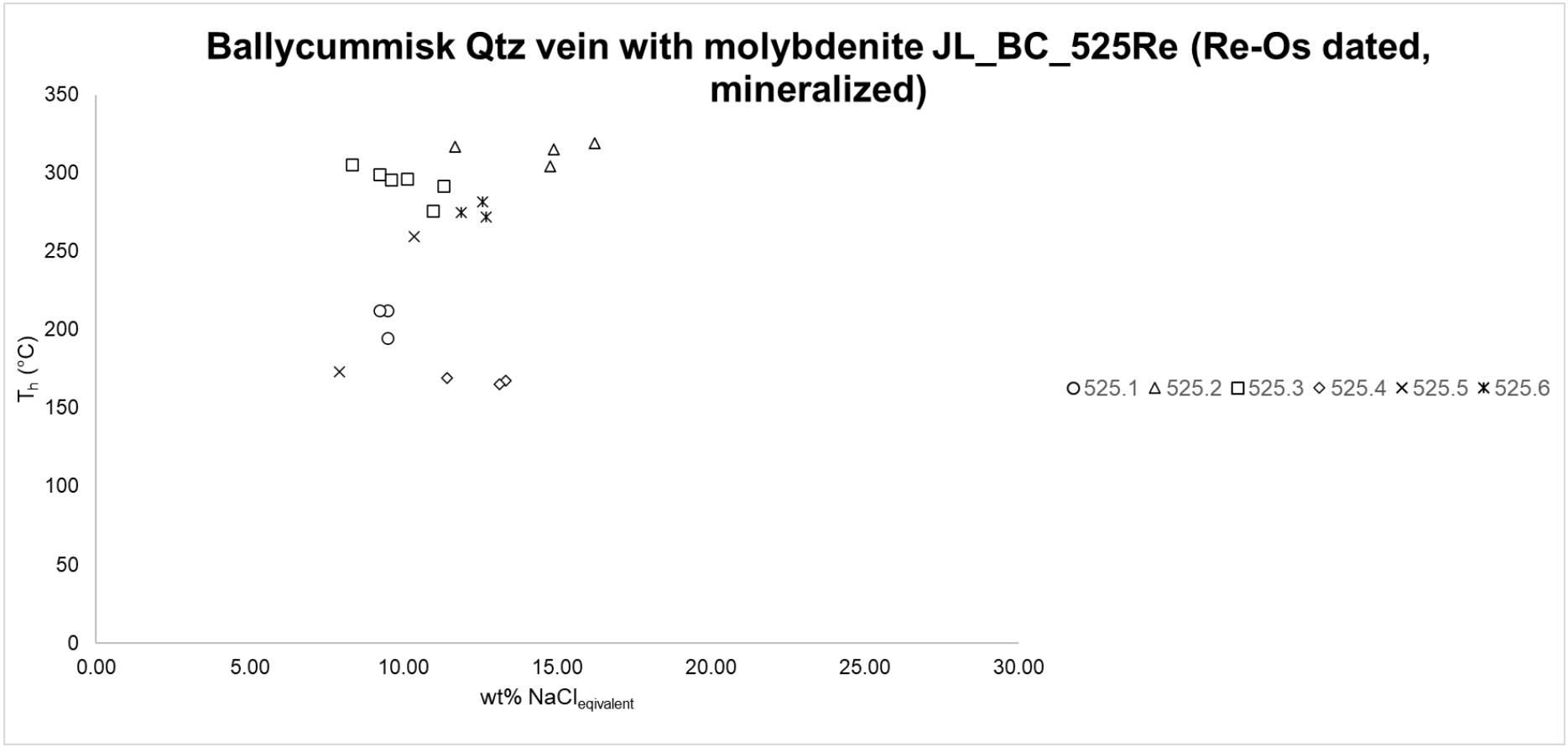

Crookhaven Mine Qtz vein Purple Lode JL_CH_518 (mineralized)
350
300
250
200
150
100
50
0
T_h (°C)
0.00
5.00
10.00
15.00
20.00
25.00
30.00
wt% $NaCl_{eqivalent}$
518.1
518.2
518.3
518.4

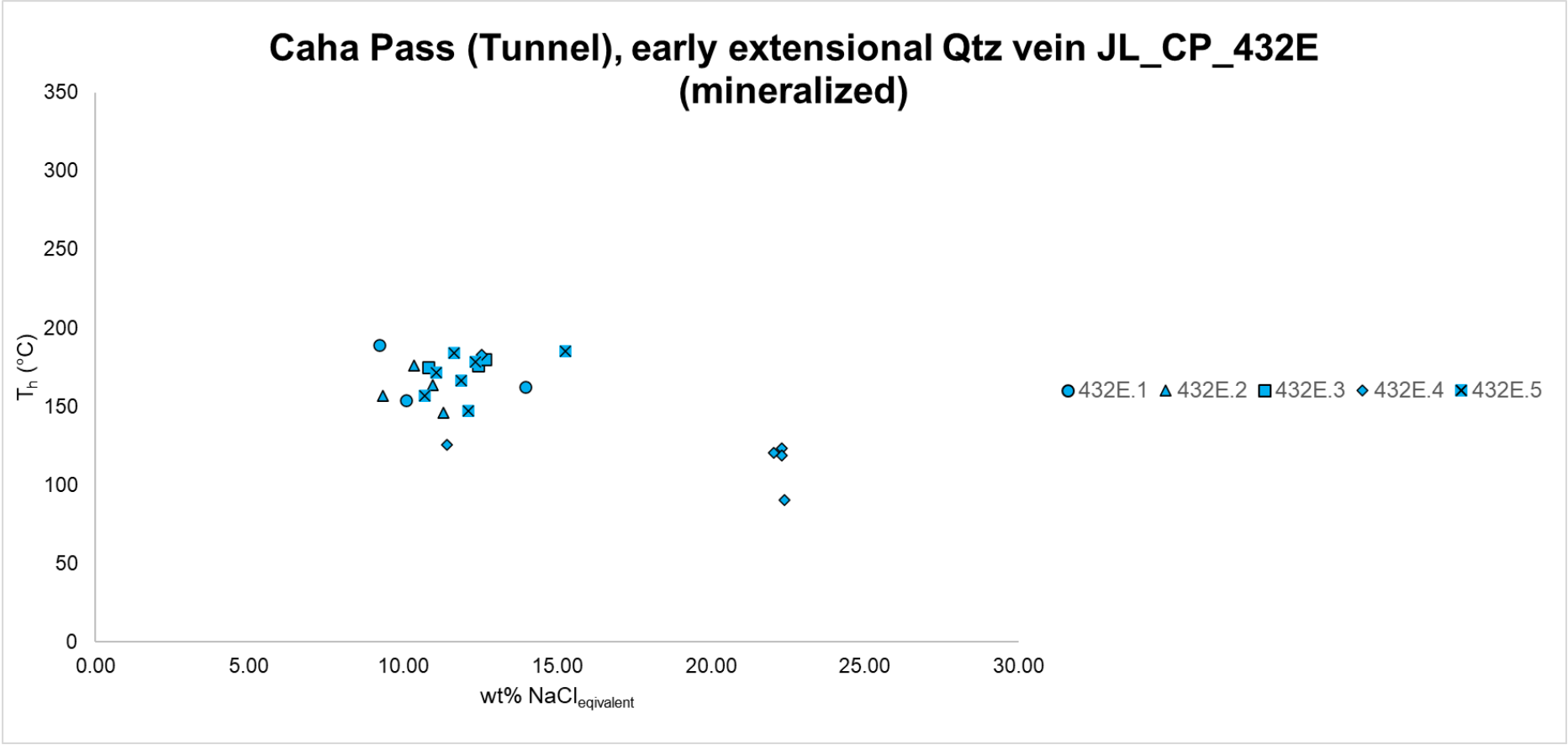

Gortavallig Mine Qtz vein JL_GV_512 (mineralized)
350
300
250
200
150
100
50
0
T_h (°C)
0.00
5.00
10.00
15.00
20.00
25.00
30.00
wt% $NaCl_{eqivalent}$
512.1
512.2
512.3
512.4
512.5

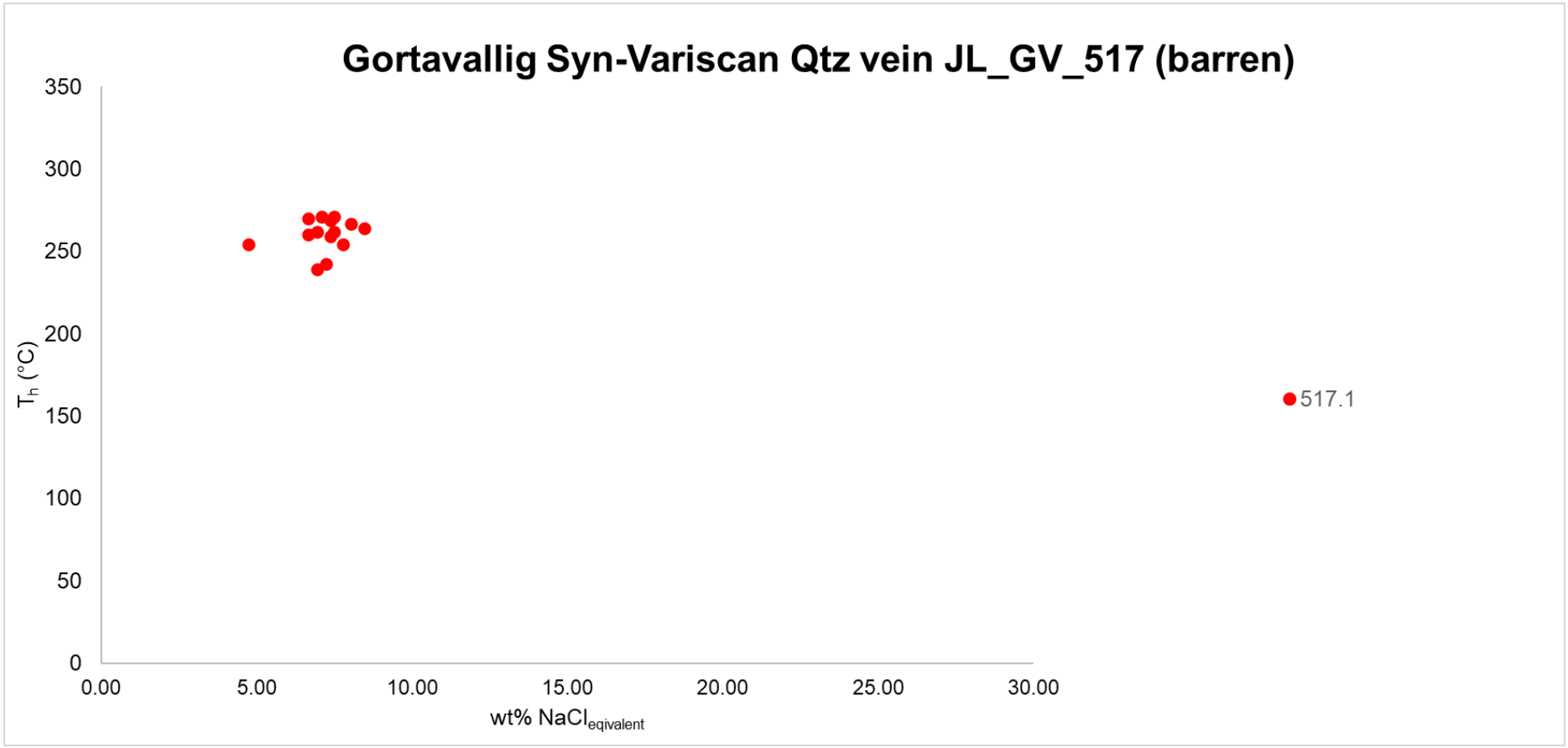

Crookhaven, vuggy Qtz crystal JL_CH_488 (barren)
350
300
250
200
150
100
50
0
T_h (°C)
0.00
5.00
10.00
15.00
20.00
25.00
30.00
wt% $NaCl_{eqivalent}$
488.1
488.2
488.3
488.4
488.5

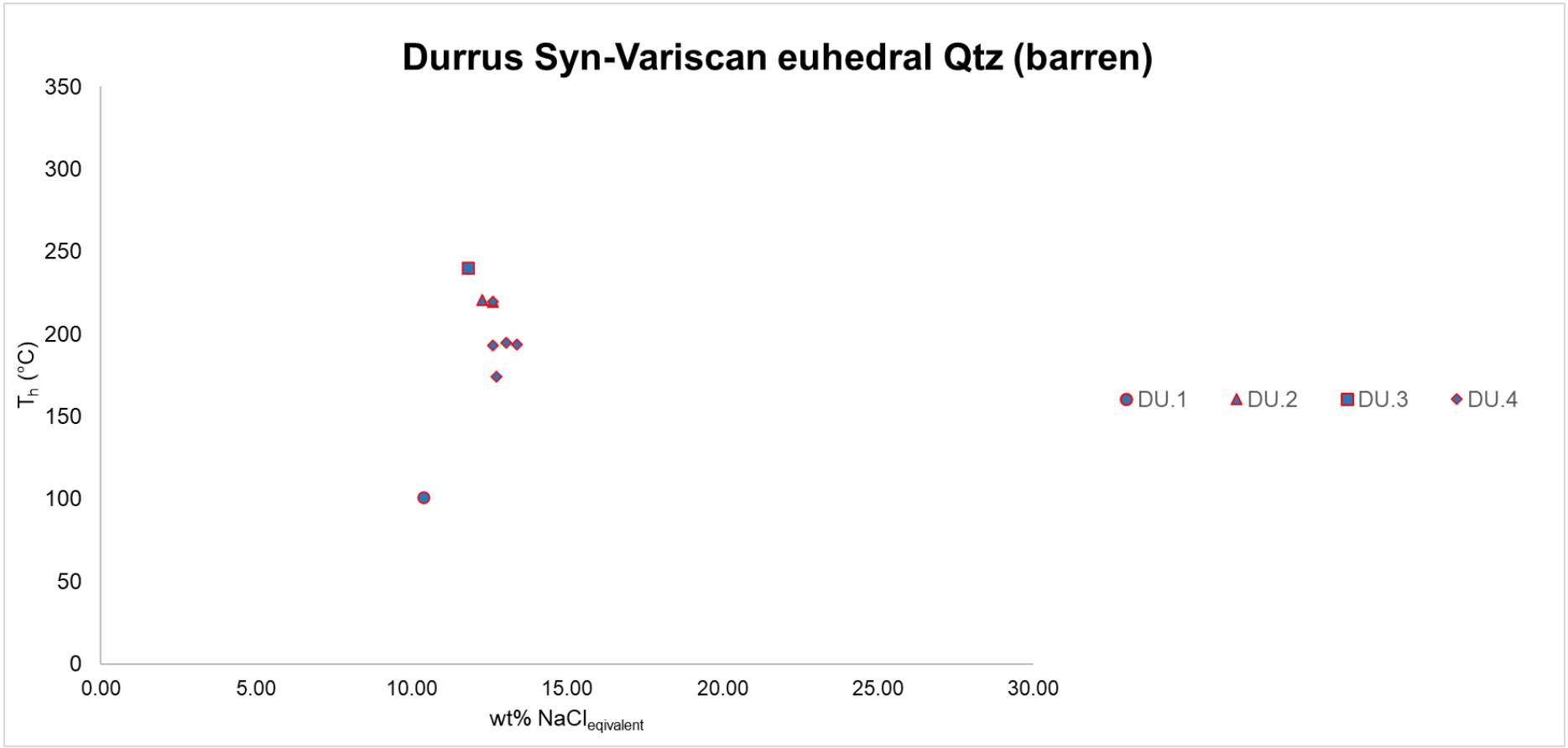

Dhurode Mine, Qtz vein JL_DH_522 (mineralized)
350
300
250
200
150
100
50
0
T_h (°C)
0.00
5.00
10.00
15.00
20.00
25.00
30.00
wt% $NaCl_{eqivalent}$
522.1
522.2
522.3
522.4
522.5
522.6
522.7

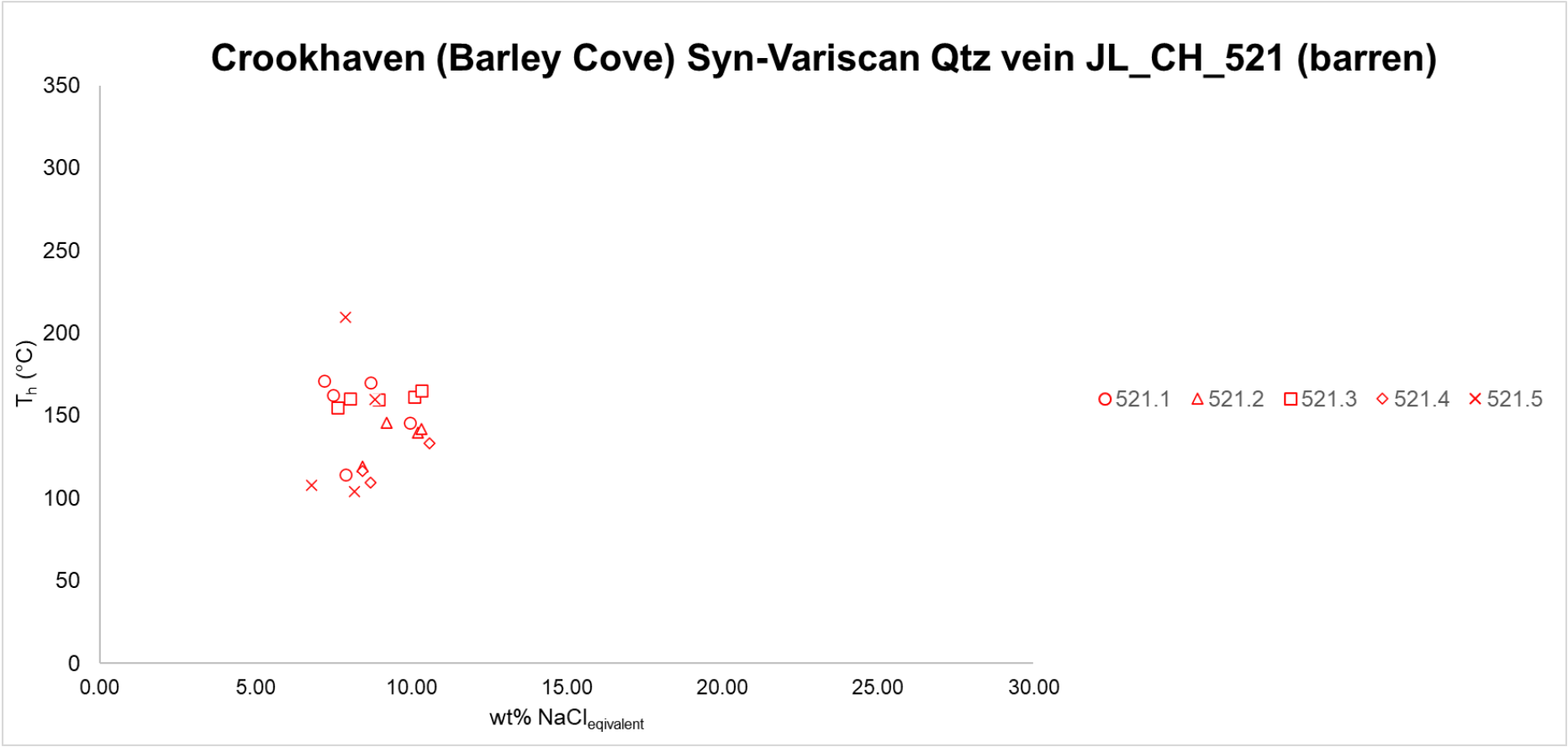

Bauregragh, early extensional Qtz vein JL_BH_475 (barren)
350
300
250
200
150
100
50
0
T_h (°C)
0.00
5.00
10.00
15.00
20.00
25.00
30.00
wt% $NaCl_{eqivalent}$
475.1
475.2
475.3

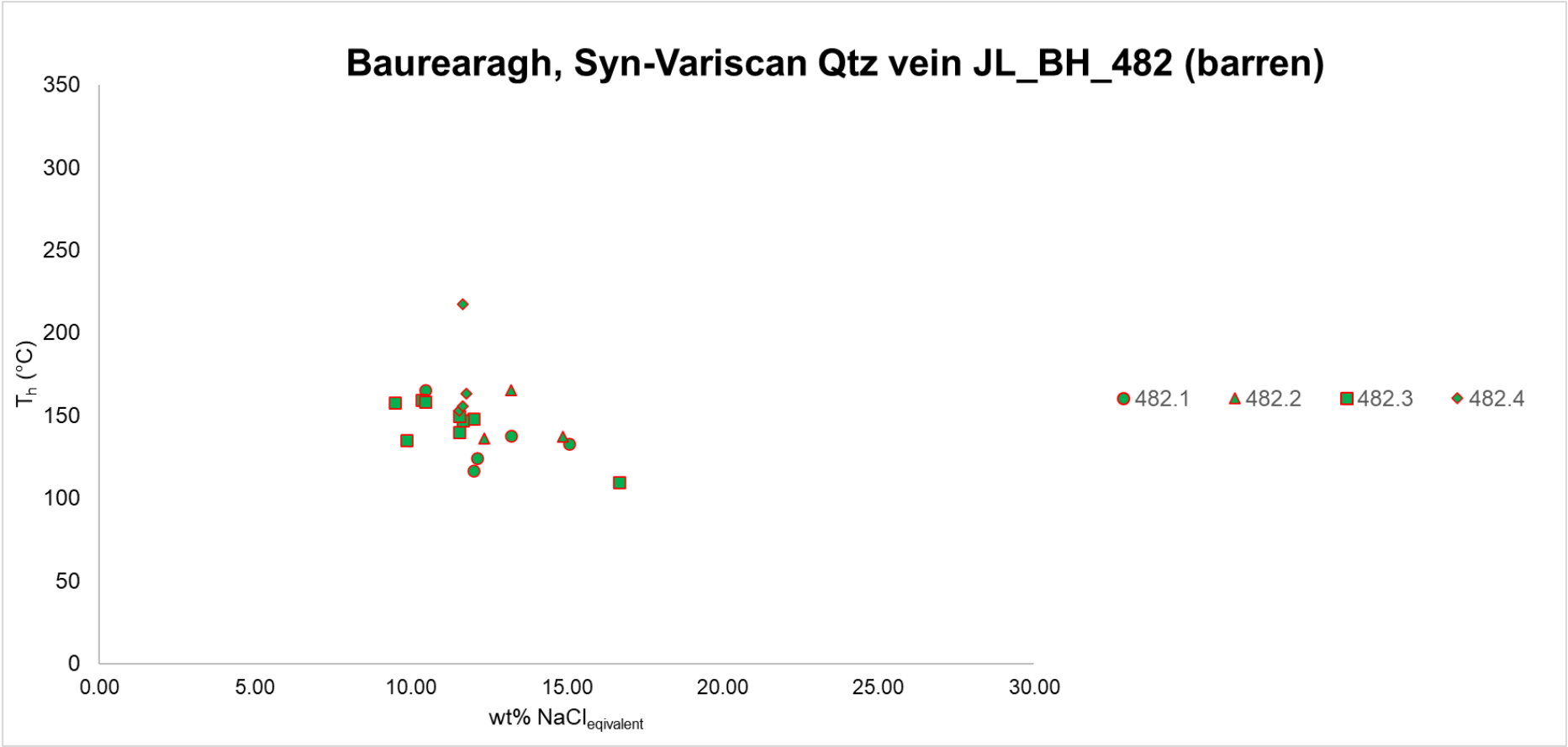

Ballycummisk Qtz vein with molybdenite JL_BC_525Re (Re-Os dated, mineralized)
350
300
250
200
150
100
50
0
T_h (°C)
0.00
5.00
10.00
15.00
20.00
25.00
30.00
wt% $NaCl_{eqivalent}$
525.1
525.2
525.3
525.4
525.5
525.6

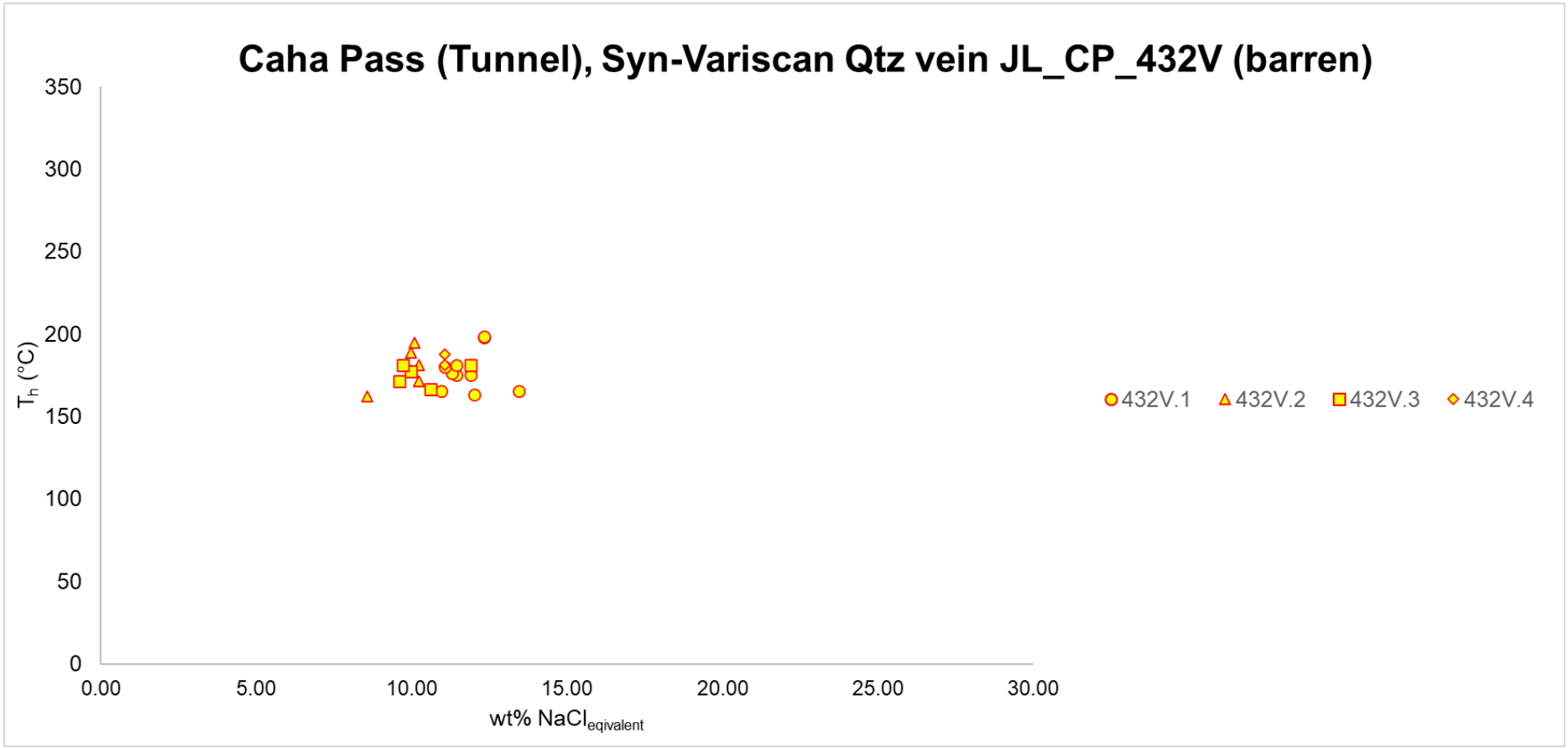

Caha Pass (Tunnel), early extensional Qtz vein JL_CP_432E (mineralized)
350
300
250
200
150
100
50
0
T_h (°C)
0.00
5.00
10.00
15.00
20.00
25.00
30.00
wt% $NaCl_{eqivalent}$
432E.1
432E.2
432E.3
432E.4
432E.5


Gortavallig Syn-Variscan Qtz vein JL_GV_517 (barren)
350
300
250
200
150
100
50
0
T_h (°C)
0.00
5.00
10.00
15.00
20.00
25.00
30.00
wt% $NaCl_{eqivalent}$
517.1


Durrus Syn-Variscan euhedral Qtz (barren)
350
300
250
200
150
100
50
0
T_h (°C)
0.00
5.00
10.00
15.00
20.00
25.00
30.00
wt% $NaCl_{eqivalent}$
DU.1
DU.2
DU.3
DU.4


Crookhaven (Barley Cove) Syn-Variscan Qtz vein JL_CH_521 (barren)
350
300
250
200
150
100
50
0
T_h (°C)
0.00
5.00
10.00
15.00
20.00
25.00
30.00
wt% $NaCl_{eqivalent}$
521.1
521.2
521.3
521.4
521.5


Bauregragh, Syn-Variscan Qtz vein JL_BH_482 (barren)
350
300
250
200
150
100
50
0
T_h (°C)
0.00
5.00
10.00
15.00
20.00
25.00
30.00
wt% $NaCl_{eqivalent}$
482.1
482.2
482.3
482.4


Caha Pass (Tunnel), Syn-Variscan Qtz vein JL_CP_432V (barren)
350
300
250
200
150
100
50
0
T_h (°C)
0.00
5.00
10.00
15.00
20.00
25.00
30.00
wt% $NaCl_{eqivalent}$
432V.1
432V.2
432V.3
432V.4

Appendix F (Chapter 4)

Locations of selected samples from West Cork, SW Ireland:

Geographic Coordinate System:	GCS_WGS_1984
Datum:	D_WGS_1984
Prime Meridian:	Greenwich
Angular Unit:	Degree

last updated: 12/01/2021

Sample/Location	Lat (°N)	Long (°E)	Location Name/Description	Comments
JL_BH_475	51.781766	-9.650353	Baurearagh, early extensional Qtz vein	
JL_BH_482	51.786223	-9.646912	Baurearagh, Syn-Variscan qtz vein	
JL_CP_432E	51.785218	-9.590671	Caha Pass (Tunnel), early extensional qtz vein	mineralized
JL_CP_432V	51.785218	-9.590671	Caha Pass (Tunnel), Syn-Variscan qtz vein	
JL_GV_512	51.575887	-9.784587	Gortavallig Mine, early extensional qtz vein	mineralized
JL_GV_517	51.574580	-9.787685	Gortavallig Syn-Variscan Qtz vein	
JL_DH_522	51.516135	-9.757177	Dhurode Mine, early extensional qtz vein, spoil material	mineralized
JL_CH_518	51.469561	-9.711099	Crookhaven Mine mineralized qtz vein Purple Lode	mineralized
JL_CH_488	51.469559	-9.711211	Crookhaven, vuggy qtz crystal	next to sample JL_CH_518
JL_CH_521	51.467396	-9.772248	Crookhaven (Barley Cove) Syn-Variscan vein	
JL_BC_525Re	51.533050	-9.476797	Ballycummisk, mineralized qtz vein with molybdenite (Re-Os dated, 315.5 Ma)	Re-Os dated
BM.1964,R230	51.533050	-9.476797	Ballycummisk Mine historic molybdenite sample (Russell collection) 311.8 Ma	No coordinates available, but sample was collected probably close to JL_BC_525Re by Sir Arthur Russell (National History Museum London)
Durrus crystals	51.625133	-9.469875	Euhedral, single crystals, no thin section, Syn-Variscan	qtz vein, road outcrop

Bauriearagh	51.781766	-9.650353		
Caha Pass	51.785218	-9.590671	Turners Rock Tunnel between Cork and Kerry	
Gortavallig Mines	51.575887	-9.784587		
Killeen North Mines	51.597905	-9.727637	Plant fossil (permineralized with chalcopyrite)	Conglomerate with mineralized clasts
Dhurode Mines	51.516135	-9.757177		spoil material
Crookhaven Mines	51.469561	-9.711099		
Ballycummisk Mines	51.533050	-9.476797		spoil material

Appendix G: Additional Field Locations

In order to support the hypothesis stated in Chapter 3 and 4, additional field locations within the Munster and South Munster Basins were selected (Fig. G.1a and G.1b). These locations show Pre-Variscan, basin-related extensional fault systems with associated quartz veins (and Cu mineralization), and Syn-Variscan compressional overprint. The sites were visited as a reconnaissance exercise.

An overview of the selected locations is listed in **Table G.1**.

All structural data is available in **Appendix A**.

The high-resolution maps of these locations can be found as PDF files in **Appendix J.**

Sample/Location	Lat (°N)	Long (°E)	Description
Caherdaniel (Behaghane)	51.788749	-10.066989	Historic mining site with small quarries and mining trials (quartz lodes), County Kerry
Healy Pass	51.741746	-9.728918	Large qtz veins (km scale), no mineralization, about 2 km east of Healy Pass
Pass of Keimaneigh	51.822914	-9.305159	Forestry area with road outcrops, larger qtz veins (metre scale)
Goleen	51.492122	-9.734049	Metre scale quartz veins, road follows major fault zone, Mizen Head
Dunmanus	51.530444	-9.661434	Larger qtz veins (metre scale), field outcrop
Mount Corin (Dereennalomane)	51.592364	-9.514255	Historic mining trials, most of the area is covered by vegetation and bog material
Durrus	51.625524	-9.471486	Forestry area, metre scale quartz veins, road outcrops
Seven Heads	51.573031	-8.706729	Coastal outcrop, metre scale quartz veins, strong tidal influence
Geographic Coordinate System:	GCS_WGS_1984		
Datum:	D_WGS_1984		
Prime Meridian:	Greenwich		
Angular Unit:	Degree		

Table G.1) Additional Field Locations in County Cork and County Kerry; Munster Basin, SW Ireland.

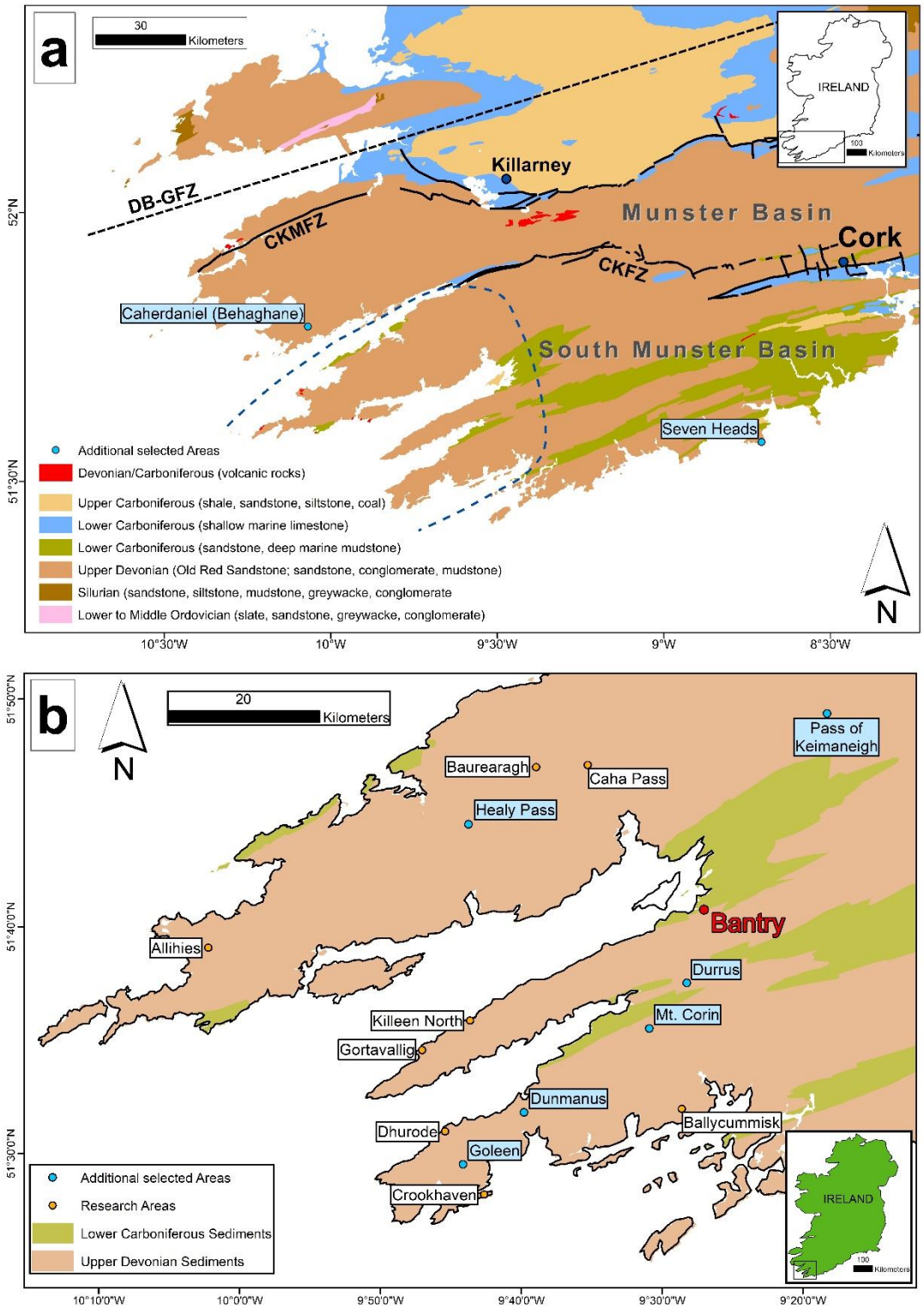


Fig. G.1) Simplified geological map of the Munster Basin and the South Munster Basin in SW Ireland. a) The Munster Basin is defined by the Coomnacronia-Killarney-Mallow Fault Zone (CKMFZ) or alternatively by the Dingle Bay-Galtee Fault Zone (DB-GFZ) in the North. The Cork-Kenmare Fault Zone (CKFZ) marks the rim to the South Munster Sub-Basin. An NNW directed

compression indicates the Variscan Orogeny (modified from Sanderson 1984; Williams 2000; MacCarthy et al. 2002; Landes et al. 2003; MacCarthy 2007; Ennis et al. 2015). b) West Cork with its peninsulas Beara (North), Sheep's Head (Middle) and Mizen Head (South).

G.1 Research Locations

G.1.1 Caherdaniel (Behaghane; 51.788749 °N, -10.066989 °E)

Caherdaniel is a small village located at the southern coast of Iveragh Peninsula (Kerry, Fig. G.1a). Behaghane is located about 3 km NE of Caherdaniel and was historically mined for copper (GSI 2016, GSI Jetstream 2019). Behaghane is located north of the Cork-Kenmare Fault Zone (Fig. G.1a) and belongs to the (North) Munster Basin. The lithology is a reddish-brown sandstone (Valentia Slate Formation, GSI 2016).

Pre-Variscan Structures

A series of conjugate extensional faults strike E-W to ENE-WSW (Fig. G.2a). Related to these faults occur quartz veins with a width of up to 70 cm and a maximum length of 50 m. Some of these quartz veins show hydrobreccias with host rock clasts (red sandstone) and green malachite staining (Fig. G.2b). Small amounts of specular hematite can be found within the quartz vein (Fig. G.2c).

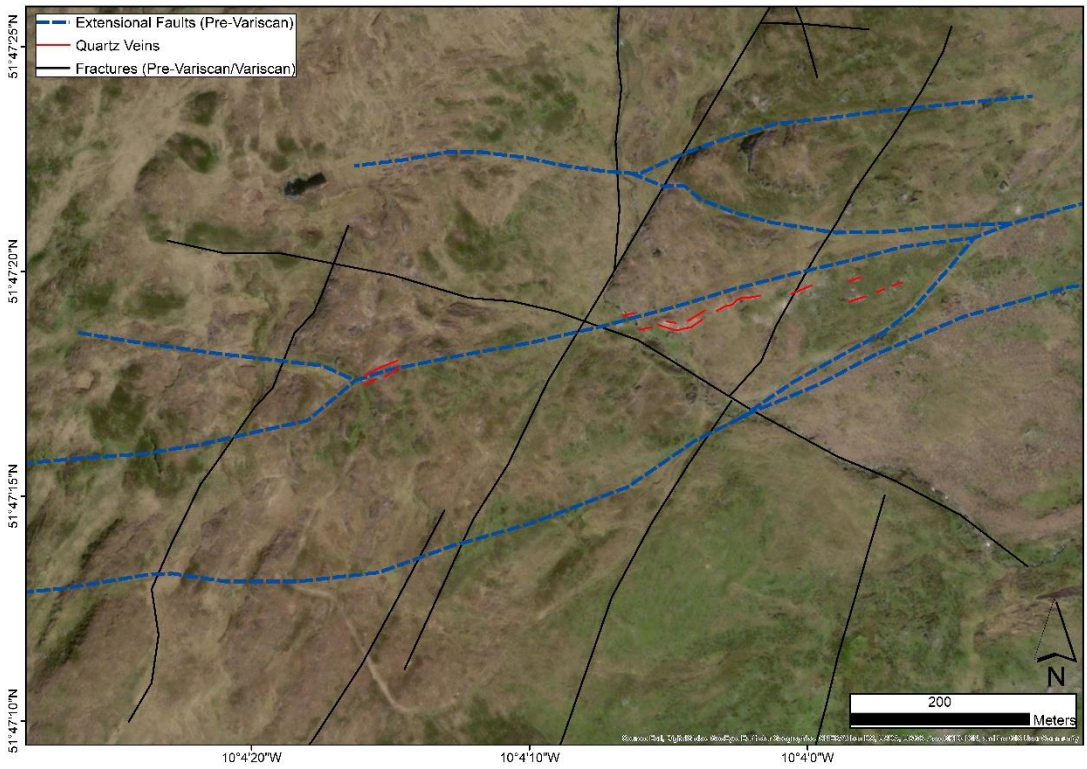
Syn-Variscan Structures

NE-SW striking, as well as WNW-ESE striking faults are possibly related to the NNW-directed compression of the Variscan Orogeny (Sanderson 1984; Ford 1987; Meere 1995b; Quinn *et al.* 2005). The Pre-Variscan quartz veins show compressional folding, as well as cleavage within thinner parts of the veins (Fig. G.2c).

Mineralization and Microstructures

The mineralization is formed by disseminated copper sulphites within the pre-Variscan quartz veins. Supergene covellite was identified together with a grey Cu sulphide (tennantite-tetrahedrite or digenite/djurleite?, Fig. G.2d). Compressional stylolites are formed within the quartz veins and show a partial dissolving of host rock fragments (Fig. G.2d).

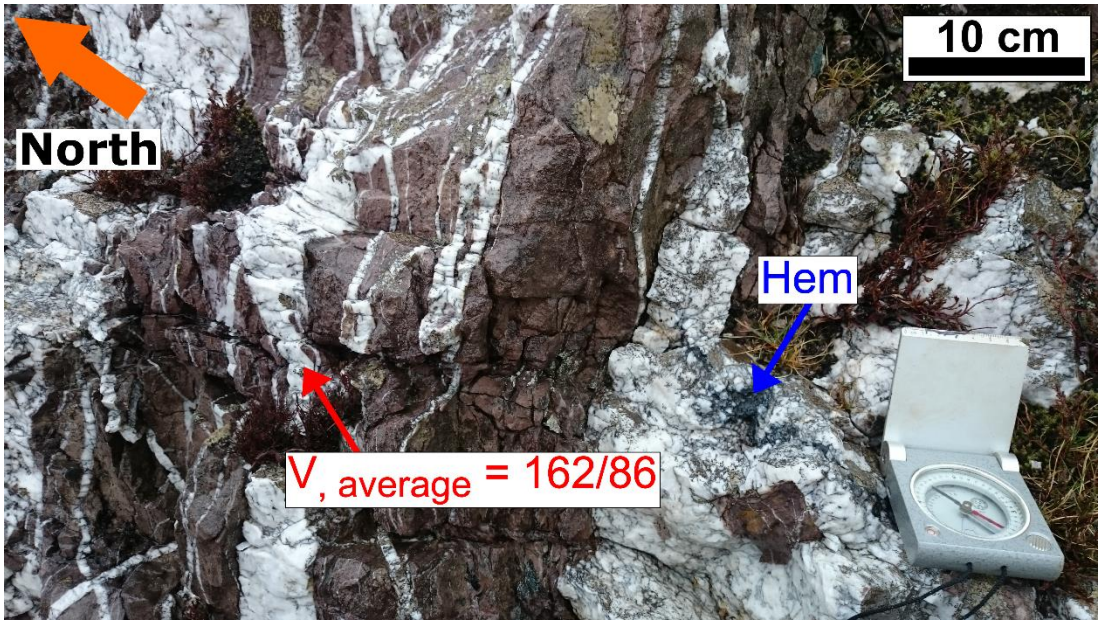
Fig. G.2a)



G.2b)



G.2c)



G.2d)

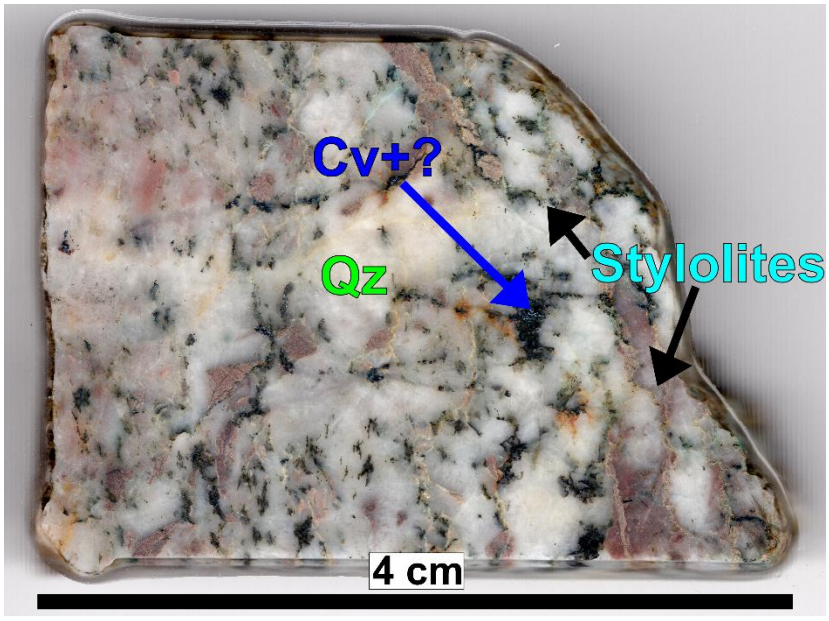


Fig. G.2a) Structural map of Behaghane showing large quartz veins related to ENE-WSW Pre-Variscan striking faults. b) Hydrobreccia of veining quartz with host rock clasts and green malachite staining. c) Folded and cleaved quartz veins with specular hematite. d) Cut hand specimen of mineralized quartz (Qz) vein showing silver-grey disseminated Cu sulphites (Cv = covellite) and stylolites.

G.1.2 Healy Pass (51.741746 °N, -9.728918 °E)

About 3 km NE of the Healy Pass (Fig. G.1b) occurs a large quartz vein which was identified by satellite imagery (Bing™ Satellite Maps, 2016-2019; Google Maps, 2016-2019; ArcGIS BaseMaps, 2016-2020). The host lithology is formed by reddish-brown silty sandstones and siltstones (Caha Mountain Formation, GSI 2016).

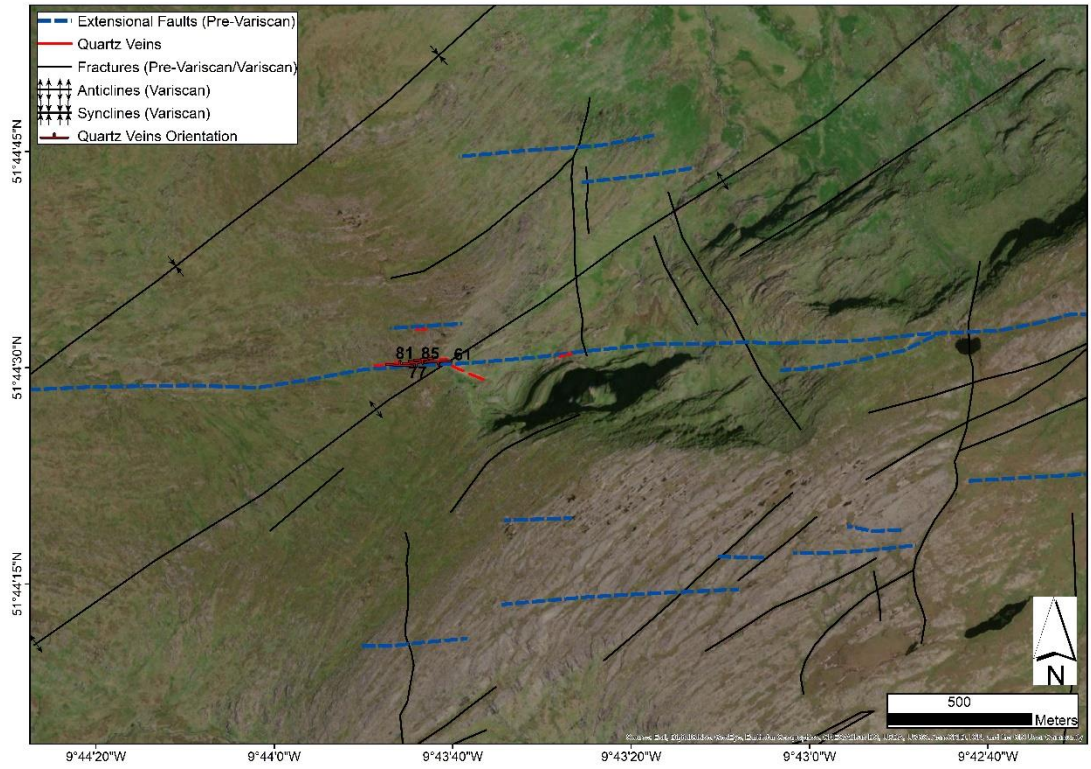
Pre-Variscan Structures

A major E-W striking extensional fault can be traced for over 3 km (Fig. G.3a). A further series of E-W striking faults up to 600 m length run parallel to this structure. A N-S striking fracture to the East of the mapping area (Fig. G.3a) shows intense folding due to Variscan compression and is therefore interpreted as Pre-Variscan feature. Related to the major E-W fault is a series of E-W striking, amorphous white quartz veins. Single veins have a width of up to 40 cm (Fig. G.3b) and the series of the veins form a traceable length of over 400 meters. Smaller amounts of specular hematite were found within the quartz veins. Vugs of euhedral quartz crystals occur in the amorphous white veining quartz.

Syn-Variscan Structures

The host rock is folded with a NE-SW strike whereby the fold axis of an anticline intersects the Pre-Variscan quartz veins (Fig. G.3a). NE-SW striking compressional fractures occur parallel aligned. Few fractures show an NNW-SSE strike. The Pre-Variscan quartz veins show an intense cataclastic deformation as well as strong folding and cleavage formation within the thinner veins (Fig. G.3b).

Fig. G.3a)



G.3b)

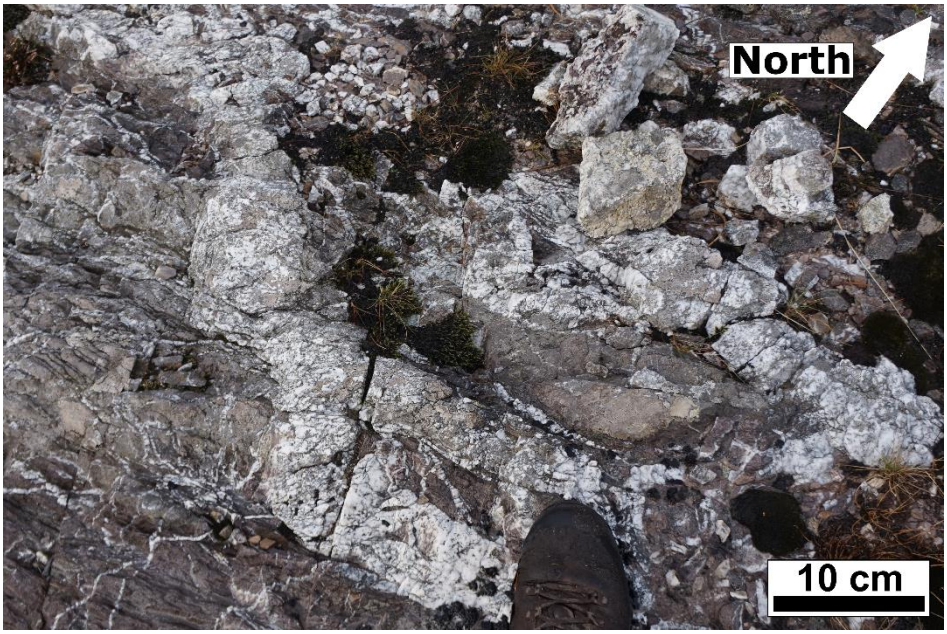


Fig. G.3a) Structural map of the location Healy Pass showing a large E-W striking fault with quartz veining. b) Pre-Variscan quartz veins with cataclastic deformation, folding and cleavage.

G.1.3 Pass of Keimaneigh (51.822914 °N, -9.305159 °E)

The Pass of Keimaneigh is located about 17.5 km NNE of Bantry (Fig. G.1b). This location was selected to examine if extensional faults are generally associated with large quartz veins. The extensional fault was traced by satellite imagery (Fig. G.4a, Bing™ Satellite Maps, 2016-2019; Google Maps, 2016-2019; ArcGIS BaseMaps, 2016-2020). There were no previous recordings of larger quartz vein occurrences. The lithology is dominated by greyish-green silty mudstone of the Caha Mountain Formation (GSI 2016).

Pre-Variscan Structures

The extensional fault strikes ENE-WSW (Fig. G.4a) and can be traced on satellite images (Bing™ Satellite Maps, 2016-2019) for 2.3 km. Drone imagery show large quartz veins occurring North of the extensional faults with a length of up to 11 m and an ENE-WSW strike. The individual quartz veins are max. 20 cm wide. Several veins form vein zones of up to 50 cm width. The quartz veins show strong Fe-staining and contain aggregates of chlorite as well as smaller amounts of specular hematite.

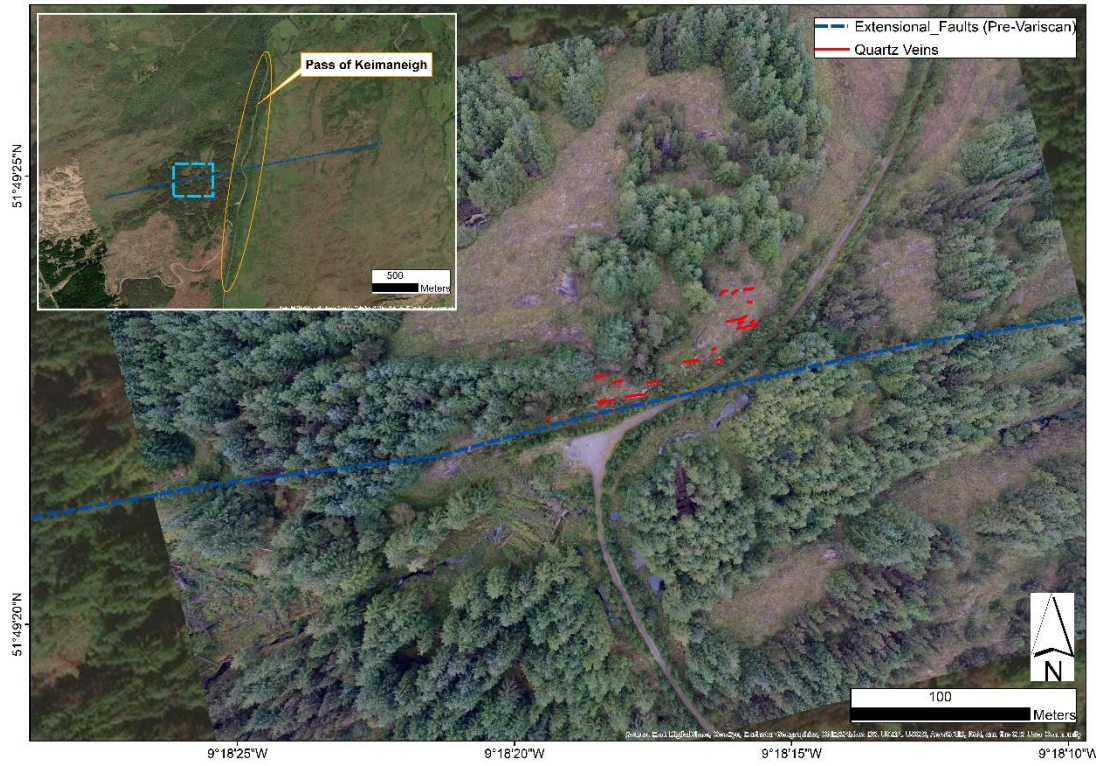
Syn-Variscan Structures

About 400 m NE of the extensional fault smaller quartz veins have been found (Fig. G.4b). They occur in compressional tension gashes with an NNW-SSE strike of the semi-brittle shear zone. These quartz veins consist of pure milky quartz and show a maximum length of 1 m and 4 cm width.

Microstructures

The specular hematite within the extensional quartz veins shows intense compressional folding (Variscan overprint) with deformation twinning (Fig. G.4c).

Fig. G.4a)


Pass of Keimaneigh
500
Meters
Extensional_Faults (Pre-Variscan)
Quartz Veins
N
100
Meters
51°49'25"N
51°49'20"N
9°18'25"W
9°18'20"W
9°18'15"W
9°18'10"W

G.4b)


South
10 cm

G.4c)

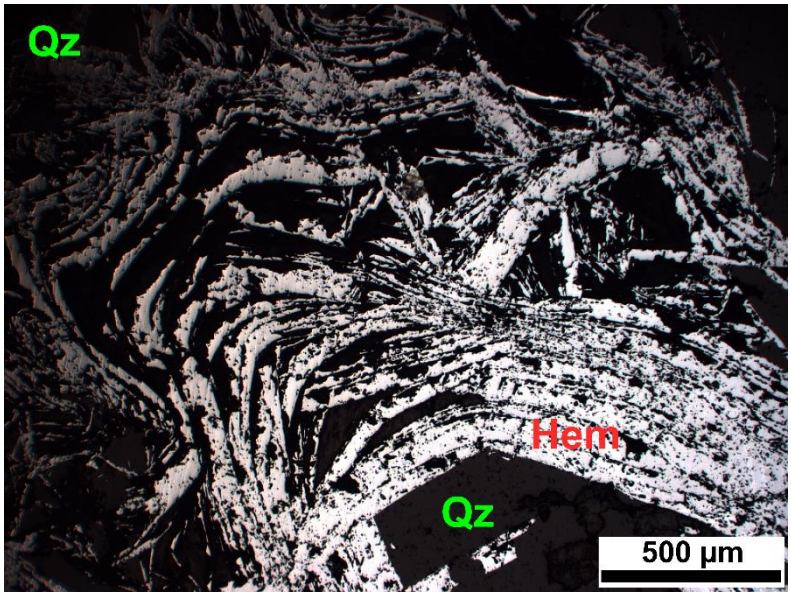


Fig. G.4a) Structural map of extensional fault with related quartz veining near Pass of Keimaneigh (ArcGIS BaseMaps, 2016-2020 and drone aerial imaging). b) Syn-Variscan quartz veins formed within tension gashes. c) Microphotograph of folded specular hematite (Hem) within Pre-Variscan quartz vein (Qz).

G.1.4 Goleen (51.492122 °N, -9.734049 °E)

The mapping area is about 1.5 km West of the village Goleen near the western end of Mizen Peninsula (Fig. G.1b). Fine-grained reddish-grey siltstone of the Upper Devonian Castlehaven Formation forms the host lithology (GSI 2016).

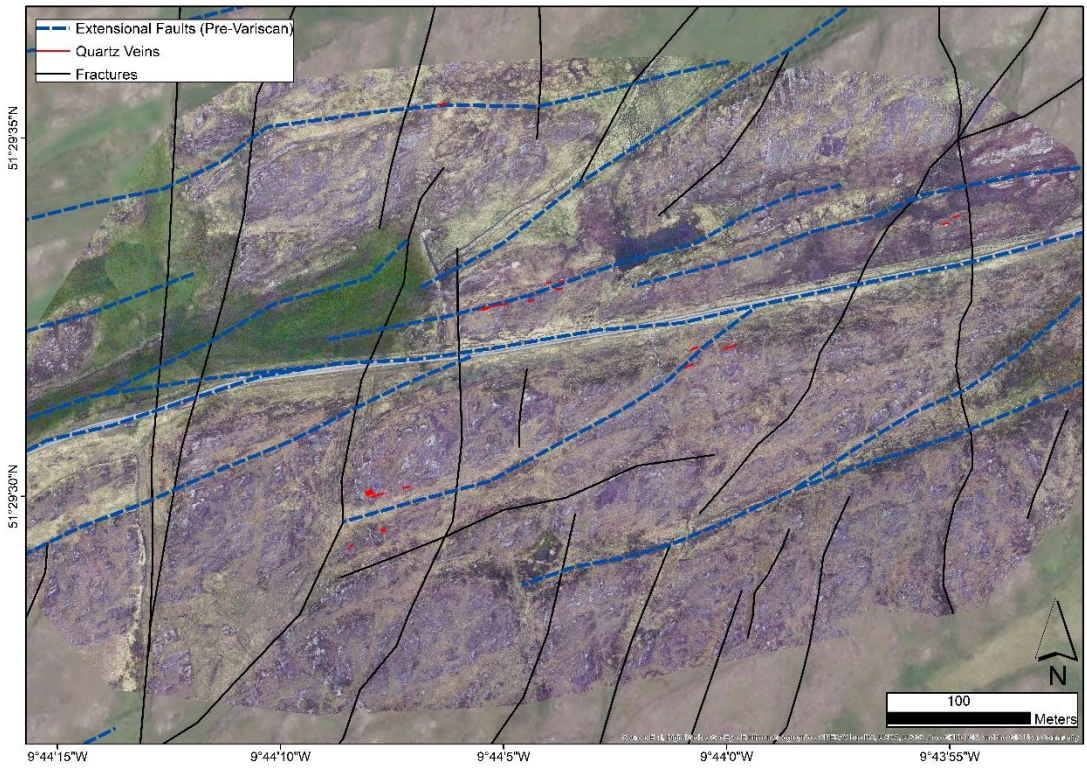
Pre-Variscan Structures

A drone orthophoto (Fig. G.5a) shows E-W to ENE-WSW striking extensional conjugate faults. Some of the larger N-S striking fractures show evidence of Variscan folding. E-W striking quartz veins with tens of meters length and a max. width of 50 cm are related to the E-W faults. The quartz veins show hydrobrecciation with sandy siltstone clasts (Fig. G.5b). Parallel aligned quartz veins form vein zones of 0.5 to 1 m width. Within the veins small amounts of specular hematite have been found (Fig. G.5b).

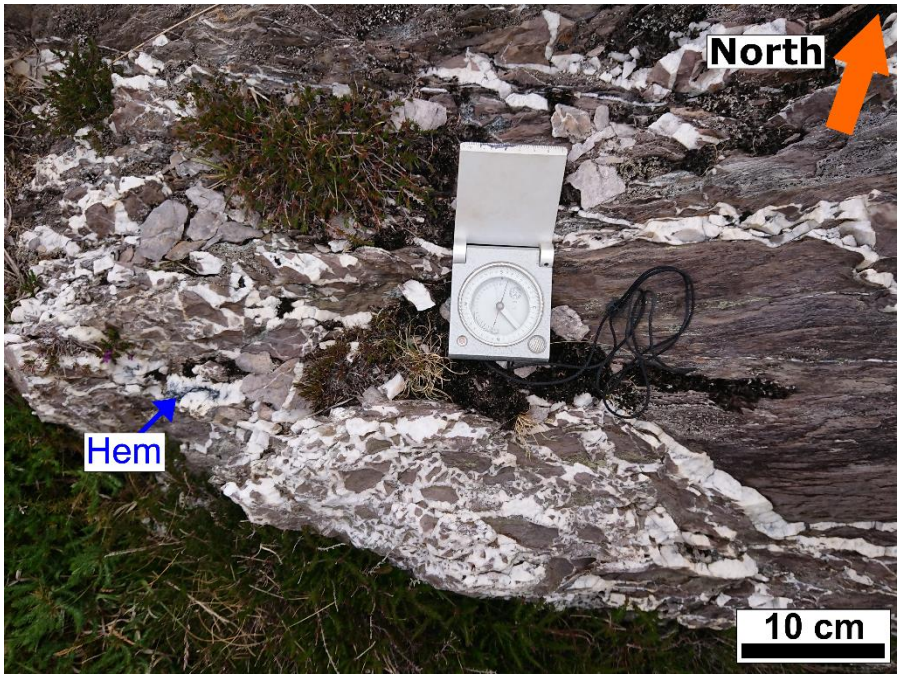
Syn-Variscan Structures

Fractures (mainly joints) have an ENE-WSW to NNE-SSW strike (Fig. G.5a). Pre-Variscan quartz veins are folded and cleaved due to Variscan compression (Fig. G.5c).

Fig. G.5a)



G.5b)



G.5c)

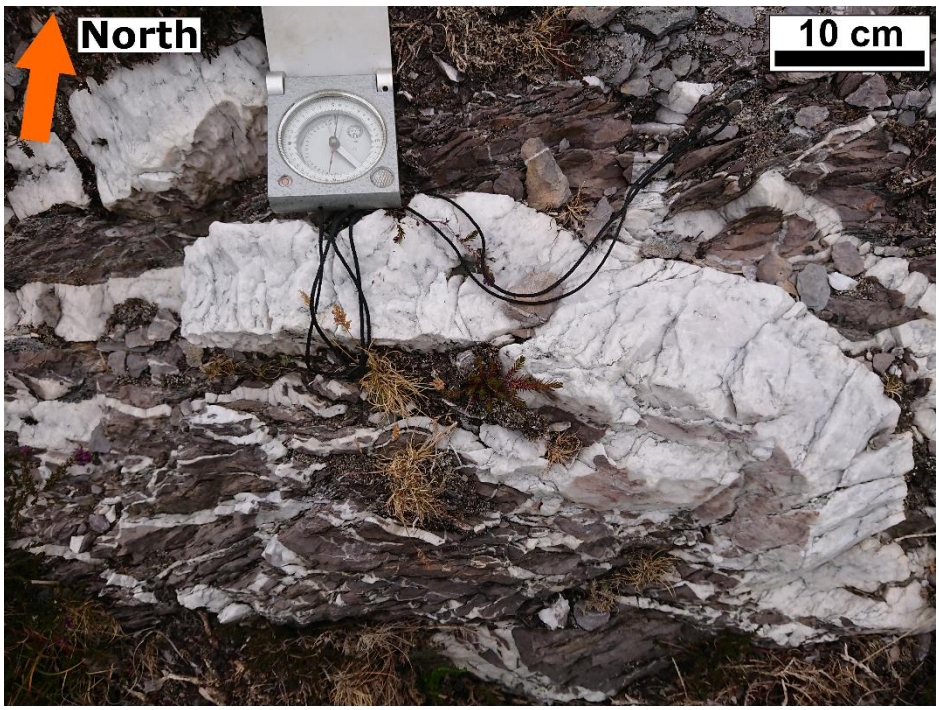


Fig. G.5a) Aerial drone map from area located west of Goleen shows Pre- and Syn-Variscan structures. b) Hydrobrecciated quartz vein with small amounts of specular hematite (Hem). c) Folded and cleaved quartz vein.

G.1.5 Dunmanus (51.530444 °N, -9.661434 °E)

Dunmanus is located in the middle of Mizen Peninsula, about 26.5 km SW of Bantry (Fig. G.1b). On an old GSI map (GSI Mineral Localities, 2016) the occurrence of malachite and chalcopyrite has been noted within a large quartz vein. The host lithology is a grey sandstone with an alternating siltstone belonging to the Upper Devonian Castlehaven Formation, (GSI 2016).

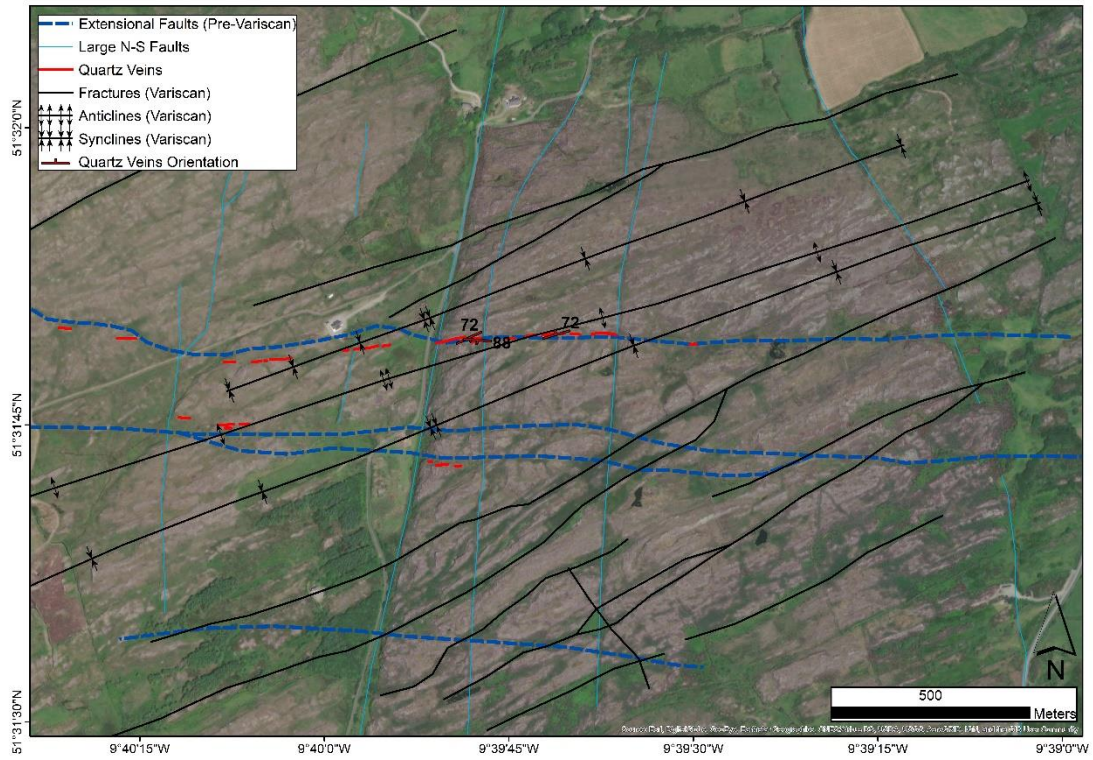
Pre-Variscan Structures

Three parallel aligned E-W striking extensional faults were identified in the mapping area (Fig. G.6a). N-S striking faults with several kilometres length occur perpendicular to the E-W faults. Related to the E-W faults are large E-W striking quartz veins with a maximum width of 1 m and up to 70 m length (Fig. G.6b). Parts of the quartz veins show intense Fe-staining (leached sulphides?) and small amounts of specular hematite.

Syn-Variscan Structures

A series of ENE-WSW striking folds has been identified at the Northern part of the mapping area (Fig. G.6a). Parallel to the folds are ENE-WSW striking faults which offset the Pre-Variscan N-S faults of up to 25 m.

Fig. G.6a)



G.6b)



Fig. G.6a) Structural map of Dunmanus showing E-W striking faults with quartz veins, as well as early N-S faults and compressional ENE-WSW striking Variscan structures. b) Outcrop of large E-W striking quartz veins.

G.1.6 Mount Corin (Dereennalomane; 51.592364 °N, -9.514255 °E)

Mount Corin is located about 3 km South of Durrus Village (Fig. G.1b). Several thousand tons of baryte (southern slope of Mt. Corin), as well as small amounts of copper were exploited for over the last hundred years (e.g. Dixon 1946, GSI mining report Dereenalomane). The lithology is a transition between purple sandstones (Castlehaven Formation, GSI 2016) to the south and grey, silty cross bedded sandstone at the northern slope of Mt. Corin (Toe Head Formation, GSI 2016).

Pre-Variscan Structures

Due to the poor outcrop pre-Variscan structures can only be identified via drone and satellite imagery (ArcGIS BaseMaps, 2016-2020). E-W striking extensional faults occur over the entire research area (Fig. G.7a). To the western part of the mapping area these E-W faults show a minor change in strike to ESE-WNW.

Syn-Variscan Structures

NE-SW striking faults form natural trenches with a cleavage parallel strike (Fig. G.7a). Some of these compressional NE-SW faults offset the Pre-Variscan E-W faults. Minor N-S to NNE-SSW fractures were identified as well. They show no interference with the pre-Variscan structures.

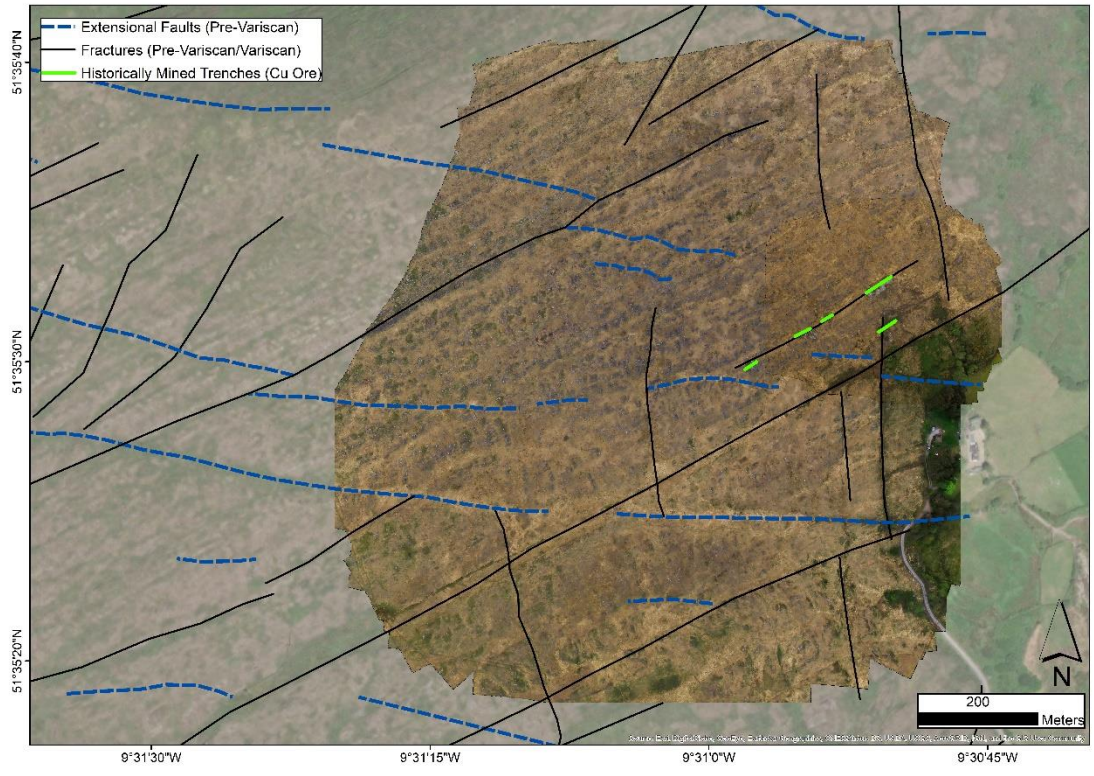
Mineralization

Smaller, historically mined trenches occur on the eastern slope of Mt. Corin (Fig. G.7a). These trenches follow the syn-Variscan NE-SW strike. The walls within the trenches are stained with green malachite and minor blue azurite.

Spoil samples show euhedral, clear quartz crystals with up to 4 cm length, chlorite, as well as minor chalcocite. Some quartz crystals have minor inclusions of specular hematite and chlorite needles (Fig. G.7b).

Ryczek (M.Sc. Thesis 2016) mapped the sediment hosted Cu mineralization parallel to the historic mining trenches and identified NE-SW striking zones of pyrite, chalcopyrite + pyrite, bornite + chalcopyrite, bornite, and chalcocite + bornite. According to Ryczek (2016) these Cu zones are related to the transition zone sediments between the Castlehaven and Toe Head Formations (see Chapter 4 Fig. 4.2b). The mineral zonation could be as a result of Cu remobilisation during the Variscan compression.

Fig. G.7a)



G.7b)

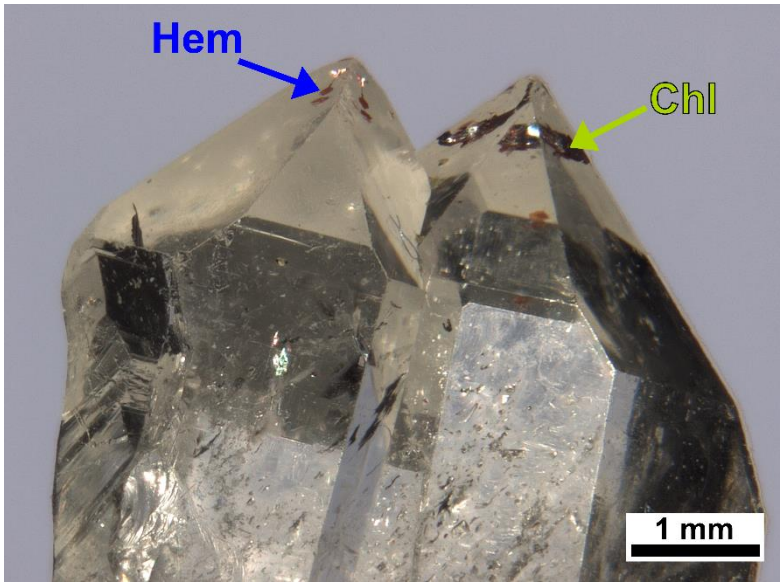


Fig. G.7a) Structural map of Mount Corin (Dereennalomane). Extensional faults were identified via drone imagery. b) Euhedral quartz twins from historically mined trenches showing specular hematite (Hem) and chlorite (Chl) inclusions.

G.1.7 Durrus (51.625524 °N, -9.471486 °E)

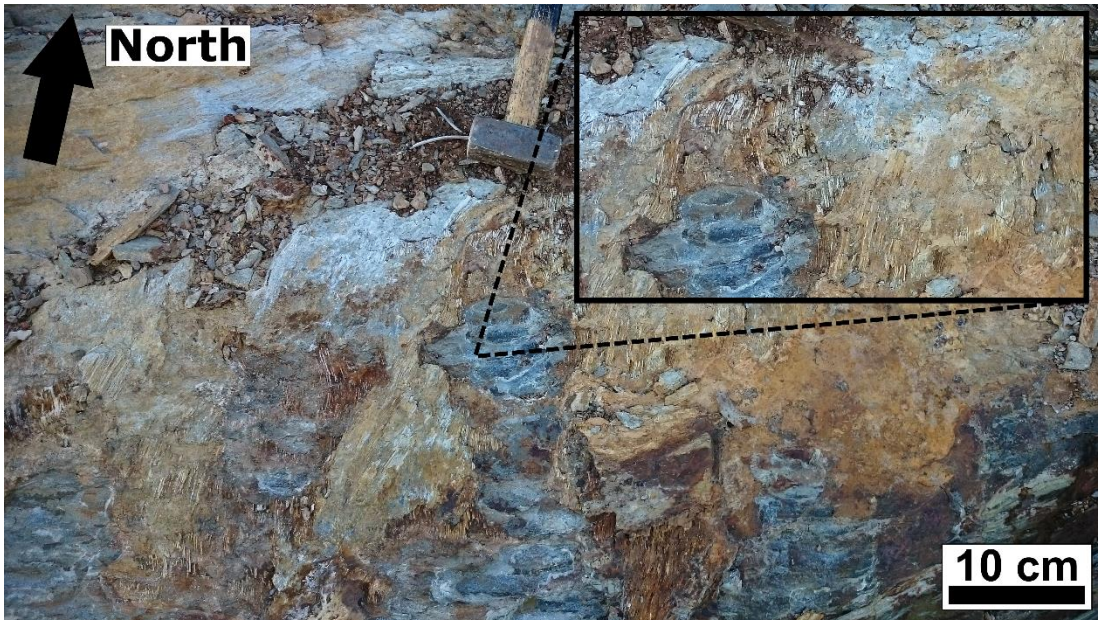
The study area is located about 4.4 km East of Durrus village (Fig. G.1b). A recently constructed forestry trail forms a several hundred-metre-long outcrop striking E-W. The host rocks are mica-rich greenish siltstones and brownish, beige to grey mudstones of the Lower Carboniferous Old Head Sandstone Formation (GSI 2016).

Quartz veins of few meters length (< 5 m) and a maximum width of 40 cm strike N-S (minor E-W) with a nearly vertical dip. The majority of the veins is formed by fibrous, Fe-stained quartz crystals with syngenetic kink crystal growth (Fig. G.8a). Some of the veins show a later generation of large (up to 5 cm) euhedral quartz crystals formed within tension gashes (up to 10 cm width). The euhedral quartz crystals are clear and can form twinning as well as doubly termination. Some quartz crystals are syngenetically intergrown with radial yellow-brownish muscovite and minor chalcopyrite (Fig. G.8b).

The fibrous quartz crystals could represent an ongoing stress-field with syngenetic crystallisation during the Variscan compression including minor

changes of stress-direction (kinks). The larger euhedral crystals must have been formed within a larger space (tension gash opening). A possibility would have been the post-Variscan relaxation phase. The mica, as well as the minor chalcopyrite was probably remobilised from the mica-rich host rock sediments.

Fig. G.8a)



G.8b)



Fig. G.8a) Durrus: Fibrous quartz crystals with kinks growing along greyish-brown mudstone. b) Euhedral quartz crystals with minor chalcopyrite (Ccp) and radial crystallized yellow muscovite (Ms).

G.1.8 Seven Heads (51.573031 °N, -8.706729 °E)

The mapped location is along the coastline at the southern tip of Seven Heads, about 13.5 km ESE of Clonakilty (Fig. G.1a). Purple siltstone of the Upper Devonian Castlehaven Formation forms the host lithology (GSI 2016).

Pre-Variscan Structures

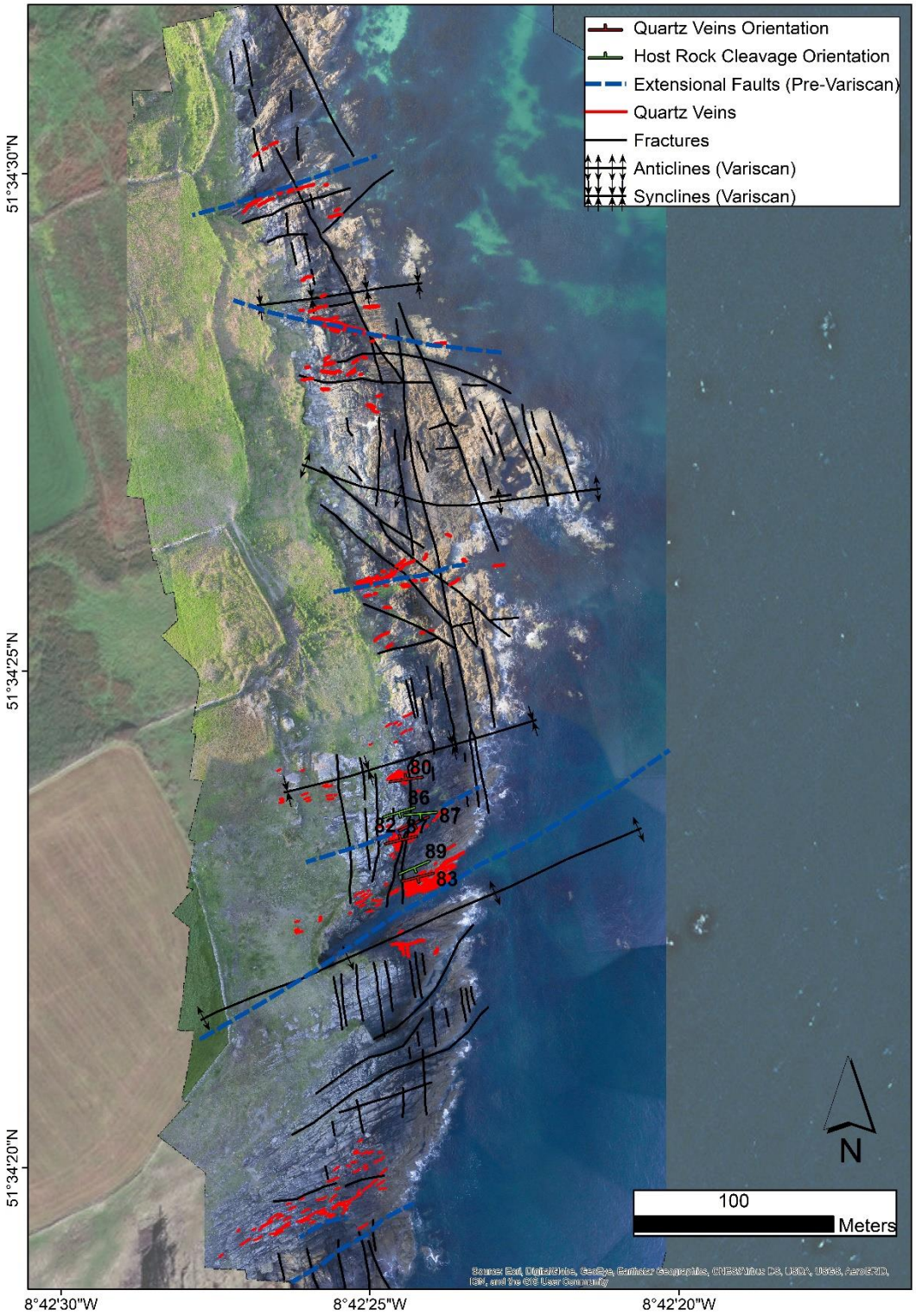
ENE-WSW to ESE-WNW striking extensional faults form up to 13 m wide fracture zones which show strong coastal erosion (Fig. G.9a + G.9b). Water filled trenches (below sea level) and caves occur at these fault zones. Related to the extensional faults are E-W to ENE-WSW striking quartz veins with a maximum width of 2 m and up to 25 m length (Fig. G.9b). A series of quartz veins can form zones of up to 25 m width and over 100 m length. Barite, aggregates of chlorite, and smaller amounts of specular hematite were found within the quartz veins.

Large N-S to NNW-SSE striking fractures occur along the coastal outcrop. It is unclear whether these fractures were formed either pre-Variscan extensional or syn-Variscan compressional.

Syn-Variscan Structures

Compressional folds show an E-W to ENE-WSW strike (Fig. G.9a). To the South and the North of the mapping area are NE-SW striking, cleavage parallel fractures. Smaller N-S striking joints were identified at the entire mapping area.

Fig. G.9a)


Quartz Veins Orientation
Host Rock Cleavage Orientation
Extensional Faults (Pre-Variscan)
Quartz Veins
Fractures
Anticlines (Variscan)
Synclines (Variscan)
51°34'30"N
51°34'25"N
51°34'20"N
8°42'30"W
8°42'25"W
8°42'20"W
80
86
82
87
87
89
83
N
100
Meters

G.9b)

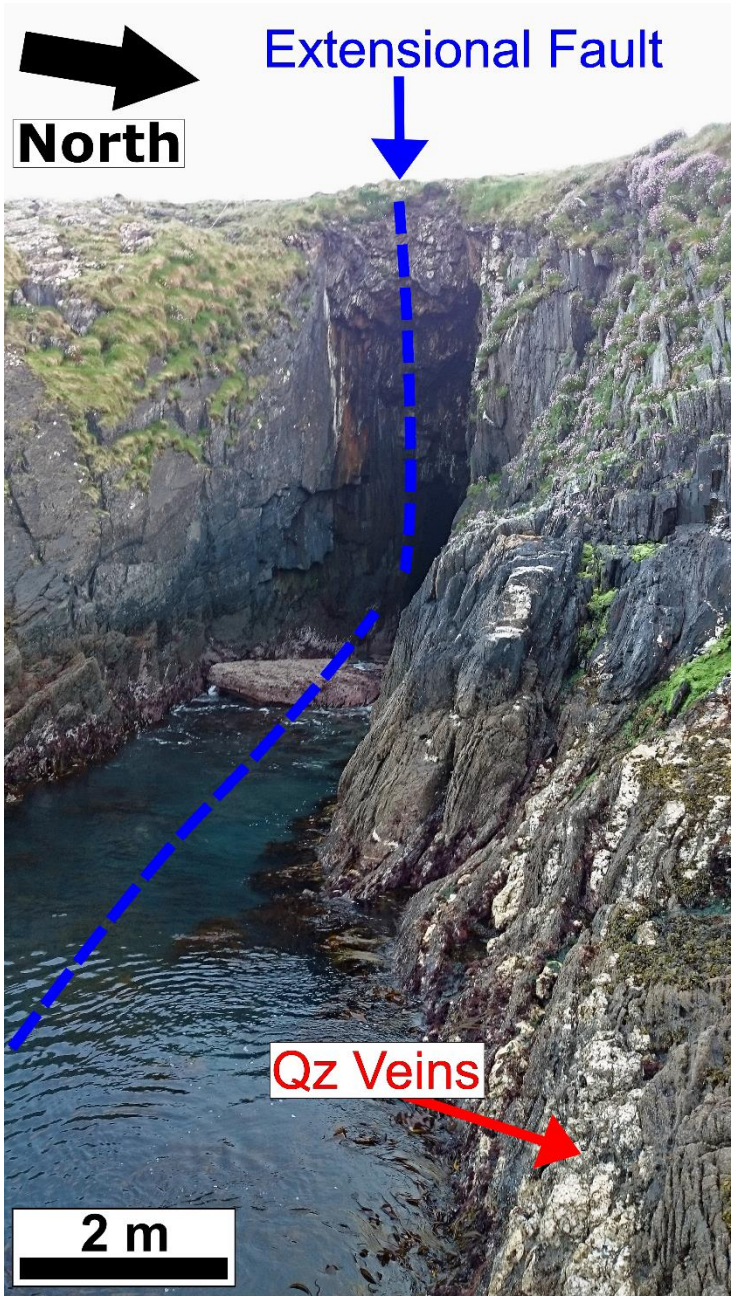


Fig. G.9a) Drone map showing the structures of the Seven Heads coastal outcrop. Large quartz veins are related to extensional fault zones. b) Coastal erosion of extensional fault. Parallel aligned are larger quartz veins with up to 2 m width.

G.2 Chapter References

Dixon 1946. Mianrai Teoranta, GSI mining report Dereenalomane, GSI Goldmine, https://secure.dccae.gov.ie/goldmine/search.html [last accessed 17/01/2021]

Ennis, M., Meere, P.A., Timmerman, M.J. and Sudo, M. 2015. Post-Acadian sediment recycling in the Devonian Old Red Sandstone of Southern Ireland. Gondwana Research, 28, 1415–1433, https://doi.org/10.1016/j.gr.2014.10.007

Ford, M. 1987. Practical application of the sequential balancing technique: an example from the Irish Variscides. Journal of the Geological Society, London, 144, 885–891, https://doi.org/10.1144/gsjgs.144.6.0885

Geological Survey of Ireland, GSI 2016. Bedrock 100k (scale 1:100,000), Bedrock Geology, Coordinate System: Irish Transverse Mercator / ITM. https://www.gsi.ie/en-ie/data-and-maps/Pages/Bedrock.aspx# [last accessed 20/04/2020]

Geological Survey of Ireland, GSI 2016. Mineral Localities (scale 1:100,000), Coordinate System: Irish National Grid / ING. https://www.gsi.ie/en-ie/data-and-maps/Pages/Minerals.aspx#MinLocs [last accessed 17/01/2021]

Geological Survey of Ireland, GSI Jetstream 2019. Historical Maps of Copper Deposits in SW Ireland. https://jetstream.gsi.ie [last accessed 08/03/2019]

Landes, M., O'Reilly, B.M., Readman, P.W., Shannon, P.M. and Prodehl, C. 2003. VARNET-96: three-dimensional upper crustal velocity structure of SW Ireland. Geophysical Journal International, 153, 424–442, https://doi.org/10.1046/j.1365-246X.2003.01911.x

MacCarthy, I.A.J. 2007. The South Munster Basin of southwest Ireland. Journal of Maps, 3, 149–172, https://doi.org/10.1080/jom.2007.9710835

MacCarthy, I.A.J., Pracht, M. and Sleeman, A.G. 2002. Geology of West Cork, Scale 1:100000, Sheet 24. Geological Survey of Ireland, Dublin.

Meere, P.A. 1995b. Sub-greenschist facies metamorphism from the Variscides of SW Ireland an early syn-extensional peak thermal event. Journal of the Geological Society, London, 152, 511–521, https://doi.org/10.1144/gsjgs.152.3.0511

Quinn, D., Meere, P.A. and Wartho, J.A. 2005. A chronology of foreland deformation: Ultra-violet laser 40Ar/39Ar dating of syn/late-orogenic intrusions from the Variscides of southwest Ireland. Journal of Structural Geology, 27, 1413–1425, https://doi.org/10.1016/j.jsg.2005.02.003

Ryczek, D.J. 2016. Investigation of Cu-Ag mineral zonation and stratigraphic-structural controls of syn-orogenic SSC deposits of the West Carbery area, County Cork, Ireland. M.Sc. Thesis, University College Cork, Ireland.

Sanderson, D.J. 1984. Structural variation across the northern margin of the Variscides in NW Europe. Geological Society, London, Special Publications, 14, 149–165, https://doi.org/10.1144/GSL.SP.1984.014.01.15

Williams, E.A. 2000. Flexural cantilever models of extensional subsidence in the Munster Basin (SW Ireland) and Old Red Sandstone fluvial dispersal systems. Geological Society, London, Special Publications, 180, 239–268, https://doi.org/10.1144/GSL.SP.2000.180.01.12

Software and satellite map sources:

Microsoft (Bing™ Satellite Maps, 2016-2019), Google Maps (2016-2019) and ESRI (ArcGIS BaseMaps, 2016-2020).

Appendix H: Stable Isotopes Geochemistry

Appendix H.1 Methodology

Mineralized quartz vein samples from the Allihies Mining Area (Fig. H.1) were chosen for $\delta^{34}S_{CDT}$ value, $\delta^{18}O_{SMOW}$ value and δD_{SMOW} value analysis. Special care was taken to select pure quartz veins from one mineralization generation (main generation, with no cross cuttings), which contain chalcopyrite (one generation) as the only sulphide mineralization. Three samples are from Mountain Mine Underground (Fig. H.1) and were extracted from E-W striking veins of the major E-W Lode (sample JL_AH_60, JL_AH_62, JL_AH_63; Fig. H.1). Sample JL_AH_263 (Caminches Mines) and sample JL_AH_197 (Coom Mine) are spoil samples from the major tailings next to the mine shafts (Fig. H.1).

The vein samples were carefully extracted from the host rock material at the School of BEES (UCC) rock preparation laboratory by rock cutting. The pure vein material (one generation per sample) was then crushed, washed and sieved at the Trinity College Dublin Crushing Laboratories. Grains > 1 mm were handpicked into fractions of pure, unaltered chalcopyrite and pure vein quartz.

Stable isotope measurements were conducted at the Stable Isotope Analysis Laboratory Nucleus at University of Salamanca in Spain. For $\delta^{34}S$ values 14.5 to 15.6 mg of chalcopyrite was heated in an oven (1160 °C) together with Cu_2O to produce SO_2 gas (e.g. Coleman and Moore 1978). The SO_2 gas was measured in a SIRAII mass spectrometer by using the CHONI standard (Appendix H.2).

Water from fluid inclusions in the quartz samples was extracted by heating the material within a vacuum chamber. An amount 0.892 to 1.088 g vein quartz was used per sample. The gas was measured for δD_{SMOW} values in a SIRA 10 mass spectrometer (VG Isogas). NBS 30-Biotite was used as standard

(Appendix H.2). It needs to be noted that the typical vein samples from Allihies contain several assemblages of fluid inclusions, inclusive primary and secondary fluid inclusions (Chapter 3 and Appendix B). Therefore, the measured δD_{SMOW} values represent a bulk value of several fluid inclusion assemblages per individual sample.

$\delta^{18}O_{SMOW}$ values were measured by using the laser fluorination line on the vein quartz. An amount of 2.0 to 2.4 mg quartz from one vein generation was used for each sample. O_2 was released by laser ablation with a SYNRAD 25W CO_2 laser in an atmosphere of ClF_3. The O_2 gas was then converted to CO_2 over hot graphite. The isotopic values ($^{18}O/^{16}O$) were measured in a dual-inlet, SIRA-II mass spectrometer (Appendix H.2). NBS 28-Quartz was used as standard (Appendix H.2).

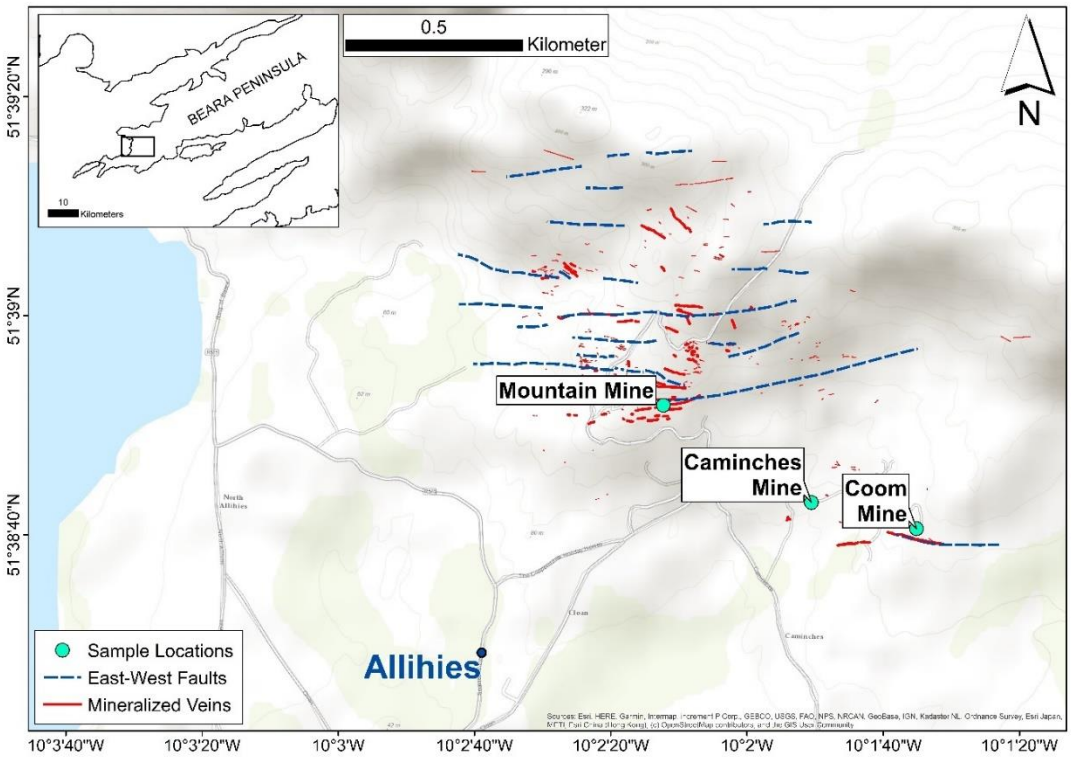


Fig. H.1) Map of Allihies Mining Area (Beara Peninsula, SW Ireland, modified from Chapter 3) showing the sample locations (historic Cu mines) selected for vein hosted Cu ore used in this study to measure stable isotopes.

Appendix H.2 Sample List and Calibration Settings

Sample locations for stable isotopes measurements (quartz veins with chalcopyrite, see Fig. H.1):

Name	Sample	Lat (°N)	Long (°E)	Location Name/Description
Caminches Mines	JL_AH_263	51.645731	-10.030541	Caminches Mines Spoil (quartz vein with chalcopyrite)
Coom Mine	JL_AH_197	51.644991	-10.026458	Coom Mine Spoil (quartz vein with chalcopyrite)
Mountain Mine Underground	JL_AH_62	51.647103	-10.037573	Mountain Mine Underground (E-W Lode, quartz vein with chalcopyrite)
Mountain Mine Underground	JL_AH_60	51.647103	-10.037573	Next to location JL_AH_62, inside Mountain Mine, from the roof (E-W Lode, quartz vein with chalcopyrite)
Mountain Mine Underground	JL_AH_63	51.647103	-10.037573	Next to location JL_AH_62, inside Mountain Mine, from the roof (E-W Lode, quartz vein with chalcopyrite)

Geographic Coordinate System:	GCS_WGS_1984
Datum:	D_WGS_1984
Prime Meridian:	Greenwich
Angular Unit:	Degree

Standardisation measurements for $\delta^{34}S$ values (measured at Department of Geology, University of Salamanca, Spain):

Analysis	**Nº Line**	**Sample**	**Mineral**	**Raw Delta**	**Precision**	**$d^{34}S_{CDT}$**	**Yield** %
20 September '16				Measured			Certified
SS-7642	S-7207	CHONI	S°	0.868	0.008	**7.7**	**7.6**
SS-7643	S-7208	CHONI	S°	0.661	0.004	**7.5**	**7.6**
SS-7644	S-7209	NBS-123	Sph	9.319	0.005	**17.1**	**17.1**
SS-7645	S-7210	NBS-123	Sph	9.331	0.019	**17.1**	**17.1**
SS-7646	S-7211	NZ-1	Ag_2S	-6.380	0.016	**-0.3**	**-0.3**
SS-7647	S-7212	NZ-1	Ag_2S	-6.222	0.007	**-0.1**	**-0.3**
SS-7648	S-7219	NBS-123	Sph	9.227	0.006	**17.0**	**17.1**
SS-7649	S-7220	CHONI	S°	0.687	0.012	**7.5**	**7.6**
SS-7650	S-7221	NZ-1	Ag_2S	-6.503	0.018	**-0.4**	**-0.3**

Sample measurements for $\delta^{34}S$ values (chalcopyrite, measured at Department of Geology, University of Salamanca, Spain):

Analysis	**Nº Line**	**Sample**	**Mineral**	**Raw Delta**	**Precision**	**$d^{34}S_{CDT}$**	**Yield %**
SS-7686	S-7255	CHONI	S°	0.905	0.008	7.8	75.7
SS-7687	S-7252	**JL-AH-263**	Cpy	-17.080	0.007	**-12.2**	84.2
SS-7688	S-7253	**JL-AH-197**	Cpy	-16.948	0.003	**-12.0**	81.0
SS-7689	S-7254	**JL-AH-62**	Cpy	-19.739	0.004	**-15.1**	72.4
SS-7690	S-7258	**JL-AH-60**	Cpy	-19.587	0.006	**-15.0**	68.3
SS-7691	S-7259	**JL-AH-63**	Cpy	-20.084	0.003	**-15.5**	71.5

Sample measurements for δD_{SMOW} values (bulk fluid inclusions within quartz, measured at Department of Geology, University of Salamanca, Spain):

Spectrometer	Line	Sample	Mineral	δD_{SMOW}	Project	% H_2O
S10-189	D/H-2014	**JL-AH-197**	Q (IncFl)	**-23,1**	Ireland, P1066/16	0,4
S10-190	D/H-2015	**JL-AH-60**	Q (IncFl)	**-27,3**	Ireland, P1066/16	0,4
S10-191	D/H-2016	**JL-AH-62**	Q (IncFl)	**-22,0**	Ireland, P1066/16	0,4
S10-192	D/H-2017	**JL-AH-263**	Q (IncFl)	**-26,6**	Ireland, P1066/16	0,3
S10-193	D/H-2018	**JL-AH-63**	Q (IncFl)	**-22,1**	Ireland, P1066/16	0,3

Standards and calibration used for δD_{SMOW} values: NBS 30-Biotite (-66 ‰), Seawater (-6 ‰), Water (-27.6 ‰), DWI (-51.9 ‰), LTSTD (-93.7 ‰), Snow Melt (-120.2 ‰), Natural Gas (-167.8 ‰).

Sample measurements for $\delta^{18}O_{SMOW}$ values (bulk quartz by laser fluorination, measured at Department of Geology, University of Salamanca, Spain):

Sample	Type	$\delta^{18}O_{SMOW}$
JL-AH-263	Q	13.3
JL-AH-62	Q	12.8
JL-AH-197	Q	13.9
JL-AH-60	Q	12.6
JL-AH-60	Q	12.9
JL-AH-63	Q	12.9

Standards and calibration used for $\delta^{18}O_{SMOW}$ values: NBS 28-Quartz, NBS 30-Biotite.

H.3 Results

Overview of all measured stable isotope delta values from selected mineralized vein samples from the Allihies Copper Mines. Sulphur isotope $\delta^{34}S_{CDT}$ values (chalcopyrite) range from -15.5 to -12.0 ‰. Hydrogen isotope δD_{SMOW} values (bulk fluid inclusions) show a span between -27.3 and -22.0 ‰. Oxygen isotope $\delta^{18}O_{SMOW}$ values (veining quartz) are between 12.8 and 13.9 ‰:

Name	**Sample**	**$\delta^{34}S_{CDT}$ (‰)**	**$\delta^{18}O_{SMOW}$ (‰)**	**δD_{SMOW}, bulk (‰)**
Mountain Mine Underground	JL_AH_60	-15.0	12.9	-27.3
Mountain Mine Underground	JL_AH_62	-15.1	12.8	-22.0
Mountain Mine Underground	JL_AH_63	-15.5	12.9	-22.1
Caminches Mines	JL_AH_263	-12.2	13.3	-26.6
Coom Mine	JL_AH_197	-12.0	13.9	-23.1

H.4 References

Coleman, M.L., Moore, M.P. 1978. Direct reduction of sulfates to sulfur dioxide for isotopic analysis. Analytical Chemistry 50 (11), 1594-1595, https://doi.org/10.1021/ac50033a056

Appendix I: Trace Element Analysis (LA-ICP-MS)

Appendix I.1 Methodology

Mineralized samples from the historic copper mines in West Cork (Fig. I.1) were cut and prepared as highly polished thin and thick sections. The samples are mainly mineralized quartz veins as well as mineralized sediments (see Appendix I.2 for detailed description). Petrographic examination via reflected and transmitted light microscopy was conducted at University College Cork. The primary copper ore is chalcopyrite with smaller amounts of tetrahedrite/tennantite, covellite and chalcocite. Each individual sample shows only one primary chalcopyrite generation. Other sulphides are syngenetic arsenopyrite and molybdenite. Gangue minerals are mainly quartz and minor baryte (Appendix I.2).

The chalcopyrite within the samples was analysed at the LA-ICP-MS lab at iCRAG Trinity College Dublin. Trace elements (^{51}V, ^{53}Cr, ^{55}Mn, ^{59}Co, ^{60}Ni, ^{66}Zn, ^{71}Ga, ^{73}Ge, ^{75}As, ^{77}Se, ^{95}Mo, ^{107}Ag, ^{111}Cd, ^{115}In, ^{118}Sn, ^{121}Sb, ^{125}Te, ^{182}W, ^{195}Pt, ^{197}Au, ^{202}Hg, ^{208}Pb, ^{209}Bi) as well as major elements (^{34}S, ^{57}Fe) were measured. The ablation laser is a Teledyne Photon Machines G2 (Teledyne Technologies, Inc., Thousand Oaks, CA, USA) 193 nm excimer Ar-F laser, which is combined with a HelEx ll active 2-volume ablation cell (Teledyne Cetac Technologies, Omaha, NE, USA). The laser is connected with a tubing system (polytetrafluoroethylene tube with 1.3 mm diameter) to a ThermoFisher Scientific iCAP-Qc quadrupole mass spectrometer (MS, Thermo Fisher Scientific, Waltham, MA, USA). The laser was operated with Chromium 2.1 software (Teledyne Photon Machines, Inc., Thousand Oaks, CA, USA), while element concentrations were collected with Qtegra (version 2.2, ThermoFisher Scientific, Waltham, MA, USA). Helium flow into the cell was set to 0.25 L/min, the sampling cup was flushed with 0.2 L/min He, make-up gas Ar was at 0.65 L/min, 14 L/min Ar was used as cool flow, as well as 0.7 L/min Ar as auxiliary

flow. N_2 as make-up gas (ca. 13 mL/min) was used to reduce oxide formation and increased the signal sensitivity. UQAC-FeS-1 was selected as quality control standard (Fig. I.2). Chalcopyrite grains with a diameter from 0.1 to 10.8 mm were selected from the individual samples (Appendix I.2). The laser beam size was set to square shaped (25 x 25 µm). A shot count of 200, combined with a laser repetition rate of 5Hz, resulted in 40 seconds of ablation for each spot. Depending on size and internal complexity of target mineral grains, spot numbers vary between 1 (single) and 13 (multiple) per chalcopyrite grain (Appendix I.4). Ten seconds were set to flush the system after each measurement.

The software package Iolite 4 (The University of Melbourne, VIC, Australia, Paton *et al.* 2011) was used for data reduction. Time-resolved waves were processed in Iolite, including definition of baseline intervals. Baseline integrations were then reviewed for each of the analyte channels and adjusted, if necessary. The MS data was synchronised with the laser log file to integrate the standards and samples. MASS1 was used as the calibration standard while UQAC-FeS-1 was selected as quality control standard (Table I.1). A 2 SD outlier rejection was performed for all integration intervals. By monitoring the time-resolved signals of major elements (^{34}S, ^{57}Fe and ^{65}Cu), sample integration intervals were either shortened or deleted, if sudden signal drops were recorded.

^{65}Cu served as the internal standard element. A constant Cu concentration of Cu = 34.63 wt.% for stoichiometric chalcopyrite (source: webmineral.com) was applied in the data reduction.

The quantitative output was checked for data errors, especially outliers, potentially caused by micro-inclusions of other minerals. Integrations of these outliers were screened for signal spikes that mark the presence of micro-inclusions. Individual measurements, that seem biased by micro-inclusions according to this approach are highlighted in the data output (I.4).

The detection limit (LOD, I.4) was calculated after Pettke *et al.* (2012), which uses an approximation to Poisson distribution statistics for the estimation of

LOD (iolite 4 Documentation, 2021). The formula incorporates the background count rate, the dwell time, the number of sweeps for the analyte, as well as the sensitivity of the element (iolite 4 Documentation, 2021). QAQC was performed by monitoring the secondary quality control standard UQAC-FeS-1 (Table I.1 and Fig. I.2)

Additional to the individual data reduction (mineral inclusions) by using Iolite 4, the measured values of the major element compositions (^{34}S and ^{57}Fe) were compared with the trace element concentrations of all samples (Appendix I.3). Spikes were cross-checked in the MS spectra for further mineral inclusions which are marked in Appendix I.4

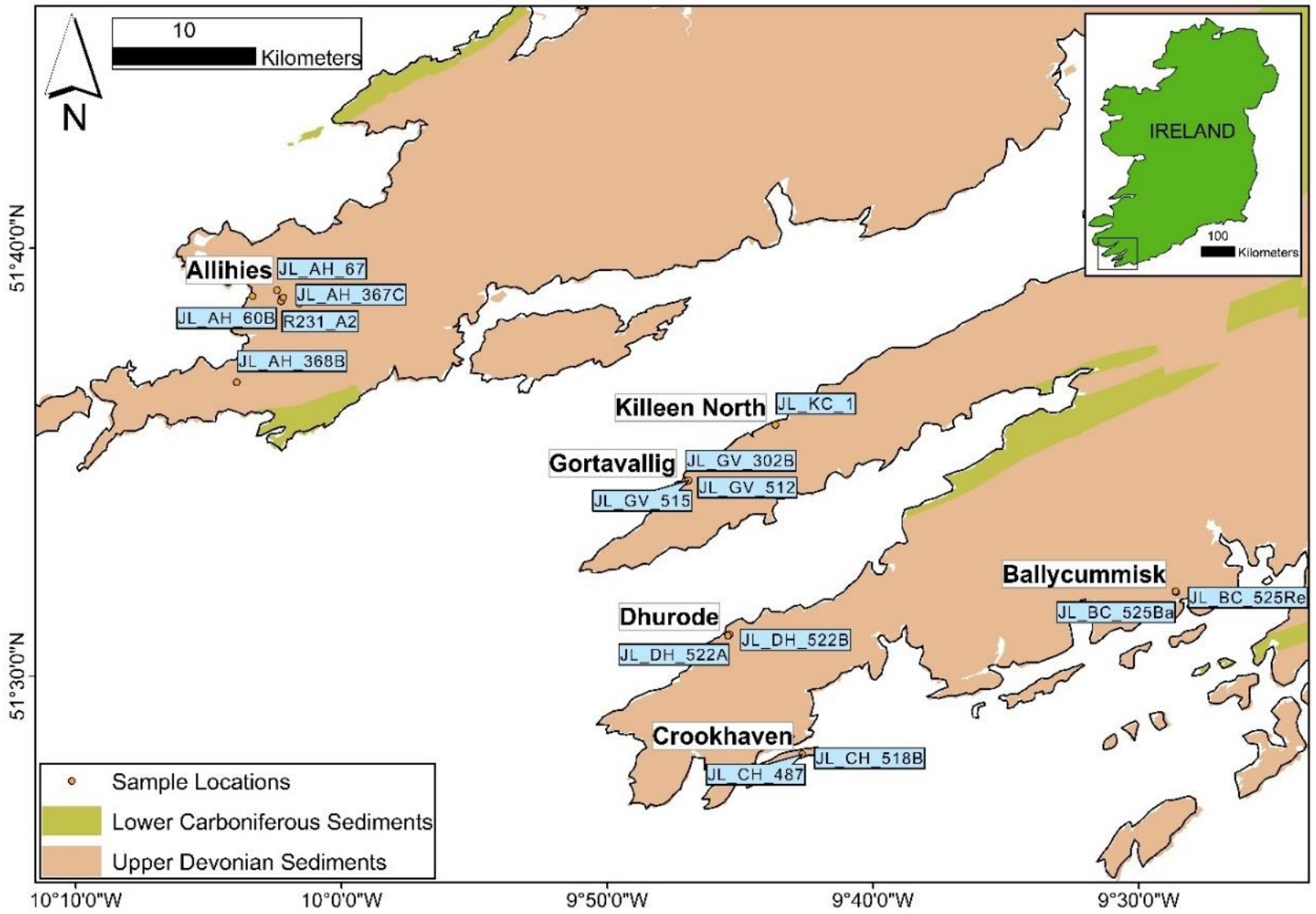


Fig. I.1) Sample localities for chalcopyrite LA-ICP-MS trace element measurements.

Table I.1)

Channel	Element	Measured	Accepted	% Diff	Variation (%RSD)	Minimum	Maximum	< LOD	Calibrant
S34_ppm	S	498157	410000	21.5	15.48	375358	594649	No	S_MASS1
V51_ppm	V	24.1408	21	14.96	22.64	18.2826	39.8756	No	S_MASS1
Cr53_ppm	Cr	290.568	250	16.23	62.49	191.386	881.512	No	S_MASS1
Mn55_ppm	Mn	73.131	58	26.09	56.27	-20.2955	136.497	No	S_MASS1
Fe57_ppm	Fe	544146	450000	20.92	14.4	473014	675296	No	S_MASS1
Co59_ppm	Co	653.071	637	2.52	13.57	531.417	773.97	No	S_MASS1
Ni60_ppm	Ni	28847.1	25000	15.39	13.51	24118.6	33612.5	No	S_MASS1
Zn66_ppm	Zn	287.548	275	4.56	50.76	216.043	789.71	No	S_MASS1
Ga71_ppm	Ga	11.4987	10	14.99	33.75	7.89727	18.3689	No	S_MASS1
As75_ppm	As	1501.6	1050	43.01	29.47	1126.43	2818.1	No	S_MASS1
Se77_ppm	Se	389.212	310	25.55	18.71	316.873	516.398	No	S_MASS1
Mo95_ppm	Mo	68.9158	66	4.42	16.87	56.0206	82.5051	No	S_MASS1
Ag107_ppm	Ag	153.246	155	-1.13	20.48	126.593	229.733	No	S_MASS1

In115_ppm	In	10.0224	9.4	6.62	21.32	8.21097	15.3318	No	S_MASS1
Sn118_ppm	Sn	241.587	180	34.22	74.8	144.922	886.827	No	S_MASS1
Sb121_ppm	Sb	97.1468	88	10.39	72.01	53.4747	264.339	No	S_MASS1
Te125_ppm	Te	186.441	170	9.67	18.65	146.099	250.22	No	S_MASS1
W182_ppm	W	1645.99	1500	9.73	58.18	866.704	3081.29	No	S_MASS1
Pt195_ppm	Pt	69.6822	50	39.36	78.64	33.2665	175.069	No	S_MASS1
Au197_ppm	Au	74.2086	65	14.17	57.48	48.4403	160.809	No	S_MASS1
Hg202_ppm	Hg	43.582	50	-12.84	103.35	23.884	145.237	No	S_MASS1
Pb208_ppm	Pb	95.0698	90	5.63	29.6	77.2752	186.277	No	S_MASS1
Bi209_ppm	Bi	134.185	120	11.82	42.03	104.787	368.935	No	S_MASS1

Table I.1) QAQC using MASS1 as calibration standard and UQAC-FeS-1 as quality control standard.

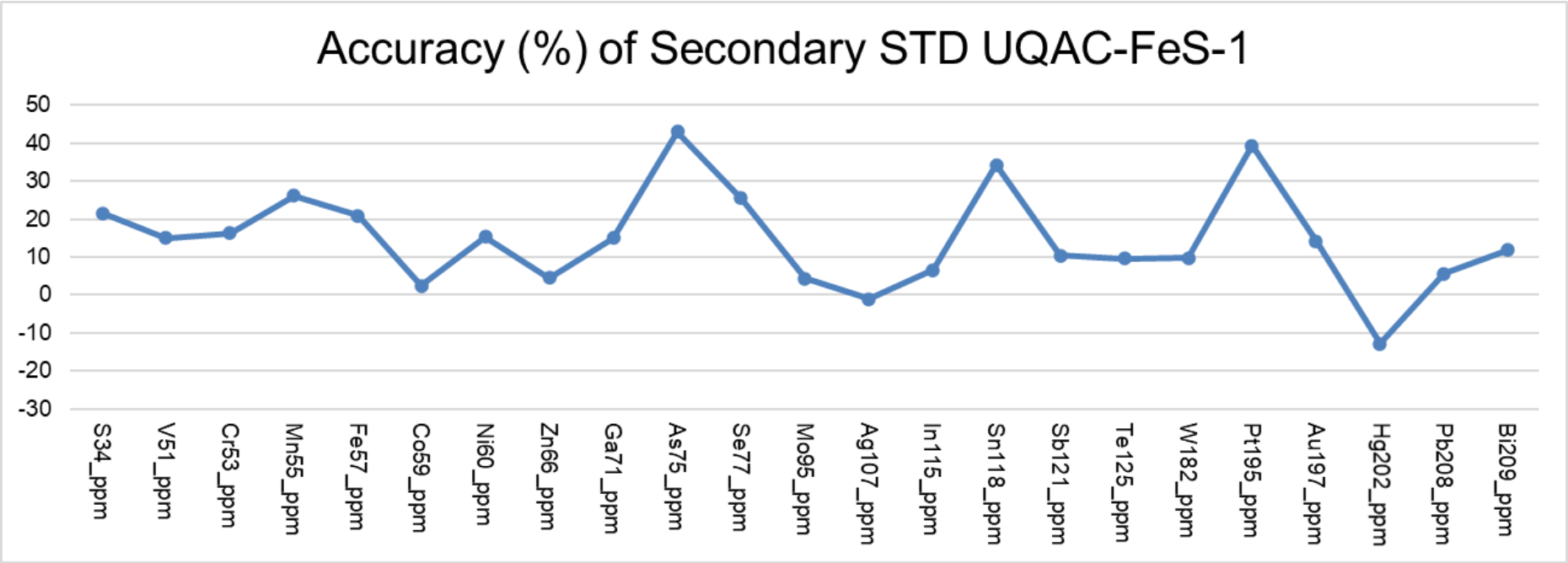


Fig. I.2) Accuracy (%) of the UQAC-FeS-1 quality control standard, calibrated with the MASS1 calibration standard (Table I.1)

Appendix I.2 Sample list + Slides images

Sample locations for LA-ICP-MS trace elements measurements (chalcopyrite):

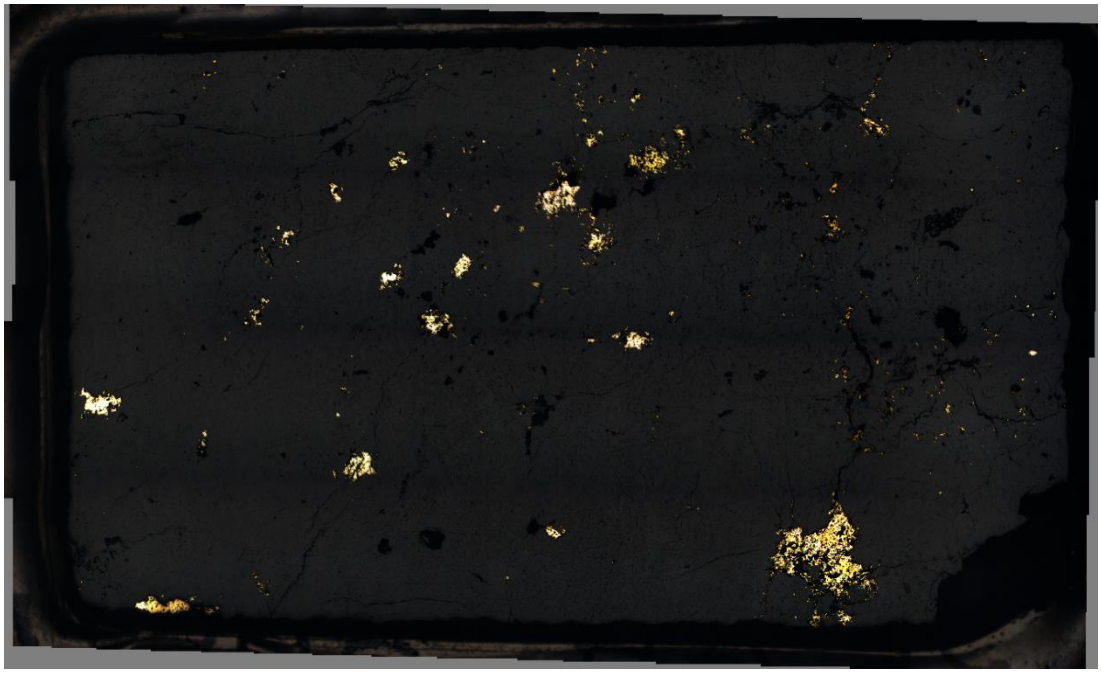
Location	Lat (°N)	Long (°E)	Sample Name	Description	Chalcopyrite Grain Size
Allihies Dooneen Mine	51.648064	-10.055819	JL_AH_365A	spoil sample, quartz vein with chalcopyrite	0.2 - 3.8 mm
Allihies Marion Lode	51.650379	-10.040490	JL_AH_67	spoil sample, massive chalcopyrite with minor covellite and tetrahedrite	0.1 - 6.6 mm
Allihies Mountain Mine	51.647103	-10.037573	JL_AH_60B	in situ sample from Mountain Mine Underground, chalcopyrite in quartz vein, hosted in siltstone	0.8 - 5.8 mm
Allihies Molybdenite Sample	51.646068	-10.037864	R231_A2	Sample was used for Re-Os dating! Historic sample from NHM London (BM.1964,R231), collected by Sir Arthur Russell (Mountain Mine dumps in 1918). Quartz vein with molybdenite with minor chalcopyrite	0.8 mm (single grain)
Allihies Gunpowder Mine	51.647532	-10.036469	JL_AH_367C	underground spoil sample, quartz vein with chalcopyrite and tetrahedrite/tennantite, with later tetrahedrite/tennantite vein cross-cutting	0.2 - 3.6 mm
Allihies Coom Mine	51.645138	-10.026552	JL_AH_333	spoil sample, quartz vein with some chalcopyrite	0.1 - 1.1 mm
Allihies Dursey Crossing Mine	51.614517	-10.065739	JL_AH_368B	underground spoil sample, quartz vein with chalcopyrite and minor covellite	0.1 - 3.0 mm

Gortavallig Mineralized Sandstone	51.575883	-9.784627	JL_GV_302B	in situ sample, mineralized sandstone, disseminated chalcopyrite, minor chalcocite? Dark grey mineral (tetrahedrite?)	0.1 - 0.4 mm
Gortavallig Vein Sample	51.575887	-9.784587	JL_GV_512	in situ sample, quartz vein with fractured arsenopyrite, nearby chalcopyrite with minor tetrahedrite intergrowths	0.1 - 7.7 mm
Gortavallig Spoil Sample with Galena	51.576339	-9.782435	JL_GV_515	spoil sample, quartz vein with major pyrite, minor chalcopyrite with traces of tetrahedrite, minor galena	0.1 - 0.8 mm
Killeen North Fossil	51.597944	-9.727817	JL_KC_1	spoil sample, mineralized conglomerate! Rounded siltstone and mudstone clasts. Some rounded clasts are replaced by chalcopyrite. One clast shows cellular fossil plant structures! Mineralized (chalcopyrite) plant fossil clast!	0.2 - 7.2 mm
Dhurode Mine A	51.516135	-9.757177	JL_DH_522A	spoil sample, quartz vein with euhedral arsenopyrite (early), chalcopyrite intergrown with tetrahedrite	1.3 - 5.6 mm
Dhurode Mine B	51.516135	-9.757177	JL_DH_522B	spoil sample, quartz vein with euhedral arsenopyrite (early), tetrahedrite with 'inclusions' of chalcopyrite	0.1 - 1.0 mm

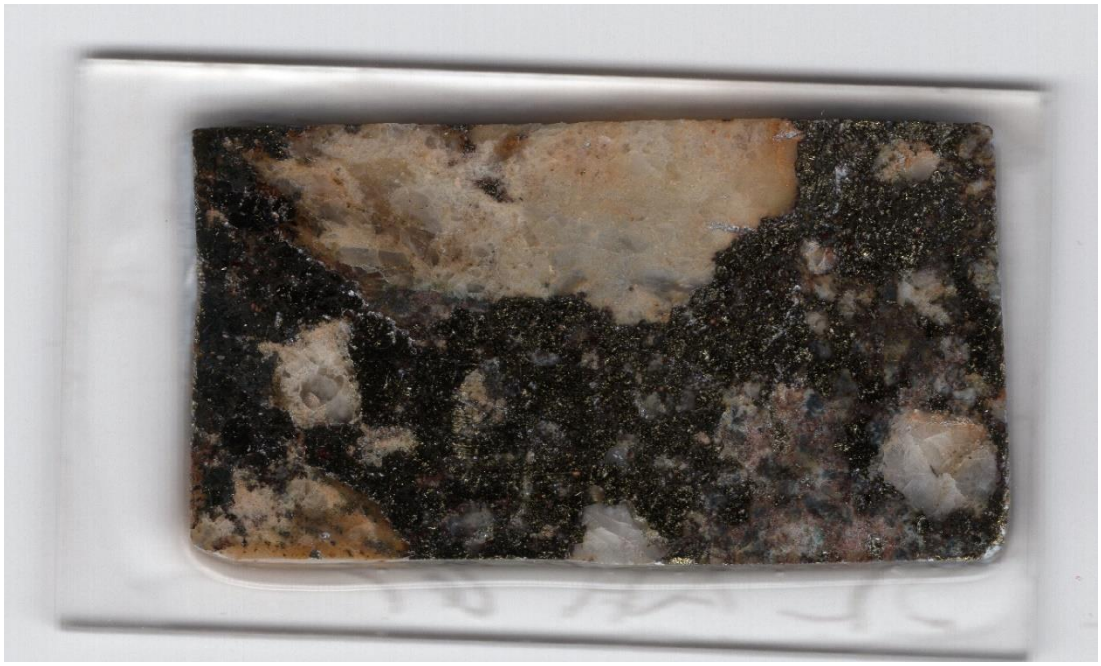
Crookhaven Sediment Hosted Cu	51.469536	-9.711183	JL_CH_487	in situ sample, sediment hosted copper ore, sampled next to mineralized quartz vein, disseminated chalcopyrite in porous sandstone, minor malachite	0.1 - 2.4 mm
Crookhaven Quartz Vein	51.469561	-9.711099	JL_CH_518B	in situ sample, quartz vein with chalcopyrite (next to sample JL_CH_487_PB)	1.5 - 10.8 mm
Ballycummisk (Sample with Baryte)	51.533050	-9.476797	JL_BC_525Ba	spoil sample, quartz vein with baryte, with specularite with late chalcopyrite	0.4 - 5.4 mm
Ballycummisk (with Molybdenite)	51.533050	-9.476797	JL_BC_525Re	spoil sample, sample was used for Re-Os dating! quartz vein with minor baryte? With specularite, molybdenite and chalcopyrite	0.1 - 2.0 mm
Datum:	**D_WGS_1984**				
Prime Meridian:	**Greenwich**				
Angular Unit:	**Degree**				

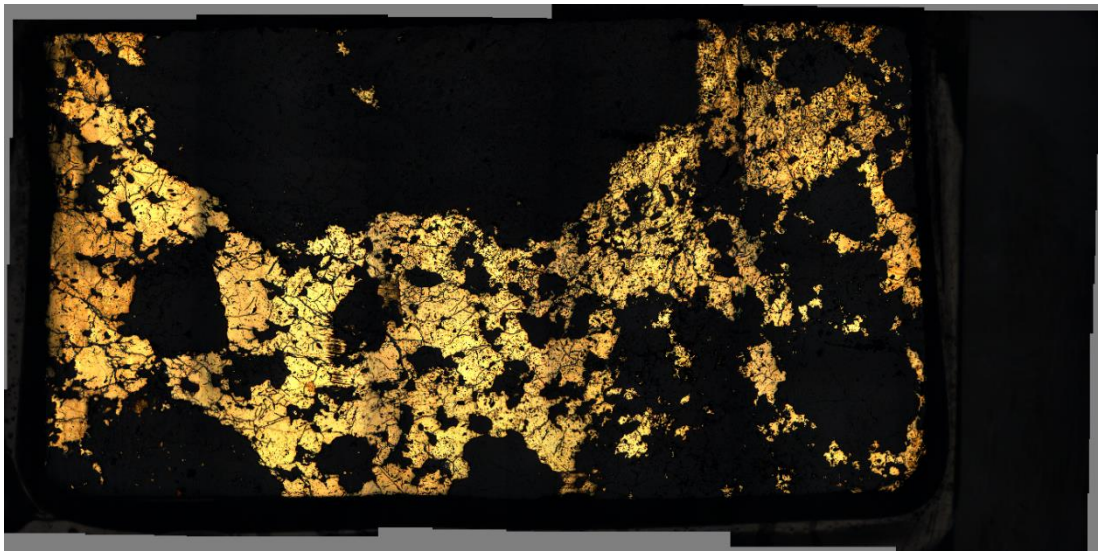
Sample **JL_AH_365A** (scanned slide and reflected light microscopy map, width of slide 46 mm):





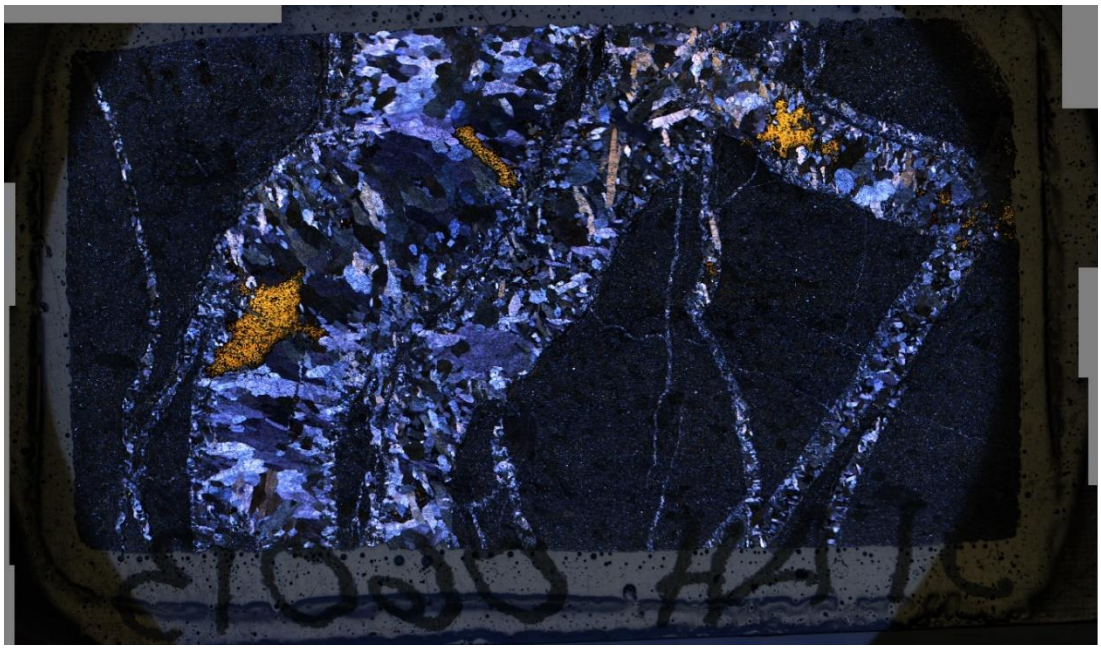
Sample **JL_AH_67** (scanned slide and reflected light microscopy map, width of slide 46 mm):





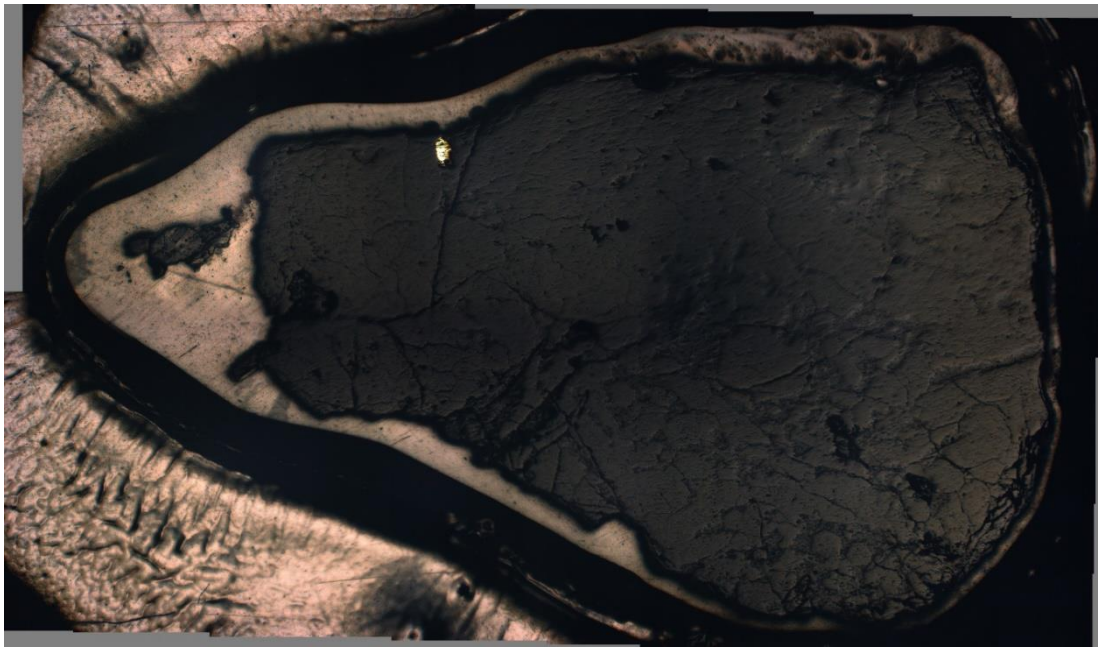
Sample **JL_AH_60B** (scanned slide and reflected and transmitted light microscopy map, width of slide 46 mm):





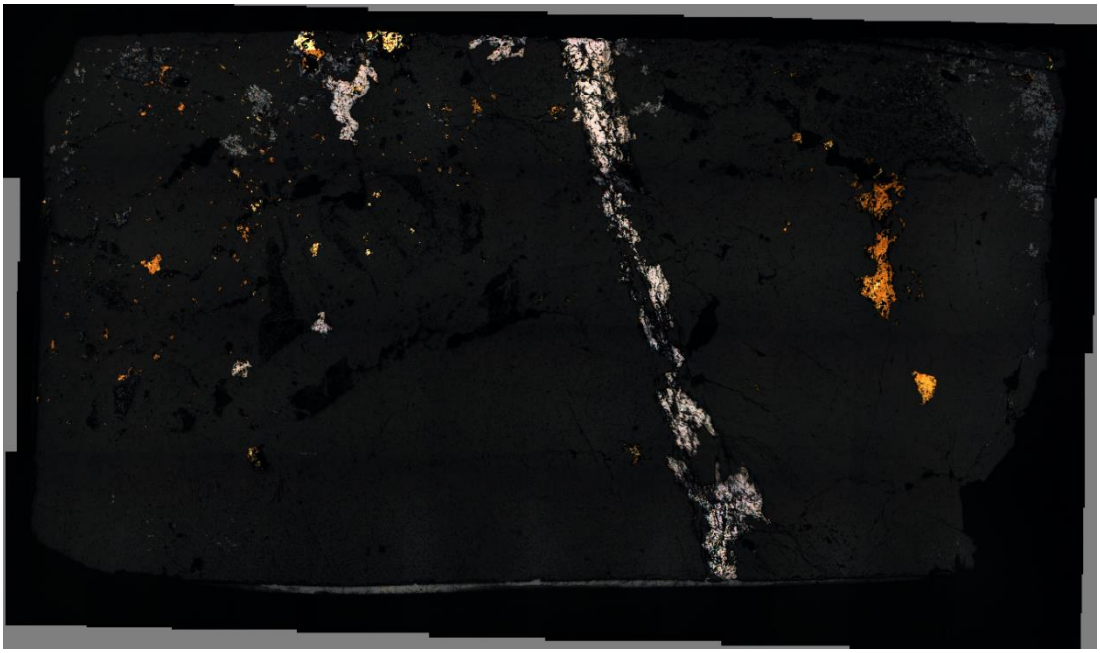
Sample **R231_A2 (BM.1964, R231)** (scanned slide and reflected light microscopy map, width of slide 46 mm):





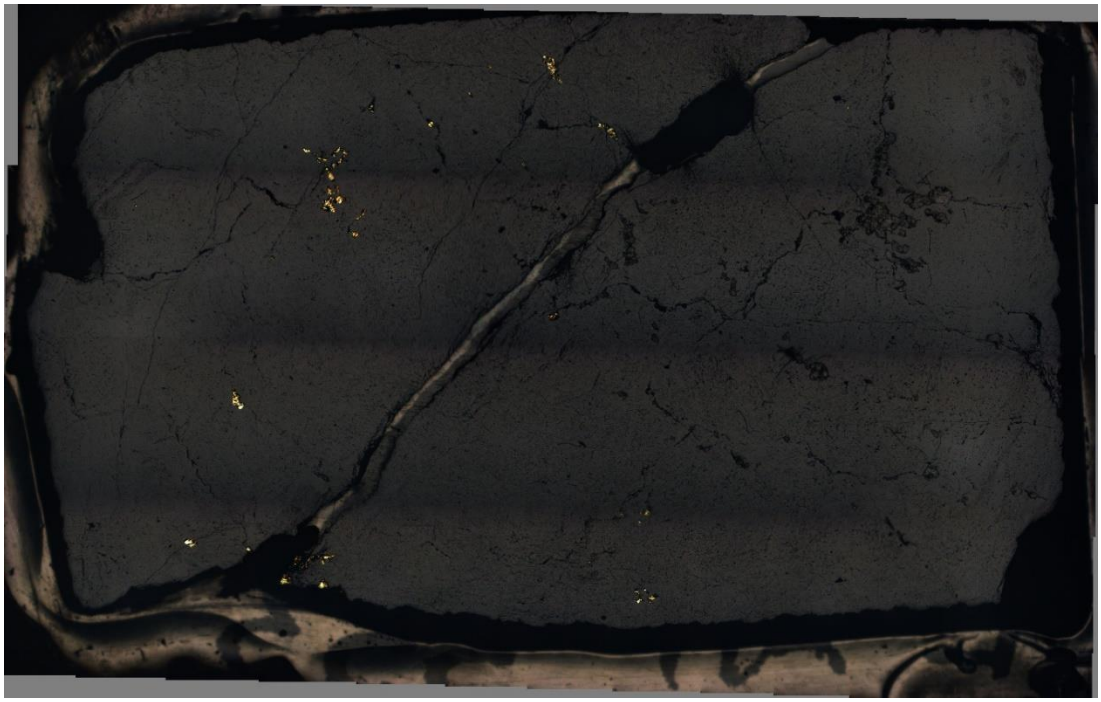
Sample **JL_AH_367C** (scanned slide and reflected light microscopy map, width of slide 46 mm):





Sample **JL_AH_333** (scanned slide and reflected light microscopy map, width of slide 46 mm):



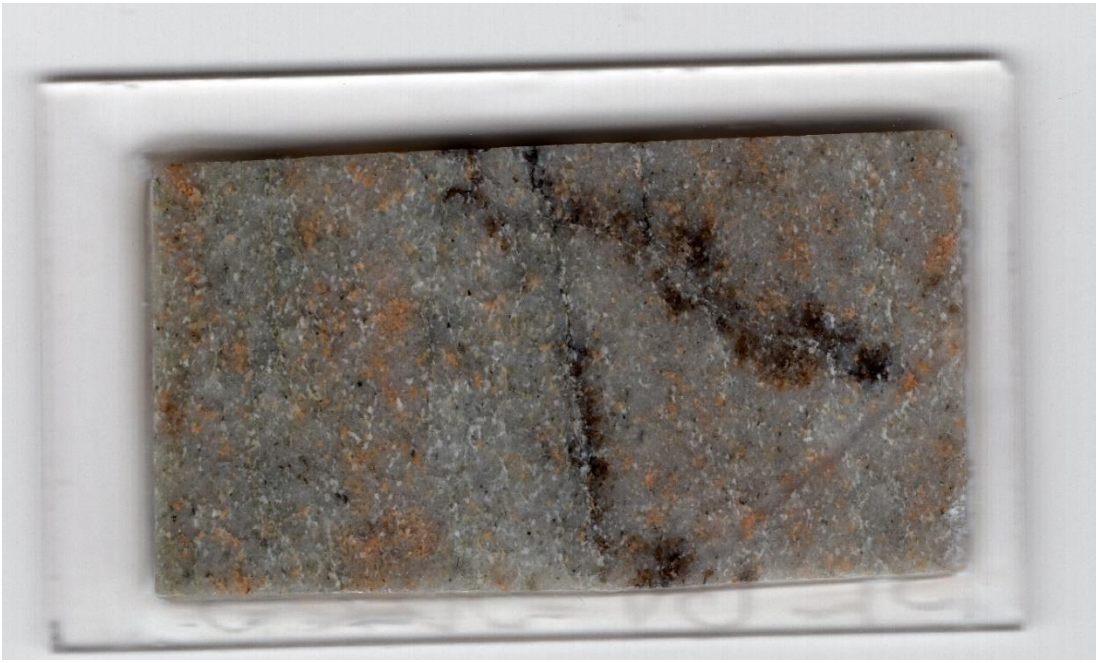


Sample **JL_AH_368B** (scanned slide and reflected and transmitted light microscopy map, width of slide 46 mm):





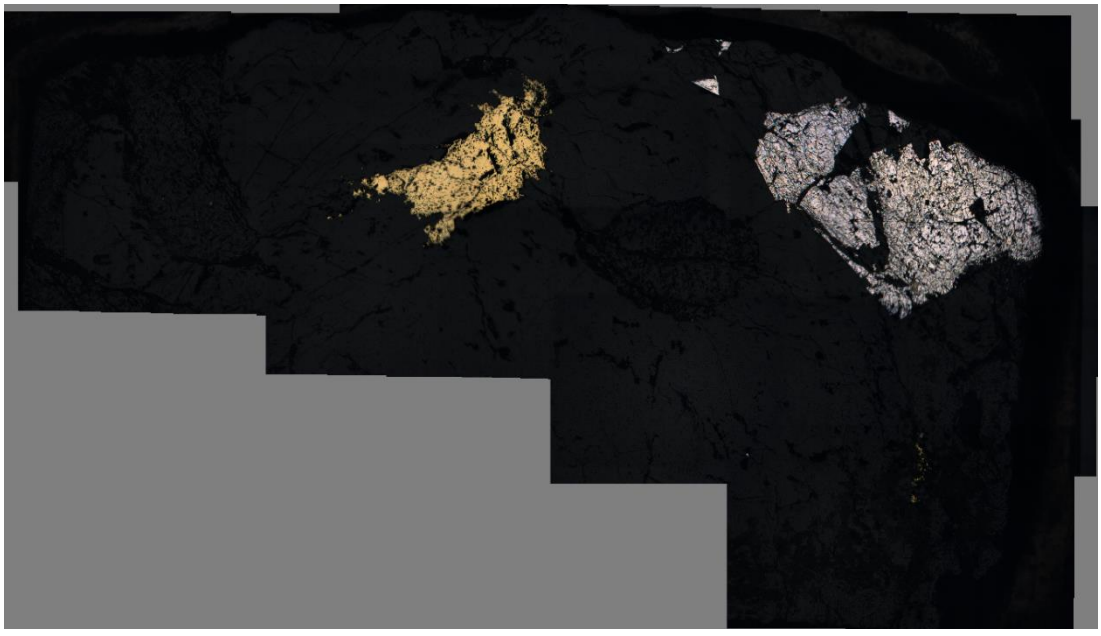
Sample **JL_GV_302B** (scanned slide and reflected light microscopy map, width of slide 46 mm):





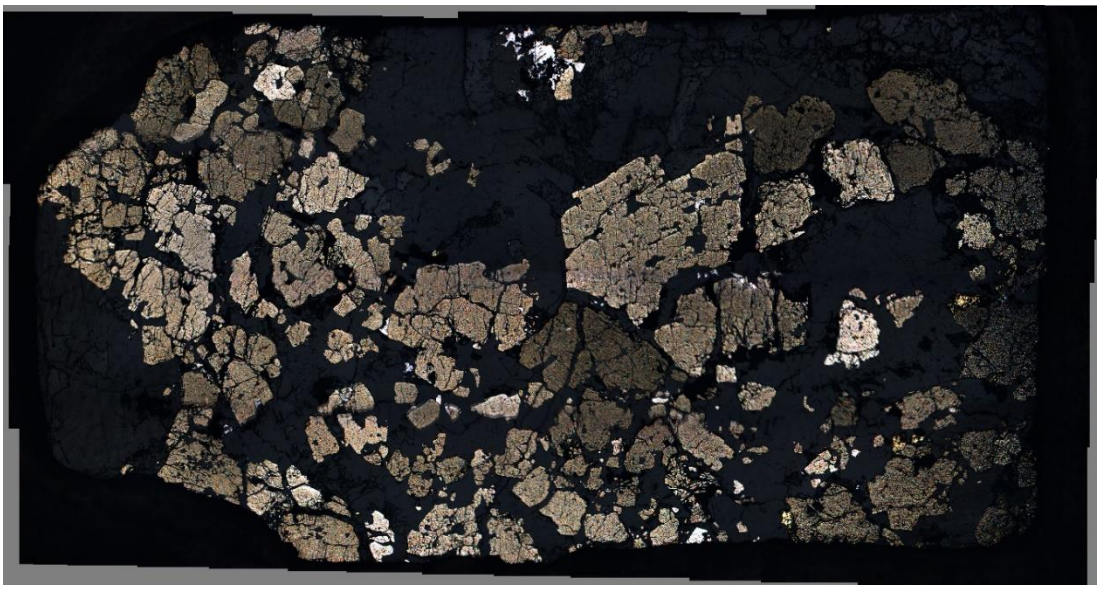
Sample **JL_GV_512** (scanned slide and reflected light microscopy map, width of slide 46 mm):





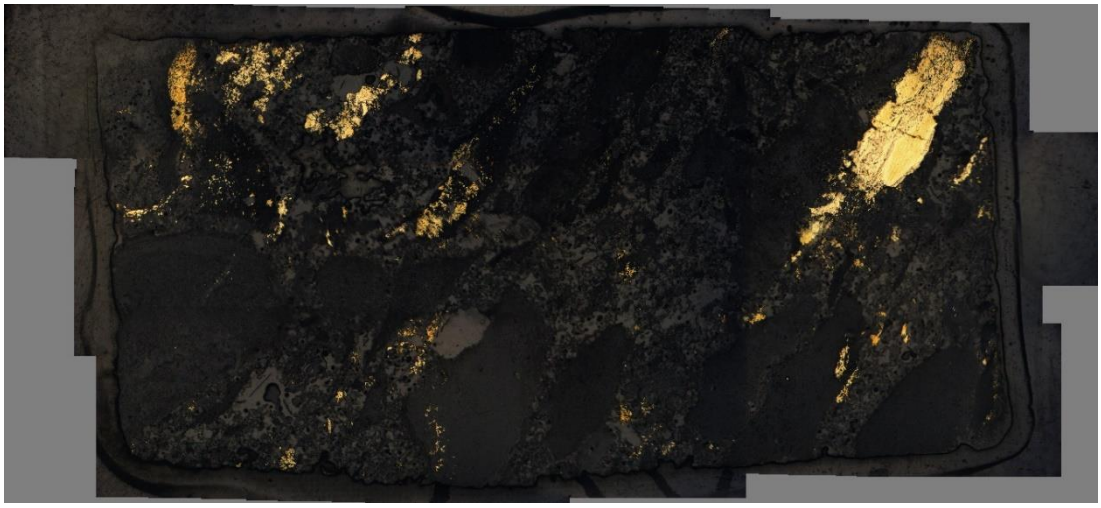
Sample **JL_GV_515** (scanned slide and reflected light microscopy map, width of slide 46 mm):





Sample **JL_KC_1** (scanned slide and reflected light microscopy map, width of slide 46 mm):





Sample **JL_DH_522A** (scanned slide and reflected light microscopy map, width of slide 46 mm):





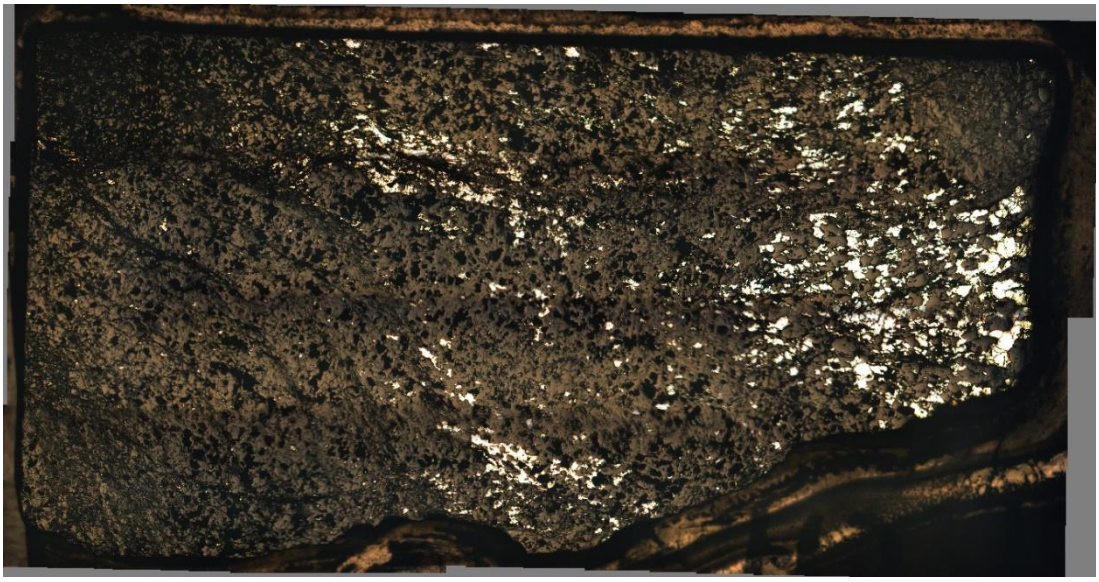
Sample **JL_DH_522B** (scanned slide and reflected light microscopy map, width of slide 46 mm):





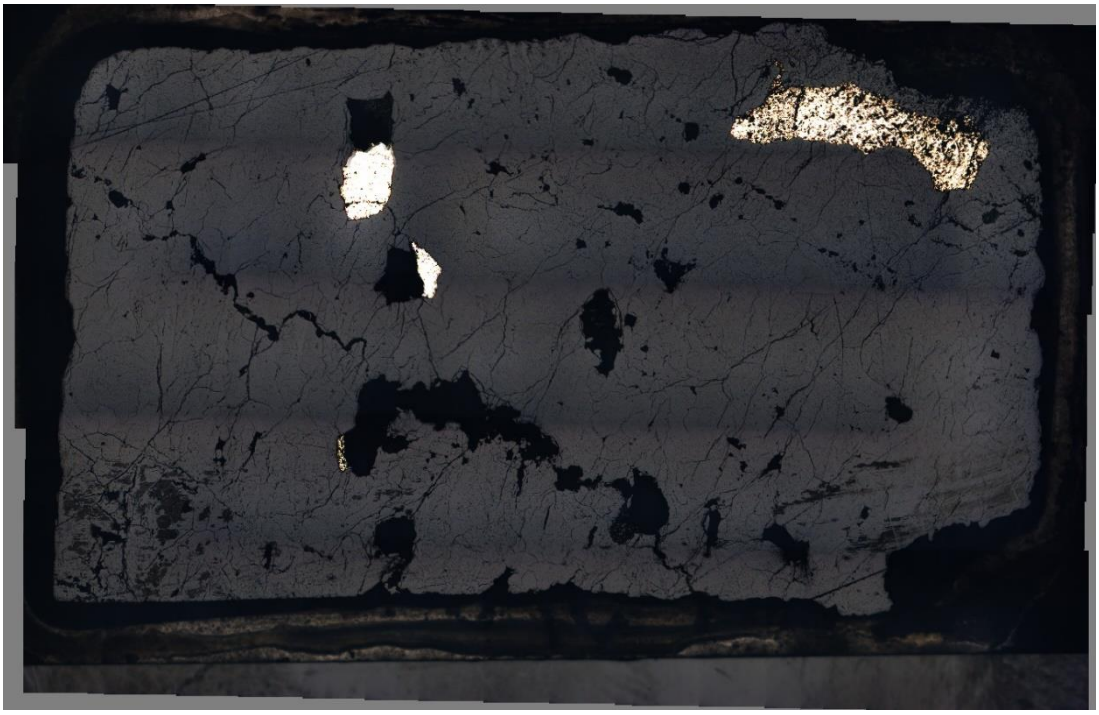
Sample **JL_CH_487** (scanned slide and reflected light microscopy map, width of slide 46 mm):



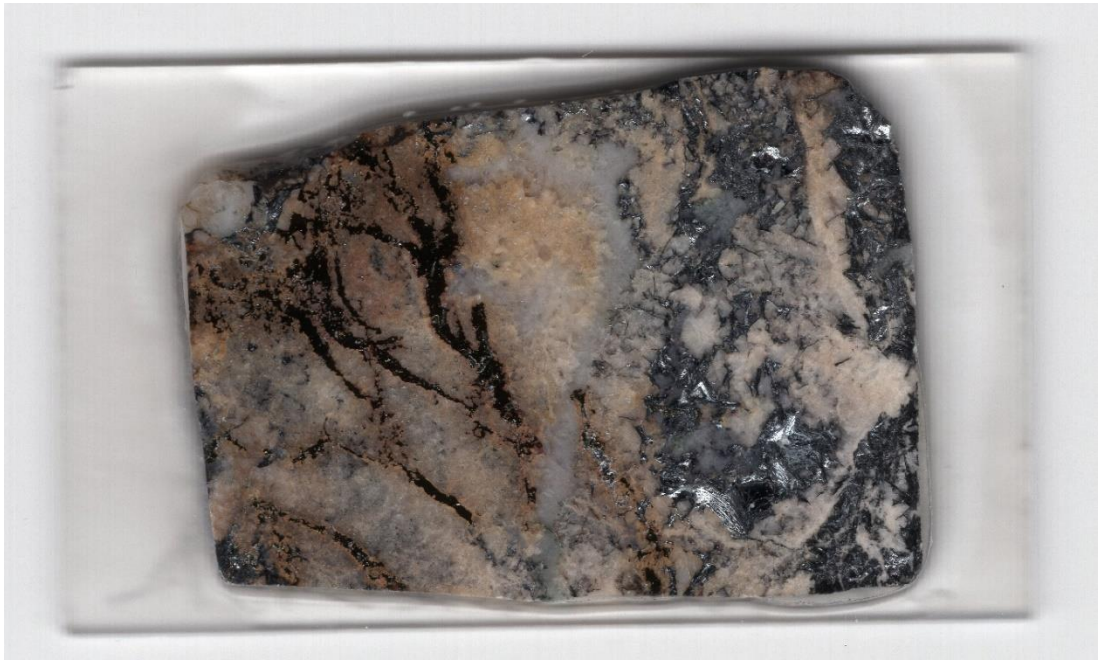


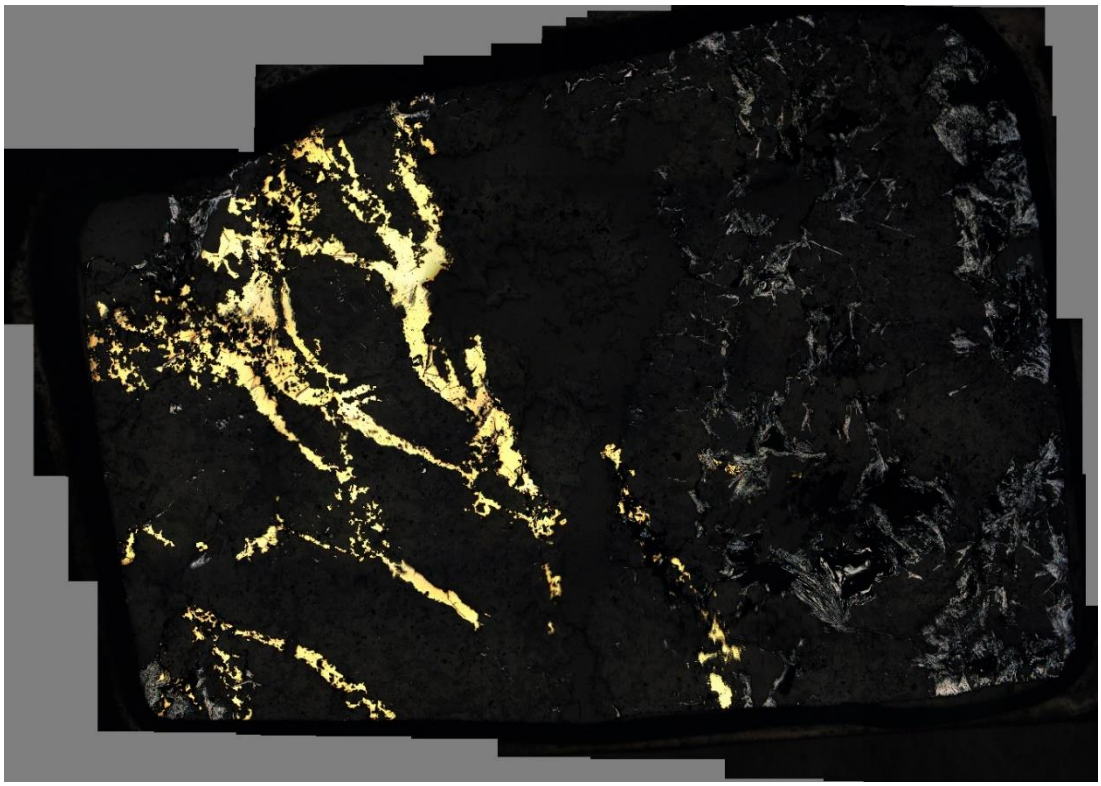
Sample **JL_CH_518B** (scanned slide and reflected light microscopy map, width of slide 46 mm):



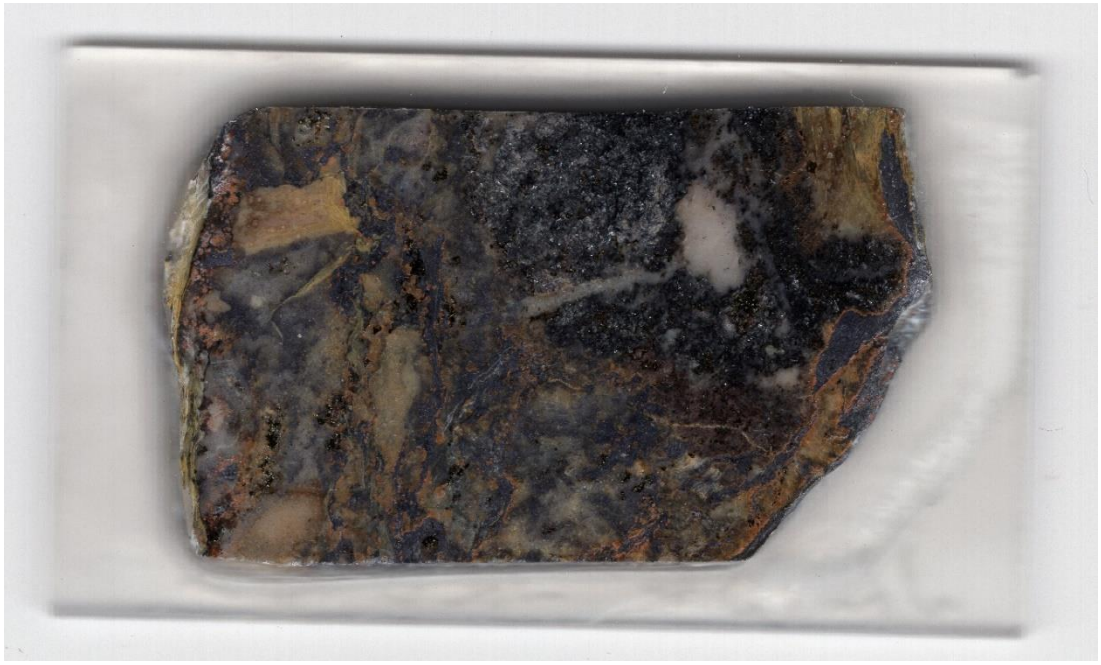


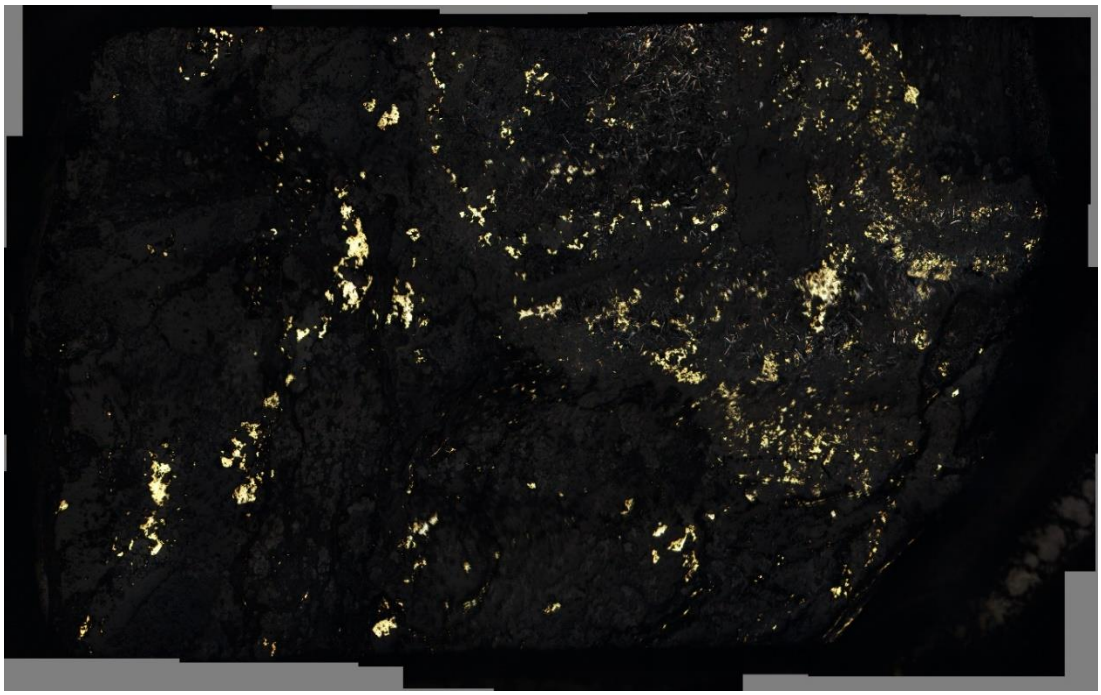
Sample **JL_BC_525Ba** (scanned slide and reflected light microscopy map, width of slide 46 mm):





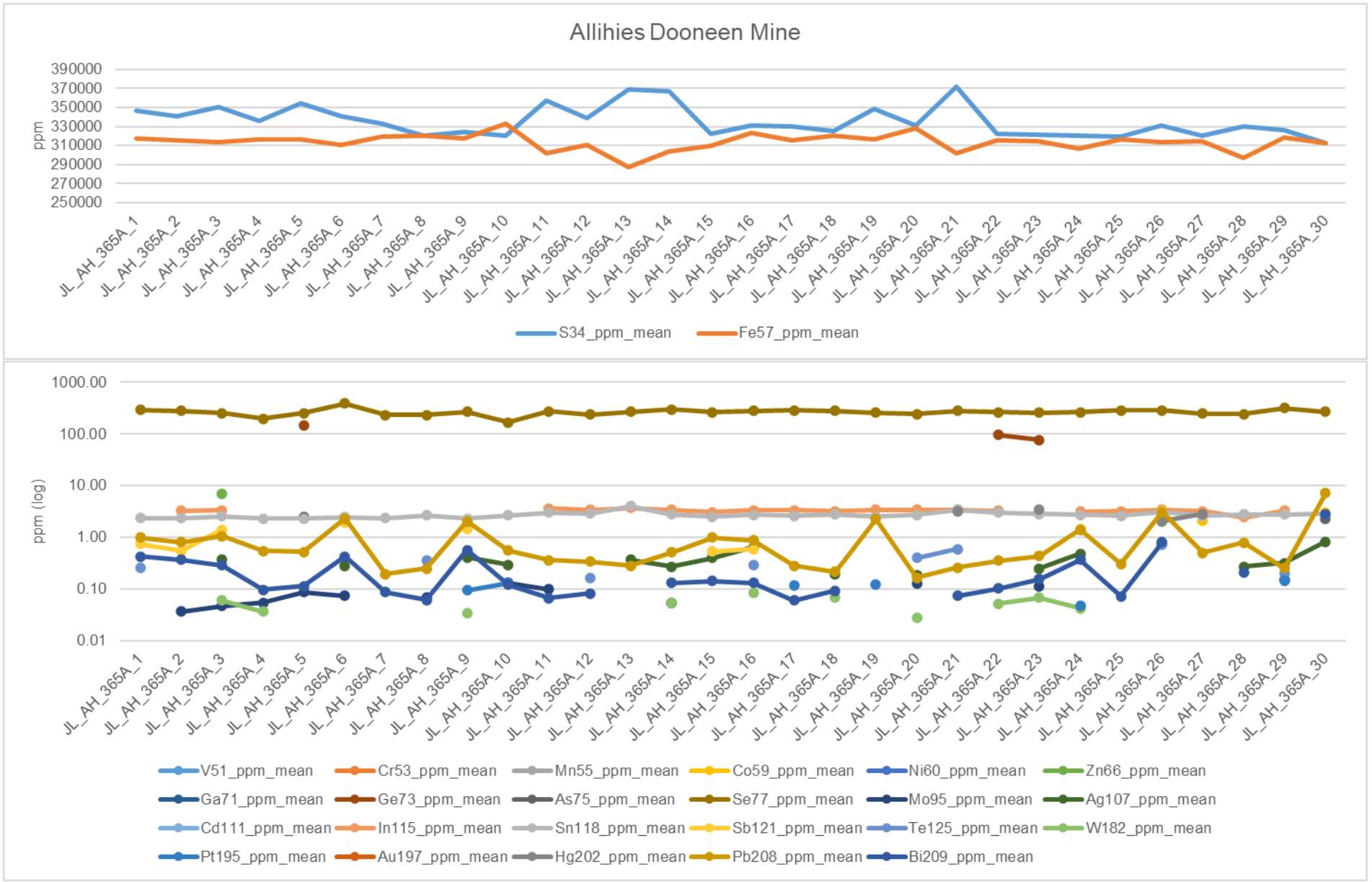
Sample **JL_BC_525Re** (scanned slide and reflected light microscopy map, width of slide 46 mm):

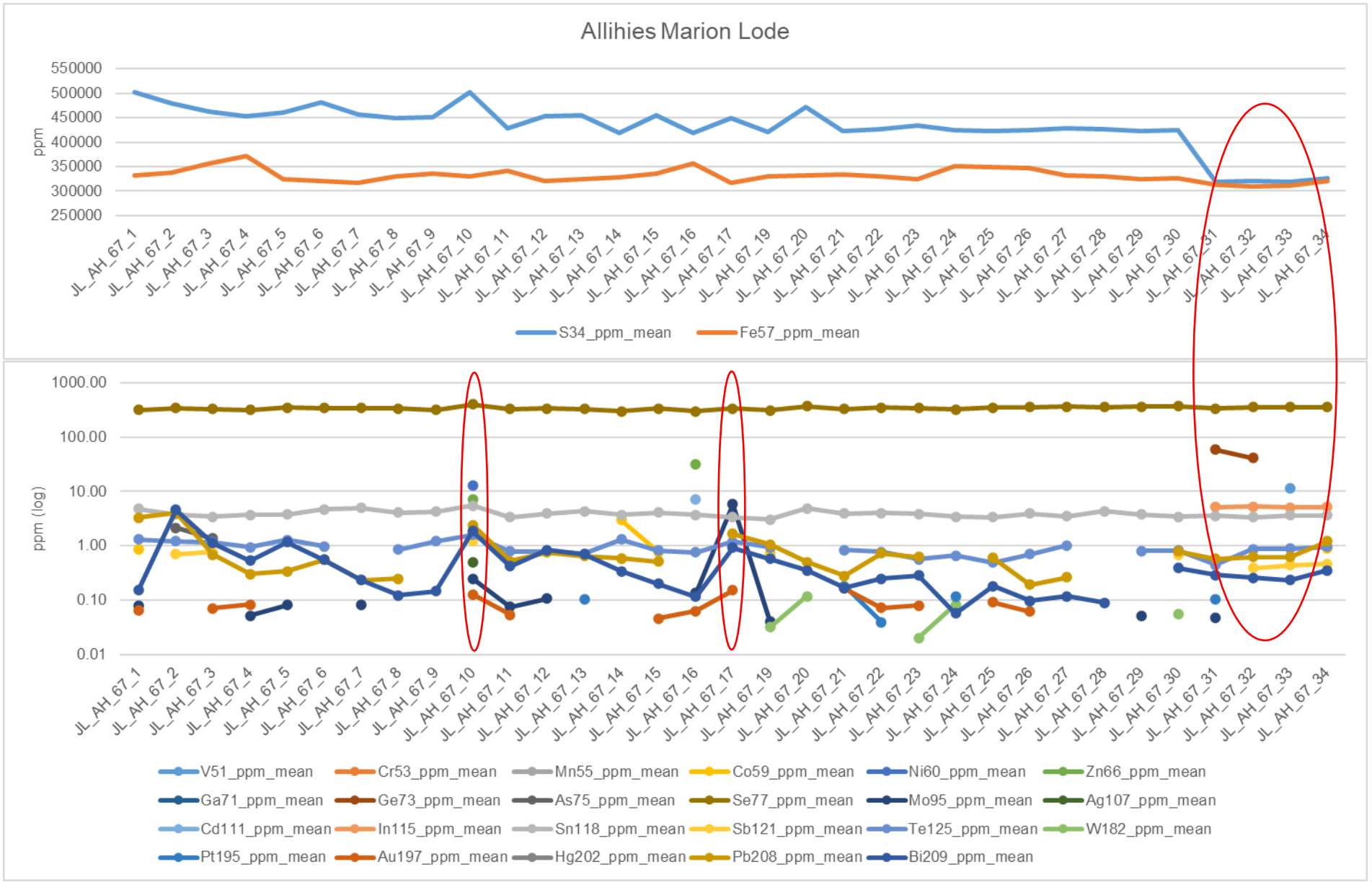




Appendix I.3 (Laser Ablation ICP-MS) Additional Quality Control: Micro Inclusions – Element plots

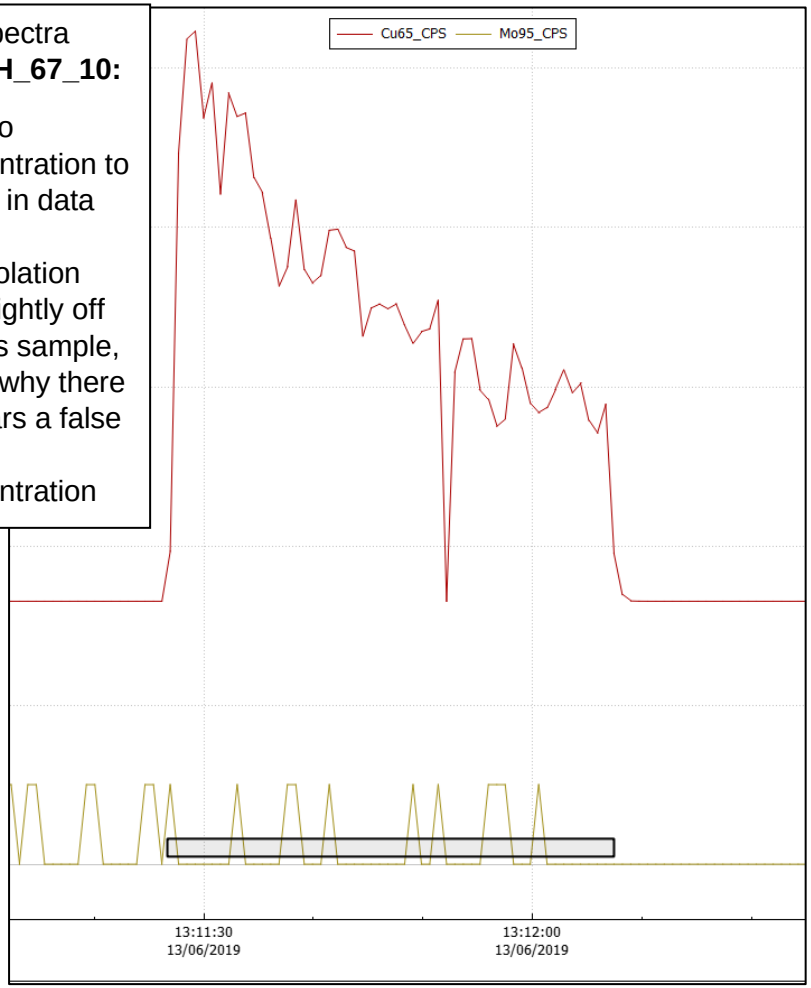
The following plots show the mean concentrations of each measurement point (in ppm). Spikes were cross-checked in the MS spectra for further mineral inclusions which are marked in Appendix I.4 The according standard deviations and detection limits (LOD) are shown in Appendix I.4.


Allihies Dooneen Mine
ppm
390000
370000
350000
330000
310000
290000
270000
250000
JL_AH_365A_1
JL_AH_365A_2
JL_AH_365A_3
JL_AH_365A_4
JL_AH_365A_5
JL_AH_365A_6
JL_AH_365A_7
JL_AH_365A_8
JL_AH_365A_9
JL_AH_365A_10
JL_AH_365A_11
JL_AH_365A_12
JL_AH_365A_13
JL_AH_365A_14
JL_AH_365A_15
JL_AH_365A_16
JL_AH_365A_17
JL_AH_365A_18
JL_AH_365A_19
JL_AH_365A_20
JL_AH_365A_21
JL_AH_365A_22
JL_AH_365A_23
JL_AH_365A_24
JL_AH_365A_25
JL_AH_365A_26
JL_AH_365A_27
JL_AH_365A_28
JL_AH_365A_29
JL_AH_365A_30
S34_ppm_mean
Fe57_ppm_mean
ppm (log)
1000.00
100.00
10.00
1.00
0.10
0.01
V51_ppm_mean
Cr53_ppm_mean
Mn55_ppm_mean
Co59_ppm_mean
Ni60_ppm_mean
Zn66_ppm_mean
Ga71_ppm_mean
Ge73_ppm_mean
As75_ppm_mean
Se77_ppm_mean
Mo95_ppm_mean
Ag107_ppm_mean
Cd111_ppm_mean
In115_ppm_mean
Sn118_ppm_mean
Sb121_ppm_mean
Te125_ppm_mean
W182_ppm_mean
Pt195_ppm_mean
Au197_ppm_mean
Hg202_ppm_mean
Pb208_ppm_mean
Bi209_ppm_mean


Allihies Marion Lode
ppm
550000
500000
450000
400000
350000
300000
250000
JL_AH_67_1
JL_AH_67_2
JL_AH_67_3
JL_AH_67_4
JL_AH_67_5
JL_AH_67_6
JL_AH_67_7
JL_AH_67_8
JL_AH_67_9
JL_AH_67_10
JL_AH_67_11
JL_AH_67_12
JL_AH_67_13
JL_AH_67_14
JL_AH_67_15
JL_AH_67_16
JL_AH_67_17
JL_AH_67_19
JL_AH_67_20
JL_AH_67_21
JL_AH_67_22
JL_AH_67_23
JL_AH_67_24
JL_AH_67_25
JL_AH_67_26
JL_AH_67_27
JL_AH_67_28
JL_AH_67_29
JL_AH_67_30
JL_AH_67_31
JL_AH_67_32
JL_AH_67_33
JL_AH_67_34
S34_ppm_mean
Fe57_ppm_mean
ppm (log)
1000.00
100.00
10.00
1.00
0.10
0.01
V51_ppm_mean
Cr53_ppm_mean
Mn55_ppm_mean
Co59_ppm_mean
Ni60_ppm_mean
Zn66_ppm_mean
Ga71_ppm_mean
Ge73_ppm_mean
As75_ppm_mean
Se77_ppm_mean
Mo95_ppm_mean
Ag107_ppm_mean
Cd111_ppm_mean
In115_ppm_mean
Sn118_ppm_mean
Sb121_ppm_mean
Te125_ppm_mean
W182_ppm_mean
Pt195_ppm_mean
Au197_ppm_mean
Hg202_ppm_mean
Pb208_ppm_mean
Bi209_ppm_mean

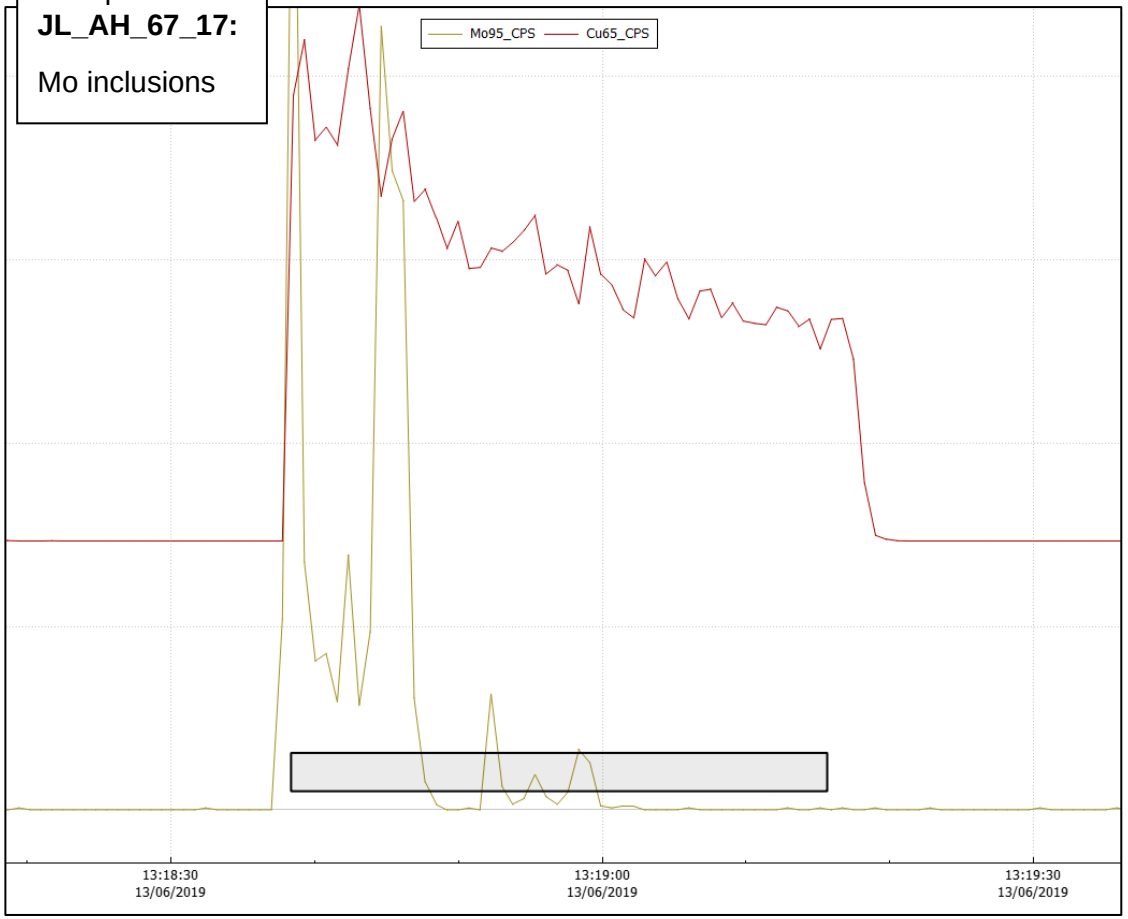
MS spectra **JL_AH_67_10:**

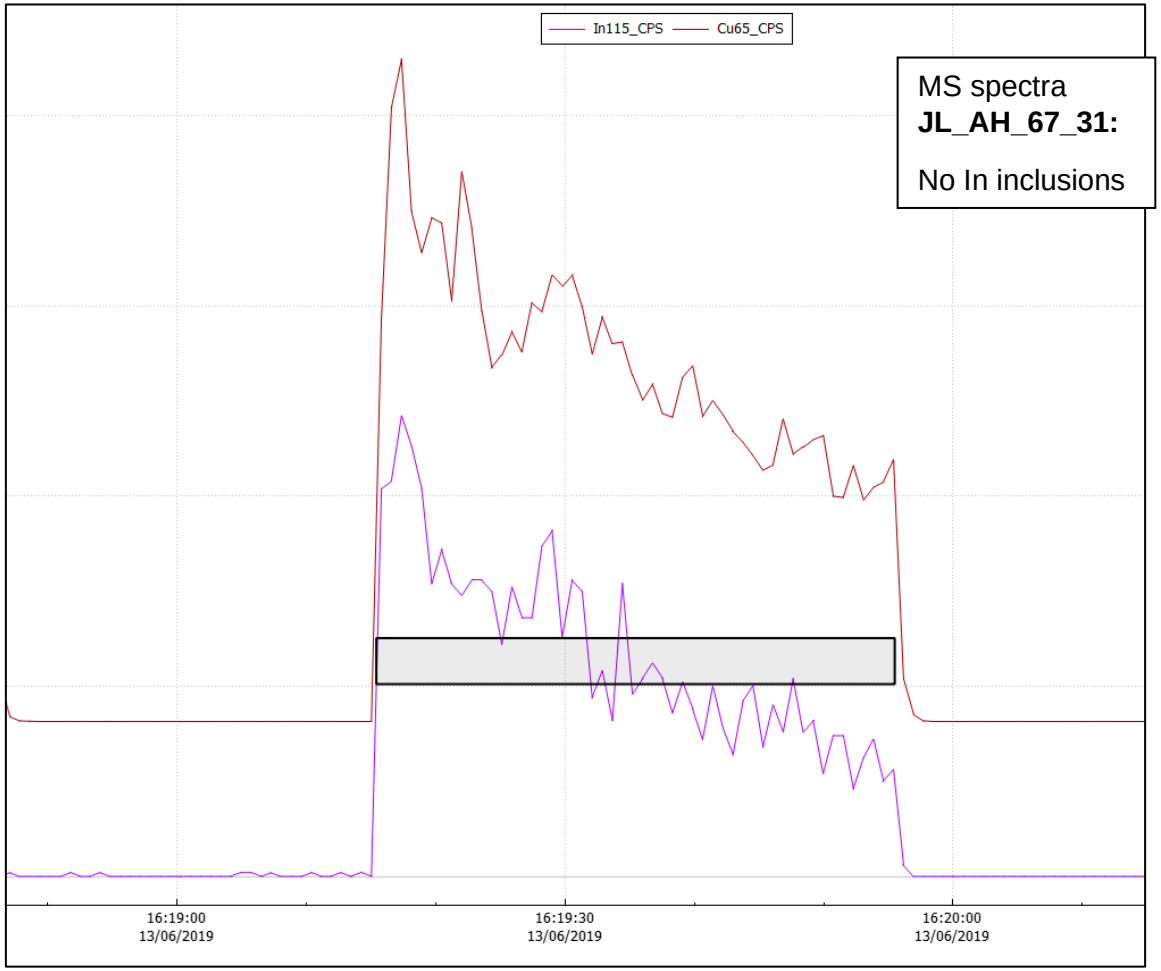
Set Mo concentration to <LOD in data table, interpolation line slightly off for this sample, that's why there appears a false Mo concentration



MS spectra **JL_AH_67_17:**

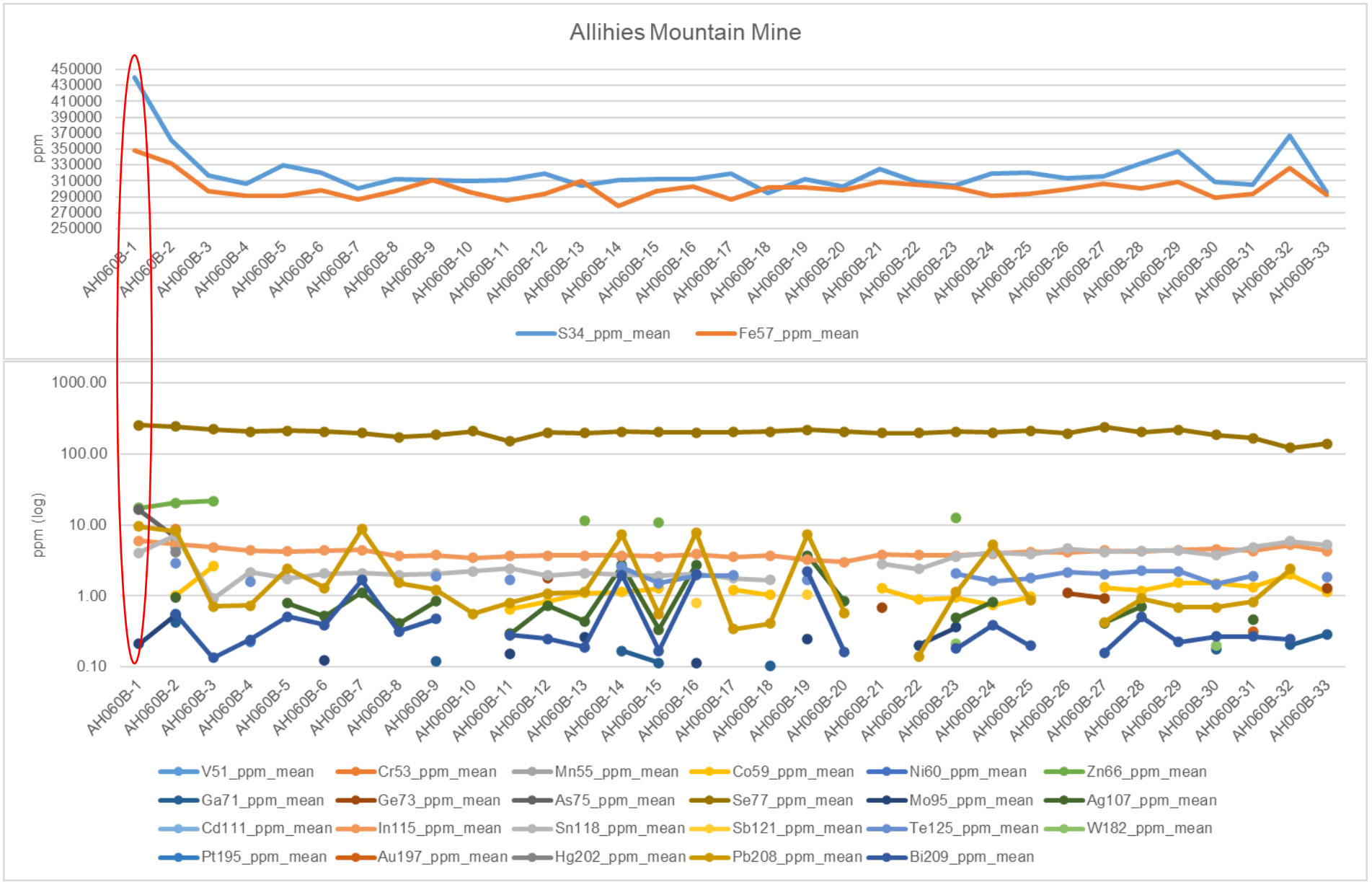
Mo inclusions

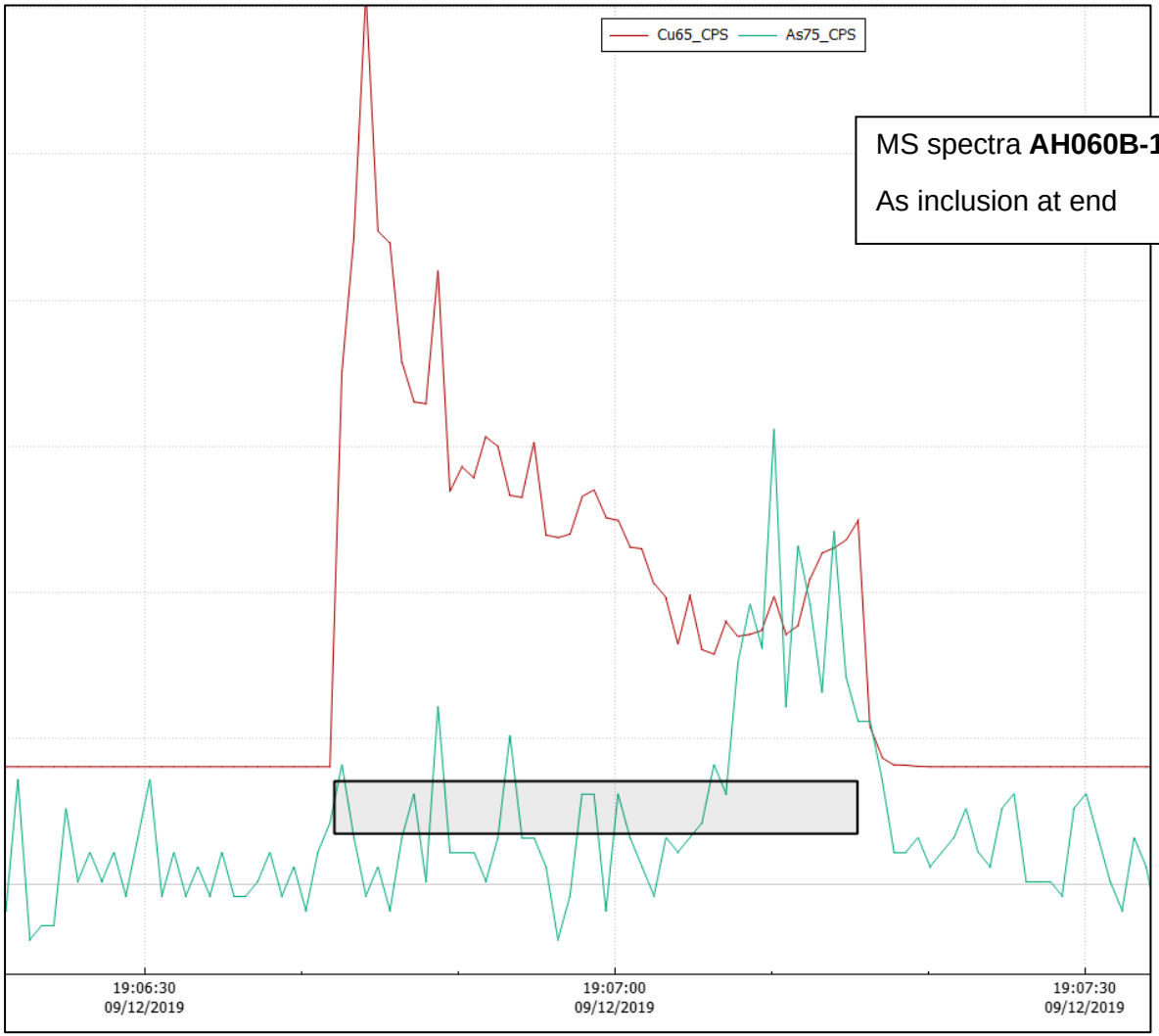




MS spectra
JL_AH_67_31:

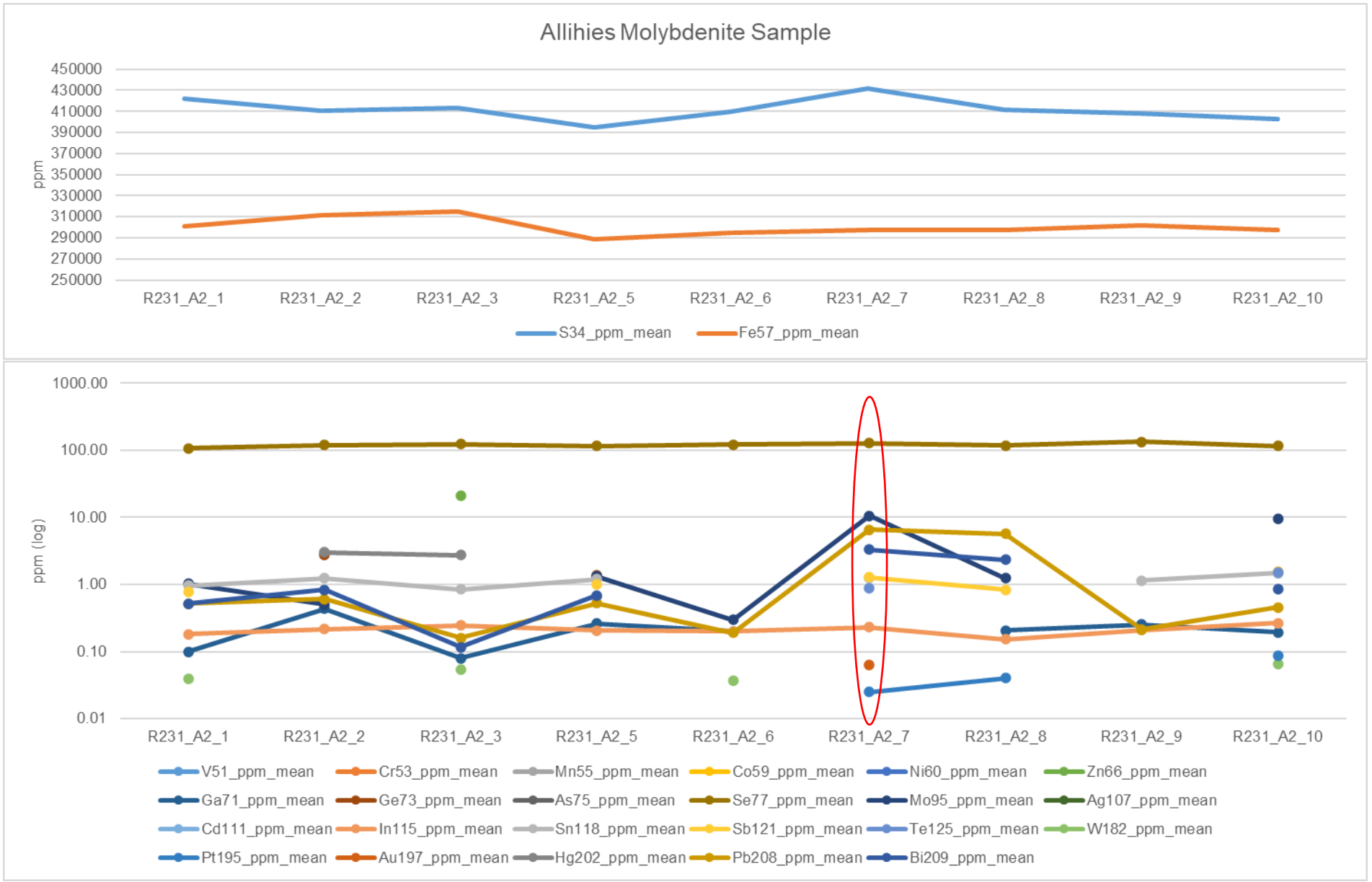
No In inclusions

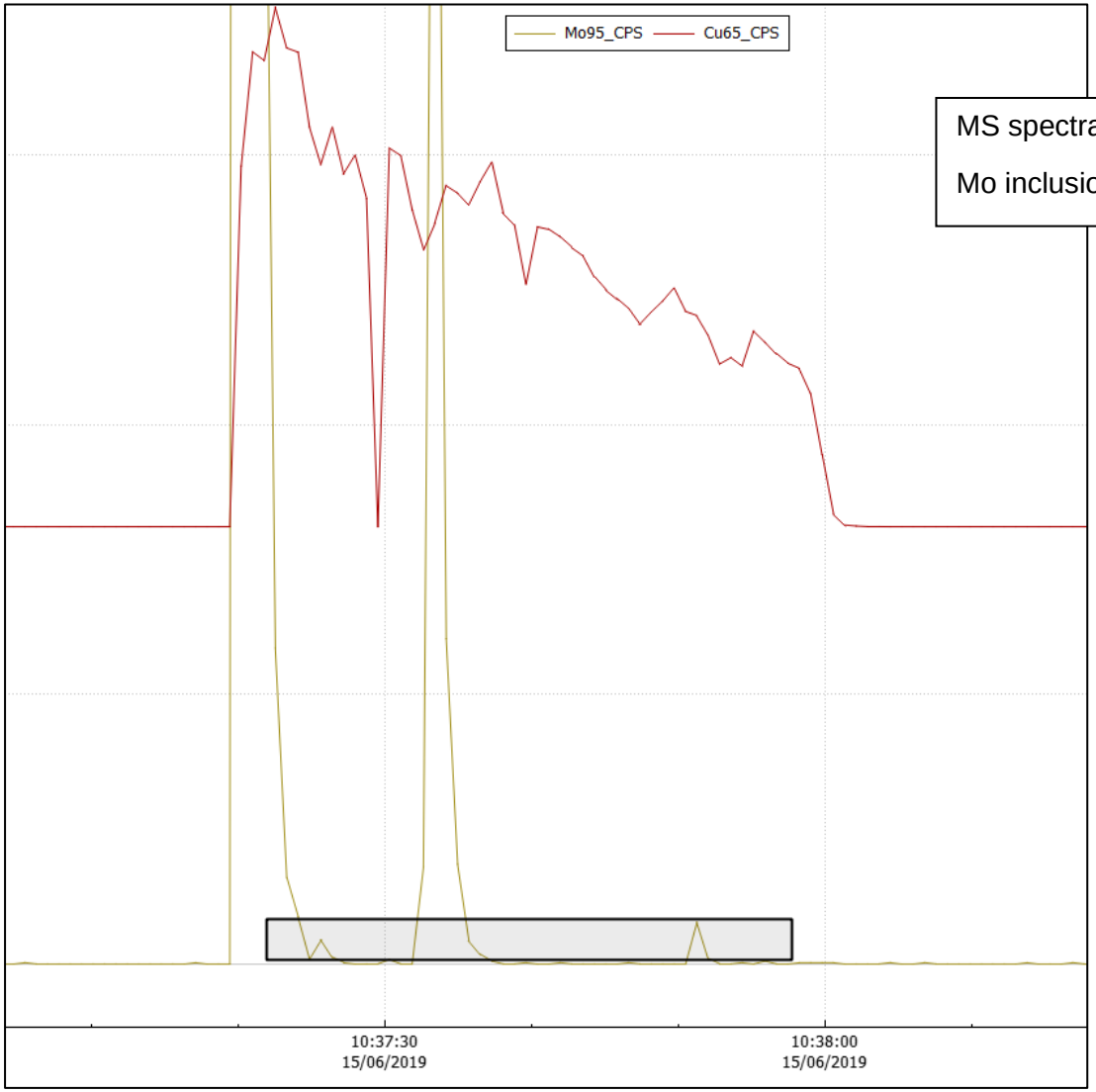

Allihies Mountain Mine
ppm
450000
430000
410000
390000
370000
350000
330000
310000
290000
270000
250000
AH060B-1
AH060B-2
AH060B-3
AH060B-4
AH060B-5
AH060B-6
AH060B-7
AH060B-8
AH060B-9
AH060B-10
AH060B-11
AH060B-12
AH060B-13
AH060B-14
AH060B-15
AH060B-16
AH060B-17
AH060B-18
AH060B-19
AH060B-20
AH060B-21
AH060B-22
AH060B-23
AH060B-24
AH060B-25
AH060B-26
AH060B-27
AH060B-28
AH060B-29
AH060B-30
AH060B-31
AH060B-32
AH060B-33
S34_ppm_mean
Fe57_ppm_mean
ppm (log)
1000.00
100.00
10.00
1.00
0.10
V51_ppm_mean
Cr53_ppm_mean
Mn55_ppm_mean
Co59_ppm_mean
Ni60_ppm_mean
Zn66_ppm_mean
Ga71_ppm_mean
Ge73_ppm_mean
As75_ppm_mean
Se77_ppm_mean
Mo95_ppm_mean
Ag107_ppm_mean
Cd111_ppm_mean
In115_ppm_mean
Sn118_ppm_mean
Sb121_ppm_mean
Te125_ppm_mean
W182_ppm_mean
Pt195_ppm_mean
Au197_ppm_mean
Hg202_ppm_mean
Pb208_ppm_mean
Bi209_ppm_mean



MS spectra **AH060B-1:**

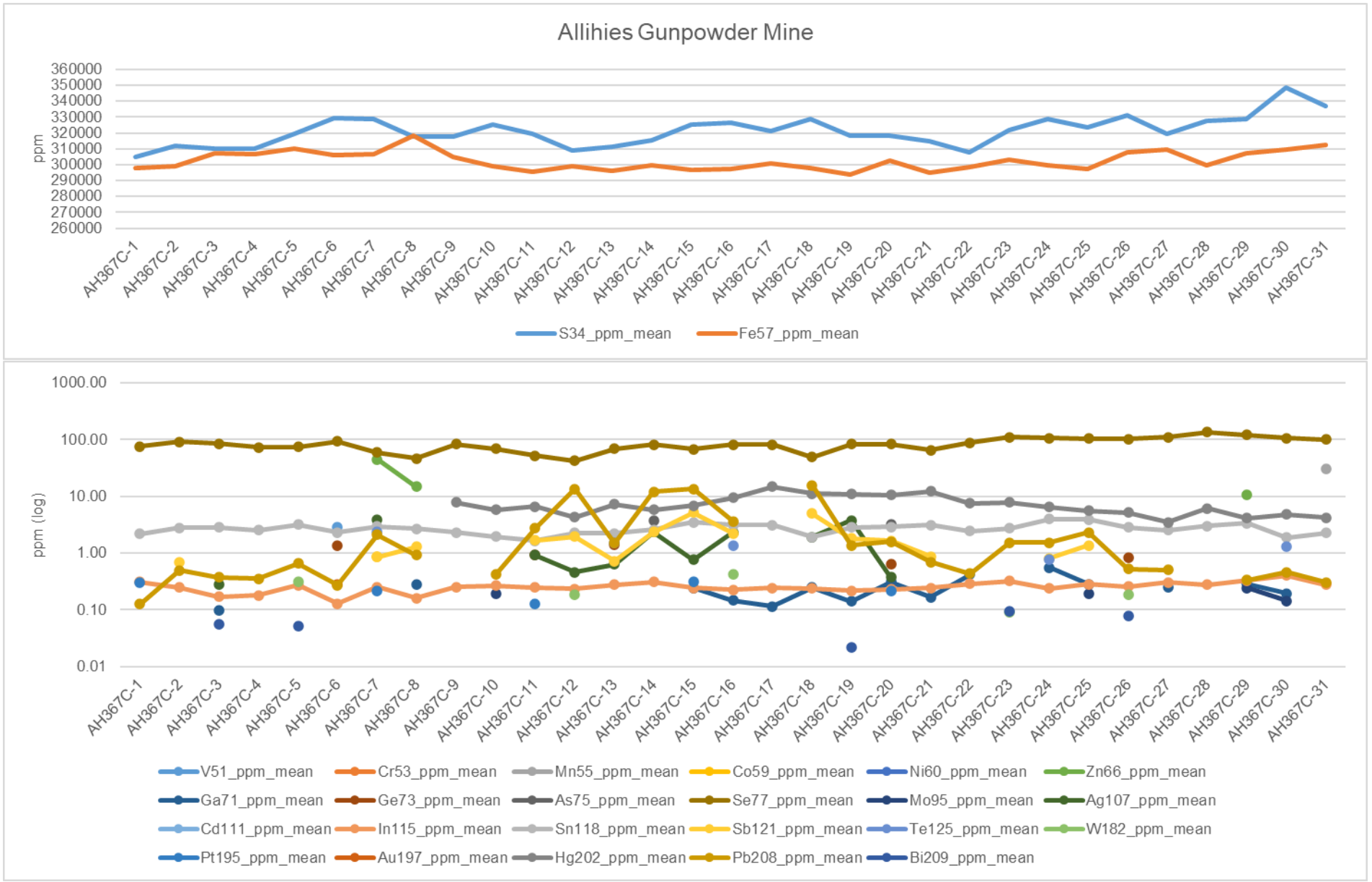
As inclusion at end

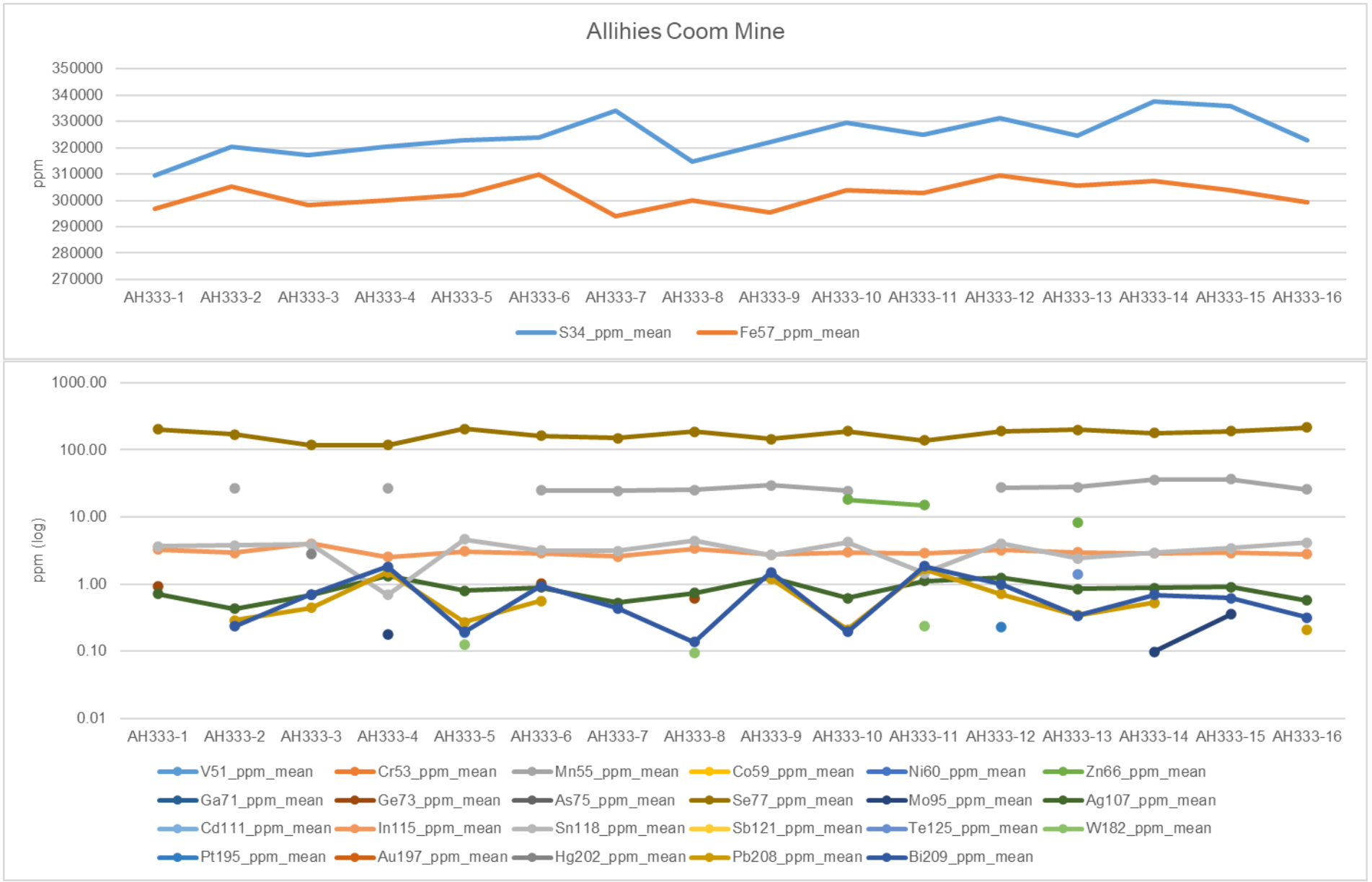

Allihies Molybdenite Sample
450000
430000
410000
390000
370000
350000
330000
310000
290000
270000
250000
ppm
R231_A2_1
R231_A2_2
R231_A2_3
R231_A2_5
R231_A2_6
R231_A2_7
R231_A2_8
R231_A2_9
R231_A2_10
S34_ppm_mean
Fe57_ppm_mean
1000.00
100.00
10.00
1.00
0.10
0.01
ppm (log)
R231_A2_1
R231_A2_2
R231_A2_3
R231_A2_5
R231_A2_6
R231_A2_7
R231_A2_8
R231_A2_9
R231_A2_10
V51_ppm_mean
Cr53_ppm_mean
Mn55_ppm_mean
Co59_ppm_mean
Ni60_ppm_mean
Zn66_ppm_mean
Ga71_ppm_mean
Ge73_ppm_mean
As75_ppm_mean
Se77_ppm_mean
Mo95_ppm_mean
Ag107_ppm_mean
Cd111_ppm_mean
In115_ppm_mean
Sn118_ppm_mean
Sb121_ppm_mean
Te125_ppm_mean
W182_ppm_mean
Pt195_ppm_mean
Au197_ppm_mean
Hg202_ppm_mean
Pb208_ppm_mean
Bi209_ppm_mean

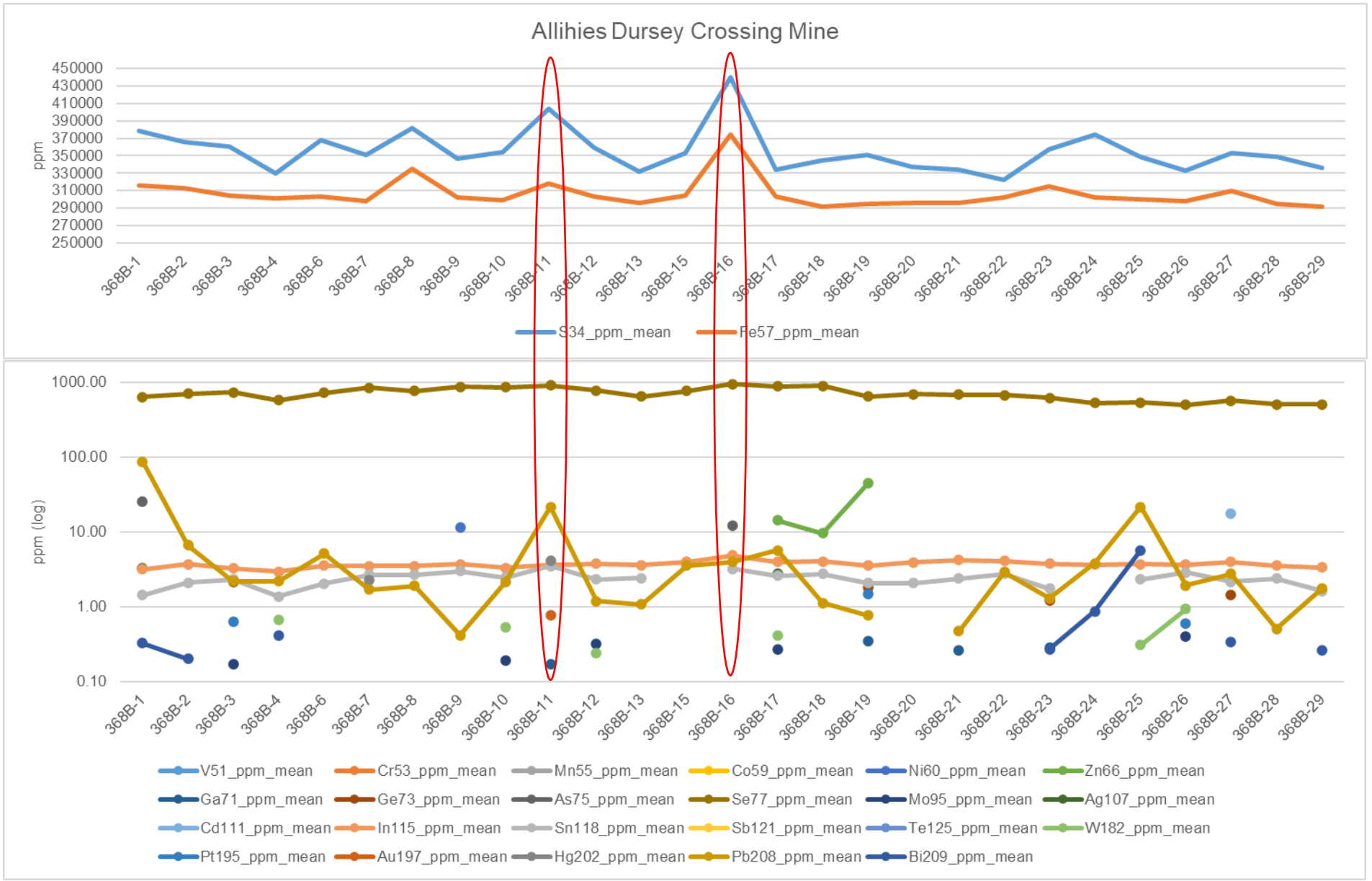


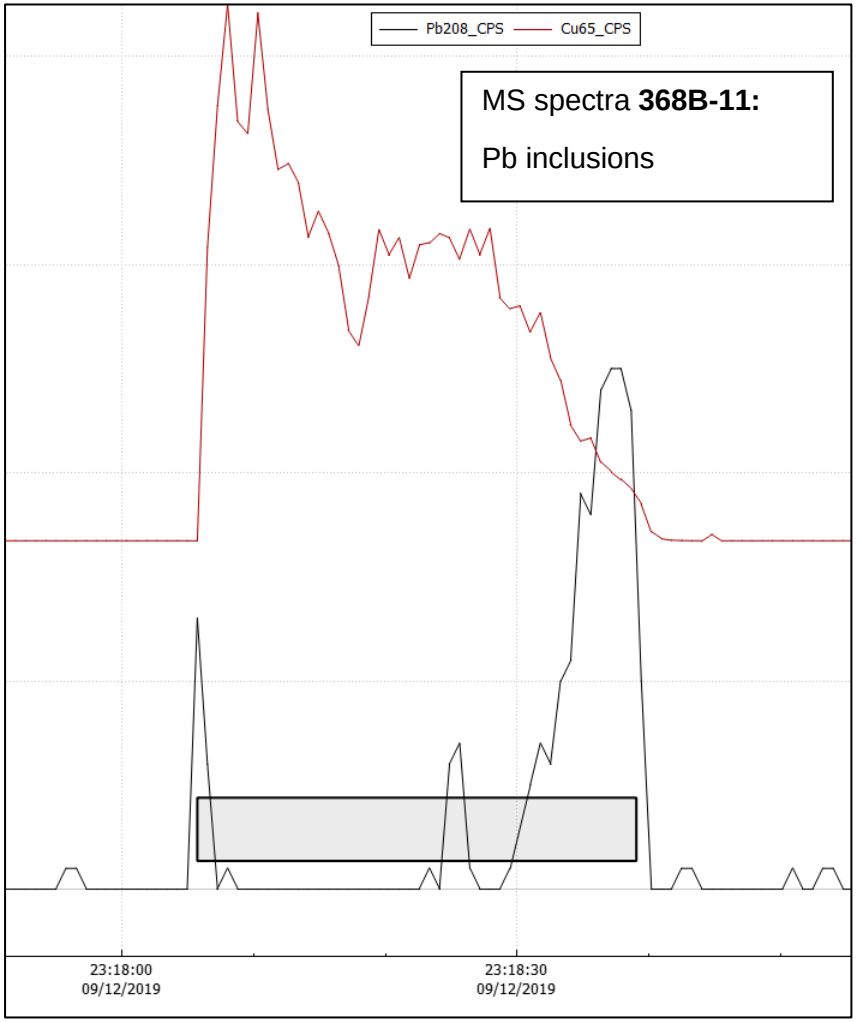
MS spectra **R231_A2_7:**

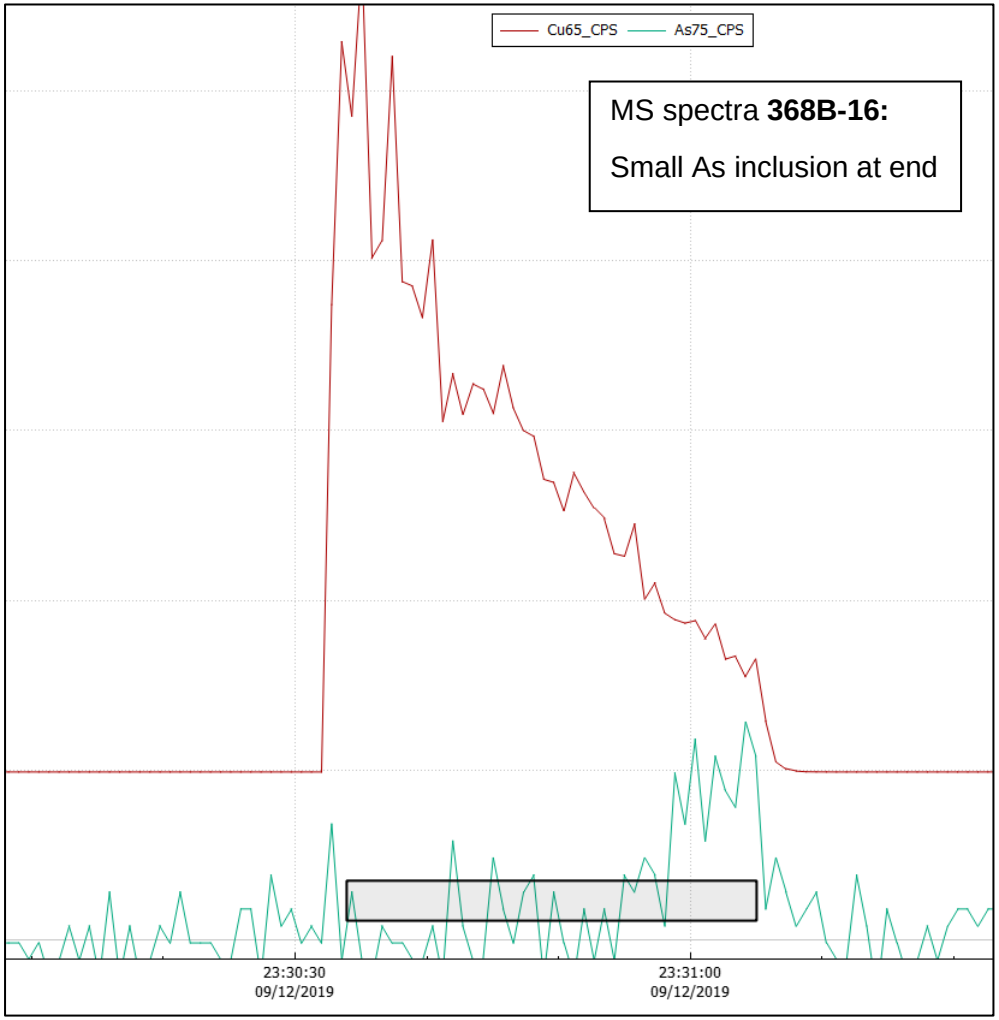
Mo inclusions

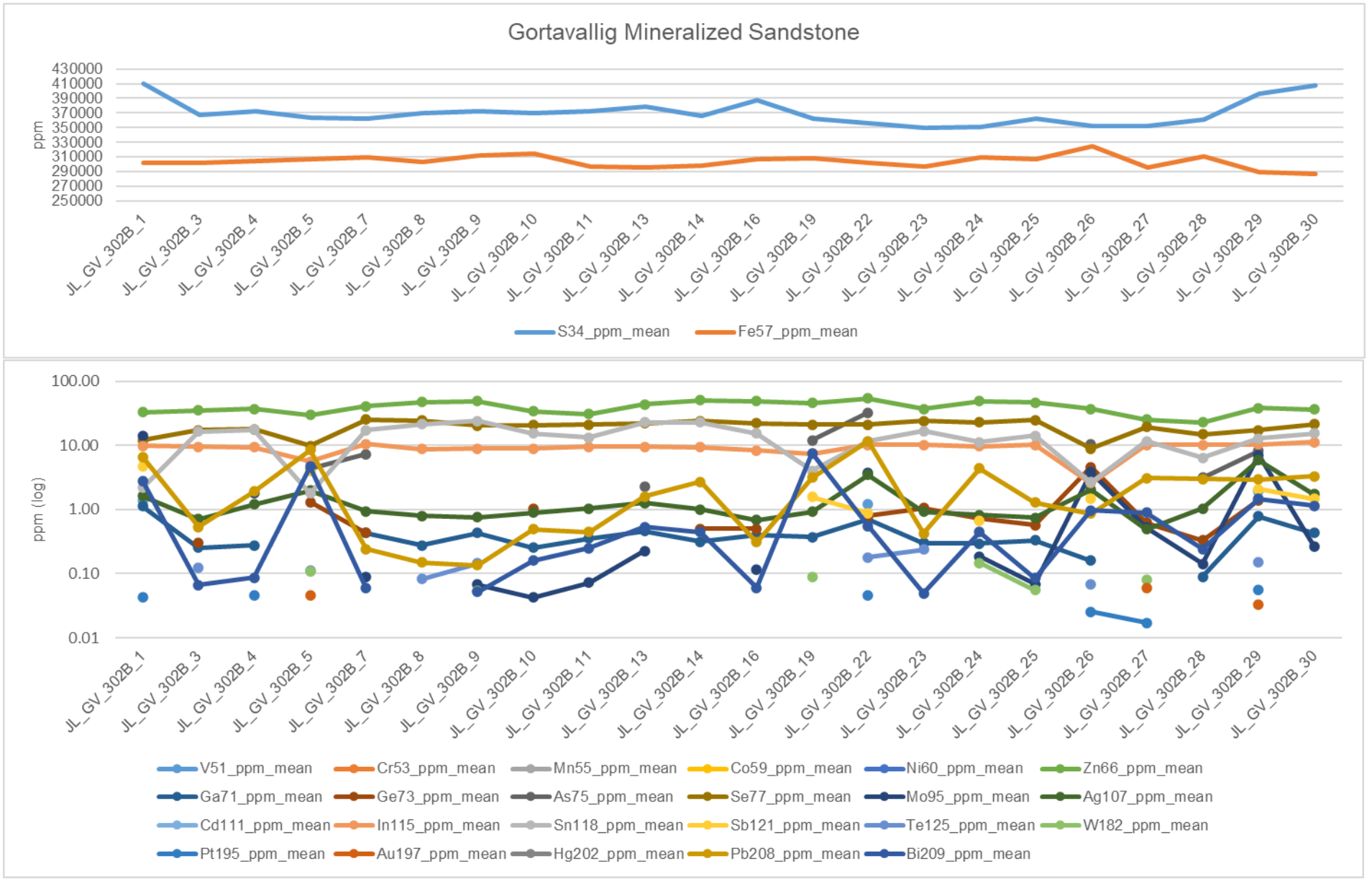

Allihies Gunpowder Mine
ppm
360000
350000
340000
330000
320000
310000
300000
290000
280000
270000
260000
AH367C-1
AH367C-2
AH367C-3
AH367C-4
AH367C-5
AH367C-6
AH367C-7
AH367C-8
AH367C-9
AH367C-10
AH367C-11
AH367C-12
AH367C-13
AH367C-14
AH367C-15
AH367C-16
AH367C-17
AH367C-18
AH367C-19
AH367C-20
AH367C-21
AH367C-22
AH367C-23
AH367C-24
AH367C-25
AH367C-26
AH367C-27
AH367C-28
AH367C-29
AH367C-30
AH367C-31
S34_ppm_mean
Fe57_ppm_mean
ppm (log)
1000.00
100.00
10.00
1.00
0.10
0.01
V51_ppm_mean
Cr53_ppm_mean
Mn55_ppm_mean
Co59_ppm_mean
Ni60_ppm_mean
Zn66_ppm_mean
Ga71_ppm_mean
Ge73_ppm_mean
As75_ppm_mean
Se77_ppm_mean
Mo95_ppm_mean
Ag107_ppm_mean
Cd111_ppm_mean
In115_ppm_mean
Sn118_ppm_mean
Sb121_ppm_mean
Te125_ppm_mean
W182_ppm_mean
Pt195_ppm_mean
Au197_ppm_mean
Hg202_ppm_mean
Pb208_ppm_mean
Bi209_ppm_mean

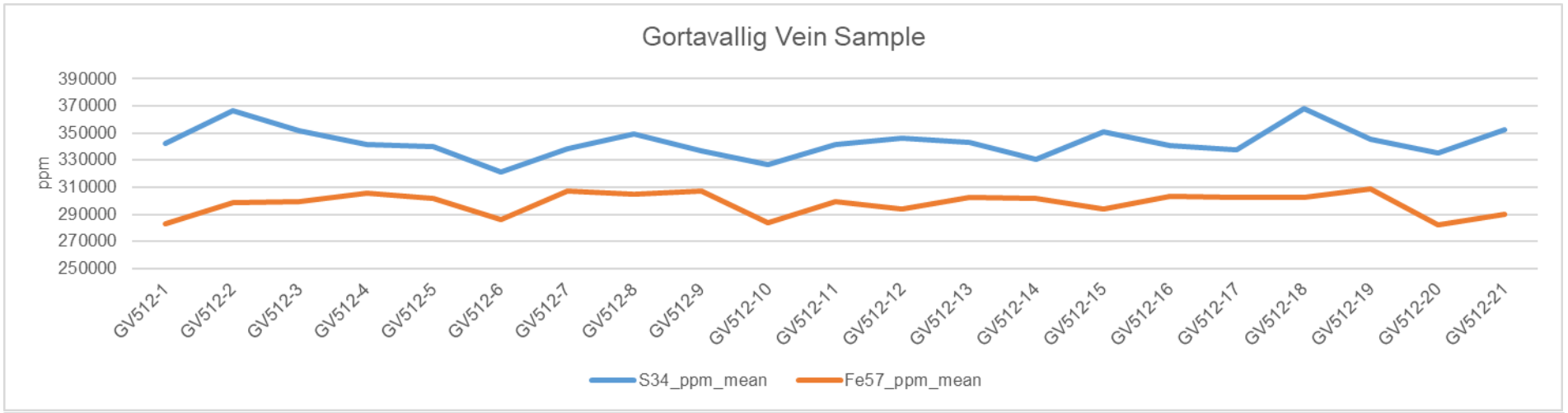

Allihies Coom Mine
ppm
350000
340000
330000
320000
310000
300000
290000
280000
270000
AH333-1 AH333-2 AH333-3 AH333-4 AH333-5 AH333-6 AH333-7 AH333-8 AH333-9 AH333-10 AH333-11 AH333-12 AH333-13 AH333-14 AH333-15 AH333-16
S34_ppm_mean
Fe57_ppm_mean
ppm (log)
1000.00
100.00
10.00
1.00
0.10
0.01
AH333-1 AH333-2 AH333-3 AH333-4 AH333-5 AH333-6 AH333-7 AH333-8 AH333-9 AH333-10 AH333-11 AH333-12 AH333-13 AH333-14 AH333-15 AH333-16
V51_ppm_mean
Cr53_ppm_mean
Mn55_ppm_mean
Co59_ppm_mean
Ni60_ppm_mean
Zn66_ppm_mean
Ga71_ppm_mean
Ge73_ppm_mean
As75_ppm_mean
Se77_ppm_mean
Mo95_ppm_mean
Ag107_ppm_mean
Cd111_ppm_mean
In115_ppm_mean
Sn118_ppm_mean
Sb121_ppm_mean
Te125_ppm_mean
W182_ppm_mean
Pt195_ppm_mean
Au197_ppm_mean
Hg202_ppm_mean
Pb208_ppm_mean
Bi209_ppm_mean

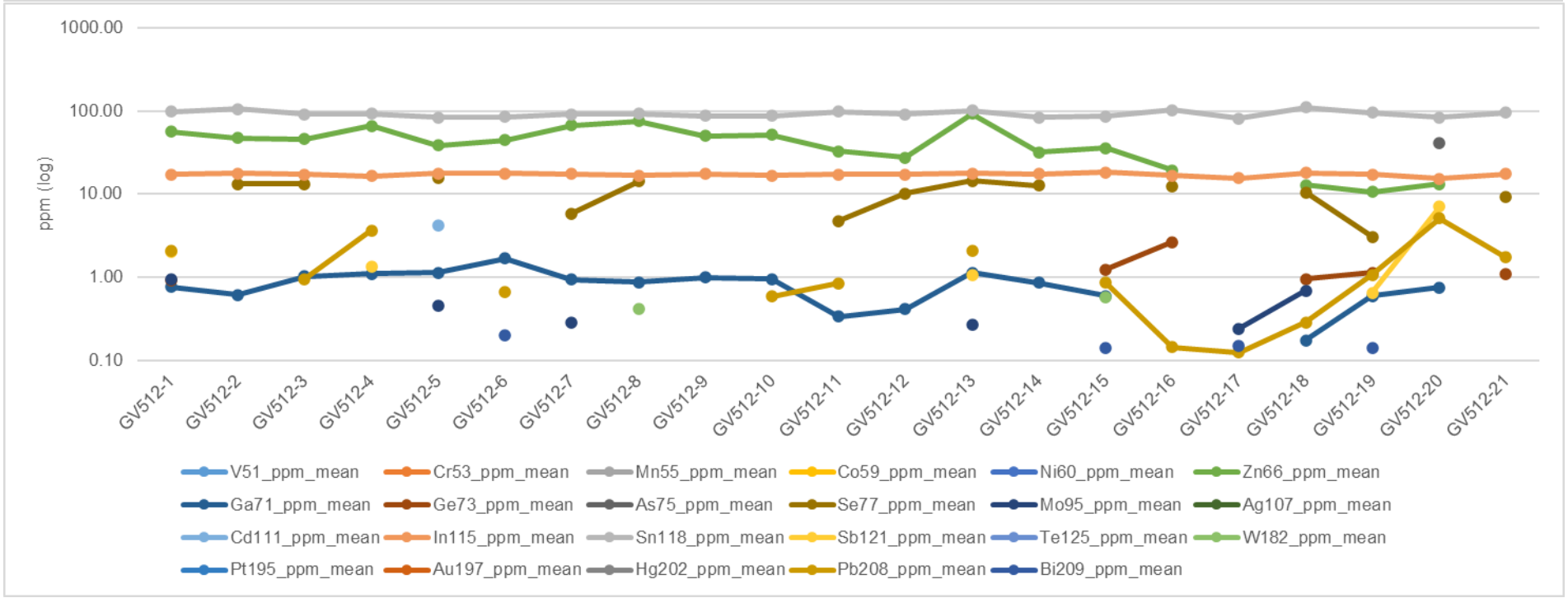

Allihies Dursey Crossing Mine
ppm
450000
430000
410000
390000
370000
350000
330000
310000
290000
270000
250000
368B-1
368B-2
368B-3
368B-4
368B-6
368B-7
368B-8
368B-9
368B-10
368B-11
368B-12
368B-13
368B-15
368B-16
368B-17
368B-18
368B-19
368B-20
368B-21
368B-22
368B-23
368B-24
368B-25
368B-26
368B-27
368B-28
368B-29
S34_ppm_mean
Fe57_ppm_mean
ppm (log)
1000.00
100.00
10.00
1.00
0.10
V51_ppm_mean
Cr53_ppm_mean
Mn55_ppm_mean
Co59_ppm_mean
Ni60_ppm_mean
Zn66_ppm_mean
Ga71_ppm_mean
Ge73_ppm_mean
As75_ppm_mean
Se77_ppm_mean
Mo95_ppm_mean
Ag107_ppm_mean
Cd111_ppm_mean
In115_ppm_mean
Sn118_ppm_mean
Sb121_ppm_mean
Te125_ppm_mean
W182_ppm_mean
Pt195_ppm_mean
Au197_ppm_mean
Hg202_ppm_mean
Pb208_ppm_mean
Bi209_ppm_mean

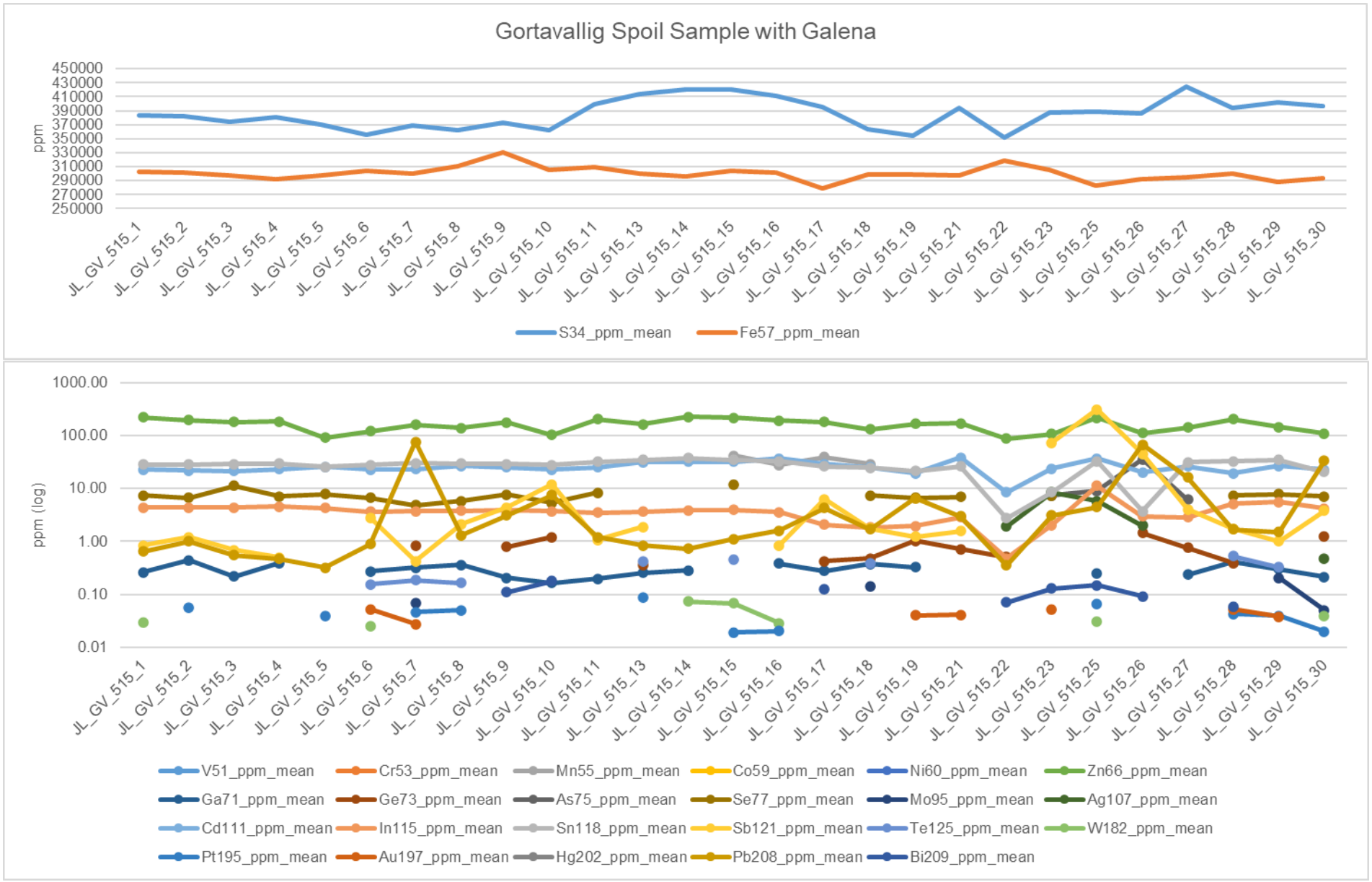

Pb208_CPS
Cu65_CPS
MS spectra **368B-11:**
Pb inclusions
23:18:00
09/12/2019
23:18:30
09/12/2019

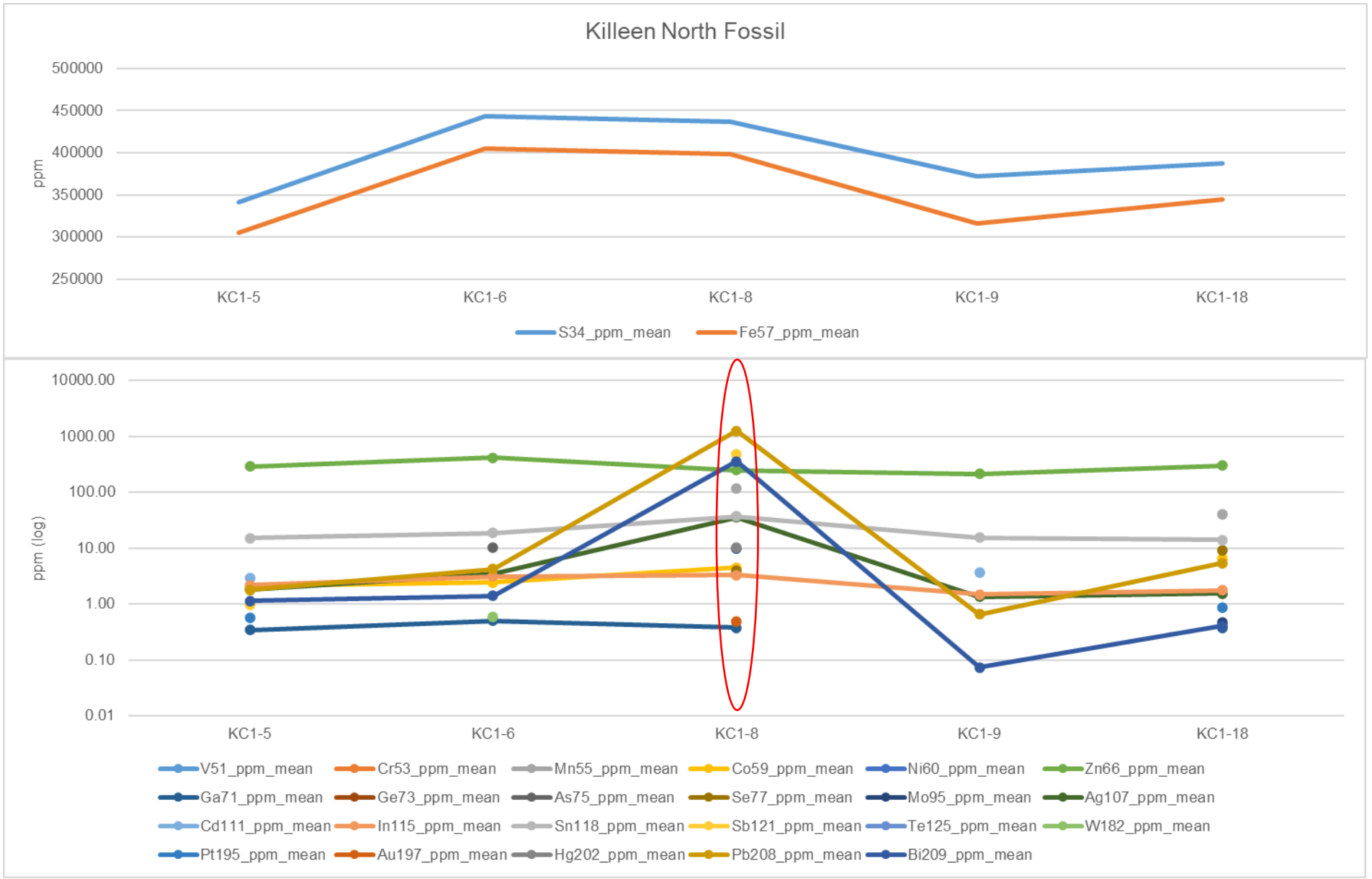

Cu65_CPS
As75_CPS
MS spectra **368B-16:**
Small As inclusion at end
23:30:30
09/12/2019
23:31:00
09/12/2019

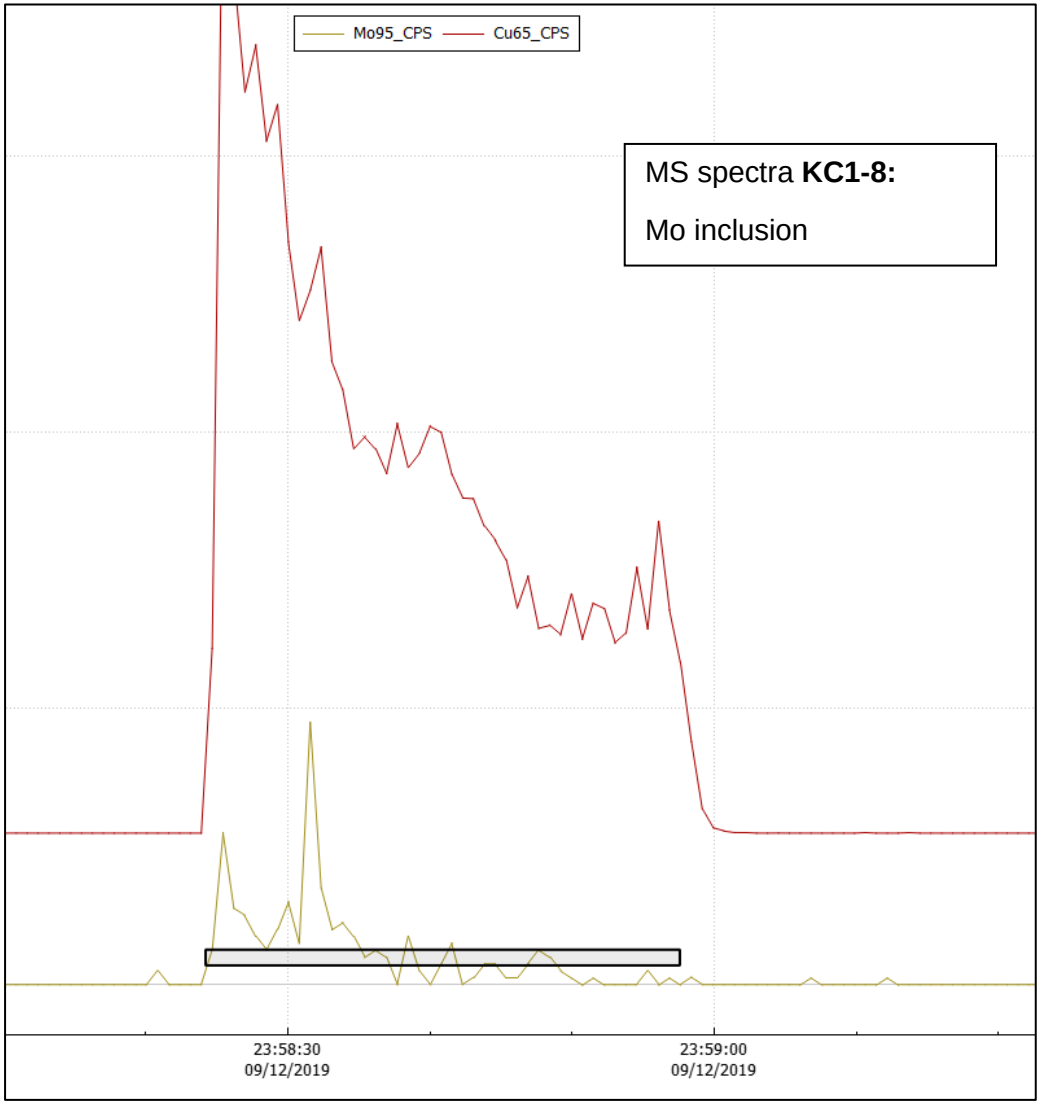

Gortavallig Mineralized Sandstone
ppm
430000
410000
390000
370000
350000
330000
310000
290000
270000
250000
JL_GV_302B_1
JL_GV_302B_3
JL_GV_302B_4
JL_GV_302B_5
JL_GV_302B_7
JL_GV_302B_8
JL_GV_302B_9
JL_GV_302B_10
JL_GV_302B_11
JL_GV_302B_13
JL_GV_302B_14
JL_GV_302B_16
JL_GV_302B_19
JL_GV_302B_22
JL_GV_302B_23
JL_GV_302B_24
JL_GV_302B_25
JL_GV_302B_26
JL_GV_302B_27
JL_GV_302B_28
JL_GV_302B_29
JL_GV_302B_30
S34_ppm_mean
Fe57_ppm_mean
ppm (log)
100.00
10.00
1.00
0.10
0.01
V51_ppm_mean
Cr53_ppm_mean
Mn55_ppm_mean
Co59_ppm_mean
Ni60_ppm_mean
Zn66_ppm_mean
Ga71_ppm_mean
Ge73_ppm_mean
As75_ppm_mean
Se77_ppm_mean
Mo95_ppm_mean
Ag107_ppm_mean
Cd111_ppm_mean
In115_ppm_mean
Sn118_ppm_mean
Sb121_ppm_mean
Te125_ppm_mean
W182_ppm_mean
Pt195_ppm_mean
Au197_ppm_mean
Hg202_ppm_mean
Pb208_ppm_mean
Bi209_ppm_mean

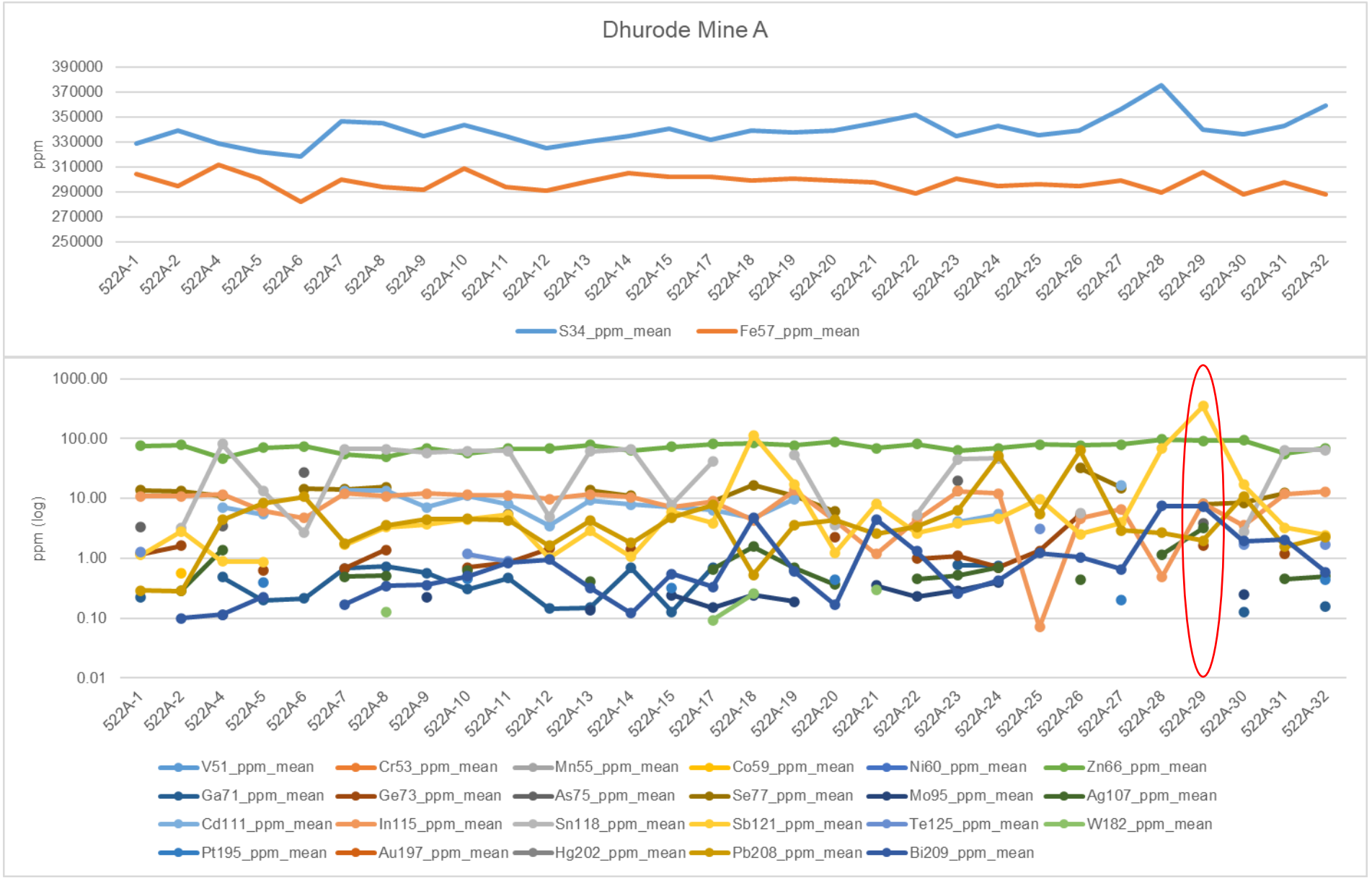

Gortavallig Vein Sample
390000
370000
350000
330000
310000
290000
270000
250000
ppm
GV512-1
GV512-2
GV512-3
GV512-4
GV512-5
GV512-6
GV512-7
GV512-8
GV512-9
GV512-10
GV512-11
GV512-12
GV512-13
GV512-14
GV512-15
GV512-16
GV512-17
GV512-18
GV512-19
GV512-20
GV512-21
S34_ppm_mean
Fe57_ppm_mean

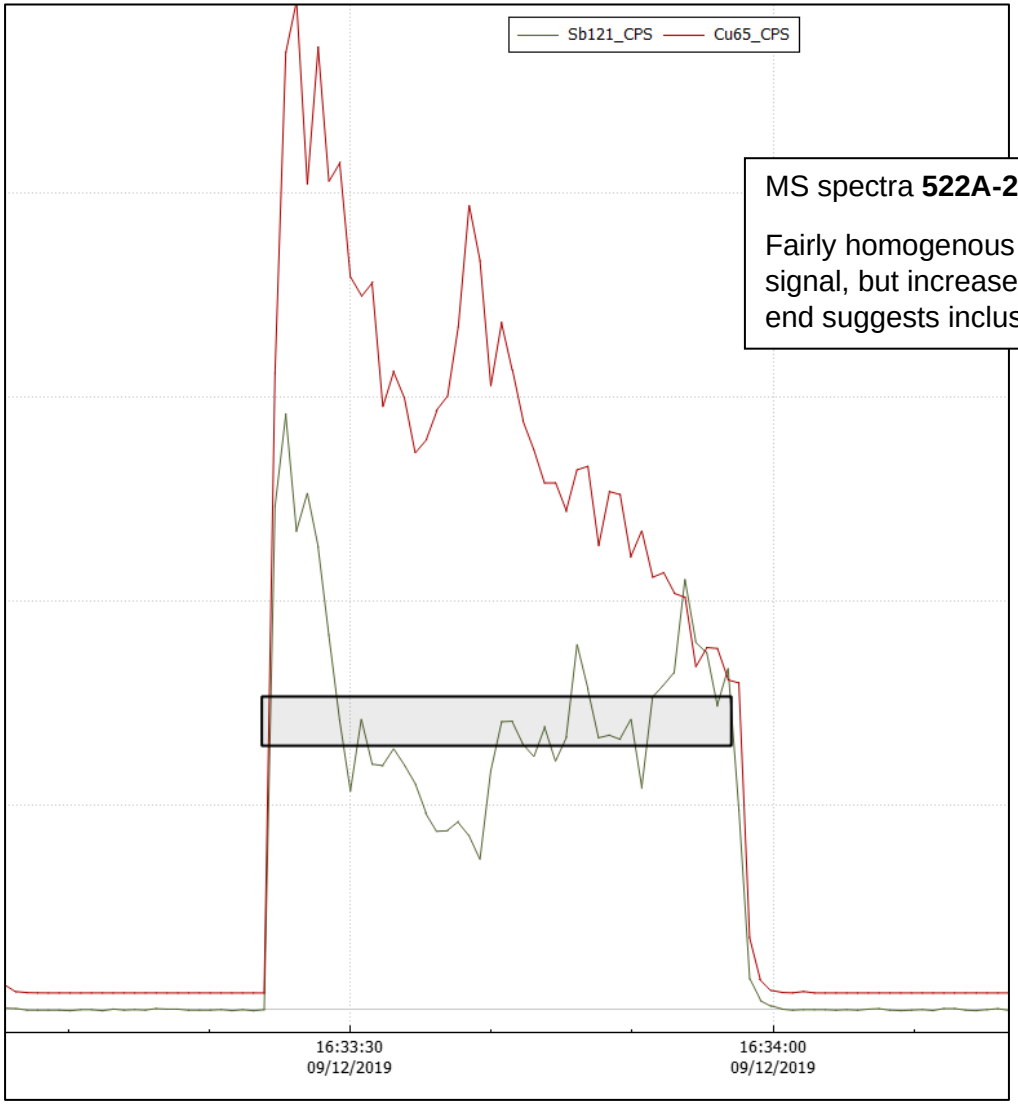

1000.00
100.00
10.00
1.00
0.10
ppm (log)
GV512-1
GV512-2
GV512-3
GV512-4
GV512-5
GV512-6
GV512-7
GV512-8
GV512-9
GV512-10
GV512-11
GV512-12
GV512-13
GV512-14
GV512-15
GV512-16
GV512-17
GV512-18
GV512-19
GV512-20
GV512-21
V51_ppm_mean
Cr53_ppm_mean
Mn55_ppm_mean
Co59_ppm_mean
Ni60_ppm_mean
Zn66_ppm_mean
Ga71_ppm_mean
Ge73_ppm_mean
As75_ppm_mean
Se77_ppm_mean
Mo95_ppm_mean
Ag107_ppm_mean
Cd111_ppm_mean
In115_ppm_mean
Sn118_ppm_mean
Sb121_ppm_mean
Te125_ppm_mean
W182_ppm_mean
Pt195_ppm_mean
Au197_ppm_mean
Hg202_ppm_mean
Pb208_ppm_mean
Bi209_ppm_mean


Gortavallig Spoil Sample with Galena
ppm
450000
430000
410000
390000
370000
350000
330000
310000
290000
270000
250000
JL_GV_515_1
JL_GV_515_2
JL_GV_515_3
JL_GV_515_4
JL_GV_515_5
JL_GV_515_6
JL_GV_515_7
JL_GV_515_8
JL_GV_515_9
JL_GV_515_10
JL_GV_515_11
JL_GV_515_13
JL_GV_515_14
JL_GV_515_15
JL_GV_515_16
JL_GV_515_17
JL_GV_515_18
JL_GV_515_19
JL_GV_515_21
JL_GV_515_22
JL_GV_515_23
JL_GV_515_25
JL_GV_515_26
JL_GV_515_27
JL_GV_515_28
JL_GV_515_29
JL_GV_515_30
S34_ppm_mean
Fe57_ppm_mean
ppm (log)
1000.00
100.00
10.00
1.00
0.10
0.01
V51_ppm_mean
Cr53_ppm_mean
Mn55_ppm_mean
Co59_ppm_mean
Ni60_ppm_mean
Zn66_ppm_mean
Ga71_ppm_mean
Ge73_ppm_mean
As75_ppm_mean
Se77_ppm_mean
Mo95_ppm_mean
Ag107_ppm_mean
Cd111_ppm_mean
In115_ppm_mean
Sn118_ppm_mean
Sb121_ppm_mean
Te125_ppm_mean
W182_ppm_mean
Pt195_ppm_mean
Au197_ppm_mean
Hg202_ppm_mean
Pb208_ppm_mean
Bi209_ppm_mean


Killeen North Fossil
500000
450000
400000
350000
300000
250000
ppm
KC1-5
KC1-6
KC1-8
KC1-9
KC1-18
S34_ppm_mean
Fe57_ppm_mean
10000.00
1000.00
100.00
10.00
1.00
0.10
0.01
ppm (log)
KC1-5
KC1-6
KC1-8
KC1-9
KC1-18
V51_ppm_mean
Cr53_ppm_mean
Mn55_ppm_mean
Co59_ppm_mean
Ni60_ppm_mean
Zn66_ppm_mean
Ga71_ppm_mean
Ge73_ppm_mean
As75_ppm_mean
Se77_ppm_mean
Mo95_ppm_mean
Ag107_ppm_mean
Cd111_ppm_mean
In115_ppm_mean
Sn118_ppm_mean
Sb121_ppm_mean
Te125_ppm_mean
W182_ppm_mean
Pt195_ppm_mean
Au197_ppm_mean
Hg202_ppm_mean
Pb208_ppm_mean
Bi209_ppm_mean

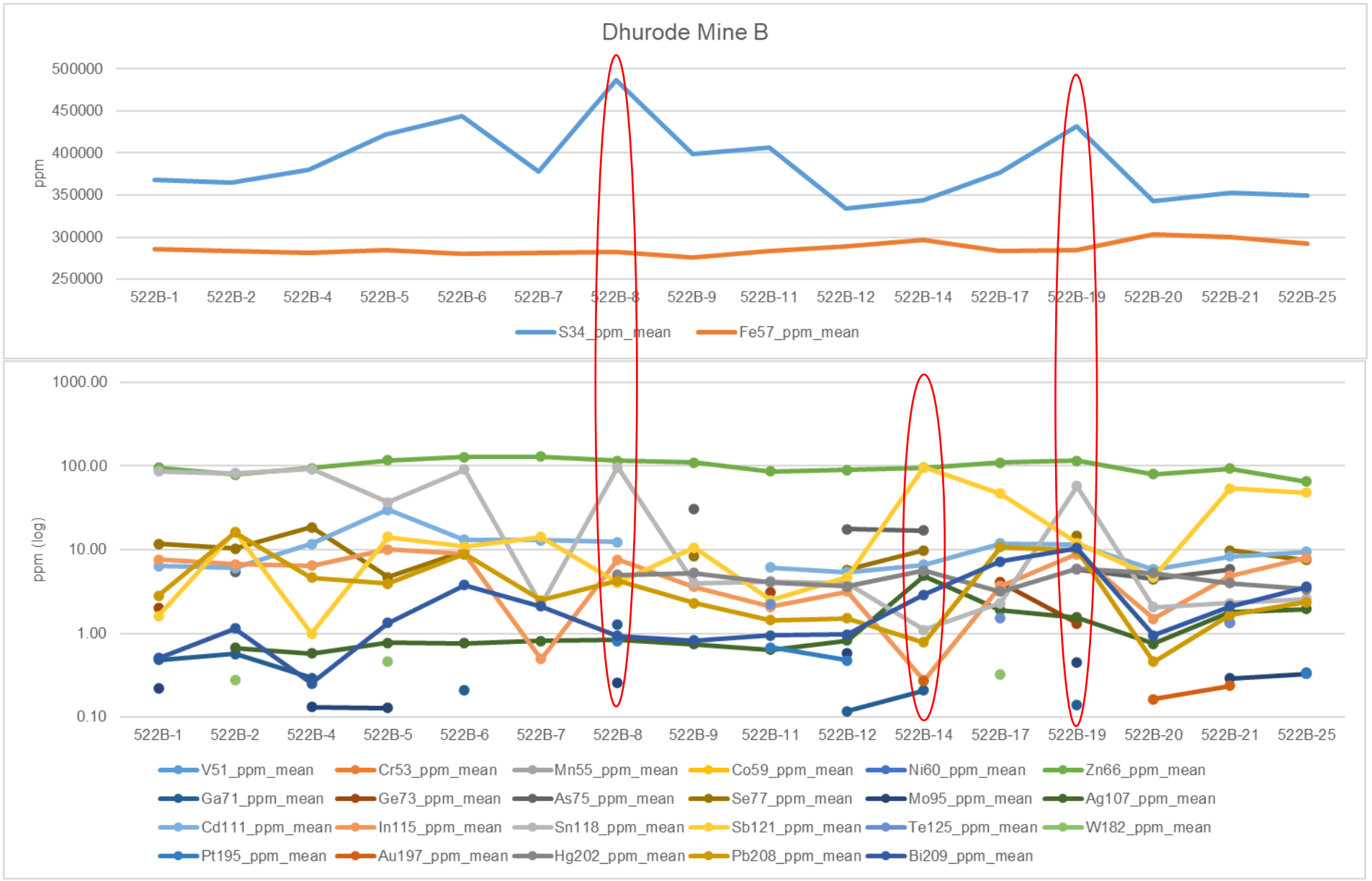

Mo95_CPS
Cu65_CPS
MS spectra **KC1-8:**
Mo inclusion
23:58:30
09/12/2019
23:59:00
09/12/2019

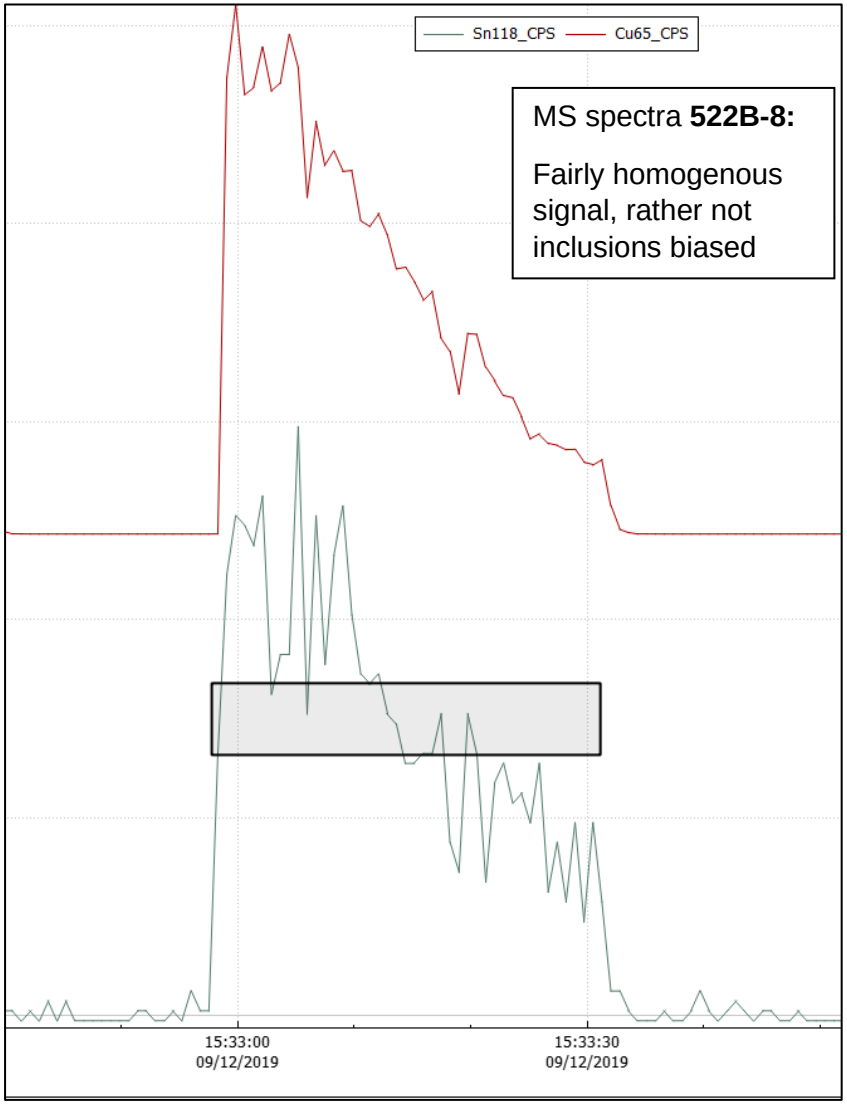

Dhurode Mine A
ppm
390000
370000
350000
330000
310000
290000
270000
250000
522A-1
522A-2
522A-4
522A-5
522A-6
522A-7
522A-8
522A-9
522A-10
522A-11
522A-12
522A-13
522A-14
522A-15
522A-17
522A-18
522A-19
522A-20
522A-21
522A-22
522A-23
522A-24
522A-25
522A-26
522A-27
522A-28
522A-29
522A-30
522A-31
522A-32
S34_ppm_mean
Fe57_ppm_mean
ppm (log)
1000.00
100.00
10.00
1.00
0.10
0.01
V51_ppm_mean
Cr53_ppm_mean
Mn55_ppm_mean
Co59_ppm_mean
Ni60_ppm_mean
Zn66_ppm_mean
Ga71_ppm_mean
Ge73_ppm_mean
As75_ppm_mean
Se77_ppm_mean
Mo95_ppm_mean
Ag107_ppm_mean
Cd111_ppm_mean
In115_ppm_mean
Sn118_ppm_mean
Sb121_ppm_mean
Te125_ppm_mean
W182_ppm_mean
Pt195_ppm_mean
Au197_ppm_mean
Hg202_ppm_mean
Pb208_ppm_mean
Bi209_ppm_mean

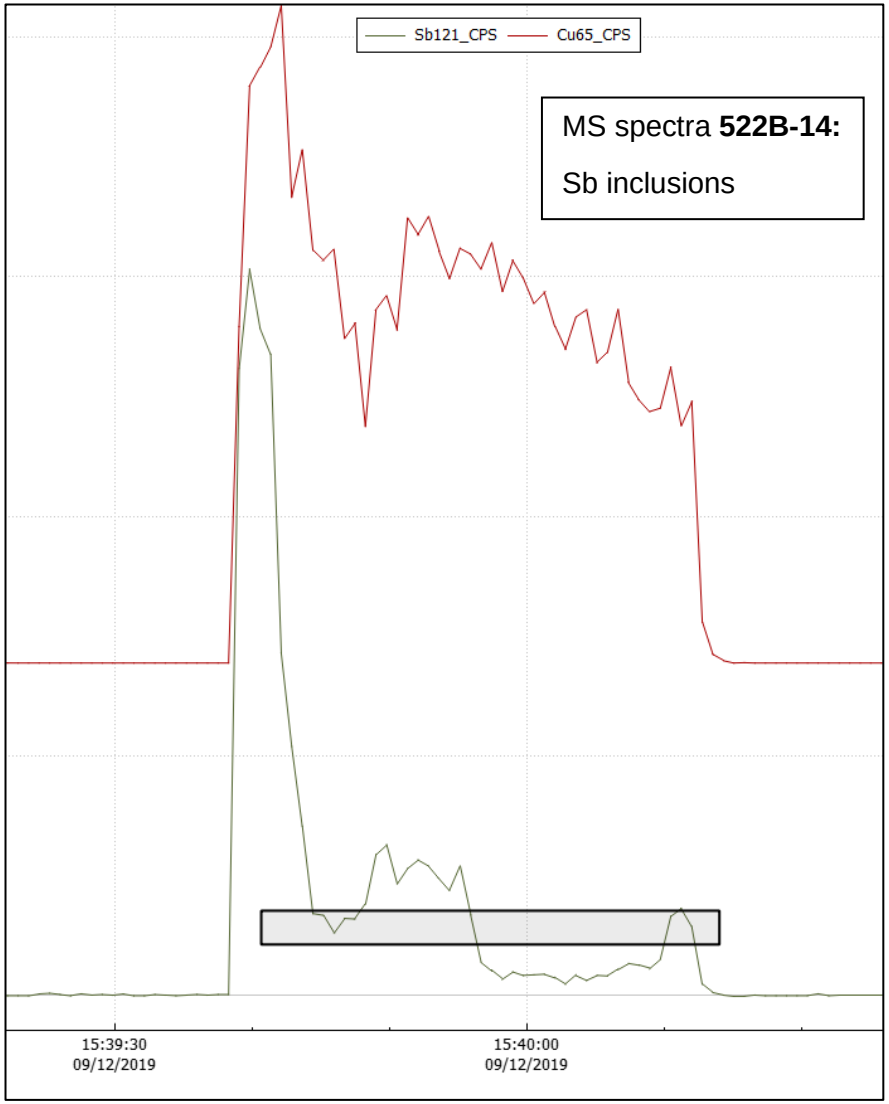


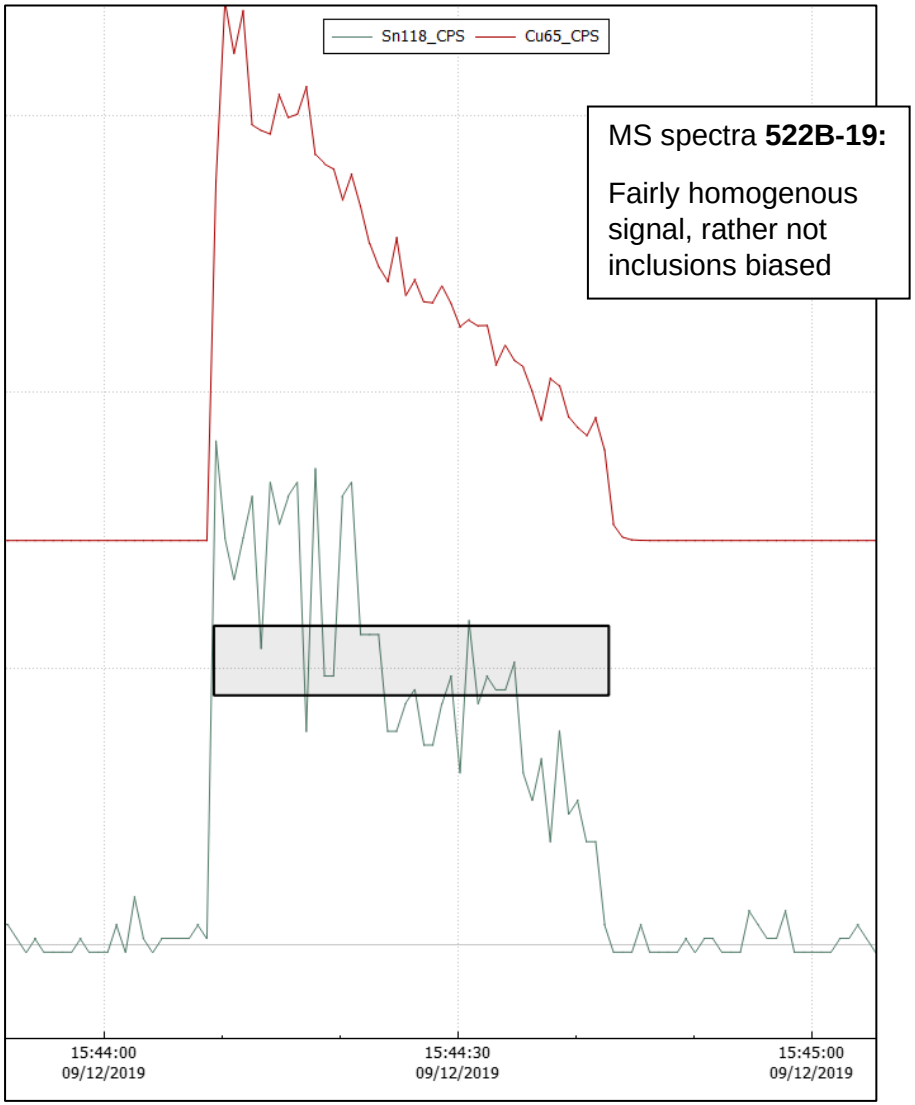
MS spectra **522A-29:**

Fairly homogenous signal, but increase at end suggests inclusions


Dhurode Mine B
ppm
500000
450000
400000
350000
300000
250000
522B-1
522B-2
522B-4
522B-5
522B-6
522B-7
522B-8
522B-9
522B-11
522B-12
522B-14
522B-17
522B-19
522B-20
522B-21
522B-25
S34_ppm_mean
Fe57_ppm_mean
ppm (log)
1000.00
100.00
10.00
1.00
0.10
V51_ppm_mean
Cr53_ppm_mean
Mn55_ppm_mean
Co59_ppm_mean
Ni60_ppm_mean
Zn66_ppm_mean
Ga71_ppm_mean
Ge73_ppm_mean
As75_ppm_mean
Se77_ppm_mean
Mo95_ppm_mean
Ag107_ppm_mean
Cd111_ppm_mean
In115_ppm_mean
Sn118_ppm_mean
Sb121_ppm_mean
Te125_ppm_mean
W182_ppm_mean
Pt195_ppm_mean
Au197_ppm_mean
Hg202_ppm_mean
Pb208_ppm_mean
Bi209_ppm_mean

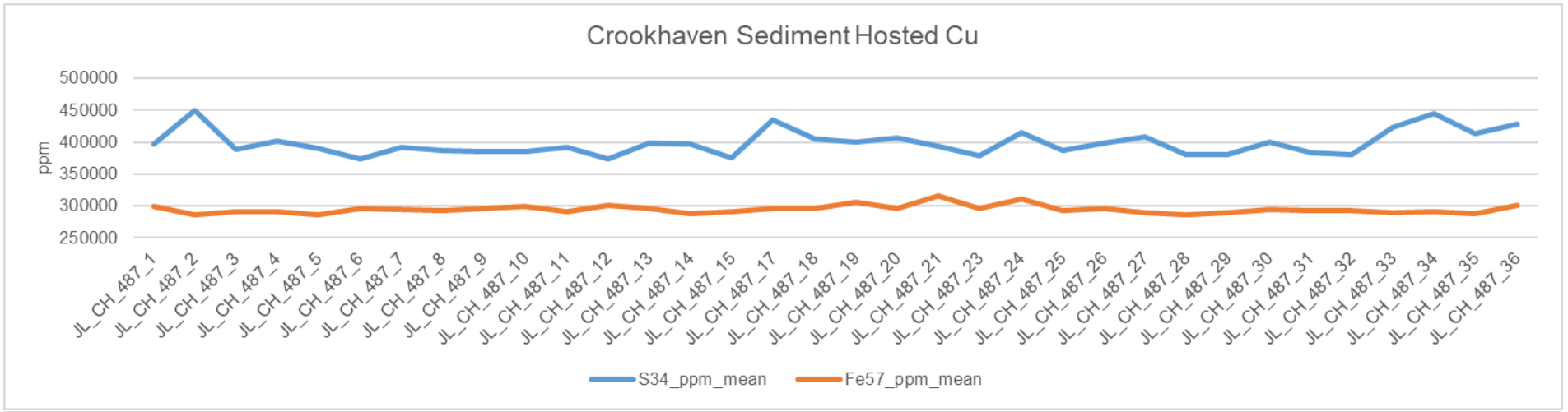

Sn118_CPS
Cu65_CPS
MS spectra **522B-8:**
Fairly homogenous signal, rather not inclusions biased
15:33:00
09/12/2019
15:33:30
09/12/2019

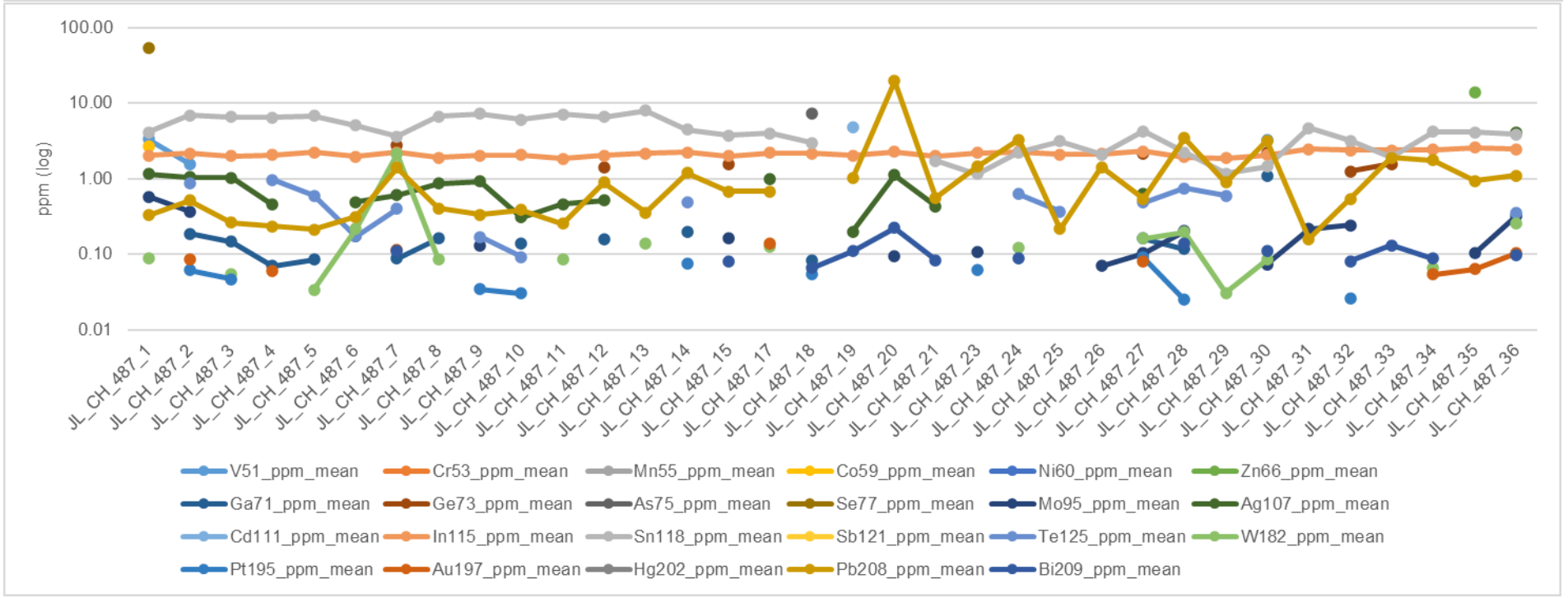

Sb121_CPS
Cu65_CPS
MS spectra **522B-14:**
Sb inclusions
15:39:30
09/12/2019
15:40:00
09/12/2019

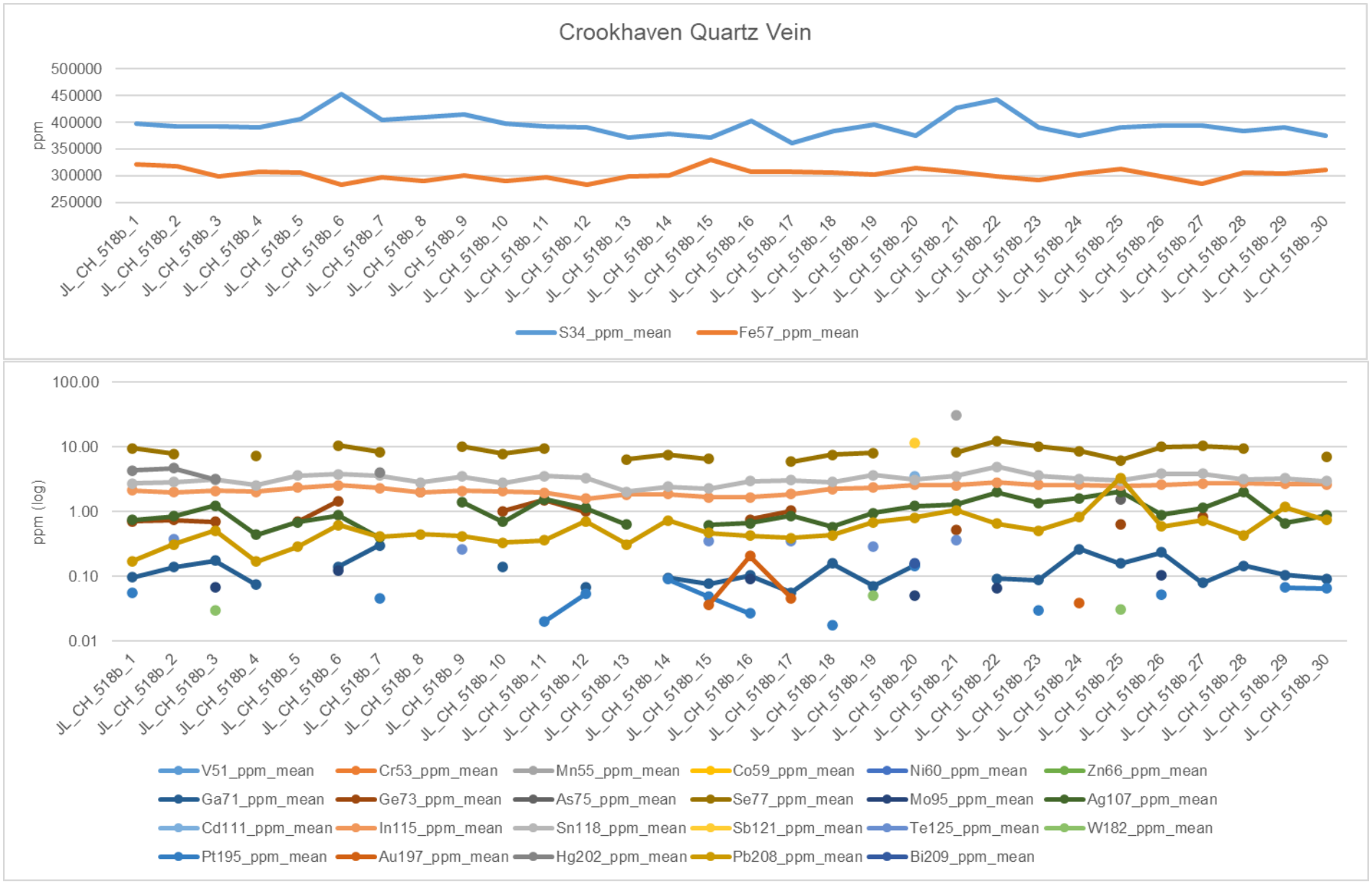


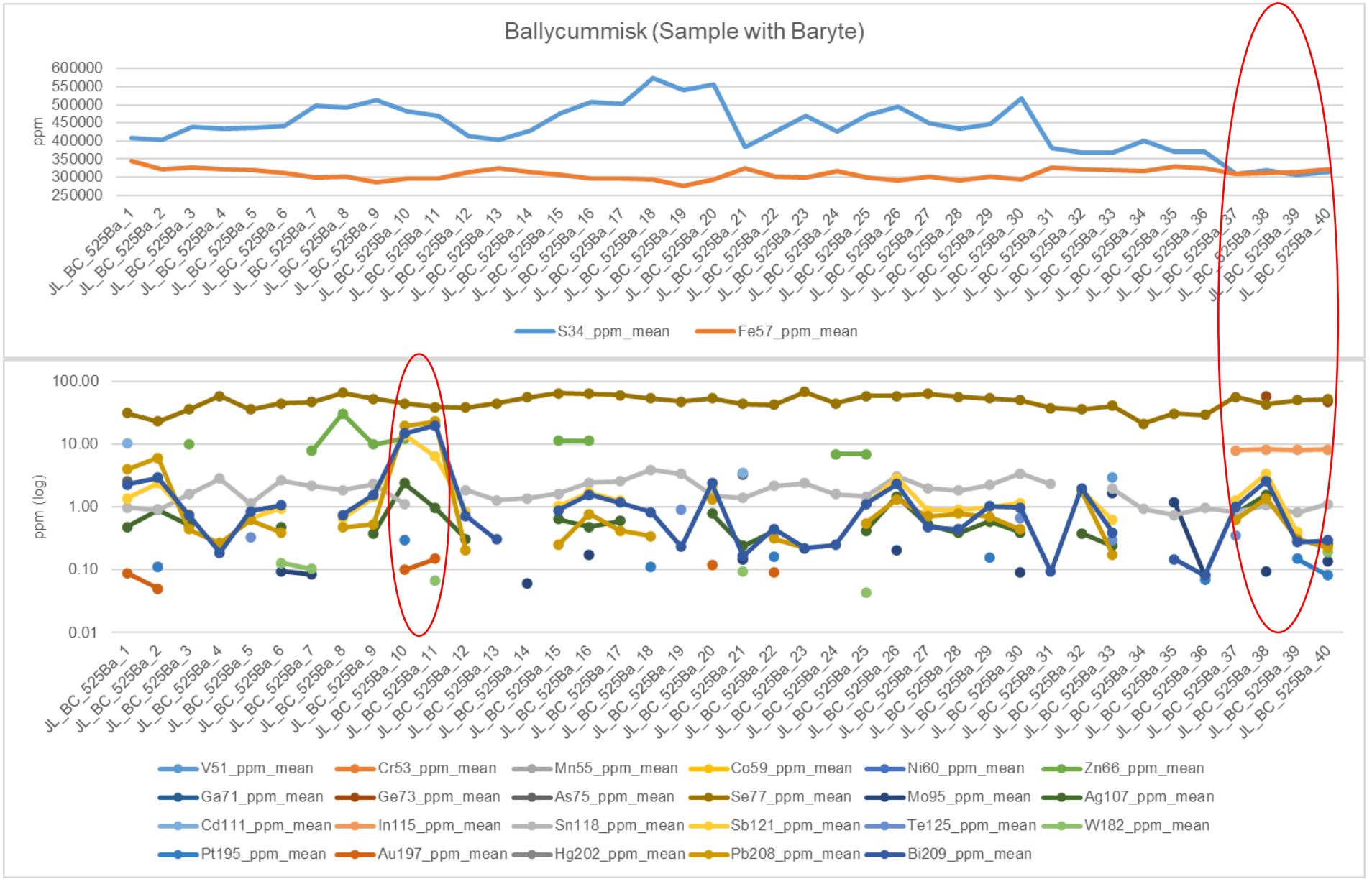
MS spectra **522B-19:**

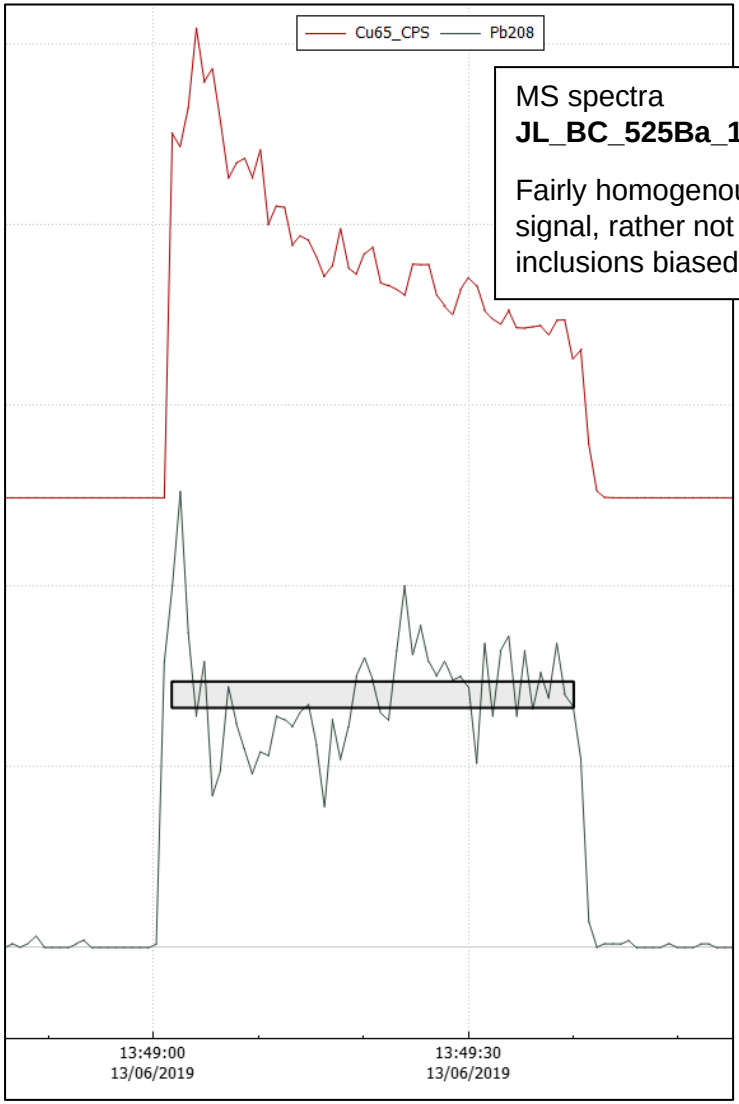
Fairly homogenous signal, rather not inclusions biased


Crookhaven Sediment Hosted Cu
ppm
500000
450000
400000
350000
300000
250000
JL_CH_487_1
JL_CH_487_2
JL_CH_487_3
JL_CH_487_4
JL_CH_487_5
JL_CH_487_6
JL_CH_487_7
JL_CH_487_8
JL_CH_487_9
JL_CH_487_10
JL_CH_487_11
JL_CH_487_12
JL_CH_487_13
JL_CH_487_14
JL_CH_487_15
JL_CH_487_17
JL_CH_487_18
JL_CH_487_19
JL_CH_487_20
JL_CH_487_21
JL_CH_487_23
JL_CH_487_24
JL_CH_487_25
JL_CH_487_26
JL_CH_487_27
JL_CH_487_28
JL_CH_487_29
JL_CH_487_30
JL_CH_487_31
JL_CH_487_32
JL_CH_487_33
JL_CH_487_34
JL_CH_487_35
JL_CH_487_36
S34_ppm_mean
Fe57_ppm_mean


ppm (log)
100.00
10.00
1.00
0.10
0.01
JL_CH_487_1
JL_CH_487_2
JL_CH_487_3
JL_CH_487_4
JL_CH_487_5
JL_CH_487_6
JL_CH_487_7
JL_CH_487_8
JL_CH_487_9
JL_CH_487_10
JL_CH_487_11
JL_CH_487_12
JL_CH_487_13
JL_CH_487_14
JL_CH_487_15
JL_CH_487_17
JL_CH_487_18
JL_CH_487_19
JL_CH_487_20
JL_CH_487_21
JL_CH_487_23
JL_CH_487_24
JL_CH_487_25
JL_CH_487_26
JL_CH_487_27
JL_CH_487_28
JL_CH_487_29
JL_CH_487_30
JL_CH_487_31
JL_CH_487_32
JL_CH_487_33
JL_CH_487_34
JL_CH_487_35
JL_CH_487_36
V51_ppm_mean
Cr53_ppm_mean
Mn55_ppm_mean
Co59_ppm_mean
Ni60_ppm_mean
Zn66_ppm_mean
Ga71_ppm_mean
Ge73_ppm_mean
As75_ppm_mean
Se77_ppm_mean
Mo95_ppm_mean
Ag107_ppm_mean
Cd111_ppm_mean
In115_ppm_mean
Sn118_ppm_mean
Sb121_ppm_mean
Te125_ppm_mean
W182_ppm_mean
Pt195_ppm_mean
Au197_ppm_mean
Hg202_ppm_mean
Pb208_ppm_mean
Bi209_ppm_mean


Crookhaven Quartz Vein
ppm
500000
450000
400000
350000
300000
250000
JL_CH_518b_1
JL_CH_518b_2
JL_CH_518b_3
JL_CH_518b_4
JL_CH_518b_5
JL_CH_518b_6
JL_CH_518b_7
JL_CH_518b_8
JL_CH_518b_9
JL_CH_518b_10
JL_CH_518b_11
JL_CH_518b_12
JL_CH_518b_13
JL_CH_518b_14
JL_CH_518b_15
JL_CH_518b_16
JL_CH_518b_17
JL_CH_518b_18
JL_CH_518b_19
JL_CH_518b_20
JL_CH_518b_21
JL_CH_518b_22
JL_CH_518b_23
JL_CH_518b_24
JL_CH_518b_25
JL_CH_518b_26
JL_CH_518b_27
JL_CH_518b_28
JL_CH_518b_29
JL_CH_518b_30
S34_ppm_mean
Fe57_ppm_mean
ppm (log)
100.00
10.00
1.00
0.10
0.01
V51_ppm_mean
Cr53_ppm_mean
Mn55_ppm_mean
Co59_ppm_mean
Ni60_ppm_mean
Zn66_ppm_mean
Ga71_ppm_mean
Ge73_ppm_mean
As75_ppm_mean
Se77_ppm_mean
Mo95_ppm_mean
Ag107_ppm_mean
Cd111_ppm_mean
In115_ppm_mean
Sn118_ppm_mean
Sb121_ppm_mean
Te125_ppm_mean
W182_ppm_mean
Pt195_ppm_mean
Au197_ppm_mean
Hg202_ppm_mean
Pb208_ppm_mean
Bi209_ppm_mean


Ballycummisk (Sample with Baryte)
ppm
600000
550000
500000
450000
400000
350000
300000
250000
JL_BC_525Ba_1
JL_BC_525Ba_2
JL_BC_525Ba_3
JL_BC_525Ba_4
JL_BC_525Ba_5
JL_BC_525Ba_6
JL_BC_525Ba_7
JL_BC_525Ba_8
JL_BC_525Ba_9
JL_BC_525Ba_10
JL_BC_525Ba_11
JL_BC_525Ba_12
JL_BC_525Ba_13
JL_BC_525Ba_14
JL_BC_525Ba_15
JL_BC_525Ba_16
JL_BC_525Ba_17
JL_BC_525Ba_18
JL_BC_525Ba_19
JL_BC_525Ba_20
JL_BC_525Ba_21
JL_BC_525Ba_22
JL_BC_525Ba_23
JL_BC_525Ba_24
JL_BC_525Ba_25
JL_BC_525Ba_26
JL_BC_525Ba_27
JL_BC_525Ba_28
JL_BC_525Ba_29
JL_BC_525Ba_30
JL_BC_525Ba_31
JL_BC_525Ba_32
JL_BC_525Ba_33
JL_BC_525Ba_34
JL_BC_525Ba_35
JL_BC_525Ba_36
JL_BC_525Ba_37
JL_BC_525Ba_38
JL_BC_525Ba_39
JL_BC_525Ba_40
S34_ppm_mean
Fe57_ppm_mean
ppm (log)
100.00
10.00
1.00
0.10
0.01
V51_ppm_mean
Cr53_ppm_mean
Mn55_ppm_mean
Co59_ppm_mean
Ni60_ppm_mean
Zn66_ppm_mean
Ga71_ppm_mean
Ge73_ppm_mean
As75_ppm_mean
Se77_ppm_mean
Mo95_ppm_mean
Ag107_ppm_mean
Cd111_ppm_mean
In115_ppm_mean
Sn118_ppm_mean
Sb121_ppm_mean
Te125_ppm_mean
W182_ppm_mean
Pt195_ppm_mean
Au197_ppm_mean
Hg202_ppm_mean
Pb208_ppm_mean
Bi209_ppm_mean

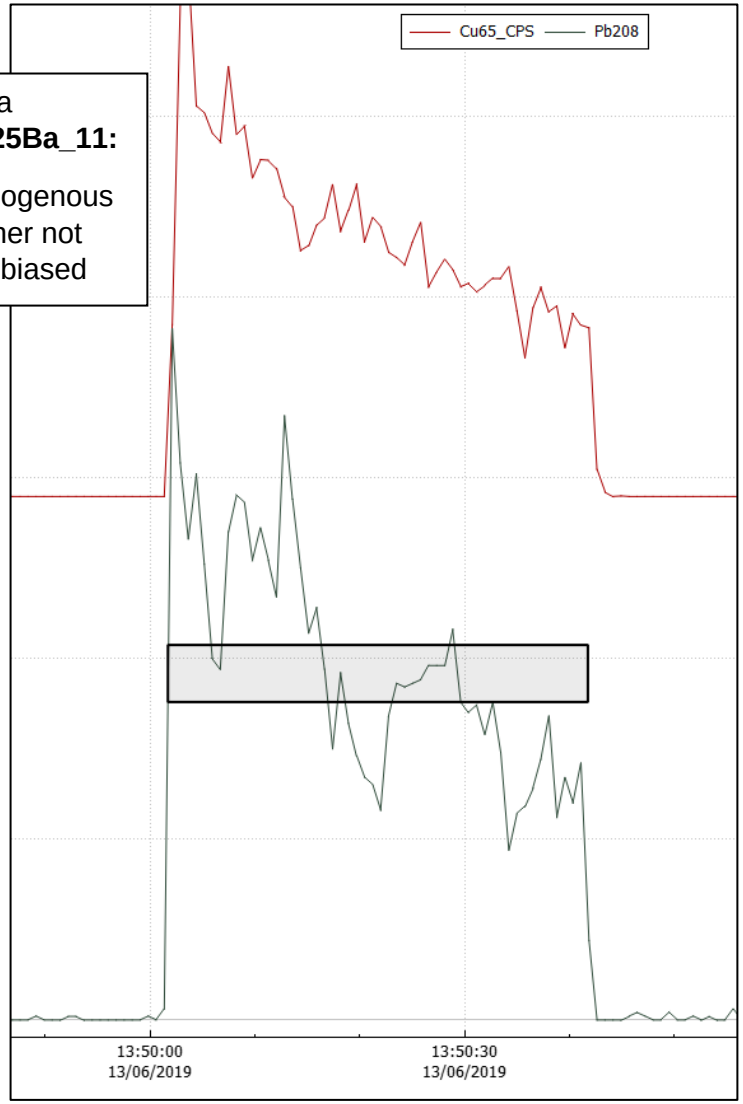


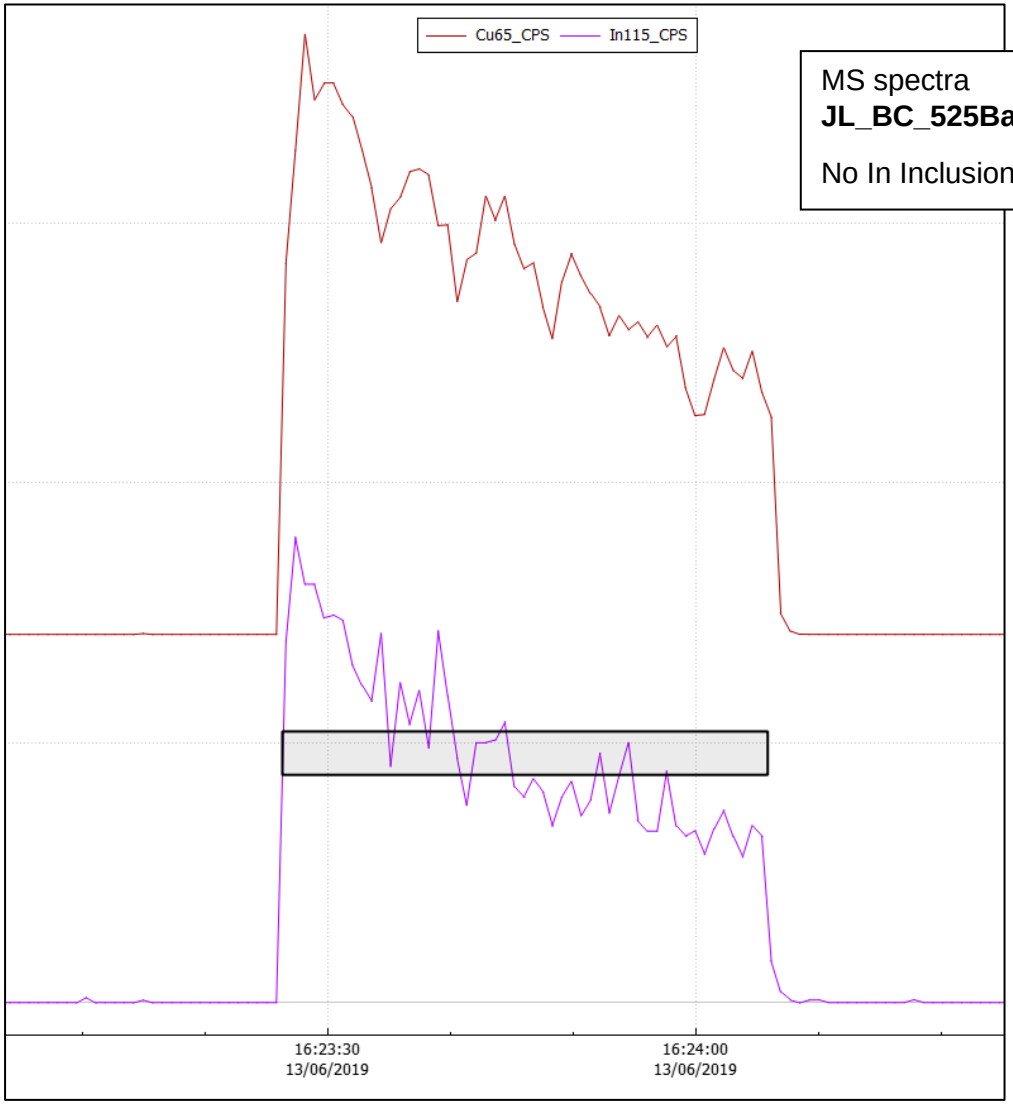
MS spectra
JL_BC_525Ba_10:

Fairly homogenous signal, rather not inclusions biased

MS spectra
JL_BC_525Ba_11:

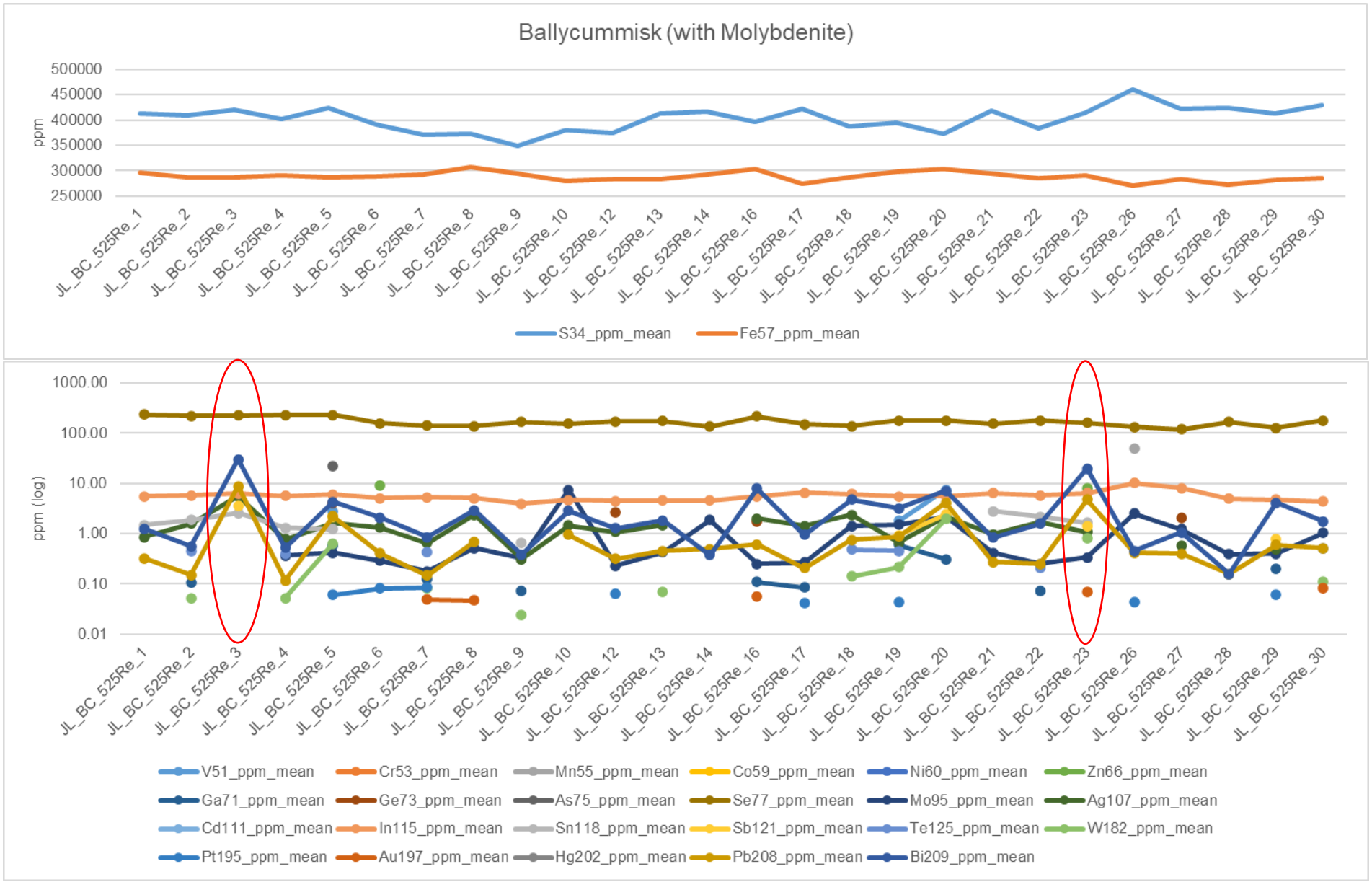
Fairly homogenous signal, rather not inclusions biased

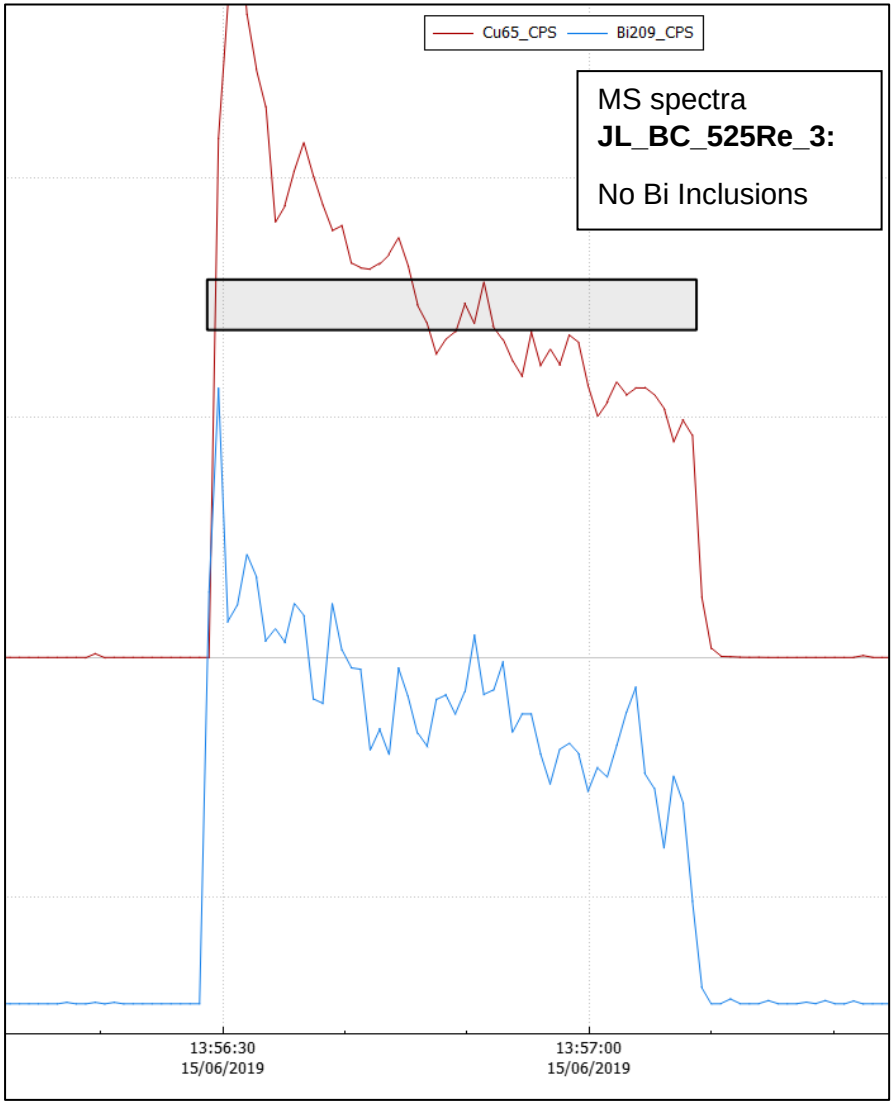


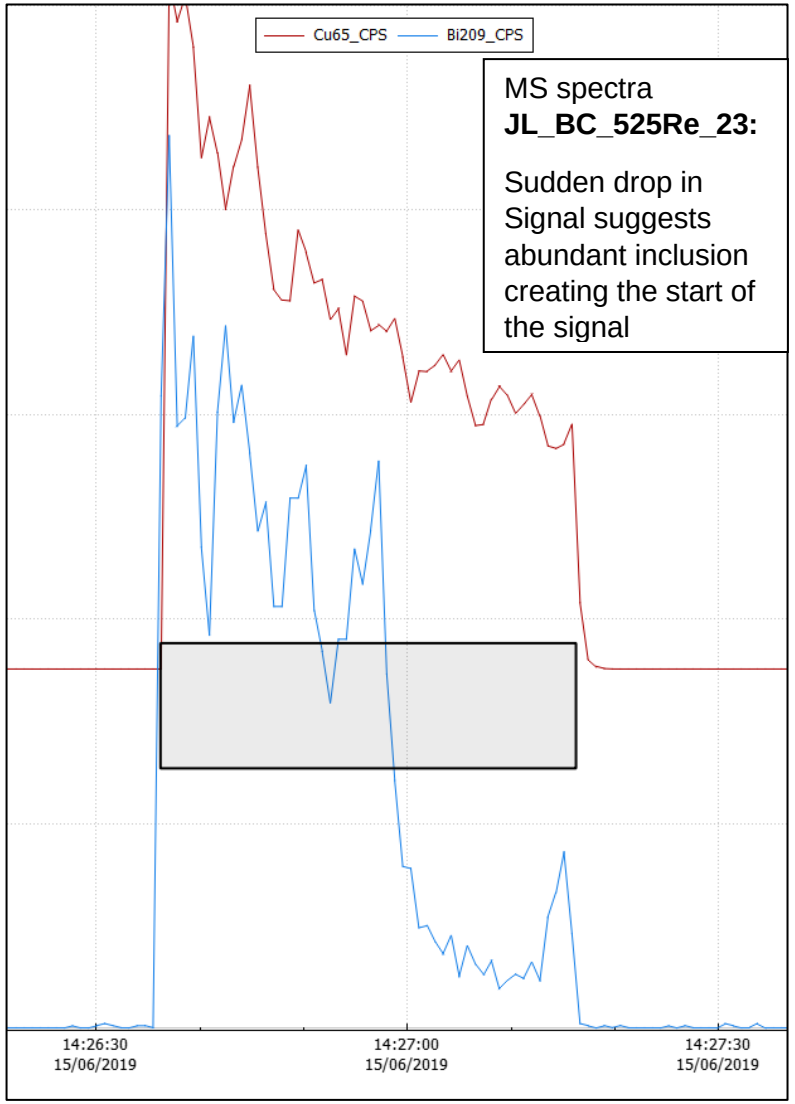


MS spectra
JL_BC_525Ba_37:

No In Inclusions


Ballycummisk (with Molybdenite)
ppm
500000
450000
400000
350000
300000
250000
JL_BC_525Re_1
JL_BC_525Re_2
JL_BC_525Re_3
JL_BC_525Re_4
JL_BC_525Re_5
JL_BC_525Re_6
JL_BC_525Re_7
JL_BC_525Re_8
JL_BC_525Re_9
JL_BC_525Re_10
JL_BC_525Re_12
JL_BC_525Re_13
JL_BC_525Re_14
JL_BC_525Re_16
JL_BC_525Re_17
JL_BC_525Re_18
JL_BC_525Re_19
JL_BC_525Re_20
JL_BC_525Re_21
JL_BC_525Re_22
JL_BC_525Re_23
JL_BC_525Re_26
JL_BC_525Re_27
JL_BC_525Re_28
JL_BC_525Re_29
JL_BC_525Re_30
S34_ppm_mean
Fe57_ppm_mean
ppm (log)
1000.00
100.00
10.00
1.00
0.10
0.01
V51_ppm_mean
Cr53_ppm_mean
Mn55_ppm_mean
Co59_ppm_mean
Ni60_ppm_mean
Zn66_ppm_mean
Ga71_ppm_mean
Ge73_ppm_mean
As75_ppm_mean
Se77_ppm_mean
Mo95_ppm_mean
Ag107_ppm_mean
Cd111_ppm_mean
In115_ppm_mean
Sn118_ppm_mean
Sb121_ppm_mean
Te125_ppm_mean
W182_ppm_mean
Pt195_ppm_mean
Au197_ppm_mean
Hg202_ppm_mean
Pb208_ppm_mean
Bi209_ppm_mean


Cu65_CPS
Bi209_CPS
MS spectra
JL_BC_525Re_3:
No Bi Inclusions
13:56:30
15/06/2019
13:57:00
15/06/2019


Cu65_CPS
Bi209_CPS
MS spectra
JL_BC_525Re_23:
Sudden drop in Signal suggests abundant inclusion creating the start of the signal
14:26:30
15/06/2019
14:27:00
15/06/2019
14:27:30
15/06/2019

Appendix I.4 Results

Please see attached Excel file:

Appendix_I_4_LA-ICP-MS_West_Cork_Thesis_JLang

Legend:

	Elements not measured in this analysis
	micro-Inclusion

Appendix I.5 Chapter References

iolite 4 Documentation, Release 4.4.0, The iolite Team, Jul 20, 2021. Available online: https://iolite.xyz/index.php (accessed on 30 October 2021).

Paton, C., Hellstrom, J., Paul, B., Woodhead, J., Hergt, J. Iolite: Freeware for the visualisation and processing of mass spectrometric data. J. Anal. Atom. Spectrom. 2011, 26, 2508–2518.

Pettke, T., Oberli, F., Audetat, A., Guillong, M., Simon, A. C., Hanley, J. J., and Klemm, L. M. 2012. Recent developments in element concentration and isotope ratio analysis of individual fluid inclusions by laser ablation single and multiple collector ICP-MS. Ore Geology Reviews 44, pp. 10-38. https://doi.org/10.1016/j.oregeorev.2011.11.001

Additional Software:

- ArcGIS (ESRI)
- Laser: Chromium 2.1 software Teledyne Photon Machines, Inc., Thousand Oaks, CA, USA
- Qtegra (version 2.2, ThermoFisher Scientific, Waltham, MA, USA
- webmineral.com, Chalcopyrite: http://webmineral.com/data/Chalcopyrite.shtml#.YX2FjByxVPY (accessed on 30 October 2021)

Appendix J: Figures as High-Resolution PDF Files

*Note: Due to the format requirements some of the figures (especially Maps) appear too small on a standard A4 page. These selected figures are attached to this thesis as high-resolution PDF files in a separate folder **Appendix J**. All references and modifications are described in the individual figure captions within the main text. The structural maps are marked in **bold**:*

Figure 2.2*	Simplified geological map of the Munster Basin and the South Munster Basin in SW Ireland
Figure 2.3a*	Geological map with research localities and major lithologies of the South Munster Basin
Figure 2.3b*	Simplified profile of the Munster Basin sedimentary formations
Figure 2.3c*	Simplified geological map with the historically mined sediment hosted copper deposits in SW Ireland
Figure 2.4*	Overview of the historical copper mines at Allihies (Beara Peninsula)
Figure 3.1*	Simplified map of the Munster Basin and the South Munster Basin in Southwest Ireland
Figure 3.2*	Overview of the historical copper mines at Allihies (Beara Peninsula, see Fig. 2.4*)
Figure 3.3a*	**The major lodes and mineralized veins of the Mountain Mine Area with pre-deformation structures**

Figure 3.5* 3D model of the major lodes and the underground workings at Mountain Mine

Figure 3.7a-c* Map with syn-Variscan structures affecting the pre-Variscan faults and veins at Allihies

Figure 3.10* False colour microphotographs of mineralized E-W veins (north of Mountain Mine)

Figure 3.12a* Schematic model of the vein development, mineralization and structural evolution of the Munster Basin and South Munster Basin (pre-Variscan)

Figure 3.12b* Schematic model of the vein development, mineralization and structural evolution of the Munster Basin and South Munster Basin (Syn-Variscan)

Figure 4.1* Simplified map of the Munster Basin and the South Munster Basin in Southwest Ireland (see Fig. 3.1)

Figure 4.2a* Geological map with research localities and major lithologies of the South Munster Basin (see Fig. 2.3a)

Figure 4.2b* Simplified profile of the Munster Basin sedimentary formations (see Fig. 2.3b)

Figure 4.3* Geological map of West Cork with E-W faults and their relation to historic copper lodes and mineralized sediments

Figure 4.4a* Structural drone map of Baurearagh

Figure 4.4b* 3D photogrammetry model of Baurearagh

Figure 4.4e* E-W striking quartz veins with reverse syn-compressional movement (Baurearagh)

Figure 4.5a* **Structural drone map of Caha Pass**

Figure 4.5b* E-W striking quartz veins with syn-compressional stylolites (Caha Pass)

Figure 4.6a* **Structural drone map of Gortavallig**

Figure 4.6h* Microphotograph of conglomerate clasts with elongated fossilised (chalcopyrite) plant cells (Killeen North)

Figure 4.7a* **Structural drone map of Dhurode**

Figure 4.7b* Aerial drone image with structures of Dhurode

Figure 4.7c* Microstructures within mineralized quartz vein from Dhurode

Figure 4.8a* **Structural drone map of Crookhaven**

Figure 4.8e* Microphotograph of a quartz vein with bornite showing a microfracture (Crookhaven)

Figure 4.9a* **Structural map of Ballycummisk**

Figure 4.9d*+e* Mineralized quartz vein with molybdenite and stylolites (Ballycummisk)

Figure 4.9f* Folded quartz vein within slate with cleavage-parallel quartz-barite-hematite-chalcopyrite mineralization (Ballycummisk)

Figure 4.12a* Block model of the South Munster Basin in West Cork: Pre-Variscan

Figure 4.12b* Block model of the South Munster Basin in West Cork: Syn-Variscan

Figure 5.1* Map of West Cork with the major research areas with the E-W extensional faults and the historically documented Cu occurrences

Figure 5.3* Geological map of Ireland with a selection of the geochronological dated Zn-Pb deposits and the Re-Os dating results of this study for the Cu mineralization in SW Ireland

Figure G.1* Simplified geological map of the Munster Basin and the South Munster Basin in SW Ireland showing additional field locations

Figure G.2a* Structural map of Behaghane (Caherdaniel, Kerry)

Figure G.3a* Structural map of the location Healy Pass (Beara Peninsula)

Figure G.4a* Structural drone map of extensional fault with related quartz veining near Pass of Keimaneigh

Figure G.5a* Structural drone map from area located west of Goleen (Mizen Peninsula)

Figure G.6a* Structural map of Dunmanus (Mizen Peninsula)

Figure G.7a* Structural (drone) map of Mount Corin (Dereennalomane, Mizen Peninsula)

Figure G.9a* Structural drone map of the Seven Heads coastal outcrop (South Cork)